

Development of The Next Generation Ceramics for Orthopaedic Application



Submitted for the Degree of Doctor of Philosophy

Zahra Pishgahi Fard

Supervisors: Professor W. Mark Rainforth

Professor Ian M. Reaney

The Department of Engineering Materials

The University of Sheffield

June 2018

به نام او

به مادرم که آغوشی از مهر کشود

و

به پدرم که سیلابی از آسایش ساخت

و

به همسرم که سنگینی کوله بار سفر بردوش کشید

و

به پسریم که روشنی چشمان و گرمای عشق چشاند

ACKNOWLEDGEMENTS

First of all, I must thank the almighty God for his grace without which it would have been all impossible.

I would like to sincerely thank my supervisor, Professor Mark Rainforth, who accepted me as a PhD student and exhausted all possible methods to guide me through learning, researching, and writing my doctoral dissertation. I am truly grateful for his constant support, valuable advice and guidance, endless help and encouragement. I would like also thank Professor Ian Reaney for his support and cooperation.

I must express my gratitude to my beloved family without whose infinite love and support this would not have been possible. To my parents, Mohammad and Batool, you have taught me how to be strong and independent and how to fight for my dreams. To my husband, Farshid, you have gone through lots of struggle and pain, but you have never stopped your love, inspiration, and unconditional emotional and financial support. To my son, Parsa, you have been there for me every step of the way with your smiles and tears, and of course, your football skills. This thesis is dedicated to you.

Abstract

Ceramic bearings have been used for femoral heads or acetabular liners of hip prosthesis due to their low wear rate arising from their high hardness and elastic modulus, as well as their excellent long-term biocompatibility as a result of their high chemical stability and resistance to corrosion. Alumina (Al_2O_3) and zirconia (ZrO_2) are two main ceramics which have been used widely in the hip joint replacements. In order to take benefit of advantages of both hardness of alumina and toughness of zirconia and eliminate or limit the disadvantages of them, ZTA (Zirconia Toughened Alumina) composites have been used widely as the hip joint prostheses in clinical surgery consisting of fine ZrO_2 particles dispersed in a dense, fine-grained Al_2O_3 matrix. However, there is still a need to improve their mechanical properties. One of the main possible improvements can be through the addition of small amounts of additives which are expected to give a measurable change in the characteristics of the composites and make a new generation of materials for orthopaedic applications. Titanium oxide is one of the additives which has been widely used in ceramics mainly as a sintering aid, and is found to improve the fracture toughness and wear resistance of alumina ceramics, as well as enhance the density and augment tetragonal phase stability of zirconia ceramics. Moreover, it has been shown that the mechanical properties of conventional ceramics, such as strength, hardness and wear resistance, could be enhanced by reducing the grain size, particularly to the nanoscale dimension. On the other hand, mechanical and tribological properties such as wear, friction and lubrication are the most important indicators to be considered in design and material selection for bearing surfaces. Although the effect of titania on mechanical and wear properties of alumina has been widely studied, there is not much research on its effect on ZTA composites, particularly in nano-sized ceramics. Thus, the current study focused on developing a new ceramic composite for hip joint replacements having higher mechanical properties and better tribological properties by both reducing the grain size and making a titania addition. The samples were prepared by mixing the starting powders, consolidation, sintering, and polishing process. The volume percent of Y-TZP used in this study was kept to 15 vol.% for all the samples, below the percolation limit of 16 vol.%, and the different composite containing no titania (pure ZTA), 0.1 mole.%, 0.5 mole.%, 2 mole.% and 5 mole.% of TiO_2 were produced. The starting powders were mixed using an attrition miller for 3.5 hours in the aqueous environment of zirconia and alumina powders and distilled water and the pH value of the slurry brought to 4.5 by adding drops of dilute nitric acid. The slurry was then freeze-dried for 48 hours and crushed using an agate mortar and pestle and passed through a 180, 90, and 45 μm sieves using sieve shaker. The samples with 20mm diameter and 3gr mass were prepared in a graphite die and processed using spark plasma sintering. A uniaxial pressure of 16 KN was applied during the sintering process from 700°C and 3, 5, 7 and 10 minutes dwell time and 1400°C, 1450°C, 1500°C, and 1550°C temperatures were selected for sintering the samples. Then, the samples were ground and polished and etched thermally in the clean furnace for 20 minutes and at the temperature 100°C below their sintering temperature. After the samples were

prepared, density measurements, XRD analysis, SEM characterisation, and mechanical testing were carried out on the samples. Due to a very difficult and time-consuming preparation process for wear samples, few samples of each series of ZTA, ZTA + 0.1 mole.% TiO₂, and ZTA + 0.5 mole.% TiO₂ showing high density and reasonable mechanical properties were selected for reciprocating wear tests. Thus, ZTA samples with sintering time of 7 minutes and temperature of 1450°C, 1500°C, 1550°C; ZTA+ 0.1 mole.% TiO₂ samples with sintering time of 5 minutes and temperature of 1450°C, 1500°C, 1550°C; and ZTA+ 0.5 mole.%TiO₂ samples with sintering time of 5 minutes and temperature of 1400°C, 1450°C, and 1500°C were prepared. The reciprocation wear test procedures were designed for 24 hours with normal load of 1N, 4N and 8N, and 8 hours with normal load of 16N. The selected reciprocating speed was 600 rpm (10 Hz) and the stroke length was set as 10 mm for all the test procedures. Fresh lubricant of 25 vol.% bovine serum was introduced every 8 hours during the test to avoid degradation. 3D optical microscopy, wear rate calculation, Raman spectroscopy, AFM, LFM and SEM microscopy were then carried out on the worn surfaces. The results showed that all the samples were reasonably dense having relative density more than 97.5% of the theoretical density with greater density at higher sintering temperature. Small amounts of 0.1 and 0.5 mole.% titania addition improved sinterability and densification of the samples; however, the relative density decreased for all sintering temperatures and times for higher content of titania to 2 and 5 mole.%. Similarly, titania addition increased the grain growth with its higher rate for alumina than zirconia. XRD patterns and SEM studies showed the formation of ZrTiO₄ occurred adjacent to monoclinic zirconia grains. No traces of aluminium titanate peaks or any particular anisotropic alumina grains or in-situ fibres in SEM images were identified in this research. The opposite effect of the amount of titania on hardness and toughness was found in which titania addition enhanced toughness significantly although it affected hardness adversely, mainly due to its improved crack deflection mechanism. The specific wear rate found to be in mild region with the specific wear rate less than 10⁻⁶ mm³/Nm, with higher amount at higher loads and coarser microstructure. Samples containing 0.5 mole.% titania showed tangibly higher wear resistance and less damaged surface, particularly at high loads. The presence of a tribolayer with a thickness around 100 nm was confirmed in this study. Wear mechanisms for tests at low loads and materials with fine microstructures were found to be polishing, differential wear, grain pull-out, 3rd body abrasion and grooves, while large microcracking and removing craters of fractured grains were found to be dominant wear mechanisms in high loads and coarser microstructures. Thus, the significant outcome of this research was that reducing the grain size using SPS technique could significantly improve mechanical and wear properties of ZTA composites and titania addition was found to be beneficially effective in improving these characteristics.

Contents

1. Introduction	1
2. Literature Review	6
2.1. Hip Joint Prostheses	6
2.1.1. Ceramic Bearings	8
2.1.1.1. Aluminum oxide (alumina) ceramics	9
2.1.1.2. Zirconium oxide (zirconia) ceramics	11
Hydrothermal degradation of zirconia	12
2.1.1.3. Composites of alumina and zirconia	14
Zirconia toughened alumina (ZTA)	15
Toughening mechanisms of ZTA	16
Hydrothermal degradation of ZTA	19
2.2. Nano-composites and nanostructures	21
2.2.1. Spark Plasma Sintering for nanostructures	23
2.3. Additives in ZTA	25
2.3.1. Al ₂ O ₃ /ZrO ₂ /TiO ₂ composites	27
2.3.1.1. Addition of titania to alumina	28
Aluminium titanate or Tialite (Al ₂ TiO ₅)	29
Densification	31
Microstructure	32
Mechanical properties	36
2.3.1.2. Addition of titania to zirconia	37
Zirconium titanate (ZrTiO ₄)	39
Densification	41
Microstructure	42

Mechanical properties	44
2.3.1.3. Addition of TiO ₂ in alumina, zirconia composites	45
Densification	48
Microstructure	49
Mechanical and wear properties	52
2.4. Tribological properties in hip joint replacements	58
2.4.1. Friction	60
2.4.2. Wear of ceramics	61
2.4.2.1. Wear transition	62
2.4.2.2. Surface Analysis	68
Wear Debris	68
Tribochemical layer	69
2.4.2.3. Additives	71
2.4.3. Wear of Alumina	72
2.4.3.1. Additives	76
2.4.4. Wear of zirconia	76
2.4.4.1. Phase Transformation	80
2.4.4.2. Additives	80
2.4.5. Wear of ZTA	81
2.4.5.1. Microstructure	82
2.4.5.2. Phase Transformation	83
2.4.5.3. Wear Transition	84
2.4.5.4. Surface analysis	86
2.4.5.5. Tribochemical	88
Water lubrication	88
Bovine serum	92

2.4.5.6. Additives	94
3. Experimental procedures	95
3.1. Sample preparation	95
3.1.1. Starting powders	95
3.1.2. Mixing and specimen preparation	96
3.1.3. Densification process	97
3.1.4. Grinding and polishing	97
3.1.5. Thermal etching	98
3.2. Sample Characterization	99
3.2.1. Density measurements	99
3.2.2. Phase analysis	99
3.2.3. Scanning Electron Microscopy (SEM)	99
3.2.4. Mechanical testing	99
3.3. Reciprocating wear testing	101
3.4. Wear scar characterization	103
3.4.1. 3D optical Microscopy	103
3.4.2. Wear rate calculation	103
3.4.3. Raman Spectroscopy	104
3.4.4. Atomic Force Microscopy (AFM) and Lateral Force Microscopy (LFM)	104
4. Results	106
4.1. Sample Characterization	106
4.1.1. Density Measurements	106
4.1.2. Phase analysis	110
4.1.3. Microstructure Characterization	115
4.1.4. Hardness and toughness characterization	128
4.2. Wear Characterization	140

4.2.1. Friction	140
4.2.2. Wear Behaviour	144
4.2.2.1. Specific wear rate	144
4.2.2.2. Worn surface analysis	148
3D surface morphology	148
Topography of wear scars	167
4.2.2.3. Worn phase analysis	209
4.2.2.4. Worn microstructure characterization	217
5. Discussion	245
5.1. Sample Characterization	245
5.1.1. Relative density	245
5.1.2. Phase analysis	249
5.1.3. Microstructure characterization	251
5.1.4. Hardness and toughness characterization	255
5.2. Wear characterization	262
5.2.1. Friction	262
5.2.2. Wear rate	264
5.2.3. Worn Surface analysis	267
5.2.4. Worn phase analysis	270
5.2.5. Worn microstructure characterisation	271
6. Conclusion	278
6.1. Sample Characterization	278
6.2. Wear characterization	283
7. Future Work	287
8. References	288

1. INTRODUCTION

Total hip and knee replacement is a very common surgery nowadays and is increasingly demanded by younger patients who still want to remain active after the surgical procedure (Rahaman, et al., 2007; Pramanik, et al., 2005; Beaulé, et al., 2006; Hamadouche, et al., 2002). In the United States and Europe, approximately 500,000 total hip and knee joint prostheses are being replaced annually which is expected to increase rapidly as the result of increasing population ages and higher life expectations (Rahaman, et al., 2007; Murphy, et al., 2006; Siopack & Jergesen, 1995). Improvements in design and materials of the total arthroplasties as well as advances in surgical techniques and instrumentations has made the hip replacement surgeries one of the most successful and long-lasting treatments in medicine with the common life time of 10 to 15 years (Antonio, et al., 2002).

However, in approximately 25% of the total hip and knee joint replacements there is a need to repeat the surgery, which are mainly because of loosening of implant due to wear debris, unstable implant, and adverse reaction of prosthesis with the host tissue (Rahaman, et al., 2007; Antonio, et al., 2002). This relatively high rate of repeated surgery, along with the pains and hardship accompanied by the failure of the implants, has made the scientists searching for new methods and materials to increase the useful life of THAs. Up to now, several kinds of materials (polymer, metal and ceramics) have been used. Systematic follow up studies and assessments have been done to evaluate the durability of the materials and the results were successful (Chevalier, 2006; Blunn, 2013; Lizaur-Utrilla, et al., 2012). However, there is still a continuous challenge to develop new bearings which has the highest wear resistance, highest toughness, and highest strength.

The ceramic bearings have been used for femoral heads or acetabular liners of hip prosthesis as monolithic ceramic oxides, such as Al_2O_3 and ZrO_2 , or nanoxide ceramics, such as Si_3N_4 , or as the ceramic composites, such as ZrO_2 -toughened Al_2O_3 (ZTA) (Rahaman, et al., 2007). Very low wear rate due to their high hardness and elastic modulus, as well as excellent long-term biocompatibility, as a result of their high chemical stability and resistance to corrosion, make the ceramics a desirable material for bearing surfaces (Rahaman, et al., 2007; Chevalier & Gremillard, 2009; Bierbaum, et al., 2002). Furthermore, the improved lubrication of ceramics

with a low coefficient of friction has the prominent effect on resulted excellent wear resistance and decreased bioactive particles compared to polyethylene or metal (Bierbaum, et al., 2002).

Alumina (Al_2O_3) and zirconia (ZrO_2) are two main ceramics which have been used widely in the hip joint replacements, while alumina has more extensive history of use (Rahaman, et al., 2007). The crystalline structures of these ceramics have a combination of strong ionic and covalent bonds (Rahaman, et al., 2007). This strong bond is the origin of favorable characteristics of ceramics, such as high compressive strength, elastic modulus, hardness and chemical biocompatibility. Their limitation for orthopaedic applications is also due to their characteristic property of brittleness, which can lead to catastrophic failure in vivo (Rahaman, et al., 2007).

In order to take benefit of advantages of both alumina and zirconia characteristics as well as eliminate or limit the disadvantages of them, several zirconia–alumina composites have been developed. In this way, two kind of ceramics can be fabricated; a phase-stabilized zirconia matrix reinforced with alumina particles (Alumina Toughened Zirconia or ATZ), or alumina matrix reinforced with zirconia particles (Zirconia Toughened Alumina or ZTA). In both of these ceramics, higher toughness values than the monolithic ceramics have been obtained, though it is found to be higher in ZTA composites (Chevalier & Gremillard, 2009). ZTA is a two-phase composite, consisting of fine ZrO_2 particles dispersed in a dense, fine-grained Al_2O_3 matrix (Rahaman, et al., 2007), in which the zirconia particles are often stabilized with small amounts of Y_2O_3 and make up 20 vol.% of the composite (Rahaman, et al., 2007; Devillea, et al., 2003). Compared to the monolithic α -alumina ceramics, ZTA combines the high hardness of the alumina matrix associated with enhanced strength and fracture toughness resulted from zirconia particles (Rahaman, et al., 2007). The recent studies in both clinical and experimental tests show the improved mechanical properties of ZTA, such as wear resistance, fracture toughness, slow crack growth propagation threshold and hydrothermal degradation, which makes ZTA a promising alternatives for hip joint prosthesis (Rahaman, et al., 2007; Chevalier & Gremillard, 2009; Benzaid, et al., 2008; Devillea, et al., 2003).

Although ZTA composites are used widely as the hip joint prostheses in clinical surgery, and they are now meeting the critical requirements for this application, there is still need for improving the mechanical properties of them. One of the main possible improvements can be through the addition of small amount of additives which are expected to give a measurable

change in the characteristics of the composites and make a new generation of materials for orthopaedic applications. Metal oxides are one of the most common additives which have been widely used in alumina, zirconia and alumina-zirconia composites to improve flexural strength, fracture toughness and tribological properties of the component. ZTA composites reinforced by some metal oxide additions has also been fabricated commercially and implanted in hip joint replacement surgeries.

Titanium oxide is one of the additives which has been widely used in ceramics mainly as a sintering aid. It has recently been reported to give promising bioactivity by forming chemical bonding with bones, which makes it suitable for implant applications (Li, et al., 1996; Fartash, et al., 1995). In alumina ceramics, it has been found to improve the fracture toughness and wear resistance of the material as well as improving flaw tolerance and thermal shock resistance, which can makes it a good candidate for tribological application such as hip joint replacement materials (Wang, et al., 2009; Yang, et al., 2009; Borrell, et al., 2013). In zirconia based ceramics, small additions of titania can improve density as well as augmenting tetragonal phase stability at room temperature (Affatato, et al., 2001). Although the effect of titania on alumina has been widely studied, there is not much research on its effect on ZTA composites.

Moreover, it has been shown that the mechanical properties of conventional ceramics, such as strength, hardness and wear resistance, could be enhanced by reducing the grain size, particularly to the nanoscale dimension (Rahaman, et al., 2007; Chevalier & Gremillard, 2009; Nawa, et al., 1998; Yang, et al., 2009). It also has been reported that the density of the nano-composites is much higher than the micron sized equivalent material (Nawa, et al., 1998; Yang, et al., 2009). In the case of nano ZTA composites which is the subject of this report, there is additional advantage; the nano size of zirconia particles, being well below the critical size, will avoid any significant transformation from tetragonal to monoclinic phase through increasing critical stress needed for t-to-m transformation and thus, increasing the strength of the alumina-zirconia nano-composites (Rahaman, et al., 2007; Nawa, et al., 1998). The ideal sintering conditions for having the nano-composite ceramics is sintering at low temperature with minimum dwell time and rapid heating and cooling rate to inhibit grain growth (Duan, et al., 2004; Yang, et al., 2008). Based on this, one of the recent processes has been used successfully to produce nanostructures is Current Activated Pressure Assisted Densification (CAPAD) also called Spark Plasma Sintering (SPS) (Garay, 2010).

Mechanical and tribological properties such as wear, friction and lubrication are the most important indicators to be considered in design and material selection for bearing surfaces. In general, wear has been defined as the unwanted removal of solid materials from rubbing surfaces, which includes many diverse phenomena such as adhesion, abrasion, corrosion, and others, operating together or separately (Burwell, 1957/58). Wear of ceramics is a complex system function, which is highly dependent on operating factors such as applied load, sliding distance, wear speed and duration; tribological factors such as contact geometry, surface roughness, environment and lubrication; and microstructural factors such as grain size and shape, and crystallographic orientation; and mechanical properties such as hardness and fracture toughness (Fischer, et al., 2000; Hsu & Shen, 2004; Rainforth, 1996).

In lubricated conditions such as real hip joint bearing system, in addition to mechanical based wear mechanisms such as microfracture or plastic deformation, tribochemical mechanisms such as chemical dissolution of the surface and the properties of the amorphous film, as well as its growth or detachment on the surface, indicate wear properties (Rainforth, 1996; Rainforth, 2004). The natural lubricant for cartilage bearings are synovial fluids with medium to high viscosity and non-Newtonian shear thinning characteristics. The most similar lubricant to the natural synovial fluid is new-born calf bovine serum which is widely used for joint simulation tests (Ma, 2010; Ma & Rainforth, 2012).

Based on this background, the current research has been carried out to study processing of ZTA ceramics with titania addition and its tribological characterization in bovine serum lubricated environment with the following objectives:

1. To produce new ZTA composite with higher mechanical properties and better tribological performance than the current materials through reducing the scale of the microstructure. This follows the trend in the history of developing alumina ceramics from 1st to 3rd generation by reducing grain size. This would be achieved using SPS, which is known to produce very fine microstructure and high density at the same time, as well as offering a very short sintering cycle, which can save energy and reduce production cost.
2. To explore the addition of titania to improve strength, toughness and wear resistance, and to understand the precise role of the titania in this respect.

In this study, samples of zirconia and alumina containing 15 vol.% of ZrO₂ (less than the percolation threshold) with titania addition of 0.1, 0.5, 2 and 5 mole.% were prepared by using

SPS technique at 1400°C, 1450°C, 1500°C, 1550°C and for 3, 5, 7, 10 minutes dwell time. The relative density, average grain sizes, hardness, and fracture toughness of the samples were measured and compared with each other. Nine samples from ZTA, ZTA+0.1 mole.%TiO₂, and ZTA+0.5 mole.%TiO₂ with similar grain sizes were selected and wear samples of them were produced. They were tested in bovine lubricated environment for 24 hours with normal load of 4N, 8N and 8 hours with normal load of 16N by using UMT tribometer with reciprocating speed of 600 rpm (10 Hz). The wear rate of each test were calculated and morphology and topography of wear scars were analyzed using 3D Contour GT optical microscope and Atomic Force Microscopy (AFM) technique. Then, microstructure characterization using scanning electron microscopy (SEM) technique were done and its effect on wear rates and involved wear mechanisms were studied.

2. LITERATURE REVIEW

2.1. Hip Joint Prostheses

The hip is one of the largest joints in the body and is a true ball-and-socket joint (Figure 2.1). The ball, called the femoral head, fits and rotates into the socket or the cup-shaped bone, called the acetabulum. This complex design provides the great stability and mobility needed for a wide range of daily activities such as walking, squatting, and stair climbing (Rahaman, et al., 2007).

In order to make a joint similar to the real hip joint with the same level of mobility, the design and materials selection are of tantamount importance. In fact, the materials used for articulating surface in the artificial hip total hip joints should yield the main critical characteristics including:

1. High mechanical reliability including high strength, high elastic modulus, high fracture toughness, and high fatigue resistance.
2. High corrosion resistance for in-vivo bio-inertness and biocompatibility.
3. High hardness, high long-term wear resistance and low friction.
4. Good wetting (low contact angle) between the bearing surface and the synovial fluids in order to make high lubrication in the body (Rahaman, et al., 2007).

It should be noted that loads of the body vary from three times to eight times of the body weight for normal walking to jogging and stumbling respectively. In addition, these properties should stay without any dramatic change in vivo for more than 20 years while tolerating two million or more motion cycles of loading each year.

Materials that have been used or been under research for bearing couples for hip joint replacements cover a wide range of classifications, which enables the orthopaedic surgeons to have many different alternatives. Each of this different range of bearings has a history of emergence and withdrawal. They were widely used for years and assessed through follow up studies and these evaluations have often led to the joint withdrawal (Chevalier, 2006; Blunn, 2013). The main classes of bearings which have

been used in the history of total hip replacement surgery are Metal-on-Metal (MOM), Metal-on-Polyethylene (MOP), Ceramic-on-Metal (COM), Ceramic-on-Polyethylene (COP) and Ceramic-on-Ceramic (COC) (Figure 2.1.c and Table 2.1). As the current study focused on the processing and characterization of ceramic bearings, this type of hip joint replacements will be discussed in the next chapters.

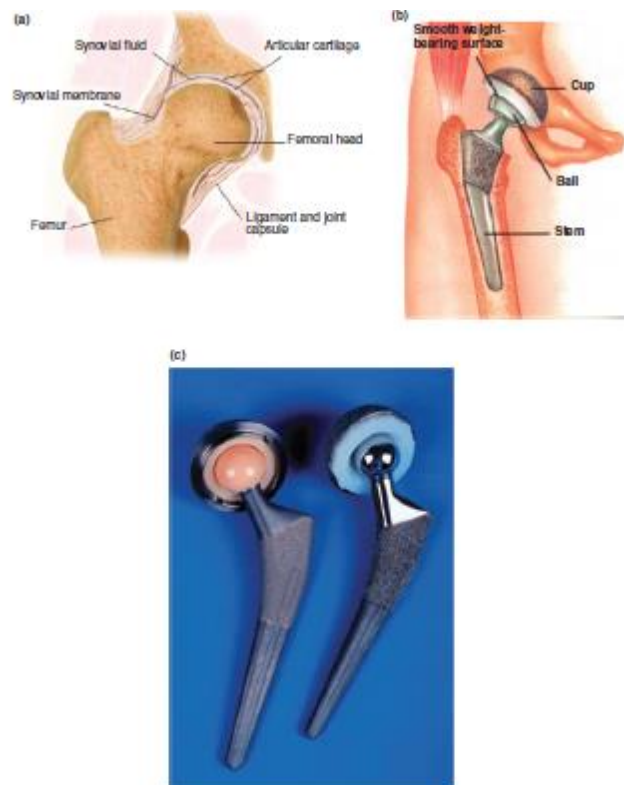


Figure 2.1. Schematic of human hip joint (a). Schematic of a prosthetic device in THA (b). Prosthetic hip implants with ceramic bearing couple (left), and metal-on-UHMWPE bearing couple (right) (c) (Rahaman, et al., 2007).

Table 2.1. Design parameters for artificial metal-on-metal (MOM) and ceramic-on-ceramic (COC) hip implants (Jin, et al., 2006).

Parameters	MOM hip implants	COC hip implants
Femoral head diameter (mm)	28	28
Diametral clearance (mm)	0.06	0.08
Elastic modulus (GPa)	210	380
Poisson's ratio	0.3 (Co-Cr)	0.3 (alumina)
Load (kN)	2.5	2.5
Angular velocity (rad/s)	1.5	1.5
Viscosity (Pas)	0.0025	0.0025
Composite R_a (μm)	0.014	0.07

2.1.1. Ceramic Bearings

Ceramic bearings have been used for femoral heads or acetabular liners of hip prosthesis for many years. Ceramics used have been monolithic oxides, such as Al_2O_3 and ZrO_2 , or nitrides such as Si_3N_4 , or as the ceramic composites, such as ZrO_2 -toughened Al_2O_3 (ZTA) (Rahaman, et al., 2007). Very low wear rates have been attained attributed to their high hardness. In addition, they exhibit excellent long-term biocompatibility, as a result of their high chemical stability and resistance to corrosion, make the ceramics a desirable material for bearing surfaces (Rahaman, et al., 2007; Chevalier & Gremillard, 2009; Bierbaum, et al., 2002).

Furthermore, the improved lubrication with a low coefficient of friction also has also resulted in excellent wear resistance and decreased bioactive particles compared to polyethylene or metal (Bierbaum, et al., 2002). Studies have shown the dramatic reduction of wear rates for the ceramics even when they have been used in combination with metals as Ceramic-on-Metal (CoM) couples (Tipper, et al., 2005). Table 2.2 shows the comparison of wear rated between different kinds of bearing surfaces (Chevalier & Gremillard, 2009).

Table 2.2. Typical values of friction values and wear volume in metal, polymer, and ceramic bearings (Chevalier & Gremillard, 2009; Jin, et al., 2006).

Materials for Cup-on-Head	Friction Coefficient	Wear Volume (mm^3/year)	Specific Wear Rate (mm^3/Nm)
UHMWPE-on-Metal	0.06-0.08	56	$\sim 10^{-7}$
MOM	0.22-0.27	0.9	$\sim 10^{-7}$
COC	0.002-0.07	0.04	$\sim 10^{-8}$

Alumina (Al_2O_3) and zirconia (ZrO_2) are two main ceramics, which have been used widely in the hip joint replacements, while alumina has more extensive history of use. The crystalline structures of these ceramics have a combination of strong ionic and covalent bonds. This strong bond is the origin of favorable characteristics of ceramics, such as high compressive strength, elastic modulus, hardness, and chemical biocompatibility. Their limitation for orthopaedic applications is also due to their characteristic property of brittleness, which can lead to catastrophic failure in vivo (Rahaman, et al., 2007).

2.1.1.1. Aluminum oxide (alumina) ceramics

Aluminum oxide is commonly called alumina (alpha alumina), or corundum, which is widely used in the industry and for biomedical applications. The crystal structure of α -alumina includes O^{2-} anions forming a hexagonal close-packed structure (hcp) with Al^{3+} cations occupying two thirds of the octahedral interstices (Figure 2.2) (Capello, et al., 2008). Therefore, each aluminum ion is surrounded by six oxygen ions which each three bonds have the length of 0.1969nm and 0.2278nm (Capello, et al., 2008). As stated before, the stability of an alumina is very high as a result of its strong ionic and covalent bond between aluminum and oxygen ions.

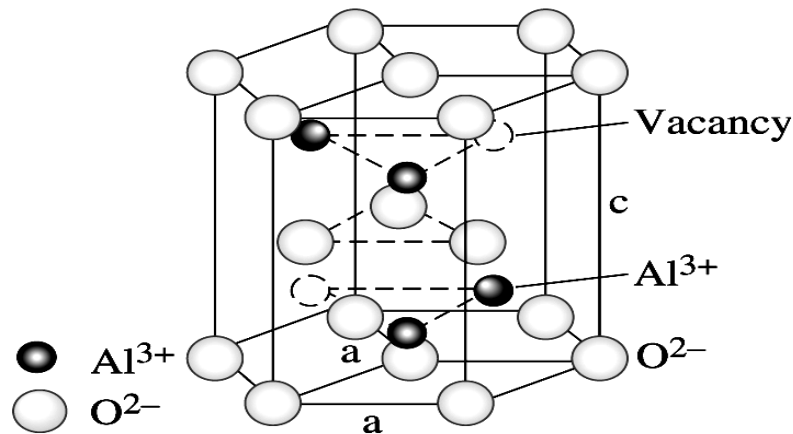


Figure 2.2. Unit cell of α -alumina (Capello, et al., 2008)

The processing of alumina for orthopaedic applications has been improved during the past 30 years. In 1970, the first generation of alumina joint replacement, made of pure Al_2O_3 with the purity of 99.5%, was developed in France to replace the traditional metal formal heads (Bar, 2004). At that time, the ceramics could not be processed to full density because of the long sintering times generating large crystal sizes. The coarse structure as well as their low density resulted in reduced strength and an increased fracture incidence and crack propagation (Rahaman, et al., 2007; Dowson, et al., 2004).

The second generation of alumina came out with the further improvements in material quality and processing techniques through adding a small amount of MgO as the sintering aid (Rahaman, et al., 2007). It was found that adding materials such as CaO or MgO could limit grain size during the long sintering process and help to achieve near theoretical density (Rahaman, et al., 2007; Dowson, et al., 2004). The 2nd generation of

alumina ceramics, which were developed from 1988 to 1994, showed an exceptionally low coefficient of friction making them desirable for THA prosthesis (Rahaman, et al., 2007; Dowson, et al., 2004).

Finally, the third generation of alumina, from 1994 to the present, emerged after the improvements evolved with isostatic pressing, laser etching and proof testing (Dowson, et al., 2004). HIPed (Hot Isostatically Pressed) alumina components represented high density with a small grain size, high chemical purity and a stable crystalline structure (Rahaman, et al., 2007) as well as very low wear rates, up to 10 times less than non-HIPed alumina components (Maccauro, et al., 2011).

The mechanical characteristics of the three generations of alumina can be seen in Table 2.3. It can be seen in the table that for achieving higher mechanical strength of alumina components, the density should be maximized, and the grain size must be kept as small as possible (Nevelos, et al., 2001).

Table 2.3. Improvement in Manufacturing and Properties of Medical Grade Al₂O₃ over Time (Rahaman, et al., 2007).

Property	Alumina: 1970s	Alumina: 1980s	Alumina: 1990s
Bending strength (MPa)	400	500	580
Compressive strength (MPa)	>4000	>4000	>4000
Fracture toughness (MPa.m ^{1/2})	4	4	4
Vickers hardness (HV)	1800	1900	2000
Wetting angle (deg)	<50	<50	<50
Grain size (µm)	4.5	3.2	1.8
Density (g/cm ³)	3.94	3.96	3.98
Young's modulus (GPa)	380	380	380
Laser making	NO	YES	YES
Hot isostatic pressed	NO	NO	YES
Proof tested	NO	NO	YES
100% inspection	YES	YES	YES
Biocompatible	YES	YES	YES
Hydrothermal stability	YES	YES	YES
Suitable for ceramic-on-ceramic	YES	YES	YES

Wide and successful employment of alumina prosthesis for hip joints is mainly due to their low failure rate in vivo. From 2000 to 2004, the reported failure rate of alumina hip prosthesis was 0.02%, which is still promising comparing with the other common surgical risks of total joint replacements (Rahaman, et al., 2007). The factors which might increase the risk of failure for these bearing surfaces are increased weight or activity of the patients (Nevelos, et al., 2001). The next improvements for achieving less failure rates can be done through superior design of the bearing or introduction of a second phase or additive to enhance the toughness of the component (Rahaman, et al., 2007).

2.1.1.2. Zirconium oxide (zirconia) ceramics

In the 1980s, zirconia-based femoral heads were introduced to use in THAs in response to concerns about alumina hip prosthesis fracture rates. Having higher flexural strength and fracture toughness resulted in reducing the fracture risks making zirconia a promising for hip joint prosthesis at that time (Rahaman, et al., 2007). This high fracture toughness also enables the manufacture to fabricate smaller head sizes and longer neck lengths (Rahaman, et al., 2007; Dowson, et al., 2004).

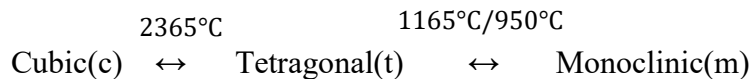
The prominent fracture resistance of zirconia, also called “ceramic steel” by Garvie et al. (1975), makes it perfect for the load bearing applications. The main phenomenon responsible for its remarkably high fracture toughness is the transformation toughening mechanism (Cahn, 2001). This mechanism happens through phase transformation of metastable tetragonal grains to monoclinic phase due to the stress induced at the crack tip (Christel, et al., 1988). The transformation produces a compressive stress at the tip of cracks which hinders the crack propagation and increases the fracture energy of the component (Christel, et al., 1988). The other toughening mechanisms contributed to raising the fracture toughness of zirconia femoral heads are microcracking, crack deflection and crack bridging (Christel, et al., 1988).

Although zirconia ceramics, having two to three times higher flexural strength than alumina and excellent fracture toughness, were expected to change the future of hip joint prosthesis, unpredictable clinical results changed this. The in vivo fracture of

zirconia femoral heads reported in 2001, associated with retrieving of more than 350 femoral heads from the patients, caused FDA to withdraw zirconia ceramics for use in THAs in 2001 (Rahaman, et al., 2007; Chevalier, 2006; Hannink, et al., 2000; Chevalier, et al., 2007). It was believed at the time that the main reason for the in vivo failure was low temperature degradation and ageing occurring in a moist atmosphere (Chevalier, 2006). However, subsequently it was shown that these particular femoral heads had not been processed correctly and had low density. However, low temperature degradation is now known to be a problem with zirconia ceramics for THA.

Hydrothermal degradation of zirconia:

Zirconia has three crystalline forms including cubic (c), tetragonal (t) and monoclinic (m), in which the transformation from one phase to another one is dependent on temperature as depicted below (Rahaman, et al., 2007):



Hence, at 950°C on cooling from the fabrication temperature, typically 1400–1600°C, the transformation from t to m occurs associated with a shear strain of ~16% and a volume expansion of ~5%. This volumetric expansion results in cracking and thus loss of structural integrity and failure of the component (Rahaman, et al., 2007). Therefore, for using zirconia as an engineering material, the tetragonal phase should be retained at room temperature. This is achieved by adding a small amount of dopant oxide such as yttria, magnesia or ceria, making Y-TZP, Mg-TZP, and Ce-TZP respectively (TZP stands for Tetragonal Zirconia Polycrystals) (Rahaman, et al., 2007; FDA, 2001). However, TZPs (e.g. Y-TZP) have the tendency to transform to the more stable monoclinic polymorph under certain conditions such as moist atmosphere at temperatures even far below 150°C (Rahaman, et al., 2007; FDA, 2001). This phenomenon, called hydrothermal degradation or low-temperature aging, limits the application of Y-TZP. This is more related for using hip joint prosthesis in the moist atmosphere of the body as the steam sterilization temperature is ~140°C and human body temperature is ~37°C (Rahaman, et al., 2007). In addition, the frictional heating between the bearing surfaces as well as localized high loads on the bearing surface can

accelerate the low-temperature of hydrothermal degradation for Y-ZTP ceramic bearings in vivo (Rahaman, et al., 2007; FDA, 2001; Nogiwa-Valdez, et al., 2014).

Hydrothermal degradation of zirconia initiates on surfaces exposed to aqueous environments, and at the first step, the single and isolated grains of the surface transform from tetragonal to monoclinic crystalline. Then the grains neighbouring the already transformed grains undergo transformation resulting in the formation of clusters of transformed grains. The formation of transformed clusters is associated with the surface roughening and micro-cracking as shown in Figure 2.3 (Chevalier, 2006; Nogiwa-Valdez, et al., 2014).

The causes for complicated and unexpected aging of zirconia under normal in vivo conditions of the body, and the temperature as low as 37°C, has been widely studied and many theories have been proposed for it. Among them, the most widely accepted mechanism is that OH⁻ diffuses into the lattice and migrates to the oxygen vacancies sites preferably. This results in the depletion of oxygen vacancies which destabilizes the tetragonal phase and provokes the t to m transformation (Nogiwa-Valdez, et al., 2014). The residual stresses arising from hard machining, sandblasting, grinding and other processes can aggravate the degradation of zirconia femoral heads in clinical practices (Nogiwa-Valdez, et al., 2014).

Low-temperature aging has two critical consequences for the use of Y-TZP in hip joint prostheses. Firstly, due to roughening and microcracking associated with aging, and surface upheaval resulted from the volume expansion of t to m transformation, the required high quality surface finish would not be achieved (Nogiwa-Valdez, et al., 2014). This would deteriorate the wear performance and increase the wear rate of the acetabulum and femoral head leading to osteolysis and implant loosening of zirconia hip prosthesis (Nogiwa-Valdez, et al., 2014). Secondly, the pull-out of zirconia grains as a result of micro cracking and aggravated wear would produce structural defects which propagates to the bulk and causes the component fracture (Nogiwa-Valdez, et al., 2014; Nogiwa-Valdez, et al., 2013).

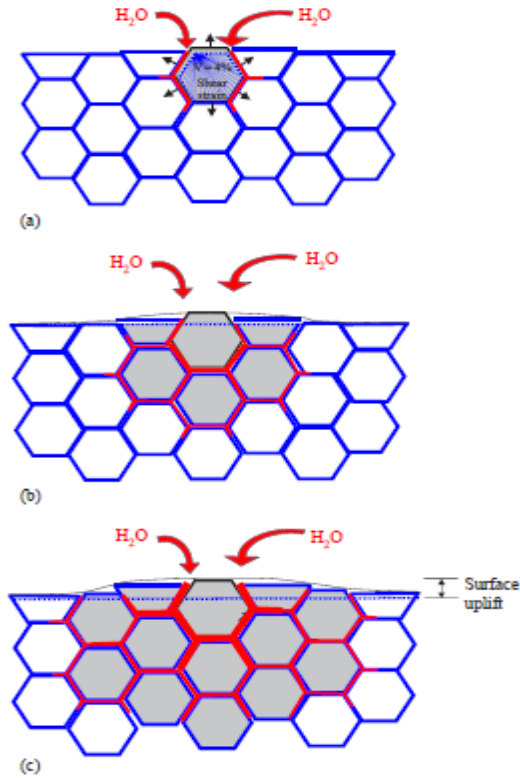


Figure 2.3. Scheme of the ageing process occurring in a cross section, showing the transformation neighbour to neighbour. (a) Nucleation on a particular grain at the surface, leading to microcracking and stresses to the neighbours. (b) Growth of the transformed zone, leading to extensive microcracking and surface roughening. Transformed grains are grey. Red path represents the penetration of water due to microcracking around the transformed grains (Chevalier, 2006)

2.1.1.3. Composites of alumina and zirconia

In order to take advantage of both alumina and zirconia characteristics as well as eliminate or limit the disadvantages of them, several zirconia–alumina composites have been recently developed. In this way, two kinds of ceramic can be fabricated; a phase-stabilized zirconia matrix reinforced with alumina particles (Alumina Toughened Zirconia or ATZ), or alumina matrix reinforced with zirconia particles (Zirconia Toughened Alumina or ZTA). In both of these ceramics, higher toughness values than the monolithic alumina ceramics have been obtained, although it is higher in ZTA composites (Chevalier & Gremillard, 2009). Moreover, the hydrothermal degradation of zirconia would still be a limitation in zirconia matrix, while in alumina matrix this phenomenon has been inhibited or at least restricted (De Azaa, et al., 2002; Benzaid, et al., 2008). This has resulted in extensive use of ZTA as bioceramics, particularly in hip

joint replacements. As this research is based on ZTA composites, we will discuss about its characteristics and developments in the next chapters.

Zirconia toughened alumina (ZTA)

ZTA is a two-phase composite, consisting of fine ZrO_2 particles dispersed in a dense, fine-grained Al_2O_3 matrix (Figure 2.4.d) (Rahaman, et al., 2007), in which the zirconia particles are often stabilized with small amounts of Y_2O_3 and make up 20 vol.% of the composite (Rahaman, et al., 2007; Devillea, et al., 2003). Compared to the monolithic α -alumina ceramics, ZTA combines the high hardness of the alumina matrix associated with enhanced strength and fracture toughness resulted from zirconia particles (Rahaman, et al., 2007). The recent studies in both clinical and experimental tests shows the improved mechanical properties of ZTA, such as wear resistance, fracture toughness, slow crack growth propagation threshold and hydrothermal degradation, which makes ZTA a promising alternatives for hip joint prosthesis (Rahaman, et al., 2007; Chevalier & Gremillard, 2009; Benzaid, et al., 2008; Devillea, et al., 2003).

The microstructures of ZTA are characterized by the presence of two specific and recognizable phases, which do not react with each other to form a solid solution (Thompson & Rawlings, 1990). Figure 2.4 shows SEM images of the typical microstructures of ceramic implant materials. As can be seen in Figure 2.4.d the two phase structure of the ZTA is clear even at low magnification. The zirconia particles can be present in their monoclinic or tetragonal phase structure (or a mixture of both), but as will discuss later, the largest improvements in strength and fracture toughness have been obtained in composites with t-phase zirconia particles (Rahaman, et al., 2007).

Among all the mechanical characteristics and issues related to ZTA ceramics, we will focus on toughening properties and mechanisms of ZTA as well as its hydrothermal degradation, which are more related to our research objectives and procedures.

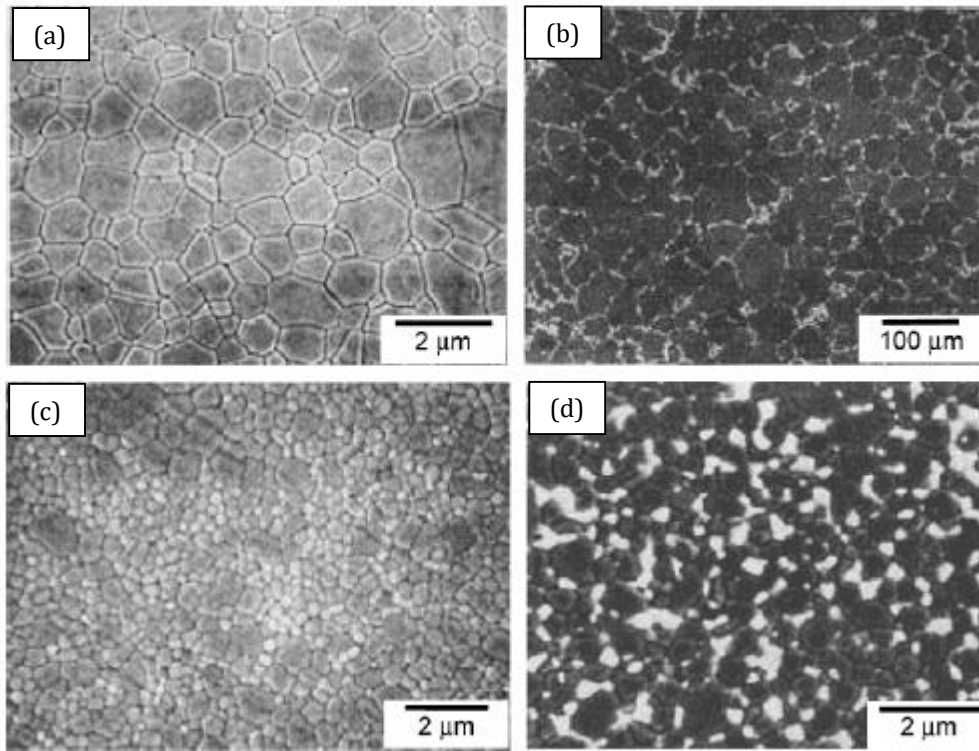


Figure 2.4. SEM images of typical microstructures of ceramic implant materials. (a) Single-phase α - Al_2O_3 with an average grain size of $1.2\ \mu\text{m}$. (b) Magnesia partially stabilized zirconia with a two-phase microstructure consisting of $50\text{--}100\ \mu\text{m}$ cubic ZrO_2 grains containing finely dispersed precipitates of sub-micron tetragonal and monoclinic ZrO_2 . (c) Single-phase yttria-stabilized tetragonal zirconia polycrystals with an average grain size of $0.5\ \mu\text{m}$. (d) ZrO_2 toughened Al_2O_3 (ZTA) with a two-phase microstructure of tetragonal or monoclinic ZrO_2 particles ($\sim 0.4\ \mu\text{m}$) dispersed in a fine-grained α - Al_2O_3 matrix ($\sim 0.6\ \mu\text{m}$) (Rahaman, *et al.*, 2007).

Toughening mechanisms of ZTA

The presence of zirconia fine grains in the alumina matrix as a distinct second phase in ZTA activates some mechanisms, which results in increasing the toughness of the composite. In fact, zirconia grains in the composite behave in their intrinsic manner in undergoing the phase transformation from tetragonal to monoclinic, or retaining the metastable tetragonal structure during cooling of the composites from its fabrication temperatures (Thompson & Rawlings, 1990). The transformation is coupled with the volume expansion and shear strain causing various toughening mechanisms such as stress induced transformation toughening, microcracking toughening, compressive surface stresses and crack deflection (Thompson & Rawlings, 1990).

Stress-induced transformation toughening: Stress-induced transformation toughening happens when the metastable tetragonal zirconia particles transform to their thermodynamically stable monoclinic form as a result of the external tensile stress applied around a crack tip (Thompson & Rawlings, 1990). The volume expansion (~5%) and shear strain (~16%) caused by transformation provide a compressive stress which reduces and eventually stops the propagation of the crack, enforcing extra work for further crack propagation (Devillea, et al., 2003; Thompson & Rawlings, 1990). Figure 2.5 shows schematically the transformation-toughening process in zirconia grains. If the transformation from the tetragonal to monoclinic phase is restricted, cracks will be self-limiting. For next crack propagation, cracks have to overcome the energy required for the t-to-m transformation in addition to the compressive stress resulted from the increased volume of the monoclinic grains (Rahaman, et al., 2007).

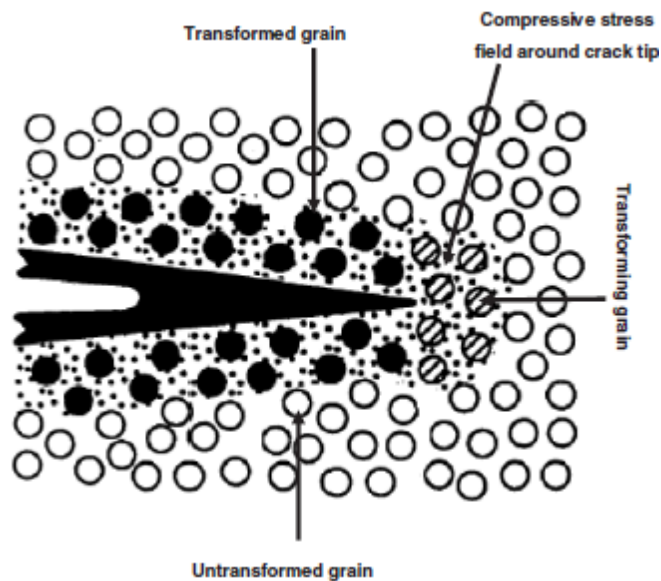


Figure 2.5. Schematic illustration of the transformation-toughening process in yttria-stabilized tetragonal zirconia polycrystals (Rahaman, et al., 2007).

Microcracking toughening: The other toughening mechanism which has been proposed to be involved in improving the toughness of ZTA is attributed to the microcracks. The microcracks in ZTA can be divided as residual microcracks and stress-induced microcracks, both generated from the phase transformation of zirconia particles (Thompson & Rawlings, 1990). The residual microcracks are generated from the volume expansion and shear strain associated with the tetragonal to monoclinic

transformation developing on cooling procedure, while the stress-induced microcracks are produced by the volume expansion and shear strain associated with the subsequent stress-induced transformation during the fracture process (Thompson & Rawlings, 1990; Wang & Stevens, 1989). The residual microcracks toughening, which occurs when the size of zirconia particles is larger than the critical size for tetragonal retention during cooling are considered to be the most commonly occurring toughening mechanism in ZTA (Thompson & Rawlings, 1990). When the ZrO_2 particles transform to the monoclinic phase, the tangential stresses are generated around the transformed monoclinic zirconia particles, which produces microcracks at the boundaries of the second phase and the matrix. The microcracks that extend in the stress field of a propagating crack, or deflect the propagating crack, will absorb fracture energy and increase the toughness of the composite (Thompson & Rawlings, 1990). However, the stress-induced or the residual microcracks can lead to a reduction of fracture strength, as a result of the presence of subcritical flaws or an increased critical flaw size, as well as the linkup or coalescence of the residual microcracks which has been shown to reduce the fracture strength significantly (Chevalier & Gremillard, 2009; Evans & Fu, 1984).

Crack deflection: In addition to the above mechanisms, cracks can also be deflected by localized residual stress fields produced as a result of phase transformation, thermal expansion mismatch or by the fracture of a second phase, which reduces forces on deflected part of the propagating crack (Thompson & Rawlings, 1990). The crack deflection toughening mechanism induced by a second phase in the matrix would be dependent to volume fraction, particle morphology and aspect ratio of the second phase (Chevalier & Gremillard, 2009; Thompson & Rawlings, 1990).

Compressive surface stresses: Compressive stresses at the surface can commonly be achieved by using techniques such as grinding, impact, surface chemical reactions, and low-temperature quenching and are localized at a depth up to $20\mu\text{m}$ from the surface (Thompson & Rawlings, 1990). In addition, in ZTA ceramics, more compressive stresses can be formed as a result of the compressive strain induced by the volume expansion and shear strain produced by the t-to-m transformation, which also have a positive effect on the fracture strength of the composite (Thompson & Rawlings, 1990).

In conclusion, it can be found from the main toughening mechanism discussed above that the stress-induced transformation toughening, compressive surface stresses, and crack deflection can all enhance both toughening and strengthening, while microcracks would result in improved toughness and a decreased strength.

Hydrothermal degradation of ZTA

As discussed before, the hydrothermal degradation known as low temperature aging is the phase transformation of tetragonal zirconia grains to monoclinic structure accelerated in moist atmosphere and accompanied by volume expansion and micro-cracking. Low temperature ageing is a serious limiting factor for using of zirconia in hip replacements. In ZTA, since zirconia has been added as the second phase, the content limit of it beyond which hydrothermal degradation is mostly avoided, is critical.

Aging of zirconia grains occurs by a nucleation and growth mechanism, initiating at the surface of the component. Therefore, in order to avoid degradation of the composite, the zirconia particles should not be connected and form a contiguous network (Rahaman, et al., 2007). This percolation limit of zirconia content in ZTA composites has been found to be 6.7 vol.% for pure ZrO_2 and 16 vol.% for Y-TZP. The difference is due to the higher stability of the tetragonal phase in Y-TZP, below which there is not percolating and not diffusing of water and aging (Rahaman, et al., 2007; Wang & Steven, 1987). This small amount of zirconia also helps to avoid aggregate formation within the composite material, which leads to additional degradation resulted in grain pull-outs and surface degradation (Thompson & Rawlings, 1990; Wang & Steven, 1987). However, it has been proposed that in the ZTA composite, due to the presence of a higher strain energy barrier induced by the alumina grains, which prevent the adjacent zirconia grains to be transformed, only a third of the agglomerates would transform (Wang & Steven, 1987).

Increasing the zirconia content up to about 10 vol.% has been found to result in microcracks toughening; in fact, increasing the number of zirconia particles results in increasing the number of microcracks created during cooling process and leads to increasing toughness of the composite. However, beyond the percolation level, those microcracks tend to join up between the particles and leads to abrupt decrease of

toughness. In addition, as commonly microcracks are present along the grain boundaries of the alumina matrix, they could act as preferential paths for the water diffusion inside the bulk of the composite (Wang & Steven, 1987).

Thus, it is critical for higher performance of ZTA composites that the zirconia content to be kept below the percolation limit and the zirconia grains should be well dispersed in the matrix to reach very fine and very homogeneous microstructures. This kind of microstructure would help the starting monoclinic phase fraction to be much lower, therefore keeping all the potential for transformation toughening (the advantageous aspect of phase transformation) as well as avoiding to form the contiguous network of zirconia grains resulted in aging (the disadvantageous aspect of phase transformation) and failure of the composite.

2.2. Nano-composites and nanostructures

The term ceramic nano-composites refers to a ceramic composites with more than one solid phase, in which at least one of the phases has dimensions in the nanoscale range ($\leq 50\text{--}100\text{ nm}$) (Rahaman, et al., 2007). It has been shown that the mechanical properties of conventional ceramics, such as strength, hardness and wear resistance, could be enhanced by reducing the grain size, particularly to the nanoscale dimension (Rahaman, et al., 2007; Chevalier & Gremillard, 2009; Nawa, et al., 1998; Yang, et al., 2009). It also has been reported that the density of the nano-composites is much higher than the micron sized equivalent material (Nawa, et al., 1998; Yang, et al., 2009).

In the case of nano ZTA composites which is the subject of this thesis, there is additional advantage; the nano size of zirconia particles, being well below the critical size, will avoid any significant transformation from tetragonal to monoclinic phase through increasing critical stress needed for t-to-m transformation and thus increasing the strength of the alumina-zirconia nano-composites (Rahaman, et al., 2007; Nawa, et al., 1998).

Figure 2.6 shows a schematic drawing and two typical microstructures of each type of micro-nano and nano-nano composite of ZTA. For both of these structures, the strategy aims to increase crack propagation threshold, tensile strength and material stability in comparison with the micro-scale ceramics and composites (Chevalier & Gremillard, 2009).

From a toughening point of view, there is an important difference between the micron and nano-composites of alumina and zirconia. In micron size ZTA composites, the increase in crack resistance is mostly due to the phase transformation toughening and micro-cracking mechanism and to a lower extent to crack bridging. However, it has been suggested that in micro-nano-composites, another toughening mechanism plays a significant role, which is the presence of large residual compressive stresses around the zirconia nanoparticles (up to 150MPa compressive stress in the alumina grains with only 1.7 vol.% zirconia transgranular particles) (Chevalier & Gremillard, 2009). Residual stresses are highly dependent to the volume fraction, the size and the location

of the zirconia particles, for example the zirconia particles at grain boundaries would not give rise to the residual stresses (Chevalier & Gremillard, 2009).

On the other hand, although the nano-ceramics have been reported to have higher density and mechanical properties than the micron-sized equivalent, the effect of this structure on wear properties is more complicated. Wang et al. (2009) reported lower average of coefficient of friction and the smoother wear surface for micro-composites in load range of 4N and 6N, which is in contrast with what were reported by Rahaman et al. (2007), Chevalier and Gremillard (2009), De Azaa et al. (2002), and Yang et al. (2009).

Wang et al. (2009) attributed higher wear volume in the case of nano-composites to intergranular fracture and grain pull-out while the wear layer in micro-composites has been shown to be associated with plastic deformation. They found that when chemical properties of the wear debris led to a tendency to adhere, especially in a humid atmosphere, the debris were compacted and formed a tribolayer, which distributed the contact stress and reduce wear (Figure 2.7) (Wang, et al., 2009).

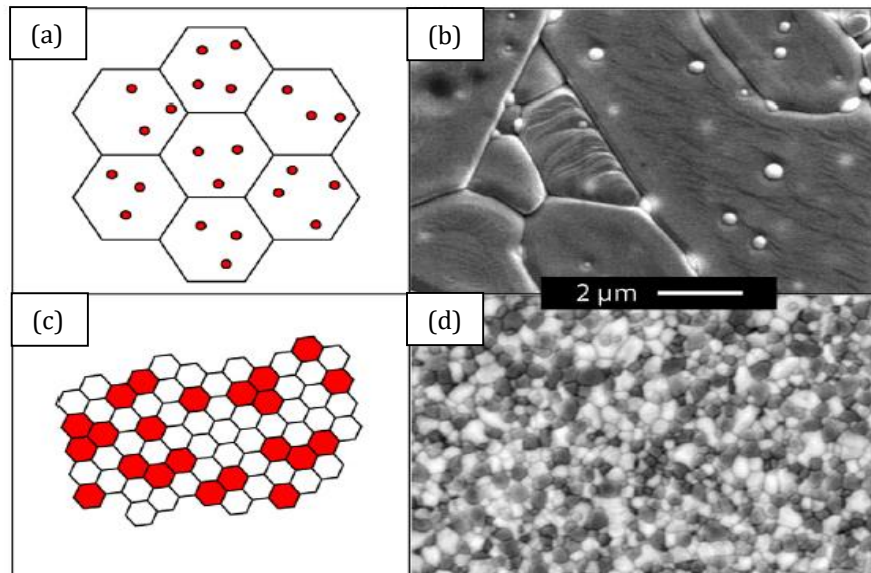


Figure 2.6. Schematic drawing of micro-nano-composite (a), example of such micro-alumina nano-zirconia composite (b), schematic drawing of nano-nano-composite (c), and nano-nano-composite (d) (Chevalier & Gremillard, 2009).

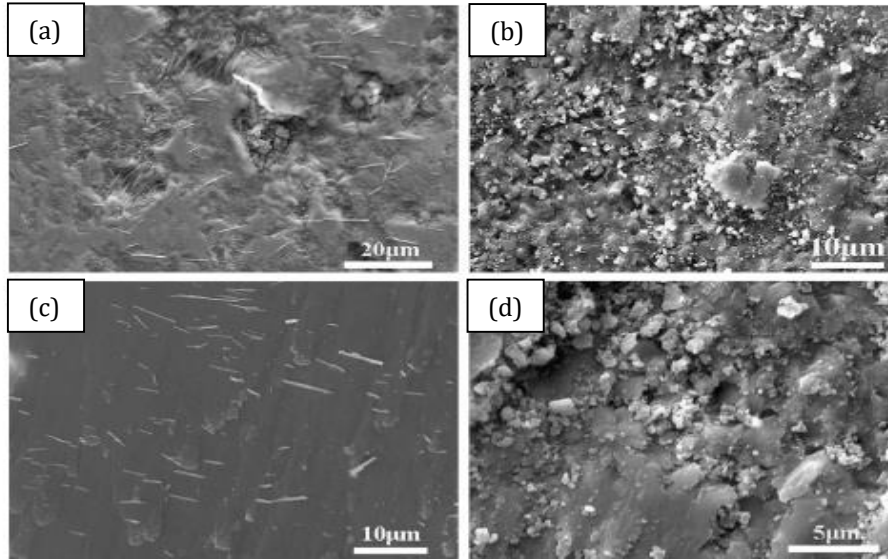


Figure 2.7. Wear debris on the worn surfaces of microstructured and nanostructured: cylindrical wear debris in the middle of the wear track of microstructured (a), granular wear debris in the middle of the wear track of nanostructured (b), cylindrical wear debris in the edge of the wear track of microstructured (c), and granular wear debris in the edge of the wear track of nanostructured (d) (Wang, *et al.*, 2009).

2.2.1. Spark Plasma Sintering for nanostructures

As stated above, the improved relative density and enhanced mechanical properties of nanostructures makes them attractive for technical research and application. The ideal sintering conditions for having the nano-composite ceramics is sintering at low temperature with minimum dwell time and rapid heating and cooling rate to inhibit grain growth (Duan, *et al.*, 2004; Yang, *et al.*, 2008). Based on this, one of the recent processes has been used successfully to produce nanostructures is Current Activated Pressure Assisted Densification (CAPAD) also called Spark Plasma Sintering (SPS) (Garay, 2010).

It is well known that in all sintering methods, densification is based on mass transport and atomic diffusion in solid state, which is driven by the kinetic energy of the atoms at higher temperature (Richerson, 2006). However, in SPS sintering method, there are three other factors contributing to the rapid densification process: the application of a mechanical pressure, the use of rapid heating rates, and the use of pulsed direct current (Shen, *et al.*, 2002).

The benefit of applying mechanical pressure is well known in removing pores from compacts, which improves diffusion and also the fact that each particle would be surrounded by an increasing number of particles when pressure increases (Shen, et al., 2002; Lee & Rainforth, 1994). Moreover, it is found by Shen et al. (2002) that the enhancement of density in SPS is due to the exposure to a pulsed direct current, which generates spark discharges between the adjacent contacting particles and the occurrence of plasma formation. The generated spark discharge and/or plasma is said to clean the surfaces from absorbed species and enhance the grain-boundary diffusion (Shen, et al., 2002).

The formation of plasma is still in debate and as stated by Garay (2010) there is little convincing evidence that sparks or plasma are beneficial or even occur in the process; however, an electric discharge process that happens on a microscopic level sounds to be widely accepted (Garay, 2010; Shen, et al., 2002). In the case of ceramic with no electrical conductivity, none or only a very low current passes through the samples and the heat as well as electric discharge would be generated as a result of the electric field applied by the pulsed direct current. This electric discharge process has been proposed to clean the surface of powder particles and create various types of surface defects, which enhance both grain-boundary diffusion and grain-boundary migration in the first stage of sintering (Shen, et al., 2002; Borrell, et al., 2013).

It has been stated that during SPS the sintering necks would be formed faster during initial stage, and its rapid heating rate can separate kinetically the densification process from grain growth stage by rapid reaching to favourable densification temperature (Borrell, et al., 2013). The sintering additives and their effect on SPS sintering can also be explained through their contribution to increasing electrical conductivity, or additional electric fields (Borrell, et al., 2013).

Whatever the mechanisms would be, it is clear that using SPS can produce high density as well as nano scale grains. For instance, Borrell et al. (2013) reached high density (>98.6% TD) with fine grain sizes (~0.5–1.4 μm) for alumina and titania composite with SPS sintering method, with the full reaction of titania and alumina to produce $\text{Al}_2\text{O}_3/\text{Al}_2\text{TiO}_5$ composite at temperatures around 1300°C (Borrell, et al., 2013).

2.3. Additives in ZTA

Although ZTA composites are used widely as the hip joint prostheses in clinical surgery, and they are now meeting the critical requirements for this application, there is still a need for improving the mechanical properties of them. One of the main possible improvements can be through the addition of small amount of additives, which are expected to give a measurable change in the characteristics of the composites and make a new generation of materials for orthopaedic applications.

Metal oxides are one of the most common additives, which have been widely used in alumina, zirconia and alumina-zirconia composites to improve flexural strength, fracture toughness, and tribological properties of the component. ZTA composites reinforced with some metal oxide additions has also been fabricated commercially and implanted in hip joint replacement surgeries. For instance, the Biolox delta® femoral heads (CeramTec, Germany) is an improved version of these composites reinforced with SrO and Cr₂O₃ additions with alumina grains in platelet-like morphology (Chevalier & Gremillard, 2009; Ceramtec Website). They show remarkable improvement in aging resistance of the composite in comparison to Y-TZP, and significant crack resistance (Chevalier & Gremillard, 2009; Ceramtec Website).

MgO, as discussed before, has been added to alumina matrix to enhance the densification and sintering properties of this ceramics and to make the fine microstructures. It also have used for ZTA composites in combination with ZrO₂ to increase the densification as well as to enhance the stabilization of the incorporated zirconia particles (Thompson & Rawlings, 1990).

Ceria (cerium oxide) is another additive, which has been studied widely in the alumina and zirconia composites, especially in ATZ composites (Benzaid, et al., 2008; Ban, et al., 2008; Tanaka, et al., 2002; Nawa, et al., 1998; Takano, et al., 2012; Kern, 2012). It has been found that adding ceria develops stabilisation of zirconia, which leads to higher resistance to low temperature degradation (Benzaid, et al., 2008; Tanaka, et al., 2002) as well as improving the composite toughness (Benzaid, et al., 2008; Tanaka, et al., 2002; Nawa, et al., 1998; Kern, 2012) and strength (Ban, et al., 2008; Kern, 2012). The soft tissue response to the Ce-doped composite has been reported to be almost the

same as that to alumina by Tanaka et al. (2002) showing the good biocompatibility of this composite. The experiments by Tanaka et al. (2002) also showed a higher friction coefficient than that of alumina, in which both the wear rate of the pin and the wear track depth of the disk were much lower in comparison to alumina. In addition, recent results have shown high resistance to subcritical crack growth and cyclic fatigue strength for these composites represented by Kern (2012) and Takano et al. (2012) respectively, making it interesting for applications operating under cyclic load such as dental implants.

Dey et al. (2009) studied the tribological behaviour of ZTA with different metal oxide additives (MO_x ; $M = \text{Cu, Ti, Mg, Zn, Mn}$). These solid oxide were added in small quantities (~8–11 wt.%) to provide a self-lubrication action and therefore to decrease the coefficient of dry friction. The results demonstrated the lowest specific wear rate and coefficient of friction in Ti-Mn-ZTA system, while the highest specific wear rates were obtained for Mn-Zn-ZTA, then Ti-Cu-ZTA and Mn-Cu-ZTA. The main wear mechanisms in these cases were suggested to be the grain pullout and removal of secondary phases. Grain coarsening has also been observed in the additions of CuO through enhancing liquid phase diffusion, MnO_2 through forming solid solution, and TiO_2 through substituting Al ions and enhancing their diffusions. This coarsening can also be retarded by adding MgO as conventional grain-growth inhibitor (Dey & Biswas, 2009).

TiO_2 also has been added to monolithic alumina and zirconia matrix composite, alone or with cerium oxide (Nawa, et al., 1998; Lee, et al., 2003). Adding TiO_2 to alumina has made an improvement of fracture toughness due to the particle bridging mechanism, but the most significant effect has been seen in the wear resistance of the composite (Lee, et al., 2003). The wear rate of alumina has been reported to be reduced greatly by increasing the amount of TiO_2 up to 10 mol.% in the nanocomposite (Figure 2.8), which has been attributed to its microstructure and mechanical properties such as fine grains and boundary chemistry (Lee, et al., 2003).

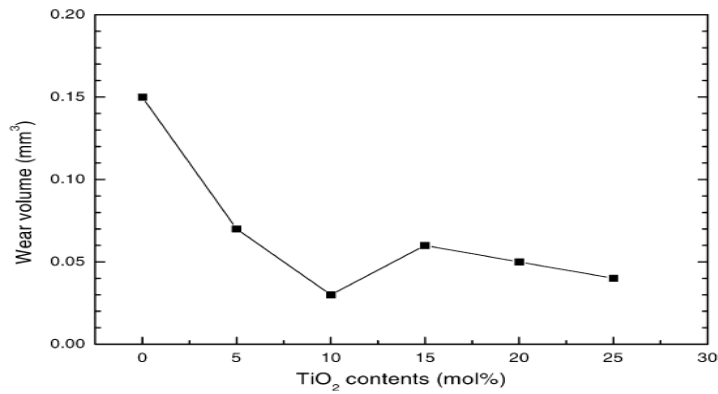


Figure 2.8. Variations of wear volumes of Al₂O₃/TiO₂ nanocomposites with the TiO₂ contents (Lee, et al., 2003)

2.3.1. Al₂O₃/ZrO₂/TiO₂ composites

Titanium oxide also called titania is one of the most attractive materials for engineering applications, which is widely used as pigments in painting, food and cosmetics industry as well as optical catalysts and oxygen sensors in automobiles (Ohama & Gemert, 2011; Shim & Lee, 2002). Titanium oxide has three crystal structure, anatase, rutile and brookite with tetragonal, tetragonal and orthorhombic crystal structure respectively (Ohama & Gemert, 2011).

Titanium oxide has been widely used as an additive in ceramics mainly as a sintering aid. It has recently been reported to give promising bioactivity by forming chemical bonding with bones, which makes it suitable for implant applications (Li, et al., 1996; Fartash, et al., 1995). In alumina ceramics, it has been found to improve the fracture toughness and wear resistance of the material as well as improving flaw tolerance and thermal shock resistance, which can make it a good candidate for tribological application such as hip joint replacement materials (Wang, et al., 2009; Yang, et al., 2009; Borrell, et al., 2013). The improved mechanical properties of alumina/titania composites has been attributed to the presence of anisotropic grains formed in an equiaxed matrix making it a whisker self-reinforced material (Kebbede, et al., 1997) and the large mismatch of thermal expansion coefficient between alumina and alumina/titania promoting the local residual stresses (Borrell, et al., 2013). In zirconia based ceramics, small additions of titania can improve density as well as augmenting tetragonal phase stability at room temperature (Affatato, et al., 2001).

Although the effect of titania on alumina has been widely studied, there is not much research on its effect on ZTA composites. In the following sections, the addition of titania to alumina, zirconia and ZTA composites, and its effect on microstructure, sintering, and mechanical and wear properties of these composites will be discussed.

2.3.1.1. Addition of titania to alumina

The typical phase diagram of alumina and titania is shown in Figure 2.9. As can be seen, the solid solution of alumina and titania is formed at a wide range of temperatures (Berger & Sayir, 2008).

The solubility limit of titanium oxide in alumina has been widely investigated and different amounts at different temperatures were reported by the researchers from both diffuse reflectance measurements and the characteristic cathodoluminescence (Winkler, et al., 1966; Horn & Messing, 1995; Kim, et al., 2000). These amounts varied from 800 ppm to 0.27 wt.% at temperatures between 1250° and 1700°C (Winkler, et al., 1966; Kim, et al., 2000; Bagley, et al., 1970; Roy & Coble, 1968). Winkler et al. (1966) found the solubility limit of titanium dioxide in alumina was between 0.25 and 0.30 mol.% for samples fired in air at 1300°C, while this amount was reported by McKee and Aleshin (1963) to be 1.0, 1.8, and 2.5 mol.% at 1400°C, 1600°C, and 1700°C, respectively for the hydrogen fired samples. This solubility was reported to be 0.2 mol.% and 0.15 mol.% by other researchers (Smothers & Reynolds, 1954; Cahoon & Christensen, 1956). As described by Winkler et al. (1966), even small additions, around 0.1 to 0.2 mol.% of TiO₂ to Al₂O₃, will alter the effective diffusion constant by a factor of more than 100. In addition, it has been suggested that the solubility of TiO₂ is dependent to the grain size, which the finer particles have higher solubility for TiO₂ (Bagley, et al., 1970).

In Figure 2.10, the fracture surfaces of the composites sintered at 1300°C and 1400°C studied by Borrell et al. (Borrell, et al., 2013) can be seen at higher magnification. The nano-sized aluminium titanates were homogeneously distributed and mainly located at alumina triple points and grain boundaries, and no titania was detected, according to XRD (Borrell, et al., 2013).

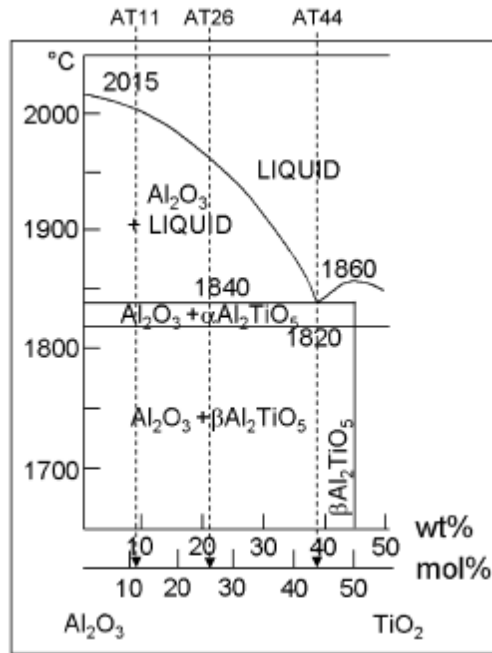


Figure 2.9. Al₂O₃-rich side of the phase diagram (Berger & Sayir, 2008).

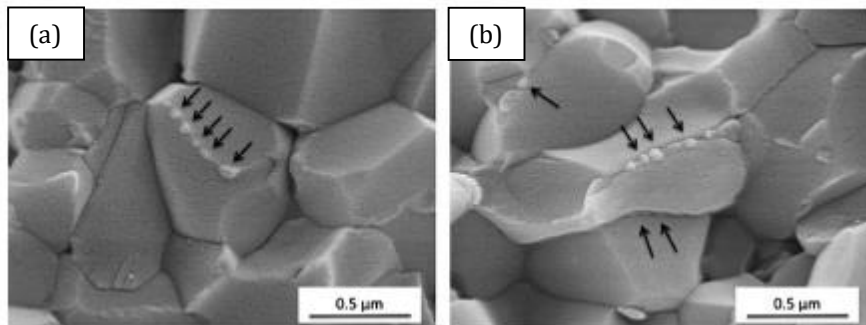


Figure 2.10. Composite Al₂O₃/Al₂TiO₅ sintered by SPS at: (a) 1300°C and (b) 1400°C. Nanometric second phase grains of aluminium titanate located at the boundaries between the alumina grains are pointed by narrows (Borrell, et al., 2013).

Aluminium titanate or Tialite (Al₂TiO₅)

Alumina and titania can react to form a solid solution above their eutectoid temperature, 1280°C, and produce Al₂TiO₅ according to the following reaction (Yang, et al., 2008):



Aluminium titanate or Tialite, Al₂TiO₅, is considered as a potential candidate for refractory and engine components application and thermal barriers due to its high

melting point, low thermal expansion coefficient, low thermal conductivity, and excellent thermal shock resistance (Duan, et al., 2004; Yang, et al., 2008). For small additions, Al_2TiO_5 can progress the thermal properties of ceramic composites (Duan, et al., 2004). However, it has reported that Al_2TiO_5 can be formed only when titania is added beyond the solubility limit (Kim, et al., 2000).

Despite its promising applications, Al_2TiO_5 has two main disadvantages to use as an engineering material; decomposition into alumina and titania (Rutile) at the temperature below 1280°C , and poor mechanical properties due to grain-boundary microcracking as the result of highly different thermal expansion coefficients of Al_2TiO_5 ceramics along its three crystalline axes (Duan, et al., 2004; Yang, et al., 2008). These disadvantages along with degradation of densification by microcracking have convinced researchers to avoid formation of Al_2TiO_5 during the process of alumina/titania composites (Duan, et al., 2004; Yang, et al., 2008; Berger & Sayir, 2008). However, some researchers has been reported that incorporation of Al_2TiO_5 in Al_2O_3 matrix leads to better flaw-tolerance properties as well as maintaining the structural integrity (Borrell, et al., 2013).

Duan et al. (2004) claimed that at temperatures below 900°C , the decomposition rate of Al_2TiO_5 was too low to be detected, and the maximum rate of decomposition would be in the temperature range of 1100°C - 1150°C . However, as the decomposition is considered to be a nucleation-growth process, it is reported to be completed when applying the high pressure to the composite even at low temperatures, which is attributed to the increased diffusion coefficient and decreased kinetic energy barrier induced by pressure (Duan, et al., 2004).

The influence of pressure on the formation of Al_2TiO_5 was also studied by Borrell et al. (2013) through SPS technique at a range of temperatures between 1250°C and 1400°C in vacuum with holding time for one minute. Their results showed the complete formation of Al_2TiO_5 after sintering above 1300°C under a pressure of 80 MPa; while after SPS sintering under a pressure of 30MPa, this complete formation of Al_2TiO_5 happened at 1250°C . They concluded that although the reaction temperature to form Al_2TiO_5 in oxidizing atmospheres has been widely reported to be above 1280°C , it is only under the ambient air pressure and the SPS processing can lower the formation

temperature of Al₂TiO₅. This effect might be useful in producing the Al₂O₃/Al₂TiO₅ composites with fine-grained microstructure (Yang, et al., 2009).

Densification

One of the main applications of adding titania to the ceramic composite is for improving the density during the sintering process and achieving up to 100% relative density (Kim, et al., 2000; Hwang & Chang, 1996; Lartigue-Korinek, et al., 2006). This characteristic has been attributed to its effect on increasing aluminium vacancy concentration to maintain the charge neutrality, as shown in following reaction, causing the increase in intergranular diffusion and grain boundary mobility, and this vacancies concentration is dependent to the titanium content (Kim, et al., 2000; Hwang & Chang, 1996; Lartigue-Korinek, et al., 2006). However, this defect model was argued to need unusual large concentration of additives in alumina (Kroger, 1984). The presence of liquid phase and its enhancing effect on densification was also proposed to explain the improved density by adding titania (Kim, et al., 2000).



What is obvious and frequently reported from many researchers is that without titanium oxide the sintered samples were more porous and had smaller grain sizes in comparison with the samples containing titania. Therefore, the effects of Ti ions on diffusion was studied to discover the origin of these changes in density and microstructure.

The effect of metal ions on grain boundary diffusion in alumina was found through the results of creep experiments showing the decrease of GB diffusion by adding zirconium and yttrium and increase of it by adding titanium and magnesium compared to undoped alumina (Lartigue-Korinek, et al., 2006).

Lartigue-Korinek et al. (2006) conducted a survey on the effect of Ti on densification and illustrated a schematic model to explain the densification mechanisms through formation of colonies and anisotropic growth of elementary bricks favored by adding titania (Figure 2.11). They mentioned that adding titania to alumina will result in anisotropic surface energies regarding to different morphologies of internal pores for

titania doped alumina compared with undoped ones (Lartigue-Korinek, et al., 2006). Thus, a stacking of elongated elementary bricks would form inside the porous single-crystalline colonies and their anisotropic growth or coalescence would remove intracolony porosity leading to the faceted fully dense α -grains (Figure 2.11.a and Figure 2.11.b) (Lartigue-Korinek, et al., 2006). It should be noted that colonies consists of nano-sized elementary bricks with close crystallographic orientations (Figure 2.11.a) and resulted from coupled mechanisms of nucleation during phase transformation from γ to α alumina (Lartigue-Korinek, et al., 2006).

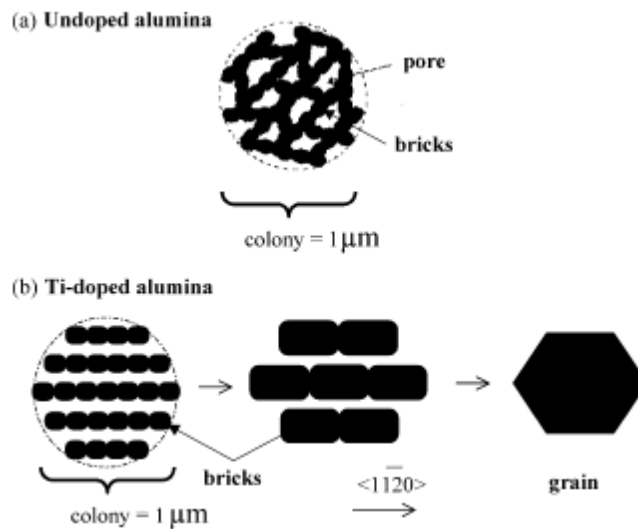


Figure 2.11. Schematic illustration of (a) the colony microstructure in undoped alumina and (b) the mechanism of colony densification in Ti-doped alumina: the stacking of elongated bricks transforms the single crystalline porous colony into a dense faceted grain; in comparison the vermicular microstructure of undoped colonies (a) delays to much higher temperature the elimination of the intracolony porosity (Lartigue-Korinek, et al., 2006).

Microstructure

One of the main advantages of adding TiO_2 in alumina is producing the anisotropic grains, which are embedded in an equi-axed matrix (Richerson, 2006; Kebbede, et al., 1997; Horn & Messing, 1995; Kim, et al., 2000; Lartigue-Korinek, et al., 2006; Kwon, et al., 2002). This characteristic can generate a composite having self-reinforcing microstructure with chemically identical anisotropic fibers or whiskers, which can improve the toughness of the composite without any risks in handling with whiskers (Kebbede, et al., 1997; Horn & Messing, 1995). To obtain such a microstructure, an

understanding and accurate controlling of effective mechanisms and parameters of anisotropic grain growth is needed which will be discussed.

Some researchers attributed the formation of in-situ fibres to the presence of liquid phases at the boundaries of anisotropic grains, which could be controlled by interfacial reactions (Kebbede, et al., 1997; Horn & Messing, 1995; Kim, et al., 2000; Kwon, et al., 2002). They mainly attributed the formation of the liquid phase to the presence of silica with co-doping of TiO_2 and SiO_2 , which formed a glassy phase with low viscosity and enhances the boundary migration (Kebbede, et al., 1997; Kim, et al., 2000; Lartigue-Korinek, et al., 2006; Kwon, et al., 2002). It also was reported the amount of TiO_2 were critical as it decreased the viscosity of silicon oxide substantially (Kim, et al., 2000).

It was found that the long facets in the platelet grains produced after adding small amounts of titania were basal planes (0001) and the short facets appeared at the edge of platelets were pyramidal planes mostly $\{1012\}$ plates (Kebbede, et al., 1997; Kim, et al., 2000; Kwon, et al., 2002).

The segregation of titanium reportedly occurred at the boundaries of both plate-like and equiaxed grains, but the silicon segregated at the basal plates of anisotropic grains and was not found on any of curved or faceted end of plates (Kebbede, et al., 1997). The presence of silicon and amorphous phase in EDS results of Kebbede et al. (1997) was attributed to the cooperation of SiO_2 and TiO_2 , which formed the glassy phase and was responsible for anisotropic grain growth of these composites (Figure 2.12) (Kebbede, et al., 1997) due to the ternary eutectic liquid phase occurred during sintering process (McKee & Aleshin, 1963; Kwon, et al., 2002). The presence of liquid phase during sintering, resulting the anisotropic microstructure, was also reported by Kwon et al. (2002); however, they attributed this phenomenon to the accumulation of impurities at the boundaries, which became liquid after heat treatment. They reported that at initial stages of anisotropic grain growth, the liquid layer on the basal or the non-basal planes was difficult to observe as it disappeared during cooling, while when grains were grown significantly, it would be detected easily (Kwon, et al., 2002). They also showed by EDS results that the concentration of Ti and Si ions were much higher along the basal plane in comparison with the non-basal planes (Kwon, et al., 2002). Consequently, they

developed a model which showed why the grains would prefer to grow in one direction resulting in anisotropic grain morphology, which is shown in Figure 2.13 (Kwon, et al., 2002). As can be seen in the model, the atomic attachment onto the basal plane, which is atomically smooth, would require the 2D nucleation process. However, a reduction in activation energy, even as less as 10%, would result in a significant increase in nucleation rate as much as few hundreds which results in much higher growth rate of non-basal planes rather than basal planes as depicted in Figure 2.13. Thus, it is the enhanced growth rate by grain boundary re-entrant edges formed at the non-basal planes of alumina, which induces the faster migration of these planes and results in anisotropic growth of alumina grains (Kwon, et al., 2002).

In contrast to the above studies, some researchers showed that the anisotropic grain growth could be observed even in the high purity composite of alumina and titania in which did not contain any silica and no clear amorphous layer was found at the grain boundaries (Horn & Messing, 1995).

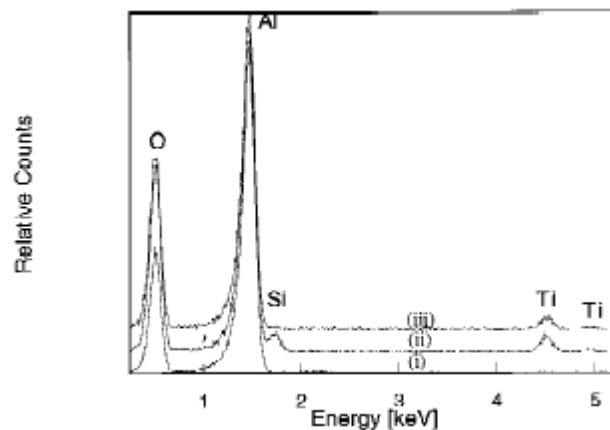


Figure 2.12. EDS spectra from (i) an alumina grain, (ii) a long faceted boundary of a platelet with an intergranular phase, and (iii) a short faceted boundary (Kebbede, et al., 1997).

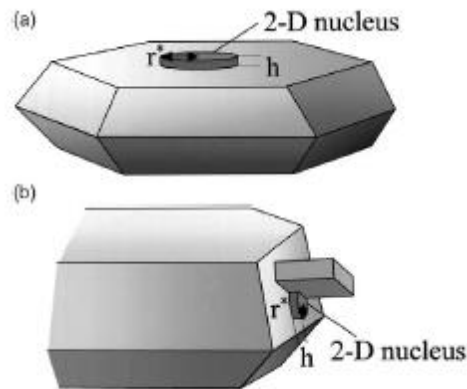


Figure 2.13. Schematic illustrations of 2D nucleus on the (a) basal plane and (b) non-basal plane (Kwon, *et al.*, 2002).

It was also found that there was a critical size for the grains after which they would grow anisotropically and the morphology of the grains was dependent to the TiO₂ amount as well as sintering conditions (Kebbede, *et al.*, 1997; Lartigue-Korinek, *et al.*, 2006), and the initial microstructure was important in forming the anisotropic grains (Horn & Messing, 1995). It was reported that the nucleation of anisotropic grains happened when a small amount of grains reached a critical size while the other grains did not coarsen highly and this happened only after an incubation period (Horn & Messing, 1995).

Horn and Messing's (1995) studies showed that the addition of titania above 0.6 wt.% would induce the abnormal grain growth during incubation which would lead to anisotropic grain microstructure while this abnormal grain growth did not occur for any of incubation times and temperatures in the undoped samples. To study this microstructure, they proposed that the anisotropic grain growth in a polycrystalline matrix is similar to the single crystal grain growth in which the shaped grains needed slower diffusion and therefore enough driving force for atom transport and coarsening. They then concluded that when the temperature is low, fewer grains would reach the critical size and instead of matrix coarsening, the driving force would be used for anisotropic grains growth (Horn & Messing, 1995). They also attributed the effect of TiO₂ for this abnormal grain growth to the balance between the processes of TiO₂ segregation at the boundaries which might poison and inhibit growth on some specific surfaces such as basal planes, and its adsorption to particular surfaces leading to changing the surface energies or local changing of diffusional grain growth (Horn &

Messing, 1995). They finally concluded that the anisotropic grain growth after incubation period which happened at low titania concentration needed these requirements:

- A fully dense matrix to avoid boundary-pore interactions
- An ultrafine matrix to provide enough anisotropic growth driving force
- Transport regulation to initiate anisotropic grain growth but restrict matrix coarsening
- Dopants to modify the growth process

and

- Preferably a material with non-isometric crystal structure (Horn & Messing, 1995).

Mechanical properties

One of the main effects of TiO₂ additives is on the mechanical properties of the composite. It has been reported that density is increased by adding TiO₂ at lower sintering temperatures (1250°C-1450°C) due to grain growth and reduced pores and then decreased at 1550°C as a result of formation of Al₂TiO₅ and macrocracks (Yang, et al., 2009). These changes in density of the composite affect the flexural strength, fracture toughness and Vickers hardness in the same manner, i.e. increased from 1250°C to 1450°C as a result of less porosity, but decreased at 1550°C because of microcracks (Yang, et al., 2009).

The toughness of alumina ceramics with the addition of titania has also been affected by the presence of elongated and plate-like alumina grains discussed above. For instance, greater high-temperature creep resistance and higher toughness were reported in this kind of microstructure due to the significant alteration of the crack path in comparison with the uniform alumina microstructure (Nawa, et al., 1998; Horn & Messing, 1995). In fact, this microstructure shows the good properties of whisker reinforced composites without the mishandling disadvantages of these composites which implies serious health risks during implementation (Horn & Messing, 1995).

2.3.1.2. Addition of titania to zirconia

There are a variety of proposed $\text{ZrO}_2\text{-TiO}_2$ phase diagrams with slight differences, which shows that there is no definitive version of this diagram yet (Brown & Duwez, 1954; Pandolfelli, et al., 1991; Bannister & Barnes, 1986; Noguchi & Mizuno, 1968). For instance, at the zirconia rich side of the diagrams, different researchers reported a different solubility limit of TiO_2 in ZrO_2 . While Brown and Duwez (1954) found the maximum solubility of TiO_2 in ZrO_2 to be approximately 18 mol.% which decreased with decreasing the temperature to nearly 6 mol.% about 980°C , Bannister and Barnes' findings (1986) showed the solubility limit of TiO_2 in tetragonal zirconia to be 13.8 ± 0.3 mol.% at 1300°C , 14.9 ± 0.2 mol.% at 1400°C , and 16.1 ± 0.2 mol.% at 1500°C .

Figure 2.14 illustrates one of these suggested phase diagrams, which has been more accepted and used by different authors (Bannister & Barnes, 1986; Noguchi & Mizuno, 1968). It can be seen that ZrO_2 and TiO_2 can form a solid solution of $(\text{Zr,Ti})\text{O}_2$ (Hwang & Chang, 1996) and ZrTiO_4 or ZT (Brown & Duwez, 1954; Pandolfelli, et al., 1991). Figure 2.15 shows the same phase diagram in ZrO_2 rich side regions illustrating solid solution boundaries between tetragonal and monoclinic zirconia and two-phases regions formed at lower temperatures (Noguchi & Mizuno, 1968). Figure 2.15 also demonstrates that the addition of TiO_2 to ZrO_2 lowers the tetragonal to monoclinic transformation temperature and makes a large area for having the tetragonal zirconia solid solution (Hwang & Chang, 1996; Brown & Duwez, 1954; Pandolfelli, et al., 1991; Noguchi & Mizuno, 1968; Chevalier & Gremillard, 2009).

Adding titania to zirconia has been reported to decrease both lattice constants and lattice volume of tetragonal zirconia showing that titanium ion with its smaller ionic radius than zirconium ions will dissolve into tetragonal zirconia (Nawa, et al., 1998). Despite uncertainty about the exact configuration of this solid solution, it is clear that this tetragonal phase stability and strengthening of zirconia composites by adding titania can be attributed to the formation of this solid solution (Nawa, et al., 1998). Moreover, it has been found that by reducing grain size, the critical stresses responsible for t to m transformation is increased resulting in increased strength of the composite (Nawa, et al., 1998).

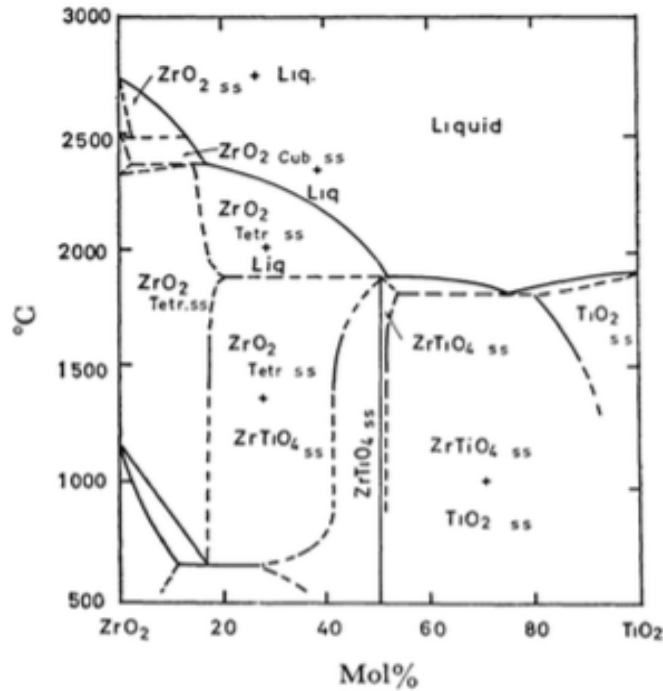


Figure 2.14. Tentative phase diagram of ZrO_2 - TiO_2 system at high temperature (Noguchi & Mizuno, 1968).

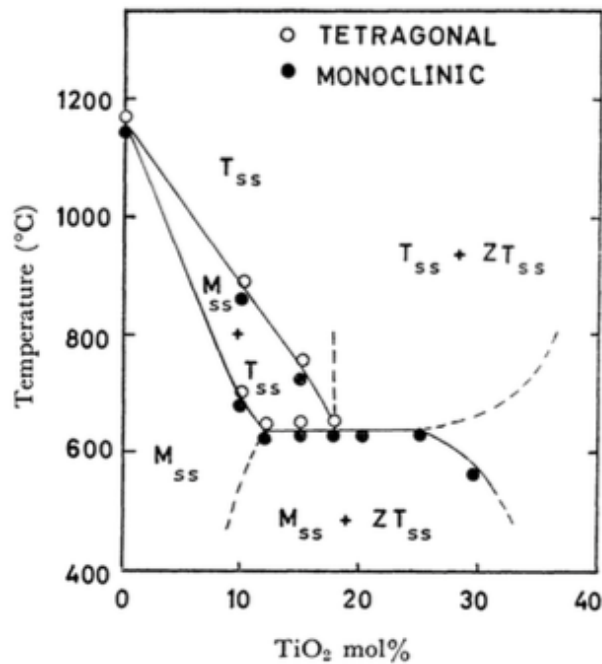


Figure 2.15. High temperature X-ray diffraction data in ZrO_2 rich side region (Noguchi & Mizuno, 1968).

To see the effect of stabilizing ions on zirconia, Pandolfelli et al. (1990) examined the addition of TiO_2 and CeO_2 to zirconia for sintering temperatures of $1300^\circ C$ to $1600^\circ C$ and found that at temperatures above $1450^\circ C$, formation of titanium and cerium rich liquid phase resulted in loss of tetragonal stabilizers. Thus, they could only obtain

tetragonal zirconia phase at 1350°C, which possessed high stability and high resistance to stress-assisted transformation and consequently low strength and low toughness (Pandolfelli, et al., 1990). This stability even existed for larger grain sizes and resulted in incomplete and transformation half way across a grain (Pandolfelli, et al., 1990). Similarly, Hughes et al. (1995) showed that by adding Al₂O₃ and TiO₂ to YSZ, the onset of tetragonal to monoclinic transformation could be retarded, and discussed this phenomenon based on chemical free energy changes.

By considering different results of tetragonal stabilization of zirconia, it has been concluded that at the condition of same grain morphology and no glassy phase at grain boundaries, the factors which can control the retention of tetragonal zirconia consist of: *thermodynamical factors* such as size, charge, concentration, and crystal structure of dopant ions, and concentration and role of anion vacancies; and *kinematical and stress field factors* such as the thermal expansion anisotropy, and the effect of dopant ions on the sintered microstructure of the zirconia matrix (Pandolfelli, et al., 1991).

Despite the differences in plotted phase diagrams for ZrO₂-TiO₂ system, what seems to be clear in all is that TiO₂ solubility in tetragonal zirconia is more than that in monoclinic phase and would result in formation of ZrTiO₄ plus monoclinic solid solution with lower titania content at eutectoid decomposition temperature (Brown & Duwez, 1954; Pandolfelli, et al., 1991; Bannister & Barnes, 1986; Noguchi & Mizuno, 1968; Pandolfelli, et al., 1990).

Zirconium titanate (ZrTiO₄)

Formation of ZrTiO₄, or zirconium titanate, in ZrO₂-TiO₂ system was first reported by Brown and Duwez (1954) through weight changes and XRD diffraction pattern studies. Their results based on different TiO₂ content samples sintered for 980°C, 1370°C and 1760°C showed the existence of ZrTiO₄ for 15 to 45 mol.% TiO₂ at all three sintering temperatures. However, other researchers' findings cast doubt on its formation at minimum threshold of titania content suggested by Brown and Duwez (1954). For instance, the existence of ZrTiO₄ was reported only in 17.9 and 21.5 mol.% TiO₂ content samples by Pandolfelli et al. (1991), 20.2, 22.5, and 29.6 mol.% TiO₂ by Bannister and Barnes (1986), and 20 and 40 mol.% TiO₂ by Miao et al. (2004). In

addition, the formation of ZrTiO_4 was also reported to be dependent to sintering temperature, as it was not found on sintering temperature below 1400°C by Miao et al. (2004).

TEM studies on ZrTiO_4 undertaken by Pandolfelli et al. (1990) showed its structure to be extensively twinned resulting in spot splitting in its diffraction pattern (Figure 2.16). It was also showed that it was monoclinic or glassy phase which surrounded ZrTiO_4 grains, supporting the theory of diffusion of Ti^{4+} ions from the matrix to the ZrTiO_4 over a short distance (Pandolfelli, et al., 1990). It was also found that when this formation was not complete, ZrTiO_4 regions were formed within the grains, which could be seen as twinned area in TEM images (Pandolfelli, et al., 1990).

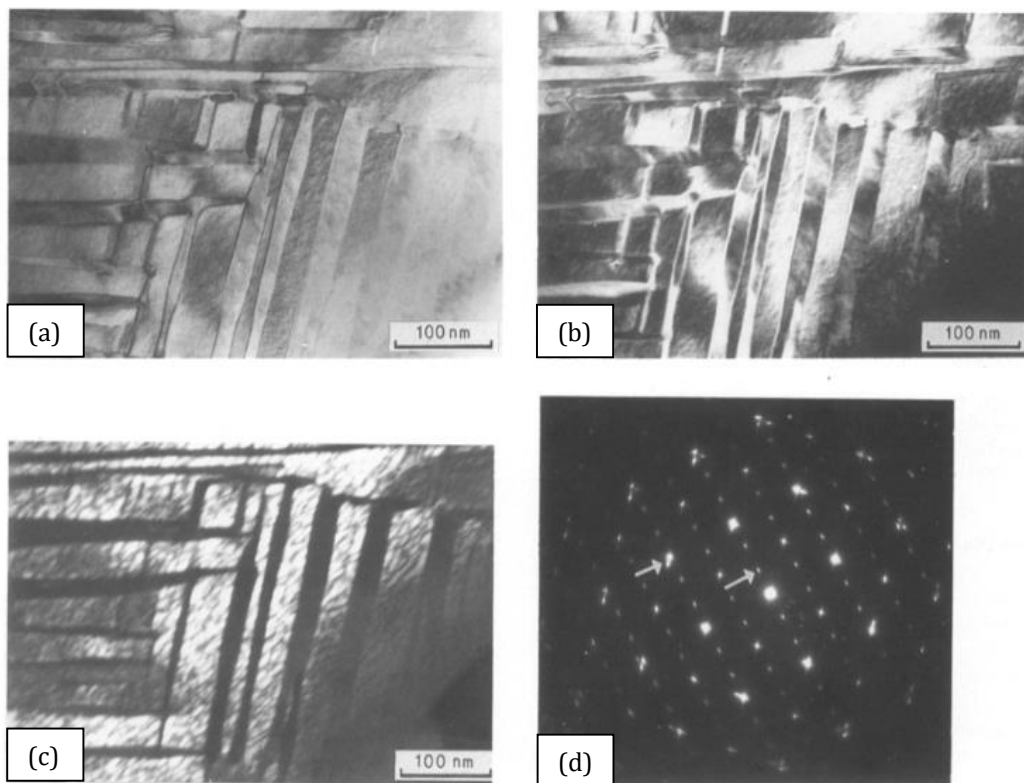


Figure 2.16. (a) Bright-field micrograph of a heavily twinned zirconium titanate particles; (b) dark-field micrograph of the same area using a fundamental diffraction spot; (c) dark-field micrograph of the same area using a superlattice diffraction spot, showing a very fine structure to the ordered lattice; (d) selected-area diffraction pattern from this area, $B = [001]$, with the diffraction spot used for the dark fields arrowed (Pandolfelli, et al., 1990).

Densification

Small additions of TiO_2 were reported to enhance density due to the defects caused by increasing temperature or in reducing conditions, which promoted diffusion (Pandolfelli, et al., 1991), or due to chemical changes in the bound nearest neighbours, which affected the diffusion rate, particularly of oxygen ions (Horn & Messing, 1995; Kim, et al., 2000) and lead to higher density and coarser microstructure. However, the densification rate was reported to decrease by increasing the amount of titania. This result could be attributed to the fact that reduction of surface area is the main driving force for both densification and coarsening of the grains, and sintering behaviour of different materials would be a mixture of these two mechanisms contributed together (See Figure 2.17) (Pandolfelli, et al., 1991). Thus, by increasing the amount of titania, the coarsening mechanism would overcome densification, until it reaches 21.5 mol.% in which pure coarsening happens (Pandolfelli, et al., 1991). Thus, adding a large amount of titania to zirconia would suppress its densification and would not allow very high density to be achieved because of its dominant grain growth mechanism resulted from its high surface diffusion coefficient (Pandolfelli, et al., 1991). This coarser microstructure would lead to the formation of microcracks due to higher thermal mismatch stresses and consequently has adverse effect on density (Horn & Messing, 1995; Kim, et al., 2000).

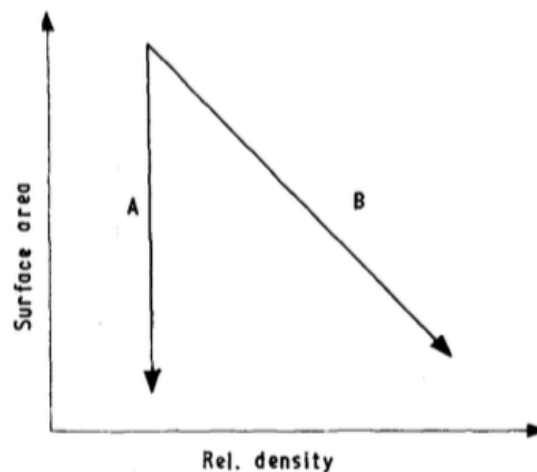


Figure 2.17. Surface area and relative density relationship during sintering. A is the trajectory for pure coarsening and B that for pure densification (Pandolfelli, et al., 1991).

Pandolfelli et al. (1990) reported reaching full density for the $\text{ZrO}_2\text{-TiO}_2$ composites

occurred only when it was doped with ceria, and at sintering temperatures range 1350-1400°C. As they considered the sintering mechanism of this composite to be liquid-phase sintering, the decreasing density for sintering at 1500-1600°C was attributed to large amount of liquid phase and formation of monoclinic phase resulting in microcracking and low density. On the other hand, Miao et al. (2004) reported reaching high densities and low residual porosity for zirconia stabilized with 3 mol.% yttria by adding TiO₂ when samples sintered 1400-1500°C.

Thus, it can be concluded that adding titania is not enough for promoting density and other additives such as yttria and ceria which are often doped in zirconia as tetragonal stabilizers can affect the degree of densification at different temperatures. It also can be concluded that increasing temperatures can not absolutely result in increasing density as it can lead to grain growth or formation of monoclinic which has detrimental effect on densification of zirconia ceramics due to forming of microcracks.

Microstructure

As stated above, adding titania to zirconia works by increasing sintering temperature and time, and can affect the diffusion rate and lead to grain growth and coarser microstructure. In addition, increasing the amount of defects by increasing the amount of titania was found for YSZ composites, particularly at low sintering temperature such as 1300°C by Miao et al. (2004) (Figure 2.18). They also reported that matrix grain size was growing by increasing titania amount until 20 vol.%, and is decreasing after that which could be as a result of raising formation of ZrTiO₄ and its effect in inhibiting matrix grain growth (Figure 2.19) (Miao, et al., 2004).

On the other hand, the glassy phase at triple points was found in the study done by Pandolfelli et al. (1990) on the microstructure of zirconia with addition of ceria and titania, which was considered to be the proof of liquid phase sintering. The amount of this glassy phase would be increasing with increasing sintering temperature and collecting on the surface as a result of capillary forces. This phenomenon formed small ellipsoid features, as seen by Pandolfelli et al. (1990) for sintering temperatures above 1400°C, which were rich in cerium and titanium (Figure 2.20).

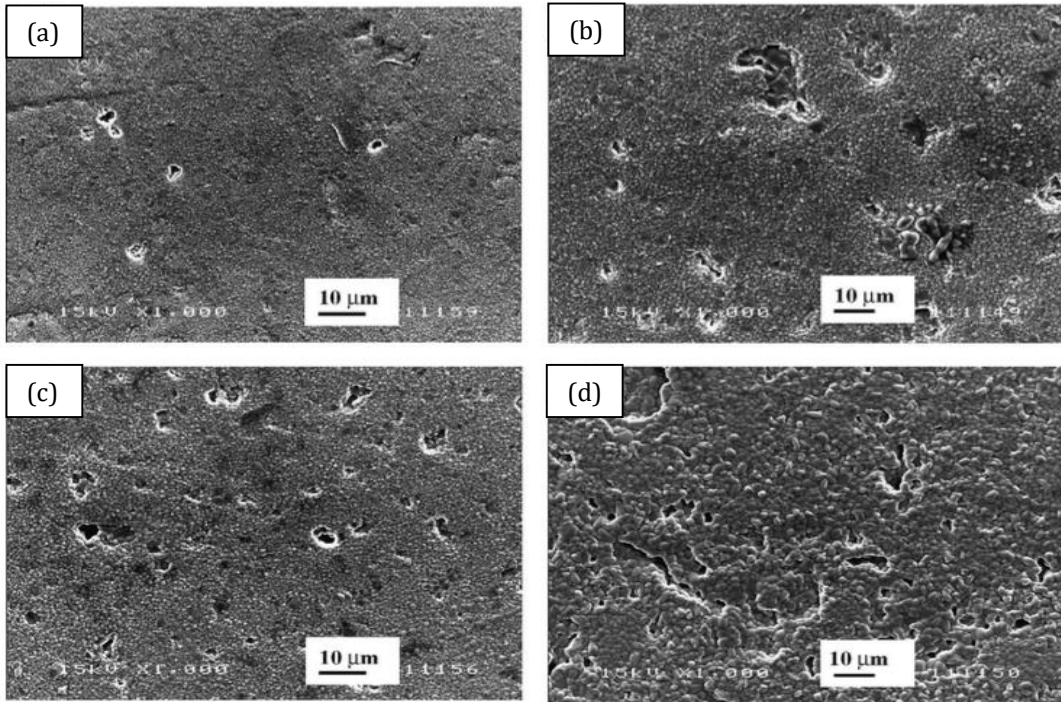


Figure 2.18. SEM micrographs of the thermally etched surfaces of the Y-ZrO₂-TiO₂ composites sintered at 1300°C with TiO₂ content of 0 vol.% (a), 10 vol.% (b), 20 vol.% (c), and 30 vol.% (d) (Pandolfelli, *et al.*, 1990).

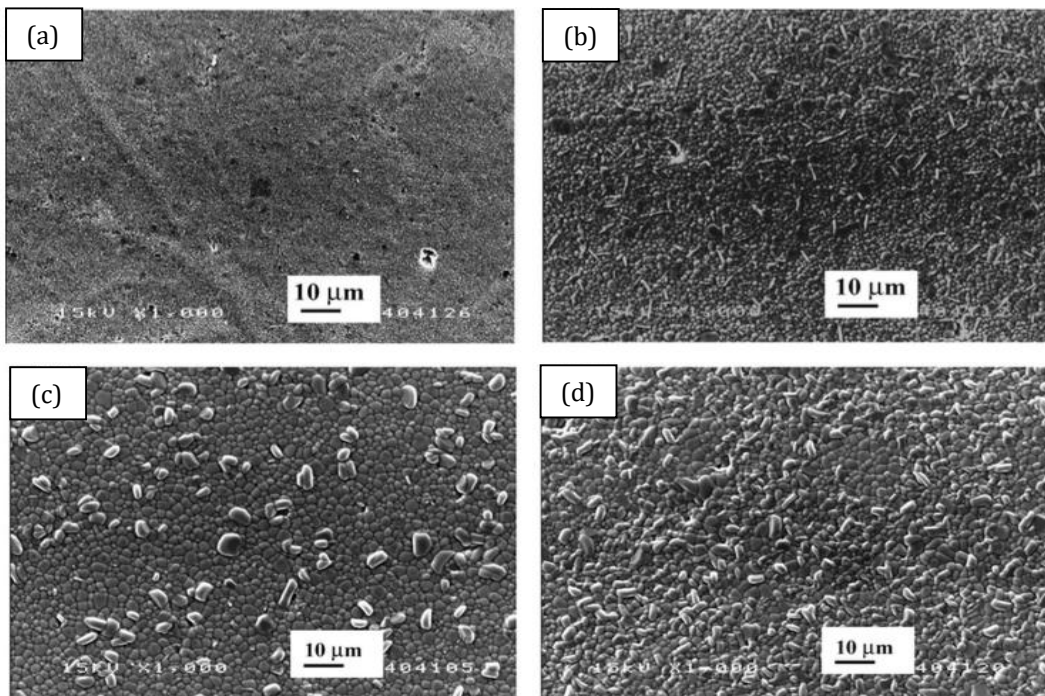


Figure 2.19. SEM micrographs of the thermally etched surfaces of the Y-ZrO₂-TiO₂ composites sintered at 1400°C with TiO₂ content of 0 vol.% (a), 10 vol.% (b), 20 vol.% (c), and 30 vol.% (d) (Pandolfelli, *et al.*, 1990).

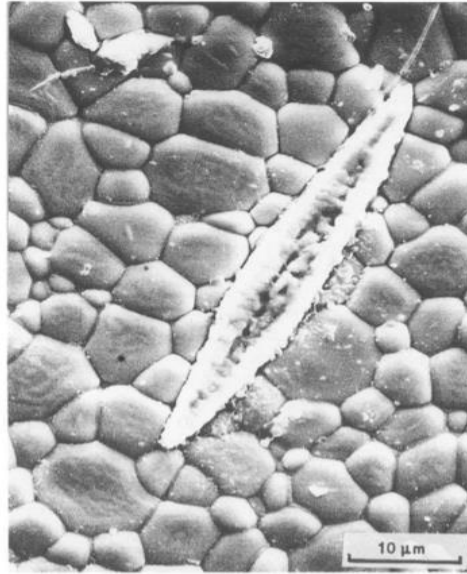


Figure 2.20. Scanning electron micrograph of sintered surface of the 1450°C sample, showing one of the many ellipsoid features, believed to be formed by capillary of the liquid phase to the surface (Pandolfelli, et al., 1990).

Mechanical properties

The mechanical properties of zirconia-titania composites are highly sensitive to the amount of titania as a result of its effect on densification, microstructure, and its effect of stabilization of tetragonal zirconia. Small additions of titania is reported to improve mechanical properties through its effect on densification and retention of tetragonal zirconia (Osendi & Moya, 1988). However, having higher and more stabilized zirconia by adding titania seems to not necessarily lead to better mechanical properties; for instance, Pandolfelli et al. (1990) found that the tetragonal zirconia added ceria and titania was highly stabilized and showed high resistance even against stress induced transformation which resulted in lower strength and toughness of the composite.

On the other hand, a large amount of titania can lead to a coarser microstructure resulting in reduction of strength and toughness due to intense microcracking (Osendi & Moya, 1988). Formation of $ZrTiO_4$, as discussed above, is another factor affecting mechanical properties. $ZrTiO_4$ can reduce hardness and toughness of the composite with its poorer mechanical properties in comparison with Y-TZP, which can affect total hardness and toughness adversely regarding mixture law (Figure 2.21) (Miao, et al., 2004; Osendi & Moya, 1988). It was also reported, as can be seen in Figure 2.21, that for the same amount of titania composites having $ZrTiO_4$ at 1500°C showed relatively

higher hardness and toughness in comparison with samples sintered at 1300°C with only Y-ZrO₂ and TiO₂, which could be the result of residual thermal stresses caused by interphase boundaries of ZrTiO₄ (Miao, et al., 2004).

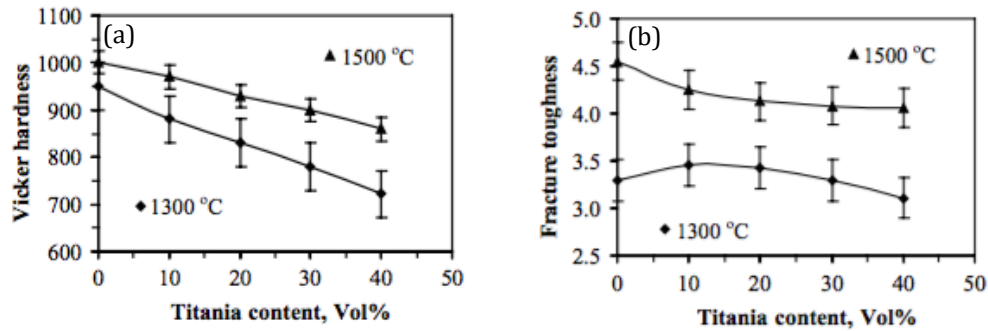


Figure 2.21. Vickers hardness (units: kg/mm²) (a), and fracture toughness (units: MPa.m^{0.5}) as a function of titania content for the T-ZrO₂-40 vol.% TiO₂ mixtures sintered at 1300 and 1500°C (Miao, et al., 2004).

2.3.1.3. Addition of TiO₂ in alumina, zirconia composites

Although adding titania to alumina and zirconia has been widely studied, there is not much research working on its effect of composite of alumina and zirconia. One of the works that has been done is by Hwang and Chang (1996) on a composite of 15 mol.% ZrO₂ + (1.5–7.5 mol.%) TiO₂ + (83.5-77.5 mol.%) Al₂O₃. Dissolution of titania in zirconia and increasing the grain sizes of both Al₂O₃ and ZrO₂ by raising TiO₂ content were reported (Hwang & Chang, 1996). The existence of Al₂TiO₅ phase was only reported for the specimen with 7.5 mol.% TiO₂, which was considered to contain titania higher than the solubility limit of zirconia (Figure 2.22) (Hwang & Chang, 1996). Through more detailed examinations, it was argued that the most Ti ions were found in (Zr,Ti)O₂ grain, and Ti ion concentration decreased from the center to the grain boundary of (Zr,Ti)O₂ grains (Figure 2.23 and Figure 2.24) (Hwang & Chang, 1996). In addition, during the hot pressing process, the small number of Ti ions would diffuse to the alumina grains to form Al₂TiO₅; therefore, it could be concluded why the aluminium titanite phase was only present in samples containing 7.5 mol.% TiO₂ (Figure 2.25) (Hwang & Chang, 1996).

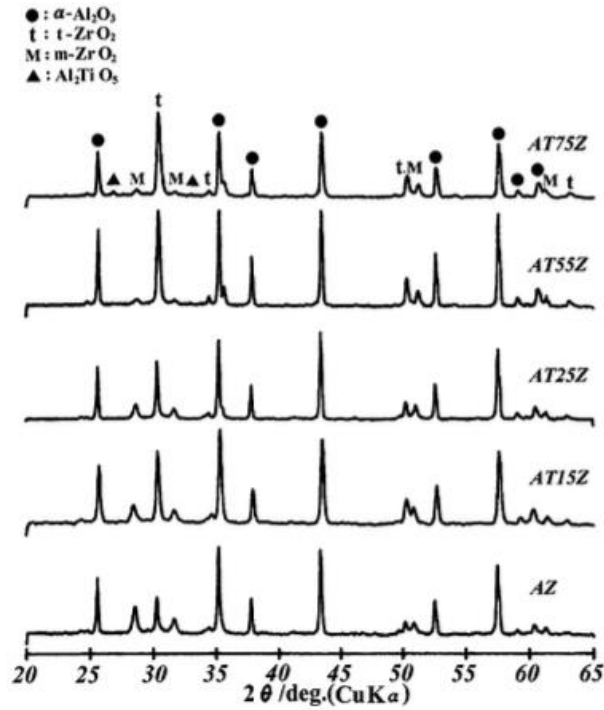
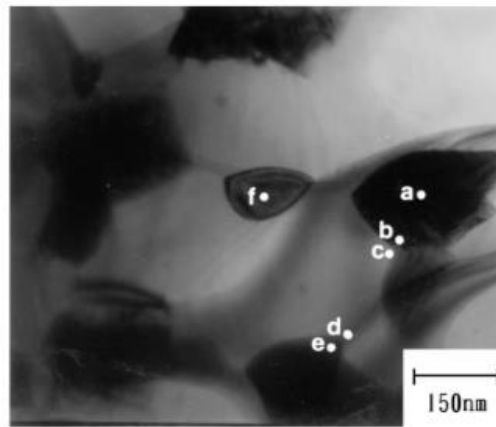
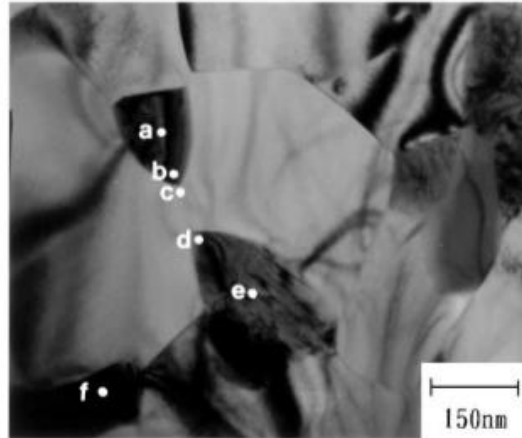


Figure 2.22. X-ray diffraction patterns of ZTA specimen hot-pressed at 1350°C for 1 h (Hwang & Chang, 1996).



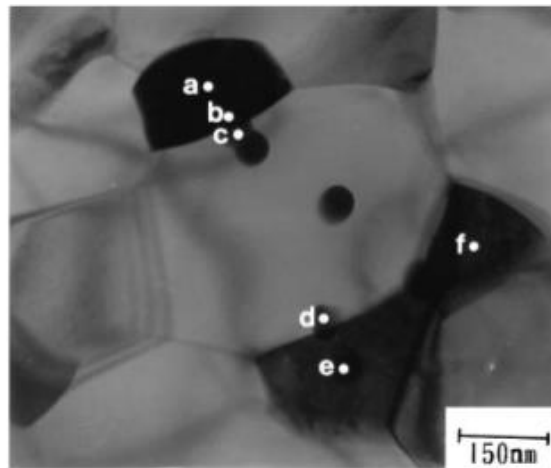
	a	b	c	d	e	f
I_{Ti}	4667	558	146	166	950	2192
I_{Zr}	24262	1968	12	34	3430	12656
I_{Al}	6003	21317	15485	12040	9387	3087
Ti (%)	13.4	2.3	0.9	1.1	6.9	12.2

Figure 2.23. AEM micrograph and relative element concentration of the specimen with ZTA+2.5 mol.% TiO_2 (AT25Z) hot-pressed at 1350°C for 1 h (Hwang & Chang, 1996).



	a	b	c	d	e	f
I_{Ti}	1819	1323	49	985	1223	1418
I_{Zr}	6257	4576	7	3174	3369	4021
I_{Al}	137	1387	5125	1013	440	150
Ti (%)	22.2	18.2	0.9	19.0	24.3	25.4

Figure 2.24. AEM micrograph and relative element concentration of the specimen with ZTA+5.5 mol.% TiO₂ (AT55Z) hot-pressed at 1350°C for 1 h (Hwang & Chang, 1996).



	a	b	c	d	e	f
I_{Ti}	4696	1717	103	2522	5150	5151
I_{Zr}	11454	4357	159	3931	11138	13537
I_{Al}	867	8928	12713	10974	640	908
Ti (%)	27.6	11.5	0.8	14.5	30.4	26.3

Figure 2.25. AEM micrograph and relative element concentration of the specimen with ZTA+7.5 mol.% TiO₂ (AT75Z) hot-pressed at 1350°C for 1 h (Hwang & Chang, 1996).

Similarly, dissolution of titania in the zirconia lattice improved tetragonal phase stability but also could enhance grain growth, which resulted in increased intragranular nano dispersion, were reported by Nawa et al. (1998) on addition of 0-3 mol.% titania in 12Ce-TZP-Al₂O₃ composite.

The same effect of titania addition on improving of densification and sintering of the composite was reported by Osendi and Moya (1988) for the composites of Al₂O₃+8vol.% ZrO₂ and adding up to 5mole.% TiO₂, though this study's results did not support the effect of titania on enhancing stabilization of tetragonal zirconia for these composites.

Densification

Adding titania to ZTA composites was found to promote densification at the initial stage of sintering like the same effect on densification of alumina and zirconia individually. In fact, the same argument can be applied for the effect on titania on composite of alumina and zirconia, ZTA. Based on this argument, titanium ions, Ti⁴⁺, improve sintering by substituting of Al³⁺ ions and creating aluminium vacancies and enhancing the diffusion of Al³⁺ (Hwang & Chang, 1996; Osendi & Moya, 1988). On the other hand, as stated above, titania first dissolves in zirconia rather than alumina, and in the reducing atmosphere such as Ar, (Zr,Ti)O₂ might be reduced to (Zr,Ti)O_{2-x} which generates the lattice defects (Hwang & Chang, 1996). In this case, by increasing the content of TiO₂ in the composite, the more Ti ions will diffuse out of (Zr,Ti)O_{2-x} to the alumina and the more Ti⁴⁺ will be generated, which will improve the sintering of the composite (Hwang & Chang, 1996).

Increasing amount of titania has, however, not had the same observed effect on densification among researchers. In work by Nawa et al. (1998), a decrease of density was reported by increasing titania content (especially more than 1 mol.%) to 12Ce-TZP+30vol.% Al₂O₃ composites and increasing temperature (Figure 2.26), which was attributed to forming solid solution of titania in tetragonal zirconia. This is in contrast with the findings of Pandolfelli et al. (1991) who reported relative density of 100% for ZTA samples containing 2.5 mol.% titania compared to that of 98% for samples with 1.5 mol.%. Pandolfelli et al. (1991) argued this enhancement of densification by titania

addition based on the lattice defects created by sintering zirconia-titania solid solution discussed above, which higher amount of titania could increase them.

However, at the final stage of sintering, this effect was not recognized by Osendi and Moya (1988) through reaching the same level of densification at 1600°C in both samples of with and without doped titania.

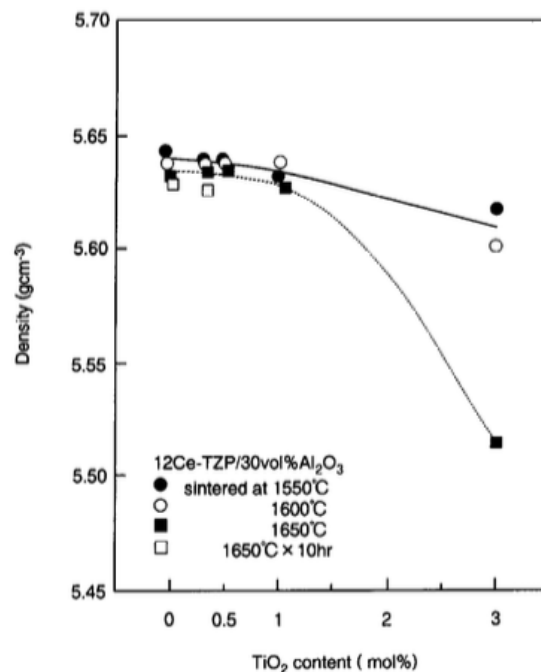


Figure 2.26. The density as a function of TiO₂ content for the 12Ce-TZP+30 vol.% Al₂O₃ composites sintered at various conditions. The solid line represents the variation of the results taken at all sintering temperatures except for 1650°C, while the dotted line shows the variation of the result of 1650°C (Nawa, *et al.*, 1998).

Microstructure

Adding titania is reported to cause grain growth in ZTA composites during sintering process as a result of the effect of Ti ions on increasing mobility of grain boundaries and diffusion rate as discussed above (Hwang & Chang, 1996; Osendi & Moya, 1988). Although grain growth occurred for both alumina and zirconia particles, it has been reported to affect alumina grains more significantly (Osendi & Moya, 1988). As discussed before, increasing TiO₂ content can promote diffusion rate and therefore

grain growth, while at higher amount of titania; e.g. more than 7.5 mol.% (Hwang & Chang, 1996); forming of Al_2TiO_5 phase can result in finer microstructure (Figure 2.27).

In the work done by Nawa et al. (1998) adding 0-1 mol.% titania in 10Ce-TZP+30 vol.% Al_2O_3 , two type of transgranular alumina grains were found; nano-dispersion particles trapped within zirconia grains during the initial sintering stages, and triple junction particles trapped into the zirconia grains during intermediate sintering stage when grain boundaries of zirconia disappeared. The second type of these transgranular grains had larger grain sizes (Figure 2.28) (Nawa, et al., 1998).

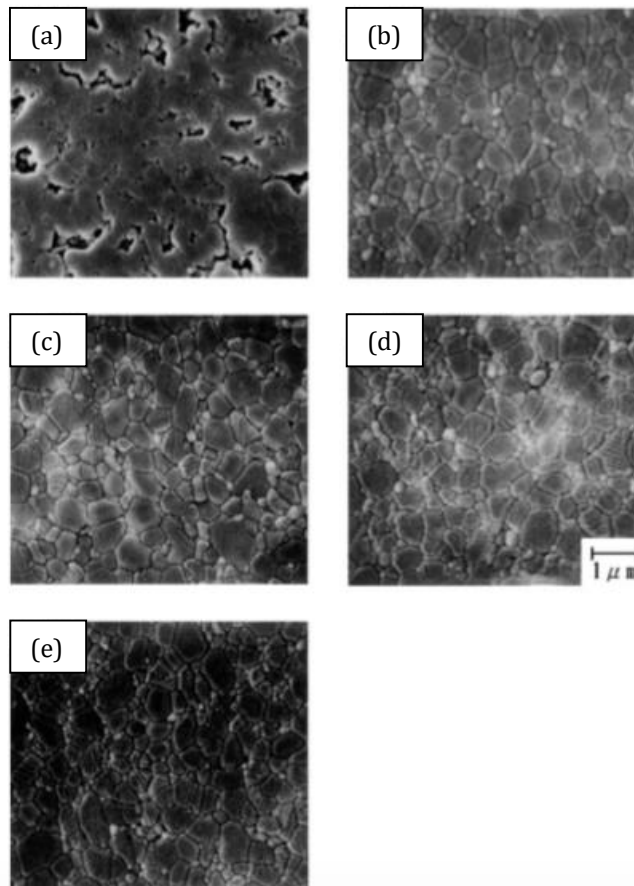


Figure 2.27. Scanning electron micrographs of thermally etched surfaces of ZTA specimen with 0 mol.%(a), 1.5 mol.%(b), 2.5 mol.%(c), 5.5 mol.%(d), and 7.5 mol.%(e) TiO_2 hot-pressed at 1350°C for 1 h (Hwang & Chang, 1996).

It has been discussed in chapter 2.3.1.1 that elongated grains would be formed by adding titania in alumina ceramics. This kind of microstructure for alumina-zirconia

composites was not reported by most of researchers worked on addition of titania to this composites (Nawa, et al., 1998; Hwang & Chang, 1996; Osendi & Moya, 1988). However, Nawa et al. (1998) found elongated Al_2O_3 -like phase at the grain boundaries of zirconia for all addition of 0.05, 0.2, 0.5 and 1 mol.% TiO_2 doped 10Ce-TZP+30 vol.% Al_2O_3 composites with relatively same distribution ratio (Figure 2.29).

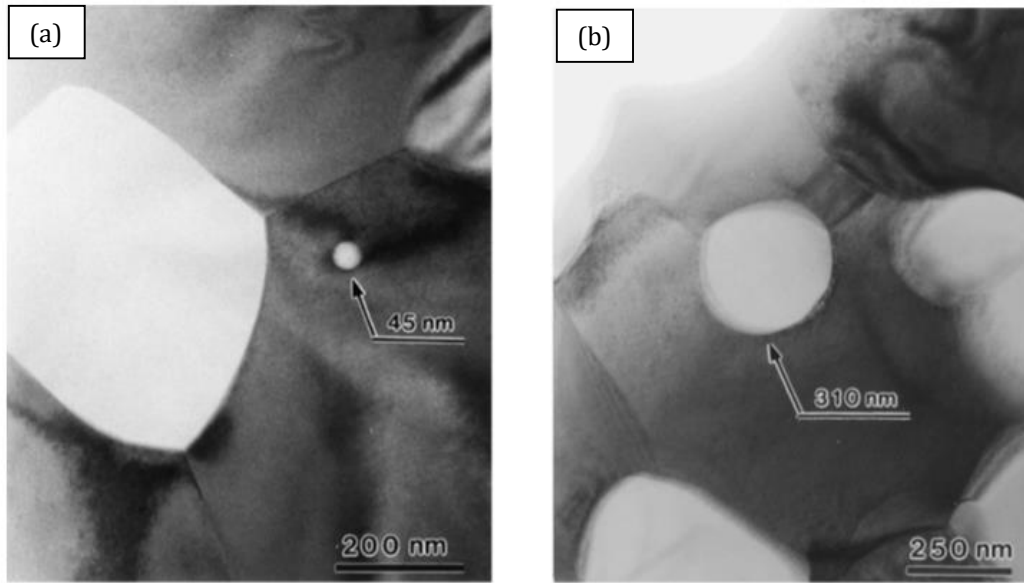


Figure 2.28. TEM images of the different sizes Al_2O_3 particles trapped within the zirconia grains for the 10Ce-TZP+30 vol.% Al_2O_3 composite sintered at 1500°C : (a) several 10 nm sized Al_2O_3 particles, (b) larger Al_2O_3 particle of about 300 nm (Nawa, et al., 1998)

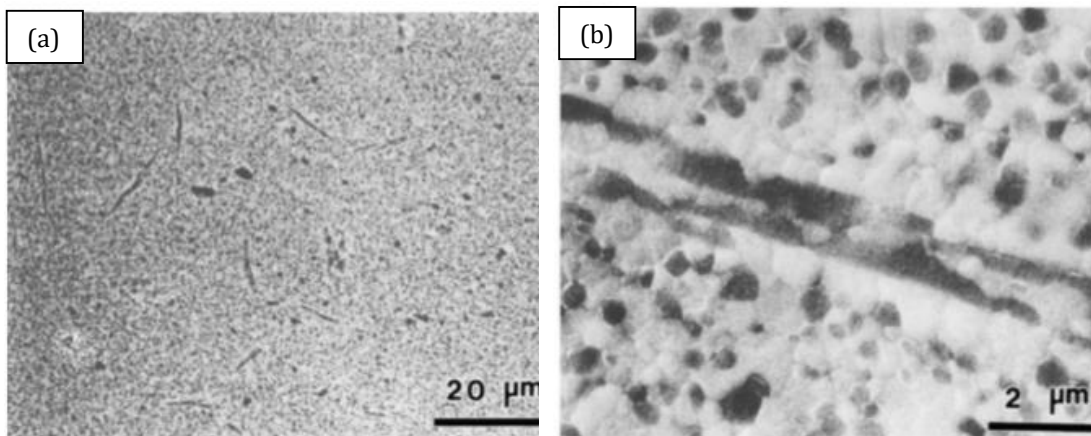


Figure 2.29. SEM photographs of thermal-etched surfaces for the 10Ce-TZP+30vol.% Al_2O_3 composite sintered at 1500°C : (a) microstructure including elongated Al_2O_3 -like phases, (b) at higher magnification (Nawa, et al., 1998).

Mechanical and wear properties

It is clear that mechanical properties of the ZTA composites, are strongly related to size, size distribution and location of zirconia particles as well as stabilization of tetragonal zirconia (Hwang & Chang, 1996; Osendi & Moya, 1988), and as titania affects all of these microstructural features it is expected to impact these properties to great extent.

Adding titania was reported to decrease the lattice constant and lattice volume of zirconia as a result of smaller ionic radius of titania ion than that of Zr^{4+} , and its dissolution in tetragonal zirconia lattice leading to stabilization of tetragonal zirconia discussed above (Nawa, et al., 1998). It was also reported that small addition of titania promoted flexural strength of the composite (Figure 2.30.a), which could be due to its beneficial effect on pore reduction and composite densification (Yang, et al., 2009; Nawa, et al., 1998; Hwang & Chang, 1996), and on increasing intragranular nano dispersions due to its ability to increase grain growth (Figure 2.30.b) (Hwang & Chang, 1996).

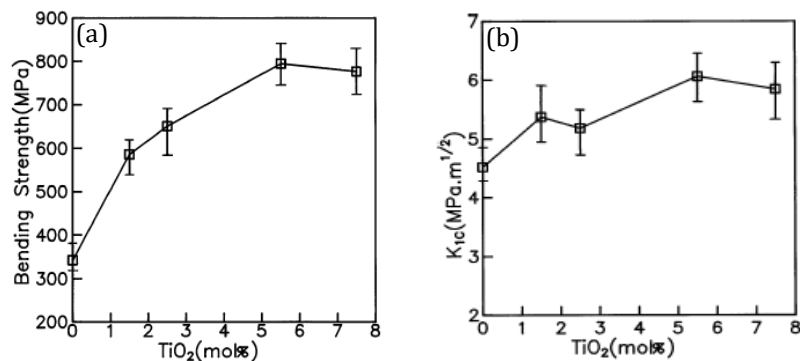


Figure 2.30. (a) Bending strength of hot-pressed ZTA specimens containing various amounts of TiO_2 , (b) Fracture toughness of hot-pressed ZTA specimens containing various amounts of TiO_2 (Hwang & Chang, 1996).

Although small additions of titania seems to improve strength of the composite, its high content can cause an adverse effect as a result of zirconia excessive grain growth (Nawa, et al., 1998; Hwang & Chang, 1996). For instance, the decrease of strength was reported by Nawa et al. (1998) for titania addition of more than 1 mole.% in alumina-zirconia composites and 3 mole.% samples for higher sintering temperature (Figure 2.31.a).

Through studying effect of titania on hardness of alumina-zirconia composites, the improved Vickers hardness was achieved by Yang et al. (2009), which was due to the raising the cohesion between grains of alumina, titania and zirconia, as well as purifying and strengthening the phase interfaces and/or the grain boundaries. In contrast, Nawa et al. (1998) reported decrease of Vickers hardness by increasing titania content and increasing temperature, which could be resulted from formation of tetragonal zirconia. However, a slight hardening was confirmed by them for titania addition of 0.2 to 0.5 mole.%, which was attributed to higher amount of transgranular nanodispersion (Figure 2.31.b) (Nawa, et al., 1998).

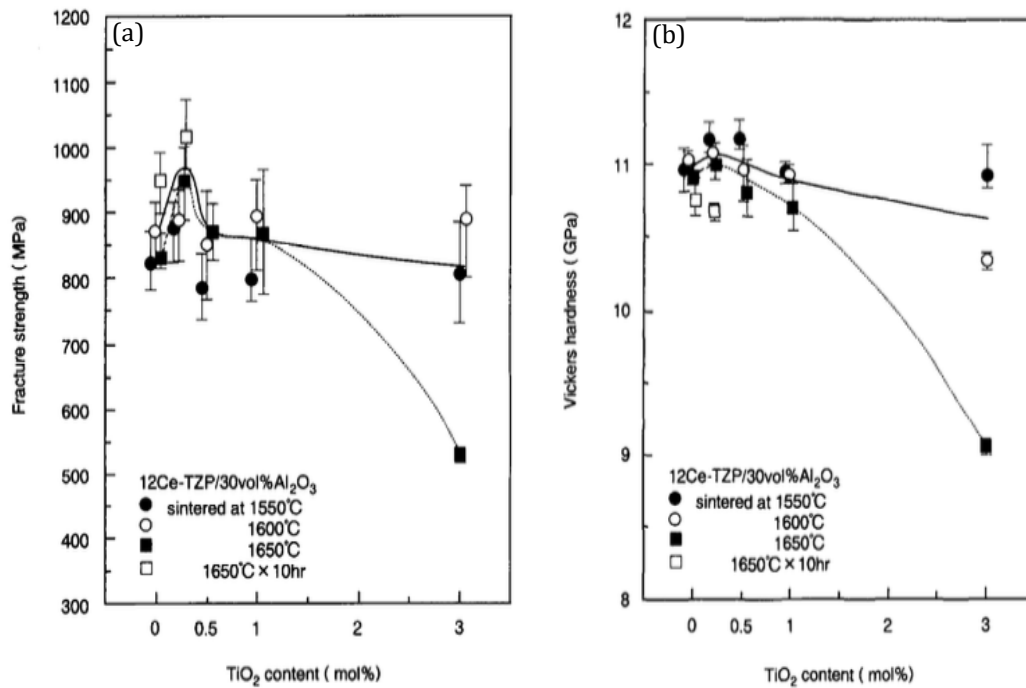


Figure 2.31. The fracture strength (a) and Vickers hardness (b) as a function of TiO₂ content for the 12Ce-TZP+30vol.% Al₂O₃ composite sintered at various conditions. The solid line represents the variation of the results taken at all sintering temperatures except for 1650°C, while the dotted line shows the variation of the results of 1650°C (Nawa, et al., 1998).

On the other hand, studying the effect of titania on toughness of the composite is more complicated due to different toughening mechanisms involved, which seems to be responsible for contradictory results reported by researchers.

Degradation of toughness with an exception for small additions (less than 1 mol.%) was

reported by Nawa et al. (1998) for titania doped alumina-zirconia composites. This tendency was attributed to the effect of titania on high stabilization of tetragonal phase and its resistance to stress induced transformation. Similar results were achieved by Osendi and Moya (1988) for titania doped ZTA composite and related to the changes of zirconia size distribution occurred by high amount of titania, which could influence the population of transformable particles inside the critical transformation zone.

For the small addition of titania, it was reported that toughness does not show noticeable changes compared with non-doped samples (Figure 2.32), which was supposed to be due to crack deflection by elongated Al_2O_3 particles working against toughness degradation mechanisms (Nawa, et al., 1998; Nawa, et al., 1998; Osendi & Moya, 1988). Consequently, the optimum amount of titania addition to alumina-zirconia composites was reported to be 0.05 mole.% (Nawa, et al., 1998), and 0.2 mole.% (Nawa, et al., 1998), which gave both high strength and high toughness.

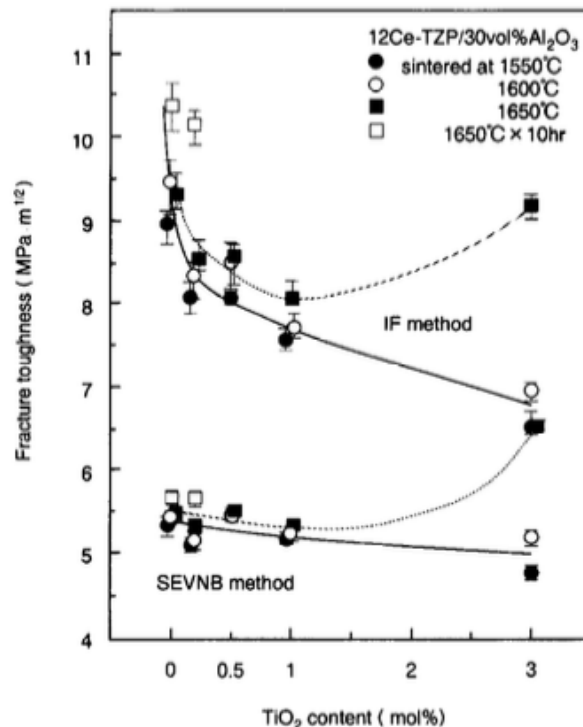


Figure 2.32. The fracture strength as a function of TiO_2 content, while was evaluated by both the IF (Indentation-Fracture) method and SEVNB (Single Edge V Notched Beam) method, for the 12Ce-TZP+30vol.% Al_2O_3 composite sintered at various conditions. The solid line represents the variation of the results taken at all sintering temperatures except for 1650°C , while the dotted line shows the variation of the results of 1650°C (Nawa, et al., 1998).

In contrast to the mentioned studies showing a decrease in toughness by added titania, it was found by Hwang and Chang (1996) that ZTA samples with 5.5 mole.% titania had higher strength and toughness in comparison with samples having 1.5, 2.5, as well as 7.5 mole.% TiO_2 (Figure 2.30.a). They discussed in their work that in titania doped ZTA composites, $(\text{Zr,Ti})\text{O}_2$ grains were surrounded and compressed by alumina grains; these compressive stresses would be decreased by adding more titania content as a result of increasing molar ratio of $(\text{ZrO}_2 | \text{TiO}_2) \text{Al}_2\text{O}_3$. However, the amount of tetragonal zirconia phase was increased by increasing titania content while its transformation to monoclinic would be limited by high titania addition, as stated above. Therefore, in the absence of transformation mechanisms for toughening for 5.5 mole.% TiO_2 , it is residual stresses from thermal expansion mismatch of alumina and zirconia which generates microcracking and crack deflections (Hwang & Chang, 1996).

As a result, it can be concluded that for the composites of zirconia toughened alumina by addition of titania residual stress played the main role for toughening (Hwang & Chang, 1996). It was also claimed that hot pressed ZTA composites doped with titania revealed higher bending strength rather than pressureless sintering as a result of their higher density and finer microstructure (Hwang & Chang, 1996).

In addition to improving and deteriorating effect of titania on strength and toughness discussed, it has been used widely as an additive to alumina-zirconia composites as a self-lubricating material resulting in reducing the friction coefficient and decreasing wear debris on the surface (Morillo, et al., 2009). To study the effect of TiO_2 on alumina and zirconia composites, Morillo et al. (2009) investigated the different nanocomposites of alumina, alumina-titania (10mol.%), and alumina-YTZP(15mol.%)-titania(10mol.%) in different wear conditions against alumina and silicon nitride balls. Their results showed that the steady minimum friction and wear rate in distilled water were found in the samples containing both titania and zirconia. They attributed these better wear properties to the formation of a tribofilm on the surface which removed and formed again during the sliding test, which is a competition between wear and film formation that protects the surfaces (Morillo, et al., 2009). This tribofilm was a smooth layer of silicon oxide in presence of water which formed on all of these three samples when using silicon nitride balls, significantly reducing the friction and wear. In addition, silicon oxide was reported to react slowly to produce a

more stable oxide and/or oxynitride when it was worn in water (Morillo, et al., 2009), which was believed to be the reason for their very low wear rate in comparison with the results of tests done against alumina balls (Figure 2.33). This decrease of coefficient of friction up to 0.2 for all samples was also seen for silicon nitride balls when the test was done in vivo condition in Fetal Bovine Serum Solution (FBSS) simulating atmosphere, while particularly ATZ showed the minimum wear in this condition as well (Figure 2.33 and Figure 2.34). The tribofilm composition in this case was found to be made of protein and phospholipids which left traces of carbon on alumina and Si_3N_4 balls after the test (Morillo, et al., 2009).

In conclusion, although titania is considered to be a good sintering aid for ZTA ceramics, there should be a careful control over its addition as its effect on microstructure can adversely affect mechanical properties.

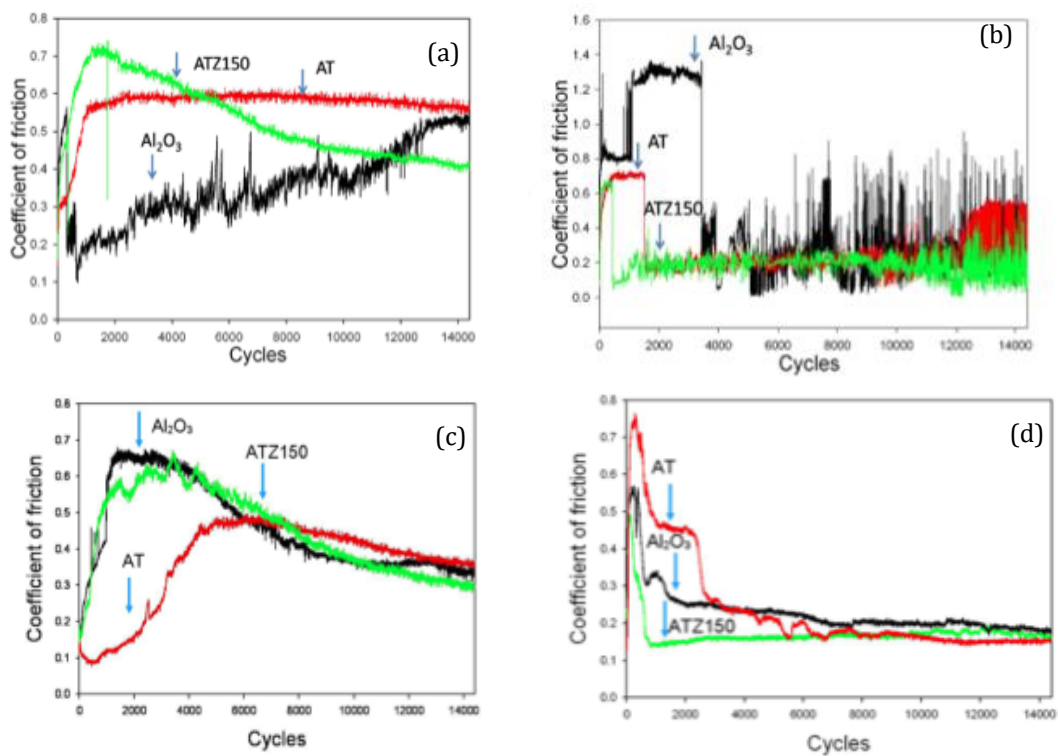


Figure 2.33. Coefficient of friction of Al_2O_3 nanocomposites slid (a) against alumina ball in distilled water, (b) against silicon nitride ball in distilled water, (c) against alumina ball in FBSS, (d) against silicon nitride ball in FBSS (Morillo, et al., 2009).

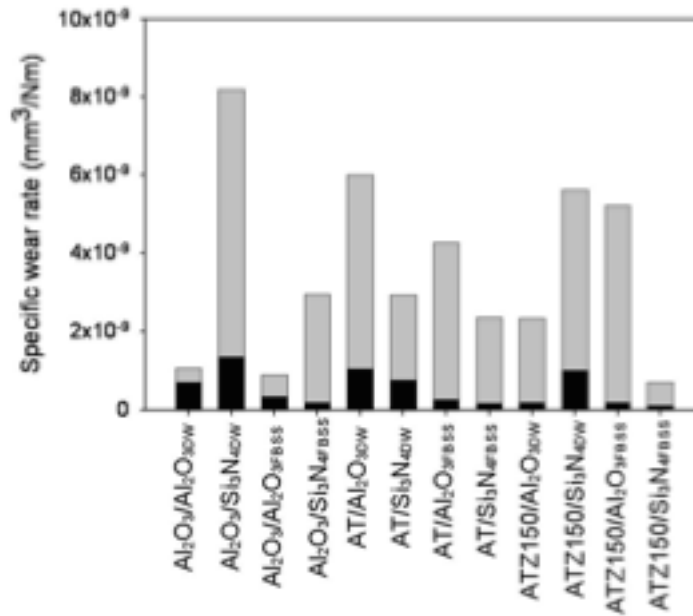


Figure 2.34. Specific wear rate of plate sample and counterface ball tested against Al₂O₃ and Si₃N₄ ball in distilled water and fetal bovine serum solution. Superior part of each bar corresponds to counterface ball (Morillo, *et al.*, 2009).

2.4. Tribological properties in hip joint replacements

In section 2.1, hip joint prostheses and their main critical characteristics were discussed. It has been mentioned that mechanical and tribological properties such as wear, friction and lubrication are the most important indicators to be considered in design and material selection for these bearing surfaces. It also has been noted that these properties should stay without any dramatic change in vivo for more than 20 years while tolerating two million or more motion cycles of loading each year.

In general, wear has been defined as the unwanted removal of solid materials from rubbing surfaces, which includes many diverse phenomena such as adhesion, abrasion, corrosion, and others, operating together or separately (Burwell, 1957/58). It also has been defined as the response of material to the localized stresses caused by normal forces and friction when surfaces are rubbed on each other (Fischer, et al., 2000).

According to Burwell (1957/58), there are at least four dominant and independent mechanisms for removing materials in rubbing surfaces with which understanding and predicting wear would be more comprehensive. He categorized these four mechanism as adhesive or galling wear, abrasive and cutting wear, corrosive wear, and surface fatigue (Burwell, 1957/58). He also classified one group as minor type including other instances of wear types which doesn't fall in any of those four main categories (Burwell, 1957/58). Today, these wear mechanisms have been developed and classified into eleven mostly observed types outlined in Table 2.4 (Ma, 2010; Hutchings, 1992).

Table 2.4. Definition and description of the common wear mechanisms (*Ma, 2010*).

Mechanism	Description
Adhesion	The transfer of material from one mating surface to another through atomic attraction. The bond formed is usually stronger than the shear strength of the softer material. Also defined as galling or scuffing.
Abrasion	Softer material is removed by ploughing or gouging by harder particles. These particles can be embedded into the mating counterface (2-body) or loose (3-body). Also defined as scoring.
Corrosion	A corrosive environment produces a reaction production on one or both sliding surfaces, which is subsequently removed by the relative motion between the two. Also includes metallic oxidation.
Fatigue	Repeated cyclic sliding stresses cause sub-surface cracks which eventually result in spalling of large material fragments.
Erosion	Can be also grouped into abrasion wear, but material is removed by the particles striking the surface, which are carried by a gas stream entrained in a flowing liquid.
Delamination	Removal of sheet-like wear debris due to the nucleation and propagation of sub-surface cracks parallel to the sliding surface.
Fretting	Wear of material due to oscillatory movement. Includes the generation of wear debris by adhesive and corrosive mechanisms.
Impact Chipping	Small-scale spalling as though small chips knocked out of the hard material surface due to brittle fracture under high impact.
Tribochemical Wear	Very important to the wear of ceramics. Environmental factors influence plastic flow by affecting the mobility of near-surface dislocations, and also lead to the formation of transfer films.
Cavitation	Occurs via the collapse of vapour bubbles in the lubricant which causes acceleration and impingement of liquid at high velocity on the surface.

2.4.1. Friction

Friction is one of the main engineering fields in tribology applications. Friction of two contacting materials is a very complicated physical phenomenon, which includes elastic and plastic deformation between two surfaces, microfracture, interaction of wear debris and particles, chemical reactions, excitation of electrons and phonons, and adhesion of two contacting surfaces (Popov, 2010).

Like metals, ceramics show an anisotropic friction characteristic, and the lowest coefficient of friction of them have been reported when rubbing is placed on their preferred slip plane and in preferred slip direction (Buckley & Miyoshi, 1984). However, in ceramics, plastic deformation of contacting bodies is very limited and it is mostly elastic deformation which occurs at counterfaces rather than plastic deformation (Fischer, et al., 2000; Buckley & Miyoshi, 1984; Miyoshi, 1988). When this elastic deformation exceeds its limit, brittle fracture happens; therefore, friction in ceramics is a function of shear strength of the elastic contact area (Fischer, et al., 2000; Buckley & Miyoshi, 1984; Miyoshi, 1988). The drawback of brittle wear in ceramics for tribology application can be retreated by lubricating through using lubricant fluids or by developing self-lubricating ceramics to diminish thermal stresses in friction and raise the critical load of initial fracture (Buckley & Miyoshi, 1984; Rainforth, et al., 2002).

In lubricated systems, there are lots of factors affecting friction, the two most important of them are lubricant viscosity and sliding velocity, which are combined and formed a dimensionless parameter called Sommerfeld number as following (Ma, 2010; Hutchings, 1992):

$$Z = \frac{\eta v}{N}$$

η	=	Viscosity of the lubricant (Pa.s)
v	=	Sliding speed (m/s)
N	=	Normal load (N)

This value is used in plotting Stribeck curve, which shows variation of friction coefficient against Sommerfeld number in lubricated system (Ma, 2010). The Stribeck curve indicates the lubrication regimes, defined as full-film or fluid-film lubrication (HL), mixed lubrication (ML) and boundary lubrication (BL) (Figure 2.35) (Ma, 2010; Dowson, 2001; He, et al., 1997). In the full-film lubrication regime, the contact surfaces are separated by the lubricant with a comparably thick film. However, in boundary lubrication, direct contact occurs between

asperities because the film thickness is low (Hutchings, 1992; Dowson, 2001). The mixed lubrication regime occurs when some asperities are in contact while other asperities are separated by a fluid lubricant (Hutchings, 1992; Dowson, 2001). The typical friction coefficient for various bearings of artificial hip joints were reported by Jin et al. (2006) to be 0.1-0.7 in boundary, 0.01-0.1 in mixed, and 0.001-0.01 in full-film lubrication regime. In general, it is preferred for practical application that tribosystem is in fluid-film or mixed lubrication regime (He, et al., 1997).

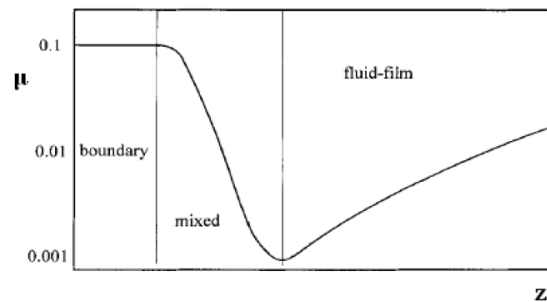


Figure 2.35. Schematic of stribeck curve and different regimes (Dowson, 2001)

2.4.2. Wear of ceramics

Wear of ceramics is a complex system function, which is highly dependent on operating factors such as applied load, sliding distance, wear speed and duration; tribological factors such as contact geometry, surface roughness, environment and lubrication; and microstructural factors such as grain size and shape, and crystallographic orientation; and mechanical properties such as hardness and fracture toughness (Fischer, et al., 2000; Hsu & Shen, 2004; Rainforth, 1996).

Both ceramics and metals show elastic and plastic deformation at contact areas during the wear procedure; for ceramics, however, with increasing the contact stresses and exceeding a very low critical value, fracture happens (Fischer, et al., 2000; Miyoshi, 1988). The brittleness of ceramics in comparison with metals has been attributed to their limited number of slip systems and difficult dislocation glide (Fischer, et al., 2000; Miyoshi, 1988). This inherent characteristic of ceramics clarifies why, despite the observation of dislocations and their pile-ups at grain boundaries, no distinct plastic deformation has been reported during the wear test, like the deformation seen in wear of metals (Erickson, et al., 1993; Wang & Hsu, 1996; Steijn, 1961; Yust & Allard, 1989; Park, et al., 1990; Zutshi, et al., 1994; Rigney, 1988; Rigney & Hammerberg, 1998). Consequently, in spite of the common dependence of wear resistance to

hardness in other materials, for ceramics fracture toughness would be a more reliable factor to predict wear behaviour (Fischer, et al., 1989).

From the mechanical point of view contact stresses play a key role in wear characteristics of ceramics. Contact stresses are mainly inhomogeneous and tri-axial stresses determined by mechanics of the test such as load, initial contact area and friction coefficient as well as microgeometry of the counterface like surface roughness (Hutchings, 1992; Williams, 1994). The difference of the nature of contact stresses between metals and ceramics is that in metals, plastic deformation of asperities cause the local compressive stresses under the asperities to be equal to the material's hardness while in ceramics, elastic deformation of asperities cause these stresses to be dependent on the initial contact radius of asperity (Fischer, et al., 2000; Rainforth, 1996).

Fischer (2000) showed that despite independence of contact stresses to applied load in metals, this independency in ceramics happens only at various depth from the contact surface (Fischer, et al., 2000). He attributed this phenomenon to elastic deformation of asperities and argued that at the subsurface very close to contact counterface, the contact stress would be much higher than the macroscopic values, known as Hertzian stresses. He called these stresses “the shallow stresses”. By increasing depth, the local stress which is the sum of the stresses of neighbouring asperities would decrease and approach to the values calculated by macroscopic contact geometry. He also found that the depth of change from shallow stresses to macroscopic stresses would be decreased by increasing the load as a result of decreasing the asperity distances (Fischer, et al., 2000).

It should be pointed out the wear is a dynamic process and dominant wear mechanism in a particular operating condition would not be the same with another conditions even with the same materials (Wang & Hsu, 1996).

2.4.2.1. Wear transition

The main characteristics of wear in ceramics is based on the severity and ratio of wear rate, which categorized in two types known as “mild wear” and “severe wear”, by the specific wear rates less and more than $10^{-6} \text{ mm}^3 (\text{Nm})^{-1}$ respectively (Adachi, et al., 1997; Rainforth, 2004;

Kato & Adachi, 2002; Hsu & Shen, 2004; Kerkwijk, et al., 2004). The transition from mild to severe wear is often sudden and accompanied by large increase in coefficient of friction and wear rate (sometimes several orders of magnitude) and start of brittle surface fracture, and is determined by operating conditions such as normal load, temperature, and sliding velocity and distance (Hsu & Shen, 2004; Adachi, et al., 1997; Rainforth, 2004; Wang, et al., 1995). In addition, materials characteristics such as grain size, grain boundary energy release rate, grain fracture energy release rate, composition, defects, and residual surface stresses can affect transition from mild to severe wear (Hsu & Shen, 2004; Adachi, et al., 1997; Rainforth, 2004).

In order to map the wear of ceramics and its affecting factors, especially in severe zones, two dimensionless parameters have been proposed by researchers called mechanical severity of contact ($S_{c,m}$) and the thermal severity of contact ($S_{c,t}$) (Adachi, et al., 1997; Kato & Adachi, 2002). The mechanical severity of contact is the critical condition where in sliding contact area tensile stresses at crack tips produce vertical surface cracks, and thermal severity of contact is the condition where thermal stresses resulted from frictional heating produce mentioned vertical surface cracks (Kato & Adachi, 2002). These parameters are defined by further formula (Adachi, et al., 1997; Kato & Adachi, 2002):

$$S_{c,m} = \frac{(1+10\mu)P_{max}\sqrt{d}}{K_{IC}}$$

- $S_{c,m}$ = Mechanical severity of contact
- μ = Friction coefficient
- P_{max} = Maximum Hertzian contact pressure
- d = Crack length
- K_{IC} = Fracture toughness

and

$$S_{c,t} = \frac{\gamma\mu}{\Delta T_s} \sqrt{\frac{VWH_v}{k\rho c}}$$

- $S_{c,t}$ = Thermal severity of contact
- γ = Heat partition ratio
- μ = Friction coefficient
- ΔT_s = Thermal shock resistance
- V = Sliding velocity
- W = Load

- H_v = Vickers hardness
- k = Thermal conductivity
- ρ = Density
- c = Specific heat

Figure 2.36 shows the relationship between wear rate and mechanical and thermal severity of contact for three main engineering ceramics.

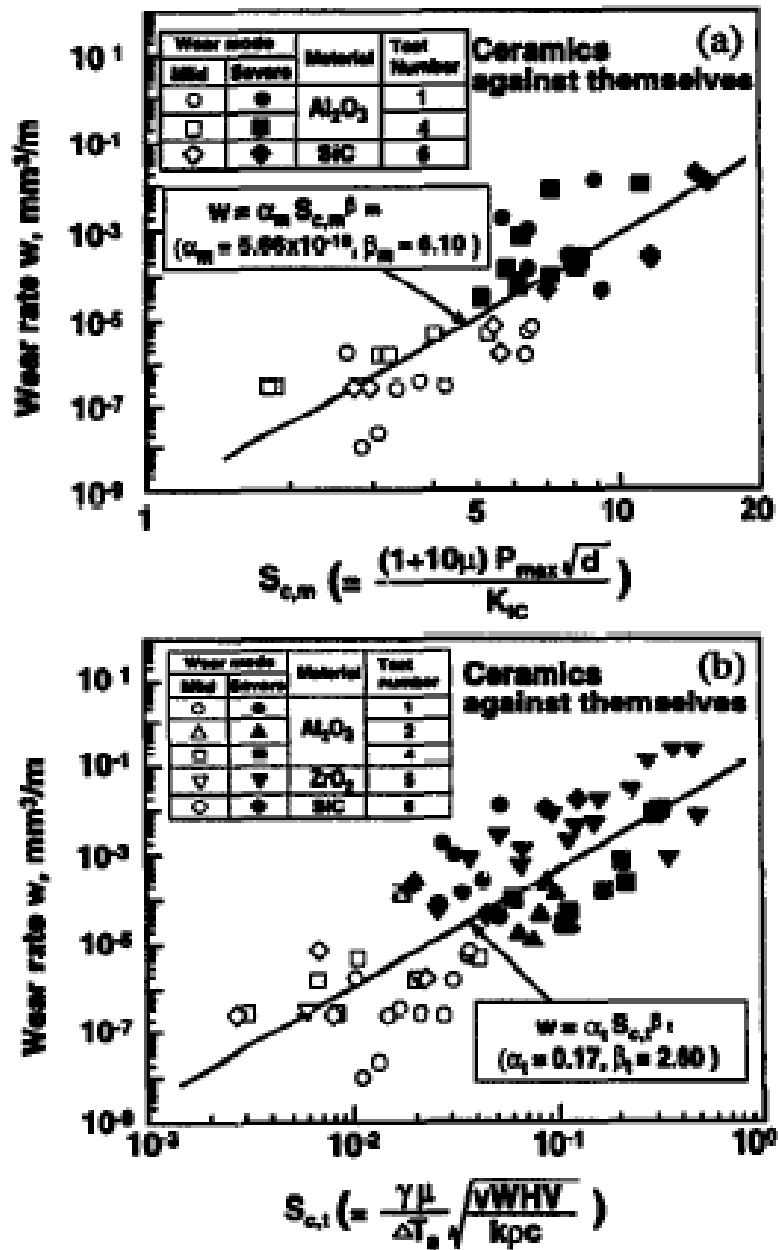


Figure 2.36. Distribution of wear rate caused by mechanical wear and the value of mechanical severity of contact $S_{c,m}$ (a), and distribution of wear rate caused by thermal wear and the value of thermal severity of contact $S_{c,t}$ (b) (Adachi, et al., 1997)

In the mild wear regime the surface is mainly smooth which means the contacting surfaces have preferably polished each other (Adachi, et al., 1997; Rainforth, 2004). Consequently, there are only some fine scale features on the surface such as very small mechanically-formed debris (one-tenth or less than grain size) (Rainforth, 2004; Kato & Adachi, 2002). Microscale abrasion, differential wear between grains, and the surface with no significant fracture are other visible features reported at this stage (Figure 2.37) (Rainforth, 2004; Kato & Adachi, 2002). However, in the severe wear regime roughening of the surfaces occurs and breaking out significant pieces of material due to mechanical cracking of grains or delamination of tribofilms can be seen on the surface (Adachi, et al., 1997; Kato & Adachi, 2002). As mentioned before, operating conditions such as normal load and sliding velocity are crucial factors in wear transition from mild to severe as is illustrated in Figure 2.38 (Kato & Adachi, 2002).

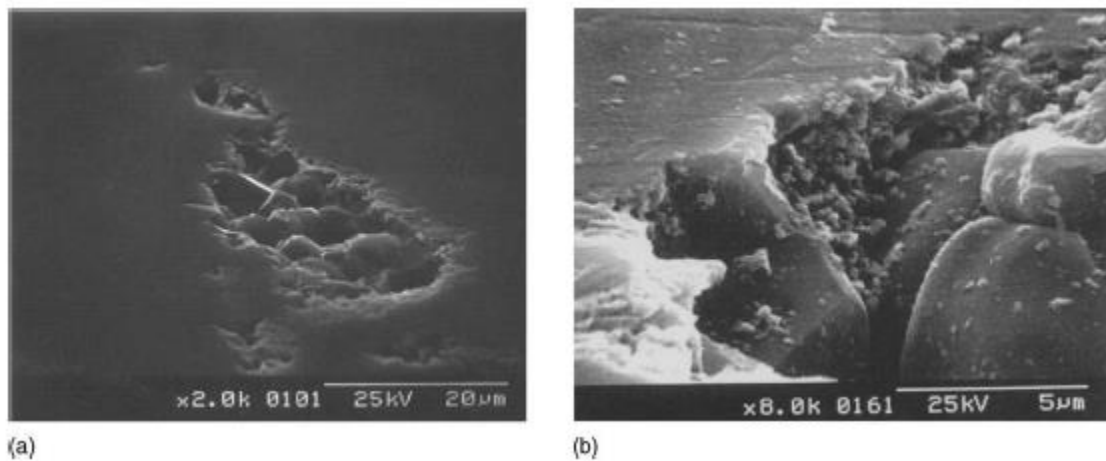


Figure 2.37. The smooth wear surface formed in mild wear (a) and the side view of the layer which shows the size of debris (b). (Kato & Adachi, 2002)

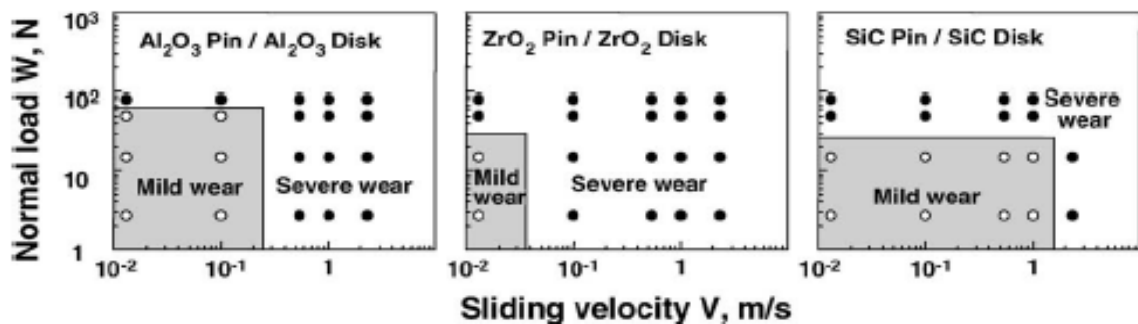


Figure 2.38. Regions of mild and severe wear observed by changing normal load and sliding velocity with Al_2O_3 , ZrO_2 , and SiC . (Kato & Adachi, 2002)

From the microstructural point of view, some researchers considered these two main wear categories as deformation-dominated and fracture-dominated wear mechanism (Hsu & Shen, 2004; Wang & Hsu, 1996; Wang, et al., 1995; He, et al., 1993). Despite the ionic and covalent atomic bonds of ceramics, dislocation accumulation and limited plastic deformation were reported in wear of ceramics, which were rarely observed in tensile or bending tests (Wang & Hsu, 1996; Wang, et al., 1995). This plastic deformation is localized and occurs at the asperity tips since they experience high flash temperature as a result of low thermal conductivity of ceramics as well as high contact stress (Wang, et al., 1995). Thus, by exceeding the plasticity limit, limited dislocation movement and twin generation occurs at the asperity tips which leads to microcracking and production of fine wear debris, as will be discussed further (Hsu & Shen, 2004; Wang & Hsu, 1996). This is why the mild wear region in ceramics has been called as the deformation-dominated mechanism whereas in severe wear or fracture-dominated regime, the microcracks propagate rapidly and macroscopic fracture occurs (Wang, et al., 1995). The importance of plastic deformation in ceramics is due to their role in further grain boundary cracking and intergranular catastrophic fracture (Rainforth, et al., 2012).

The wear transition is a time dependent mechanism due to the process of dislocation accumulation resulting in microcracks nucleation and propagation of these microcracks leading to intergranular fracture (Wang & Hsu, 1996; Adachi, et al., 1997). Changes of surface roughness or abrasive body dimension during time, which results in higher asperities contact stresses, and differential thermal stresses from high speed sliding should also be considered as contributing factors to time dependency of wear transition (Hsu & Shen, 2004; Wang & Hsu, 1996). The wear transition has also been reported to be dependent on crystallographic orientation which is consistent with plastic deformation theory in mild wear, indicating that surface and environmental factors would affect wear by controlling surface plasticity (Barceinas-Sánchez & Rainforth, 1998).

Occurrence of severe wear in sliding wear has been attributed by some researchers to maximum tensile stresses formed at the rear of sliding contact (Fischer, et al., 2000; He, et al., 1997; Adachi, et al., 1997; Wang, et al., 1995); for instance, Wang et al. (1995) defined severe wear as tensile crack-controlled wear mechanism. Similarly, Fischer et al. (2000) argued that these tensile stresses initiated a half-moon cracks perpendicular to the surface (Figure 2.39), which propagated further in a direction parallel to the surface as a result of fatigue stresses until detaching large pieces of surface happens (Fischer, et al., 2000). He et al. (1993) related

formation of these cracks to friction and tensile stresses at asperities' trailing edges and stated that maximum shear stress had been subsurface when the coefficient of friction was around 0.1. They argued that the shear stress would cause propagation of cracks at grain boundaries and tensile stress would assist the cracks to reach the surface and detach the grain or particle from the surface (He, et al., 1993). After detaching the particle, third-body abrasion occurred and the contact stress distribution underwent changes in which the most pressure concentration would be on third bodies (He, et al., 1993). When the particle tips experienced stresses greater than their fracture toughness, medium and lateral cracks began to form and propagate, and severe wear occurred in which the whole grains or a cluster of them were removed from the surface (He, et al., 1993). In contrary to the effect of tensile stresses on fracture-dominated wear regime, Hsu and Shen (2004) stated that tensile stresses were important in producing microfracture at subsurface grain boundaries in mild wear regime, and when contact pressure was high enough to induce fracture, compressive stresses would be more crucial to wear.

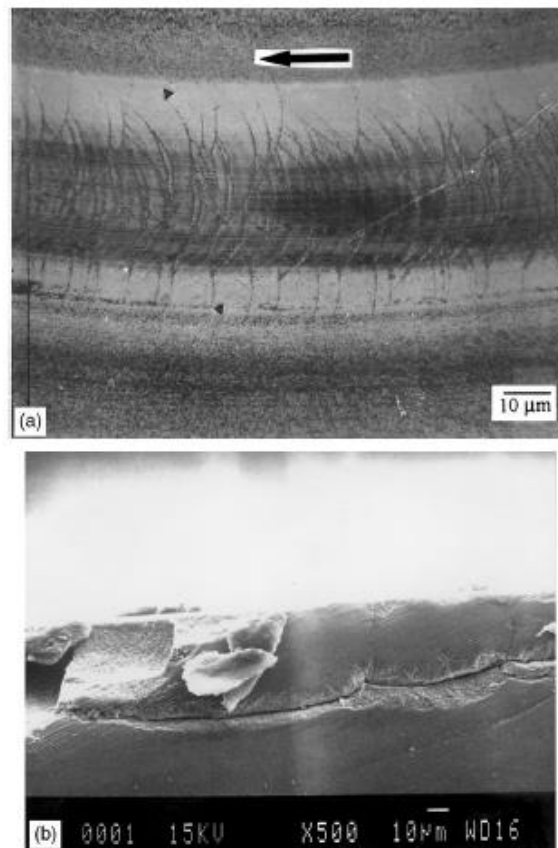


Figure 2.39. Optical micrograph of semi-circular macroscopic cracks on the worn surface of a flat Al_2O_3 specimen against an Al_2O_3 ball (a), cross-section of zirconia plate with similar semi-circular cracks shows that these cracks propagate normal to the surface, then turn abruptly parallel to the surface (b) (Fischer, et al., 2000)

It should be noted that for common tribological purposes, wear mechanism should drop in mild region having the specific wear rate less than $10^{-6} \text{ mm}^3 (\text{Nm})^{-1}$, which is the mild wear upper limit (Adachi, et al., 1997; Rainforth, 2004; He, et al., 1993).

2.4.2.2. Surface Analysis

Surface analysis of wear scars is the main method for wear evaluation and modelling wear studies. Based on a wide investigation made by Shishido et al. (2006) on the surface of several individual scars on retrieved CoC implants for total hip arthroplasty, a grading map was proposed showing the degree of wear progression as follows (Shishido, et al., 2006):

Grade I: original surface as ground by manufacturer (machine-scratches with rounded pits or craters)

Grade II: low wear as evidenced by partial removal (polishing) of the original machine scratches and with rounded pits evident

Grade III: mild wear as evidenced by total removal of the original machine tracks and relief-polishing showing grain structure

Grade IV: progressive wear as evidenced by intergranular fracture and grain pullout with formation of craters localized regions in an otherwise intact surface

Grade V: disruptive wear as characterized by intergranular fracture with total loss of bearing surface integrity.

Wear Debris

The important features of the wear of ceramics are the very fine particles generated during the wear called wear debris. Wear debris consist of detached grains, detached planes, and amorphous reaction products, which has been produced as a result of intersecting of microcracks with grain boundaries or free surfaces, or even other microcracks (Fischer, et al., 2000; Wang & Hsu, 1996). In fact, at low loads, wear debris are consequences of microfracture

due to dislocation and twins accumulation resulted in microcracking; while at intermediate loads and high loads, wear debris are formed as a result of grain boundary fatigue and macroscopic fracture respectively (Fischer, et al., 2000; Wang & Hsu, 1996).

The wear debris can be squeezed and removed from the surface by continuing the wear or they can remain and play as a third body and affect the contact stresses and wear rate (Fischer, et al., 2000). Forming wear debris and their further grinding and plastic deformation consumes energy and affects the stress distribution on the surface (Cherif, et al., 1996); however, this phenomenon would not normally occur in ceramics due to insufficient plastic deformation of ceramic wear debris (Fischer, et al., 2000; Wang & Hsu, 1996). Wear debris can be crushed to finer debris at high stresses or removed from the surface in liquid environment, and in case of tribochemical dissolution, it can lead to presenting a clean and simple surface after wear (Fischer, et al., 2000; Wang & Hsu, 1996).

Tribochemical layer

The previous discussion has mainly considered the mechanical aspect of wear while wear of ceramics is affected also by tribochemical processes such as corrosion, chemical fatigue, or lubrication in presence of humidity or fluids (Fischer, et al., 2000; Wang, et al., 1995). Although ceramics are traditionally assumed to be resistant to chemical phenomena, this is not the constant fact in all cases. It has been reported that chemical interactions can affect wear properties through modification of surface composition and topology, or through aggregation of fracture due to chemically induced cracking (Fischer, et al., 2000; Rainforth, 1996).

In a humid environment, wear debris can attach to each other and form micrometer rolls or agglomerated wear particles which can compose a compact layer on the worn surface and distribute contact stresses and consequently reduce friction and wear like a lubricant layer (Fischer, et al., 2000; Rainforth, 2004; Adachi & Kato, 2000). This surface layer has a structure that is very different with the substrate (Rainforth, 2004). It should be noted that adhesion of this compact layer is due to humidity, not mechanical alloying as can be seen in metals (Fischer, et al., 2000).

Many researchers have reported the formation of such surface layer in wear of ceramics and

called it as “tribo-film”, “transfer layer”, “interlayer”, “agglomerated film”, “debris film”, “particle layer”, “surface layer of compacted materials”, “layer of compacted wear particles”, “film-like substrate”, “border layer”, and TTS (tribologically transformed structure) (Komvopoulos & Li, 1992; Ajayi & Ludema, 1990; Zanoria & Danyluk, 1993; Denape & Lamon, 1990; Blau, 1993; Gee & Butterfield, 1993; Fischer & Tomizawa, 1985; Gates, et al., 1989; Adachi & Kato, 2000). For example, Kato and Adachi (2002) reported the formation of such layer by oxidation of silicon in Si_3N_4 in presence of oxygen and water vapour and at high contact stresses, which increased wear of asperity peaks leading to a smoother surface than the initial rough surface (Kato & Adachi, 2002). They argued that this tribochemical products can attach to fine wear debris and make a composite layer at the surface, which was defined as tribofilm in Si_3N_4 (Kato & Adachi, 2002).

In alumina a very moderate of humidity adsorption embrittlement was reported by Rainforth (1996) and Fischer et al. (2000), which increased the rate of intergranular fracture and raised the wear rate in humid environment (Fischer, et al., 2000; Rainforth, 1996). According to their findings, in alumina a surface layer of bayerite (a hydrated form of alumina) was formed which was expelled by friction and produced the roll-shaped wear debris and was beneficial for reducing friction and wear rate (Fischer, et al., 2000; Rainforth, 1996). Similarly, Kato and Adachi (2002) reported that wear of alumina against itself was accompanied by a tribochemical reaction in water resulting in aluminium trihydroxide (bayerite– $\text{Al}(\text{OH})_3$) at temperature around 100°C and aluminium oxide hydroxide (boehmite– $\text{AlO}(\text{OH})$) at temperature around 200°C (Kato & Adachi, 2002). Formation of these hydroxide composed a protective layer on the surface, which reduced both friction and wear rate (Fischer, et al., 2000; Rainforth, 1996; Kato & Adachi, 2002).

In addition to humidity, the presence of a liquid as a lubricant in the tribosystem can affect the friction and wear properties of ceramics and delay the onset wear transition from mild regime to severe regime. Figure 2.40 illustrates the effect of lubrication by water or purified paraffin oil on the size of the region of mild or severe wear observed with Al_2O_3 , Y-TZP, Si_3N_4 , and SiC sliding against themselves (Kato & Adachi, 2002).

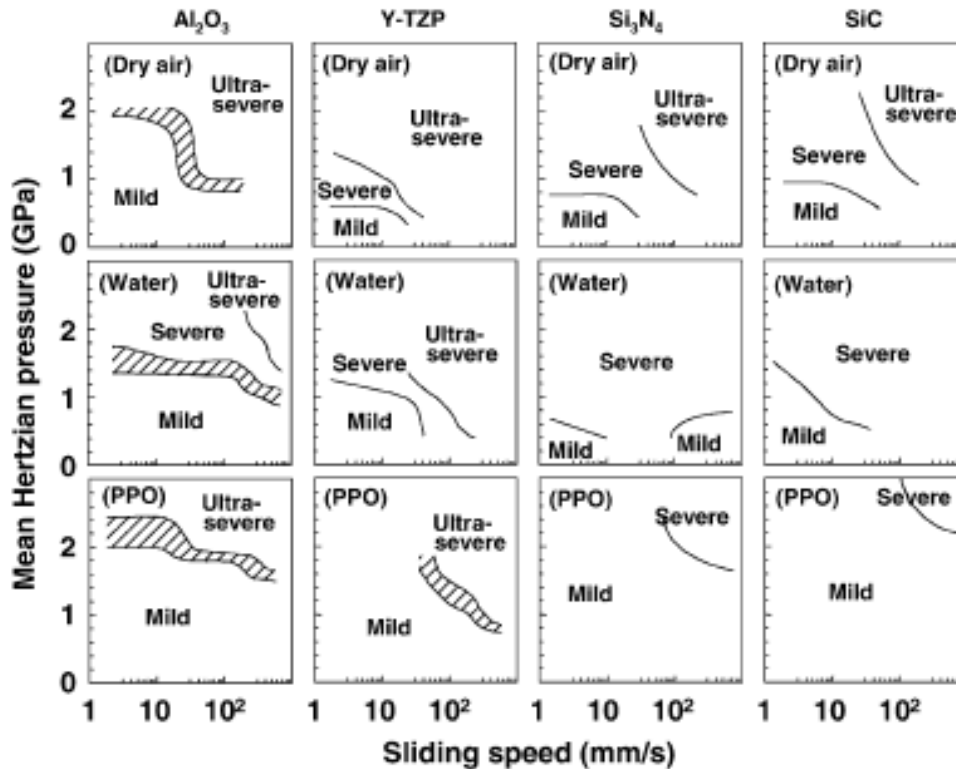


Figure 2.40. The effect of lubrication by water or purified paraffin oil on the size of the region of mild or severe wear observed with Al_2O_3 , Y-TZP, Si_3N_4 , and SiC sliding against itself (Kato & Adachi, 2002).

2.4.2.3. Additives

There are three main strategies to retard the severe wear mechanism in ZTA ceramics: (i) improving density and amending microstructure such as reducing grain size, (ii) producing duplex structures with accurate engineering design for thermal expansivity mismatches of phases and (iii) transformation toughening (Rainforth, 2004).

Rainforth (2004) reported that in improving wear by producing nanocomposites, particularly in SiC- Al_2O_3 nanocomposites, it was not only fine microstructure responsible for retarded wear transition. He argued that intergranular fracture was significantly improved due to enhancing the intrinsic grain boundaries strength and changes in dislocation density and residual stress states in nanocomposites (Rainforth, 2004). The former diminishes catastrophic nature of grain boundaries fracture happening in severe wear regime, and the latter can delay wear transition and its time dependence through generating dislocation with more homogenous density between grains and less dislocation pile-ups at grain boundaries (Rainforth, 2004). Similarly, Fischer et al. (2000) argued that enhancing the strength of grain boundaries by proper additives

could affect the wear transition regime and change the mechanism involved in it through transgranular fracture happened in weak grain boundaries replacing by fatigue cracks in strong grain boundaries which needed higher severity conditions to happen.

2.4.3. Wear of Alumina

Figure 2.41 shows the different wear regime involved in the wear of alumina at different normal loads. It is clear from the figure that at low loads (less than 19.6N), the wear volume is proportional to load and raises with the third root of sliding distance. Increasing the load (up to 80N) increased the wear to the fifth power of load and in linear relation with increasing sliding distance. This dependency of wear volume to load and sliding distance is attributed to the number of asperities under contact pressure as explained before (Fischer, et al., 2000).

As discussed before, plastic deformation occurs in ceramics in mild regime giving the smooth and polished surface. This phenomenon has been reported in wear of alumina as can be seen in Figure 2.37(a) and (b) where nano-sized wear debris have embedded in the surface voids and a smooth layer have been formed (Kato & Adachi, 2002). It should be noted that in ceramics only the top surface will undergo plastic deformation and it is when temperature is elevated enough by friction to soften the surface (Kato & Adachi, 2002).

Alumina shows a time-dependent wear transition, which is attributed to dislocation accumulation and twin formation as discussed before. It has been observed that the density of dislocations is different in adjacent alumina grains and the grains with high dislocation damage stand proud on the worn surfaces (Rainforth, et al., 2012; Barceinas-Sánchez & Rainforth, 1998). The average height difference between the grains were reported in one case by Barceinas-Sánchez and Rainforth (Barceinas-Sánchez & Rainforth, 1998) in scanning of 30 grains to be 21.2 ± 6.9 nm with the maximum of 33.2 nm (Barceinas-Sánchez & Rainforth, 1998). This differential wear, known as grain relief, can be triggered by different mechanisms involved in it like different elastic deflection of grains in an asperity contact, different worn mechanisms (e.g. microfracture and plastic flow) due to different crystal orientations, and different tribochemical wear rates (Barceinas-Sánchez & Rainforth, 1998). Barceinas-Sánchez and Rainforth (Barceinas-Sánchez & Rainforth, 1998) reported microcracks and dislocation accumulation, the main features of mechanical based mechanism, were not seen in the majority

of severe worn grains in mild region and concluded that grain relief in alumina could be attributed to tribochemical wear mechanisms (Barceinas-Sánchez & Rainforth, 1998). Thus, different rate in formation of amorphous wear debris, which composed of dissolved counterface materials, causes differential wear in alumina and this rate is a function of crystallographic orientation of grains (Rainforth, et al., 2012; Barceinas-Sánchez & Rainforth, 1998).

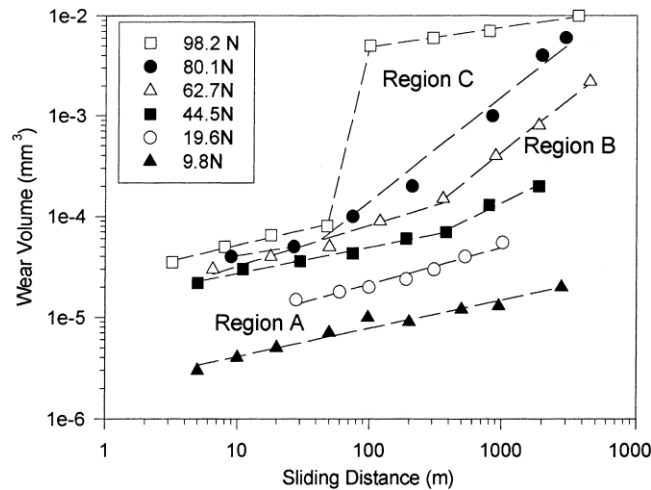


Figure 2.41. Wear volume of alumina ball against alumina plate as a function of sliding distance in air at 11.5 mm/s sliding speed. Region A: mild wear; region B: grain boundary fatigue fracture; region C: macroscopic fracture (Fischer, et al., 2000)

The unworn grains standing proud of the surface are reported to have surfaces $70\text{-}78^\circ$ to the c -axis and contain considerable dislocation density mainly on pyramidal planes due to preferred slip system on these slip planes (Rainforth, et al., 2012; Barceinas-Sánchez & Rainforth, 1998). This dislocation activity is a result of third body abrasive grooves initiating from the leading edge of grains standing proud of the surface (Figure 2.42) (Rainforth, et al., 2012; Barceinas-Sánchez & Rainforth, 1998). The width, depth and orientation of these abrasive grooves are reported to be relatively independent of grain height and more dependent on crystallographic orientation of the grains and change from one grain to its neighbouring (Rainforth, et al., 2012; Barceinas-Sánchez & Rainforth, 1998). Formation of these grooves can be accompanied by four categories different surface damages reported by Barceinas-Sánchez and Rainforth (1998) as cracking contained within the abrasive groove (Figure 2.43(a)), both high dislocation and microcracking (Figure 2.43(b)), dislocation accumulation only (Figure 2.43(c), and no dislocation or microcracking (Figure 2.43(d)) (Barceinas-Sánchez & Rainforth, 1998).

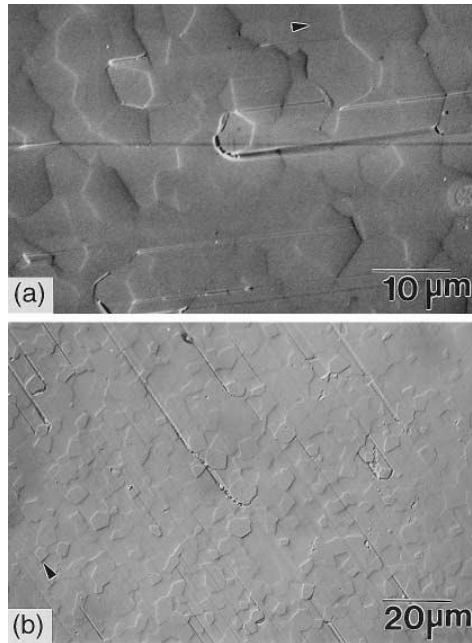


Figure 2.42. Optical (Nomarski contrast) micrograph (a) and scanning electron micrograph (backscattered including channelling contrast), (b), indicating differential wear between grains and three-body abrasive grooves initiating at those grains standing proud of the surface. Note the manner in which abrasive grooves come to an abrupt end at grain boundaries in (a), the residual abrasive fragment in the trailing edge of the groove in (b) and the cracking at the leading edge of the central grain in (b). The arrow indicates the sliding direction in each case (*Barceinas-Sánchez & Rainforth, 1998*).

In summary, the wear process of alumina can be regarded as the following process: development of grain relief results in raised contact stresses due to lower real contact area. This elevated contact stress induces dislocation flow at the unworn grains and accumulation of dislocation in grain boundaries associated with residual tensile stresses in some grains would promote crack nucleation at these grain boundaries. These cracks cause detachment of a wear particle operating as the third body and make abrasive grooves on the surface. Wide-ranging microcracking and dislocation flow occurs at the base of grooves promoting release of further abrasives. Finally, extensive microcracking and accumulation of dislocations associated with high residual asperity contact and thermal stresses cause transgranular catastrophic fracture (Rainforth, et al., 2012; Barceinas-Sánchez & Rainforth, 1998). The transgranular fracture of alumina has similarities to severe plastic deformations of metals and reveals strong crystallographic texture (Rainforth, et al., 2012).

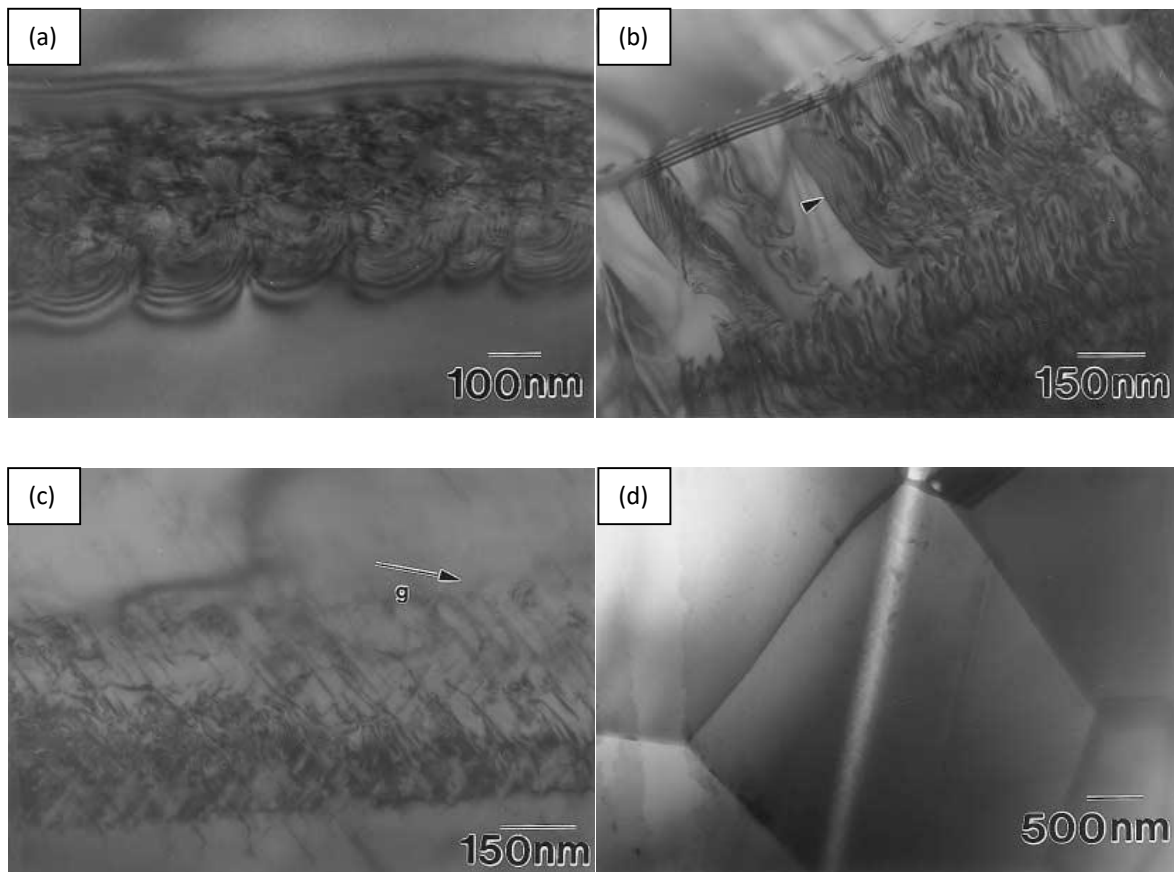


Figure 2.43. TEM bright field images of four categories of surface damages caused by grooves; fracture constrained within the groove (a), microcracking (one example arrowed) extending well beyond the edge of the abrasive groove and a high residual dislocation density at the base of the groove (b), a high dislocation density at the base of an abrasive groove, without any apparent microcrack damage (c), and an abrasive groove not associated with dislocation or microcrack damage (Barceinas-Sánchez & Rainforth, 1998).

Therefore, transition from mild to severe wear in alumina is a time-dependent process due to accumulation of density at grain boundaries and crack initiation as explained before, and the time of this transition is dependent on the grain size, in which finer grains offers lower dislocation density (Rainforth, et al., 2012; Barceinas-Sánchez & Rainforth, 1998). This effect of grain size accompanied with finer grain size effects on fracture strength has made improving impact from first to third generation of alumina for medical grains discussed in previous chapter (Rainforth, et al., 2012).

It is notable that dislocation activity in alumina surfaces is only limited to the sublayer very close to surface, and rare evidence of dislocations on the sublayers well below the surface is existed (Rainforth, et al., 2012).

2.4.3.1. Additives

Rainforth et al. (2002) reported that the addition of CuO to alumina resulted in appreciable lower coefficient of friction in comparison to monolithic alumina, and attributed it to formation of CuAlO_2 probably acting as a wear lubricant. According to their study, MgO addition did not improve wear properties as a lubricant; however, by inhibiting grain growth and microstructural alteration it also decreased friction and wear rate (Rainforth, et al., 2002). Similarly, in research done by Rainforth (2004) Al_2O_3 -SiC composites showed expanded region for mild wear compared to monolithic alumina through rare transition from intergranular to transgranular fracture. Rainforth (2004) argued that despite the greater tendency of dislocation activity in these composites rather than alumina, no damage resulting from dislocation pile-ups at grain boundaries was observed, which was attributed to improving the intrinsic grain boundaries strength by adding SiC.

2.4.4. Wear of zirconia

Figure 2.44 shows the wear transition map for Y-TZP proposed by Lee et al. (1993). Under dry sliding conditions, the wear transition in the low-speed regime is mainly dependent to the normal load and increasing the load more than 10 N gives a rapid increase in wear rate (Lee, et al., 1993). In the mild wear region, the wear mechanism has been reported to be mainly plastic deformation and microcracking (Rainforth, et al., 2012; Lee, et al., 1993; Fischer, et al., 1988), associated by formation of rolled wear debris as observed by Fischer et al (1988). However, in the high-speed regime the wear rate is controlled by both load and sliding velocity, and when it exceeds the critical speed, severe wear occurs attributed to induced thermal shock brittle fracture (Lee, et al., 1993). Additionally, Lee et al.'s (1993) wear map shows the presence of lubrication can significantly affect the beginning of the wear transition (shaded region of Figure 2.44) by reducing frictional heat as well as reducing contact stresses through tribofilm formation (Lee, et al., 1993). It should be noted that using water as the lubricant in these kind of ceramics has an adverse effect on wear properties due to hydrothermal degradation phenomenon explained before (Lee, et al., 1993; Rainforth & Stevens, 1993).

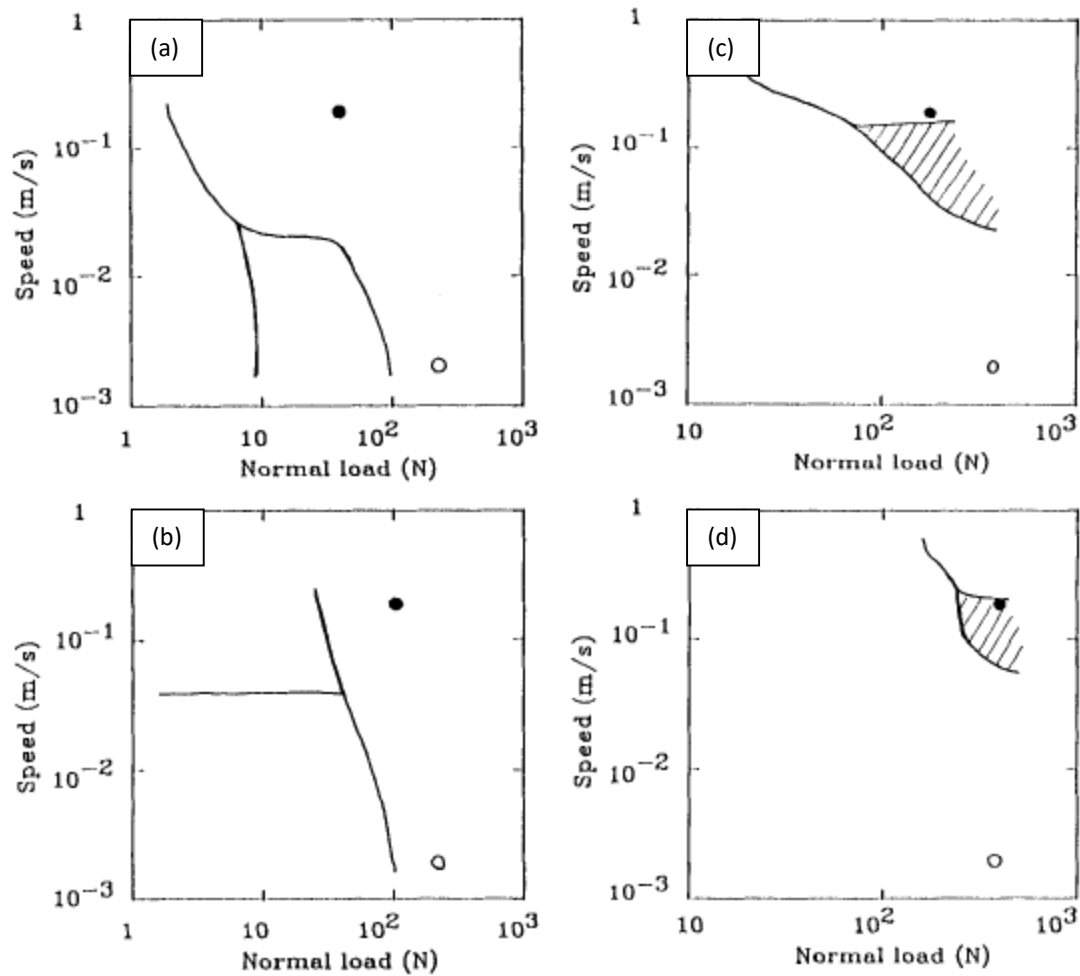


Figure 2.44. Wear transition diagrams for Y-TZP under different lubrication conditions: in dry air (a), in water (b), in paraffin oil (c), and in formulated oil (d). The solid and hollow circles represents the conditions where SEM observations were taken (Lee, et al., 1993)

The dominant cause for the wear transition from mild to severe have been reported to be low thermal conductivity of zirconia raising the flash temperature to more than 800°C at asperity contacts in unlubricated conditions, which is detrimental for both strength and toughness of the ceramic (Rainforth, 2004; Lee, et al., 1993; Stachowiak & Stachowiak, 1993; Rainforth, et al., 2012). The flash temperature or asperity temperature is the short-duration microscopic temperature pulse caused by the asperity-asperity contact and the frictional dissipation of heat, while the bulk interfacial temperature is the steady-state temperature which is controlled by the geometry of the wear tester (Lee, et al., 1993). Thus, the flash temperature can be defined as the bulk interfacial temperature plus the energy dissipation (Lee, et al., 1993). The elevated flash temperatures would trigger severe surface deformation such as changes in grain shapes by dislocation flow, similar to deformation process of metals (Rainforth, 2004).

High flash temperatures caused by low thermal conductivity of zirconia has reportedly

generated high strain deformation resulted from dislocation flow (Rainforth, 2000).

Figure 2.45.a illustrates three main zones (labelled as A,B,C) under the worn surface in sliding wear of Y-TZP with equiaxed tetragonal starting microstructure against ZTA. It is clear from this figure that at region A, the microstructure contains elongated (30:1 aspect ratio) tetragonal zirconia grains, having a clear crystallographic texture with the tetragonal {111} planes preferentially parallel to the worn surface, with high dislocation density. In region B, fine equiaxed tetragonal zirconia grains with the size around 50 nm (much finer than starting microstructure) can be seen having considerable cracks at grain boundaries. Region C is amorphous mechanically mixed layer reported to consist of Al and Zr ions as well as nano zirconia and fractured alumina particles (Rainforth, 2000). Formation of this mixed tribochemical layer, resulting from dissolution of the contacting ceramic, has been reported by other researchers and is considered to be responsible for reducing friction and wear coefficient from the start to the end of wear test (Ma, 2010; Rainforth, 1996; Rainforth, 2000). Rainforth and Stevens' results (1998) showed that transformation of monoclinic to tetragonal and deformation of monoclinic phase in sliding direction happened at region A of

Figure 2.45.a where temperature is low enough (Rainforth, 2000). Wear progress and material removal of the surface associated with raising temperature would increase temperature and re-transformation of monoclinic zirconia to tetragonal would happen around its equilibrium temperature in heating (~560C) as can be seen in region B (Rainforth, 2004).

Although formation of this kind of complex microstructure is attributed to high strain deformation due to dislocation flow, it only can be found in ceramics where frictional heating is excessive and substantial temperature is extremely high during wear (Rainforth, 2000). In the case that this frictional heat is removed by conductive counterfaces, this structure has not been observed and grain relief, similar to what happens for alumina grains in wear, has been reported (Figure 2.46) (Rainforth, 2004).

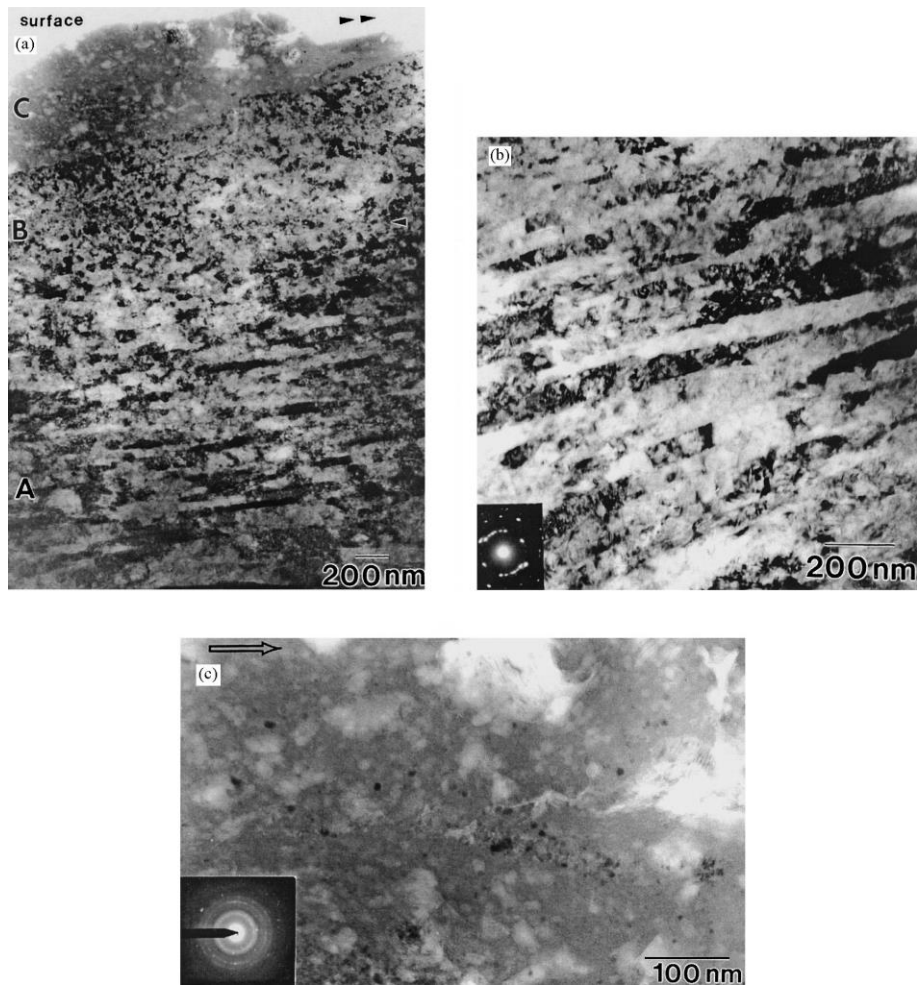


Figure 2.45. Bright field TEM micrographs from a longitudinal cross-sectional sample of a worn 3Y-TZP ceramic, tested in pure sliding at 0.24ms^{-1} , 19N against a zirconia toughened alumina counterface. (a) Low magnification micrograph showing the complete change in microstructure; region A is heavily deformed tetragonal zirconia; region B is equiaxed tetragonal zirconia which has undergone an order of magnitude reduction in grain size from the starting condition; region C is a mechanically mixed layer comprising an amorphous zirconia and alumina phase, fine zirconia precipitates, and fractured alumina particles. (b) Detail from region A, showing extensive plastic deformation (corresponding to a tensile strain of 1.7). (c) Detail from region C. (After Rainforth and Stevens (1998)) (Rainforth, 2000).

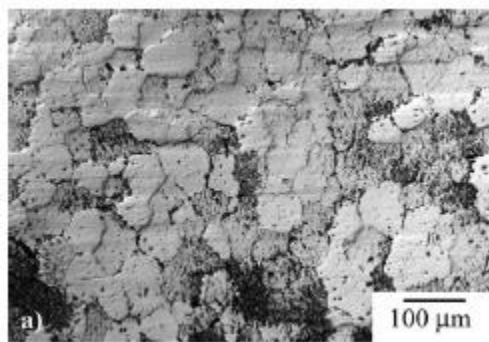


Figure 2.46. Normaski contrast optical micrograph of a worn Mg-PSZ surface, after sliding against a 316 L stainless steel, representing the differential wear between grains (After Rainforth and Stevens (1993)) (Rainforth, 2004).

2.4.4.1. Phase Transformation

As discussed earlier, the tetragonal to monoclinic transformation of zirconia is one of the main features of these ceramics, which can highly affect mechanical properties; however, the contribution of this phenomenon on wear of zirconia is controversial. Some researchers have argued that transformation would induce additional compressive strength which can inhibit formation and propagation of surface cracks (Lee, et al., 1993; Fischer, et al., 1988; Wang, et al., 1993). In contrast, other researchers have pointed out that microcracking resulted from tetragonal to monoclinic transformation enhances grain pull outs which leads to third body abrasion and higher wear rate (Rainforth, 2004; Rainforth, et al., 2012; Birkby, et al., 1989).

2.4.4.2. Additives

Effect of metallic oxides addition for wear properties of zirconia was investigated by many researchers (Kerkwijk, et al., 2004; Rainforth & Stevens, 1993; Birkby, et al., 1989; Fischer, et al., 1989). Y_2O_3 , as discussed in chapter 2.3.1.2 is widely used as the tetragonal zirconia phase stabiliser; however, regarding the controversial effect of zirconia phase transformation on its wear behaviour, its role on wear properties is not clear. For instance, although Fischer et al. (1989) showed wear resistance of the Y-TZP was dependent to its yttria content due to beneficial transformation effects, Birkby et al. (1989) reported contrary results attributed to cracking involved in phase transformation and its effect on the wear transition. CuO was reported by Kerkwijk et al. (2004) to improve wear properties of zirconia through reducing wear and coefficient of friction to about 40% due to superplastic deformation and forming a soft phase at the counterface acted like a lubricating phase. The addition of MgO to zirconia, accounted for its effect on stabilization of tetragonal phase (Kerkwijk, et al., 2004), studied by Rainforth and Stevens (1993) and showed promoting preferential wear and grain relief due to its tribochemical interaction during wear. Other metallic oxides such as ZnO, B_2O_3 , and MnO_2 were not found to improve wear properties and reduce friction in a research done by Kerkwijk et al. (2004); the latter was even reported to raise coefficient of friction due to moving and re-deposition of MnO_2 grains as clusters on the surface.

2.4.5. Wear of ZTA

As discussed in the previous sections, alumina and zirconia show different wear behaviour due to their distinctive intrinsic properties. Generally, alumina has higher hardness and Young's modulus, lower fracture toughness and bending strength, lower coefficient of linear thermal expansion and higher thermal conductivity in compare with zirconia ceramics (Zum Gahr, et al., 1993). Both alumina and zirconia ceramics show plastic deformation, intergranular microfracture, grain lamination, microcracking and tribolayer formation (Zum Gahr, et al., 1993); however, their wear resistance is quite different. Lower thermal conductivity of zirconia (around one third than that of alumina) increases the flash temperature and thermal stresses at the contacting areas and therefore cause higher wear rate of these ceramics in compare with alumina (He, et al., 1993; Zum Gahr, et al., 1993; Kerwijk, et al., 1999). Nonetheless, it has been reported that at higher applied pressure (more than 5 MPa) or in reciprocating conditions, they show greater wear resistance than alumina ceramics, which is attributed to their intercrystalline microfracture resulted from their high fracture toughness (Zum Gahr, et al., 1993).

Despite the widely accepted beneficial effect of adding zirconia to alumina in order to make ZTA composite in improving its fracture toughness, its effect on wear properties is complicated and controversial. Some researchers believe that zirconia addition reduce the wear resistance of alumina due to its lower hardness and lower thermal conductivity (He, et al., 1997; Trabelsi, et al., 1989; Krell & Blank, 1988; Dey & Biswas, 2009). The latter can cause large thermal stresses at the subsurface layer by largely localized thermal gradients, reduced fracture toughness due to high temperature, and thermal shock development at local contact spots, which all generated as a result of fast temperature rise at asperities (He, et al., 1997). The adverse effect of zirconia addition in ZTA wear behaviour have been reported to get accelerated when its amounts exceeds a threshold limit of 20 vol.% (Wang, et al., 1995; He, et al., 1993; Dogan & Hawk, 1997).

In contrast, other researchers believe that the addition of zirconia to alumina can improve the wear properties of both of these ceramics (He, et al., 1997; Wang & Hsu, 1996; Kerwijk, et al., 1999; Ma & Rainforth, 2010; Wang, et al., 1993; Krell & Blank, 1988; Kerkwijk, et al., 1999). Their argument is based on the fact that hardness indicating intensity of bond strength cannot be the accurate estimation for measuring abrasive wear properties as it is in metals, and fracture

toughness and its inhibition effect on crack propagation is more effective on wear loss, specifically at high normal loads (He, et al., 1997; Wang, et al., 1993). Advantageous effect of adding zirconia to alumina on improving the wear properties of the composite has been attributed to its effect on beneficial toughening transformation mechanisms (e.g. microcracking, compressive residual stresses, and heterogenization of the grain boundary toughness), and its inhibited effect on grain growth resulting in more fine and homogeneous microstructure (Wang, et al., 1995; Kerwijk, et al., 1999; Krell & Blank, 1988; Ma & Rainforth, 2010; Kerkwijk, et al., 1999).

2.4.5.1. Microstructure

It seems to be widely accepted by researchers that fine-grained alumina ceramics show much lower wear rate than coarse-grained structure (Wang, et al., 1995; Zum Gahr, et al., 1993; He, et al., 1993; Krell, 1996; Senda, et al., 1995). The higher wear rate has been attributed to higher anisotropic thermal expansion and elastic properties of neighbouring grains in coarse structures resulting in higher local residual stresses during cooling, which leads to grain boundary failure and intergranular microfracture during the wear tests (Zum Gahr, et al., 1993). This phenomenon was explained by Wang et al. (1995) based on Hall-Petch-type relationship between grain size and critical damage stress (stated below) in which the smaller grain sizes would result in higher critical damage stresses or higher transition resistances as discussed before (Wang, et al., 1995; He, et al., 1993). In the case of zirconia, the relationship between grain size and wear resistance is more controversial due to positive effect of coarser grain size on increasing toughness and the questionable effect of toughening transformation on wear behaviour as addressed before.

$$\sigma_D = f(d^{-\frac{1}{2}})$$

σ_D = Critical level of applied stress for producing fracture

d = Grain size

In ZTA ceramics, adding zirconia to alumina matrix would result in finer and more homogenous microstructure, which have been reported by researchers to improve wear properties (He, et al., 1997; Kerwijk, et al., 1999; Wang, et al., 1995; Kerkwijk, et al., 1999; Bartolome, et al., 2006; He, et al., 1997). According to these researchers finer grain sizes of

ZTA composites would increase the critical stresses required for mild to severe wear transition according to Hall-Petch type relation (Kerwijk, et al., 1999; Bartolome, et al., 2006). However, in a study done by He et al. (1997), wear rate of coarse-grained ZTA was found to be lower than that of fine-grained ZTA. They attributed the higher wear resistance of coarse-grained ZTA to greater compressive stresses at the surface caused by zirconia transformation and its volume expansion. They also observed that in this composite, no subsurface microcracks were formed as the detrimental effect of transformation, which was attributed to higher Young's modulus of the alumina matrix than the zirconia second phase.

2.4.5.2. Phase Transformation

Transformation of tetragonal zirconia to monoclinic in ZTA during the wear test has been reported by researchers; however, its effect on improving the wear properties has been the controversial issue. Some researchers reported beneficial effect of transformation on wear resistance and attributed it to the formation of a localised compressive layer at the surface of ZTA composites, which required higher critical tensile stress for crack propagation (He, et al., 1997; He, et al., 1993; Wang, et al., 1993; Kerwijk, et al., 1999; He, et al., 1997). They also concluded that higher amount of zirconia would lead to greater subsurface compressive stress and therefore these composites possess higher wear resistance (Wang, et al., 1993; Dogan & Hawk, 1997; He, et al., 1997). In contrast, other researchers found transformation detrimental and argued that internal stresses might inhibit crack formation and propagation, but they also could weaken grain boundaries and trigger easier delamination and grain pull-out (Bartolome, et al., 2006).

Interestingly, Dogan and Hawk (1997) categorized the effect of toughening on its involved mechanisms and interpreted that toughening mechanisms acting behind the propagating crack, or depending on the porosity or the presence of microcracks, would mainly increase wear loss through linking up with other cracks under the contact stresses. On the contrary, toughening mechanisms working at or ahead of the crack (e.g. crack deflection) would decrease wear loss of the material due to higher energy consumed and longer and more difficult path for material removals. They then concluded that as transformation toughening operates ahead of the crack by forming a compressive zone ahead of the propagating cracks, it could be considered as

improving factor for wear resistance of ZTA ceramics.

It should be noted that despite above arguments, some studies show no detectable effect of transformation on wear properties of ZTA concluding that wear of ZTA is mainly dominated by tribochemical mechanisms than toughening mechanisms (Rainforth, 1996; Rainforth, et al., 2012; Dogan & Hawk, 1997).

2.4.5.3. Wear Transition

In ZTA composites, a clear wear transition from mild to severe regime like what happens in alumina have been observed by researchers (He, et al., 1997; Wang, et al., 1995; He, et al., 1993; Kerkwijk, et al., 1999; Bartolome, et al., 2006; Huang, et al., 2008). The mild wear regime has been reported to be plastic deformation dominated (He, et al., 1997; Wang, et al., 1995; He, et al., 1993) with some grain pull-out (He, et al., 1993) and relatively smooth wear track and elongated grooves in the sliding direction which is the characteristic of a deformation-controlled wear mechanism (Wang, et al., 1995). Microchipping and microfracture occurs in the severe wear regime as a result of high frictional temperature causing transgranular and brittle fracture, and grain pull-out (He, et al., 1997; Wang, et al., 1995; He, et al., 1993).

The wear transition of ZTA have been found to occur at much higher loads than alumina and zirconia in the same operating conditions, which means that higher critical tensile stress required for crack propagation (He, et al., 1997; Wang, et al., 1995). This has been attributed to lower contact stress due to the larger contact area resulted from their lower elastic moduli of composite under the same load (Wang, et al., 1995). In addition, compressive residual stress as discussed before as well as easier dislocation and twin formation which releases energies promote wear transition loads (Wang, et al., 1995).

The important factors for improving the value of transition load in ZTA have been found by researchers to be higher zirconia content (Wang, et al., 1995; He, et al., 1993), more effective zirconia dispersion (He, et al., 1993; Huang, et al., 2008) and smaller alumina matrix grain size (He, et al., 1993). As discussed before, smaller grain sizes can improve wear resistance as well as transition resistance of ZTA composites. Similarly, dispersion of zirconia and its effect of grain size distribution is important since they can make a critical stress distribution essential

for wear transition (He, et al., 1993). In fact, it is the largest grains which determine the actual transition load rather than the mean grain size; thus, a homogeneous microstructure having a narrow grain size distribution would show a narrower damage stresses distribution and less fluctuations in wear transition results (He, et al., 1993).

For zirconia content factor, although He et al. (1993) reported improving wear transition load occurs by an increase of zirconia content up to 12 vol.%, other researcher's findings gave other values for this amount. For instance, the maximum of zirconia content reported to be 20 vol.% by Wang et al. (1995), while He et al. (1993) showed that the lowest wear rate was found for 15 vol.% ZrO₂ addition. Figure 2.47 illustrates the results for the transition load as a function of the zirconia content in ZTA composites reported by He et al. (1993). It can be seen that as the zirconia content rises from 5 to 20 vol.%, the transition load promotes from 170 to 350 N. However, they argued that when zirconia content increased from 15 to 20 vol.%, wear rate would increase although transition load is still rising as illustrated in Figure 2.48. They attributed this to dominating adverse effect addition of zirconia from hardness reduction over its beneficial effect from grain size refinement.

Additionally, Bartolome et al. (2006) study showed that for composition with zirconia content (22 vol.%) above the percolation threshold (16 vol.%), the composite was worn by two orders higher wear rate compared to the composites below the percolation threshold (14 and 7 vol.%) (Wang, et al., 1995; Bartolome, et al., 2006). They attributed this difference to different mechanisms involved, which were abrasion and chipping respectively in lower and higher loads for zirconia contents under percolation threshold and percolative mechanism and microcracks induction for zirconia content above percolation limit (Bartolome, et al., 2006).

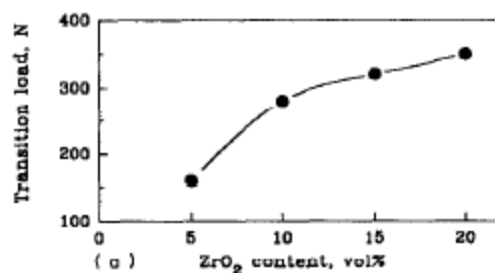


Figure 2.47. Wear transition load as a function of zirconia content for ZTA ceramics (He, et al., 1993)

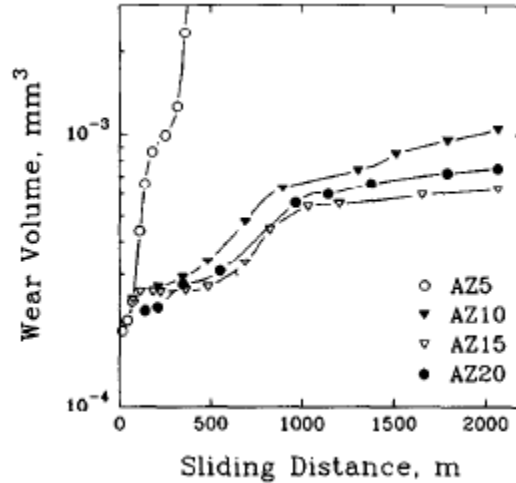


Figure 2.48. Pretransition wear resistance of ZTA sliding. Note that AZ20 has a higher wear volume than that of AZ15 for a given sliding distance (He, et al., 1993).

2.4.5.4. Surface analysis

In the mild regime, the wear surface have been reported by researchers to be relatively smooth with elongated grooves in wear direction which are the characteristics of the plastic deformation mechanism (He, et al., 1997; Rainforth, 1996; Wang, et al., 1995; He, et al., 1993; Rainforth, et al., 2012; Dogan & Hawk, 1997; Kerkwijk, et al., 1999; Bartolome, et al., 2006). Despite He et al. (1997) reported no local microcracks or microfracture in the mild wear regime for ZTA, they observed microcracks perpendicular to the sliding direction at the turning points in another study (He, et al., 1997) and Dogan and Hawk (1997) reported the pre-existing microcracks on the surface.

Figure 2.49 shows the observed wear surface by Wang et al. (1993) which is quite similar to alumina wear surface with grooves and occasional plastic flow. The depth and width of grooves were dependent on the load, the morphology of the surface of the pin and they seemed to be the result of polishing mechanism in ZTA rather than fracture as it was in alumina (Wang, et al., 1993). Some grain pull-out and pitting were also observed in this wear regime by researchers (Wang, et al., 1995; He, et al., 1993; Rainforth, et al., 2012; He, et al., 1997). This pitting associated with intergranular fracture was seen next to the grains having high dislocation density (Rainforth, et al., 2012). In ZTA, they seemed to be the result of microfracture and loss of zirconia grain(s) rather than alumina ones (Rainforth, et al., 2012; Wang, et al., 1993).

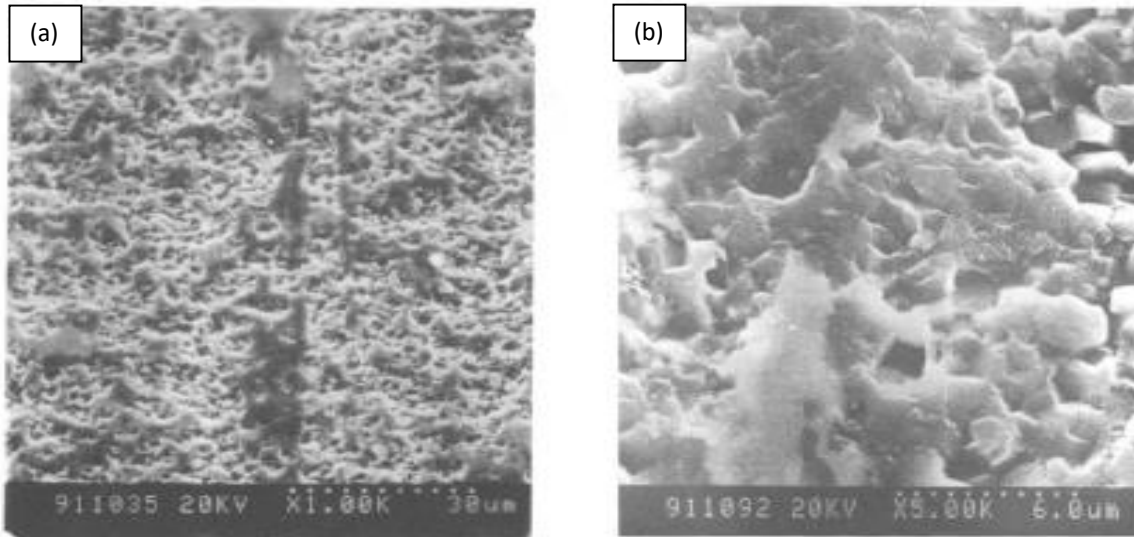


Figure 2.49. SEM image of the abraded surface of ZTA: (a) under 4 kg load with SIC after 5000 revolutions showing polishing scratches, (b) magnified image of (a) showing plastic flow and micro-fracture (Wang, *et al.*, 1993).

High density dislocation and twins were observed in both alumina and zirconia grains in ZTA composites which could absorb energy and release stresses and as described before, could improve microfracture resistance of the composite (Wang, *et al.*, 1995; Rainforth, *et al.*, 2012). In monolithic alumina formation of these dislocations and twins were not effective and thus the energy would be balance through formation of transgranular cracks (Wang, *et al.*, 1995). In the wear surface of ZTA composites, zirconia grains was present mainly as monoclinic phase and its characteristic twinned structure (Rainforth, *et al.*, 2012).

Wear debris was another feature observed by researchers in ZTA worn surfaces, which their small size implied that they were the products of plastic deformation and microcracking removal (Bartolome, *et al.*, 2006). These wear debris were reported to be a mixed structure consisting of nanocrystals in an amorphous matrix, and contain chemical mixture of all component in the tribosystem (Rainforth, *et al.*, 2012). They adhered to microcracked parts of the surface and since the local contact stresses were mainly concentrated on wear debris, they caused high local stresses which triggered crack propagation around and below the wear debris (He, *et al.*, 1997; Bartolome, *et al.*, 2006). The wear debris could also drop in and fill the pitting area and get smeared in progressive wear (Rainforth, *et al.*, 2012; He, *et al.*, 1997).

The formation of an amorphous surface layer of wear debris and grain relief were also observed in wear of ZTA (Rainforth, 1996; Rainforth, 2004; Rainforth, *et al.*, 2012). According to

Rainforth (1996) and Rainforth (2004), two kinds of wear debris could be formed in wear of ZTA, one was the smeared debris making a surface layer adhered to the surface, second was fine rods and randomly shaped debris which accumulated at the most worn grains. The latter was explained before as the result of differential wear due to tribochemical reactions.

In general, the wear mechanism of ZTA is abrasion, polishing and grain pull-out (Kerwijk, et al., 1999; Kerkwijk, et al., 1999; He, et al., 1997), while rough region with irregular and deep grooves and large microcracking have been reported in severe wear regime by researchers (He, et al., 1997; Rainforth, 1996; Wang, et al., 1995; He, et al., 1993; Rainforth, et al., 2012; Dogan & Hawk, 1997; Kerkwijk, et al., 1999; Bartolome, et al., 2006).

2.4.5.5. Tribochemical

In lubricated conditions, mechanical based wear mechanisms like microfracture or plastic deformation are not considered to have a significant effect on wear and the wear rate is more controlled by tribochemical mechanisms (Rainforth, 1996; Rainforth, 2004). Consequently, the wear rate is mainly dependent on chemical dissolution of the surface and the properties of the amorphous film (Rainforth, 1996; Rainforth, 2004). The hardness and inherent friction coefficient of the adherent film, as well as its growth or detachment on the surface, indicate if it can affect wear properties in a favourable or adverse manner (Rainforth, 1996; Rainforth, 2004).

Water lubrication

Using water as the lubricant in a tribosystem of ZTA composites was considered by many researchers (He, et al., 1997; Rainforth, 1996; Rainforth, 2004; Ma & Rainforth, 2010; Ma & Rainforth, 2012; Barceinas-Sánchez & Rainforth, 1998; Steijn, 1961; Chevalier, et al., 2007; Kelly & Francis Rose, 2002; Muddle & Hannink, 1986). Some reported that the wear rate of ZTA increased in water environment despite their reduced coefficient of friction due to formation of an amorphous layer of hydrated phases (Rainforth, 1996). They argued that the rate of surface hydration, the removal of the hydrated film, and the damage caused by the film as a 3-body abrasive would indicate the wear rate in ZTA.

However, He et al. (1997) argued that water lubrication is advantageous in ZTA as hydroxide layer had some solid lubricating ability and inhibited direct contact of the surface as in monolithic alumina. In addition, they discussed the cooling effect of water lubrication in reducing high contact temperature and thus decreasing thermal stresses in subsurface areas due to low thermal conductivity of zirconia grains. He et al. (1997) also considered a relatively larger contact area due to smooth surface in water and more homogeneous stress distribution would cause lower local contact stresses, which consequently would reduce tensile stresses at the behind of wear scar. According to their study, acceleration of wear damage due to degradation of zirconia in water was not clear since chemisorption and diffusion OH⁻ ions to zirconia lattice was a time dependent process, and it was not easy to state if water plays a detrimental or beneficial role in wear of ZTA composites. Consequently, selecting the appropriate chemical composition which can optimise the hydration resistance of the composite as well as improving the properties of hydrated films is a significant priority in these composites (Rainforth, 1996).

The surface analysis of ZTA composites in this environment done by Ma and Rainforth (2012) showed that at varied loads, different wear surfaces were observed in these ceramics. In the normal load of 1 N, grain relief associated with several fine grooves initiating from the grains standing proud of the surface observed, as illustrated in Figure 2.50.a. The differential wear seemed to be higher in neighbouring zirconia grains (~10–12 nm) than that of alumina grains (~4 nm) (Ma & Rainforth, 2010; Ma & Rainforth, 2012). The decreasing depth of grooves from their onset point showed three-body abrasive wear mechanism, and as reported by Barceinas-Sanchez and Rainforth (1998) for ZTA and Steijn (1961) for alumina grains, this depth is dissimilar in adjacent grains due to their different crystallographic orientation. It was also found that grain relief could only be observed for full fluid-film lubrication regime due to its main tribochemical feature (Ma & Rainforth, 2010; Ma & Rainforth, 2012). In addition to grain relief and fine grooves, some occasional grain pull-out is also detectable in Figure 2.50.a which were reported to be more zirconia particles rather than alumina grains considering the pitting sizes, while in larger pitting areas both alumina and zirconia might be lost (Ma & Rainforth, 2010; Ma & Rainforth, 2012).

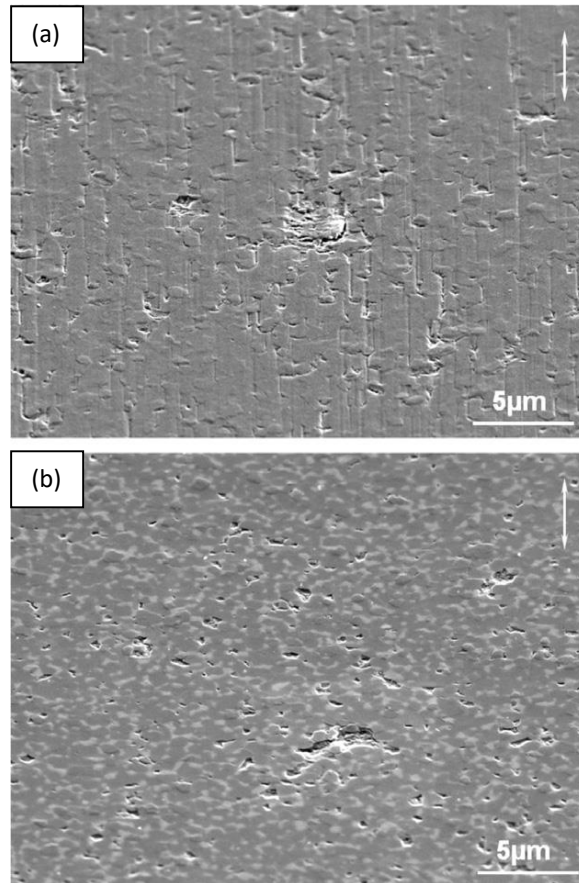


Figure 2.50. Secondary electron SEM images of typical worn surface morphology for the worn surface tested in ultra pure water: (a) 1 N load, 600 rpm speed, 24 h and (b) 4 N load, 600 rpm speed, 24 h (*Ma & Rainforth, 2012*).

In Figure 2.50.b it can be seen that for 4N, the worn surface is smooth, with the reported height differences between grains to be less than 5 nm (*Ma & Rainforth, 2012*), associated with uniformly distributed grain pull-outs; however, no differential wear or fine grooves could be detected. The lateral force microscopy (LFM) images illustrated by Ma and Rainforth (2012) for this load show non-uniformity of friction force as a function of grain orientation and highlighted grain boundaries due to different friction force (Figure 2.51.b).

Ma and Rainforth (2012) also found out from LFM images (Figure 2.51.a and b) that all the zirconia grains on the surface were transformed from tetragonal to monoclinic phase showing parallel linear features with the twin spacing for monoclinic zirconia. Similarly, transformation of all zirconia grains was reported by Chevalier et al. (2007) and TEM cross-section studies of subsurface layers done by Ma and Rainforth (2010) for 1 N contact load (Figure 2.52). In Figure 2.52, evidence of dislocation activity could be detected in alumina grains at the surface while the subsurface grains show nearly no damage and only residual strain associated with the transformation of the zirconia can be seen in them.

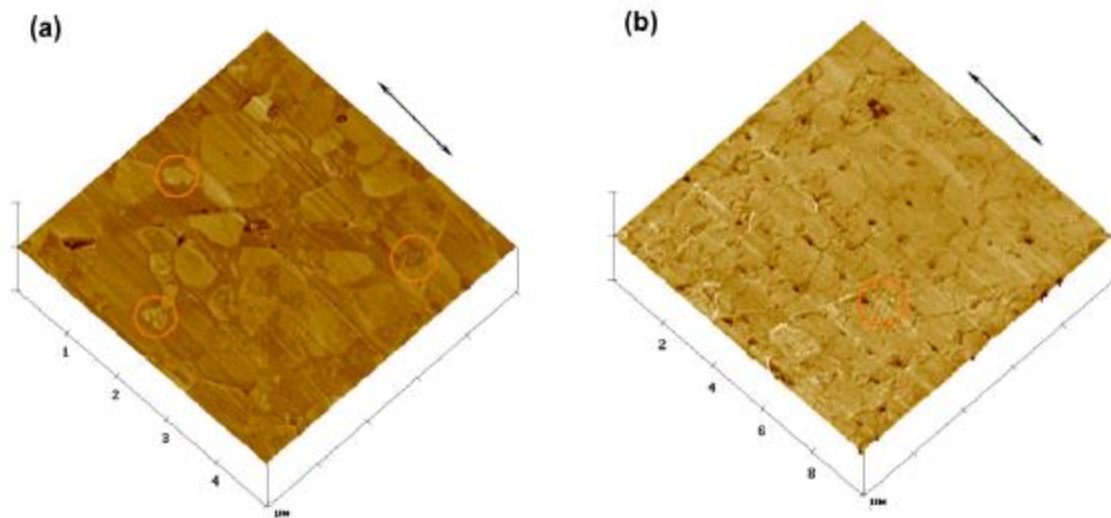


Figure 2.51. LFM images showing distinctive friction force changes of BioloX delta worn surfaces tested in ultra pure water with 600 rpm speed for 24 h under 1 N (a) and 4 N (b) contact load. The location of zirconia grains were circled (Ma & Rainforth, 2012).

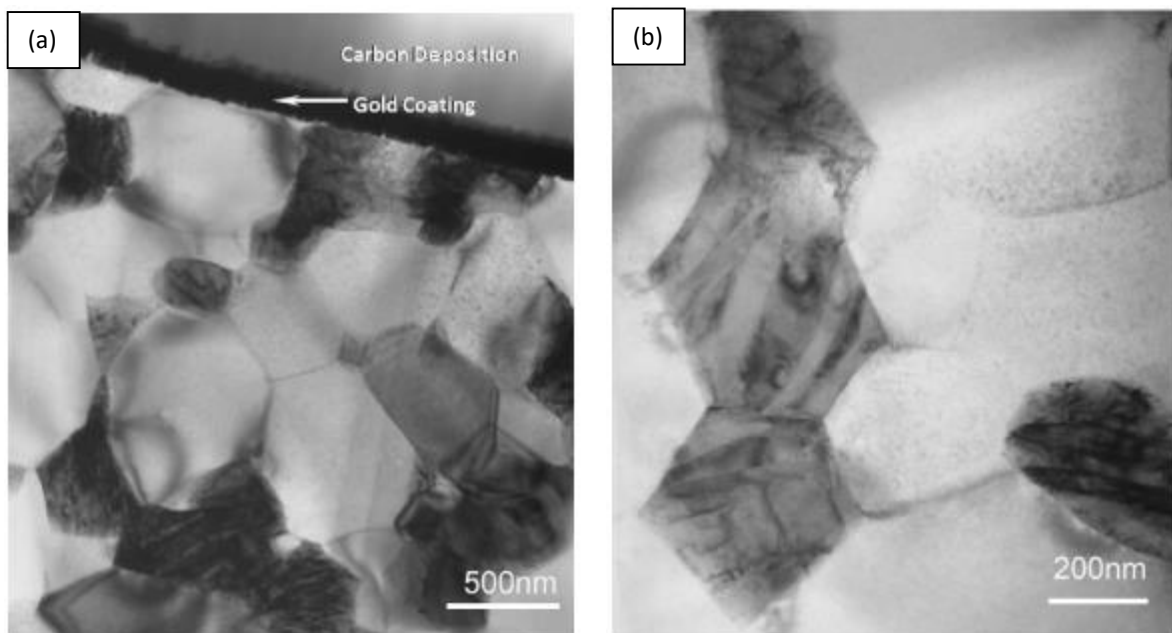


Figure 2.52. (a) Bright field TEM images of a site-specific cross-section of the worn surface from 1N contact load tested sample showing an overview of the subsurface microstructure. (b) Magnified bright field TEM showing the transformed zirconia grains (Ma & Rainforth, 2010).

This transformation and its associated grain volume expansion leading to transformed grains to stand proud of the surface, accompanied by microcracking result of transformation could be the cause of removing zirconia grains from the surface (Kelly & Francis Rose, 2002; Muddle & Hannink, 1986).

Bovine serum

The natural lubricant for cartilage bearings is synovial fluids with medium to high viscosity and non-Newtonian shear thinning characteristics. The most similar lubricant to the natural synovial fluid is new-born calf bovine serum which is widely used for joint simulation tests (Ma, 2010; Ma & Rainforth, 2012). The wear test results for ZTA ceramics in 25 vol.% bovine serum done by Ma and Rainforth (2012) showed the values of the COF was around 0.002–0.015, which was less than that one for water lubrication. The Stribeck curve depicted by this research showed full fluid-film lubrication indicating that the friction is dependent to internal friction of the lubricant (Ludema, 1996). The low coefficient of friction and wear rate for ZTA composites in bovine serum environment has been attributed to protein precipitation on the surface which can make a solid-like tribofilm with the thickness of up to 20 nm (Ma & Rainforth, 2012; Brown & Clarke, 2006; Lu & McKellop, 1997; Lu, et al., 1999).

In spite of lower coefficient of friction and wear rate of ZTA composites in bovine serum rather than water lubrication, the worn surface was reported by Ma and Rainforth (2012) to be rougher with higher pitting and more expanded grain pull-out areas (Figure 2.53). This implies that when protein is present, the local contact conditions makes more damage at individual surface grains, which is attributed to protein adsorption behaviour of alumina and zirconia grains (Ma & Rainforth, 2012). In addition, the damage accumulation such as dislocation activity was reported to be higher in bovine serum lubricated environment which supports the idea of different local contact stresses (Ma & Rainforth, 2012). LFM image of this lubrication system for ZTA composites obtained by Ma and Rainforth (2012) showed little change in friction forces between grains, except for pitting areas and grain boundaries (Figure 2.54) and the image was blurred, probably due to pulling of LFM probe by soft layer formed on the surface.

According to Ma and Rainforth's results (2012), increasing loads resulted in larger areas of grain pull-out and the pits were mainly filled with agglomerated wear debris and no grooves were seen on the surface. In lower normal load (2N), the surface was reported to be smooth with pitting sizes to be around a single grain size and some grain reliefs (Figure 2.53.a). The transformed zirconia grains were not observed by Ma and Rainforth (2012), as seen in water lubrication, but it was stated that grain pull-outs were initially formed by the loss of transformed zirconia grains. For higher loads (4N), the surface analysed by Ma and Rainforth (2012) showed some features of severe wear regimes in which the top layer of grains was

removed and large pitting areas with accumulated wear debris were seen on the surface (Figure 2.53.b).

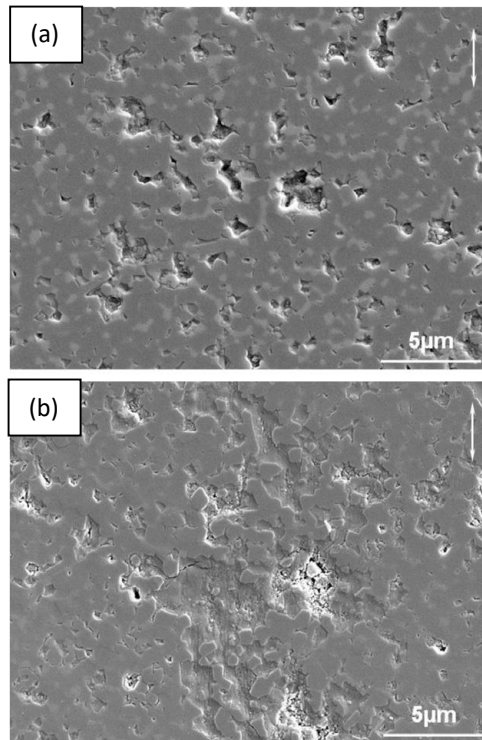


Figure 2.53. SEM images of BioloX delta worn surfaces obtained from serum solution-lubricated reciprocating wear tests at (a) 2 N and (b) 4 N load, 600 rpm speed for 24 h (Ma & Rainforth, 2012).

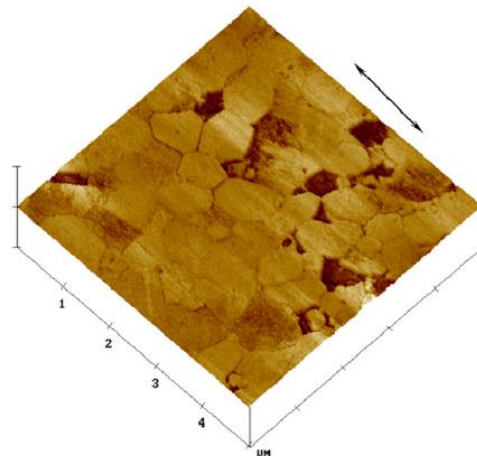


Figure 2.54. LFM images showing distinctive friction force changes of BioloX delta worn surfaces tested in 25 vol.% newborn calf serum solution under 2 N contact load with 600 rpm speed for 24 h (Ma & Rainforth, 2012)

In summary, according to five stage grading scale of wear progression by Shishido et al. (2006) explained above, wear of ZTA in bovine serum under 2N load can be classified as Grade III

regime while its scale under 4N load lays in Grade IV regime.

2.4.5.6. Additives

In a study by Dey and Biwas (2009), MnO_2 was reported to decrease the wear rate with increasing sliding distance (Figure 2.55) due to formation of compacted and smeared wear debris on the surface leading to more polished surfaces and higher contact areas. In addition, MnO_2 can form a solid solution with alumina and raise the hardness (Erkalfa, et al., 1998). Thus, its addition with TiO_2 could give a low specific wear rate and low coefficient of friction as observed by Key and Biswas (2009) with the dominant wear mechanisms of abrasion and grain pull-out.

Addition of CuO was done by Key and Biswas (2009) and as can be seen in Figure 2.55, increased friction and wear rate by increasing sliding distance occurred in this ceramics, which was attributed to the release of second phase and also enhanced superplastic deformation due to presence of CuO (Kerkwijk, et al., 2004; Kerwijk, et al., 1999). It is stated by Key and Biswas (2009) that the formation of CuO -rich grain boundaries could be beneficial for brittle fracture such as grain pull-outs since the softer phase could extend the contact area and decrease contact stresses leading to lower fracture and material loss.

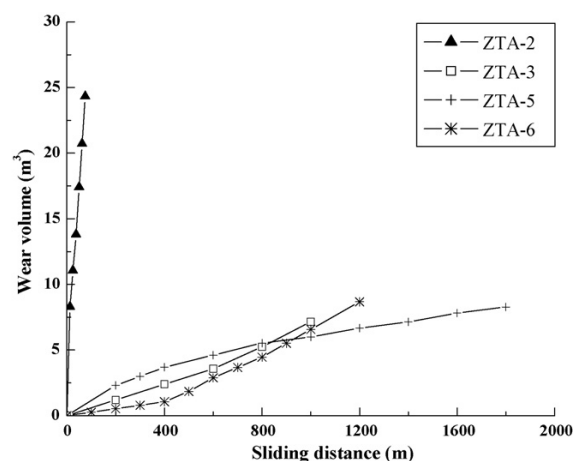


Figure 2.55. Dry sliding wear behaviour of different ZTA composites under 50 N load at a constant sliding speed of 0.5 m/s with the additives of MnO_2, ZnO for ZTA-2, MnO_2, CuO for ZTA-3, TiO_2, MnO_2 for ZTA-5, and TiO_2, CuO for ZTA-6 (Dey & Biswas, 2009).

3. EXPERIMENTAL PROCEDURES

3.1. Sample preparation

The samples were prepared by mixing the starting powders, consolidation, sintering, polishing, and thermal etching, which is shown schematically in Figure 3.1.

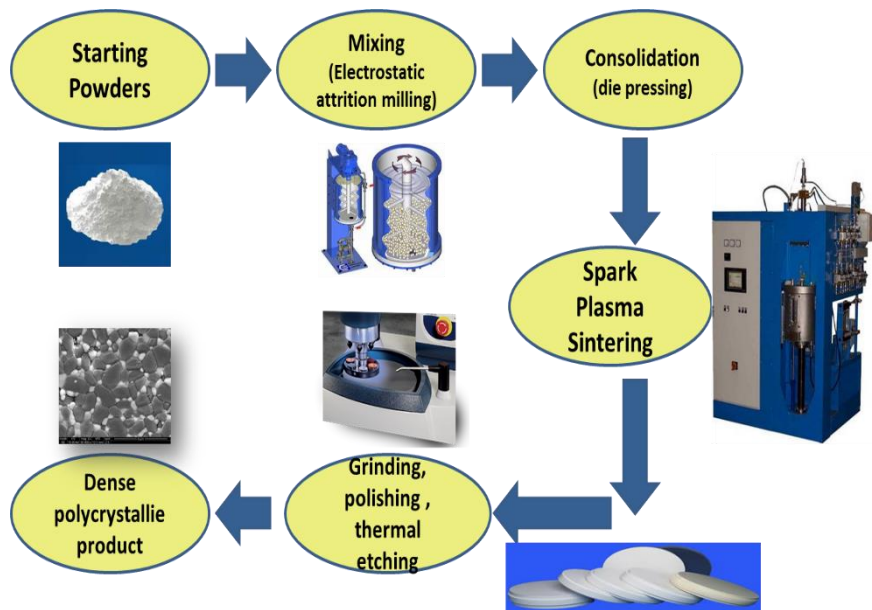


Figure 3.1. Schematic of experimental procedure

3.1.1. Starting powders

In order to study the effect of titania on microstructure, mechanical and wear properties of the composite, different compositions were selected. As mentioned before, the percolation limit of zirconia content in ZTA composites has been reported to be 6.7 vol.% for pure ZrO_2 and 16 vol.% for Y-TZP, below which there is not percolating and not diffusing of water and aging (Wang & Stevens, 1987; Rahaman, et al., 2007). Therefore, the volume percent of Y-TZP used in this study was kept to 15 vol.% for all the samples and the different composite containing no titania (pure ZTA), 0.1 mole.%, 0.5 mole.%, 2 mole.% and 5 mole.% of TiO_2 were produced.

The main objective of this research was the investigation of the nano-composite ceramics; thus, the starting materials were selected accurately to be on nano-size range having as less impurity as possible. Therefore, biomedical grade α -Al₂O₃ powder (AKP53, Sumitomo, Japan), biomedical grade 3 mol.% yttria stabilized tetragonal ZrO₂ (TZ-3Y-E, Tosoh, Japan), and rutile titanium oxide (Sigma-Aldrich, US) were used to prepare zirconia toughened alumina nanocomposites containing titania additives. The main characteristics of the starting powders are shown in Table 3.1.

Table 3.1. Characteristics of starting powders

	α - Alumina	ZrO₂(TZ-3Y-E)	TiO₂ (Rutile)
Purity	≥ 99.99%	-	≥99.5%
Mean Particle size (μm)	0.18	0.04	0.021
Specific surface area (m²/g)	11.7	16±3	35-65
Sintered density (g/cm³)	3.98	6.05	4.26
Impurity	Si ≤ 33 ppm Fe ≤ 4 ppm Na ≤ 2 ppm Mg ≤ 5ppm Cu ≤ 1ppm	Y ₂ O ₃ = 3 mole.% (5.2±0.5 wt.%) Al ₂ O ₃ = 0.1~0.4 wt.% SiO ₂ ≤ 0.02 wt.% Fe ₂ O ₃ ≤ 0.01 wt.% Na ₂ O≤ 0.04 wt.%	NA

3.1.2 Mixing and specimen preparation

The mechanical mixing route used in this study was attrition milling using zirconia ceramic balls. The first batch of the composite was prepared with a ~50 gr mixture of the starting powders blended with 120 ml of methanol. The slurry was attrition milled (Szegevari attritor, Reeves, USA) using zirconia balls for 3.5 hours. As the SEM images of the first prepared batch of samples showed a poor distribution and relatively high agglomeration of zirconia and alumina particles in the composites, a new route for mixing was developed based on the

electrostatic dispersion method in pH acidic environment. This method was suggested by Gutknecht et al. (2007) and Wang and Stevens (1989) for ZTA composites to achieve more uniform dispersion and less agglomeration.

In the new developed route, the slurry of zirconia and alumina powders and distilled water (35 wt.% solid loading) was prepared and the pH value of the slurry brought to 4.5 by adding drops of dilute nitric acid. This pH value was adopted based on the findings of Gutknecht et al. (2007) who reported the highest zeta potential and the lowest viscosity, and therefore greater electrostatic dispersion, for alumina and zirconia slurries at a pH value between 4 and 5. After magnetic stirring for one hour, the slurry was attrition milled similar to the last route for 3.5 hours. Then, the slurry was freeze-dried for 48 hours using Epsilon 1-4 LSC (SciQuip, UK), and then crushed using an agate mortar and pestle and passed through a 180, 90, and 45 μm sieves using sieve shaker (AS 200 Control, Retsch, Germany).

3.1.3. Densification process

The densification and sintering process used in this research was Spark Plasma Sintering (SPS) in which the dwell time was as low as 10 minutes and can help to achieve nanostructures of the composite. This method is also known as Current-Activated Pressure-Assisted Densification (CAPAD), and its densification procedure is that very large electric currents and applied loads are employed simultaneously to dense and sinter the powders (Garay, 2010). This method was employed rather than conventional pressing and sintering process because of its advantages for producing dense specimens with nano-size grains.

The samples with 20mm diameter and 3gr mass were prepared in a graphite die and processed using a SPS sintering machine (FCT System, GmbH, Germany). A uniaxial pressure of 16 KN was applied during the sintering process from 700°C and 3, 5, 7 and 10 minutes dwell time and 1400°C, 1450°C, 1500°C, and 1550°C temperatures were selected for investigation.

3.1.4. Grinding and polishing

After sintering, the graphite particles that remained on the samples were removed using sandblaster (Guyson, UK).

The samples prepared for microstructural analysis were then cut using an Isomet 5000 linear precision saw (Buehler, USA) to make the cross section of the specimen for the next experiments. These cut samples were then cold mounted and ground by diamond abrasive disk (Buehler, USA) using automatic grinding machine Ecomet 250 Pro (Buehler, USA), and finally polished to a 1 μm finish with diamond suspensions. The surface quality was checked after each stage of grinding and polishing using an optical microscope.

The samples prepared for reciprocating sliding wear tests were mounted on metallic stubs by a hot wax resin, and then ground deeply using coarse diamond abrasive disks (250 and 125 μm) to remove the carbon diffused layer completely. Then, the samples were ground and polished very carefully to the lowest feasible roughness (linear roughness less than 20 nm) with diamond suspensions and colloidal silica. This careful attention to the surface quality is required since topographic variations and surface defects such as scratches would cause residual strains which definitely affect the friction and wear results.

3.1.5. Thermal etching

After polishing, the cold mounted samples were placed in the oven for about an hour and the samples were removed using a spatula. The wear samples were easily removed from the metallic stubs through melting the wax resin on a hot plate. Then, all the samples were cleaned using an ultrasonic agitation in isopropanol for 5 minutes.

Both type of samples were then etched thermally in the clean furnace (Elite Thermal Systems, UK) for 20 min and at the temperature 100°C below the sintering temperature in order to release residual stresses caused in the grinding process, as well as disclosing grain boundaries for microstructural studies.

3.2. Sample Characterization

3.2.1. Density measurements

Density of the compacted samples was measured based on the Archimedes principles using the density meter New Classic MF (Mettler Toledo, Switzerland). The procedure of measuring the density was taken according to the British Standard draft for determination of density and apparent porosity for fine ceramics (ISO/DIS 18754).

3.2.2. Phase analysis

In order to investigate the phase identification of the samples, especially determining the existence of monoclinic or tetragonal zirconia, XRD analysis was performed on the samples. D2 Phaser diffractometer (Bruker, USA) was used to obtain the X-ray diffraction pattern of the specimen with setting of $\text{CuK}\alpha$ source, 2θ range of 10° - 80° , and the step size of 0.02 seconds. The ICDD PDF-4+ software and database were then used for phase analysis of the samples.

3.2.3. Scanning Electron Microscopy (SEM)

The thermally etched cross-sectioned samples were carbon coated to get ready for SEM image analysis. The FEI Inspect-F microscope and FEI Inspect-F50 microscope (FEI Company, USA) was used to take both secondary electron (SE) and back scattered electron (BSE) images of the sample to analyze the microstructure. The average grain size was determined using point counting method for measuring the volume fraction of two phases, and the linear intercept method for calculating the grain size, based on ASTM E562-02 and ASTM E112-12 principles respectively.

3.2.4. Mechanical testing

Hardness measurements (H_V) were done with Vickers indentations at a load of 10 Kgf and 20 second dwell time, with a manual hardness tester (CV Instruments, UK). Ten indentations were

made on each sample and the diagonal and the crack length were measured using optical microscope (Eclipse LV150, Nikon, Japan). The Vickers hardness was calculated by the following equation proposed by Shetty et al. (Ponton & Rawlings, 1989):

$$H_v = \frac{0.4636 P}{a^2}$$

H_v = Vickers hardness (Pa)

P = Load test (N)

a = Average half diagonal length

The fracture toughness (K_C) of the samples was measured based on the Palmqvist cracks which occurred with a Vickers indentation. This method is extensively used to determine the fracture toughness of brittle materials because of the ease of sample preparation (no need to process special samples) and the simplicity of the test; however, there is some confusion about the multiple models and equations in the literature relating the degree of cracking to the fracture toughness. Among nineteen equations suggested for toughness documented by Ponton and Rawlings (1989; 1989), the equation proposed by Shetty et al. has been used, known as SWMC (Ponton & Rawlings, 1989):

$$K_C = \frac{0.0319 P}{a\sqrt{l}}$$

K_C = Indentation toughness ($\text{Pa m}^{1/2}$)

P = Load test (N)

a = Average half diagonal length

l = Average crack length

3.3. Reciprocating wear testing

As stated before, the main objective of this research was to introduce a new range of promising materials for hip and knee joint replacements; therefore, the wear properties of the fabricated material was critical as these prostheses operate under in severe environment. Like many other biological tests, in-vitro tests were selected as the most convenient and feasible method, trying to simulate the in-vivo conditions as accurately as possible. The in-vitro equipment for tribological studies are mainly divided into three categories of pin-on-disc machines, reciprocating pin-on-flat machines and joint simulators (Dowson, 2001; Jin, et al., 2006). The first two methods are easy to operate and relatively cheap, and are beneficial for evaluating the nature of wear and friction for the contact surfaces under well controlled load, speed and environment (Dowson, 2001; Jin, et al., 2006). The reciprocating ball-on-flat have an advantage over the pin-on-disc technique as they could simulate the reciprocating actions mostly associated with the hip joint motions and can be considered as a simplified wear procedure and part representative of involving mechanisms in wear of hip joints (Saikko, 1993; Jin, et al., 2006; Rana, 2013). This is why many researchers have used this technique as the first stage of tribological characterization, which could give a valuable insight into the mechanisms of friction and wear of biomaterials for hip joint prosthesis (Saikko, 1993; Ortega-Saenz, et al., 2008; Jin, et al., 2006; Rana, 2013; Dowson, 2001; Smirnov, et al., 2011; Ma & Rainforth, 2010; Ma & Rainforth, 2012; Shirkhan, 2014; Zanoria & Danyluk, 1993). It should be mentioned that in order to simulate all aspects of motion between femoral head and cup, and the lubrication regimes at the body environment, the tests should be carried out using joint simulators, but this was not available for this study.

The reciprocating ball-on-flat wear tests were performed at room temperature using a UMT tribometer (Bruker, USA) for different loads in lubricated conditions. Figure 3.2 shows the schematic image of the performed reciprocating test. The balls used for this range of tests were high purity alumina balls (Oakwade, UK) with 4 mm diameter and approximate linear roughness of 5-8 nm.

Due to a very difficult and delicate preparation process for wear samples as well as time-consuming process for wear tests, measuring the wear properties of all samples was impossible. Therefore, few samples of each series of ZTA, ZTA + 0.1 mole.% TiO₂, and ZTA + 0.5 mole.% TiO₂ showing high density and reasonable mechanical properties were selected. For

investigating the effect of titania on the wear behavior of ZTA composites, these samples were also selected based on having comparable and close microstructure to avoid the effect of grain sizes on the wear properties. Selection was also allowed the possible effects of sintering temperature and time on wear to be studied for samples with the same composition.

ZTA samples with respective sintering temperature and time of 1450°C-7min, 1500°C-7min, 1550°C-7min; ZTA+ 0.1 mole.% TiO₂ samples with respective sintering temperature and time of 1450°C-5min, 1500°C-5min, 1550°C-5min; and ZTA+ 0.5 mole.%TiO₂ samples with respective sintering temperature and time of 1400°C-5min, 1450°C-5min, and 1500°C-5min were prepared as disc shaped samples and ground and polished very carefully to achieve the lowest feasible linear roughness being under 20 nm. They were then thermal etched to release residual stresses caused by grinding and polishing process, which might affect the wear behaviour.

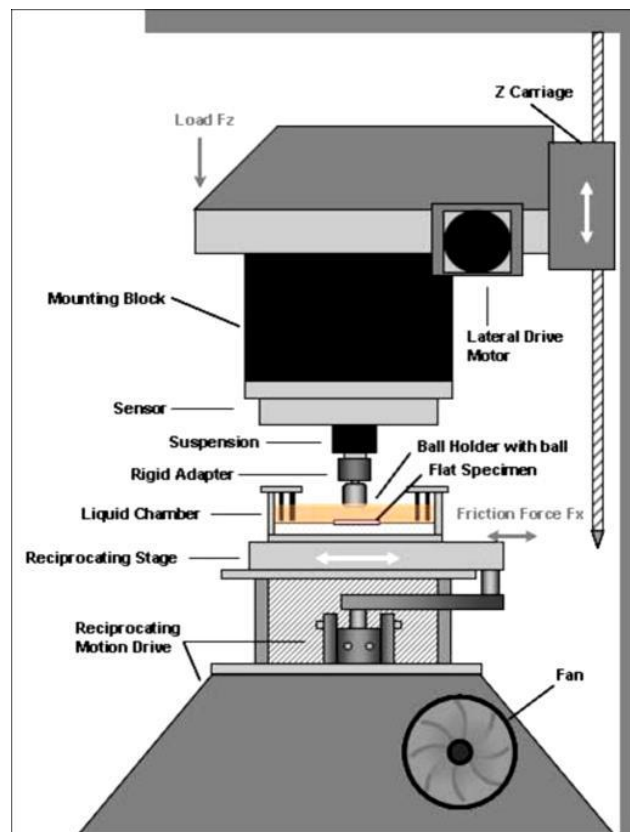


Figure 3.2. Schematic of the reciprocating test in UMT tribometer (Bruker Website)

The specimens were then cleaned in isopropanol using an ultrasonic bath and mounted in a liquid chamber and soaked in the lubricant more than 12 hours before the test. The test procedures were designed for 24 hours with normal load of 1N, 4N, 8N and for 8 hours with

normal load of 16N. The selected reciprocating speed was 600 rpm (10 Hz) and the stroke length was set as 10 mm for all the test procedures. Fresh lubricant was introduced every 8 hours during the test to avoid degradation. The friction coefficient (COF) and real sliding time were recorded by UMT software for next analysis.

The lubricant used for this study was 25 vol.% new-born calf serum which is mostly used in biological tests and cell culturing as because of its physiological range and viscosity close to synovial fluids (Dumbleton, 1981). The lubricant was made through dissolving phosphate buffered saline (Sigma-Aldrich, UK) with the ratio of one tablet per 200 mL and 0.1 wt.% sodium azide (Fisher, UK) in ultra-pure water (Fisher, UK), then adding 25 volume percent of sterile new-born calf serum (First Link, UK) to the solution. Then it was vigorously stirred using a magnetic plate for an hour and kept in the fridge to avoid degradation. The resulted solution showed a viscosity of 0.0012 Pa.s during the test.

3.4. Wear scar characterization

3.4.1. 3D optical Microscopy

After the wear test, the samples were cleaned by isopropanol to remove the loose debris on the samples and then the wear scars were studied using a 3D optical microscope, Contour GT (Bruker, USA). 3D images using VSI mode (vertical scanning interferometer) at different magnifications with green light illumination were taken, and linear roughness of the worn surfaces were measured by this microscope. In addition, the profilometers of the cross-sections from 7 different locations of the wear scars were obtained which were used further for calculating the wear rate.

3.4.2. Wear rate calculation

The wear scar profile was obtained from different locations of the worn cross-sections, as mentioned above, and transferred to an excel file. These profiles were acquired to measure the average cross-sectional wear loss area (A) through calculating the area above the worn curves. Then, the total wear volume loss (V) was measured by multiplying A to stroke length of wear track (D), as showed below:

$$V=AD$$

Specific wear rate were consequently calculated based on an equation proposed by Archard (Archard, 1953):

$$k = V / NS$$

k = Specific wear rate coefficient
(mm³/Nm)

V = Wear volume (mm³)

N = Normal load (N)

S = Sliding distance (m)

For above equation sliding distance (S) can be replaced by $S=v.t$, where v is the mean sliding rate value and t is running time.

3.4.3. Raman Spectroscopy

In order to examine the composition of wear scars and investigate if any tribolayer was formed during the test, Raman spectra of the wear scars were determined using inVia Confocal Raman Microscope (Renishaw, UK). The laser light used for this analysis was green light with 514.5 nm wavelength. The spectra was acquired for the range of 50 to 2000 cm⁻¹ and the exposure time was 10 seconds per point. Compositional mapping of the worn surfaces also were done by mapping analysis feature of the microscope.

3.4.4. Atomic Force Microscopy (AFM) and Lateral Force Microscopy (LFM)

In order to investigate the topography and surface of the wear scars to nanometer scale, AFM and LFM techniques were adopted using Dimension 3100 AFM (Veeco, USA). After the first analysis of AFM studies, it was found that tribolayer formed on the worn surfaces inhibited the exposure of the grain structures in AFM. Therefore, the samples were immersed in a solution of Vikron tablet (Antec, UK) (which is a proven chemical for safe anti-bacterial cleaning and

effective in removing biochemical substances) and warm water for 4 hours and the surface particularly the wear scars were cleaned using cotton buds.

In AFM study, tapping mode of the machine was selected in which the silicon nitride cantilever can be deflected by a very small contact force as a result of its low spring constant, i.e. 0.12 N/m. These deflections are in the vertical direction and are detected by small laser signal changes and can form pseudocolour image which gives useful information about the roughness of the surface at nanoscale.

In LFM technique, contact mode of the machine was selected. The principle of this technique is very similar to AFM with the difference that in LFM a lateral force is applied to cantilever and its deflection in the horizontal direction is measured. Thus, the extent of cantilever lateral deflection is dependent on frictional coefficient, topography of the surface, movement direction of the cantilever and its lateral spring constant. This method can be helpful for this study of composite material as can give useful information for both surface friction of each phase and topography and provide a structural map of the surface.

4. RESULTS

4.1. Sample Characterization

4.1.1. Density Measurements

The relative density at different temperatures and dwell times for samples containing 0, 0.1, 0.5, 2 and 5 mole.% TiO₂ are shown in Figure 4.1, and the values are listed in Table 4.1 to Table 4.5.

As can be seen in Figure 4.1 all the samples are reasonably dense having relative density more than 97.5% of the theoretical density. Samples containing lower amounts of titania (Figure 4.1.b and Figure 4.1.c) show generally higher relative density (more than 99% of theoretical density) in comparison with samples with high amount of titania (Figure 4.1.d and Figure 4.1.e).

The effect of higher sintering temperature and time on enhancing the density can easily be seen on ZTA samples (Figure 4.1.a), while this effect seems to be diminished in samples containing titania. In some of the samples, sintering at 1550°C shows lower density than the lower temperatures while the density is normally expected to increase with increasing the temperature.

The maximum relative density, which was very close to theoretical density, was obtained at 1500°C-3mins and 1550°C-5mins for ZTA samples, while for 0.1 wt.% and 0.5 wt.% TiO₂ samples have been reported at 1500°C-7min and 1500°C-5min respectively.

Table 4.1. Characteristics of ZTA samples at different sintering temperature and dwell time

Sintering Temperature (°C)	Sintering dwell time (min)	Relative density (%)	Grain sizes	
			Zirconia (nm)	Alumina (nm)
1400	3	98.73	110±49	172±27
	5	98.24	131±35	173±23
	7	98.26	133±75	242±55
	10	98.35	134±62	257±23
1450	3	99.79	130±23	222±26
	5	99.85	138±17	242±11
	7	99.00	140±96	244±63
	10	98.80	142±90	271±74
1500	3	99.99	164±93	283±26
	5	99.82	168±67	285±23
	7	99.04	176±110	310±13
	10	99.09	192±85	325±66
1550	3	99.64	204±65	348±35
	5	99.99	210±110	355±73
	7	99.16	212±73	418±37
	10	99.29	221±101	521±118

Table 4.2. Characteristics of ZTA+0.1 mol.% TiO₂ samples at different sintering temperature and dwell time

Sintering Temperature (°C)	Sintering dwell time (min)	Relative density (%)	Grain sizes	
			Zirconia (nm)	Alumina (nm)
1400	5	99.42	144±66	220±35
	7	99.23	NA	NA
1450	5	99.77	121±74	255±51
	7	99.89	180±101	337±73
	10	99.86	159±82	328±56
1500	5	99.85	170±71	295±60
	7	99.99	186±92	441±84
1550	5	99.73	264±152	414±81
	7	99.52	204±160	434±84

Table 4.3. Characteristics of ZTA+0.5 mol.% TiO₂ samples at different sintering temperature and dwell time

Sintering Temperature (°C)	Sintering dwell time (min)	Relative density (%)	Grain sizes	
			Zirconia (nm)	Alumina (nm)
1400	5	99.22	120±95	236±39
	7	99.43	136±58	240±39
	10	99.59	145±88	279±38
1450	5	99.86	181±96	347±72
	7	99.43	176±101	339±62
	10	99.32	181±96	347±72
1500	5	99.99	232±130	338±96
	7	99.88	224±130	462±104
	10	99.67	226±192	412±89
1550	5	99.67	264±164	478±143
	7	99.68	226±137	412±89
	10	NA	NA	NA

Table 4.4. Characteristics of ZTA+2 mol.% TiO₂ samples at different sintering temperature and dwell time

Sintering Temperature (°C)	Sintering dwell time (min)	Relative density (%)	Grain sizes	
			Zirconia (nm)	Alumina (nm)
1400	5	98.08	325±134	643±259
	7	97.98	NA	NA
1450	5	97.78	324±160	792±168
	7	97.88	NA	NA
1500	5	97.74	463±217	877±305
	7	97.67	NA	NA
1550	5	97.86	668±308	1046±263
	7	NA	NA	NA

Table 4.5. Characteristics of ZTA+5 mol.% TiO₂ samples at different sintering temperature and dwell time

Sintering Temperature (°C)	Sintering dwell time (min)	Relative density (%)	Grain sizes	
			Zirconia (nm)	Alumina (nm)
1400	5	98.22	342±263	624±140
	7	98.05	331±197	529±182
1450	5	97.86	458±272	900±243
	7	97.82	NA	NA
1500	5	98.19	785±248	1297±486
	7	NA	NA	NA
1550	5	97.98	913±497	1479±406
	7	NA	NA	NA

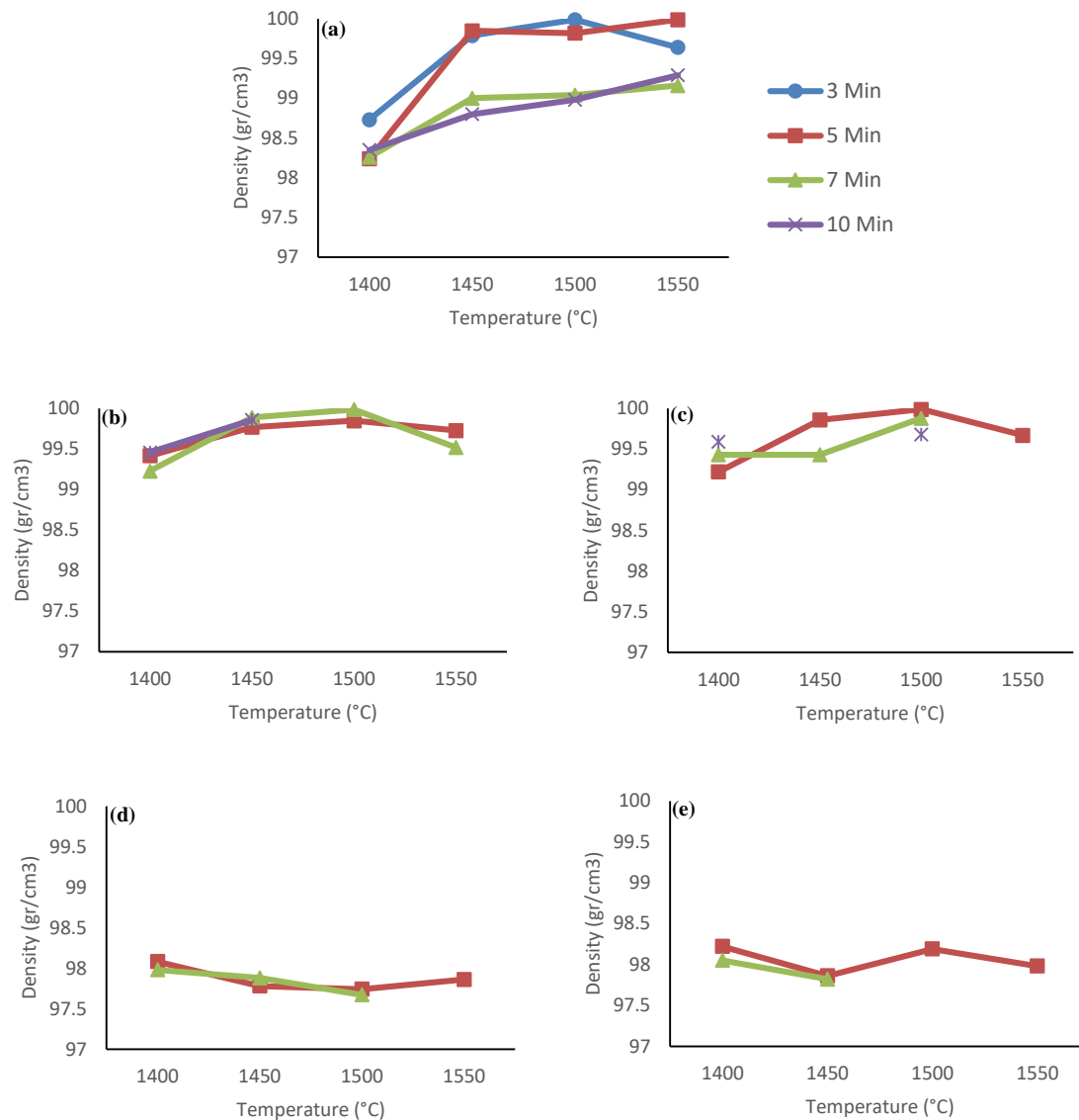


Figure 4.1. Relative density of ZTA(a), ZTA + 0.1 mol.% TiO₂ (b), ZTA + 0.5 mol.% TiO₂ (c), ZTA + 2 mol.% TiO₂ (d), ZTA + 5 mol.% TiO₂ (e) vs sintering temperature for different sintering dwell time

4.1.2. Phase analysis

The XRD patterns for ZTA, ZTA+0.1 mol.%, and ZTA+0.5 mol.% TiO₂ were found to be the same at different temperatures and times. Figure 4.2 shows one of the XRD patterns for samples sintered at 1550°C and 5 minutes. As can be seen, for ZTA samples the peaks of alumina and tetragonal zirconia have been detected, and there is no trace of monoclinic phase. For samples containing TiO₂, the same peaks of tetragonal zirconia were detected.

For the higher amount of titania addition, the XRD patterns showed different peaks with the ones detected in Figure 4.2. Figure 4.3 and Figure 4.4 give XRD patterns for ZTA samples containing 2 mol.% and 5 mol.% TiO_2 respectively, sintered for 5 minutes at different temperatures. It can be seen in Figure 4.3 that a new phase has been detected for all tested sintering temperatures, which is ZrTiO_4 . Furthermore, by increasing temperature more than 1450 °C, peaks related to monoclinic zirconia are present, Figure 4.3.c and Figure 4.3.d.

Figure 4.4 shows XRD patterns for ZTA samples containing 5 mol.% TiO_2 sintered at different temperatures for 5 minutes. It is clear from this figure that all the samples contained monoclinic zirconia and ZrTiO_4 , and the tetragonal zirconia peaks shows less intensity compared to the same peaks in Figure 4.2 and Figure 4.3.

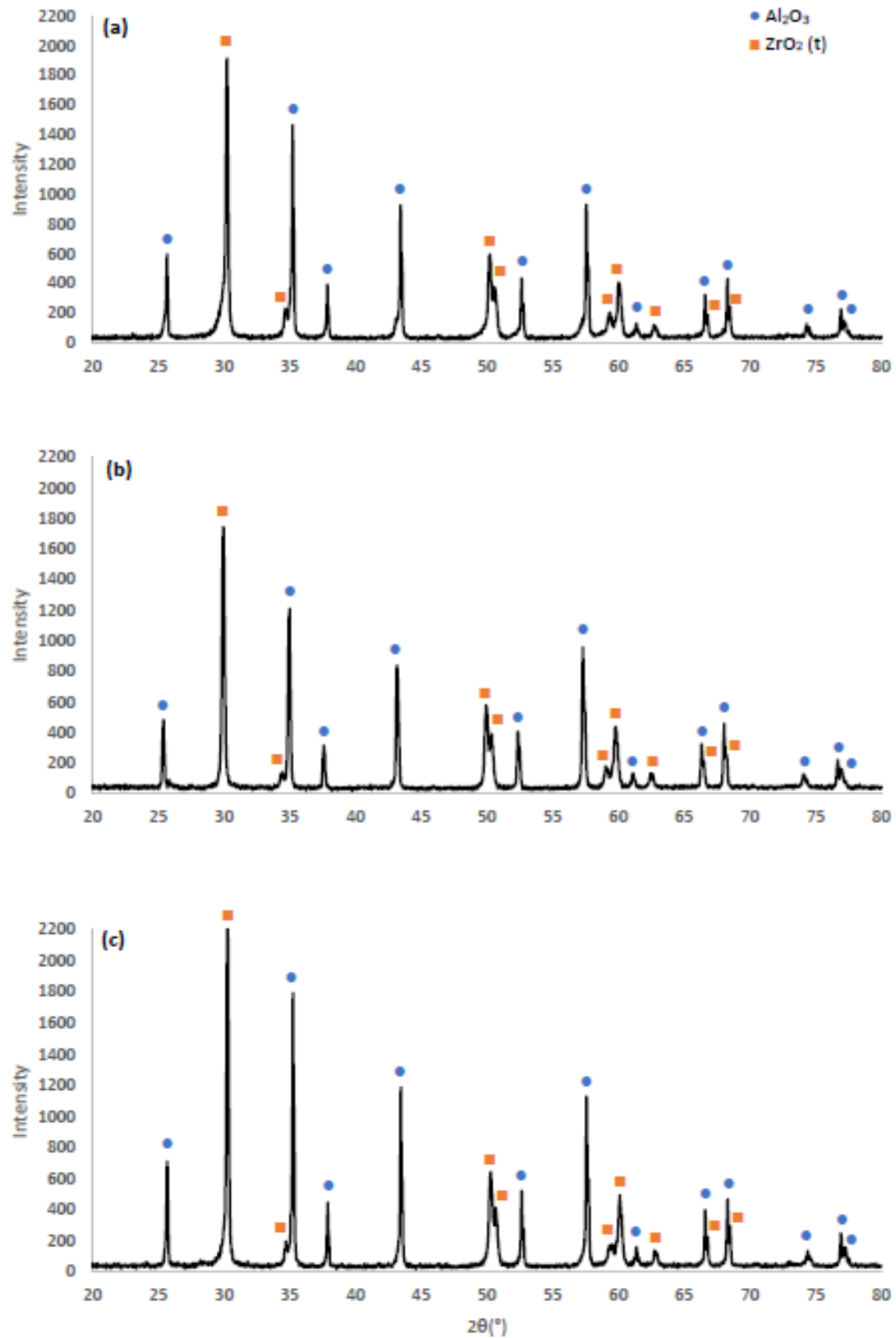


Figure 4.2. XRD patterns of (a) ZTA, (b) ZTA + 0.1 mol.% TiO₂, (c) ZTA + 0.5 mol.% TiO₂ sintered at 1550°C for 5 minutes.

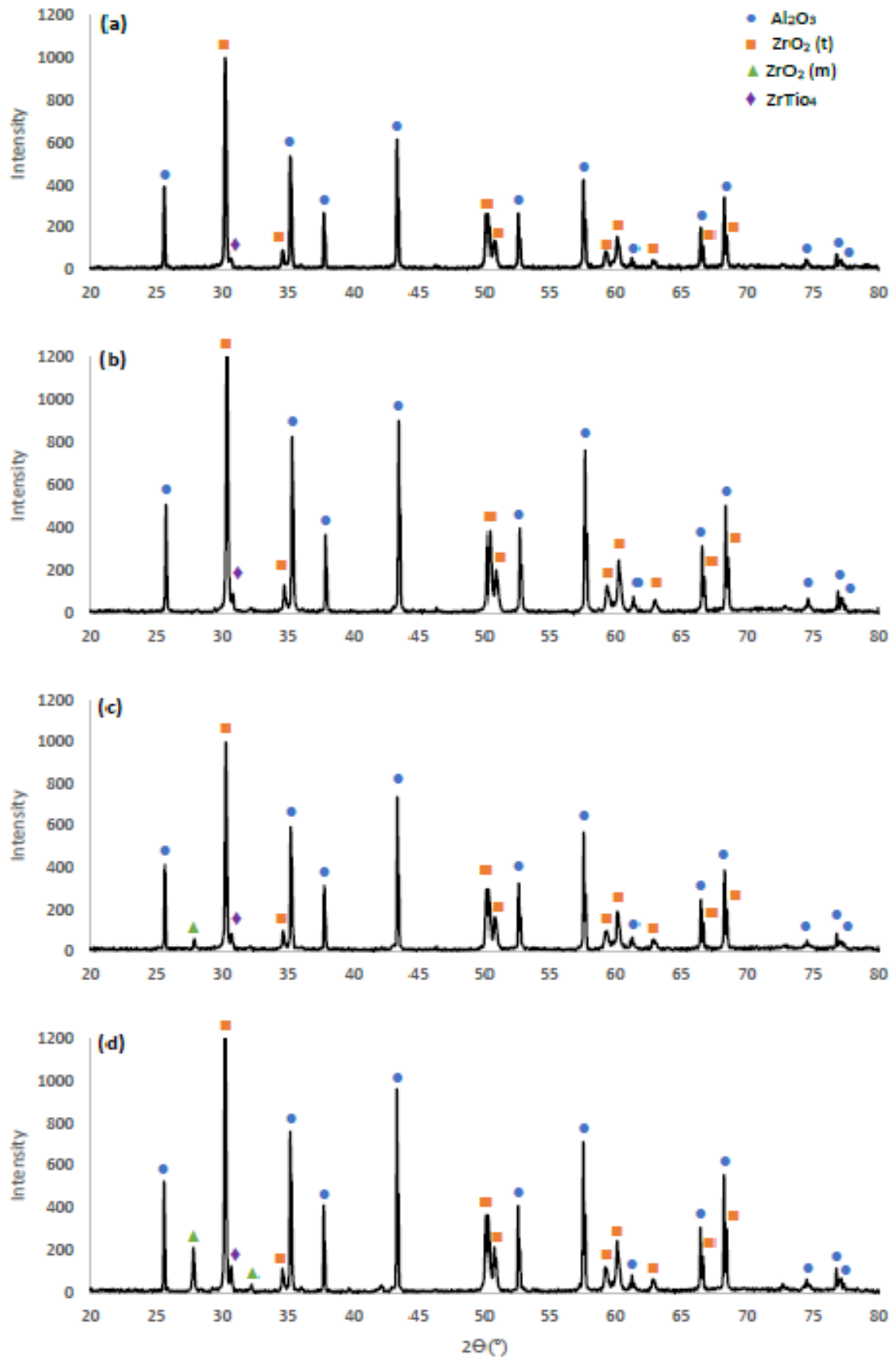


Figure 4.3. XRD patterns of ZTA + 2 mol.% TiO_2 sintered for 5 minutes at (a) 1400°C, (b) 1450°C, (c) 1500°C, and (d) 1550°C.

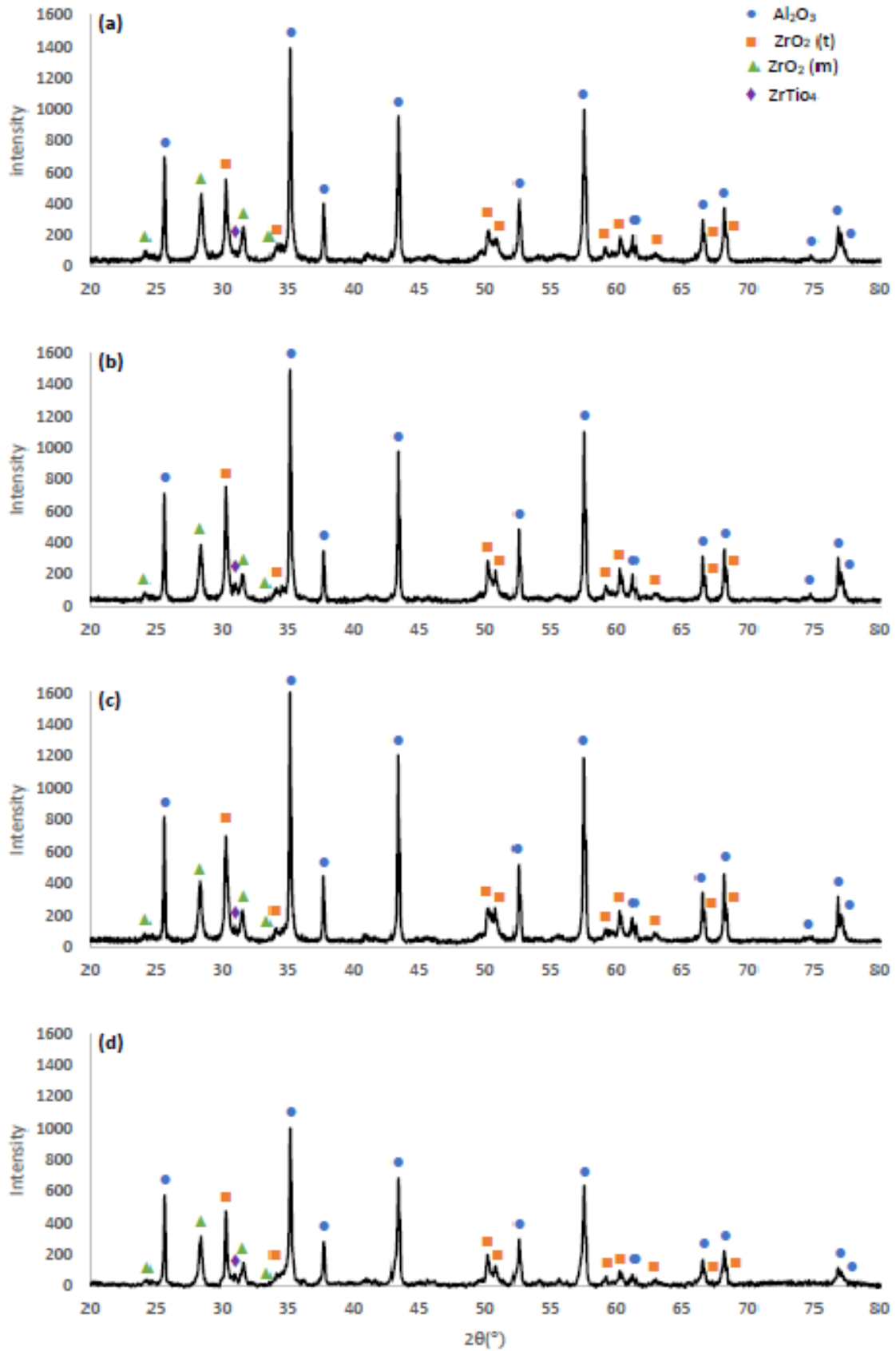


Figure 4.4. XRD patterns of ZTA + 5 mol.% TiO₂ sintered for 5 minutes at (a) 1400°C, (b) 1450°C, (c) 1500°C, and (d) 1550°C

4.1.3. Microstructure Characterization

The grain size values for both alumina and zirconia of the different samples of ZTA, ZTA with 0.1, 0.5, 2, 5 mol.% TiO_2 are listed in Table 4.1 to Table 4.5 and are shown in Figure 4.5 to Figure 4.9. It can be seen that the grain size increases with increasing time and temperature of the sintering process.

Figure 4.10 shows the effect of TiO_2 addition on the grain size, for the samples sintered at 5 minutes dwell time and different sintering temperature. The values of this graph are listed in Table 4.6. As can be seen from these table and figure both alumina and zirconia average grain sizes increased with increasing TiO_2 content, and reaching to micron size for the larger amount of titania sintered at the higher temperatures.

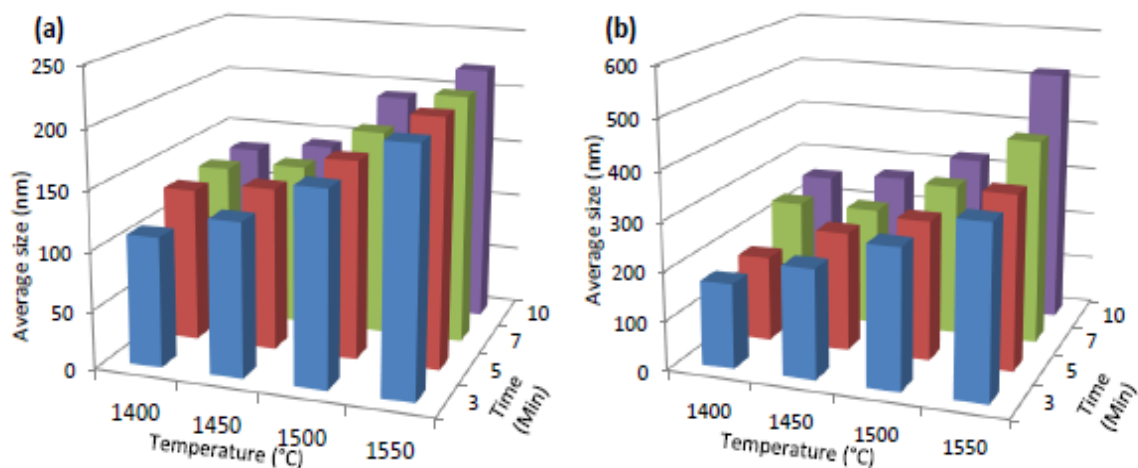


Figure 4.5. Average grain sizes for zirconia (a) and alumina (b) particles in ZTA samples at different sintering temperature and dwell time.

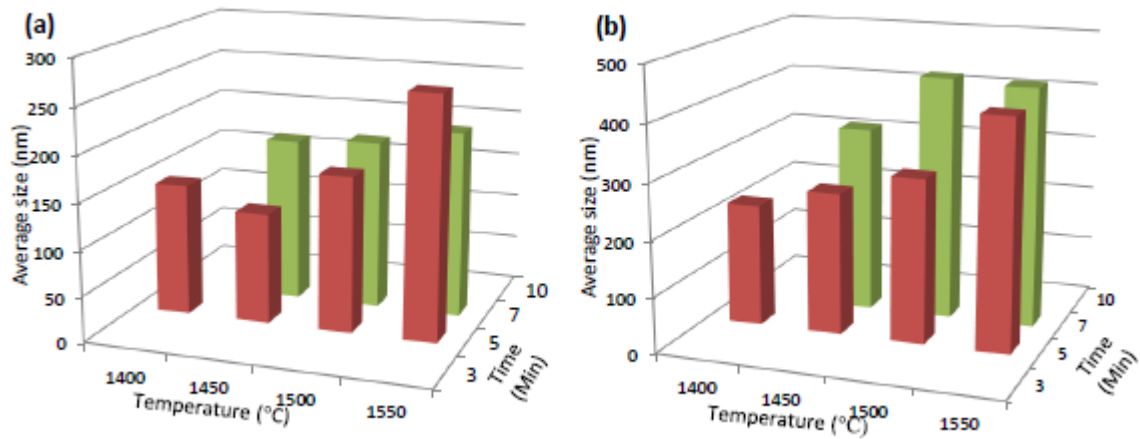


Figure 4.6. Average grain sizes for zirconia (a) and alumina (b) particles in ZTA+0.1mol.% TiO₂ samples at different sintering temperature and dwell time.

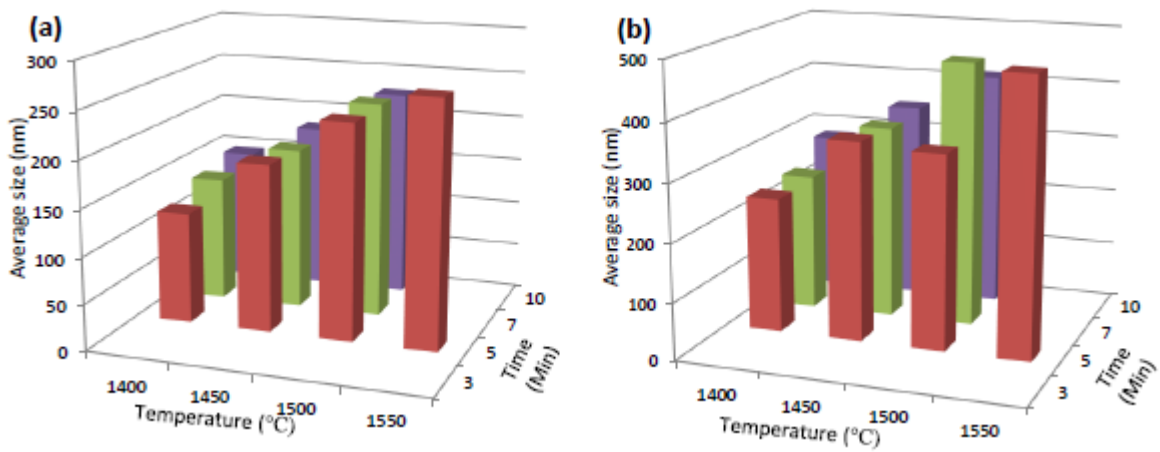


Figure 4.7. Average grain sizes for zirconia (a) and alumina (b) particles in ZTA+0.5mol.% TiO₂ samples at different sintering temperature and dwell time.

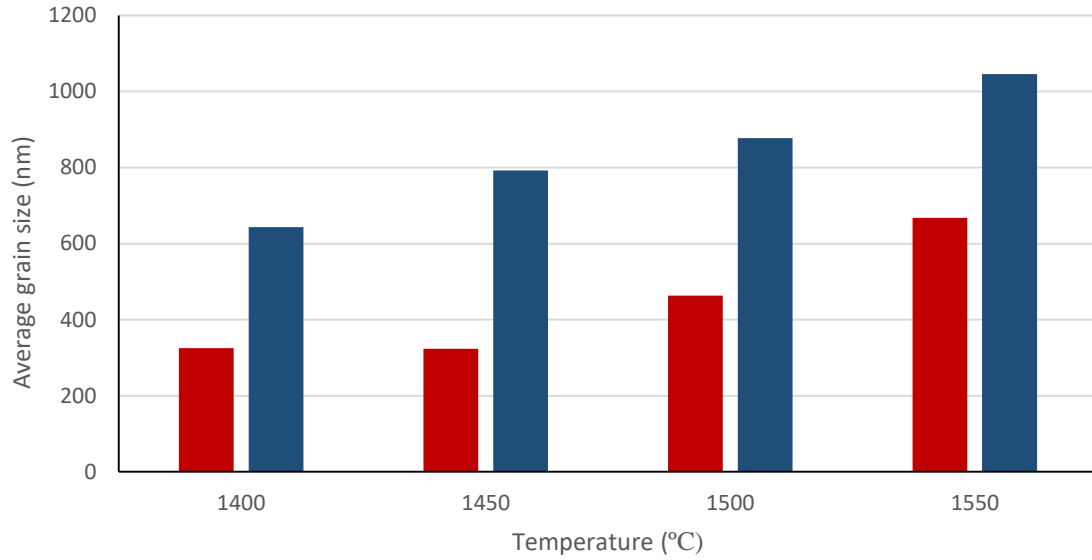


Figure 4.8. Average grain sizes for zirconia (red) and alumina (blue) particles in ZTA+2mol.% TiO₂ samples at different sintering temperature and 5 minutes dwell time.

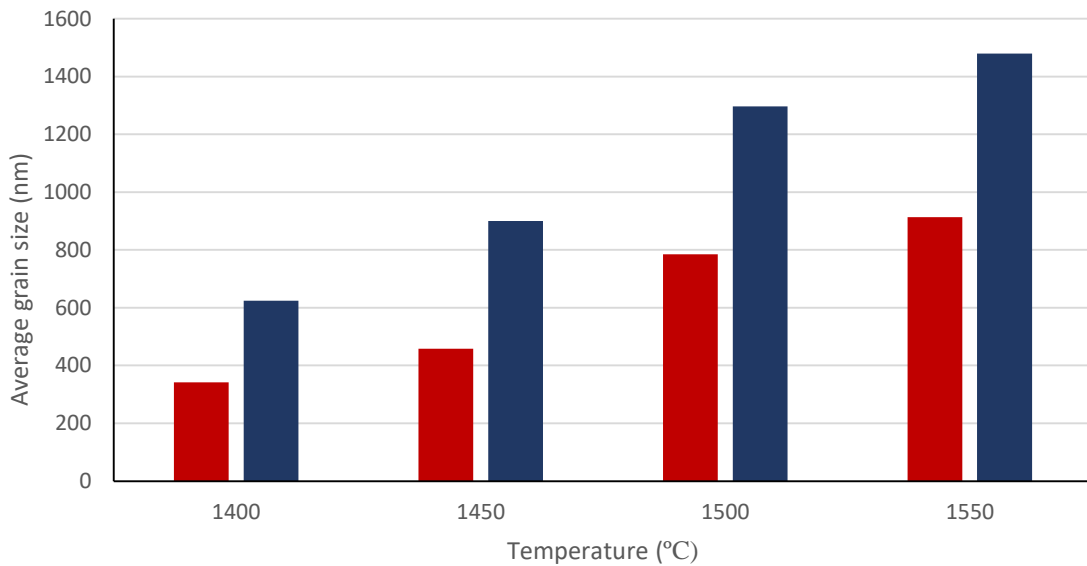


Figure 4.9. Average grain sizes for zirconia (red) and alumina (blue) particles in ZTA+5mol.% TiO₂ samples at different sintering temperature and 5 minutes dwell time.

Table 4.6. Average grain sizes of zirconia and alumina particles for samples sintered for 5 minutes

Material	Sintering Temperature (°C)	Grain sizes	
		Zirconia (nm)	Alumina (nm)
ZTA	1400	131±35	173±23
	1450	138±17	242±11
	1500	168±67	285±23
	1550	210±110	355±73
ZTA + 0.1 mol.% TiO₂	1400	144.1±66.5	220.2±35
	1450	121±73	255±51
	1500	170.5±71	295.4±60
	1550	264.1±152	414.0±81
ZTA + 0.5 mol.% TiO₂	1400	119.9±95	236.0±39
	1450	181.0±96	346.7±72
	1500	232.4±130	338.2±96
	1550	264.0±164	478.3±143
ZTA + 2 mol.% TiO₂	1400	325±134	643±259
	1450	324±161	792±169
	1500	463±217	877±306
	1550	668±308	1046±264
ZTA + 5 mol.% TiO₂	1400	342±263	624±141
	1450	458±272	900±243
	1500	785±248	1297±486
	1550	913±497	1479±406

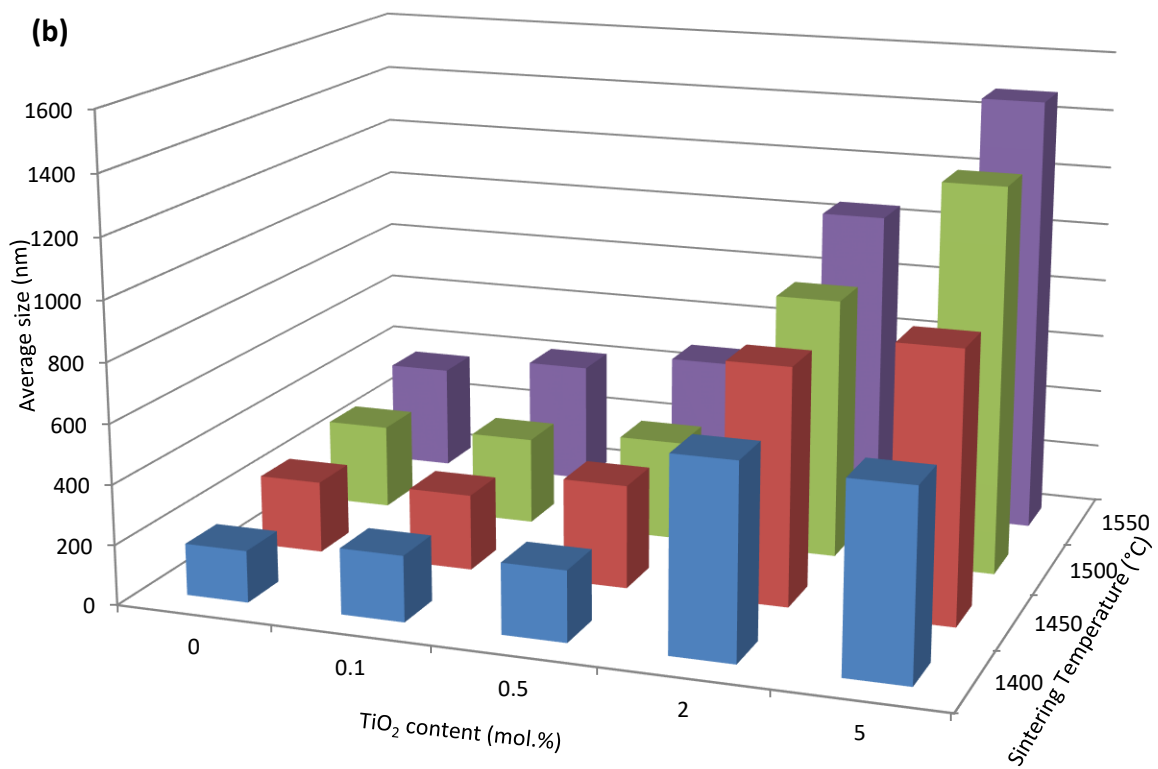
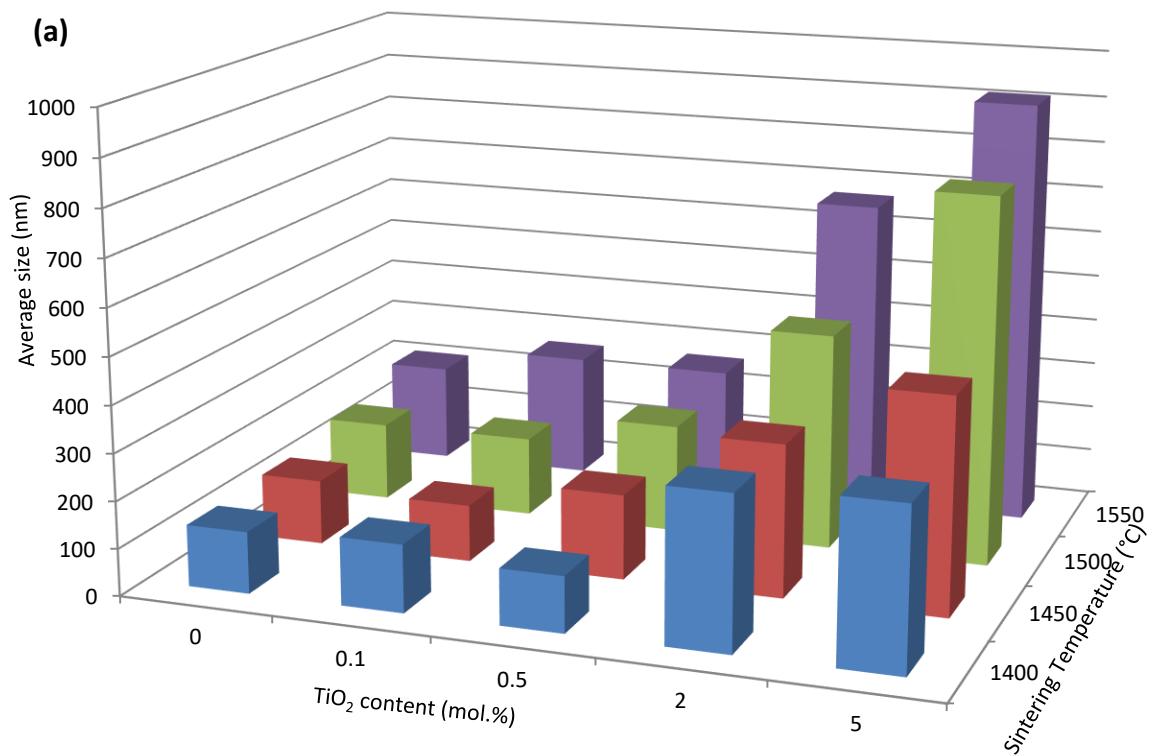


Figure 4.10. Average grain sizes of zirconia (a) and alumina (b) particles for samples sintered for 5 minutes

The SEM images of selected samples are shown in Figure 4.11 to Figure 4.14, in which alumina grains exhibit dark contrast and zirconia grains are bright. In all the images, two kinds of ZrO_2 particles can be distinguished, which are faceted intergranular ZrO_2 particles located between alumina grains (generally at the grain corners) and spherical transgranular ZrO_2 particles, located within the alumina grains (marked by arrows). Comparing the microstructure of samples with different amount of TiO_2 also shows that TiO_2 addition changed the microstructure both in aggregation and surface roughness of the grains. The samples without TiO_2 have an even and flat microstructure after thermal etching, while the grains become more faceted with the TiO_2 addition.

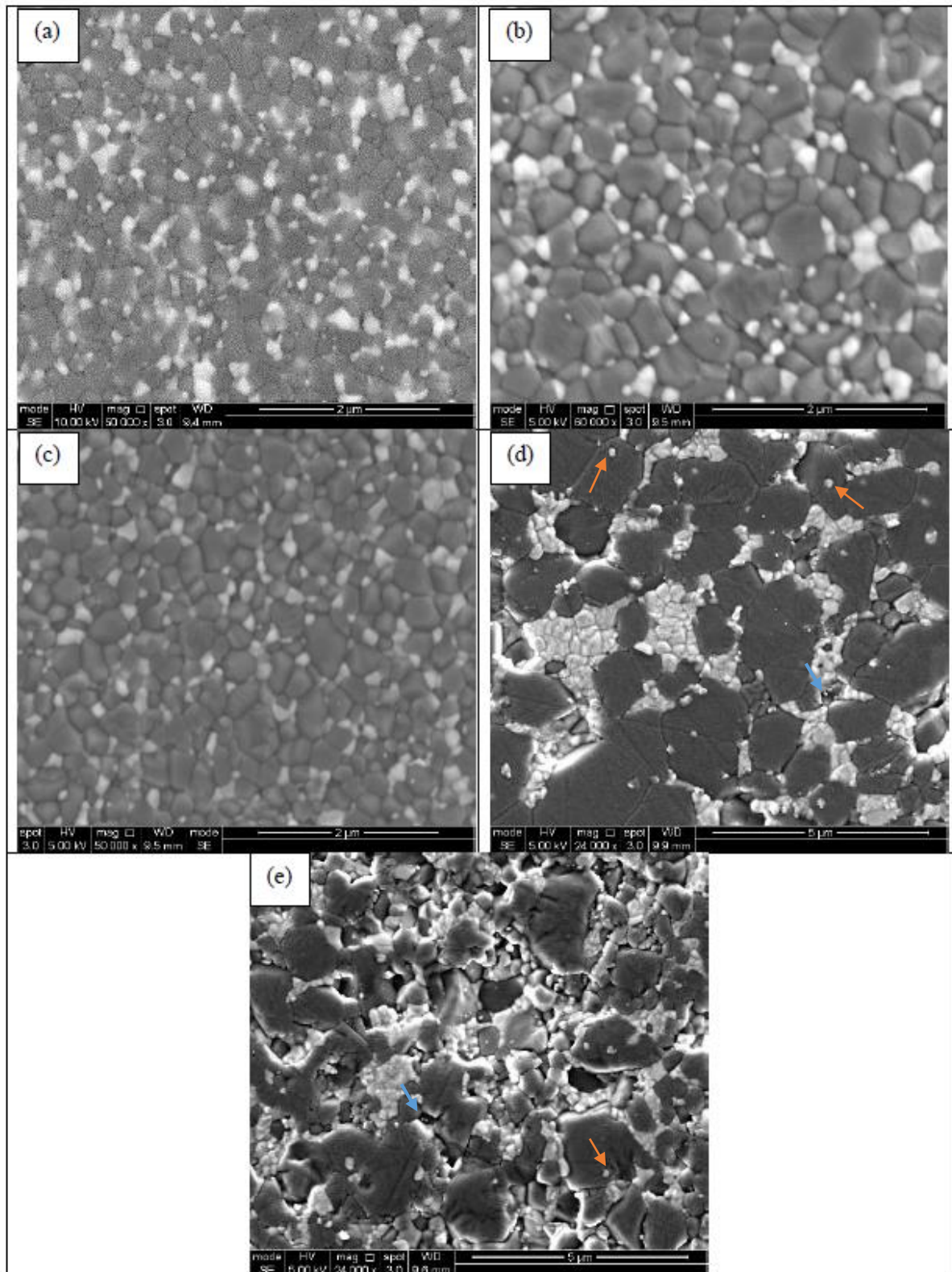


Figure 4.11. Secondary electrons SEM images of samples sintered for 5 minutes at 1400°C for ZTA (a), ZTA+0.1 mol.% TiO₂ (b), ZTA+0.5 mol.% TiO₂ (c), ZTA+2 mol.% TiO₂ (d), ZTA+5 mol.% TiO₂ (e), representing transgranular ZrO₂ particles, located within the alumina grains with orange arrows and pores with blue arrows

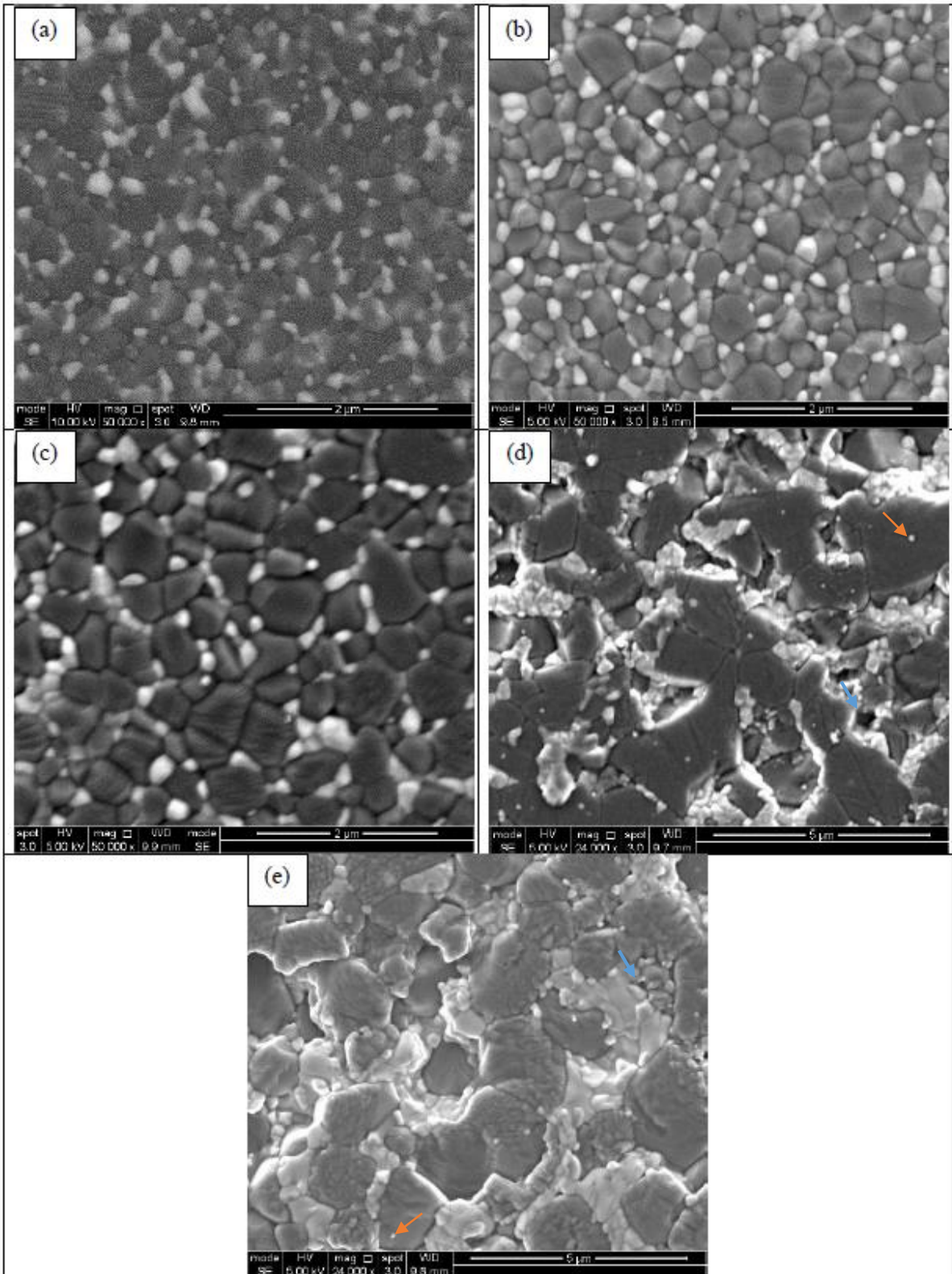


Figure 4.12. Secondary electrons SEM images of samples sintered for 5 minutes at 1450°C for ZTA (a), ZTA+0.1mol.%TiO₂ (b), ZTA+0.5mol.%TiO₂ (c), ZTA+2mol.%TiO₂ (d), ZTA+5mol.%TiO₂ (e), representing transgranular ZrO₂ particles, located within the alumina grains with orange arrows and pores with blue arrows

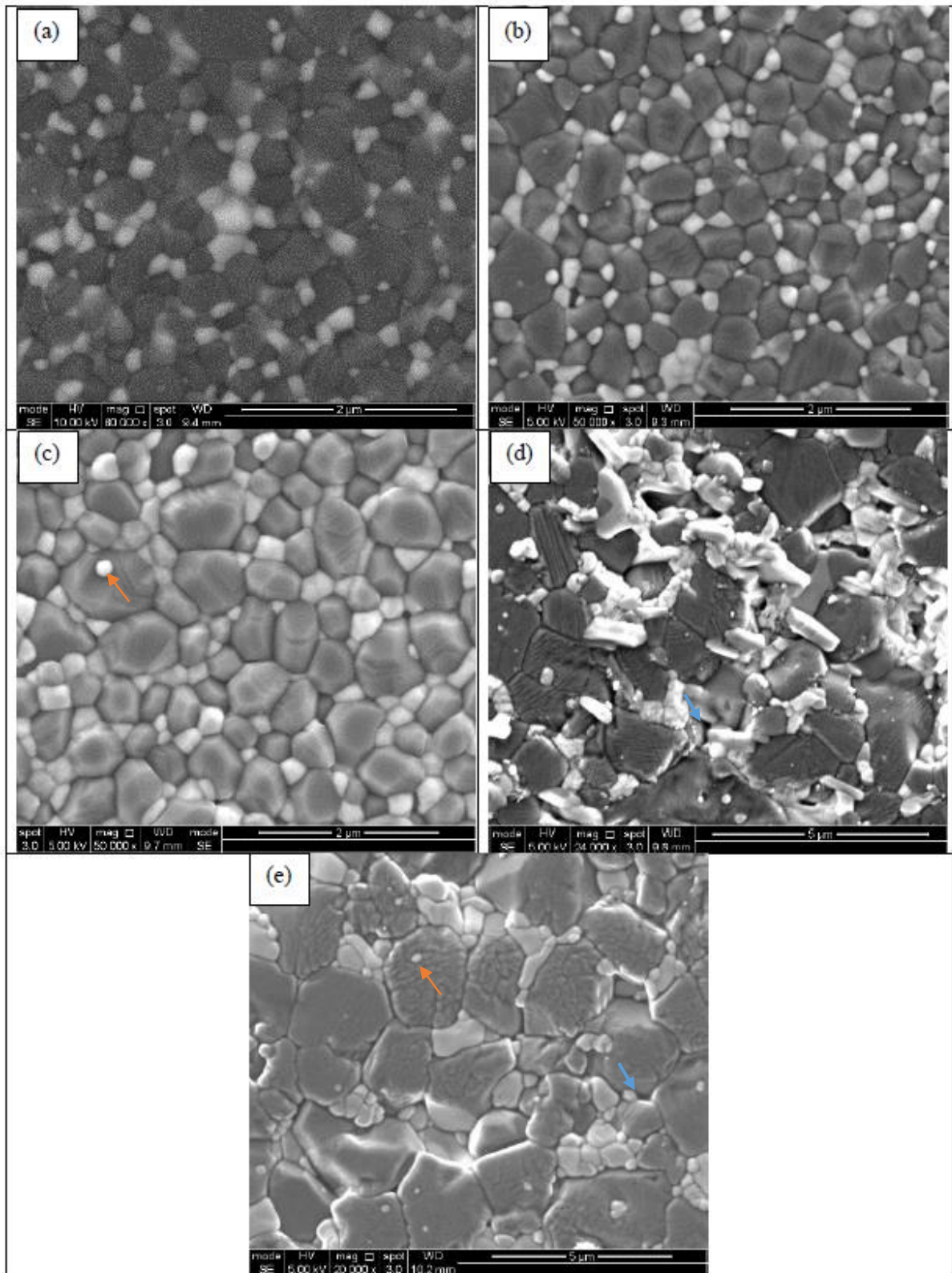


Figure 4.13. Secondary electrons SEM images of samples sintered for 5 minutes at 1500°C for ZTA (a), ZTA+0.1mol.%TiO₂ (b), ZTA+0.5mol.%TiO₂ (c), ZTA+2mol.%TiO₂ (d), ZTA+5mol.%TiO₂ (e), representing transgranular ZrO₂ particles, located within the alumina grains with orange arrows and pores with blue arrows

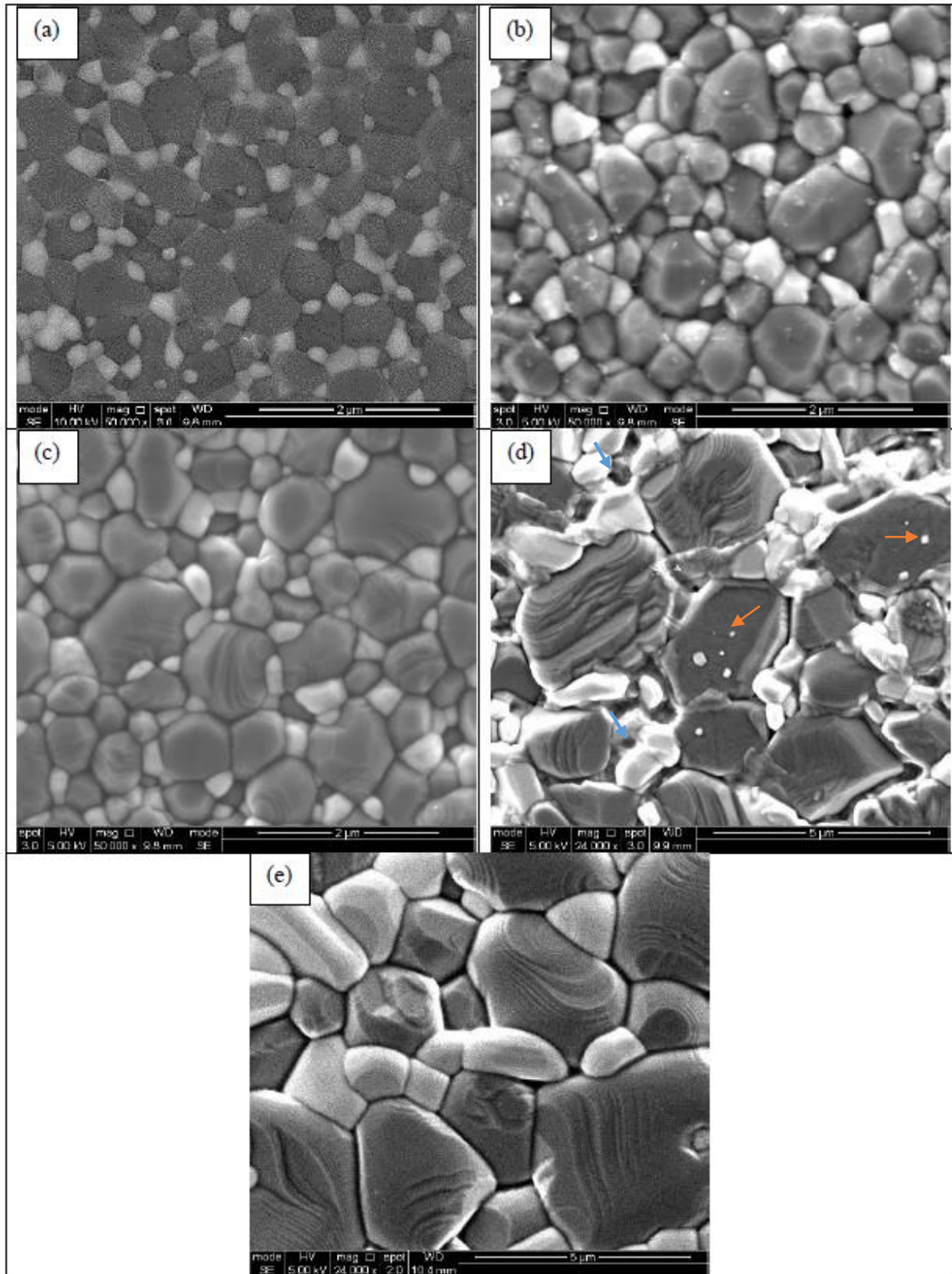


Figure 4.14. Secondary electrons SEM images of samples sintered for 5 minutes at 1550°C for ZTA (a), ZTA+0.1 mol.% TiO₂ (b), ZTA+0.5 mol.% TiO₂ (c), ZTA+2 mol.% TiO₂ (d), ZTA+5 mol.% TiO₂ (e), representing transgranular ZrO₂ particles, located within the alumina grains with orange arrows and pores with blue arrows

As the XRD patterns showed new phases of ZrTiO_4 and monoclinic zirconia for the samples containing 2 mol.% and 5 mol.% TiO_2 , the backscattered electron (BSE) images of these samples were taken to detect the compositional map in microstructure. Figure 4.15 and Figure 4.16 show BSE images of ZTA samples containing 2 mol.% and 5 mol.% TiO_2 respectively, sintered at different temperature for 5 minutes. In BSE images, which are formed based on elastic scattering of electrons, atoms with a higher atomic number have higher probability of causing elastic collision and therefore, higher number of backscattered electrons reaching the detector. Thus, the brighter areas are related to the atoms with greater atomic number, while darker areas show lower atomic number. In this study, alumina grains can be seen as the dark grains and zirconia would be detected as the white grains as a result of the differences in aluminium and zirconium atomic numbers.

The map of ZTA without TiO_2 and with smaller amounts of TiO_2 (0.1 mol.% and 0.5 mol.%) only were consisted of black and white grains. However, on adding TiO_2 particles with a new grey contrast were detected in BSE images, which is believed to be ZrTiO_4 as will be discussed later. As can be seen in Figure 4.15 and Figure 4.16 the grains with grey contrast can be hardly seen at 1400°C (Figure 4.15.a and Figure 4.16.a) while they were more detectable with increasing sintering temperature. This effect can also be found by increasing titania amount through comparing the corresponding BSE images sintered at the same conditions in Figure 4.15 and Figure 4.16.

Furthermore, Figure 4.16.b and Figure 4.16.c show the formation of the grey phase (probably ZrTiO_4) within the zirconia grains, which has been completed to form a whole grain at 1550°C (Figure 4.16.d). This structure has been demonstrated in higher magnification in Figure 4.17.

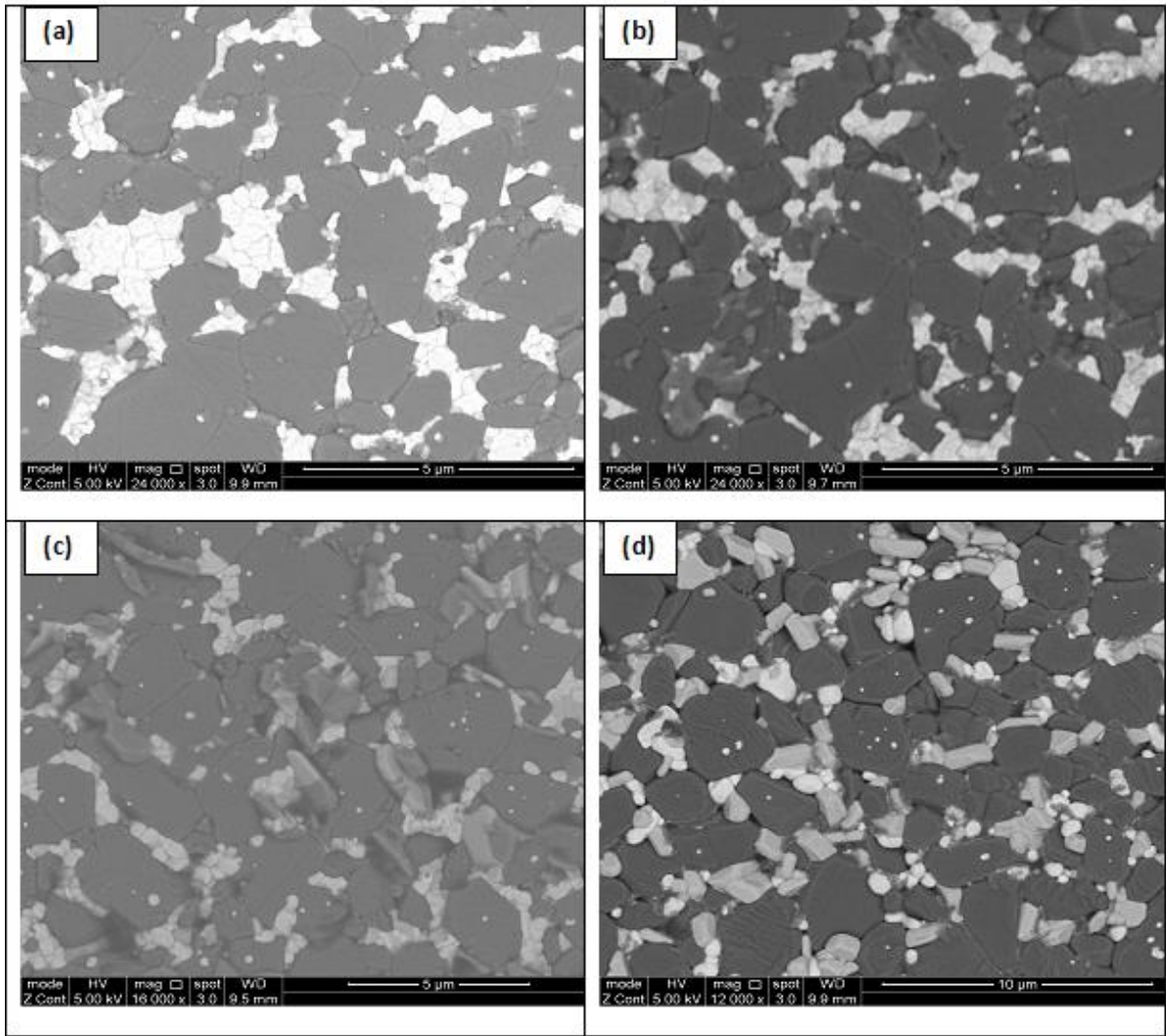


Figure 4.15. Backscattered electrons SEM images of ZTA + 2 mol.% TiO₂ sintered for 5 minutes at (a) 1400°C, (b) 1450°C, (c) 1500°C, and (d) 1550°C

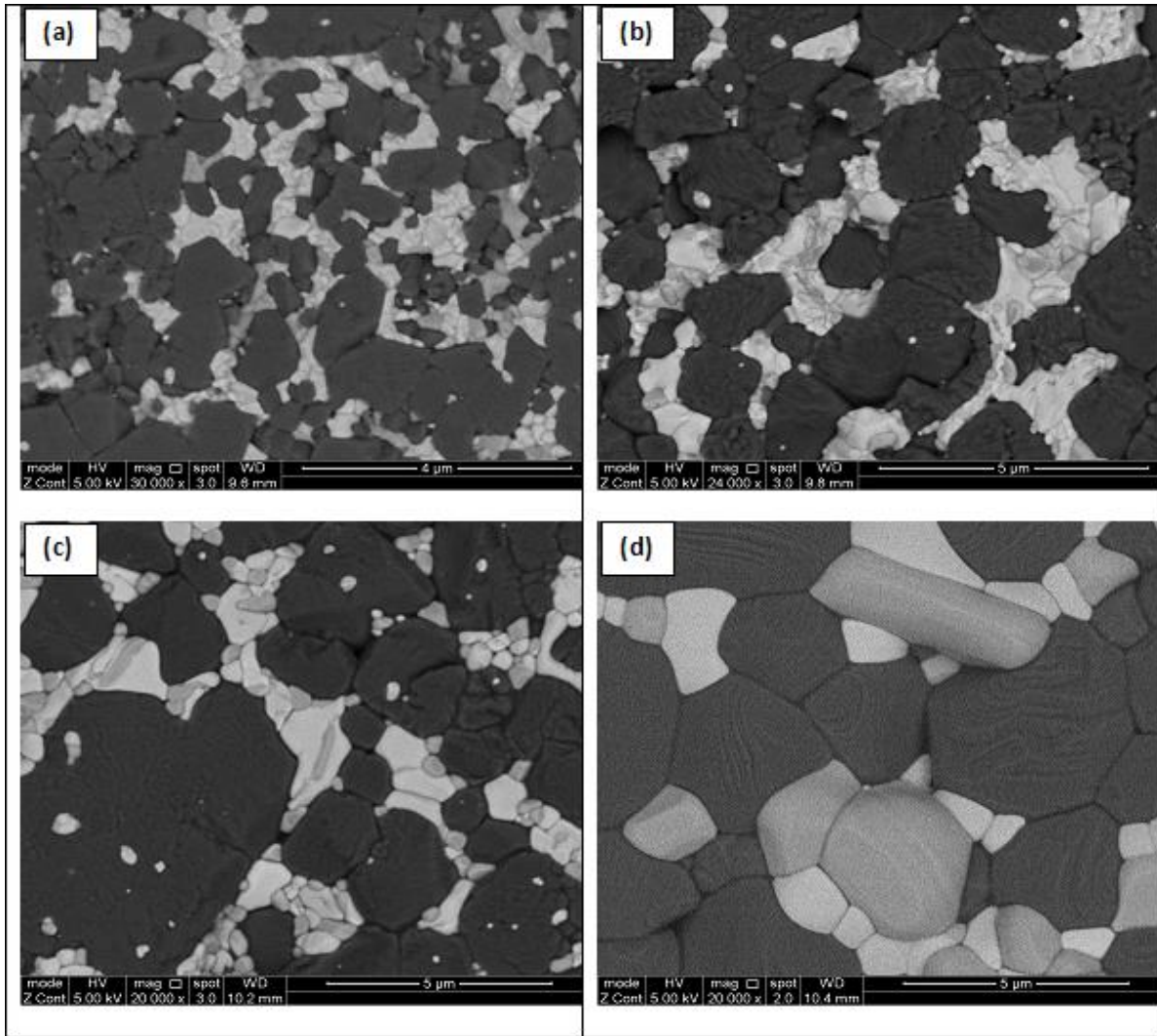


Figure 4.16. Backscattered electrons SEM images of ZTA + 5 mol.% TiO₂ sintered for 5 minutes at (a) 1400°C, (b) 1450°C, (c) 1500°C, and (d) 1550°C

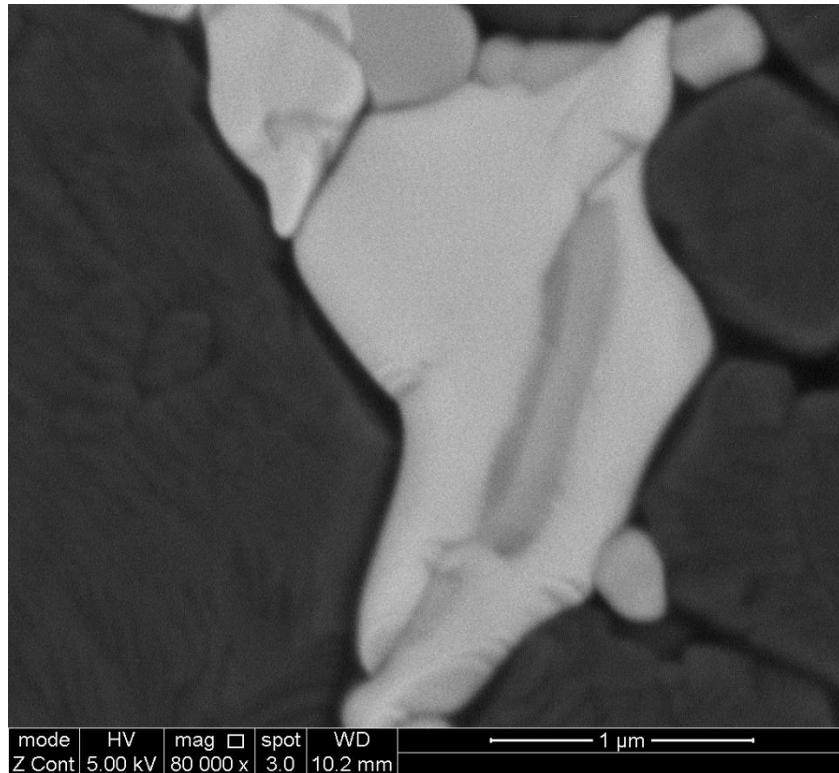


Figure 4.17. Backscattered electrons SEM images of ZTA + 5 mol.% TiO₂ sintered for 5 minutes at 1500°C at high magnification

It should be noted that numerous SEM images were taken from all the prepared samples and only a few of them were singled out to be representative of the microstructures of the samples. Similarly, every samples were analyzed by XRD, but the repeated XRD patterns, which did not give new information were not included in this chapter in order to not overload the amount of data.

4.1.4. Hardness and toughness characterization

The Vickers hardness and fracture toughness of samples with 0, 0.1, 0.5, 2 and 5 mole.% TiO₂ are listed in Table 4.7 to Table 4.11, and their graphs versus temperature for ten indentations are plotted in Figure 4.18 to Figure 4.21. Figure 4.22 shows the hardness and toughness of different prepared samples sintered at 1450°C. Similarly, Figure 4.23 shows the changes in hardness and fracture toughness of the samples with and without TiO₂ at different temperatures for dwell time of 5 minutes. As can be seen in these figures the changes are relatively in the same range, and hardly show a trend in hardness and toughness by increasing temperature, dwell time, and particularly by adding titanium oxide.

The SEM images of the Vickers indentation and formed cracks for one sample of each series of produced composites can be seen in Figure 4.24 to Figure 4.28. As it is clear adding TiO₂ at amounts of 2 and 5 mole.% has made more torturous crack propagation in comparison with ZTA and samples containing 0.1 and 0.5 mole.% TiO₂. Double cracks and microcracking can also be noticed, especially in the areas near indents (Figure 4.24.f and Figure 4.25.e). Additionally, most of the cracks seems to grow at grain boundaries as intergranular cracks, while some traces of transgranular cracks (marked by arrows), mainly at the samples having 5 mole.%, can be detected (Figure 4.26.f, Figure 4.27.e, and Figure 4.28.d,e,f).

Table 4.7. Mechanical characteristics of ZTA samples at different sintering temperature and dwell time

Sintering Temperature (°C)	Sintering dwell time (min)	Vickers Hardness (GPa)	Fracture Toughness (MPa m^{1/2})
1400	3	17.2±0.7	5.1±0.2
	5	NA	NA
	7	17.2±0.5	5.0±0.2
	10	17.3±0.3	5.3±0.2
1450	3	18.1±0.9	5.8±0.2
	5	17.1±0.6	5.8±0.3
	7	16.8±0.3	4.9±0.2
	10	17.2±0.4	5.2±0.2
1500	3	16.6±0.5	5.1±0.2
	5	17.2±0.4	5.1±0.2
	7	17.2±0.2	5.1±0.2
	10	16.8±0.3	5.2±0.2
1550	3	17.1±0.2	5.2±0.2
	5	17.0±0.2	5.3±0.3
	7	17.2±0.3	5.2±0.2
	10	16.3±0.3	5.1±0.2

Table 4.8. Mechanical characteristics of ZTA+0.1 mol.% TiO₂ samples at different sintering temperature and dwell time

Sintering Temperature (°C)	Sintering dwell time (min)	Vickers Hardness (GPa)	Fracture Toughness (MPa m^{1/2})
1400	5	18.0±0.6	5.6±0.3
	7	NA	NA
1450	5	17.6±0.5	5.4±0.2
	7	17.6±0.5	5.5±0.4
	10	18.0±0.3	5.5±0.1
1500	5	17.2±0.8	5.8±0.2
	7	NA	NA
1550	5	17.9±0.8	6.2±0.5
	7	17.6±0.4	5.5±0.2

Table 4.9. Mechanical characteristics of ZTA+0.5 mol.% TiO₂ samples at different sintering temperature and dwell time

Sintering Temperature (°C)	Sintering dwell time (min)	Vickers Hardness (GPa)	Fracture Toughness (MPa m^{1/2})
1400	5	14.8±2.1	5.1±0.6
	7	17.7±0.5	5.4±0.3
1450	5	17.6±0.3	5.4±0.1
	7	16.8±0.2	5.3±0.3
1500	5	17.1±0.5	5.9±0.14
	7	16.9±0.3	5.5±0.3
1550	5	16.4±0.2	5.8±0.3
	7	NA	NA

Table 4.10. Mechanical characteristics of ZTA+2 mol.% TiO₂ samples at different sintering temperature and dwell time

Sintering Temperature (°C)	Sintering dwell time (min)	Vickers Hardness (GPa)	Fracture Toughness (MPa m ^{1/2})
1400	5	17.9±1.2	6.4±0.3
1450	5	16.7±3.1	7.8±0.8
1500	5	16.4±1.7	7.1±0.6
1550	5	16.7±0.5	5.9±0.3

Table 4.11. Mechanical characteristics of ZTA+5 mol.% TiO₂ samples at different sintering temperature and dwell time

Sintering Temperature (°C)	Sintering dwell time (min)	Vickers Hardness (GPa)	Fracture Toughness (MPa m ^{1/2})
1400	5	14.9±2.8	6.8±0.7
1450	5	15.8±0.9	6.2±0.3
1500	5	15.4±1.3	6.1±0.3
1550	5	14.3±0.7	5.4±0.3

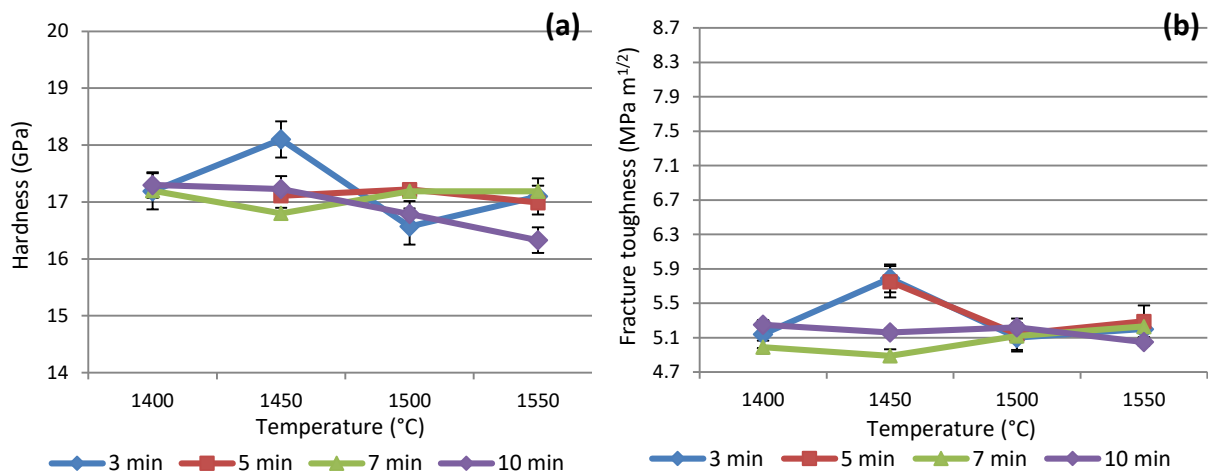


Figure 4.18. Vickers hardness (a), and fracture toughness (b) of ZTA samples vs sintering temperatures

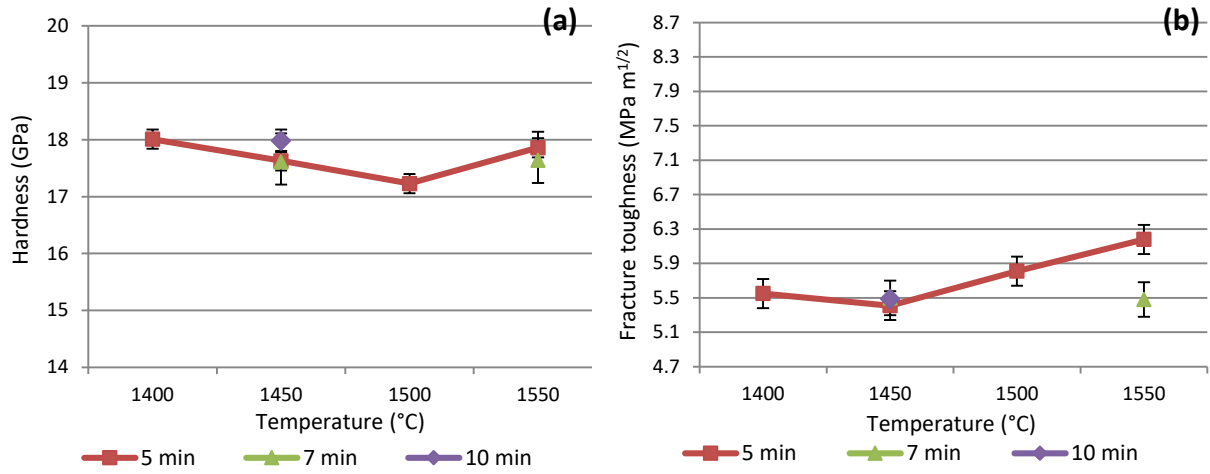


Figure 4.19. Vickers hardness (a), and fracture toughness (b) of ZTA+0.1 mol.% TiO₂ samples vs sintering temperatures

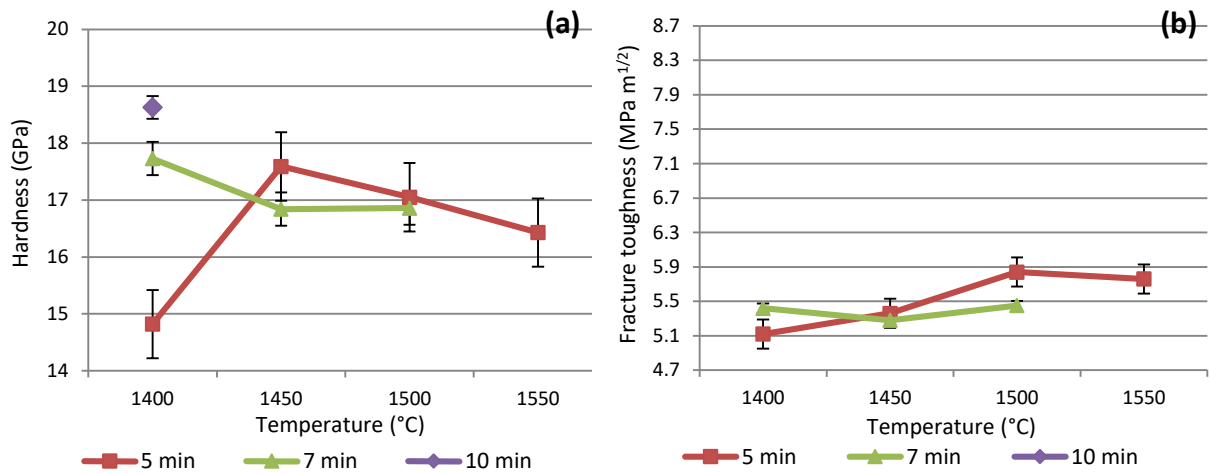


Figure 4.20. Vickers hardness (a), and fracture toughness (b) of ZTA+0.5 mol.% TiO₂ samples vs sintering temperatures

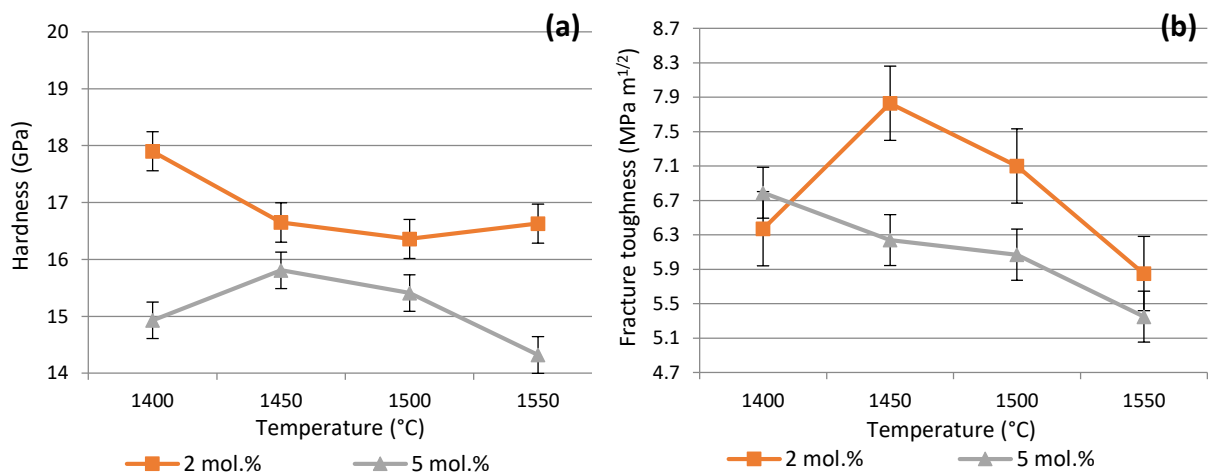


Figure 4.21. Vickers hardness (a), and fracture toughness (b) of ZTA+2 mol.% and ZTA+5 mol.% TiO₂ samples sintered for 5 minutes vs sintering temperatures

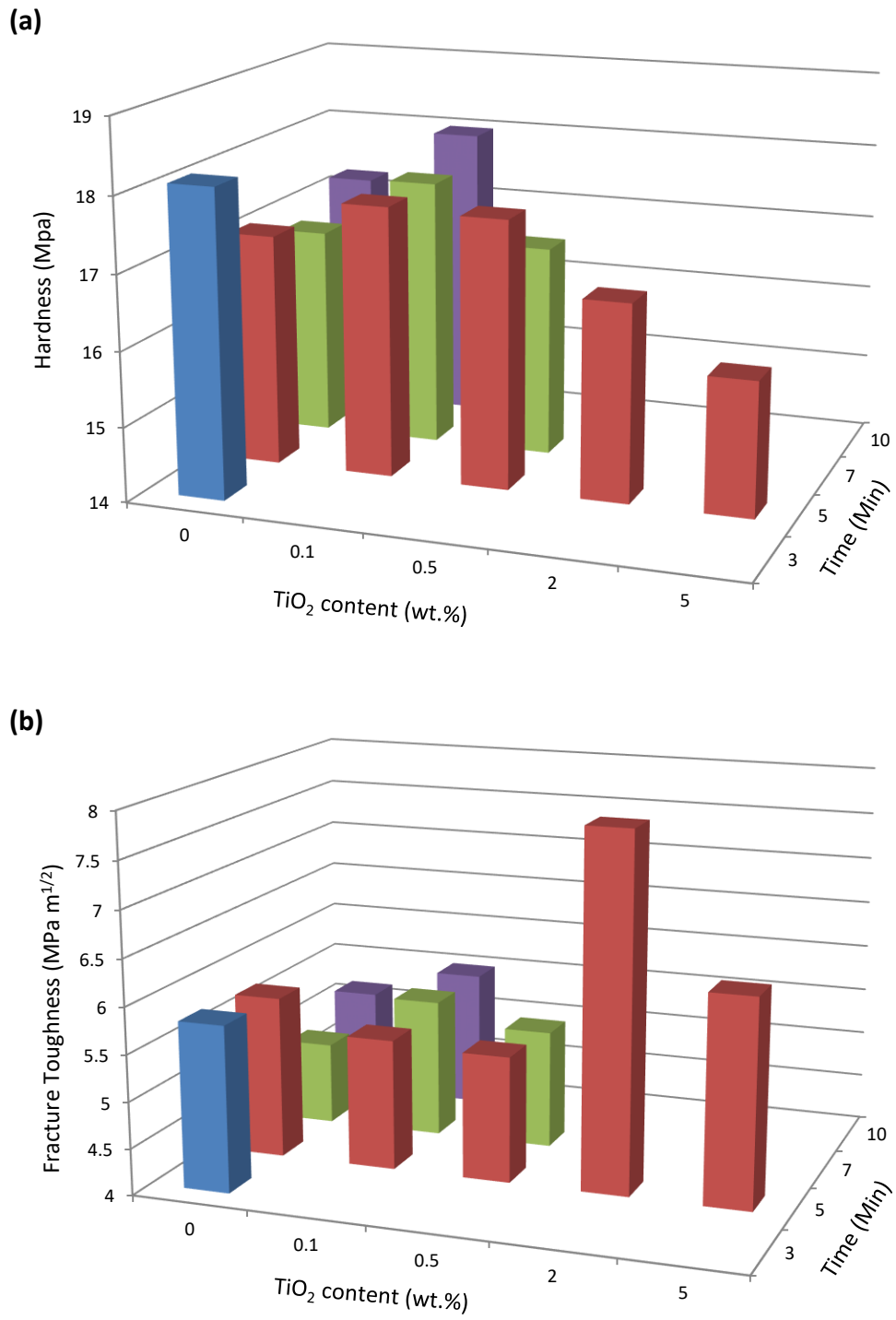


Figure 4.22. Vickers hardness (a), and fracture toughness (b) of samples sintered at 1450°C vs TiO₂ content and dwell time

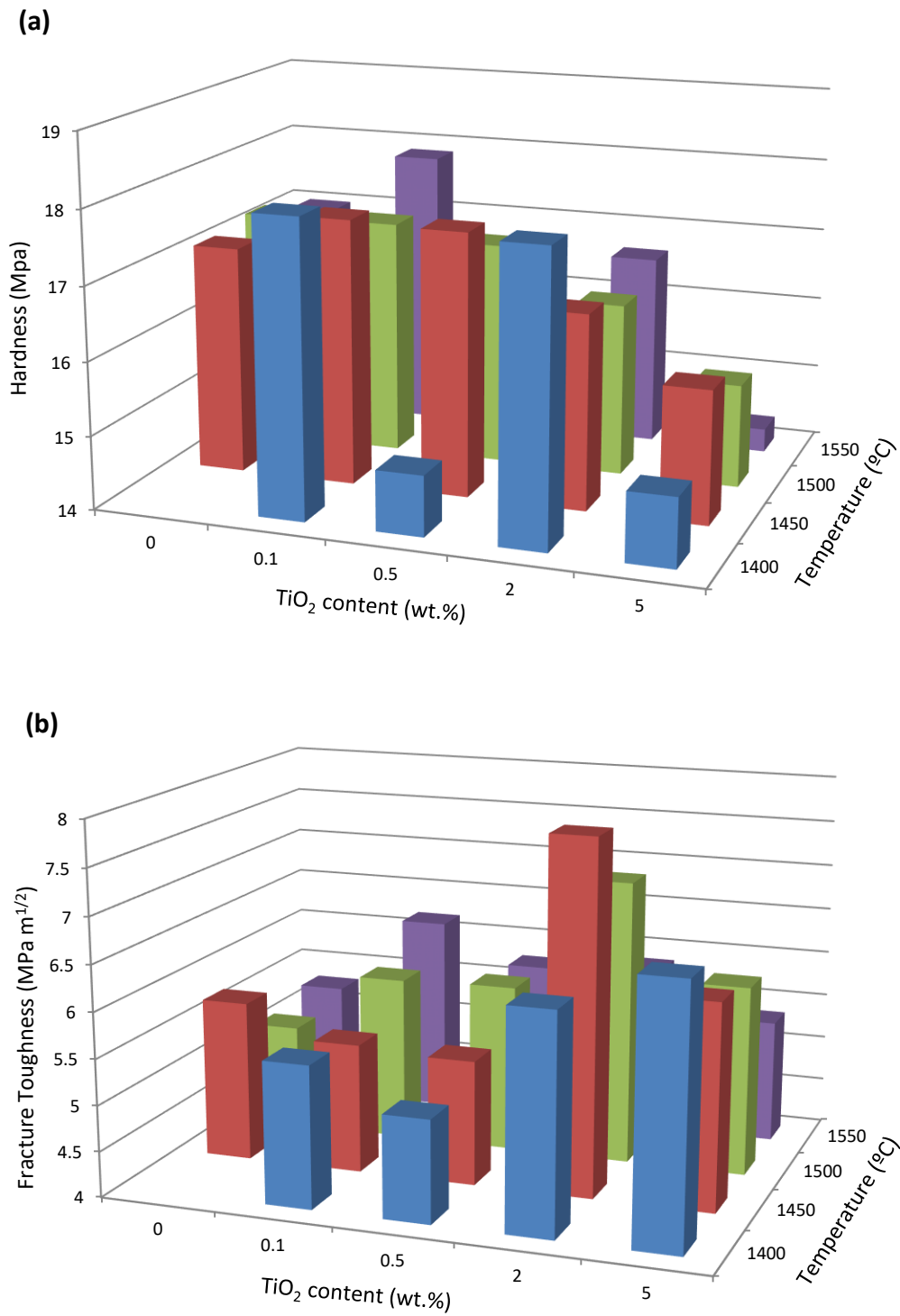


Figure 4.23. Vickers hardness (a), and fracture toughness (b) of samples sintered for 5 minutes vs TiO₂ content and sintering temperature

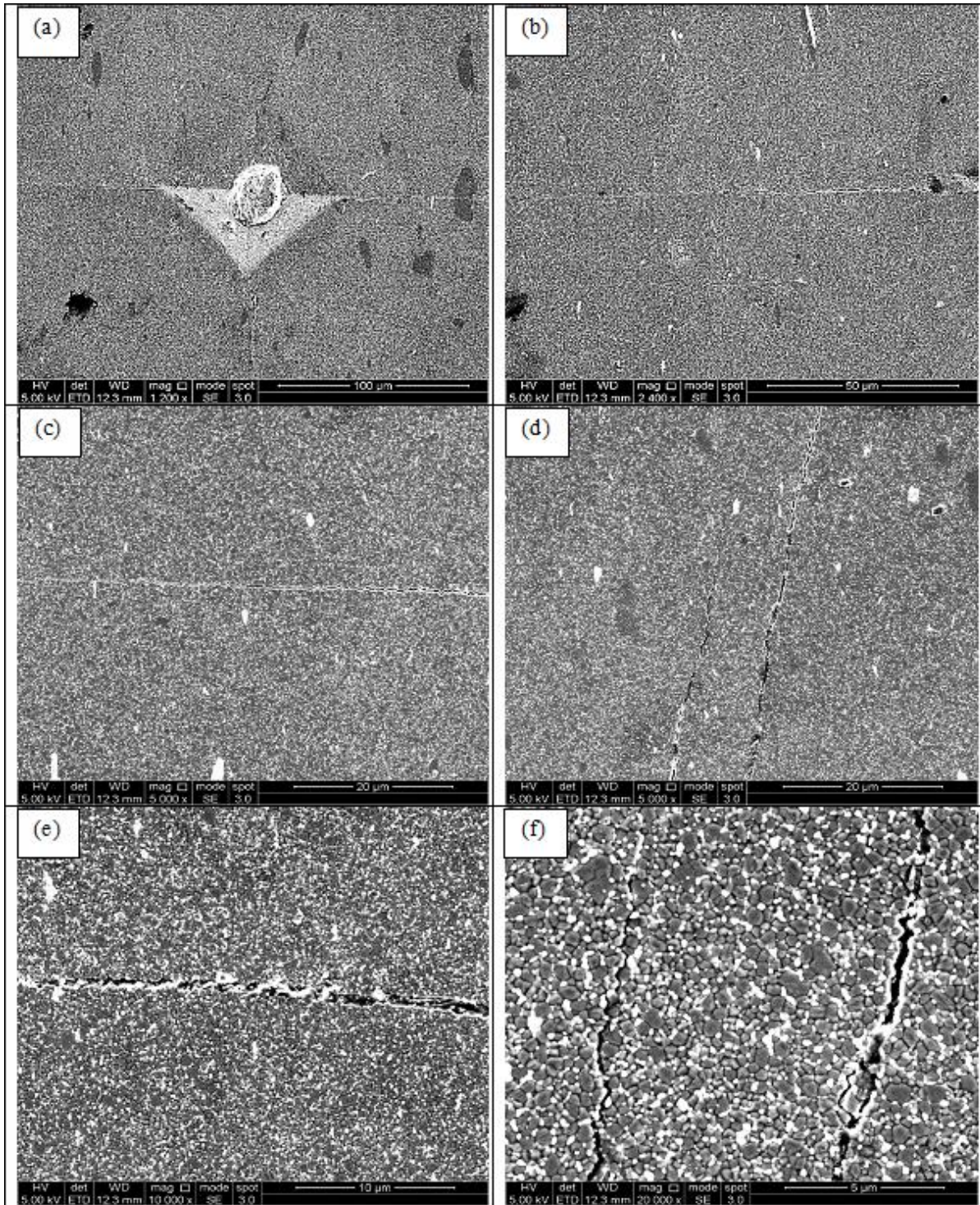


Figure 4.24. Secondary electrons SEM images of indented ZTA samples sintered for 5 minutes at 1500°C

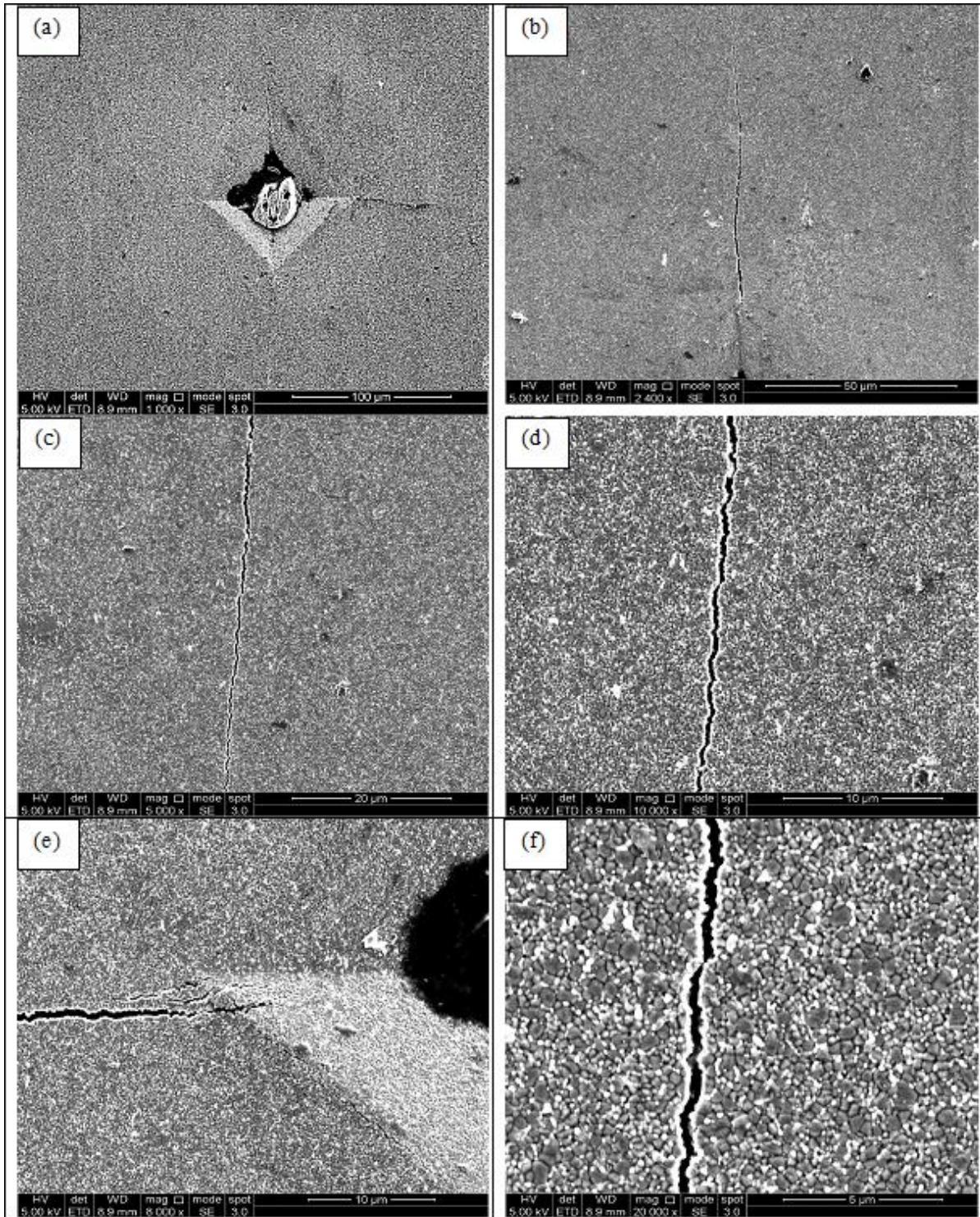


Figure 4.25. Secondary electrons SEM images of indented ZTA+0.1TiO₂ samples sintered for 5 minutes at 1450°C

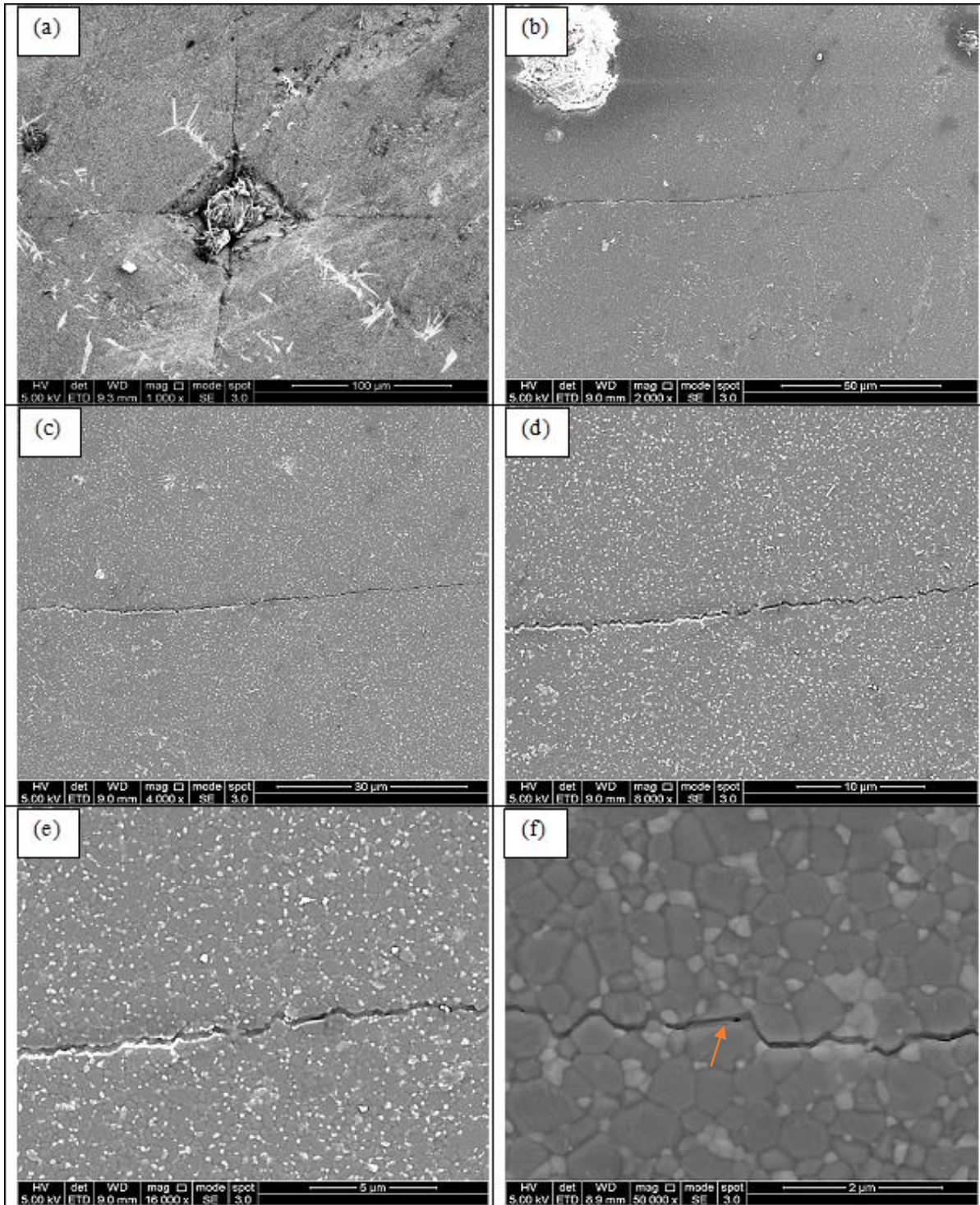


Figure 4.26. Secondary electrons SEM images of indented ZTA+0.5TiO₂ samples sintered for 5 minutes at 1450°C (The arrow shows a transgranular crack)

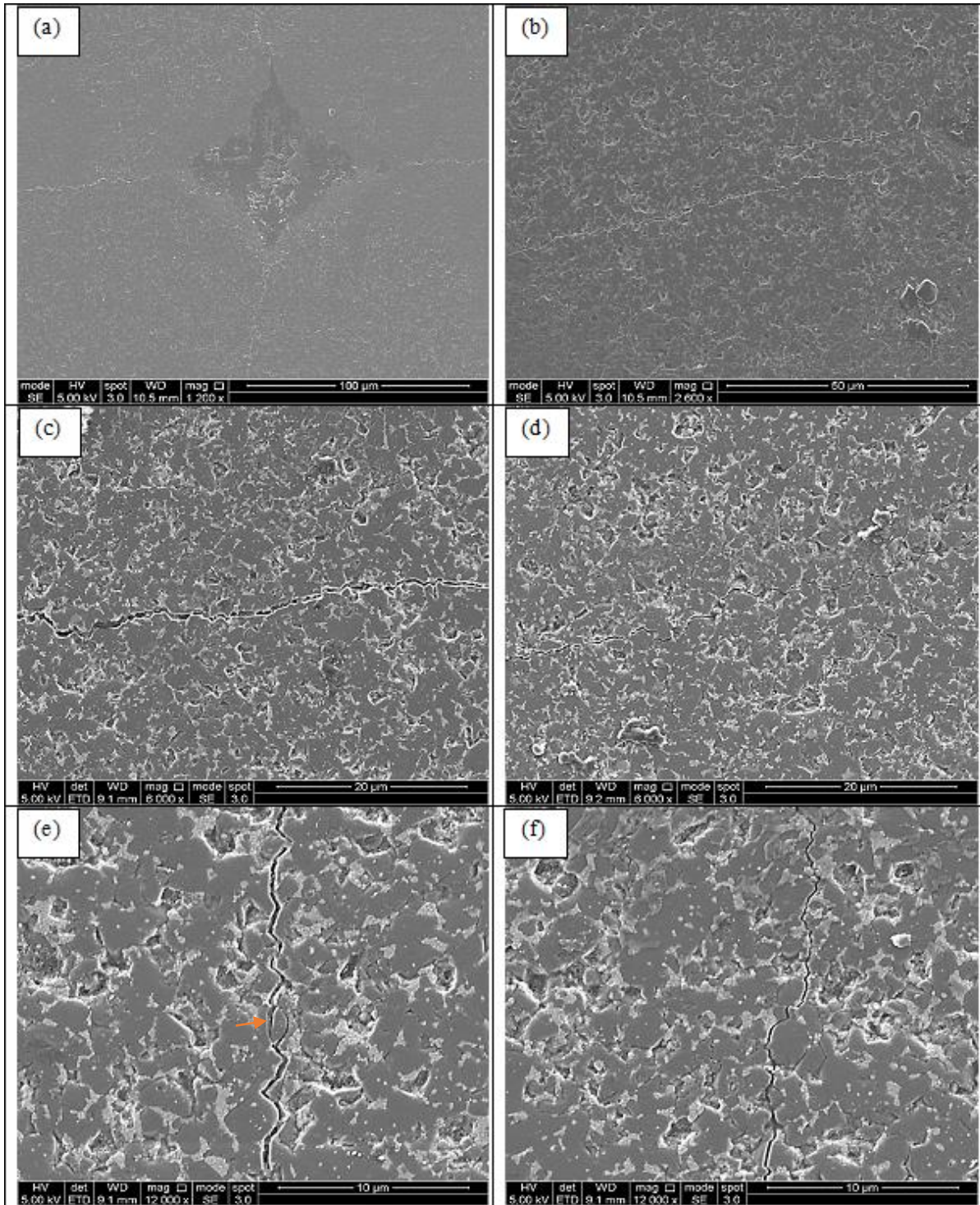


Figure 4.27. Secondary electrons SEM images of indented ZTA+2TiO₂ samples sintered for 5 minutes at 1500°C (The arrow shows a transgranular crack)

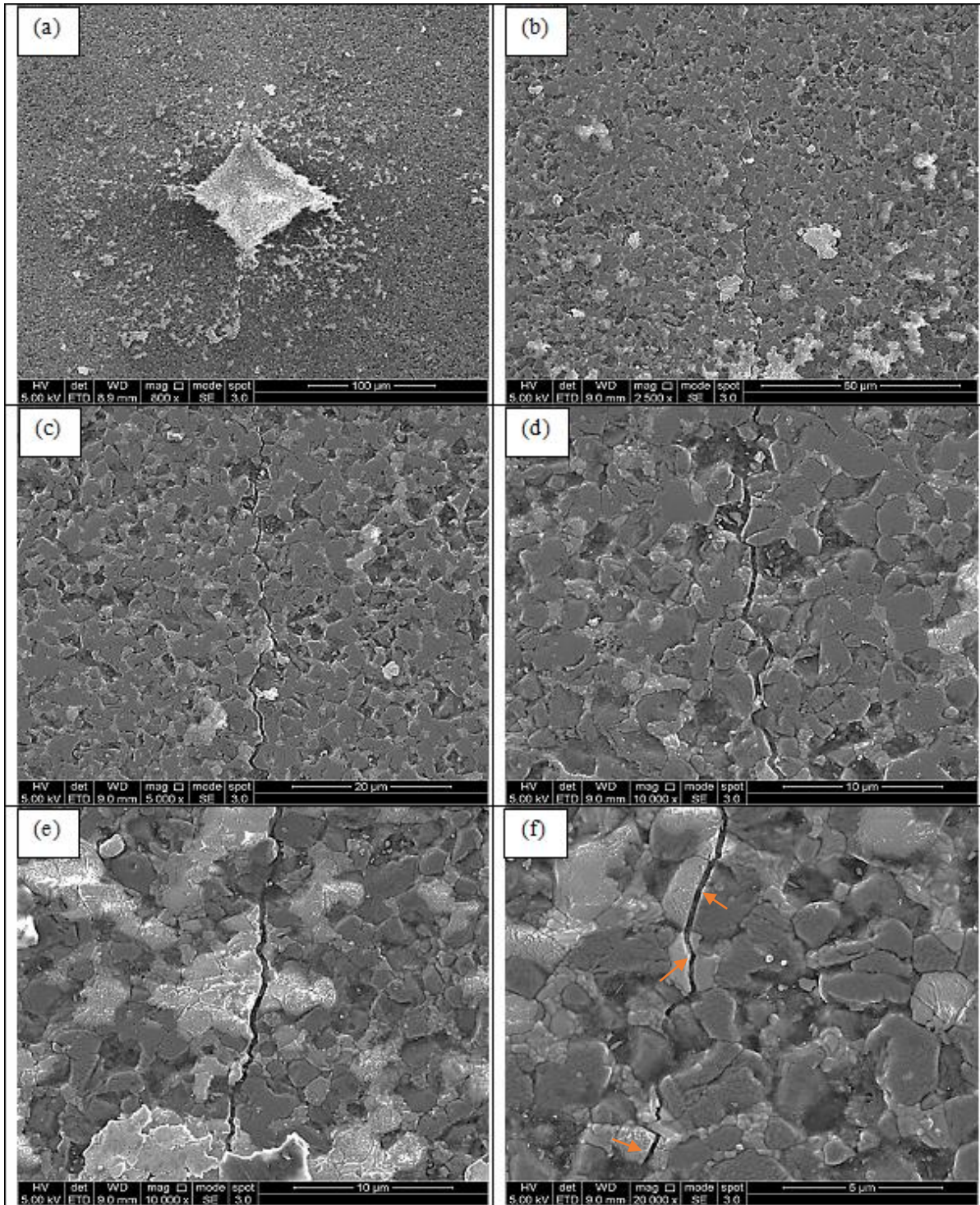


Figure 4.28. Secondary electrons SEM images of indented ZTA+5TiO₂ samples sintered for 5 minutes at 1450°C (The arrow shows a transgranular crack)

4.2. Wear Characterisation

4.2.1. Friction

The coefficient of friction (COF) for each test was plotted by the UMT tribometer software under the lubrication of 25 vol.% new-born calf serum as explained in the last chapter. In a standard COF curve versus time, there should be two separate stages as “running-in” and “steady-state” stage. In running-in stage, COF is high and erratic as a result of initial contacting two highly smooth and fresh counterfaces; while in steady-state stage, the wear scar has been formed and there is less variation in COF in time unless some changes in wear regime occurs. Figure 4.29 shows COF vs time from one of the samples and shows two distinct stage of running-in and steady-state can be detected in it. In contrast, Figure 4.30 gives a COF curve for another sample showing very erratic changes in COF, for which no reason was found and could be related to the UMT tribometer software. However, for comparing COF in different samples and materials, the steady state values were selected, listed in Table 4.12 and depicted in Figure 4.31.

In addition, as stated before, the obtained COF values in this test were found to be unreasonably low as a result of a technical problem in machine or software. This was believed to be due to machine using the frictional load in calculating the COF rather than the frictional force, giving a 9.8x error. This could not be recalibrated in the machine. Thus, although the absolute values of COF could not be used, the trends in the COF graphs are accurate. The friction values were relatively higher for samples containing titania in comparison with ZTA samples in all the test conditions.

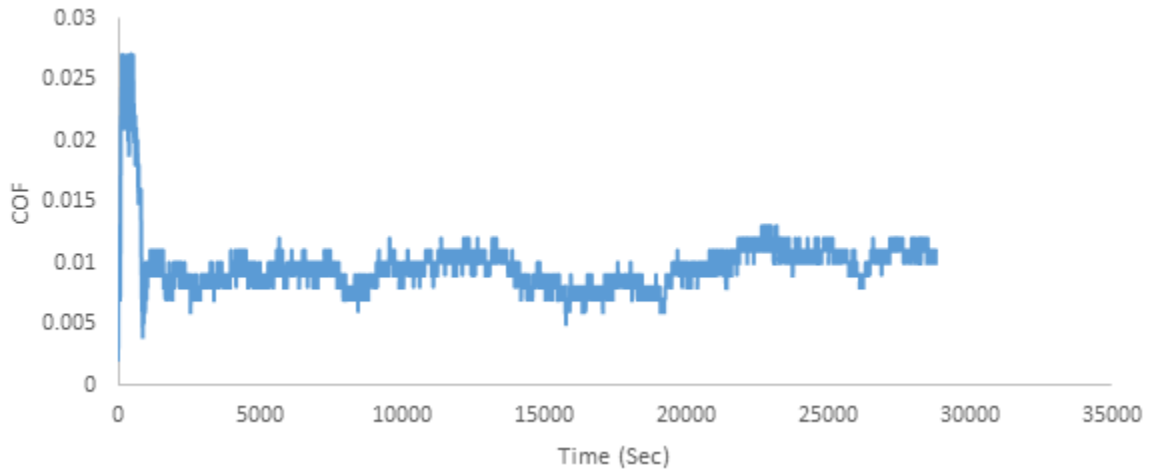


Figure 4.29. COF vs time for ZTA+0.5 mole.% TiO₂ sintered for 1500°C and 5 minutes under the wear condition of 16N for 8 hours

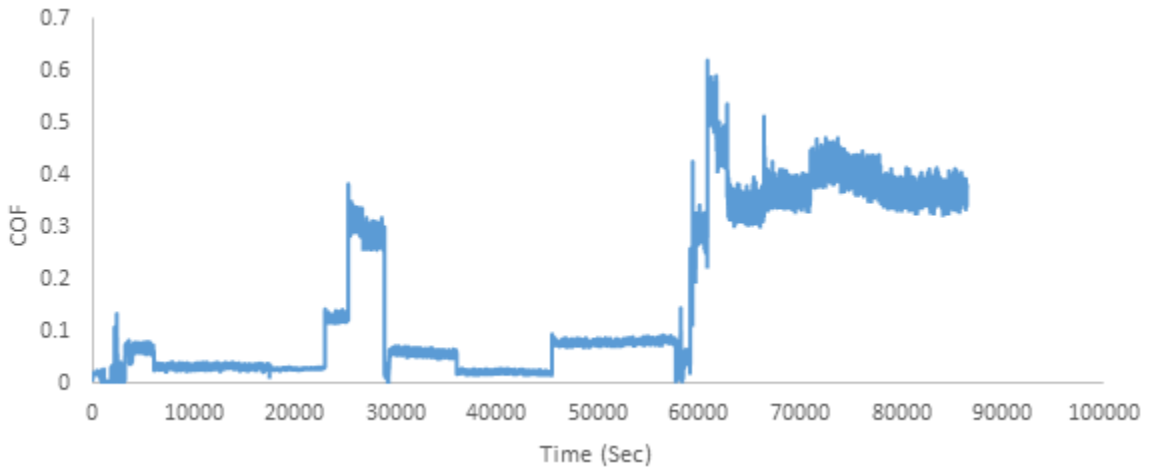


Figure 4.30. COF vs time for ZTA+0.1 mole.% TiO₂ sintered for 1450°C and 5 minutes under the wear condition of 8N for 24 hours

Table 4.12. Average COF for the samples under different wear conditions

Material	Sintering condition (Temperature (°C)- Time (min))	Average COF		
		4 N-24 h	8 N-24 h	16 N-8h
ZTA	1450 - 7	0.002	0.004	0.001
	1500 - 7	0.003	0.016	0.010
	1550 - 7	0.003	0.001	0.001
ZTA + 0.1 mole.% TiO ₂	1450 - 5	0.003	0.032	0.013
	1500 - 5	0.006	0.009	0.014
	1550 - 5	0.012	0.013	0.006
ZTA + 0.5 mole.% TiO ₂	1400 - 5	0.002	0.003	0.004
	1450 - 5	0.007	0.016	0.017
	1500 - 5	0.007	0.007	0.009

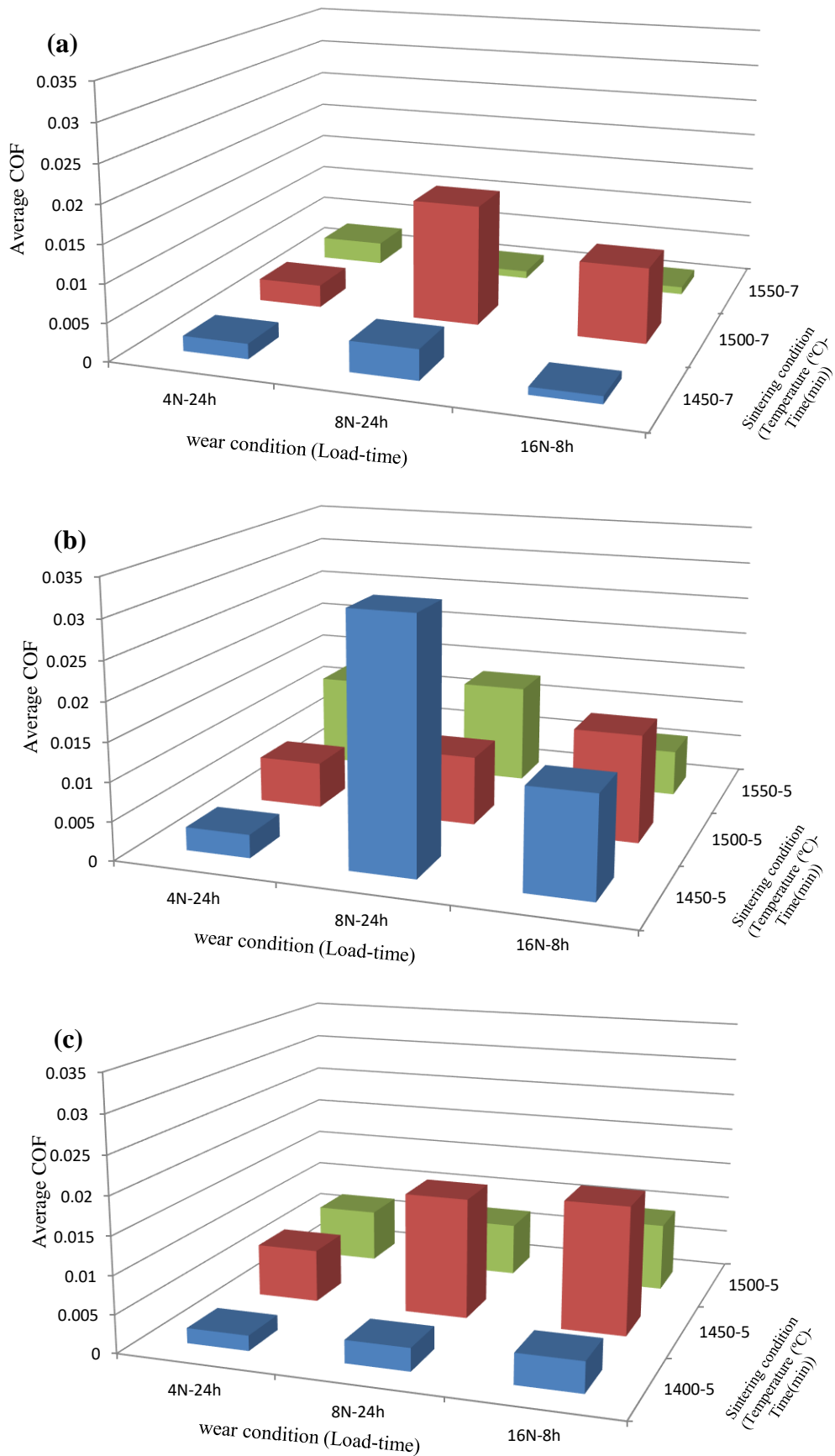


Figure 4.31. Average COF for ZTA samples (a), ZTA+0.1 mole.% TiO₂ (b), and ZTA+0.5 mole.% TiO₂ (c) under different wear conditions

4.2.2. Wear Behaviour

4.2.2.1. Specific wear rate

The calculated values of specific wear rate for ZTA, ZTA+0.1 mole.% TiO₂, and ZTA+0.5 mole.% TiO₂ at different reciprocating wear conditions are listed in Table 4.13 and their related diagrams are given in Figure 4.32, Figure 4.33, and Figure 4.34.

For ZTA samples, as can be seen in Figure 4.32, increasing load did not necessarily lead to increasing wear rate, and for samples sintered at 1500°C and 1550°C the specific wear rate under 4N load was higher than that of 8N load. It also can be found from this figure that by increasing sintering temperature, and therefore coarsening microstructure, the wear rate seems to have been increased. There is an exemption for the ZTA sample sintered at 1500°C that its wear rate is less than that of both less and higher sintering temperature.

In samples containing 0.1 mole.% TiO₂ (Figure 4.33), the same trend of ZTA samples occurred with increased load, where the wear rate did not increase for the sample sintered at 1550°C by increasing load from 4N to 8N. For the sample sintered at 1500°C, the specific wear rate was relatively similar for both 4N and 8N wear load. A coarser grain structure in this samples probably led to a higher specific wear rate at the same wear condition with a slight difference for samples sintered at 1450°C and 1500°C under 16N.

Similarly, Figure 4.34 shows the same diagrams for samples containing 0.5 mole.% TiO₂ at different wear conditions. It can be found from this diagram that increasing load in all samples was accompanied by increasing wear rate, and that increased sintering temperature led to a coarsened grain structure and a resultant increase in the wear rate.

Comparison of these three diagrams demonstrates that with approximately the same grain sizes, the samples show about the same wear rate at fine (blue columns) and moderate (red columns) microstructures, while in coarse microstructures (green columns) the samples containing 0.5 mole.% TiO₂ showed a tangible reduction (up to one third) in wear rate, especially at high load of 16N. In addition, it is notable that the minimum wear rate was obtained for the sample containing 0.5 mole.% TiO₂ worn for 24 hours under 4N load, and the maximum wear rate was for ZTA+0.1mole.%TiO₂ sample worn for 8 hours under 16N, with the values of 2.5E-09 and 4.7E-07 mm³/Nm respectively. It also should be noted that all the samples displayed the wear rate of the mild wear regime, which is under 10⁻⁶ mm³/Nm.

Table 4.13. Specific wear rates for the samples under different reciprocating wear conditions

Material	Sintering condition (Temperature (°C)- Time (min))	Specific wear rate (mm ³ /Nm)		
		4 N-24 h	8 N-24 h	16 N-8h
ZTA	1450 - 7	4.2E-09	3.5E-08	6.5E-08
	1500 - 7	2.2E-08	1.6E-08	6.5E-08
	1550 - 7	5.7E-08	3.9E-08	3.7E-07
ZTA + 0.1 mole.% TiO ₂	1450 - 5	4.9E-09	2.6E-08	5.1E-08
	1500 - 5	4.4E-09	4.1E-08	4.6E-08
	1550 - 5	7.5E-08	6.4E-08	4.7E-07
ZTA + 0.5 mole.% TiO ₂	1400 - 5	2.5E-09	2.1E-08	5.5E-08
	1450 - 5	4.6E-09	3.7E-08	4.9E-08
	1500 - 5	1.0E-08	3.8E-08	1.2E-07

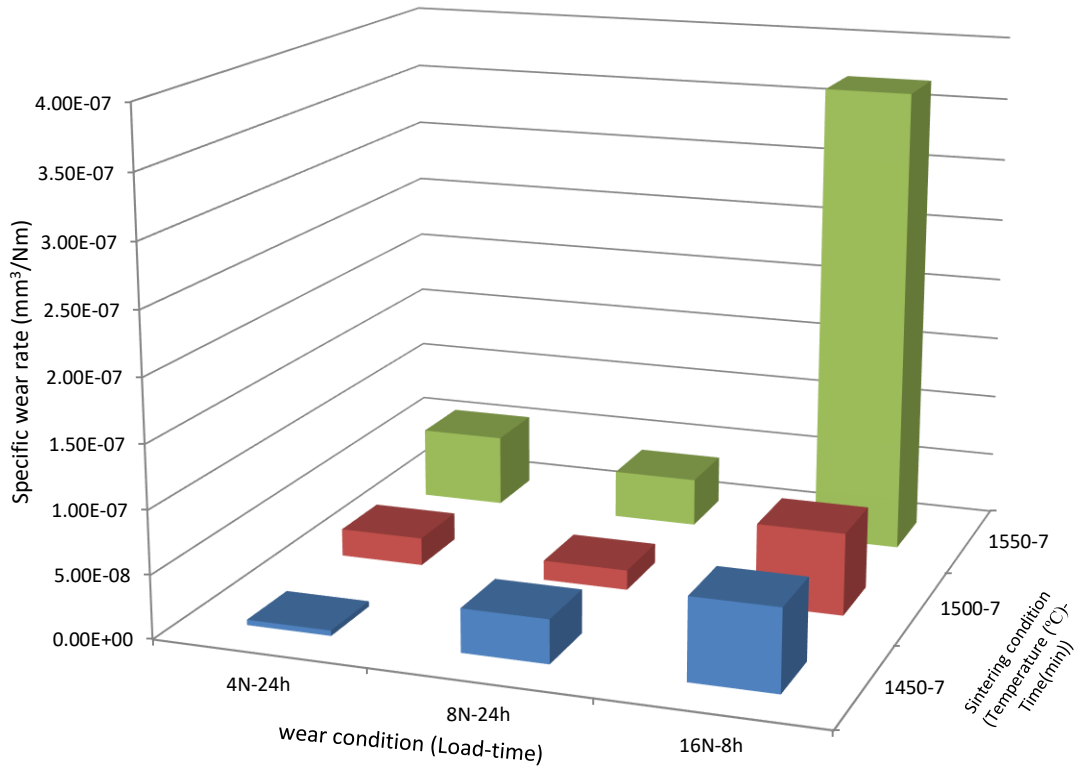


Figure 4.32. Specific wear rate for the reciprocating wear tests of ZTA samples at different wear conditions

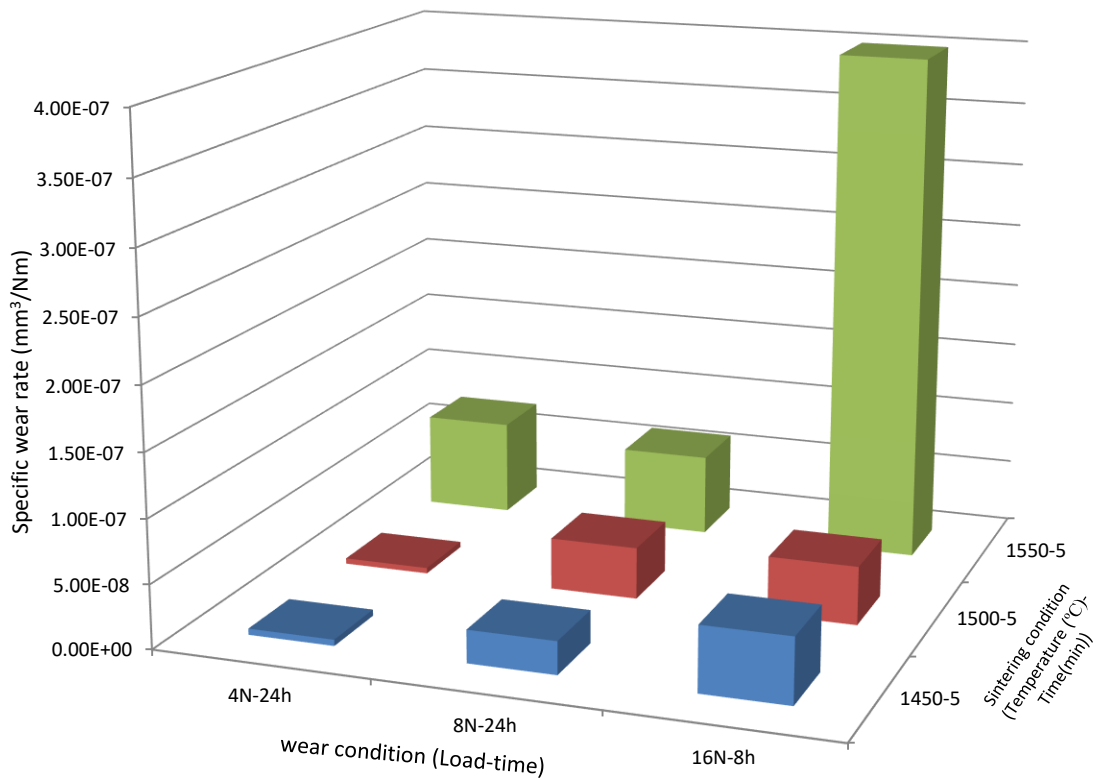


Figure 4.33. Specific wear rate for the reciprocating wear tests of ZTA + 0.1 mole.% TiO₂ samples at different wear conditions

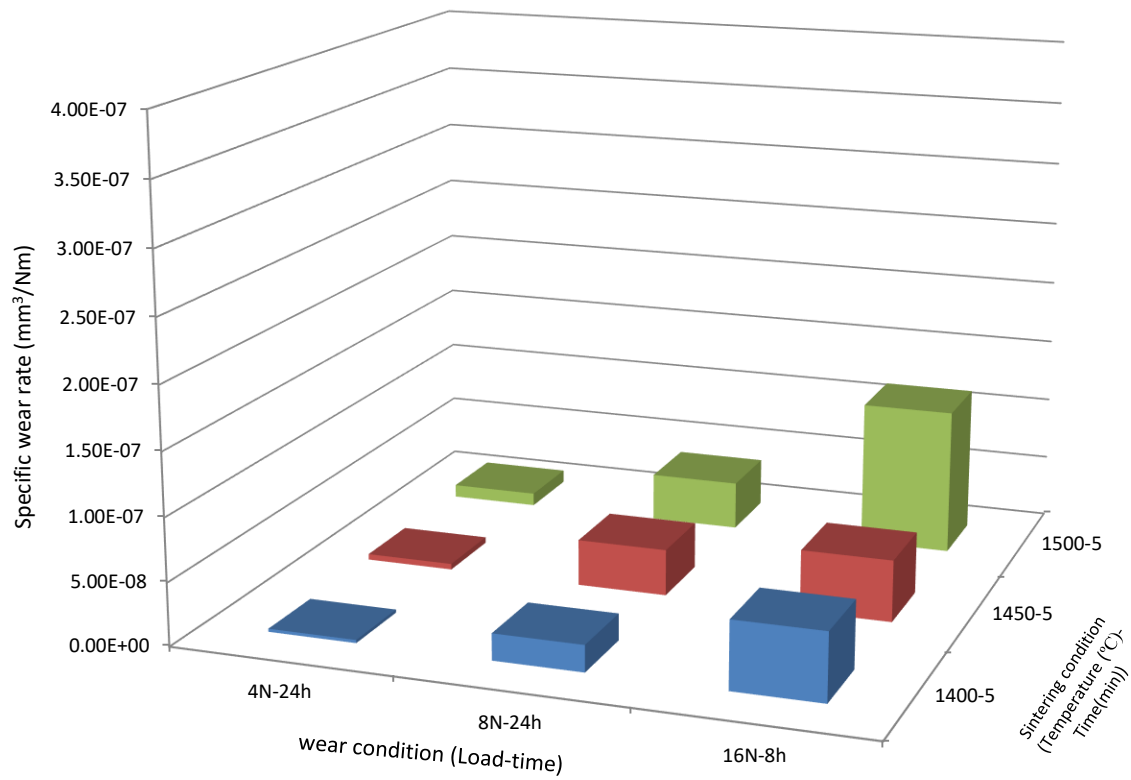


Figure 4.34. Specific wear rate for the reciprocating wear tests of ZTA + 0.5 mole.% TiO₂ samples at different wear conditions

4.2.2.2. Worn surface analysis

3D surface morphology

3D VSI images of the wear scars for the samples under different wear conditions are given in Figure 4.35 to Figure 4.43. As can be seen for all the samples, increasing normal load led to wider and deeper wear scars. Additionally, a coarser microstructure resulted in a wider wear scar for each series of samples (Figure 4.37, Figure 4.40, and Figure 4.43). In accordance with the wear rate results presented in the last chapter, the widest and deepest wear scar were related to the ZTA and ZTA+0.1 mole.%TiO₂ samples sintered for 7 minutes and 5 minutes respectively at 1550°C and worn under 16 N load (Figure 4.37(c), and Figure 4.40(c)). However, the wear scar for the sample containing 0.5 mole.% TiO₂ sintered for 5 minutes at 1500°C, with relatively the same grain size, under the same wear condition was tangibly smaller and more shallow (Figure 4.43(c)). The least surface damage was for the sample containing 0.5 mole.% TiO₂ sintered for 5 minutes at 1400°C as can be seen in Figure 4.41(a), and was in accordance with the value reported in Table 4.13.

Table 4.14 shows the values for surface roughness of the wear scars from calculating its average values for high magnification VSI images, with the height resolution of 10 nm and lateral resolution of 0.5µm, at different spots of wear scars. Some representative images of the wear scars surfaces are illustrated in Figure 4.44 to Figure 4.51. As can be seen in these figures, wear tracks with different width and depth are visible in some wear scars, and spikes can be detected in some areas and some points. However, the roughness values of wear scars are very low (less than 50 nm for most of wear conditions), and in case of low loads is very close to the surface roughness before the test, which was tried to be kept less than 20 nm. This low roughness is what expected in fine microstructure under lubricated operation systems.

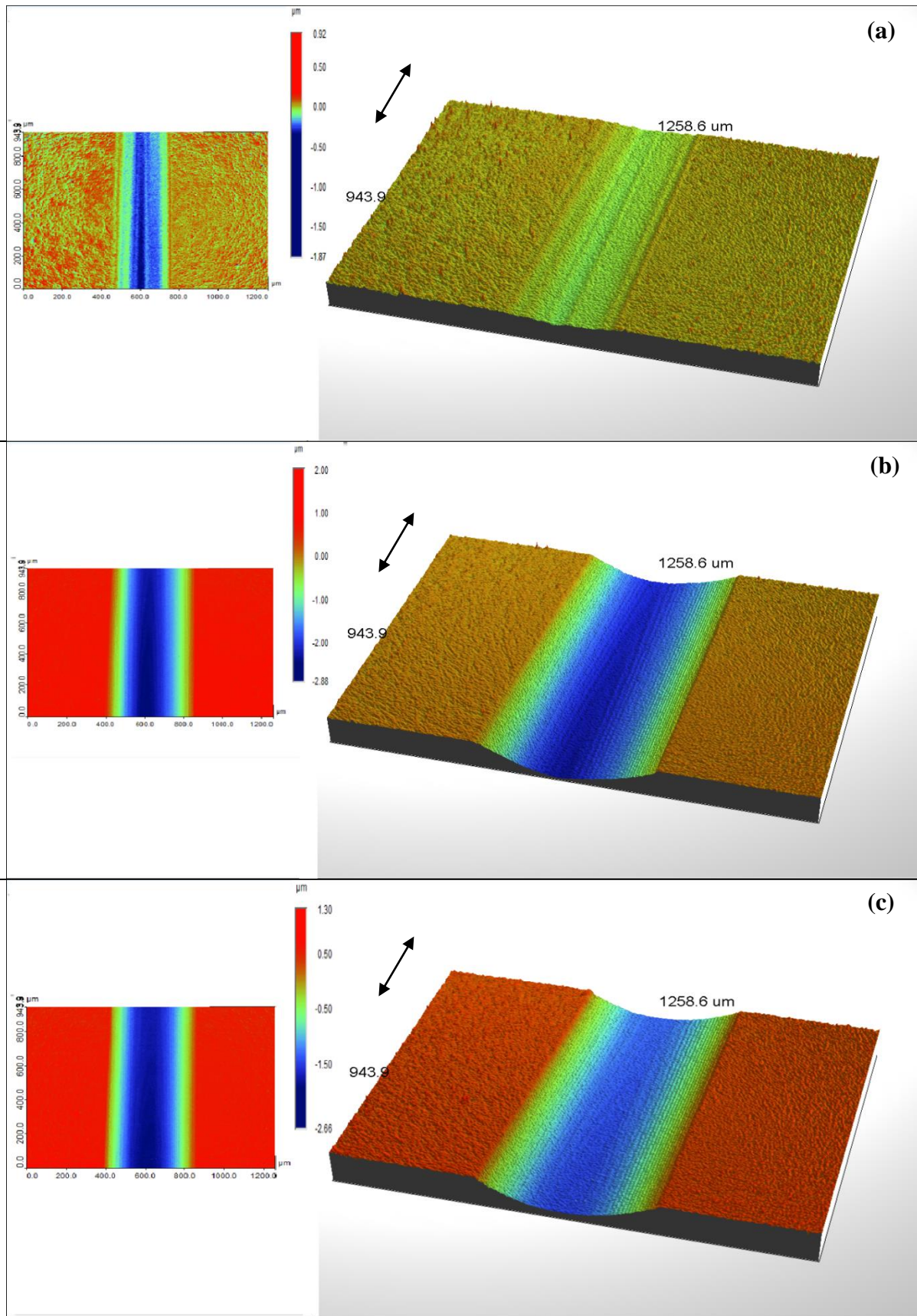


Figure 4.35. 3D VSI image of wear scars for ZTA sample sintered at 1450°C for 7 minutes under the wear condition of 4N-24hrs (a), 8N-24hrs (b), and 16N-8hrs (c)

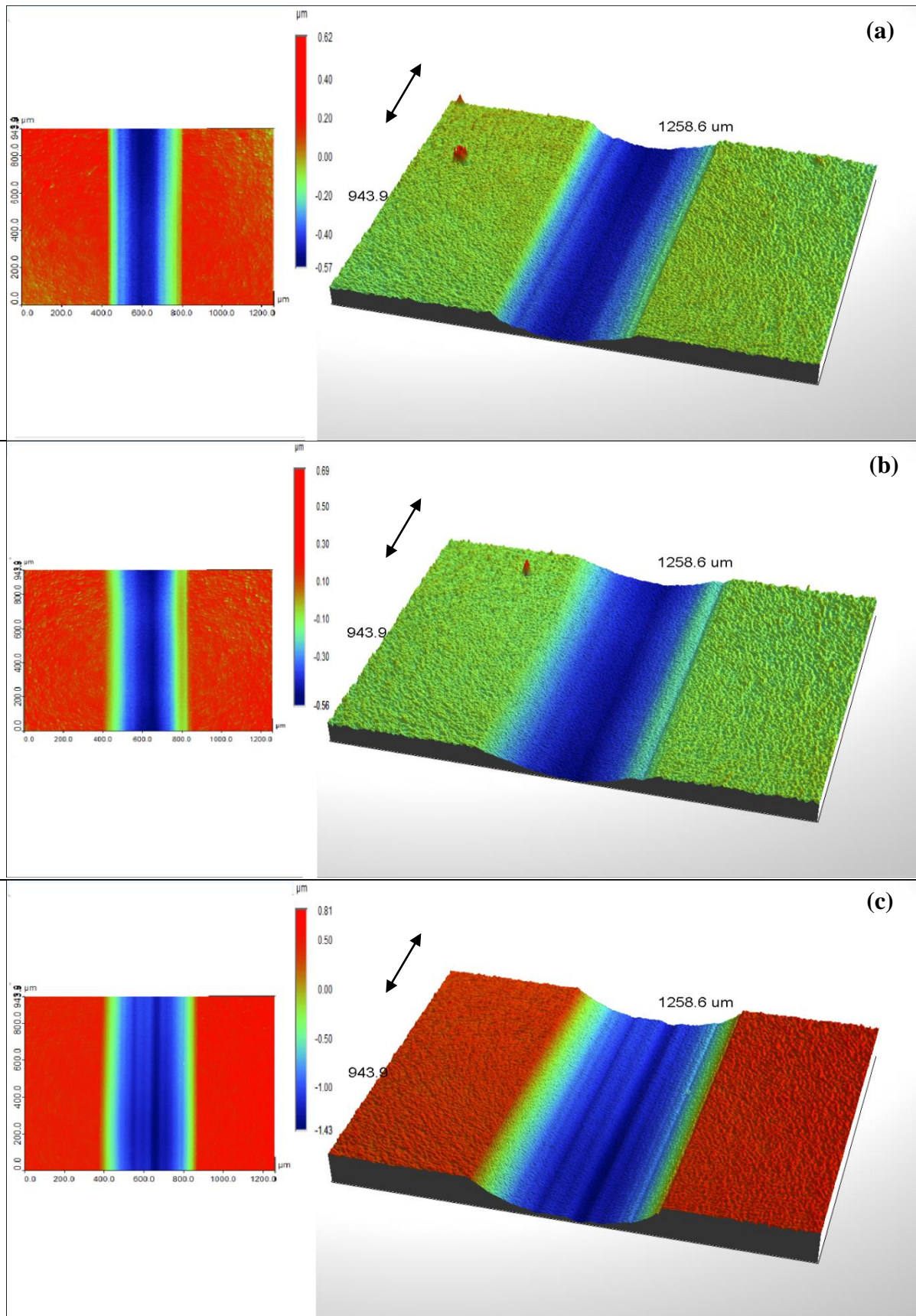


Figure 4.36. 3D VSI image of wear scars for ZTA sample sintered at 1500°C for 7 minutes under the wear condition of 4N-24hrs (a), 8N-24hrs (b), and 16N-8hrs (c)

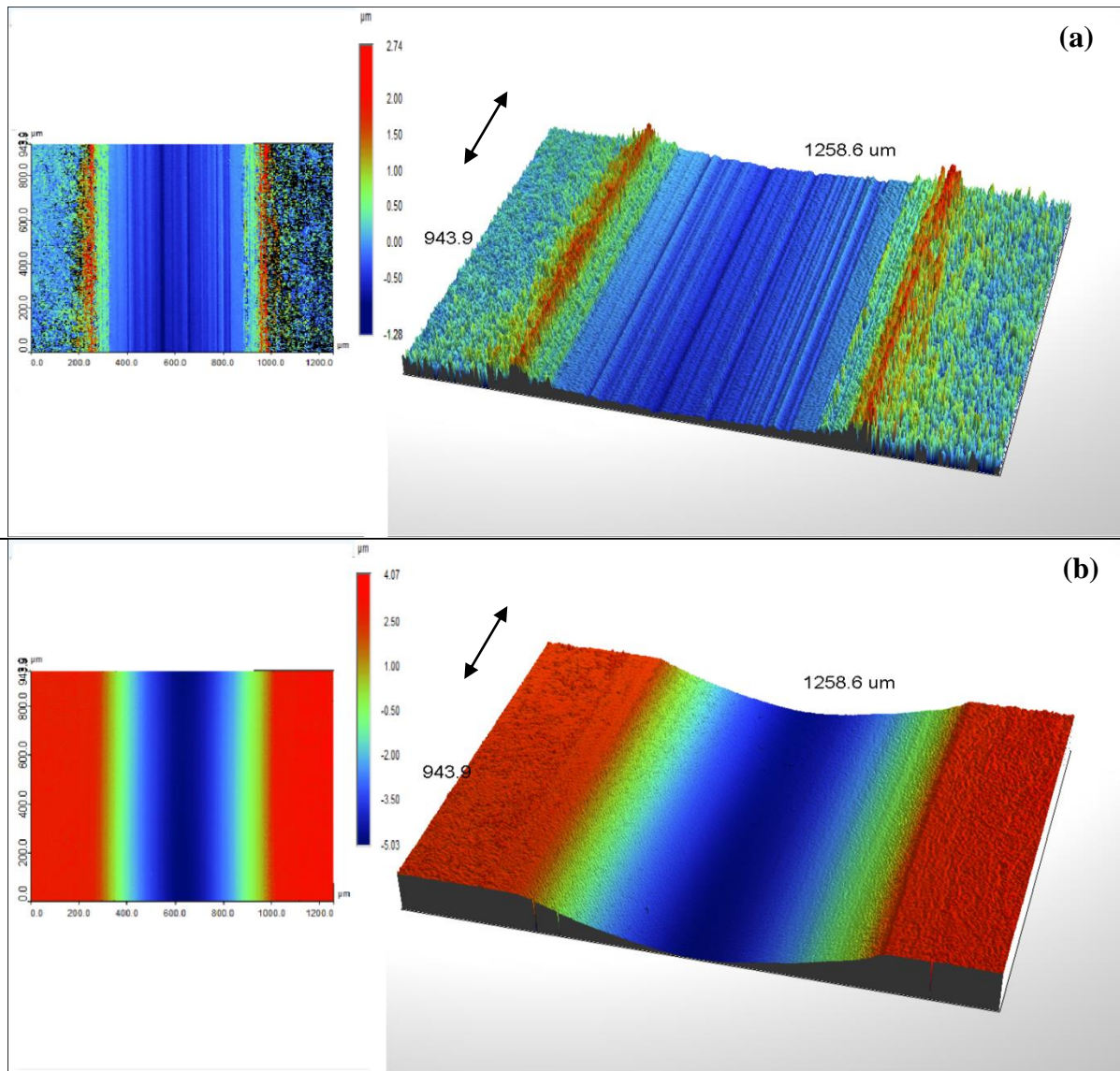


Figure 4.37. 3D VSI image of wear scars for ZTA sample sintered at 1550°C for 7 minutes under the wear condition of 4N-24hrs (a), and 16N-8hrs (b)

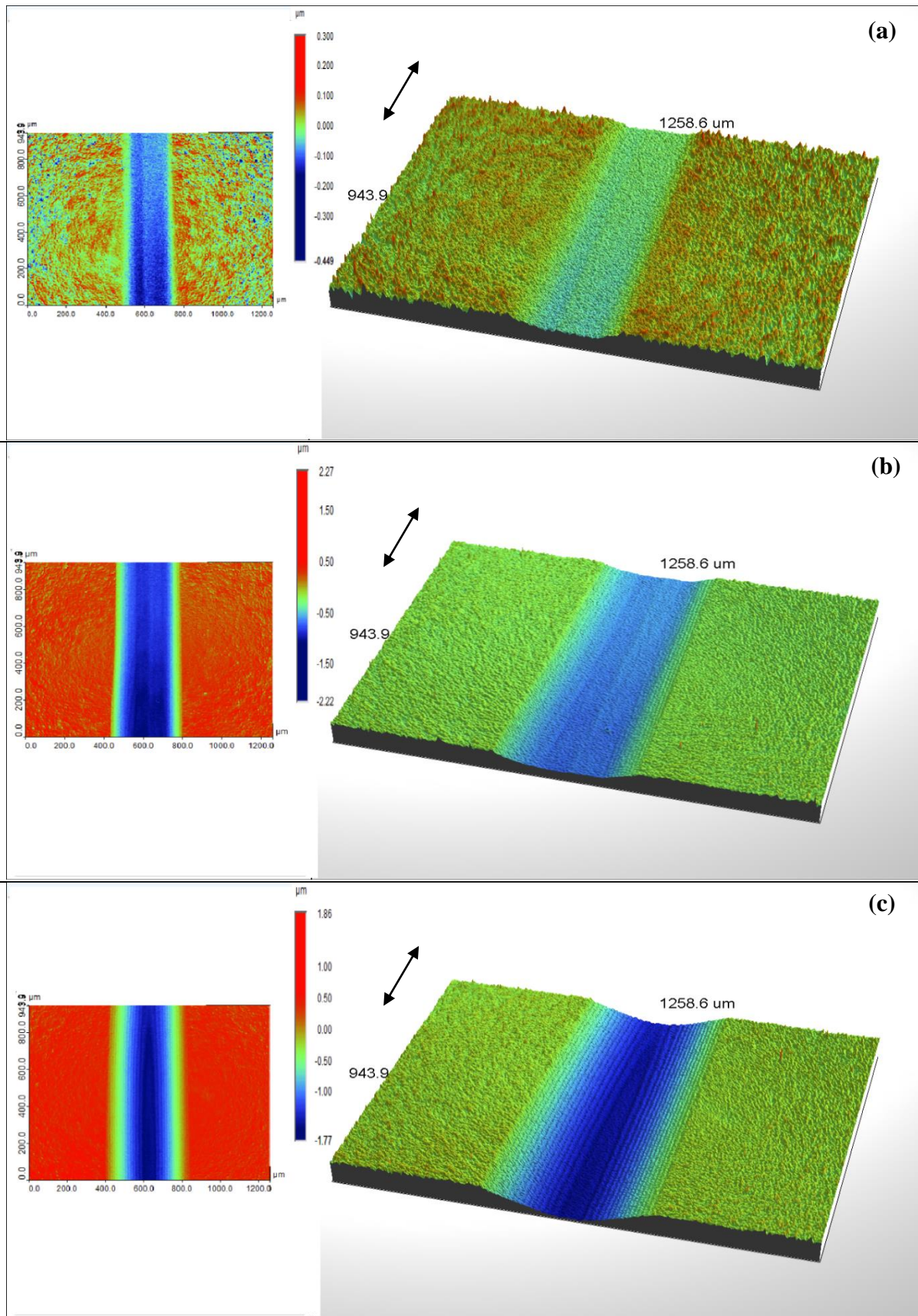


Figure 4.38. 3D VSI image of wear scars for ZTA+0.1 mole.% TiO₂ sample sintered at 1450°C for 5 minutes under the wear condition of 4N-24hrs (a), and 8N-24hrs (b), and 16N-8hrs (c)

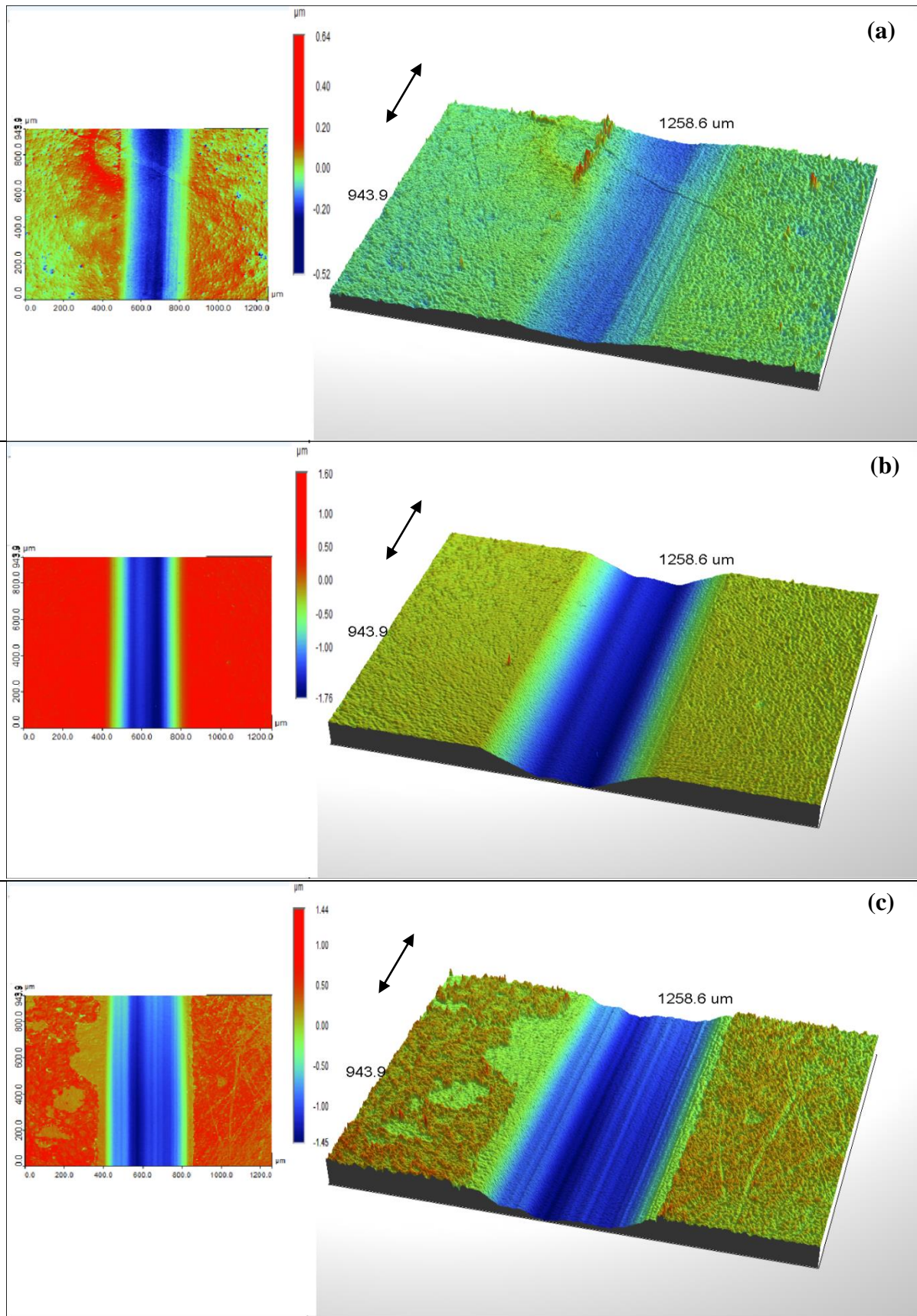


Figure 4.39. 3D VSI image of wear scars for ZTA+0.1 mole.% TiO₂ sample sintered at 1500°C for 5 minutes under the wear condition of 4N-24hrs (a), and 8N-24hrs (b), and 16N-8hrs (c)

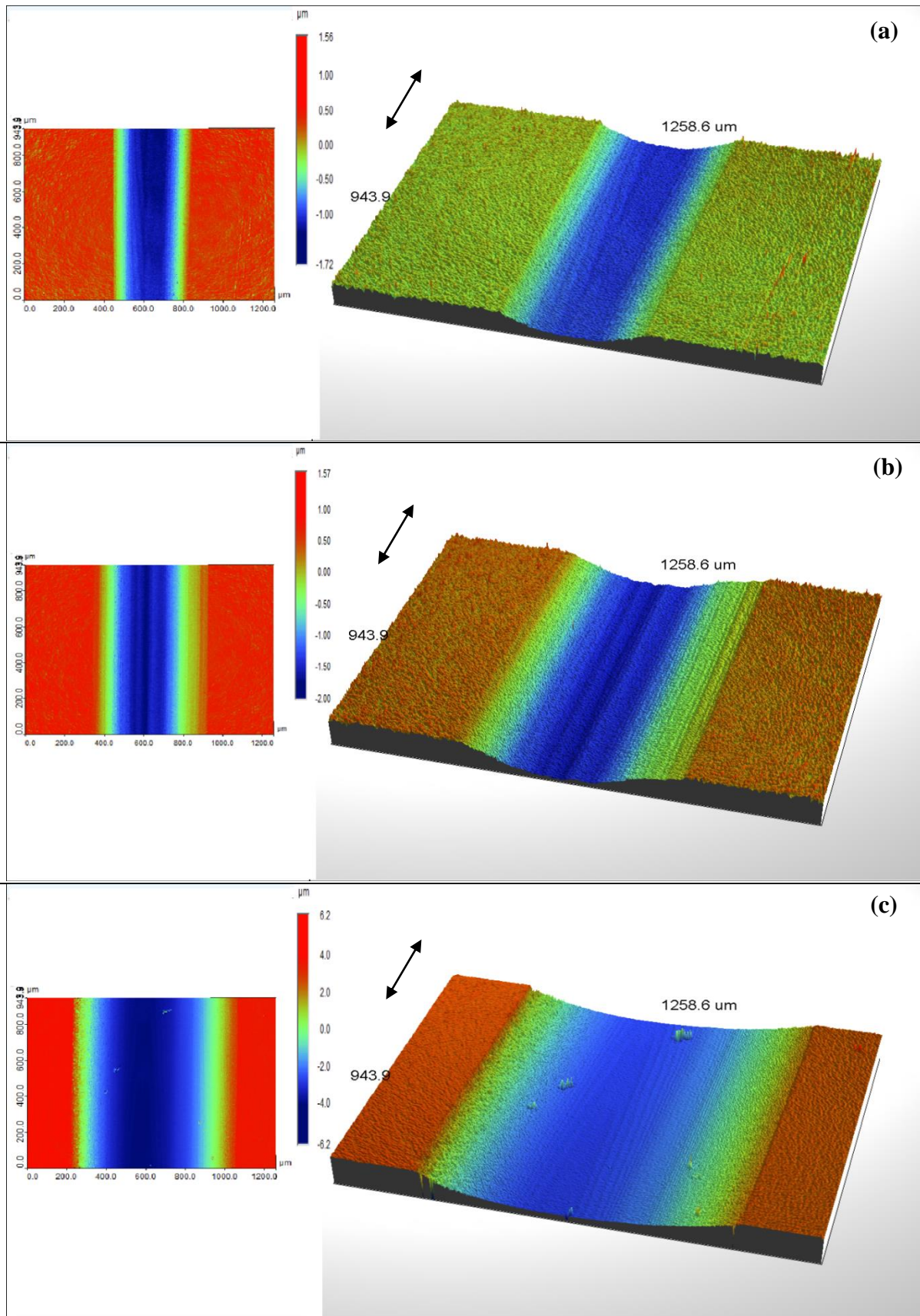


Figure 4.40. 3D VSI image of wear scars for ZTA+0.1 mole.% TiO₂ sample sintered at 1550°C for 5 minutes under the wear condition of 4N-24hrs (a), and 8N-24hrs (b), and 16N-8hrs (c)

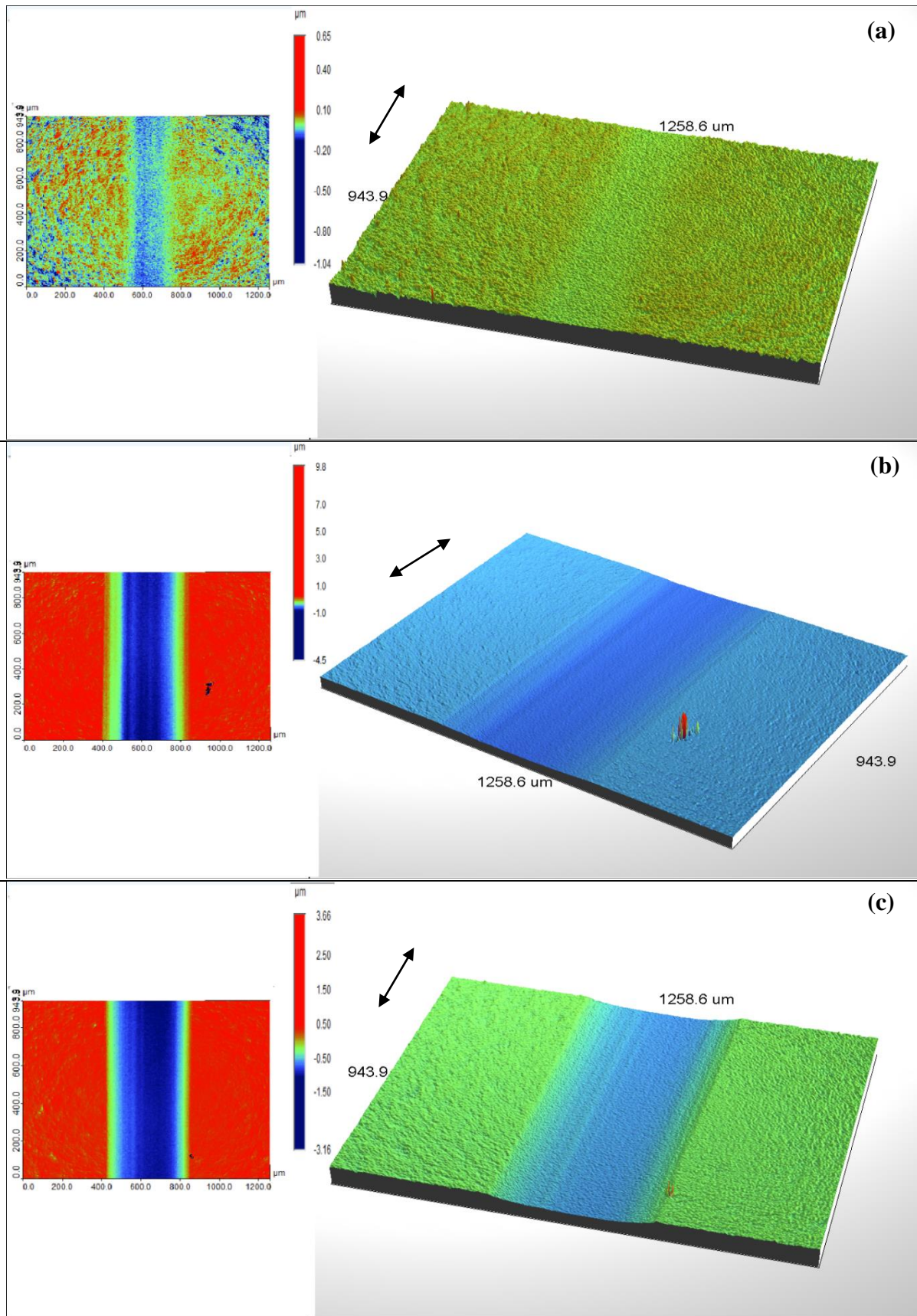


Figure 4.41. 3D VSI image of wear scars for ZTA+0.5 mole.% TiO₂ sample sintered at 1400°C for 5 minutes under the wear condition of 4N-24hrs (a), and 8N-24hrs (b), and 16N-8hrs (c)

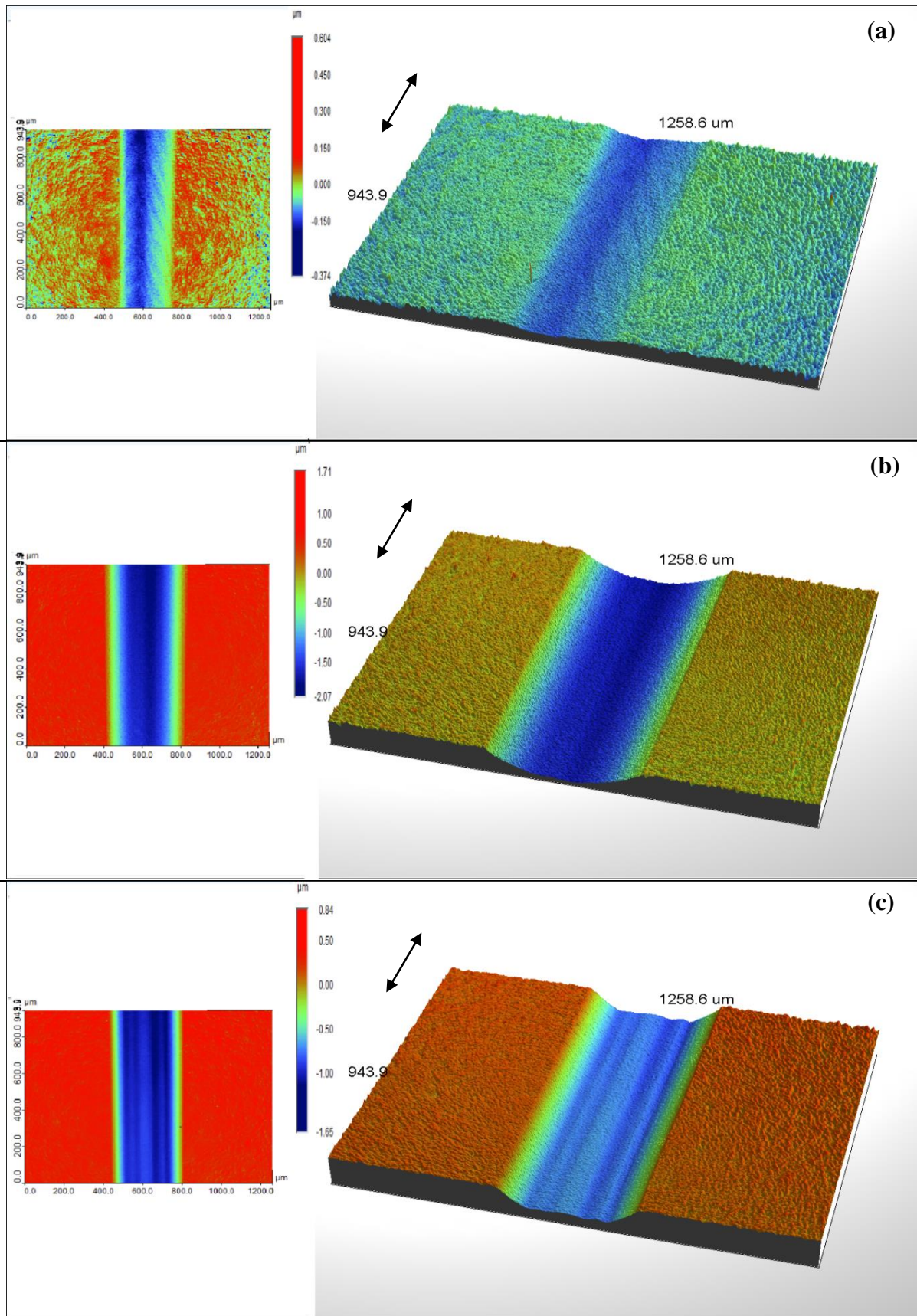


Figure 4.42. 3D VSI image of wear scars for ZTA+0.5 mole.% TiO₂ sample sintered at 1450°C for 5 minutes under the wear condition of 4N-24hrs (a), and 8N-24hrs (b), and 16N-8hrs (c)

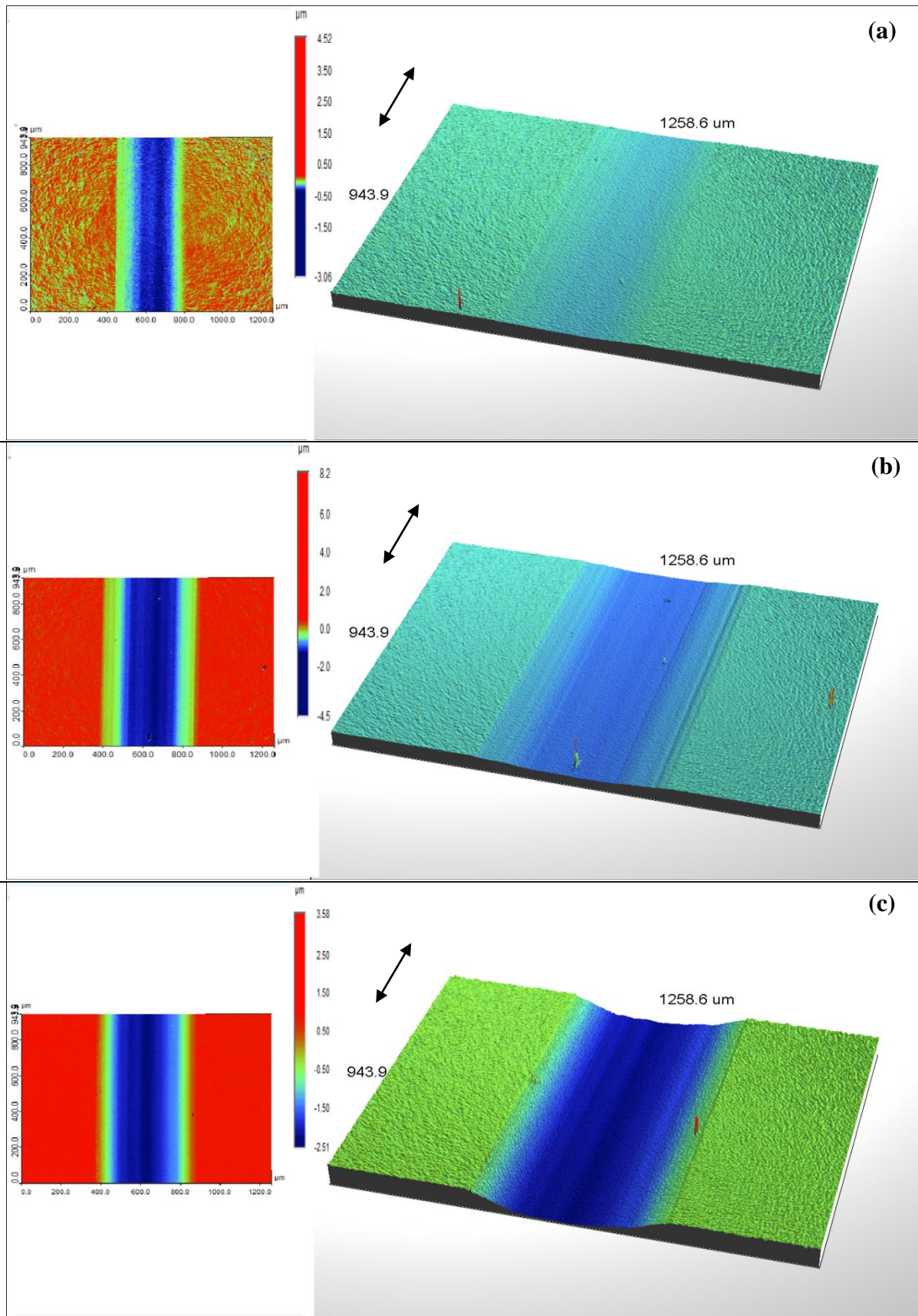


Figure 4.43. 3D VSI image of wear scars for ZTA+0.5 mole.% TiO₂ sample sintered at 1500°C for 5 minutes under the wear condition of 4N-24hrs (a), and 8N-24hrs (b), and 16N-8hrs (c)

Table 4.14. Surface roughness for the samples under different reciprocating wear conditions

Material	Sintering condition (Temperature (°C)- Time (min))	Surface Roughness (nm)		
		4 N-24 h	8 N-24 h	16 N-8h
ZTA	1450 - 7	34±9	42±7	29±4
	1500 - 7	21±2	24±4	43±7
	1550 - 7	83±7	47±5	33±1
ZTA + 0.1 mole.% TiO ₂	1450 - 5	28±2	24±2	37±5
	1500 - 5	16±6	75±1	58±5
	1550 - 5	NA	NA	NA
ZTA + 0.5 mole.% TiO ₂	1400 - 5	19±2	24±4	26±9
	1450 - 5	27±7	31±8	29±7
	1500 - 5	28±3	29±7	43±9

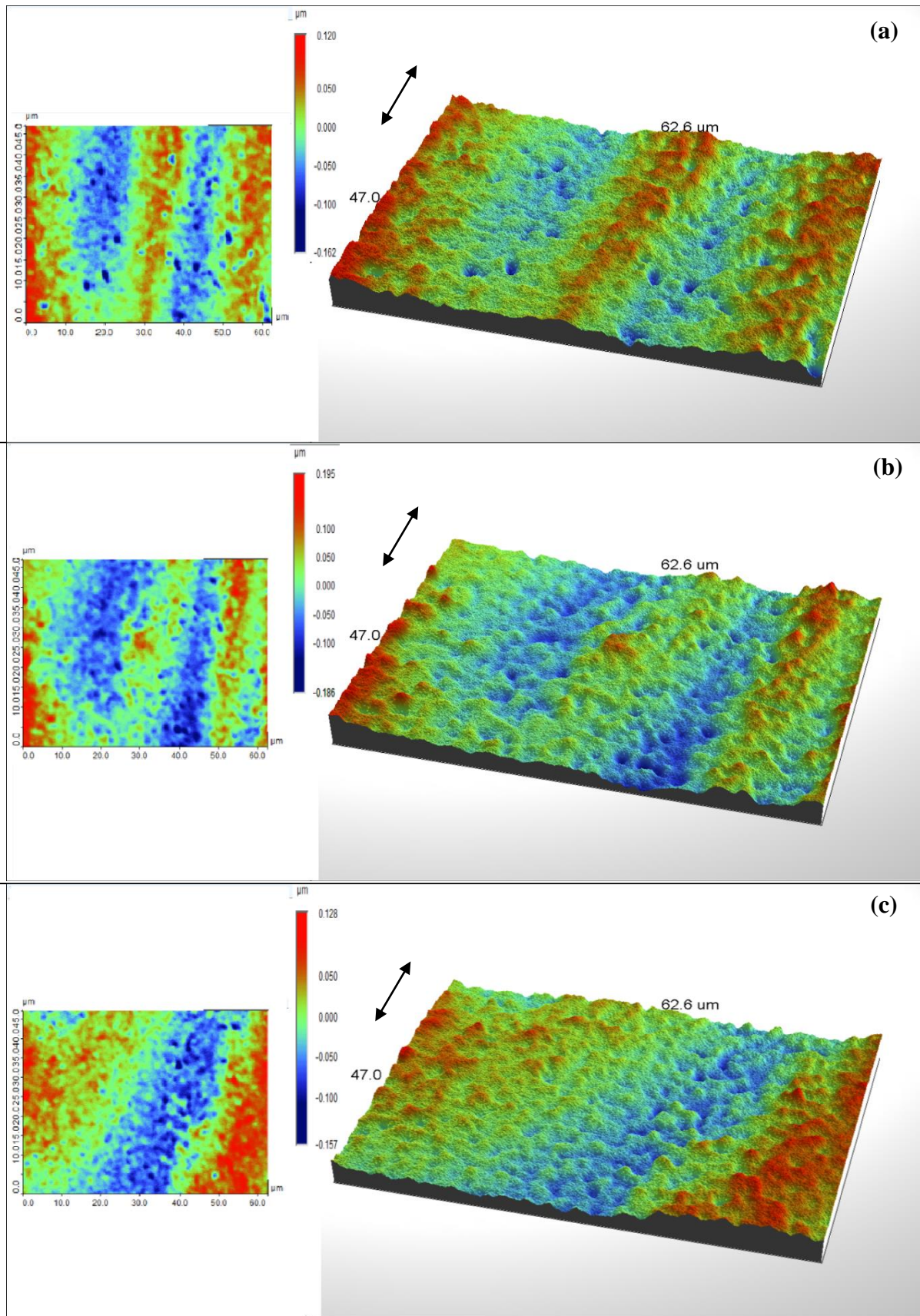


Figure 4.44. High magnification 3D VSI image of wear scars in the middle of deepest region for ZTA sample sintered at 1450°C for 7 minutes under the wear condition of 4N-24hrs (a), and 8N-24hrs (b), and 16N-8hrs (c)

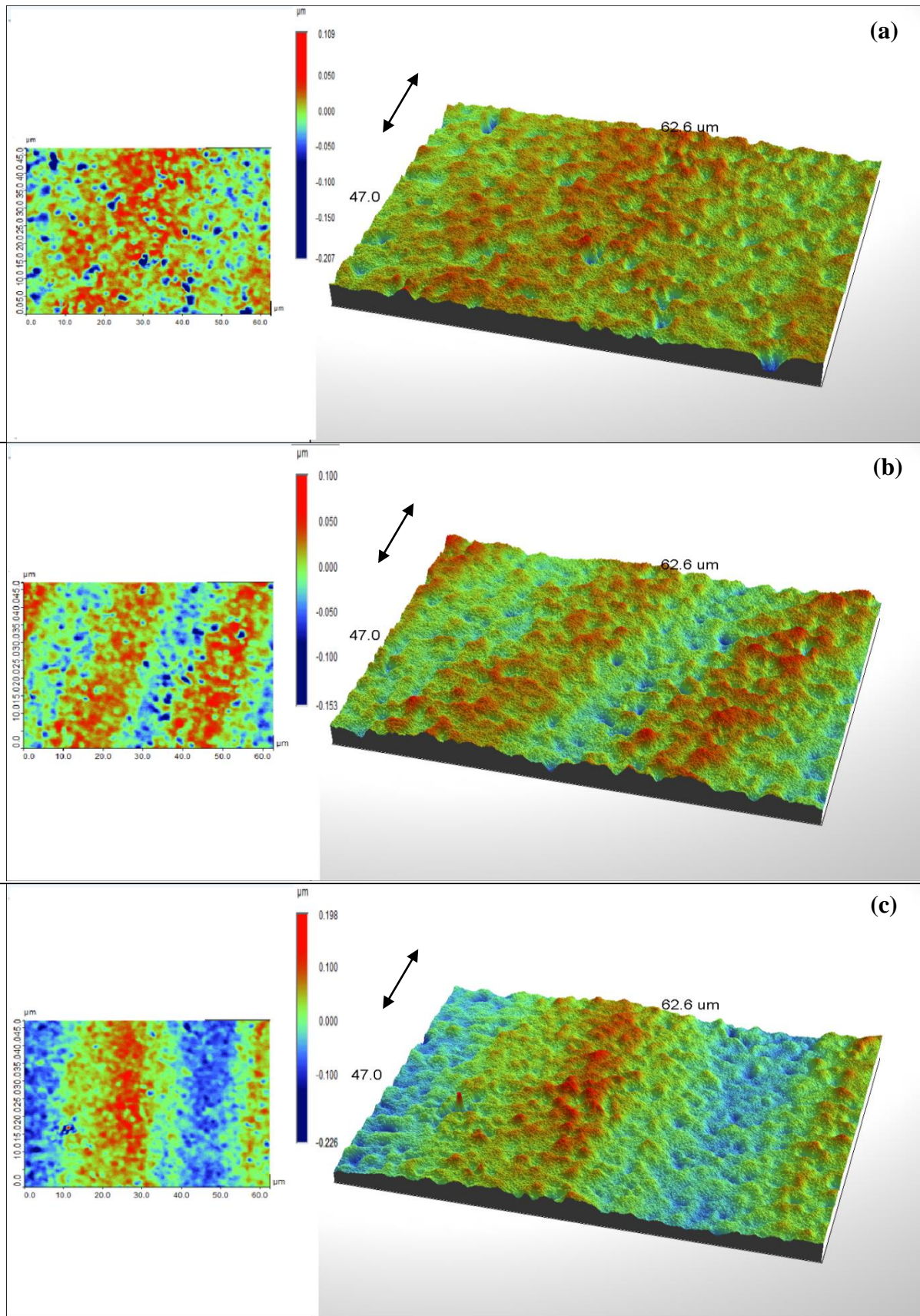


Figure 4.45. High magnification 3D VSI image of wear scars in the middle of deepest region for ZTA sample sintered at 1500°C for 7 minutes under the wear condition of 4N-24hrs (a), and 8N-24hrs (b), and 16N-8hrs (c)

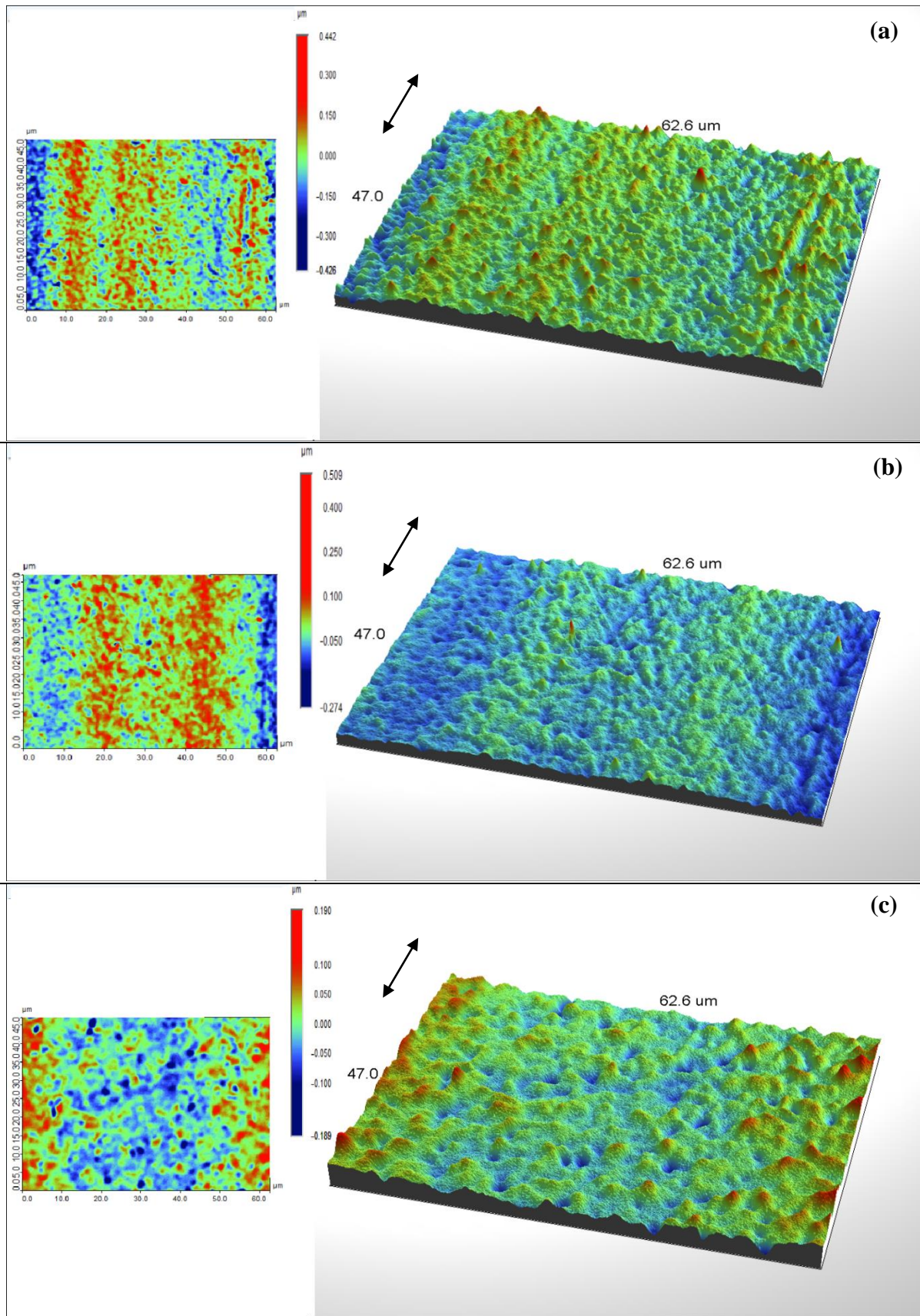


Figure 4.46. High magnification 3D VSI image of wear scars in the middle of deepest region for ZTA sample sintered at 1550°C for 7 minutes under the wear condition of 4N-24hrs (a), and 8N-24hrs (b), and 16N-8hrs (c)

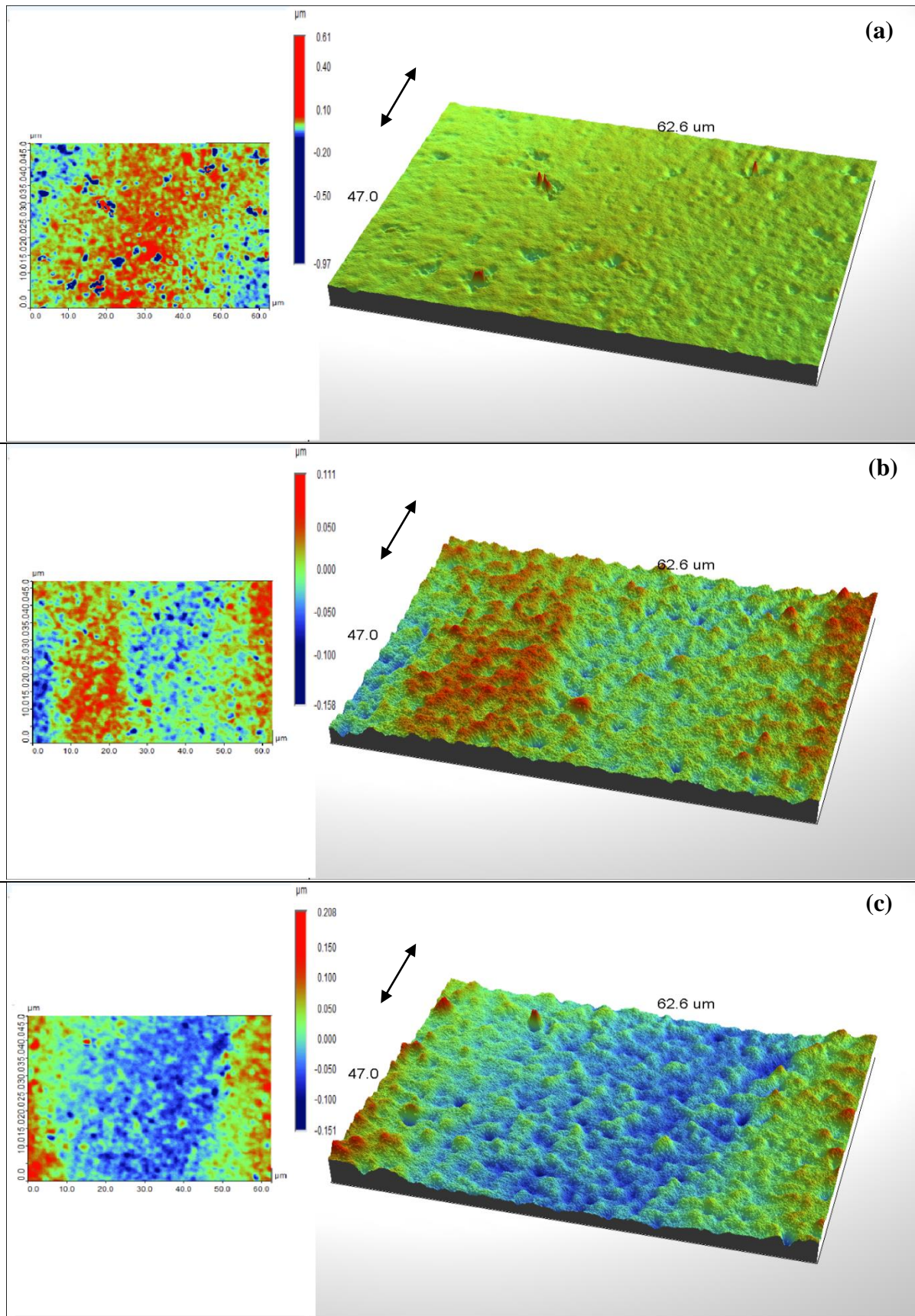


Figure 4.47. High magnification 3D VSI image of wear scars in the middle of deepest region for ZTA+0.1 mole.% TiO_2 sample sintered at 1450°C for 5 minutes under the wear condition of 4N-24hrs (a), and 8N-24hrs (b), and 16N-8hrs (c)

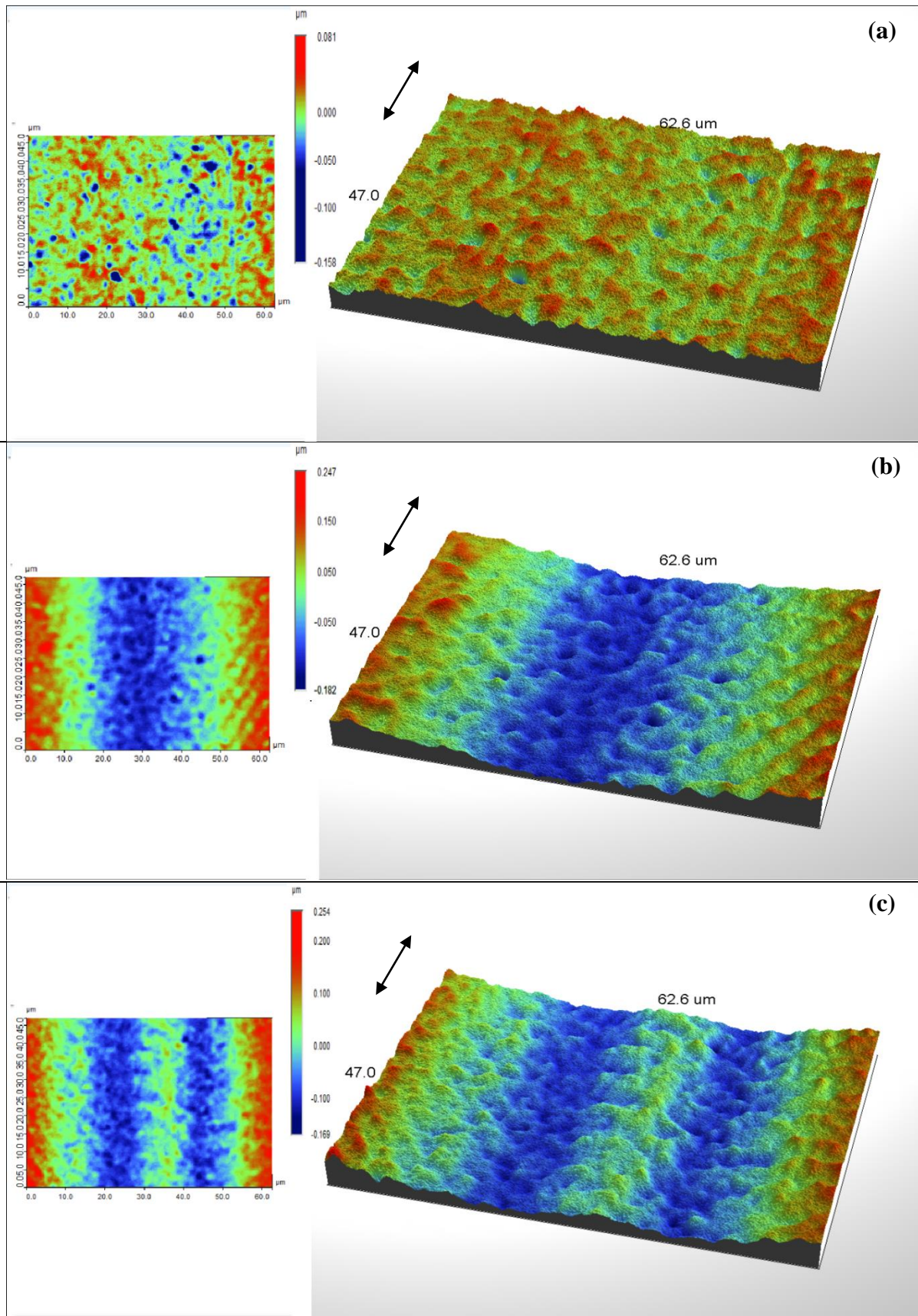


Figure 4.48. High magnification 3D VSI image of wear scars in the middle of deepest region for ZTA+0.1 mole.% TiO_2 sample sintered at 1500°C for 5 minutes under the wear condition of 4N-24hrs (a), and 8N-24hrs (b), and 16N-8hrs (c)

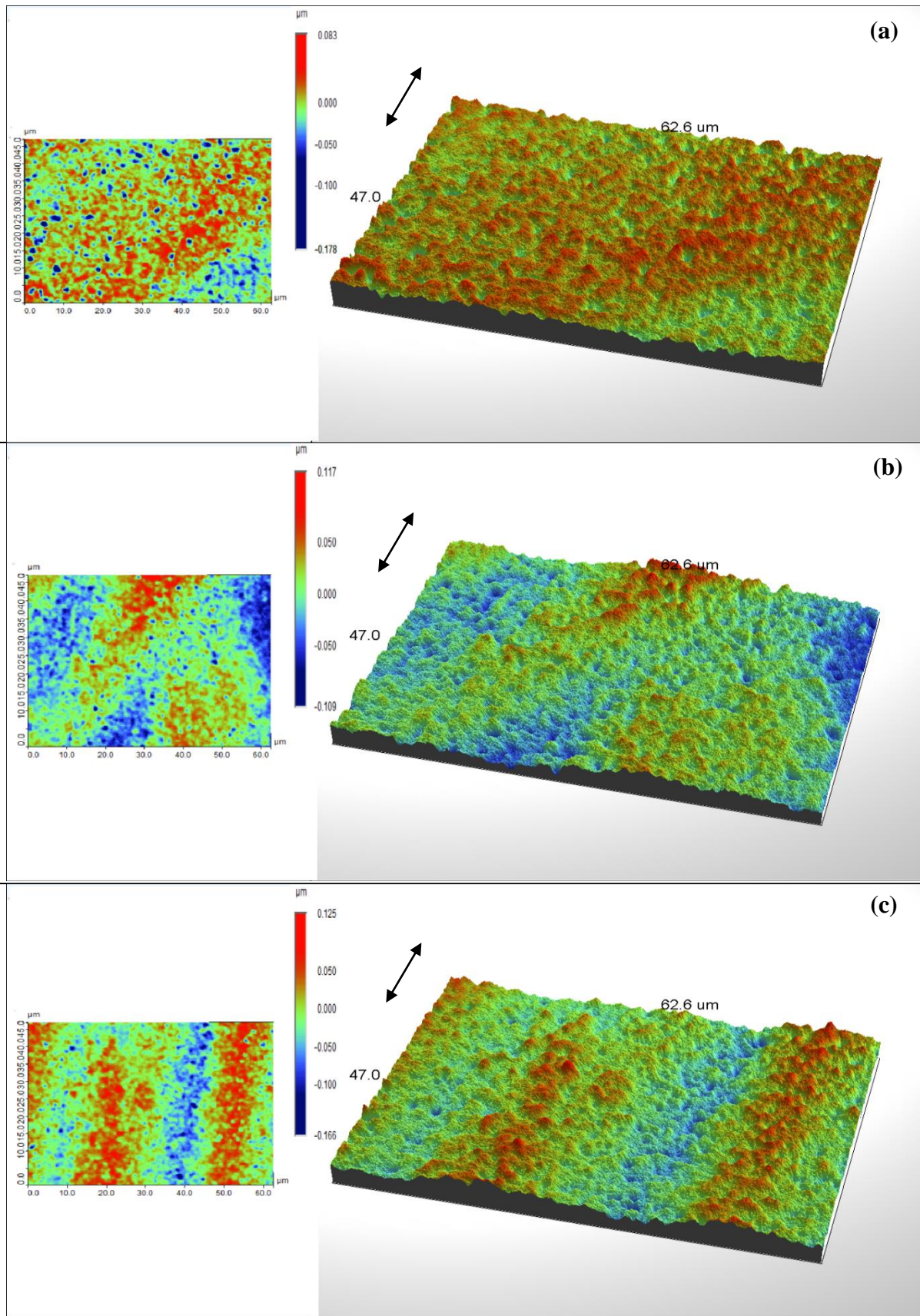


Figure 4.49. High magnification 3D VSI image of wear scars in the middle of deepest region for ZTA+0.5 mole.% TiO₂ sample sintered at 1400°C for 5 minutes under the wear condition of 4N-24hrs (a), and 8N-24hrs (b), and 16N-8hrs (c)

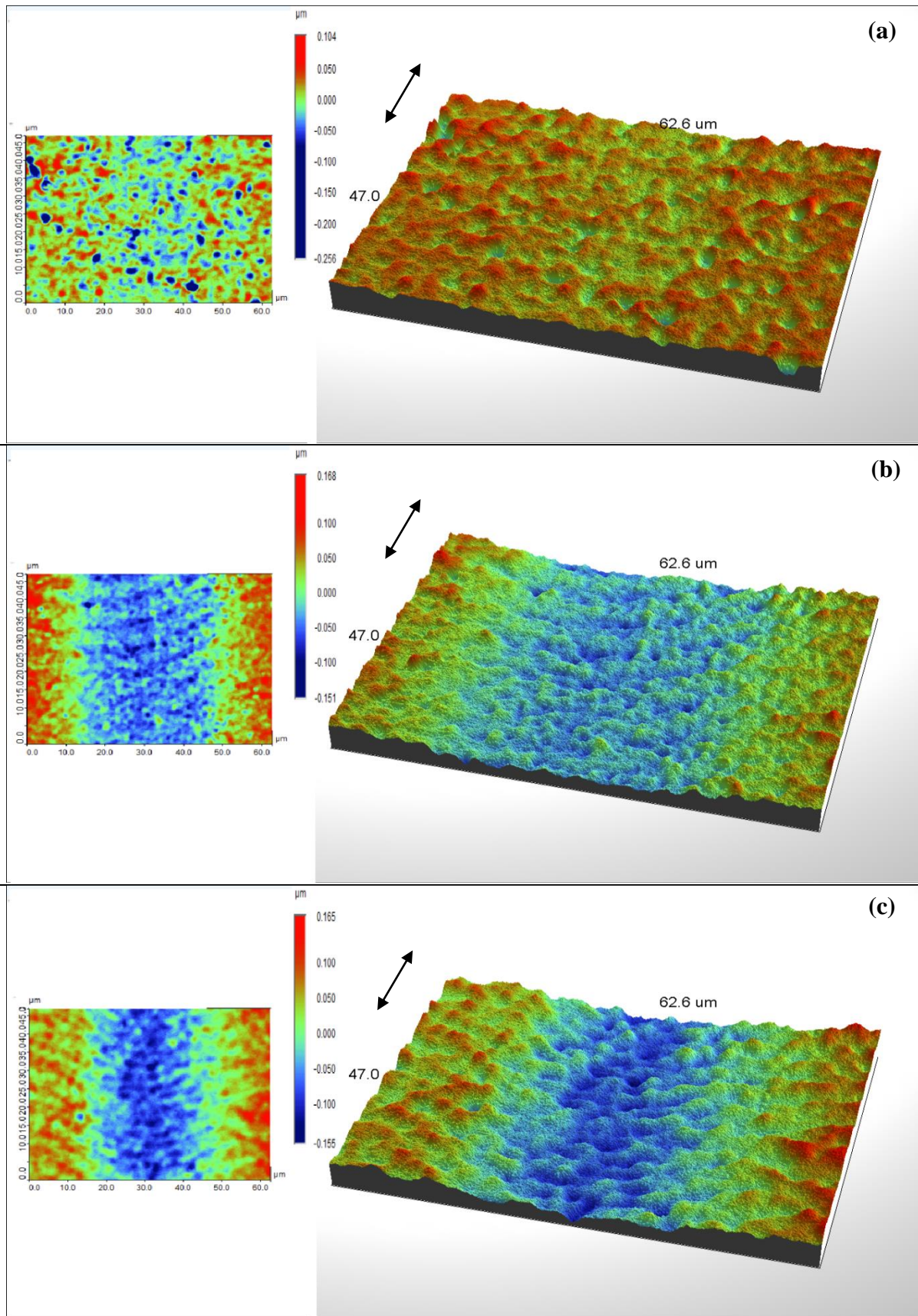


Figure 4.50. High magnification 3D VSI image of wear scars in the middle of deepest region for ZTA+0.5 mole.% TiO₂ sample sintered at 1450°C for 5 minutes under the wear condition of 4N-24hrs (a), and 8N-24hrs (b), and 16N-8hrs (c)

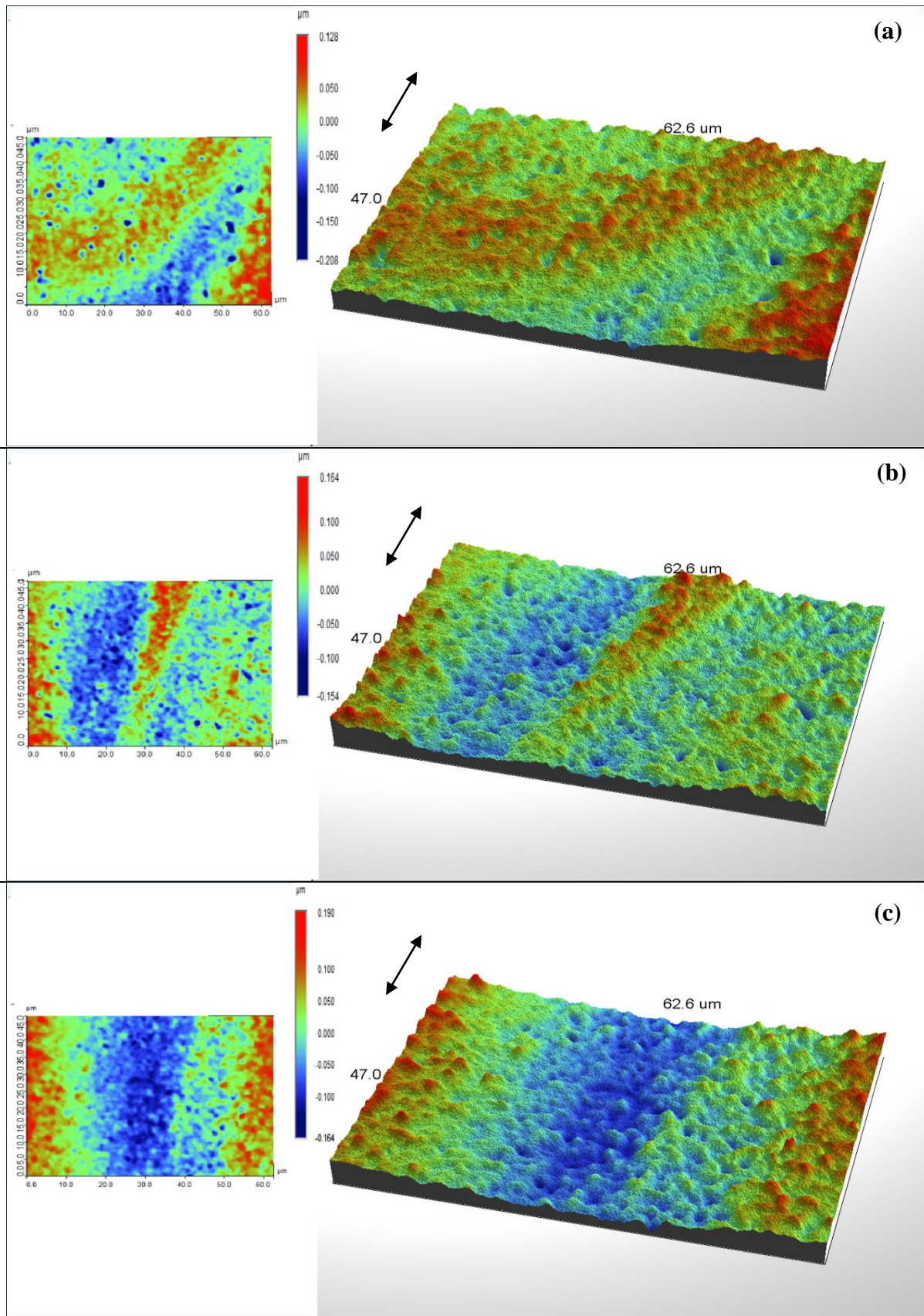


Figure 4.51. High magnification 3D VSI image of wear scars in the middle of deepest region for ZTA+0.5 mole.% TiO₂ sample sintered at 1500°C for 5 minutes under the wear condition of 4N-24hrs (a), and 8N-24hrs (b), and 16N-8hrs (c)

Topography of wear scars

In order to find out if any tribofilm was formed during the wear, the samples were analyzed by AFM after they had been rinsed in acetone. Figure 4.52 shows some representative AFM images of samples. As can be seen in this figure the surface is covered by a layer of tribofilm. The thickness of the tribofilm was variable, but an estimation was made from the AFM that it was of the order of 100 nm (Figure 4.52 (c)). It should be noted that identification of elements composed in tribofilm needs cross-sectional TEM, which was not carried out in this study.

Cleaning the sample to analyze the grain structure was very difficult, especially for samples containing 0.5 mole.% titania, which might be due to strong adhesion of tribofilm to the surface. However, after immersing and cleaning the samples with the solution made from Vikron tablets, several AFM images could be captured which some of their representative ones are illustrated in Figure 4.53 to Figure 4.77 for different samples and wear conditions. It should be noted that numerous AFM images were taken from all the wear scars and only a few of them were purposefully singled out to be representative of the topography of the samples.

Figure 4.53 and Figure 4.54 shows representative images for ZTA samples sintered at 1450°C for 7 minutes under wear condition of 8 N for 24 hours and 16 N for 8 hours respectively. The surface was rough with the grain height difference between 2.4 nm (Figure 4.53.c) to 14.9 nm (not shown) for 8N wear scar and around 1 nm for 16N wear scar (Figure 4.54.c and d). Transgranular fracture inside the grains standing proud of the surface is another feature which could be detected in Figure 4.53.b, and Figure 4.54.a and b; these grains were found to be around 13 nm higher than their neighbouring grains (Figure 4.53.b). In addition, fractured triple point is the major damage which is clear in all the figures and grain pull out could also be detected as can be seen in Figure 4.54.d.

Figure 4.55 to Figure 4.57 illustrate the AFM images for ZTA samples sintered at 1500 °C for 7 minutes under different wear conditions. The same feature of rough surface with height difference between grains to be from 1.0 nm to 13.0 nm (Figure 4.55.a) for 4N wear scar, from 1.0 nm to 9.0 nm (Figure 4.56.d) for 8N wear scar and from 3.9 nm (Figure 4.57.c) to 7.3 nm (Figure 4.57.a) for 16N wear scar could be detected. Grain pull-out from a depth of 109.4 nm (Figure 4.56.a) to 241.7 nm (Figure 4.56.c) and transgranular fractured grains with height difference around 7 nm (Figure 4.57.b) are another features identified on the wear scars of this sample.

Representative AFM images for ZTA samples sintered at 1550 °C for 7 minutes under different wear conditions are given in Figure 4.58 to Figure 4.60. The images show coarser grain sizes due to higher sintering temperature and same rough surface with height difference between grains from 9.8 nm (Figure 4.58) to 20.0 nm (Figure 4.59.b), which the latter is related to the height of transgranular fractured grain to its neighbour. Grain pull-out with the depth of 108.1 nm (Figure 4.60) has also been identified for this sample.

Figure 4.61 to Figure 4.63 show the topography of wear scars for ZTA+0.1 mole.% TiO₂ sample sintered at 1450 °C for 5 minutes under different wear conditions. The rough surface with height difference between grains from 2.7 nm for 16N wear scar to 7.5 nm for 4N wear scar was observed. Transgranular fractured grains with height difference of 11.7 nm (Figure 4.63.c) and width of 1.572 μ (Figure 4.63.d) were detected, with one of them having an inside fracture depth of 37.1 nm (Figure 4.63.b). Grain pull-outs are also clear, as expected, with the depth of 149.5 nm (Figure 4.63.c). In addition to these common features, wear grooves could be found on the 4N wear scar as can be seen in Figure 4.61.b.

Topographic characteristics of surfaces for ZTA+0.1 mole.% TiO₂ sample sintered at 1500 °C for 5 minutes under different wear conditions are illustrated in Figure 4.64 and Figure 4.65. As can be seen in these figures, transgranular fractures occurred with a height difference of 12.6 nm to 16.2 nm (Figure 4.64) were detectable for the wear scars of this sample. A cluster of removed grains in an area with the size of more than 2 μ (Figure 4.65) is another feature found for 16N wear scar.

Similarly, Figure 4.66 to Figure 4.68 gives AFM images of different wear scars for ZTA+0.1 mole.% TiO₂ sample sintered at 1550 °C for 5 minutes. Height difference between grains in this composite was found to be from 0.5 nm for neighbouring grains of 16N wear scar to 4.5 nm for 8N wear scar. Transgranular fractured grains seen in these wear scars were standing from 11.7 nm (Figure 4.67.b) to 14.8 nm (Figure 4.68.c) proud of the surface. Fractured triple points with the depth less than 35 nm (Figure 4.66 and Figure 4.67.d) and the frequent grain pull-out with the depth of 229.0 nm (Figure 4.67.c) are other features observed in wear scars of this sample.

AFM images for samples containing 0.5 mole.% TiO₂ sintered at 1400 °C for 5 minutes are given in Figure 4.69 to Figure 4.71. The rough surface with height difference in neighbouring grains from 2.9 nm in 16N wear scar to 11.3 nm (Figure 4.70.a) for 8N wear scar were detected

in this composite. Despite the relatively large deeper areas found on the surface, less grain pull-out was detected in comparison with other samples and the damage seemed to be more on triple points (Figure 4.69.c). Grooves were also detected in 4N (Figure 4.69) and 8N (Figure 4.70) wear scars with the depth up to 22.9 nm (Figure 4.69.a) and 9.3 nm (Figure 4.70.c) for 4N and 8N grooves respectively. As it is clear in Figure 4.69.a and Figure 4.70.c, the depth of grooves was changing in grooves' path. Interestingly, no transgranular fractured grains were found in any of taken images for 4N and 8N wear scars.

Figure 4.72 to Figure 4.74 shows topographic characteristics of ZTA+0.5 mole.% TiO₂ sample sintered at 1450 °C for 5 minutes under different wear conditions. The same rough surface with deep regions by having depth from 5.6 nm for 8N wear scar to 14.3 nm (Figure 4.72.b) was observed in this composites. Several transgranular fractured grains were found on the surface of all wear scars clearly illustrated in Figure 4.72.c and d, and Figure 4.74.c. No grooves were identified in the images taken for this composite.

Similarly, AFM images of ZTA samples with 0.5 mole.% addition of TiO₂ sintered at 1500°C for 5 minutes are given in Figure 4.75 to Figure 4.77. Rough surface and deep regions with depth of 5.4 nm for 8N wear scar to 16.0 nm (Figure 4.75.b) for 4N wear scar were characteristics of these surfaces. Transgranular fractured grains with height difference from 10.2 nm (Figure 4.76.c) to 14.4 nm (Figure 4.77.b) and grain pull-outs were also detected in these figures, as well as clusters of more than one removed grains (Figure 4.76.b). In addition, an area was found in 16N wear scar in which upper part of the grain seemed to be removed and its depth was around 20 to 60 nm, which is less than half of the depth for grain pull-out. This grain and its related surface profile is demonstrated in Figure 4.77.c.

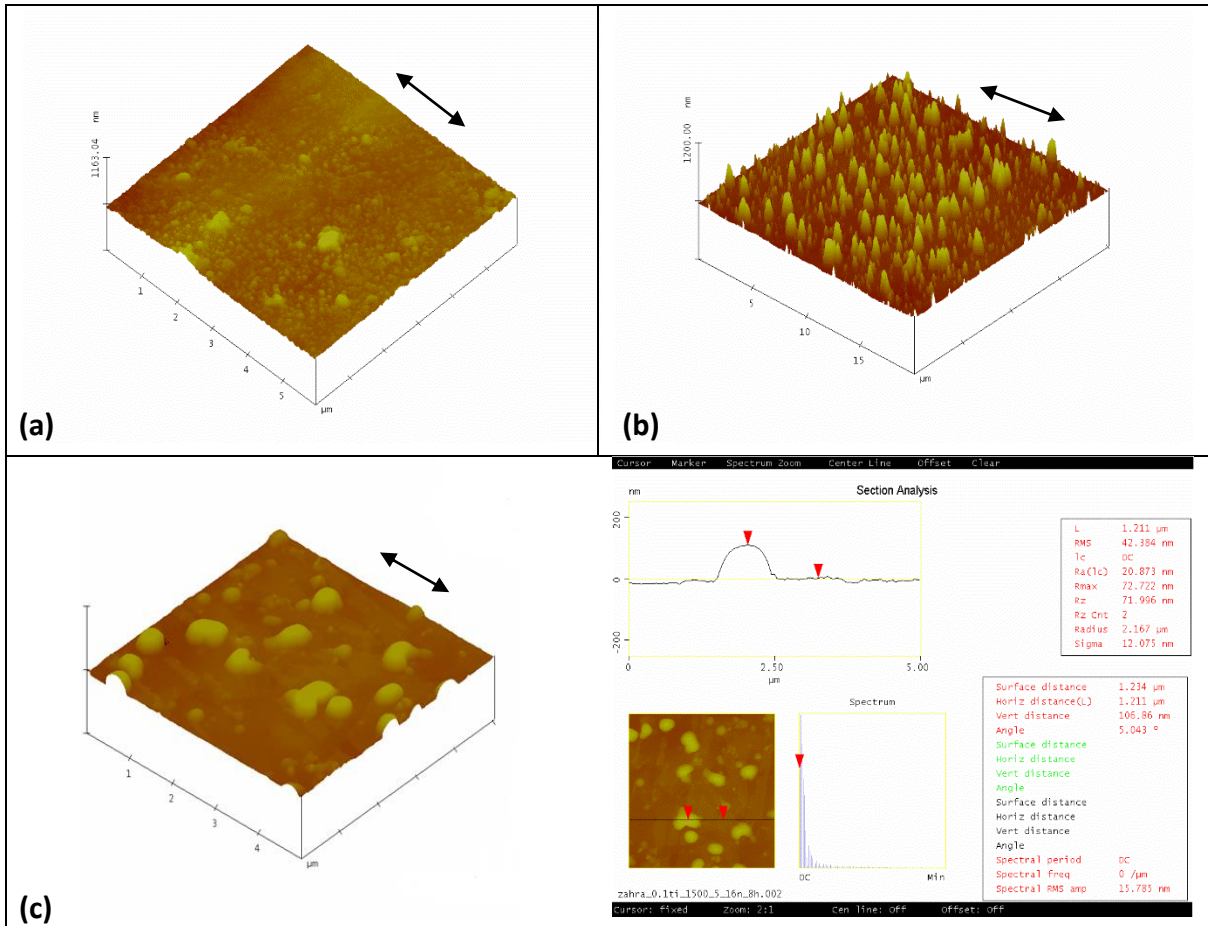
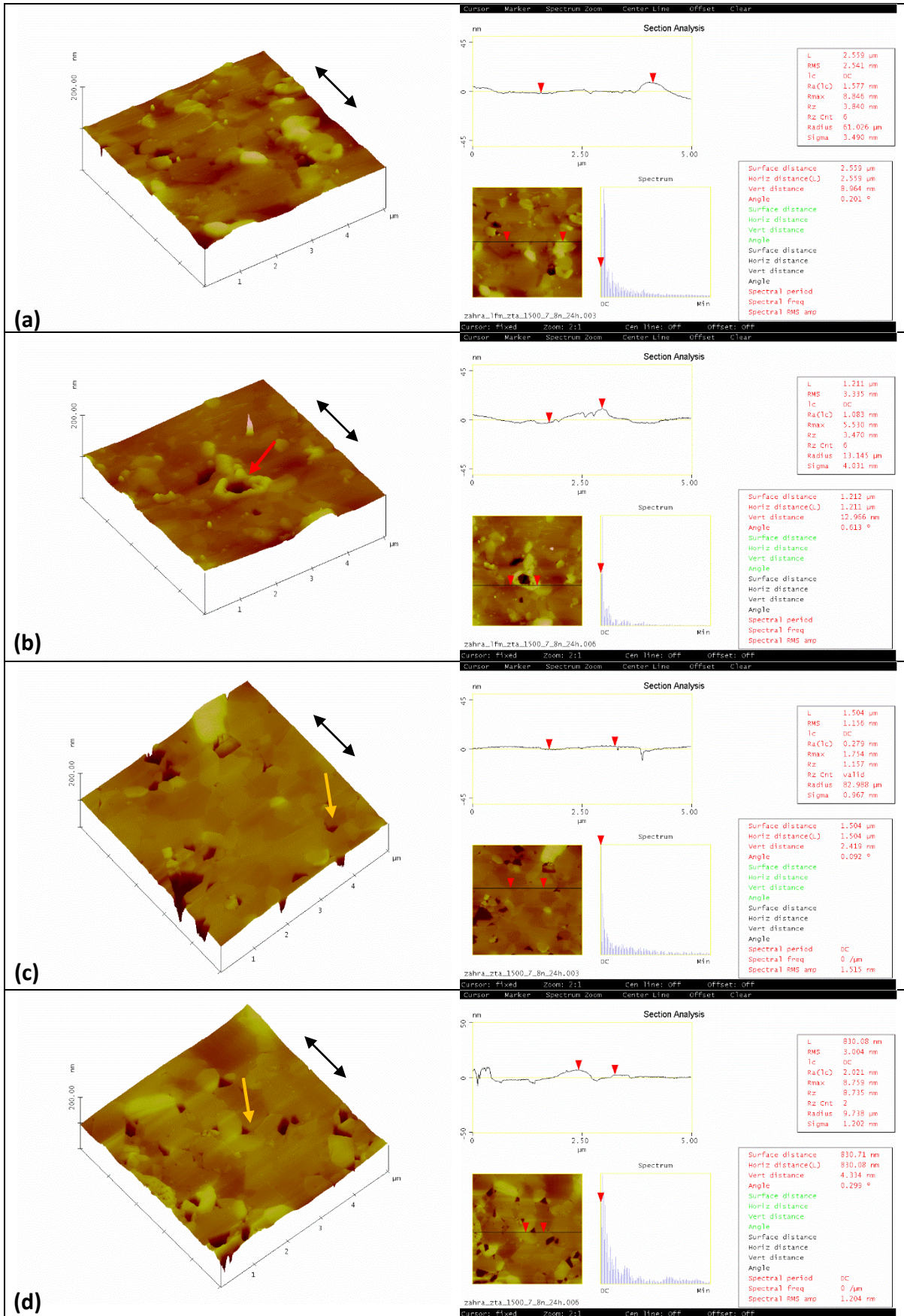


Figure 4.52. AFM image of wear scars before cleaning for ZTA sample sintered at 1550°C for 7 minutes under the wear condition of 16N-8hr (a), and ZTA+0.1 mole.% TiO₂ samples sintered at 1500°C for 5 minutes under the wear condition of 4N-24hr (b) and (c) (image width is 6 μm for (a), 20 μm for (b), and 5 μm for (c))



Continued

Continued

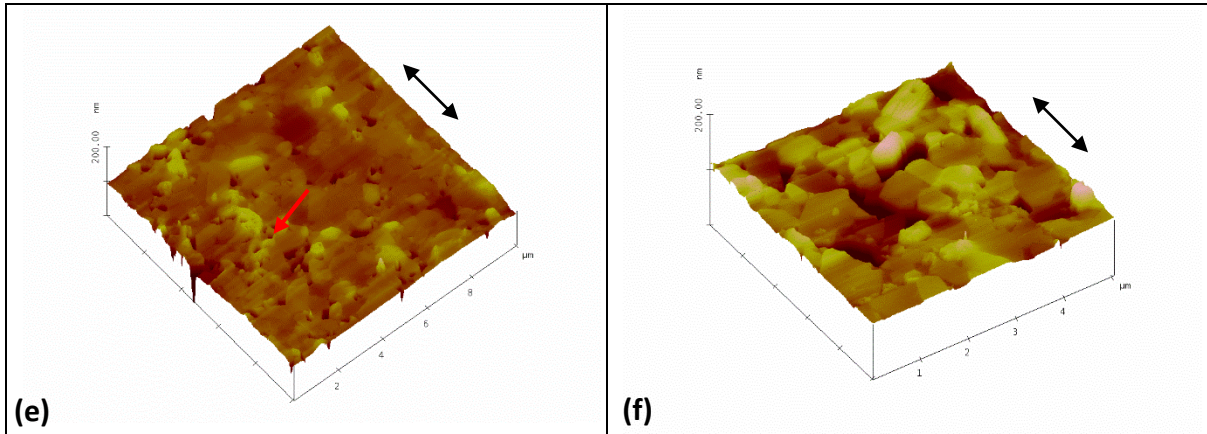


Figure 4.53. AFM image of wear scars for ZTA sample sintered at 1450°C for 7 minutes under the wear condition of 8N-24h, representing transgranular fracture with red arrows and fractured triple points with yellow arrows
(image width is 5 μm for (a), (b), (c), (d) and (f), and 10 μm for (e))

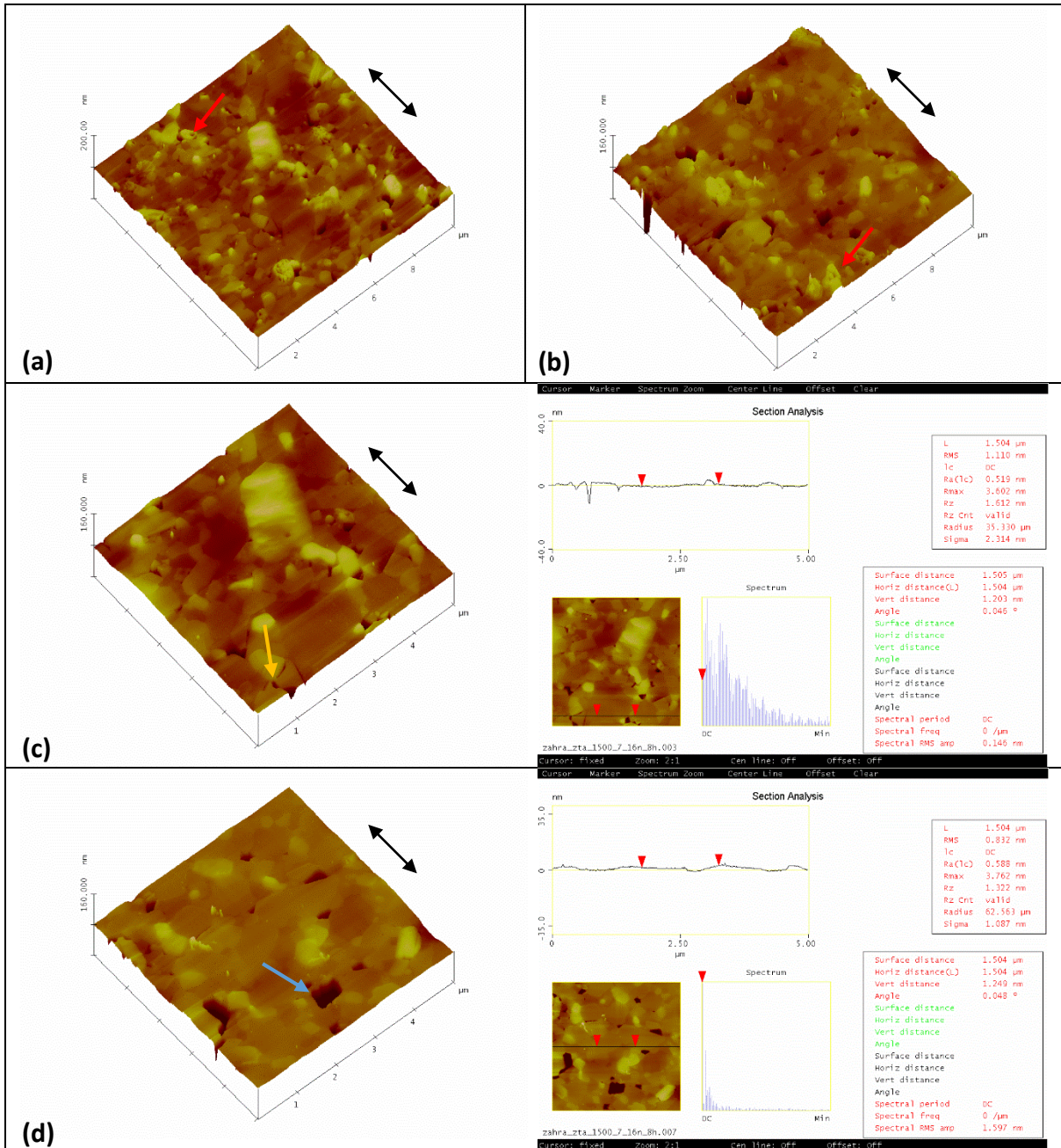


Figure 4.54. AFM image of wear scars for ZTA sample sintered at 1450°C for 7 minutes under the wear condition of 16N-8hr, representing transgranular fracture with red arrows, grain pull-out with blue arrows, and fractured triple points with yellow arrows (image width is 10µm for (a) and (b), and 5µm for (c) and (d))

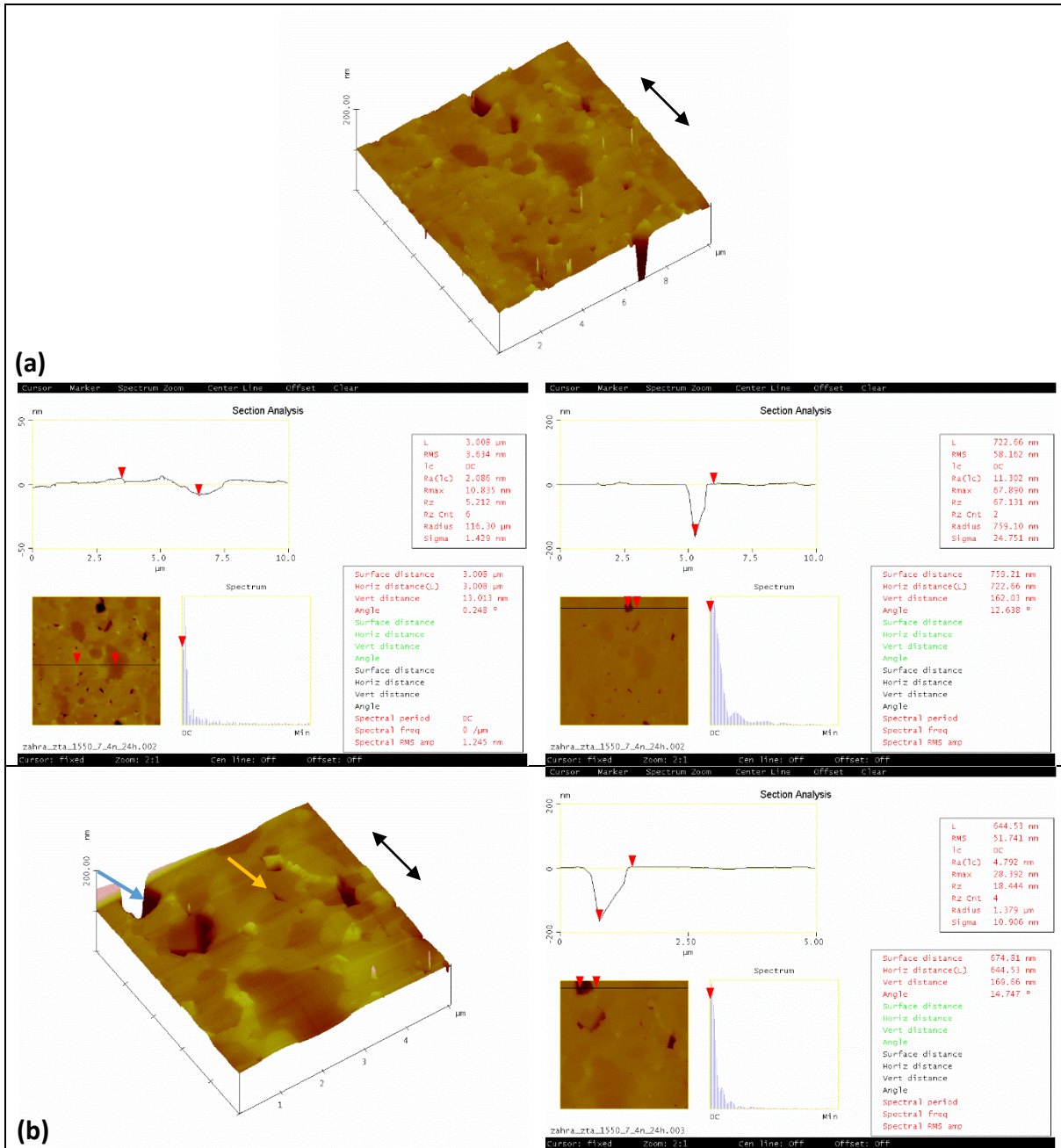
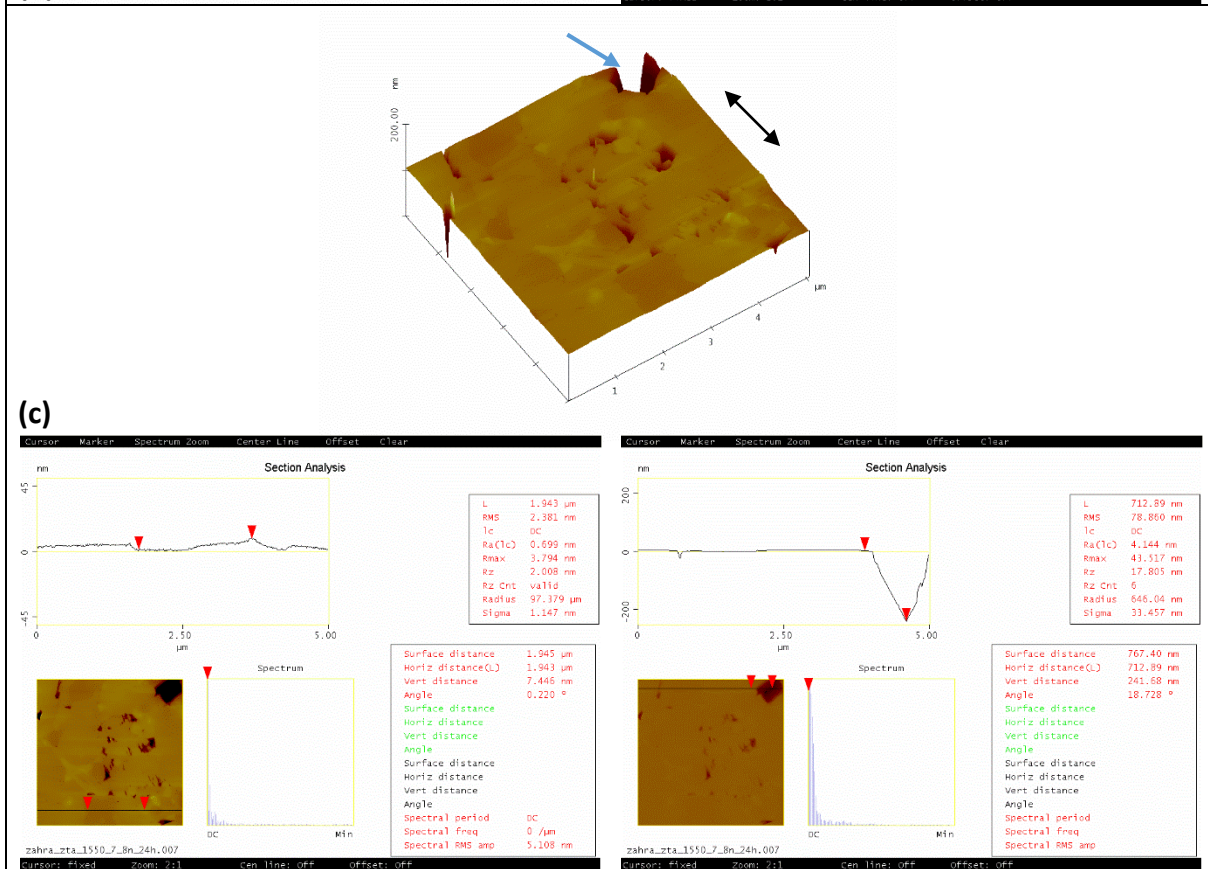
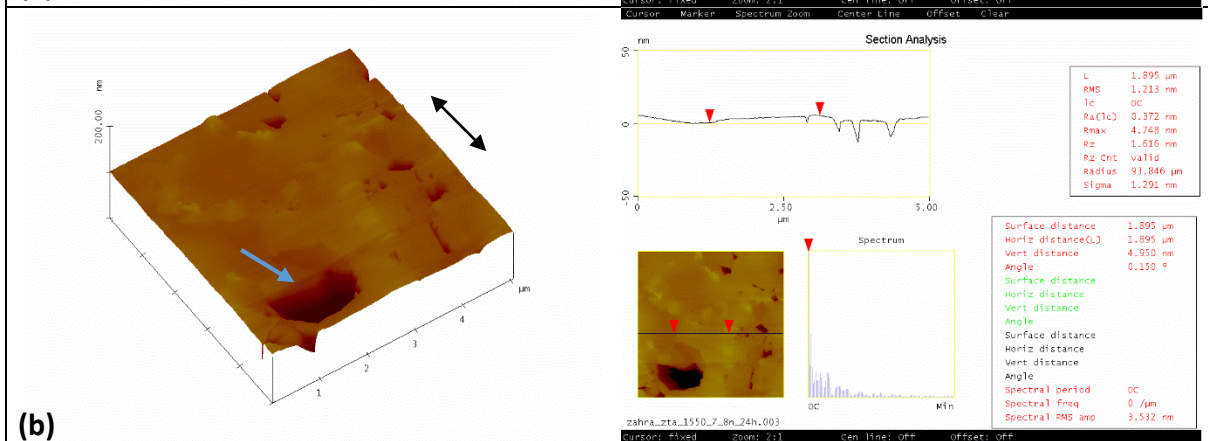
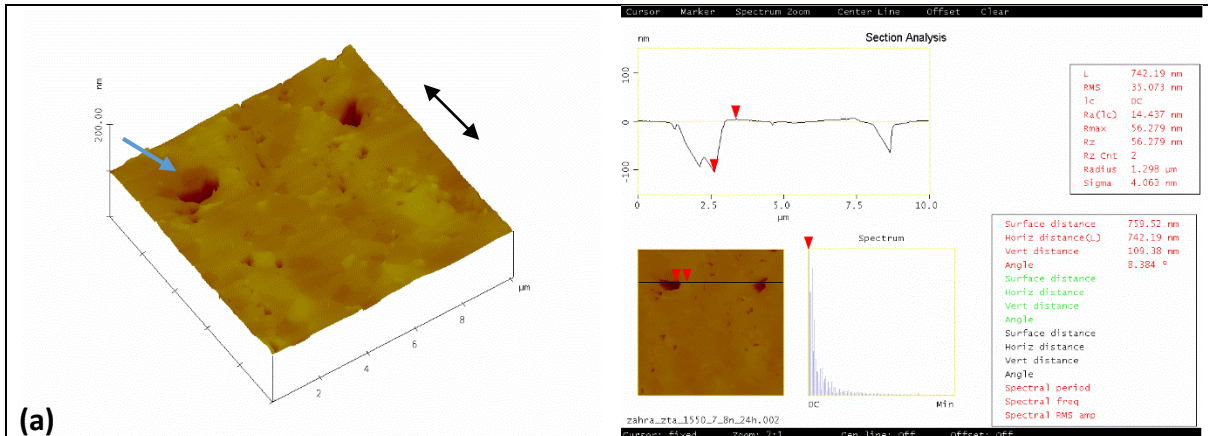


Figure 4.55. AFM image of wear scars for ZTA sample sintered at 1500°C for 7 minutes under the wear condition of 4N-24hr, representing grain pull-out with blue arrows, and fractured triple points with yellow arrows (image width is 10µm for (a), and 5µm for (b))



Continued

Continued

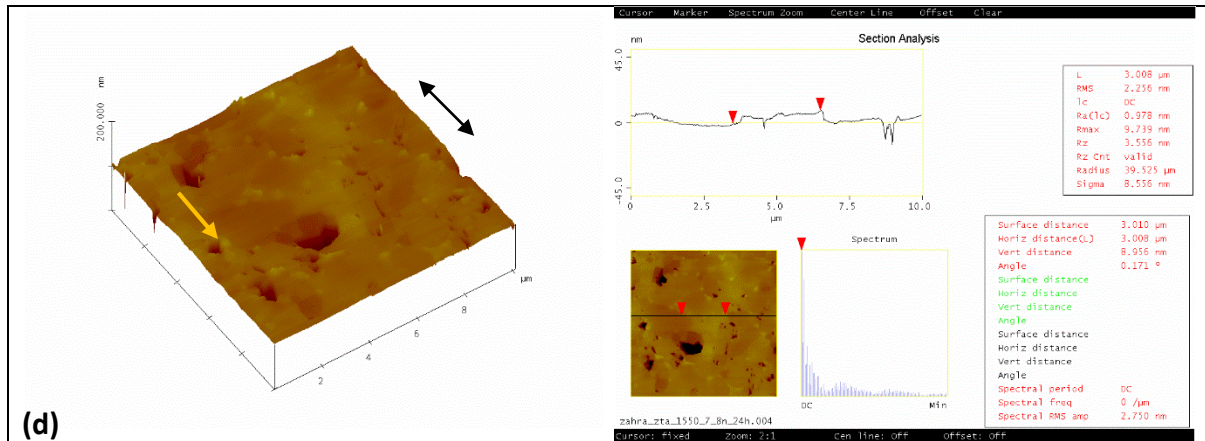


Figure 4.56. AFM image of wear scars for ZTA sample sintered at 1500°C for 7 minutes under the wear condition of 8N-24hr, representing grain pull-out with blue arrows, and fractured triple points with yellow arrows

(image width is 10 μm for (a) and (d), and 5 μm for (b) and (c))

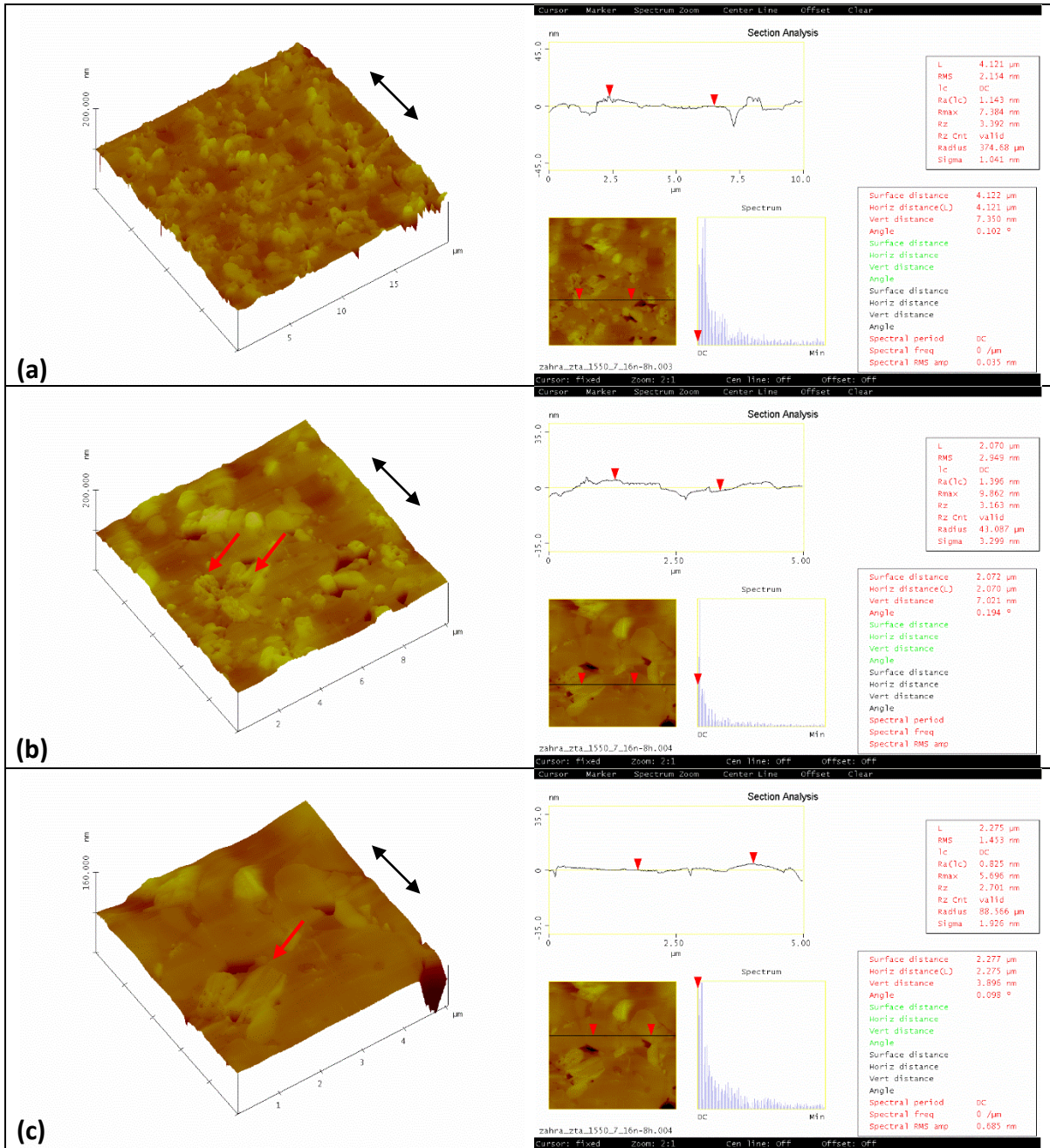


Figure 4.57. AFM image of wear scars for ZTA sample sintered at 1500°C for 7 minutes under the wear condition of 16N-8hr, representing transgranular fracture with red arrows. (image width is 30 μm, 10μm, and 5μm for (a), (b), and (c) respectively)

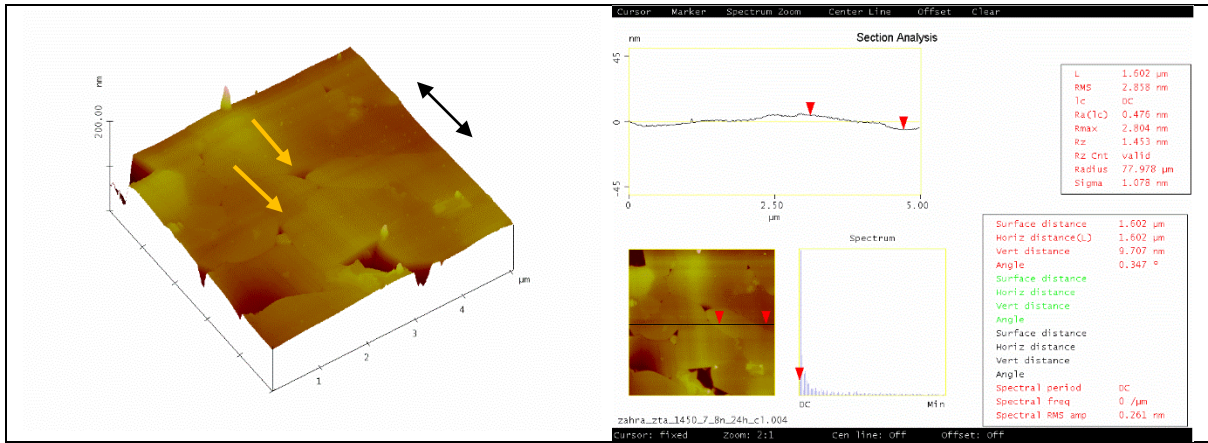


Figure 4.58. AFM image of wear scars for ZTA sample sintered at 1550°C for 7 minutes under the wear condition of 4N-24hr, representing fractured triple points with yellow arrows (image width is 5µm)

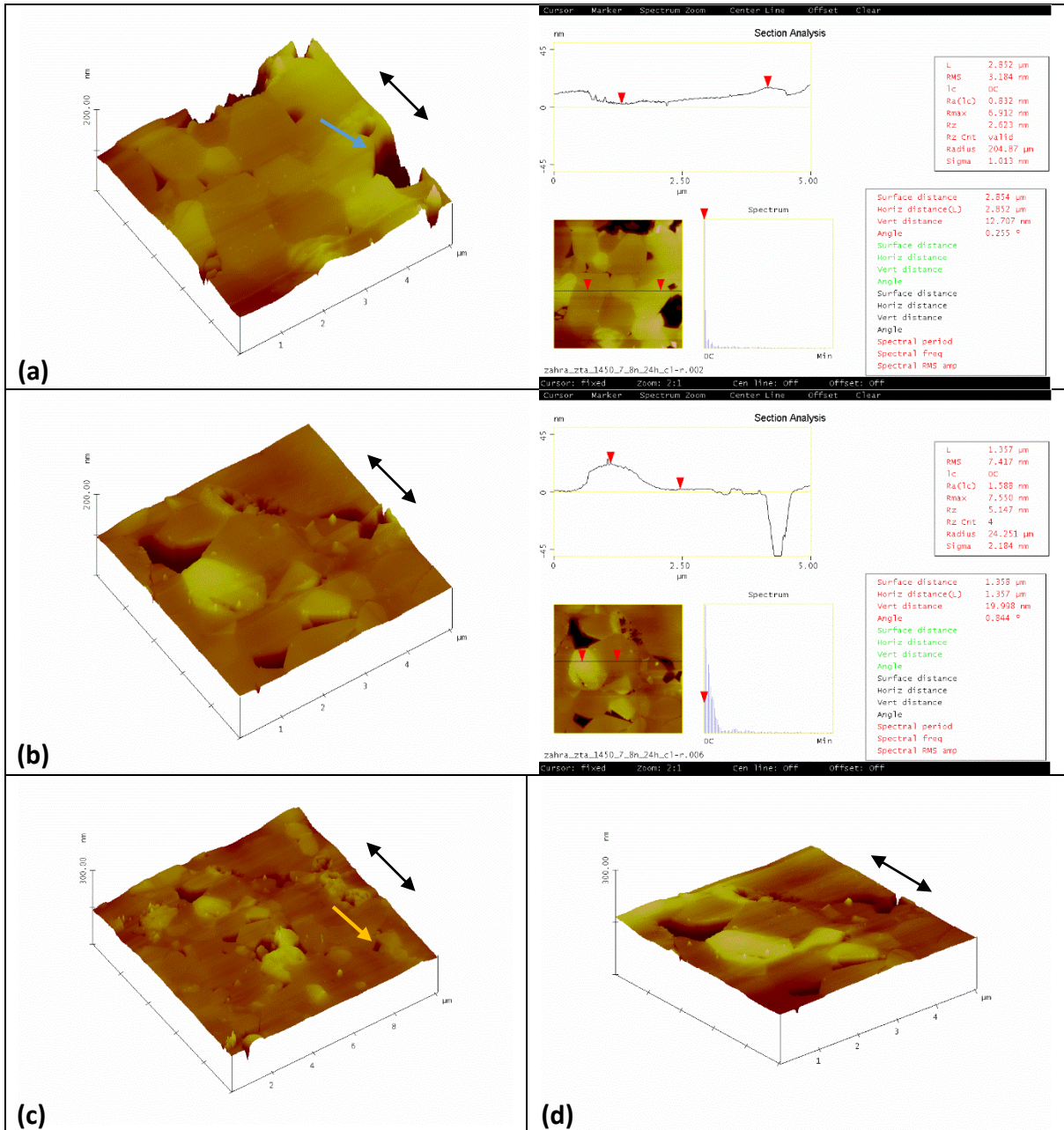


Figure 4.59. AFM image of wear scars for ZTA sample sintered at 1550°C for 7 minutes under the wear condition of 8N-24hr, representing grain pull-out with blue arrows, and fractured triple points with yellow arrows (image width is 5µm for (a), (b), and (d), and 10µm for (c))

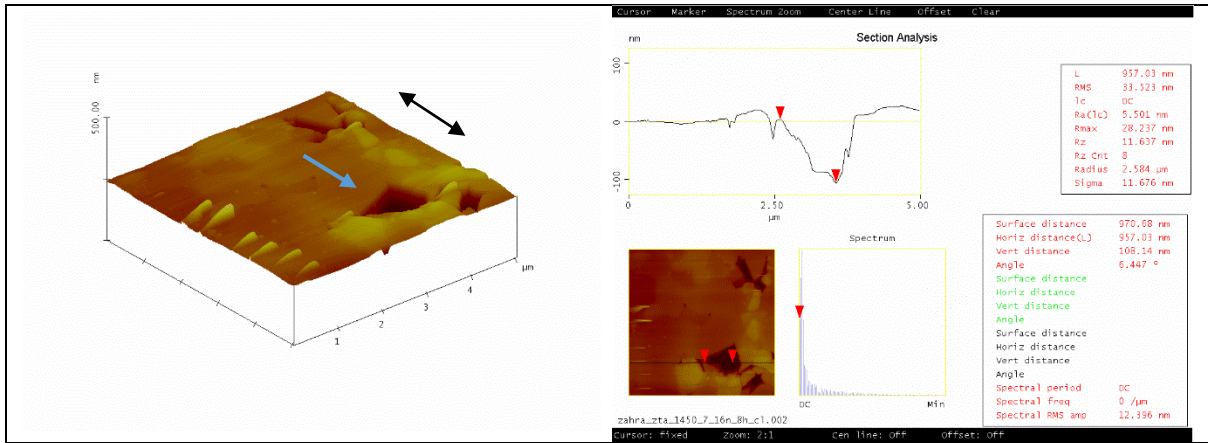


Figure 4.60. AFM image of wear scars for ZTA sample sintered at 1550°C for 7 minutes under the wear condition of 16N-8hr, representing grain pull-out with blue arrow (image width is 5μm)

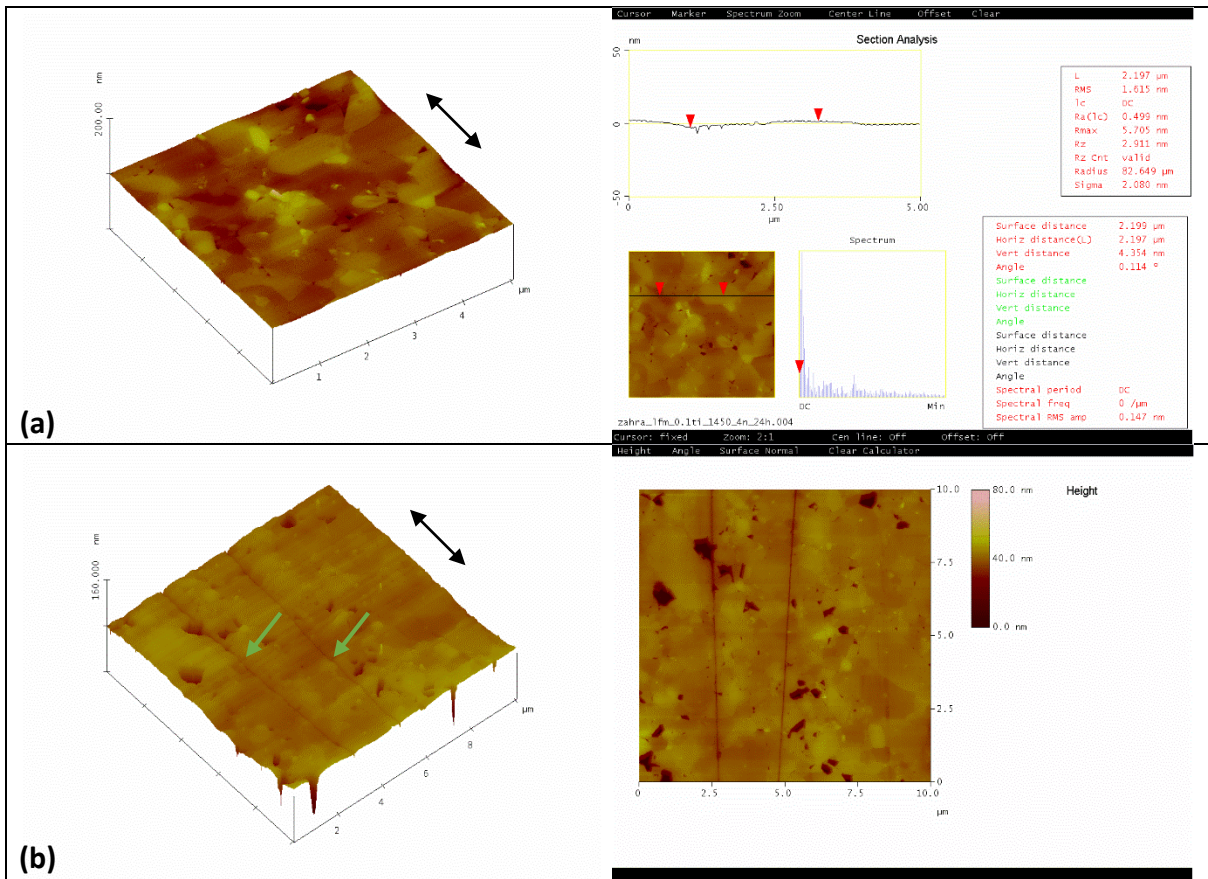


Figure 4.61. AFM image of wear scars for ZTA+0.1 mole.% TiO₂ sample sintered at 1450°C for 5 minutes under the wear condition of 4N-24hr, representing grooves with green arrows (image width is 5μm for (a), and 10μm for (b))

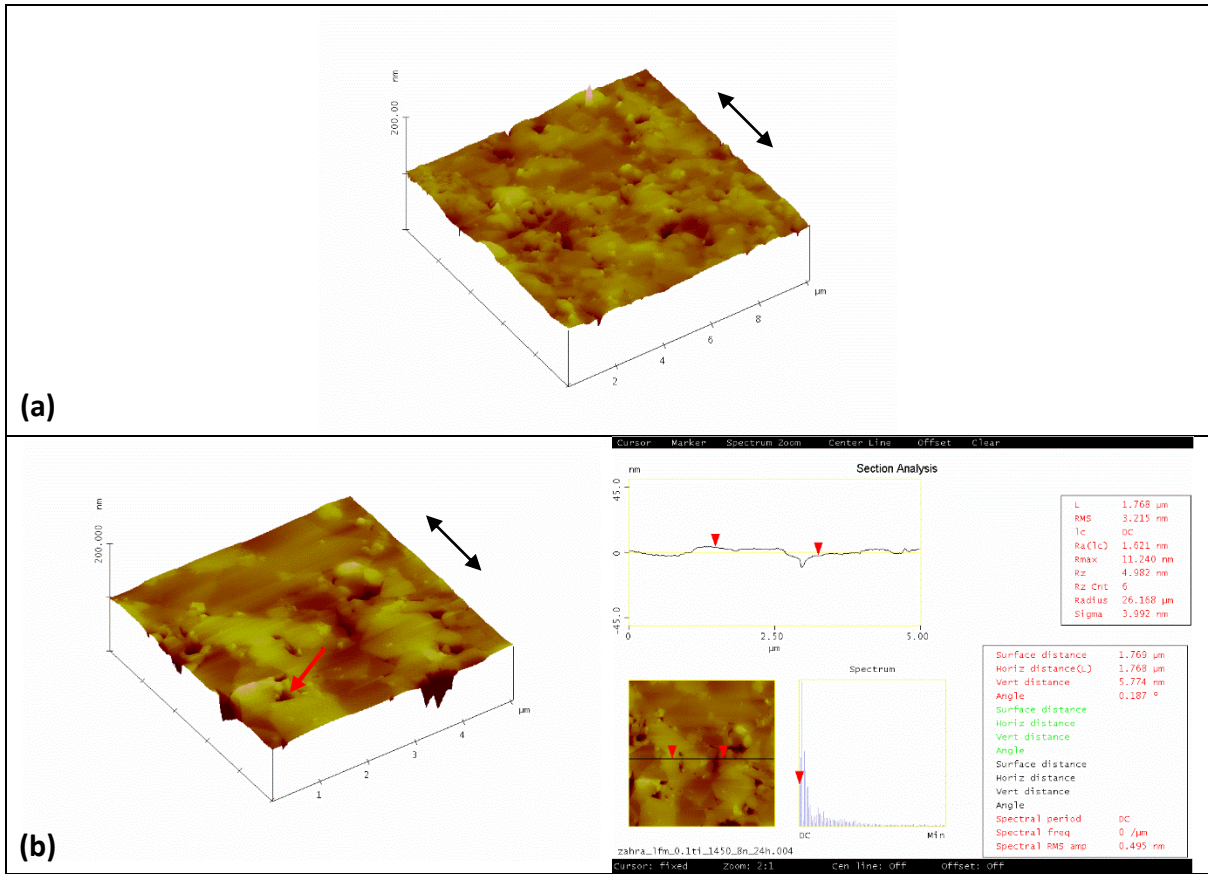
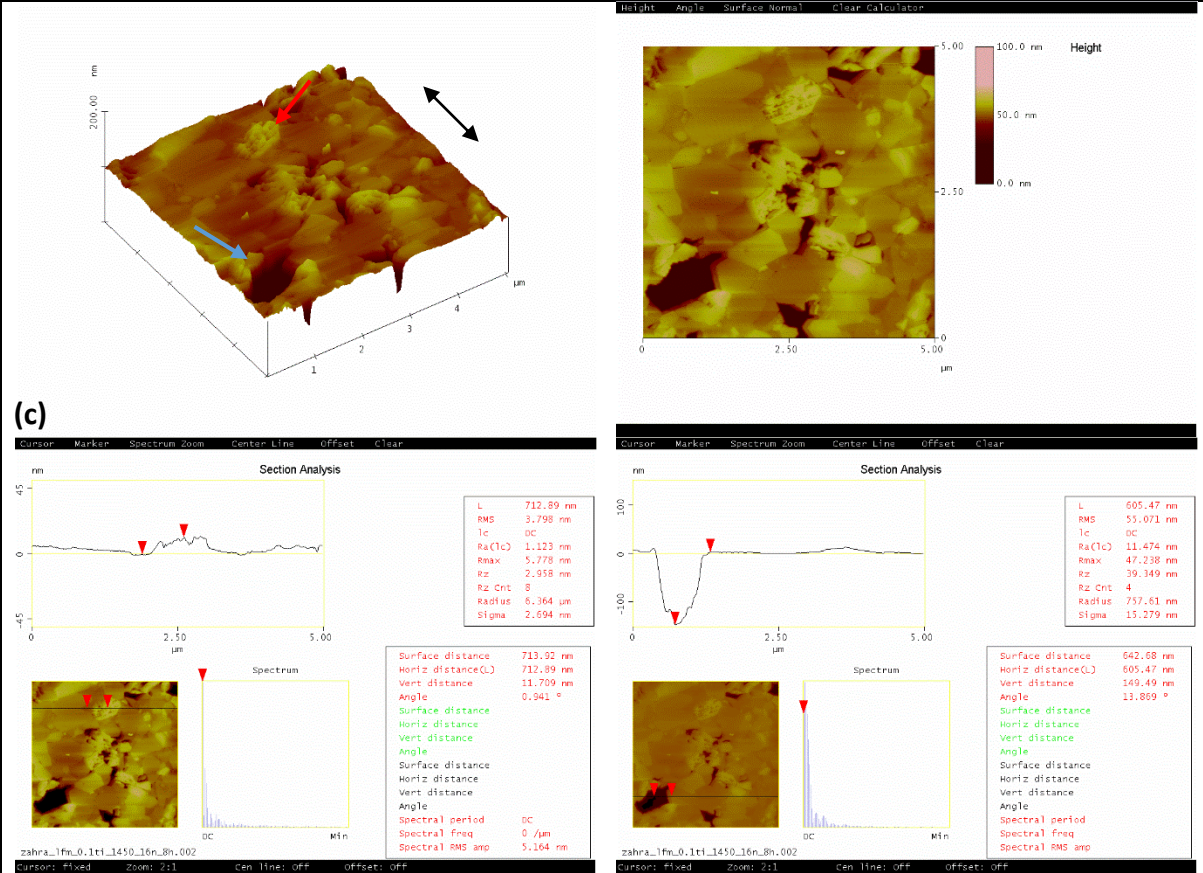
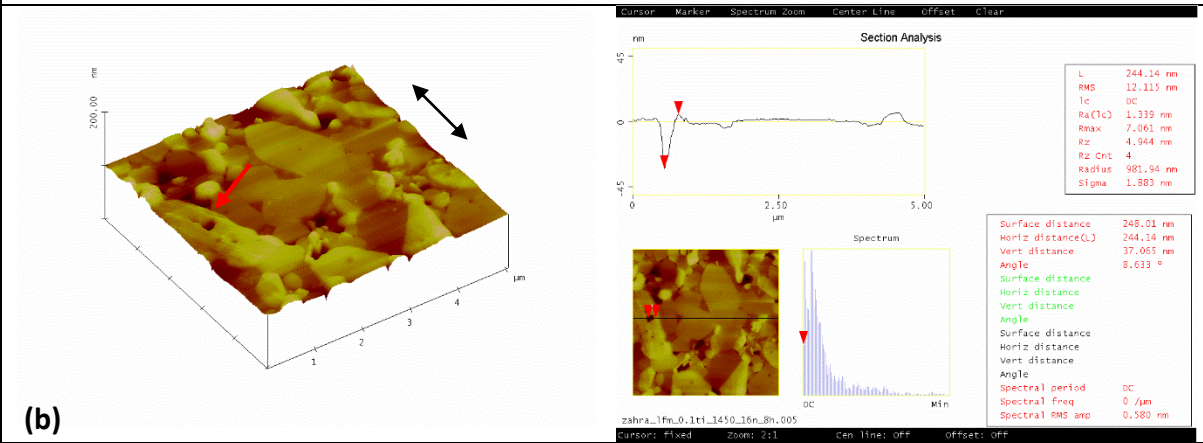
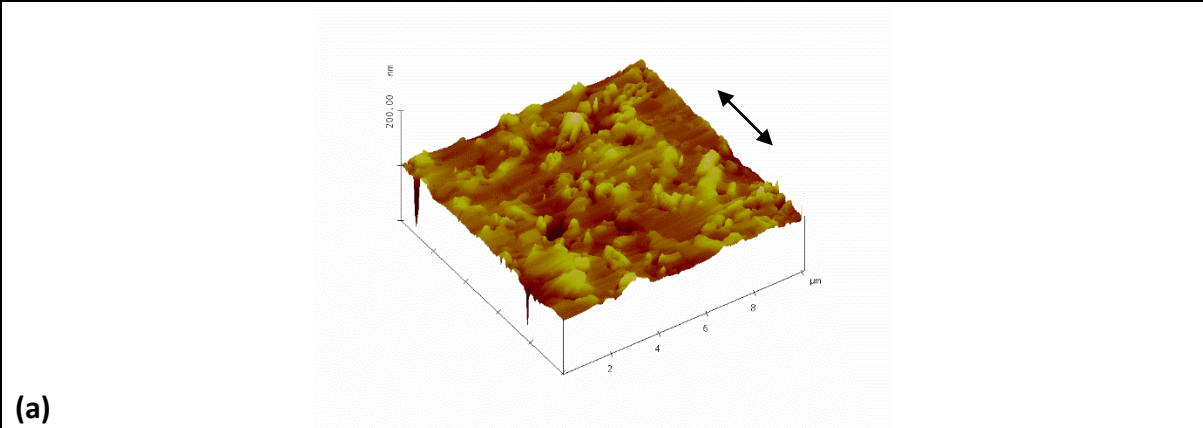


Figure 4.62. AFM image of wear scars for ZTA+0.1 mole.% TiO₂ sample sintered at 1450°C for 5 minutes under the wear condition of 8N-24hr, representing transgranular fracture with red arrow (image width is 5µm for (a), and 10µm for (b))



Continued

Continued

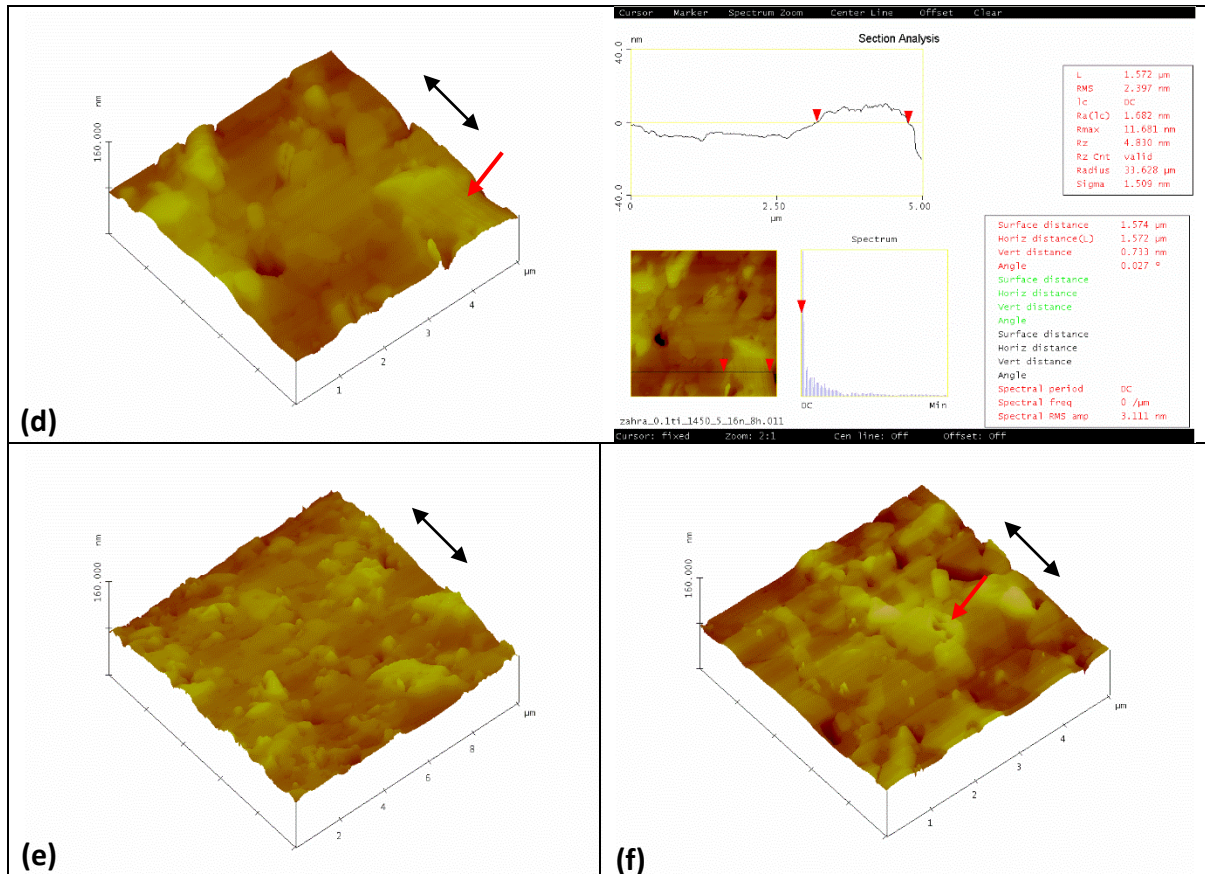


Figure 4.63. AFM image of wear scars for ZTA+0.1 mole.% TiO₂ sample sintered at 1450°C for 5 minutes under the wear condition of 16N-8hr, representing grain pull-out with blue arrows, and transgranular fracture with red arrows (image width is 10µm for (a) and (e), and 5µm for (b), (c), (d),and (f))

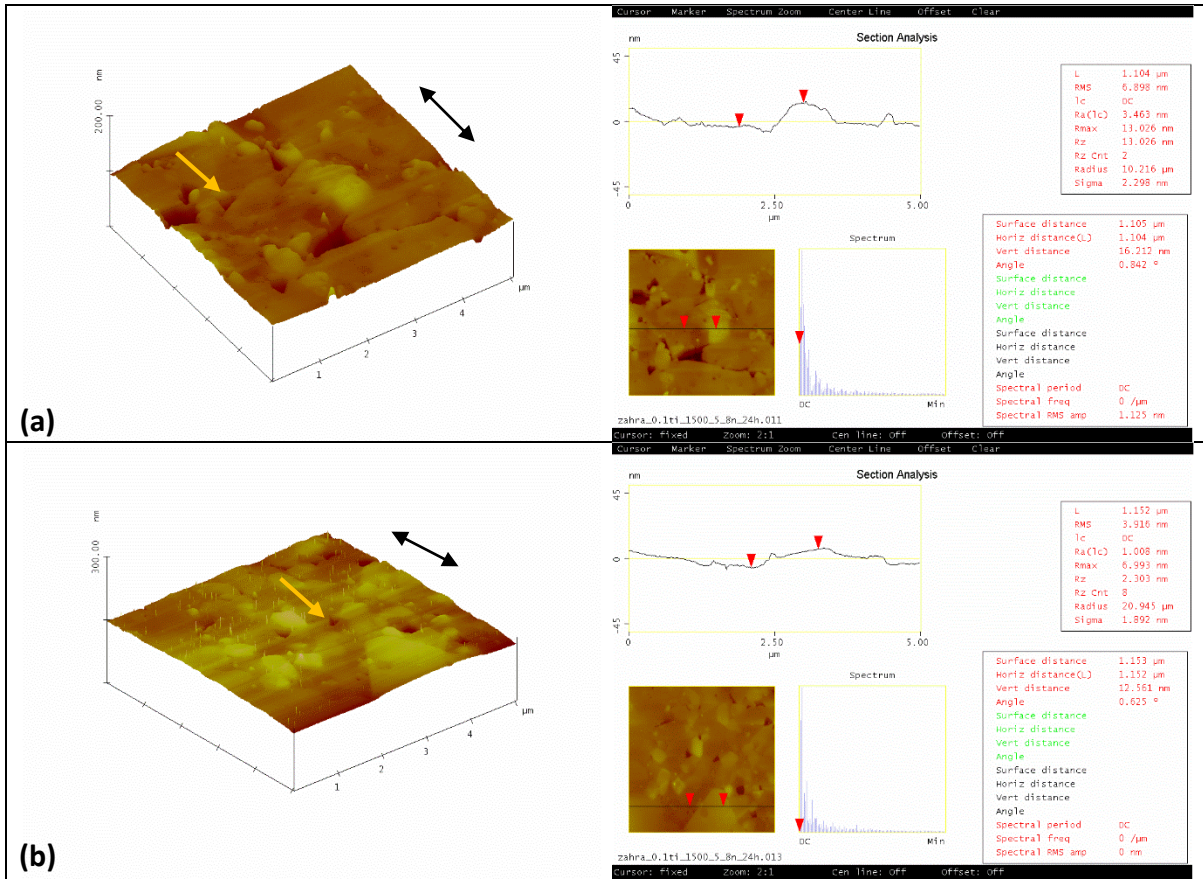


Figure 4.64. AFM image of wear scars for ZTA+0.1 mole.% TiO₂ sample sintered at 1500°C for 5 minutes under the wear condition of 8N-24hr, representing fractured triple points with yellow arrows (image width is 5 μm for (a) and (b))

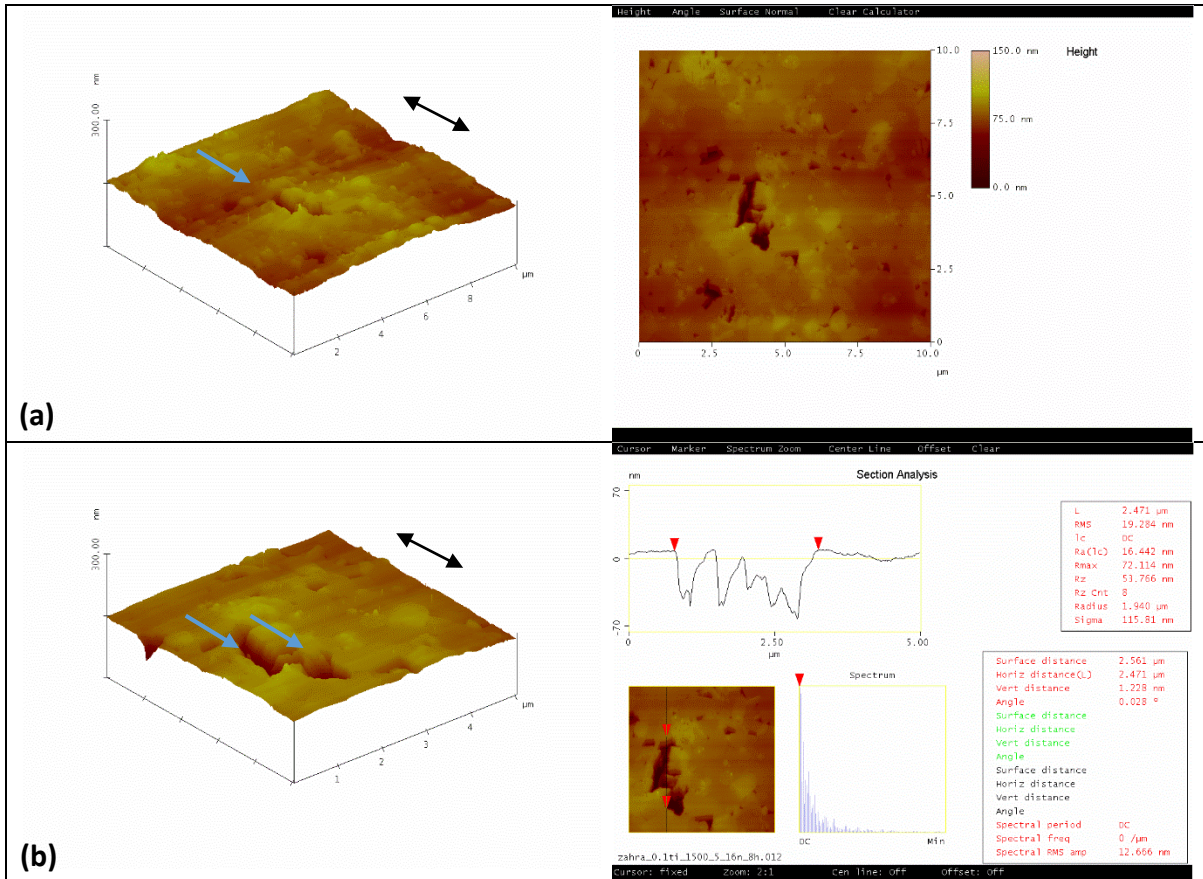


Figure 4.65. AFM image of wear scars for ZTA+0.1 mole.% TiO₂ sample sintered at 1500°C for 5 minutes under the wear condition of 16N-8hr, representing grain pull-out with blue arrows (image width is 5μm for (a) and (b))

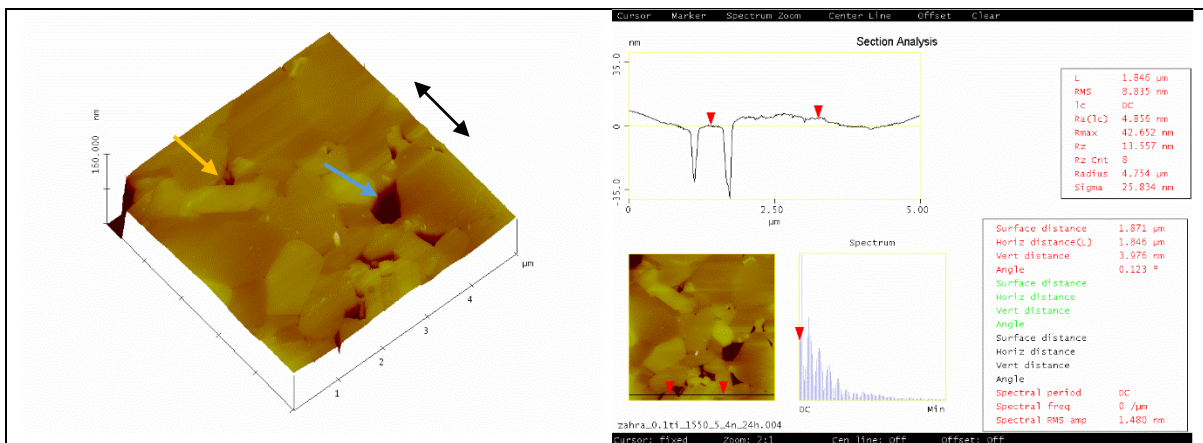


Figure 4.66. AFM image of wear scars for ZTA+0.1 mole.% TiO₂ sample sintered at 1550°C for 5 minutes under the wear condition of 4N-24hr, representing grain pull-out with blue arrow (image width is 5μm)

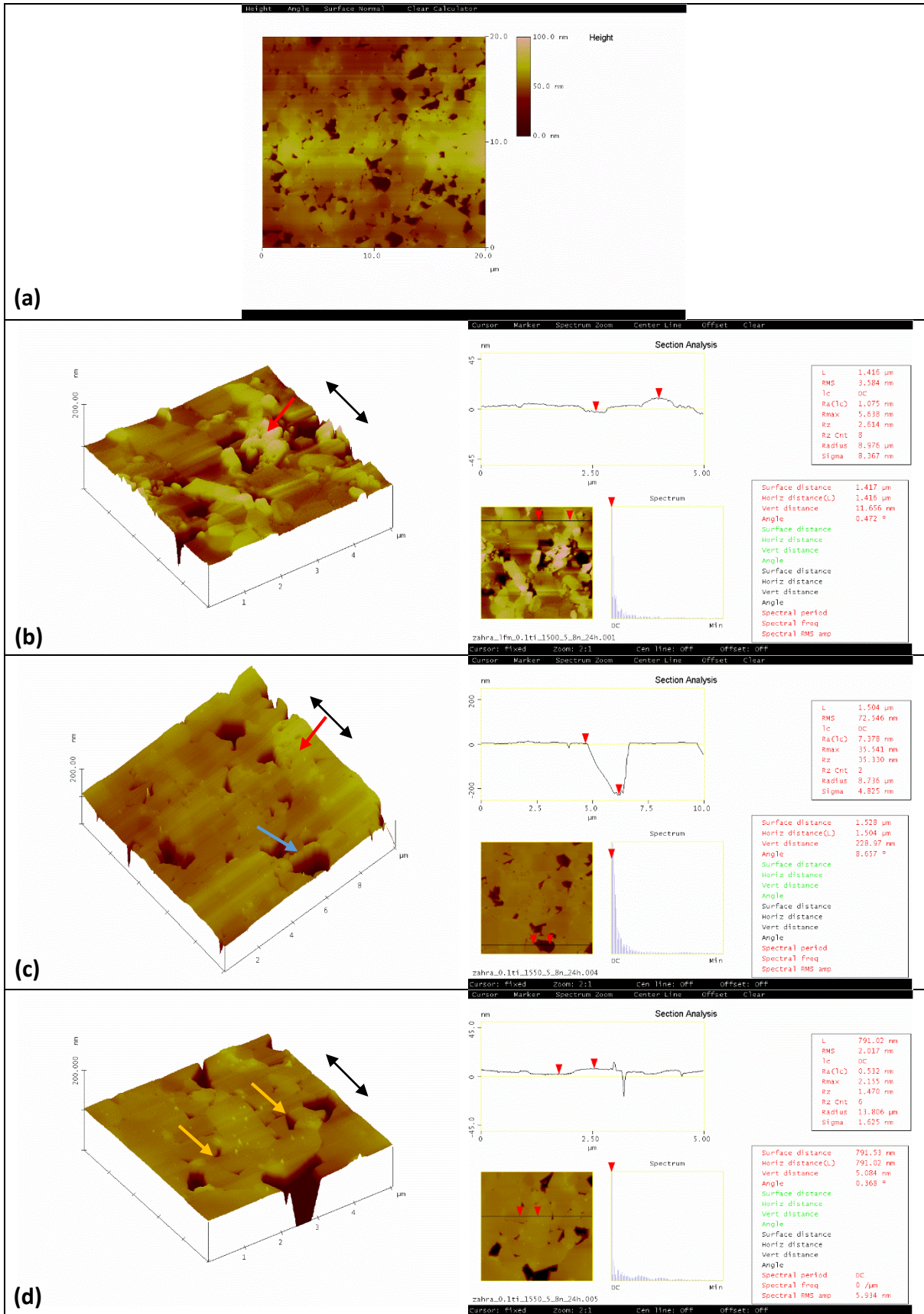


Figure 4.67. AFM image of wear scars for ZTA+0.1 mole.% TiO_2 sample sintered at 1550°C for 5 minutes under the wear condition of 8N-24hr, representing grain pull-out with blue arrows, transgranular fracture with red arrows, and fractured triple points with yellow arrows (image width is $20\mu\text{m}$ and $10\mu\text{m}$ for (a) and (c) respectively, and $5\mu\text{m}$ for (b) and (d))

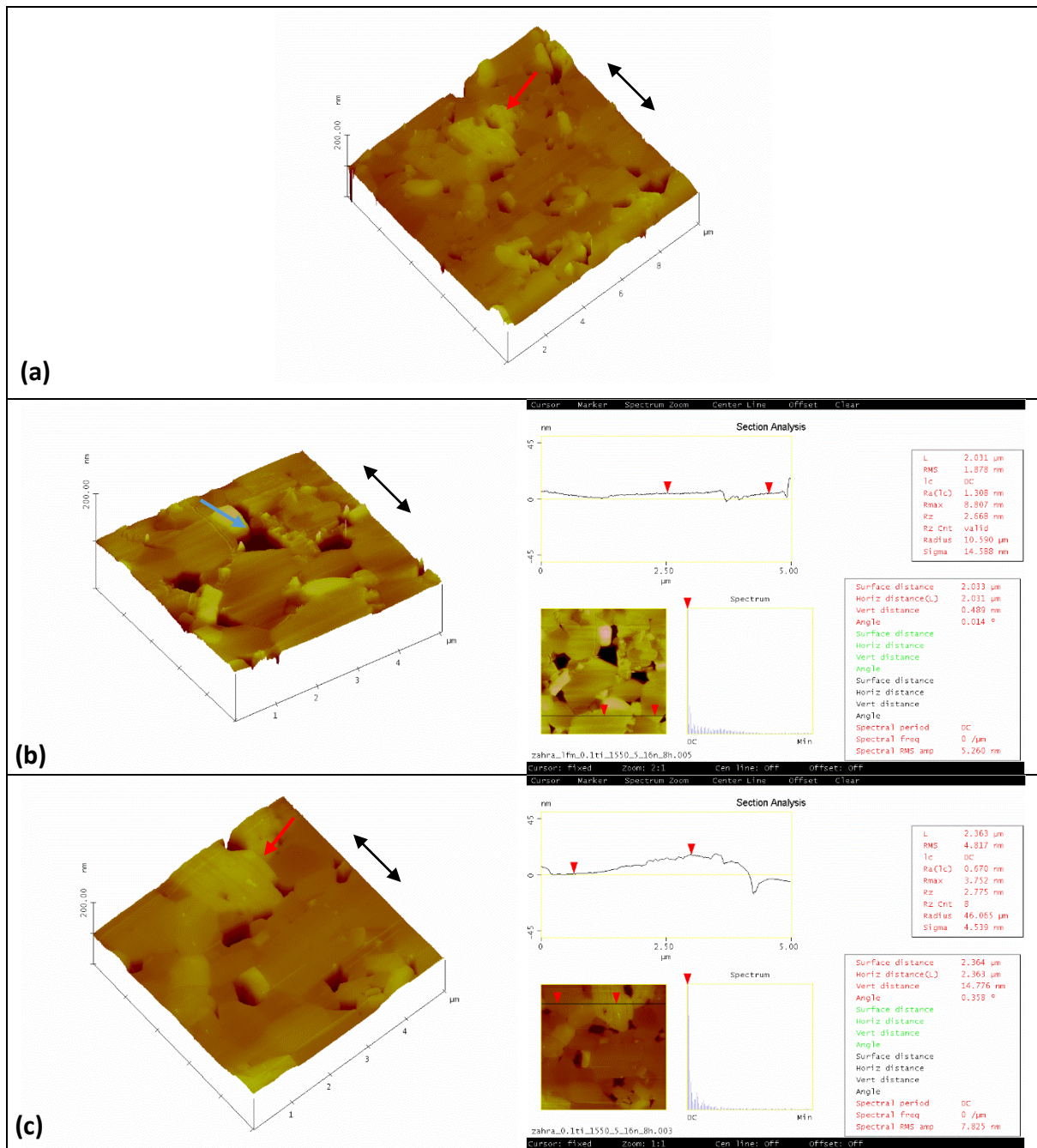


Figure 4.68. AFM image of wear scars for ZTA+0.1 mole.% TiO₂ sample sintered at 1550°C for 5 minutes under the wear condition of 16N-8hr, representing grain pull-out with blue arrows and transgranular fracture with red arrows (image width is 10µm for (a), and 5µm for (b) and (c))

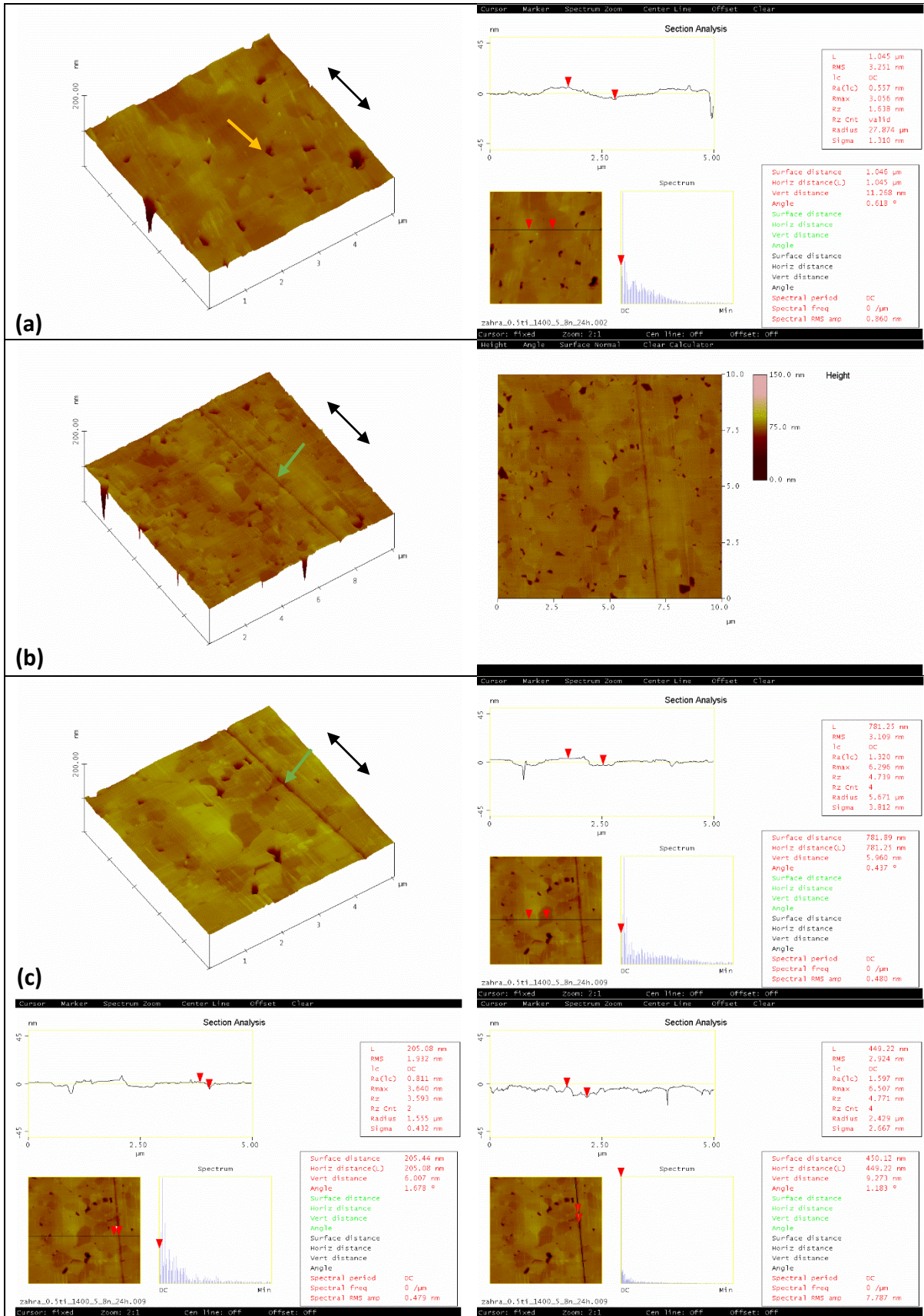


Figure 4.70. AFM image of wear scars for ZTA+0.5 mole.% TiO₂ sample sintered at 1400°C for 5 minutes under the wear condition of 8N-24hr, representing grooves with green arrows, and fractured triple points with yellow arrows (image width is 10µm for (b), and 5µm for (a) and (c))

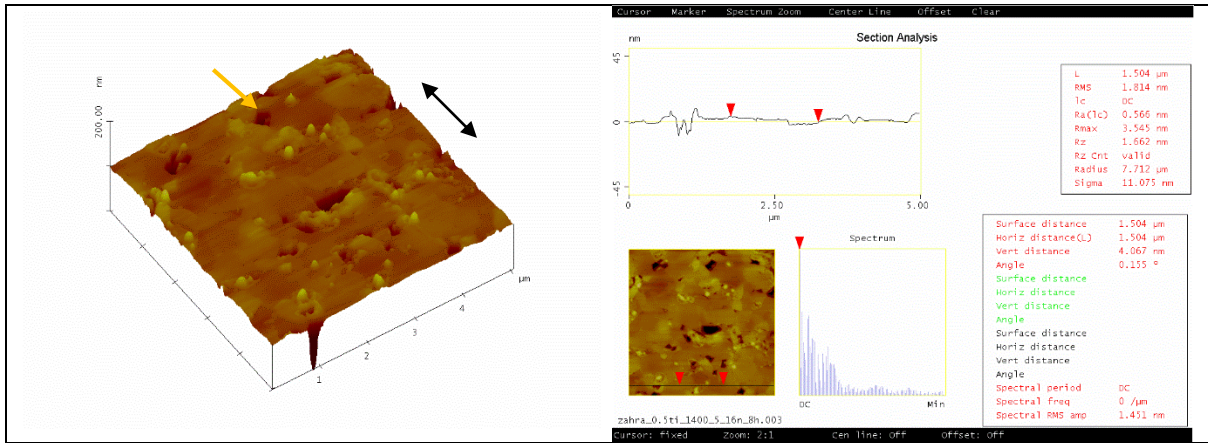


Figure 4.71. AFM image of wear scars for ZTA+0.5 mole.% TiO_2 sample sintered at 1400°C for 5 minutes under the wear condition of 16N-8hr, representing fractured triple points with yellow arrow (image width is $5\mu\text{m}$)

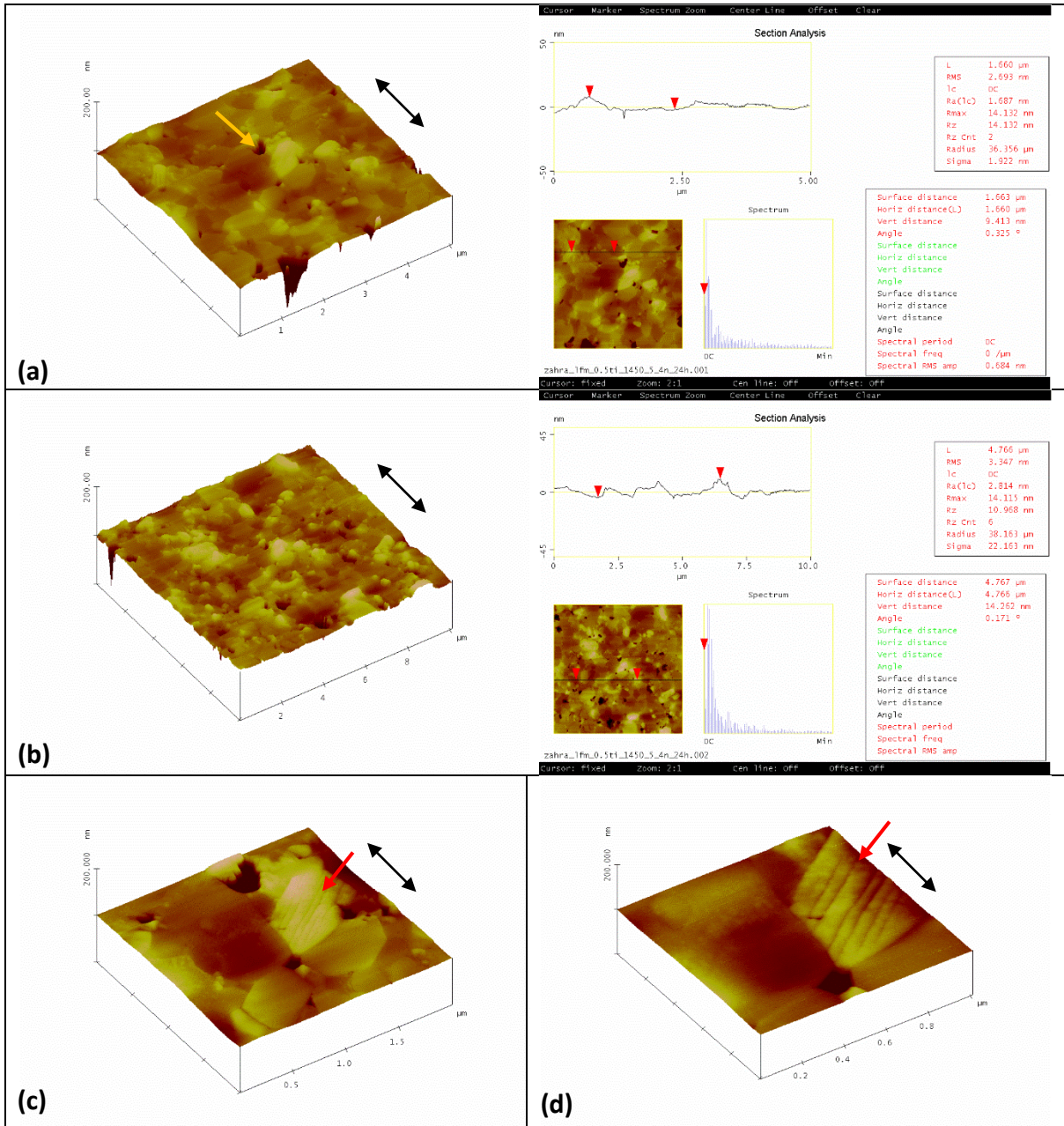


Figure 4.72. AFM image of wear scars for ZTA+0.5 mole.% TiO₂ sample sintered at 1450°C for 5 minutes under the wear condition of 4N-24hr, representing transgranular fracture with red arrows, and fractured triple point with yellow arrow (image width is 5 μm for (a), 10 μm for (b), 3 μm for (c), and 1 μm for (d))

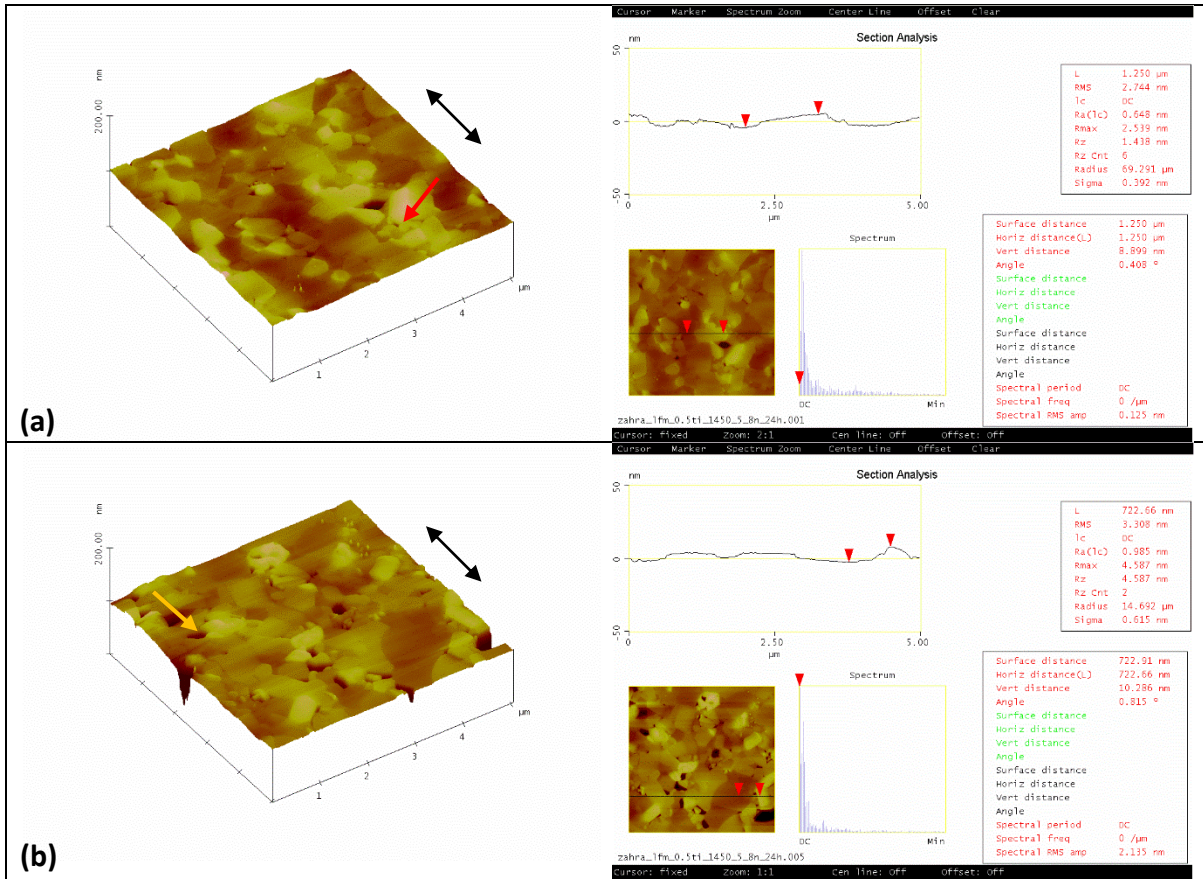


Figure 4.73. AFM image of wear scars for ZTA+0.5 mole.% TiO₂ sample sintered at 1450°C for 5 minutes under the wear condition of 8N-24hr, representing transgranular fracture with red arrow, and fractured triple point with yellow arrow (image width is 5 μm for (a) and (b))

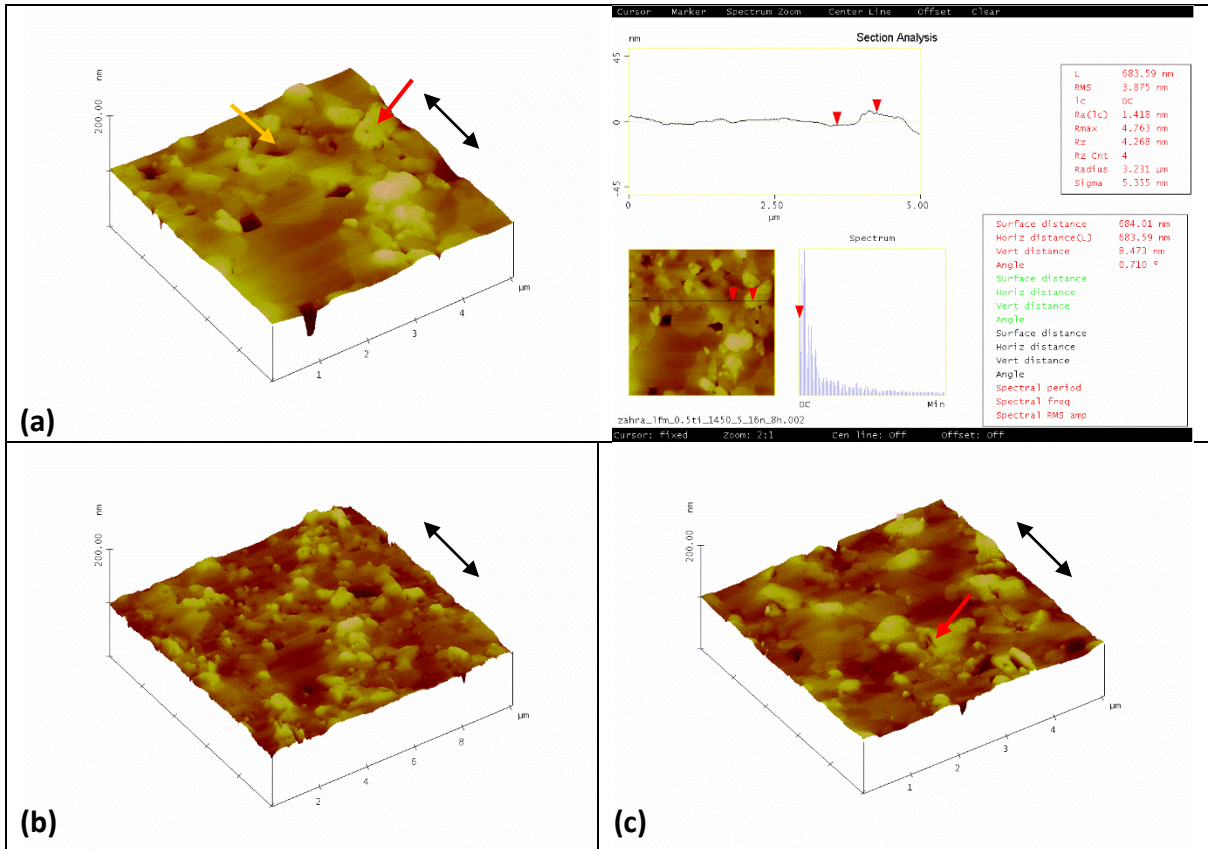


Figure 4.74. AFM image of wear scars for ZTA+0.5 mole.% TiO₂ sample sintered at 1450°C for 5 minutes under the wear condition of 16N-8hr, representing transgranular fracture with red arrows, and fractured triple point with yellow arrow (image width is 5μm for (a) and (c), and 10μm for (b))

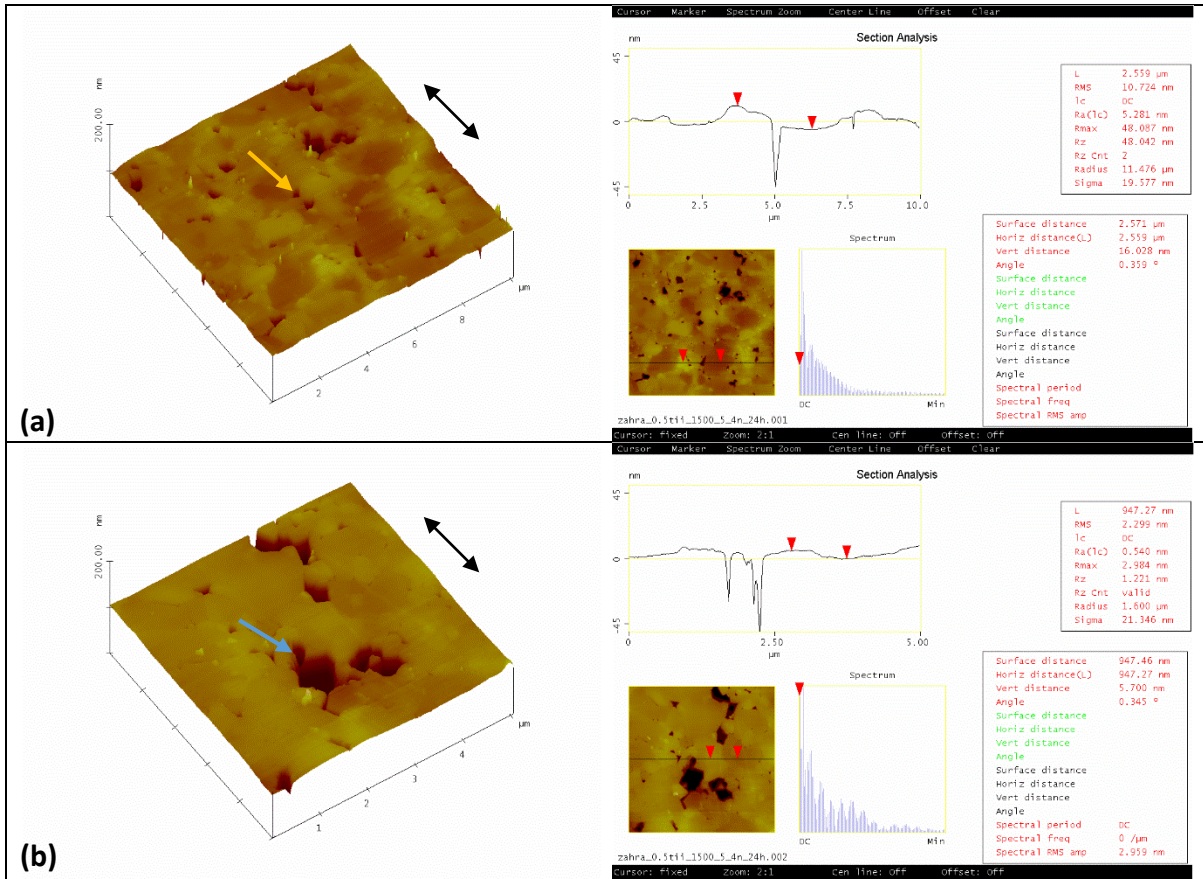


Figure 4.75. AFM image of wear scars for ZTA+0.5 mole.% TiO₂ sample sintered at 1500°C for 5 minutes under the wear condition of 4N-24hr, grain pull-out with blue arrow, and fractured triple point with yellow arrow (image width is 10µm for (a), and 5µm for (b))

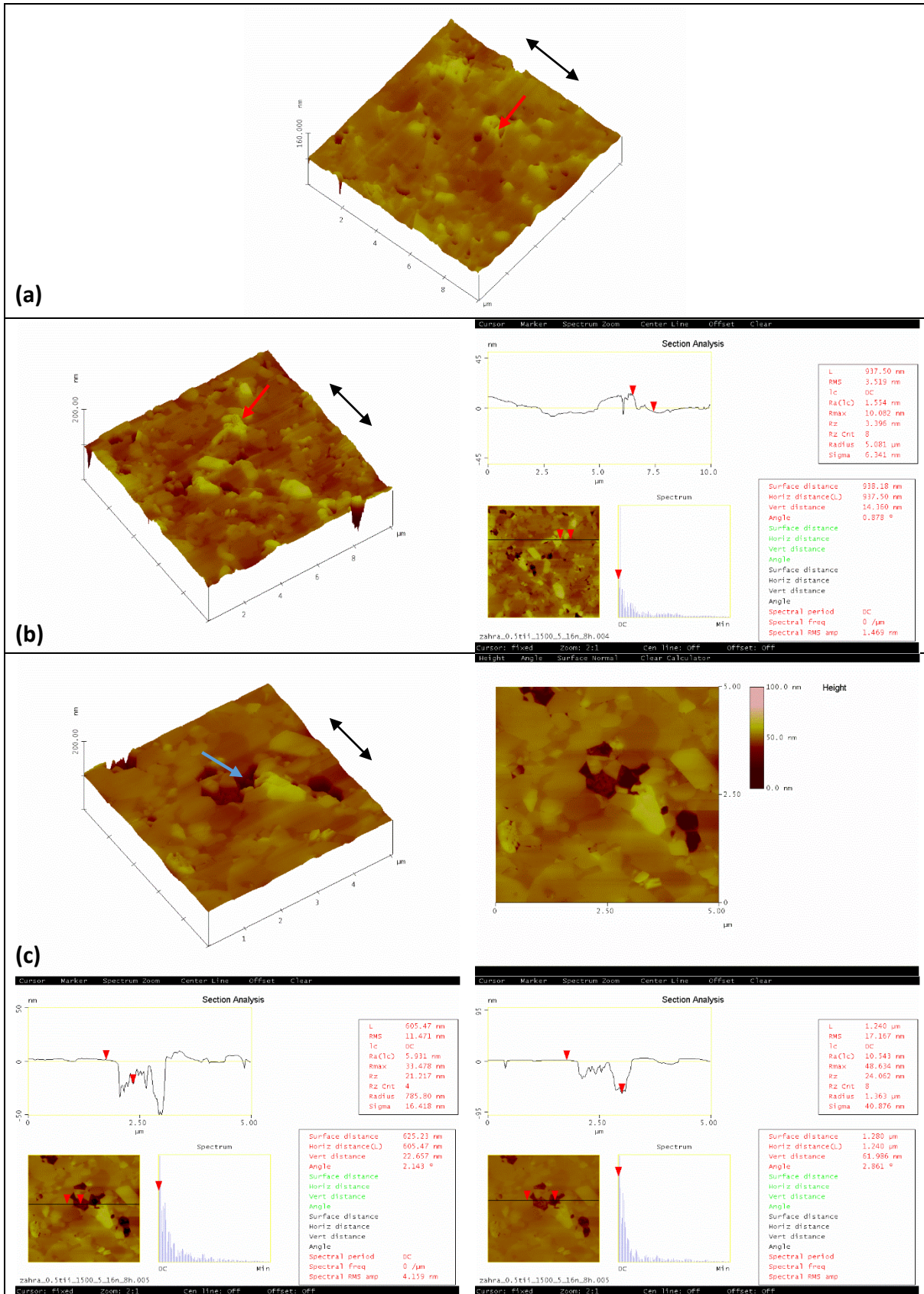
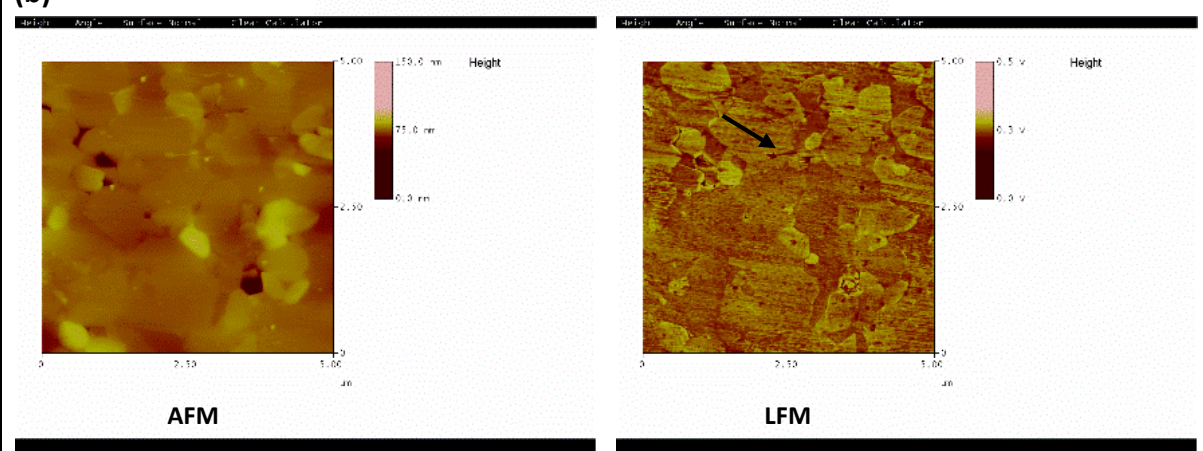
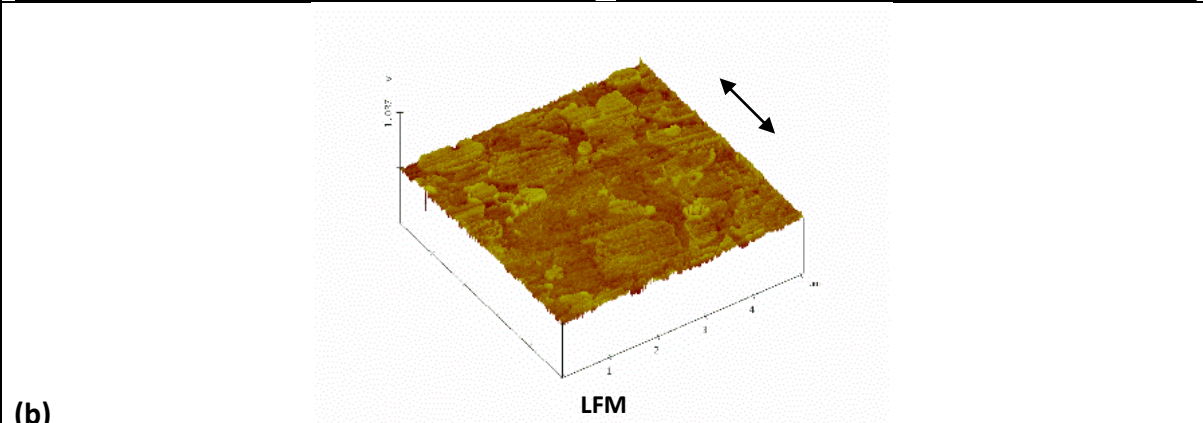
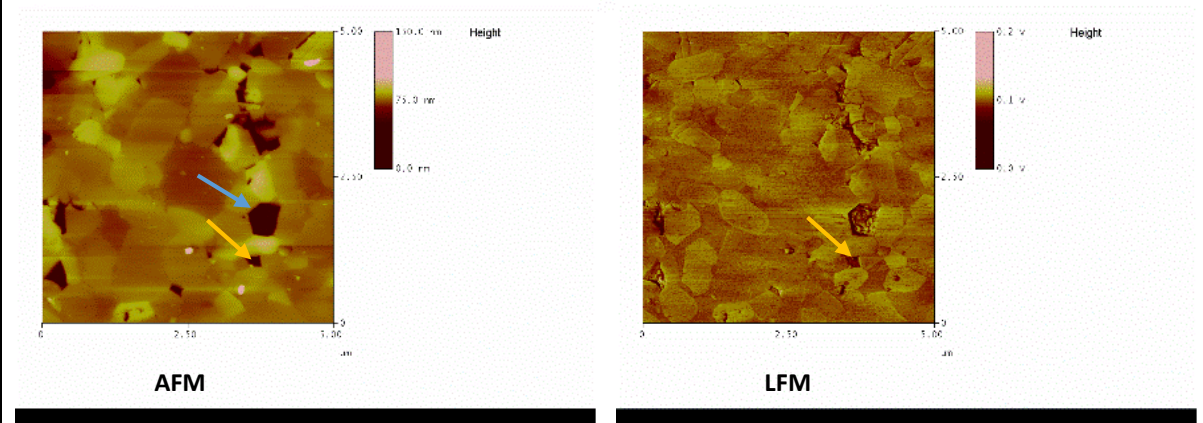
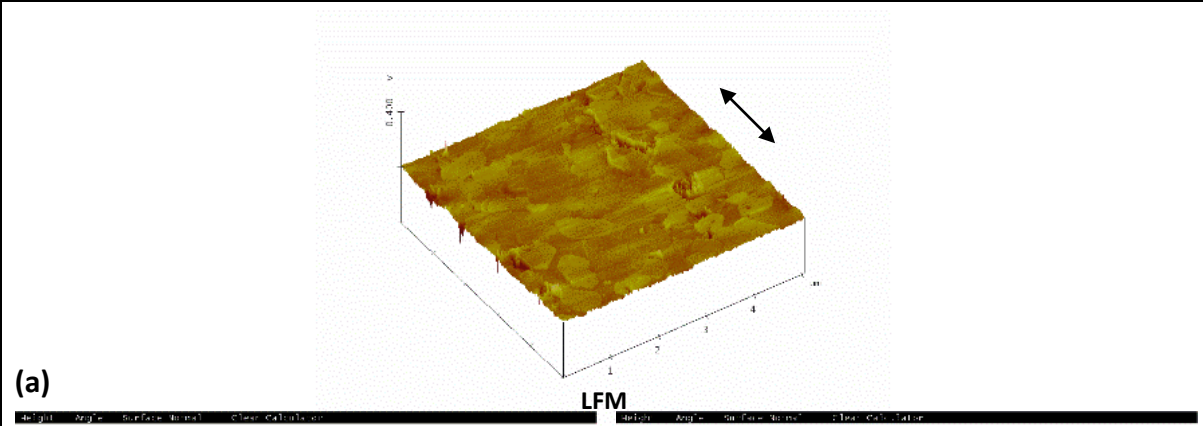


Figure 4.77. AFM image of wear scars for ZTA+0.5 mole.% TiO₂ sample sintered at 1500°C for 5 minutes under the wear condition of 16N-8hr, representing transgranular fracture with red arrows, and grain pull-out with blue arrow (image width is 10µm for (a) and (b), and 5µm for (c))

As stated in section 3, LFM analysis of the wear scars were done in order to study modification of surface friction for ZTA and ZTA containing titania samples under different wear conditions, as illustrated in Figure 4.78 to Figure 4.87. LFM images could reveal grain boundaries and transformed areas more clear than what could be seen in AFM images due to changes of friction forces.

Intergranular fracture at grain boundaries could be detected in all images of Figure 4.78 to Figure 4.87 under different conditions. It is difficult to find the location of zirconia and alumina grains; however, the size differences of zirconia and alumina can give an estimation of these grains. What is notable in LFM images is that no transformed zirconia grain with monoclinic characteristics of substructure of parallel linear features could be seen in any of the figures. In addition, none of the images show wear grooves as could be seen in AFM images. Transgranular fractured grains are more visible in these images as can be clearly detected in Figure 4.78.c and d, Figure 4.82, and Figure 4.85.b and c. Similarly, fractured triple points and grain pull-outs could be seen in these figures (e.g. Figure 4.78.d) as reported in AFM images. New features such as transgranular zirconia grains could also be found in these images (e.g. Figure 4.84), which are not detectable in AFM images.



Continued

Continued

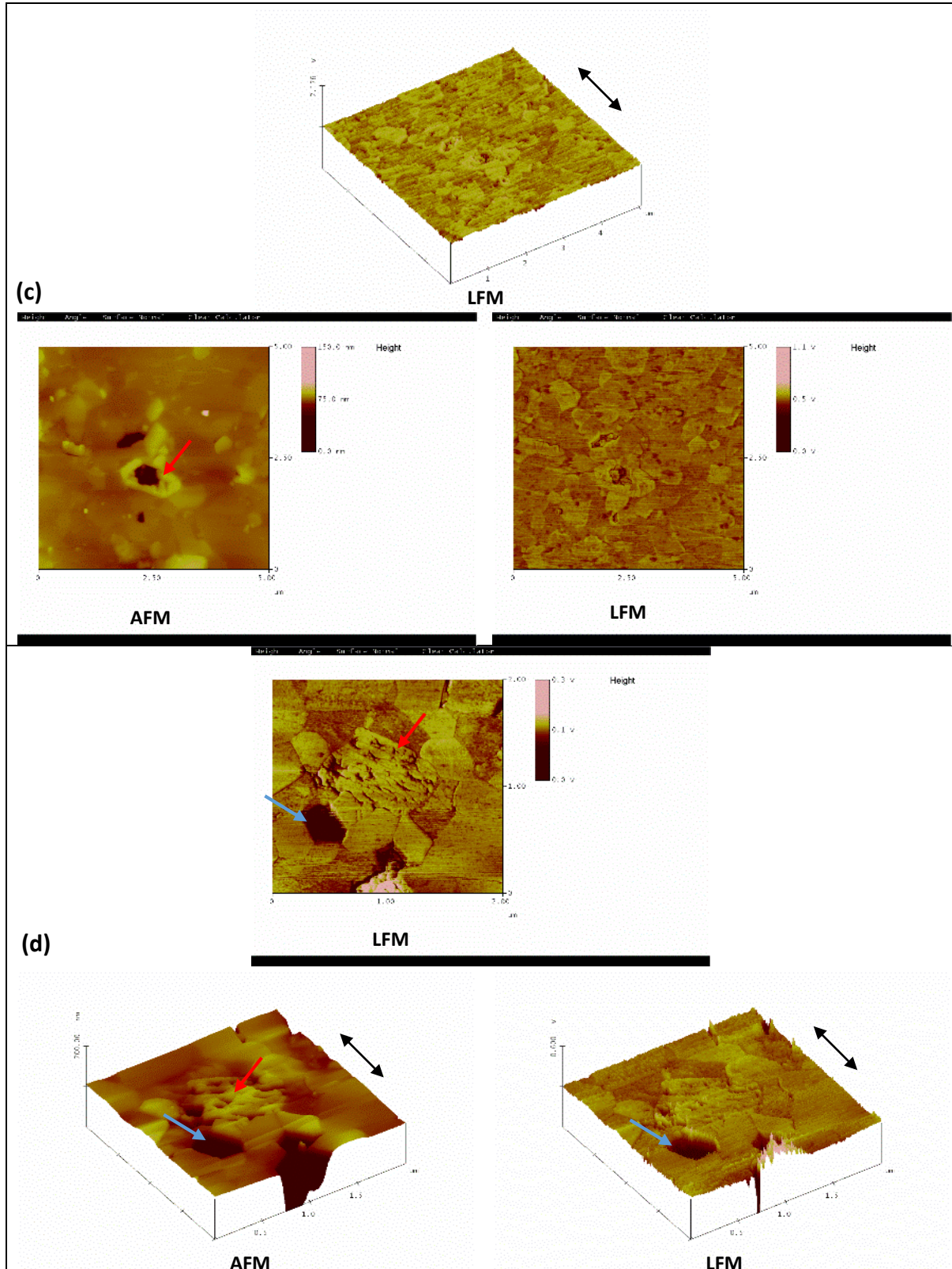


Figure 4.78. LFM images and corresponding AFM image of wear scars for ZTA sample sintered at 1450°C for 7 minutes under the wear condition of 8N-24hr, representing transgranular fracture with red arrows, fractured triple points with yellow arrow, grain pull-out with blue arrow, and intergranular fracture with black arrow
(image width is 5 μ m for (a), (b) and (c), and 2 μ m for (d))

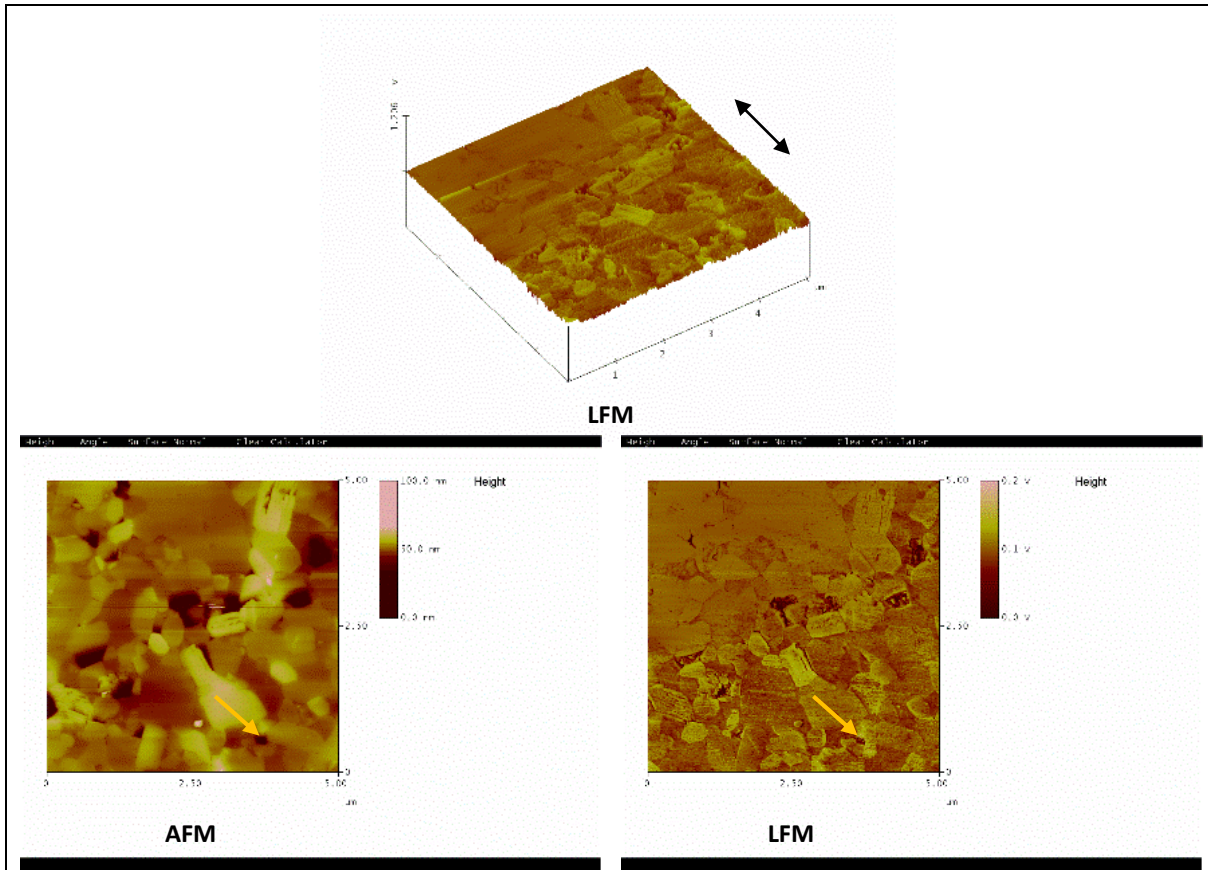


Figure 4.79. LFM images and corresponding AFM image of wear scars for ZTA sample sintered at 1450°C for 7 minutes under the wear condition of 16N-8hr, representing fractured triple points with yellow arrow (image width is 5 μ m)

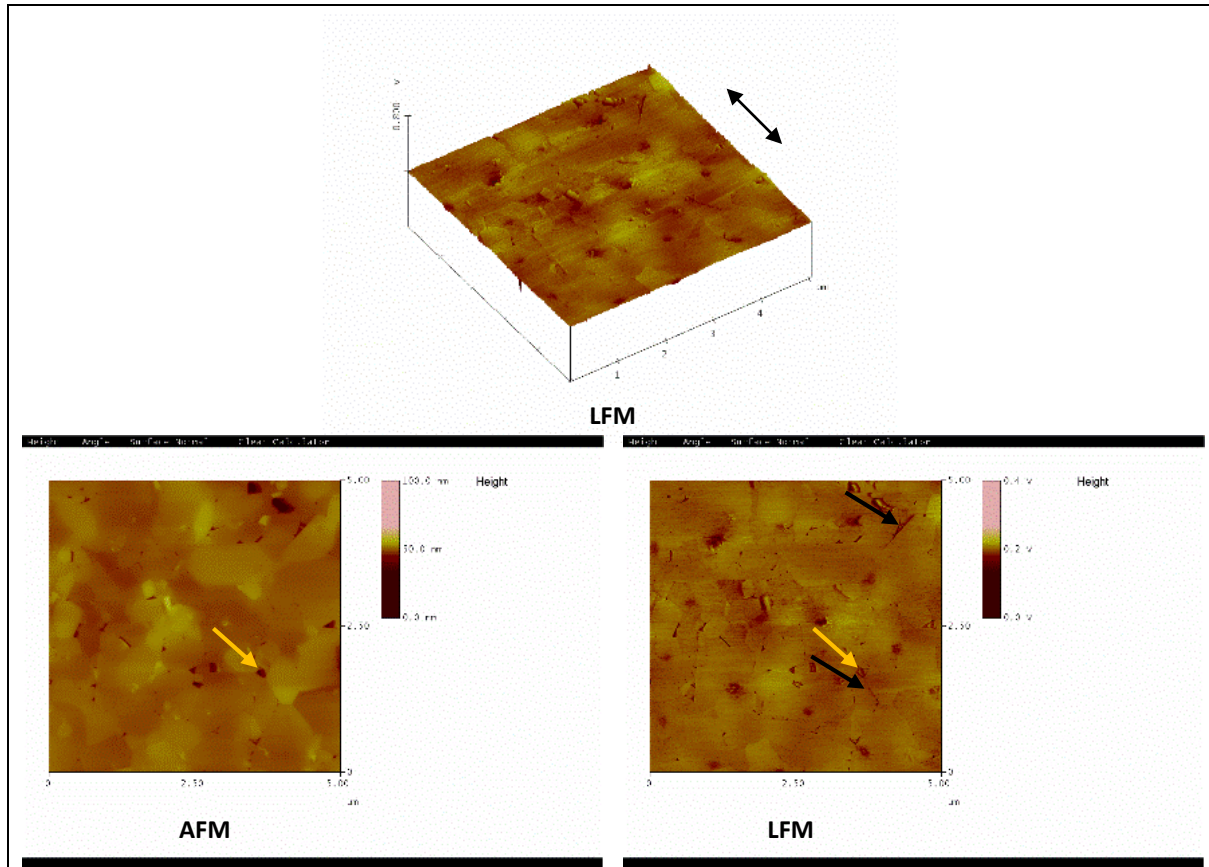


Figure 4.80. LFM images and corresponding AFM image of wear scars for ZTA+0.1 mole.% TiO₂ sample sintered at 1450°C for 5 minutes under the wear condition of 4N-24hr, representing fractured triple points with yellow arrows, and intergranular fracture with black arrow (image width is 5μm)

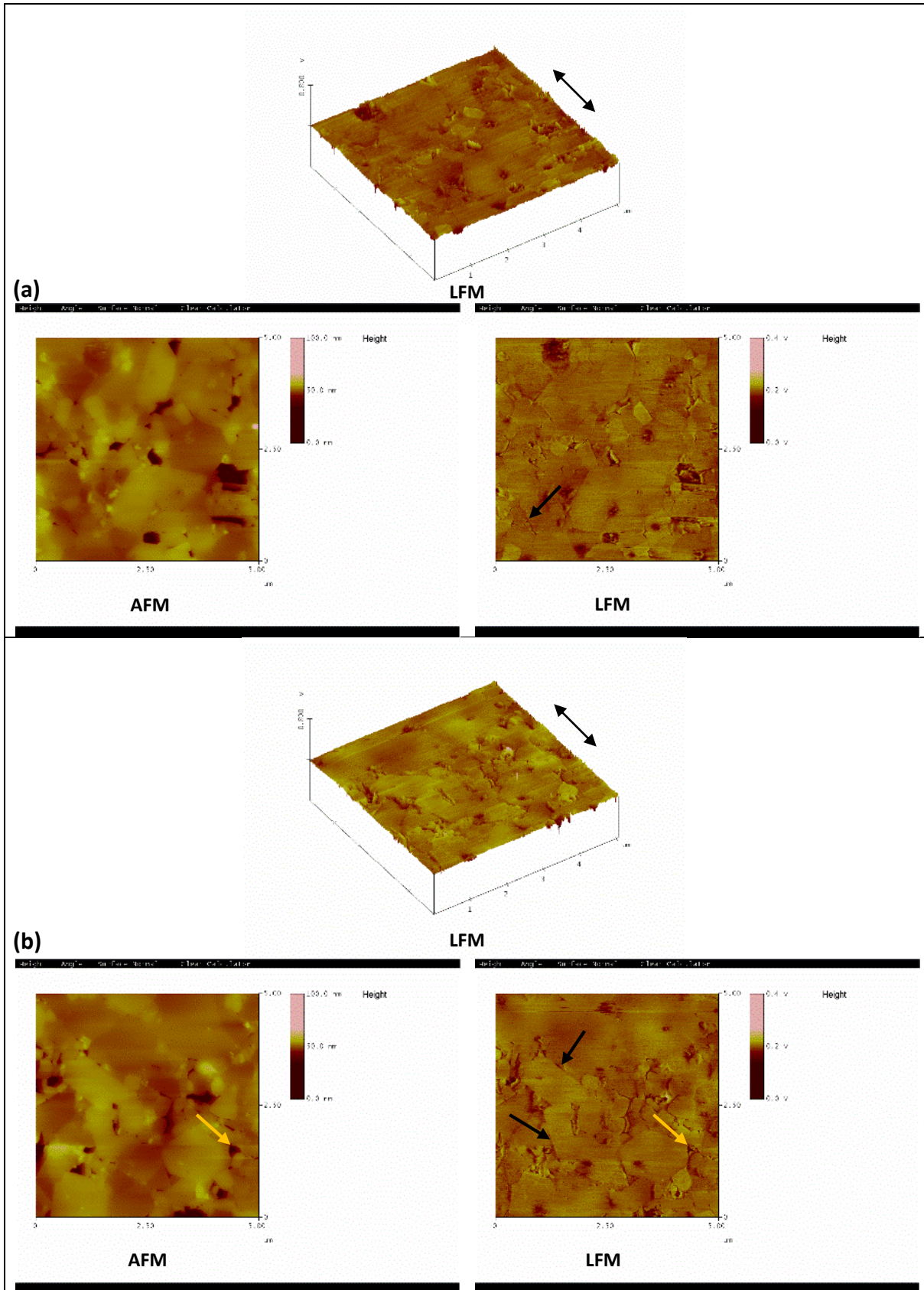
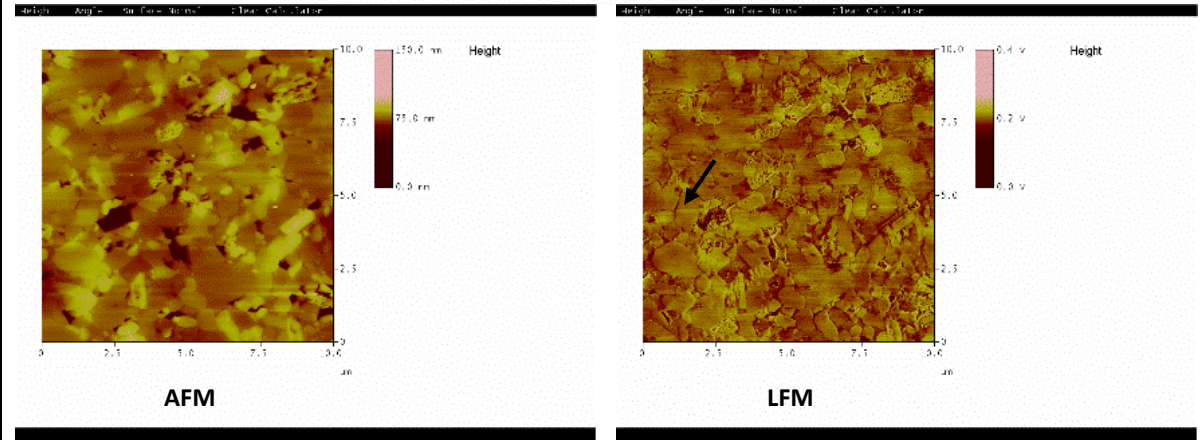
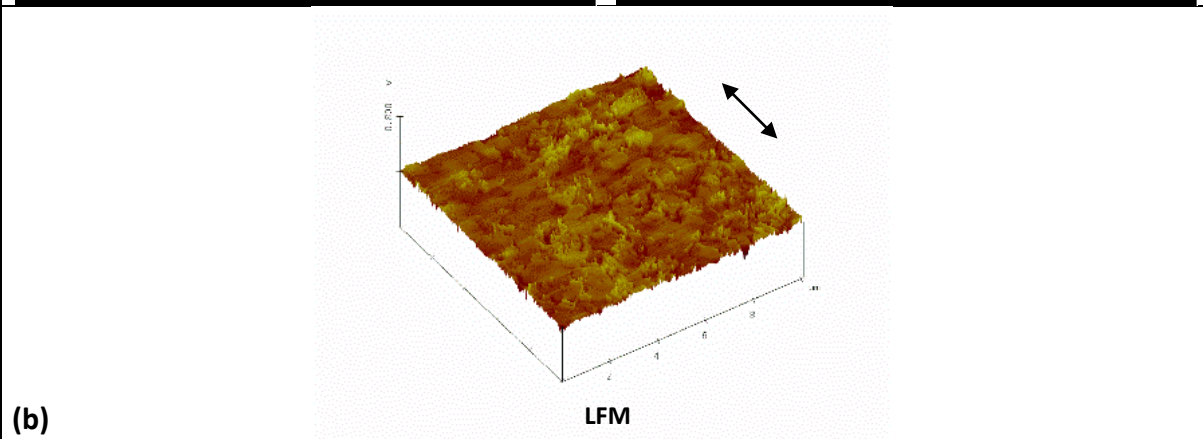
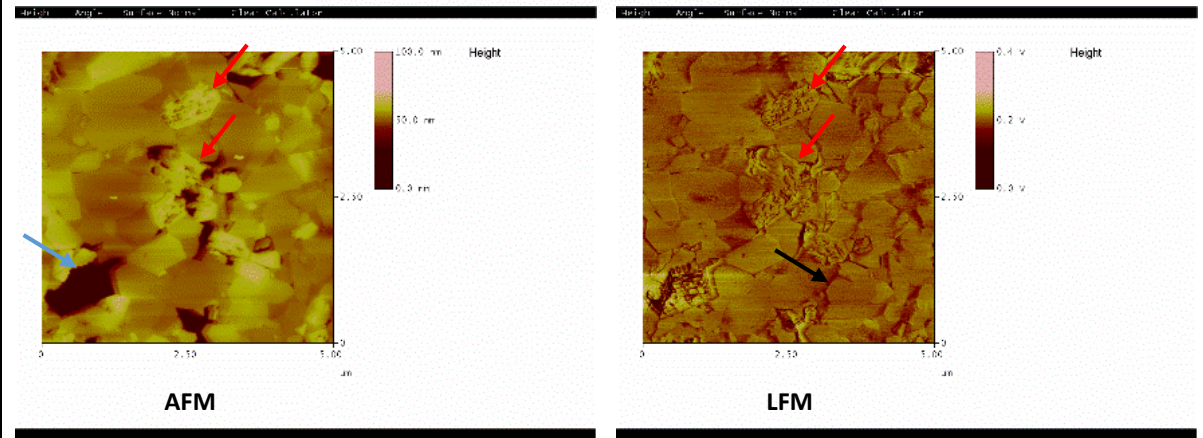
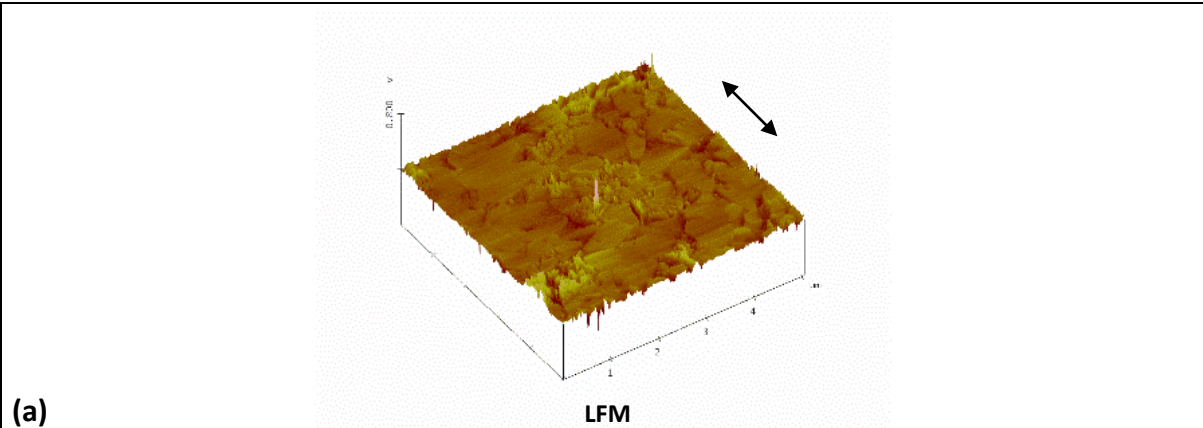


Figure 4.81. LFM images and corresponding AFM image of wear scars for ZTA+0.1 mole.% TiO₂ sample sintered at 1450°C for 5 minutes under the wear condition of 8N-24hr, representing fractured triple points with yellow arrow, and intergranular fracture with black arrow (image width is 5μm)



Continued

Continued

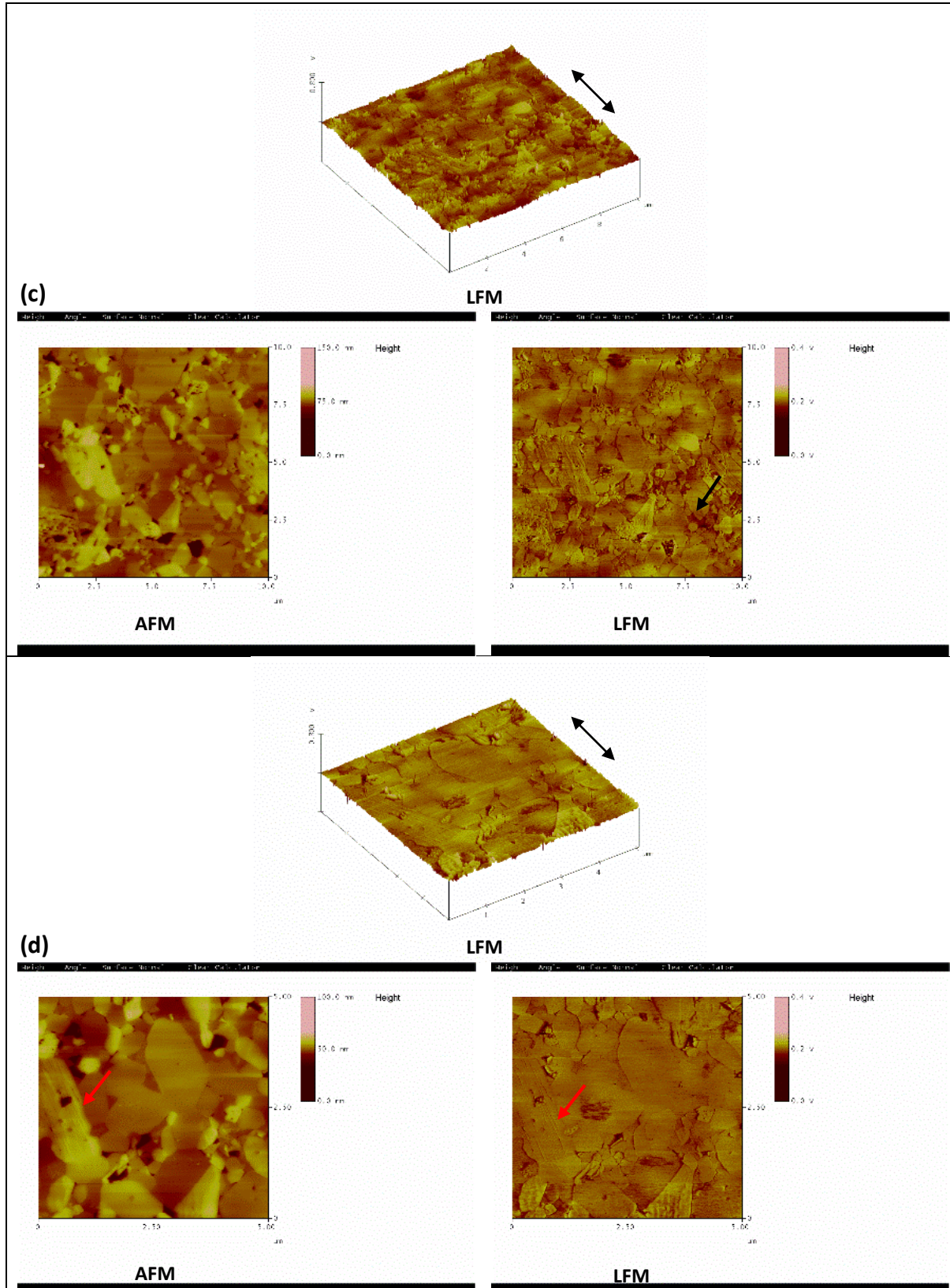


Figure 4.82. LFM images and corresponding AFM image of wear scars for ZTA+0.1 mole.% TiO_2 sample sintered at 1450°C for 5 minutes under the wear condition of 16N-8hr, representing transgranular fracture with red arrows, grain pull-out with blue arrow, and intergranular fracture with black arrow

(image width is 5 μm for (a), (c) and (d), and 10 μm for (b))

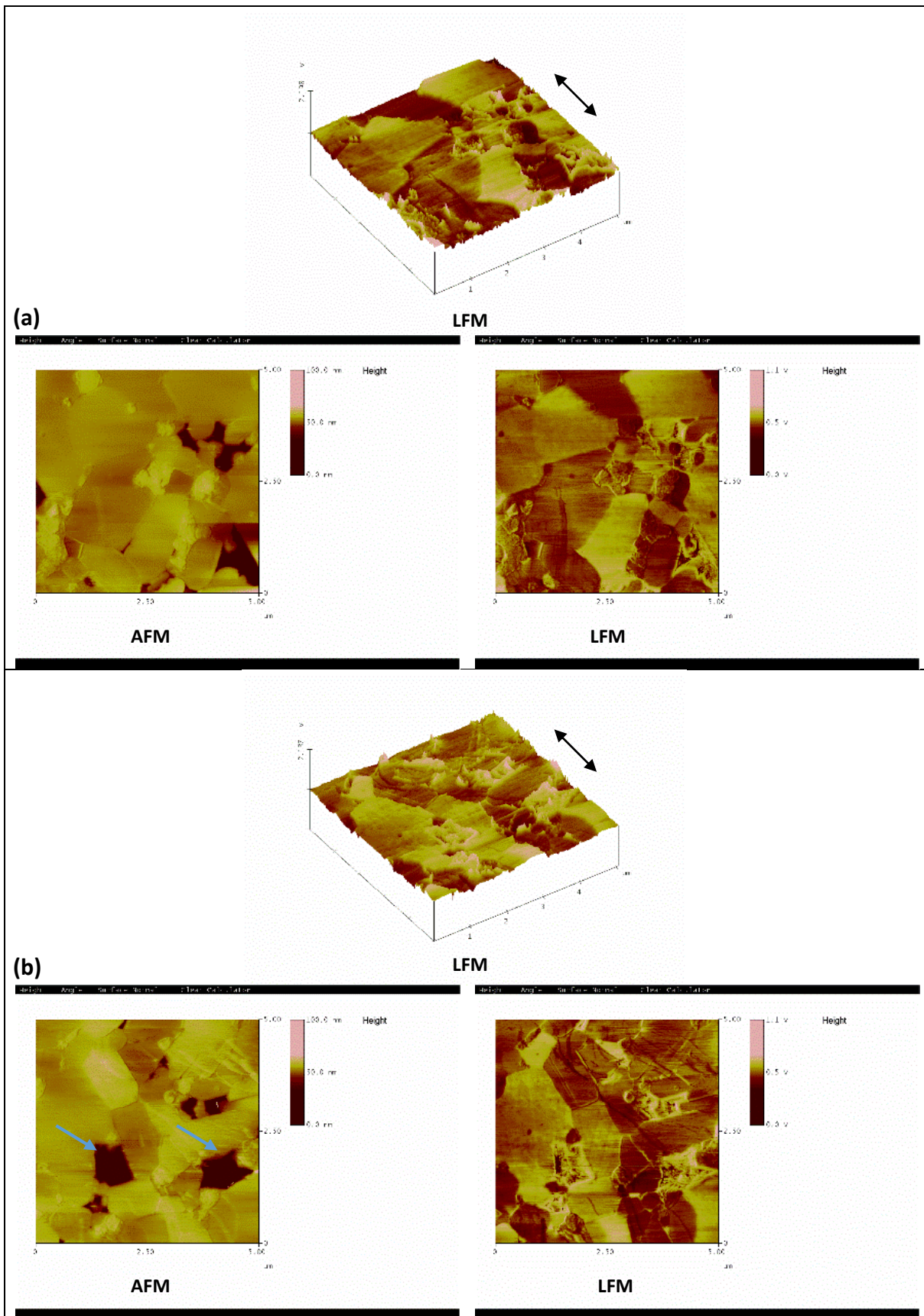


Figure 4.83. LFM image and corresponding AFM image of wear scars for ZTA+0.1 mole.% TiO₂ sample sintered at 1550°C for 5 minutes under the wear condition of 8N-24hr, representing grain pull-out with blue arrows (image width is 5μm)

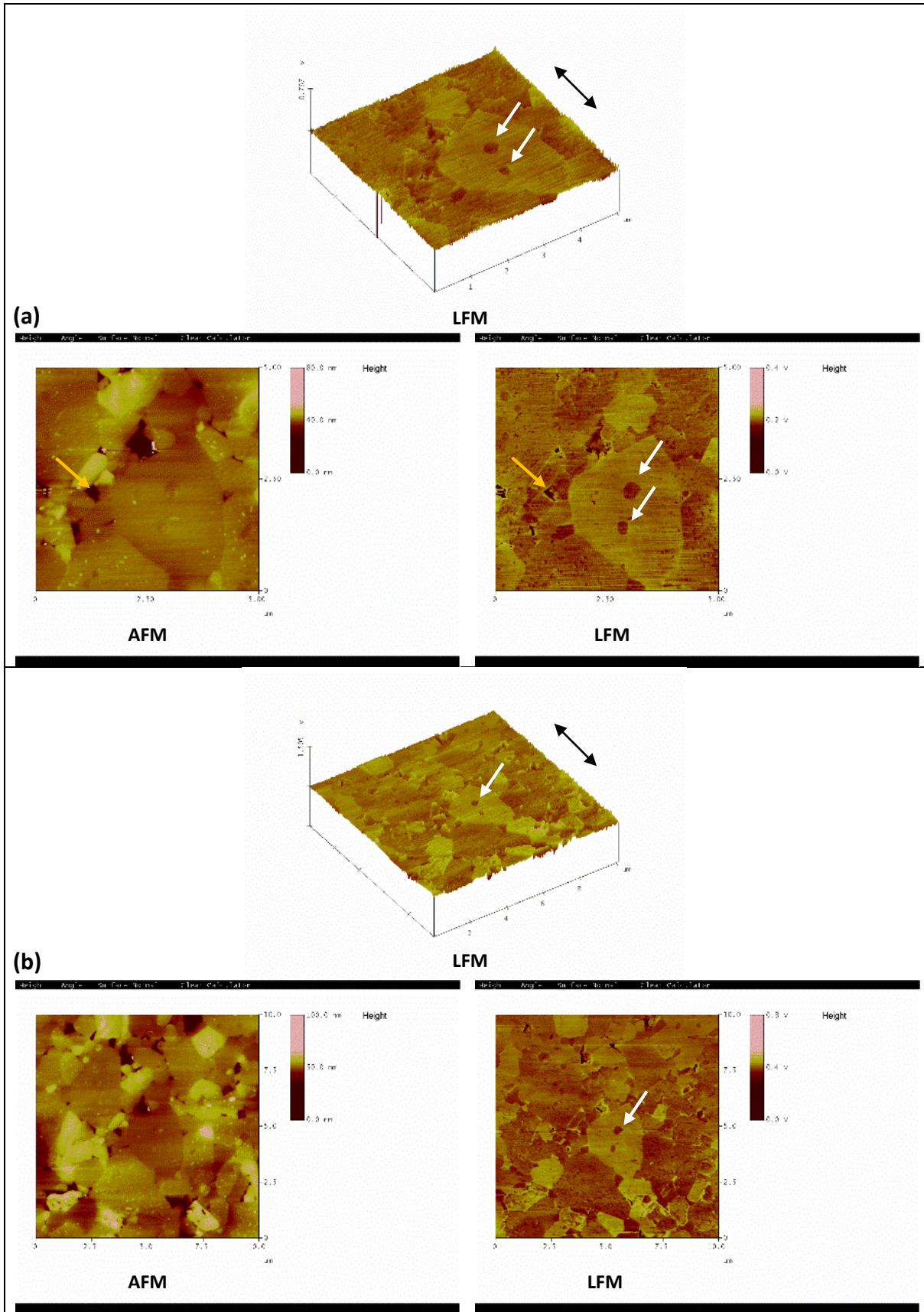
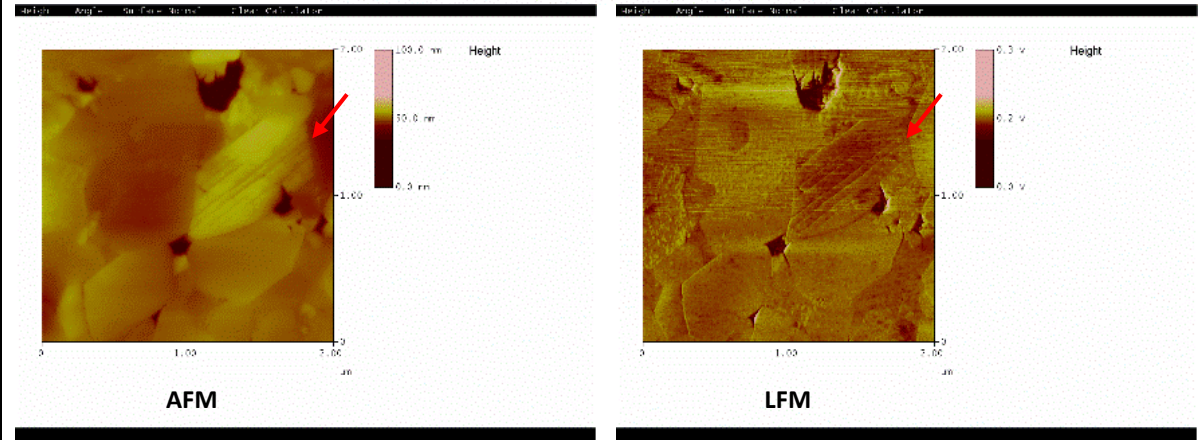
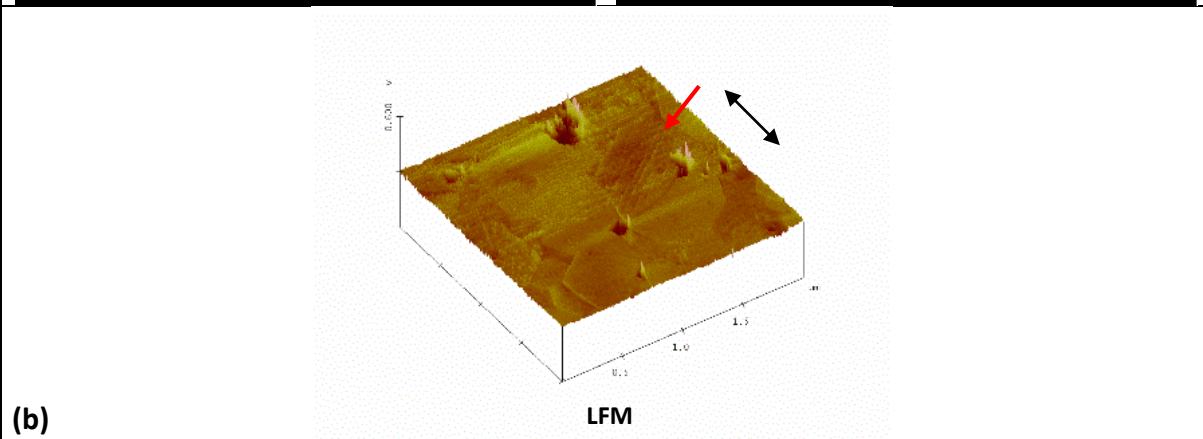
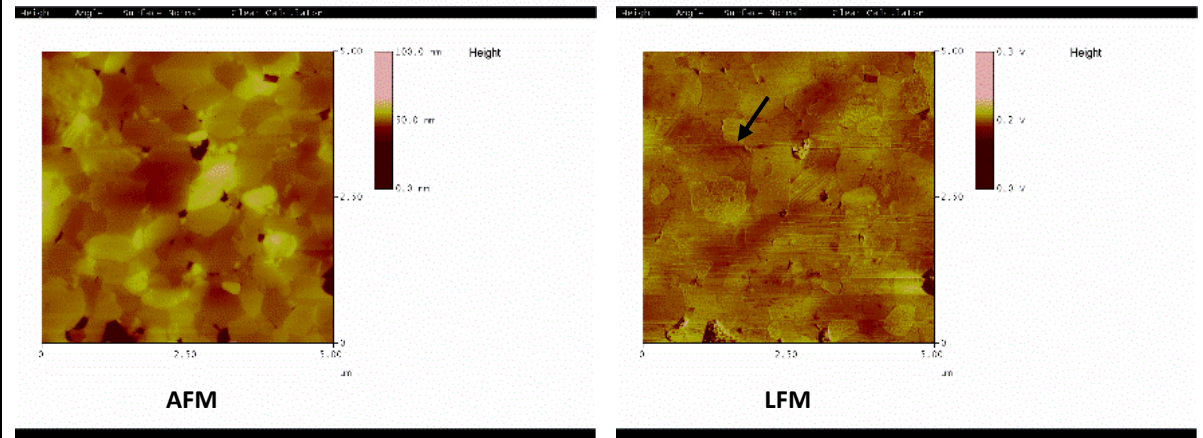
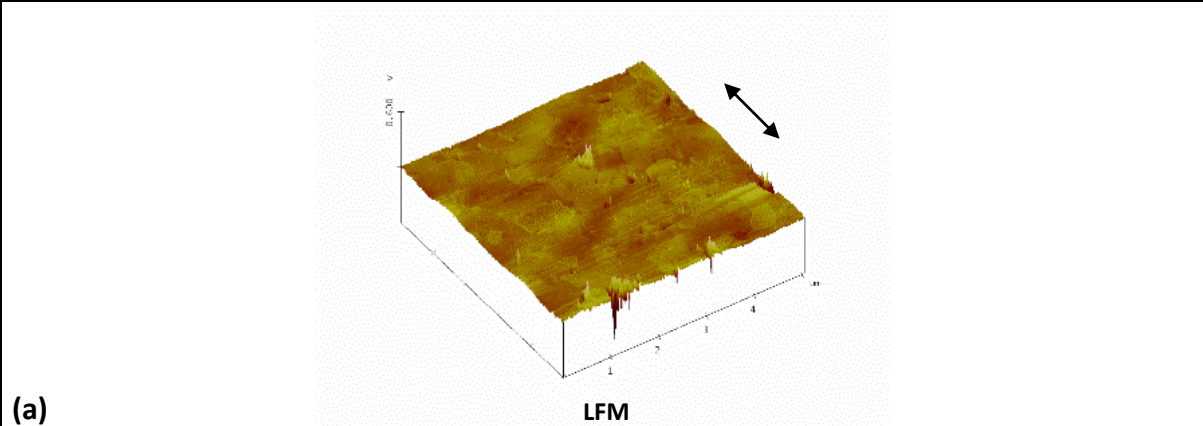


Figure 4.84. LFM images and corresponding AFM image of wear scars for ZTA+0.1 mole.% TiO₂ sample sintered at 1550°C for 5 minutes under the wear condition of 16N-8hr, representing fractured triple points with yellow arrow, and transgranular zirconia grains with white arrows (image width is 5µm for (a), and 10µm for (b))



Continued

Continued

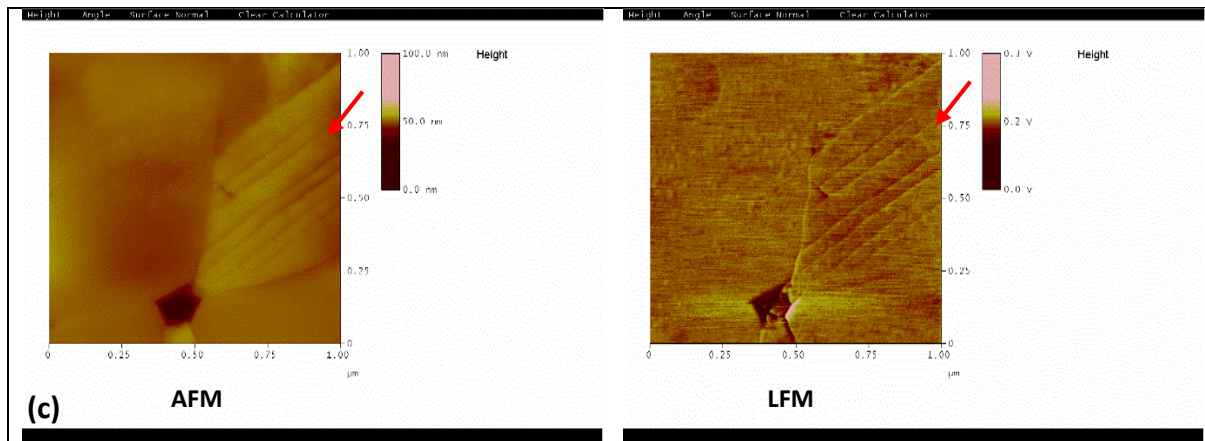


Figure 4.85. LFM images and corresponding AFM image of wear scars for ZTA+0.5 mole.% TiO_2 sample sintered at 1450°C for 5 minutes under the wear condition of 4N-24hr, representing transgranular fracture with red arrows, and intergranular fracture with black arrow (image width is $5\mu\text{m}$, $2\mu\text{m}$, and $1\mu\text{m}$ for (a), (b) and (c) respectively)

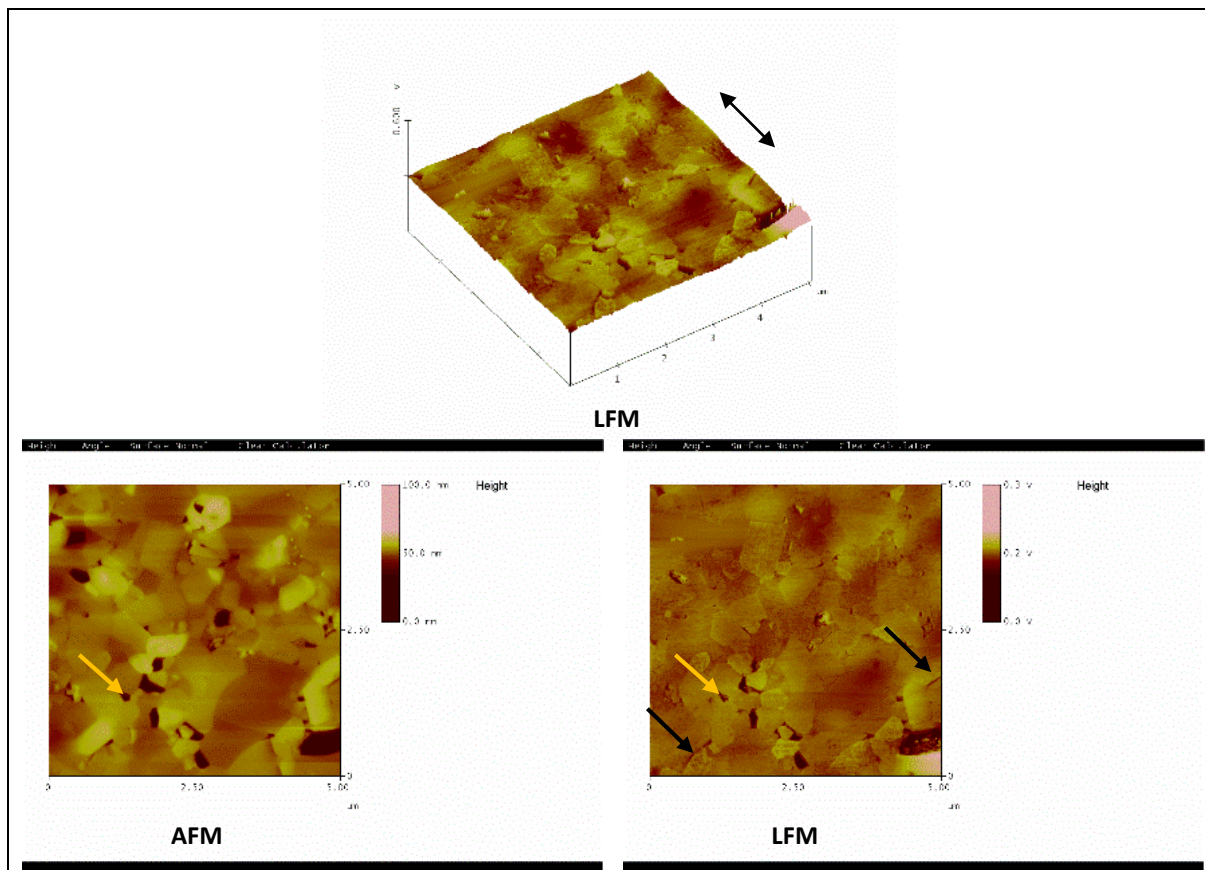


Figure 4.86. LFM images and corresponding AFM image of wear scars for ZTA+0.5 mole.% TiO_2 sample sintered at 1450°C for 5 minutes under the wear condition of 8N-24hr, representing fractured triple points with yellow arrow, and intergranular fracture with black arrow (image width is $5\mu\text{m}$)

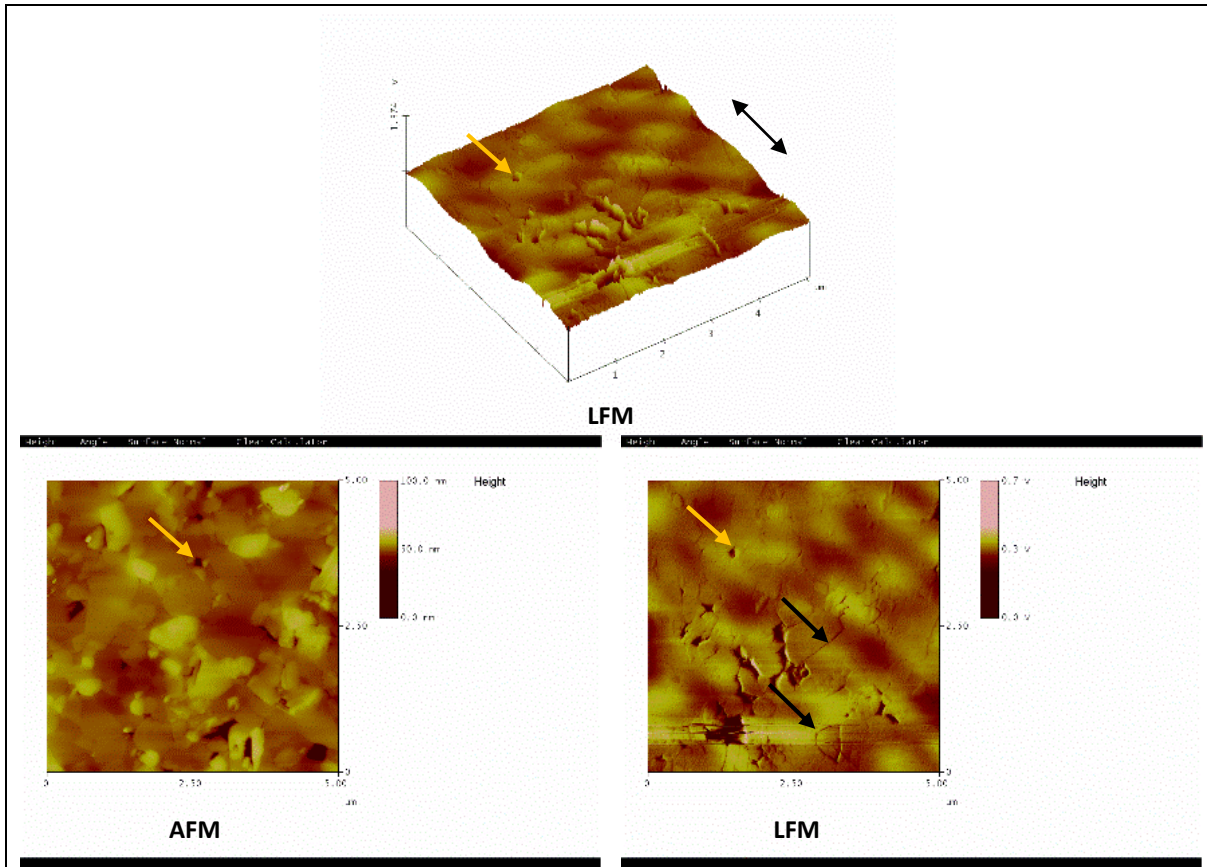


Figure 4.87. LFM images and corresponding AFM image of wear scars for ZTA+0.5 mole.% TiO₂ sample sintered at 1450°C for 5 minutes under the wear condition of 16N-8hr, representing fractured triple points with yellow arrow, and intergranular fracture with black arrow (image width is 5μm)

4.2.2.3. Worn phase analysis

As stated before, Raman spectra of the wear scars were obtained in order to examine the composition of wear scars and investigate if any tribolayer was formed during the test. After each test, samples were first rinsed with distilled water and isopropanol and tested with Raman spectroscopy. Figure 4.88 shows the Raman spectra for the surface of ZTA samples as polished (a) and unworn surface after wear (b). The worn surfaces can be seen in Figure 4.89 and Figure 4.90.a, which might contain broken parts of a tribolayer attached to the surface and remained after washing the surface with water. Raman spectra of these spots illustrate the same spectra of bovine serum reported by Lin and Koenig (Lin & Koenig, 1976). A representative Raman spectrum of these spots is shown in Figure 4.90.b demonstrating weak peaks of alumina and zirconia and high peaks of bovine serum.

After cleaning the surface with Vikron tablet as explained in chapter 3.4.5 and removing tribolayer from the surface, the samples were studied for Raman analysis again to inspect if any changes in phases happened during wear test, particularly tetragonal to monoclinic transformation was the centre of interest due to its high possibility. In order to investigate a large area of wear scar, mapping feature of the spectrometer was used and an area around 350 to 400 micron in middle of the wear scar was selected with the step of 1 micron, which resulted in obtaining more than 350 Raman spectra for each sample. The location of alumina and zirconia peaks on Raman spectra were found based on the reference spectra reported by Zhu et al. (Zhu, et al., 2013), where monoclinic zirconia peaks had a wavenumber of 178.66 and 190.99 ω/cm^{-1} . Based on these information, a peak area of 160 to 200 ω/cm^{-1} was determined for refining the data, and the locations with high probability of monoclinic phase were examined carefully, like the representative spectra and map illustrated in Figure 4.91. The representative Raman spectra of some samples are given in Figure 4.92 and Figure 4.93. It can be seen from these two figures that monoclinic peaks could be detected in ZTA samples, particularly in the sample with coarse microstructure (Figure 4.92.c); however, no evidence of monoclinic peaks were found in samples contacting titania and all the obtained results were similar to the spectra depicted in Figure 4.93.

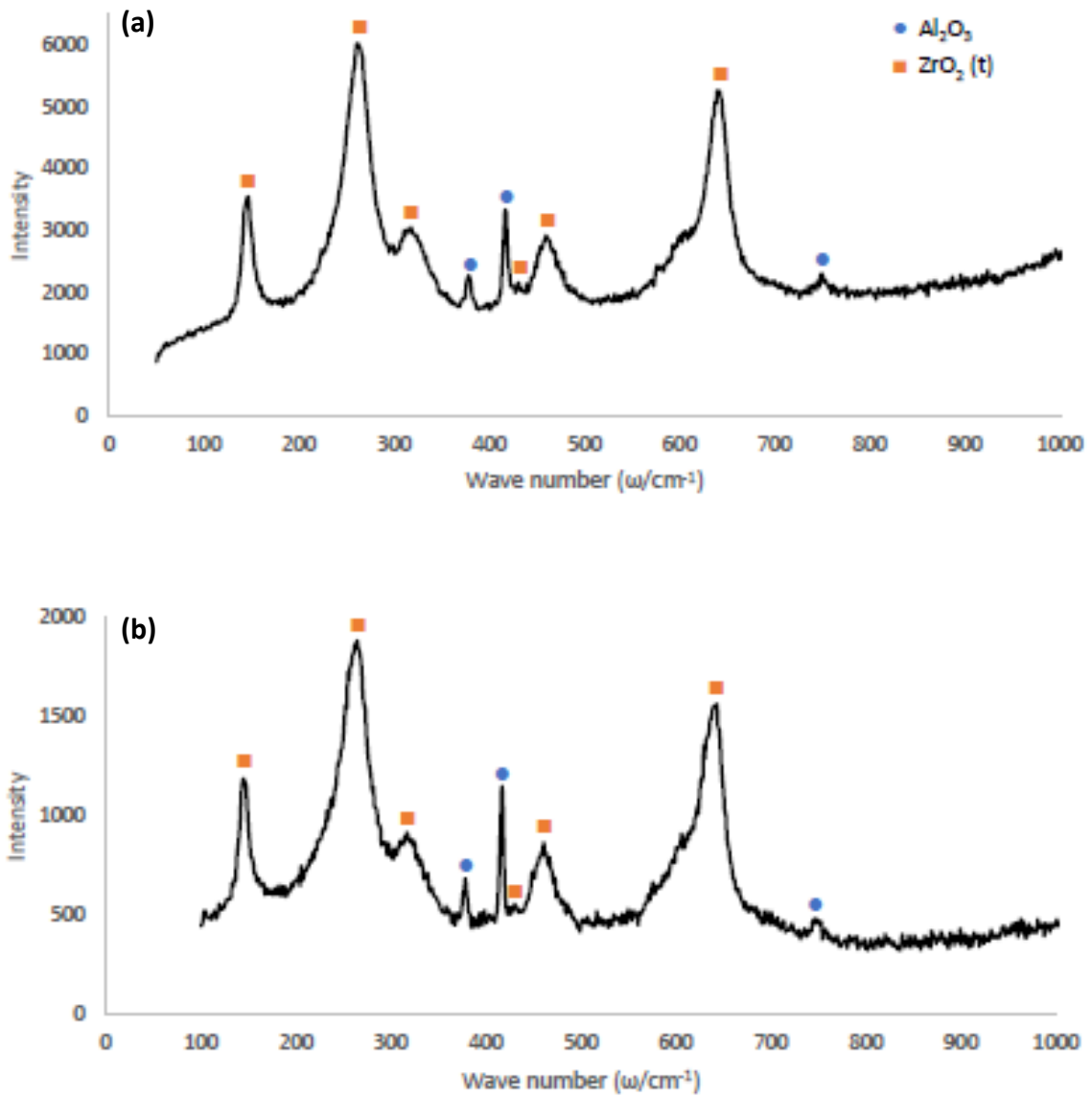


Figure 4.88. Raman spectra of the surface of ZTA sample sintered at 1450°C for 7 minutes before wear (a) and unworn surface after wear (b)

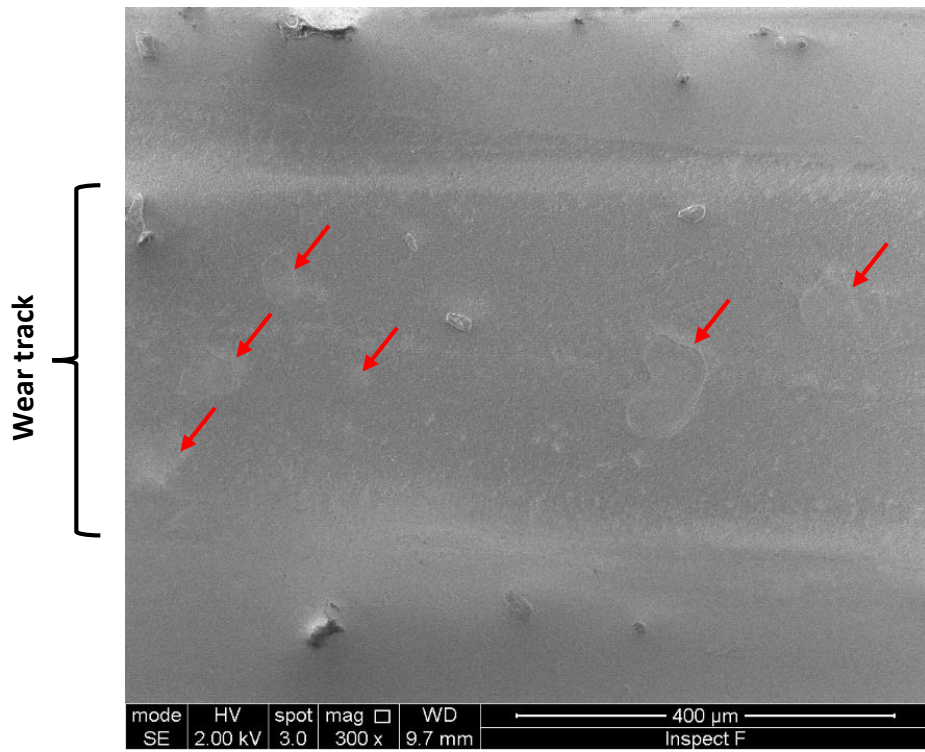


Figure 4.89. SEM image of spots representing broken attached tribolayer to the wear scar surface with red arrows for ZTA sample sintered at 1450°C for 7 minutes under wear condition of 8N-24hr

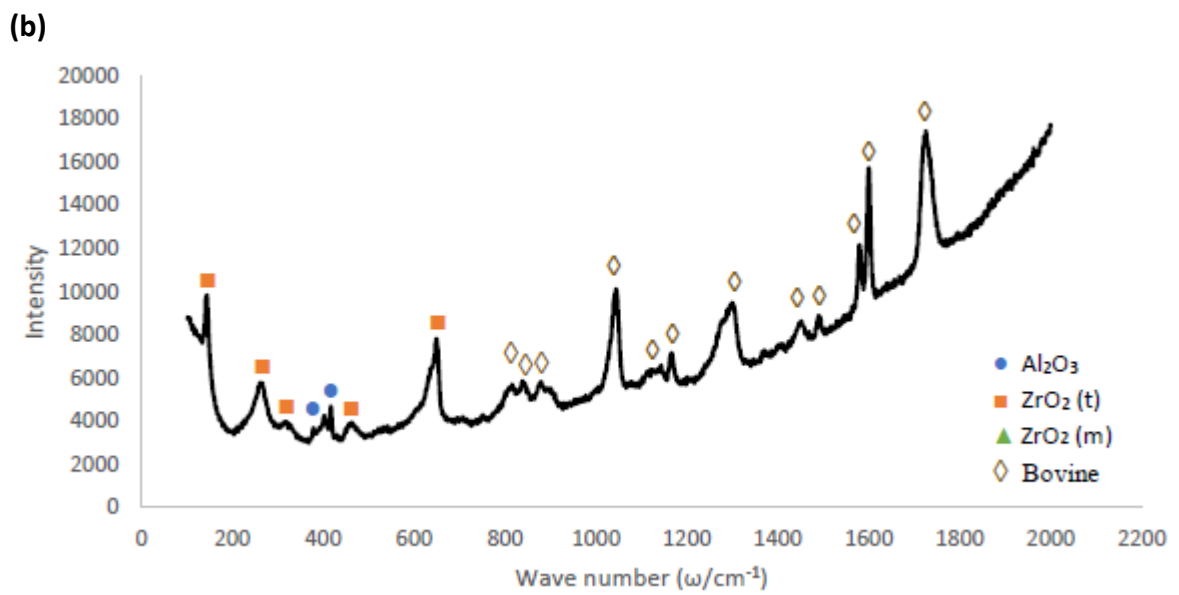


Figure 4.90. Optical image (a) and Raman spectra (b) of a spot on the wear scar of ZTA sample sintered at 1550°C for 7 minutes under wear condition of 8N-24hr

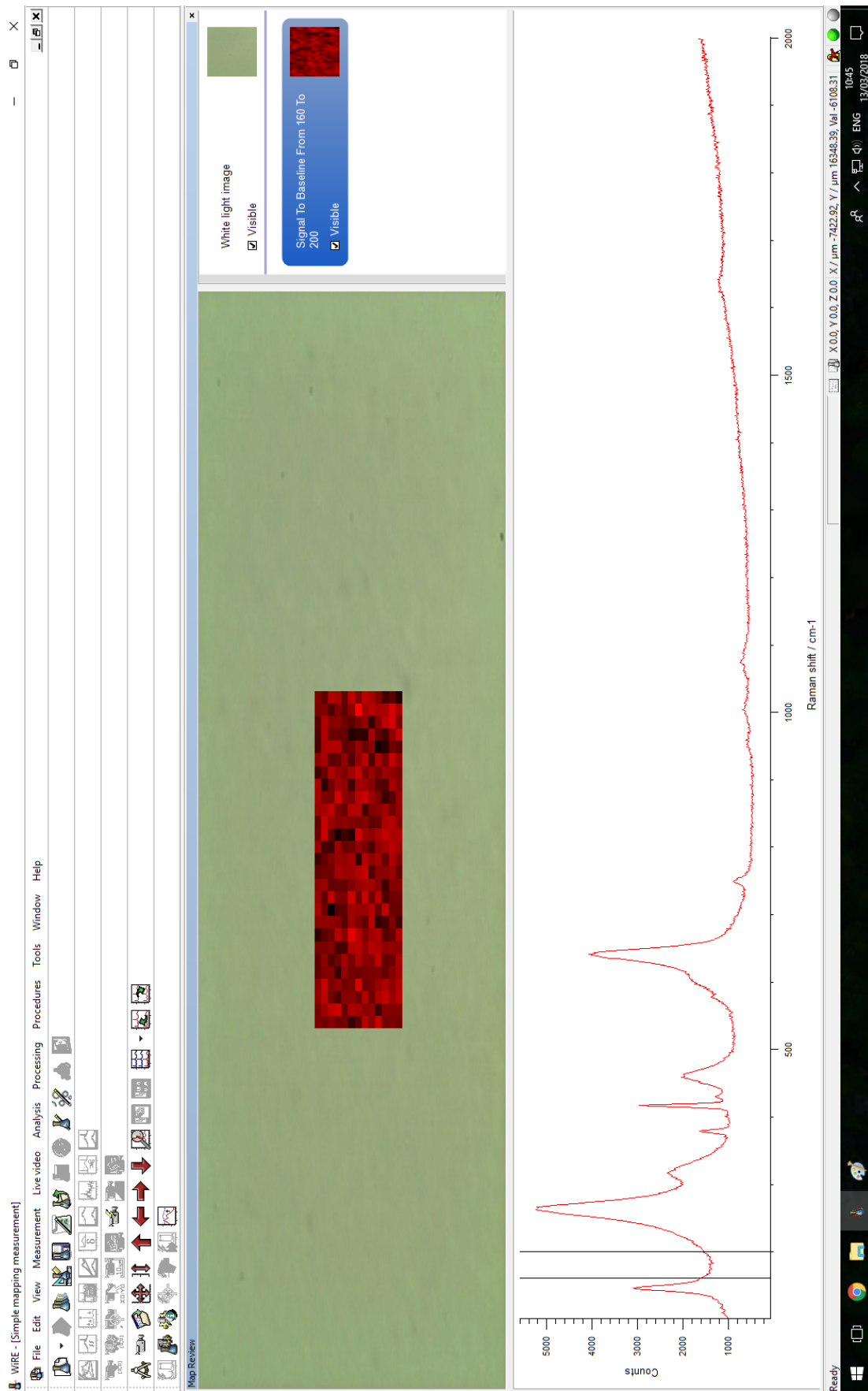


Figure 4.91. Raman spectral image and peak area acquisition map for ZTA+0.1 mole.% TiO₂ sample sintered at 1500°C for 5 minutes under wear condition of 16N-8hr

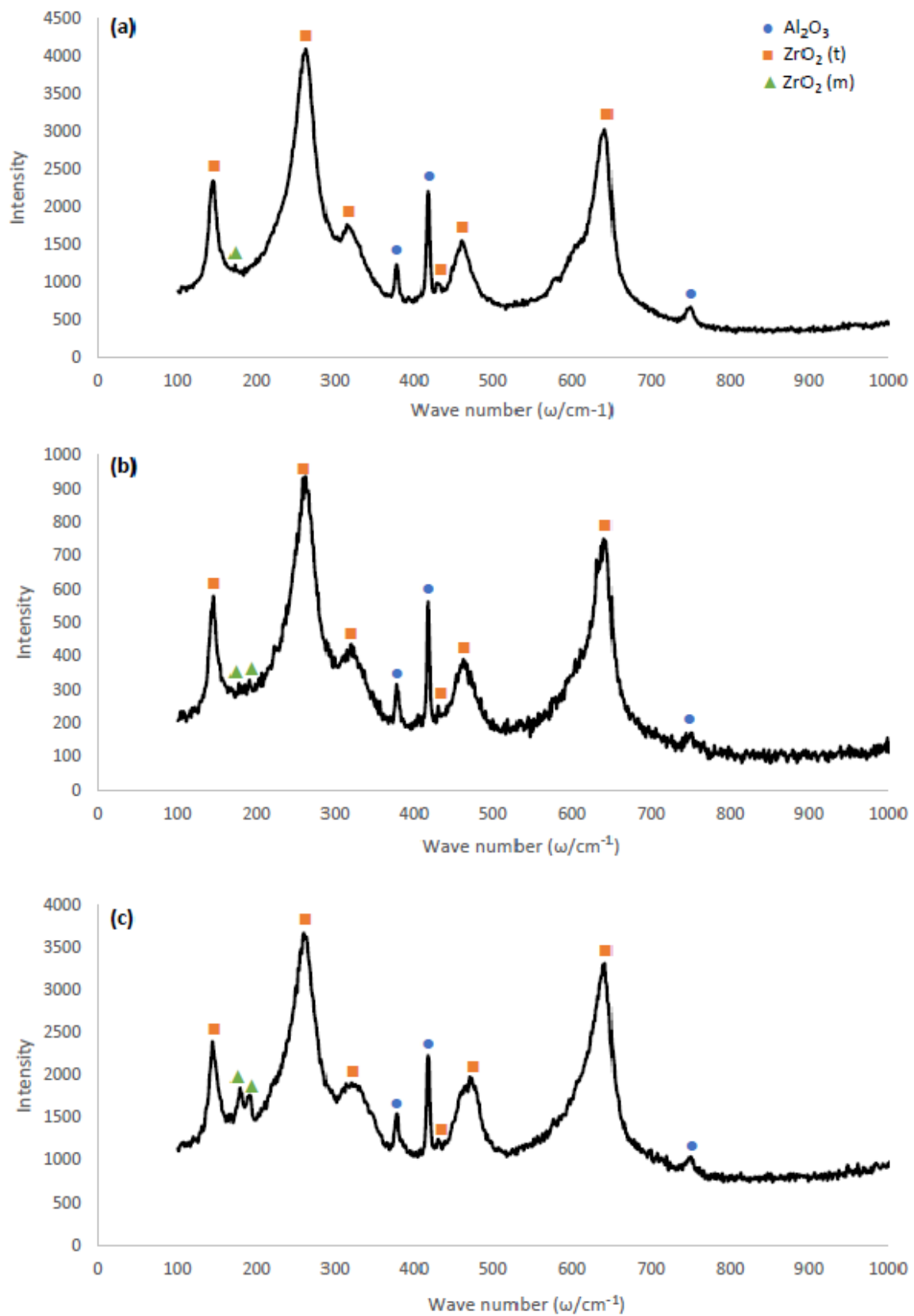


Figure 4.92. Raman spectra of ZTA samples; sintered at 1450°C for 7 minutes under the wear condition of 16N-8hr (a), sintered at 1500°C for 7 minutes under the wear condition of 16N-8hr (b), and sintered at 1550°C for 7 minutes under the wear condition of 16N-8hr (c)

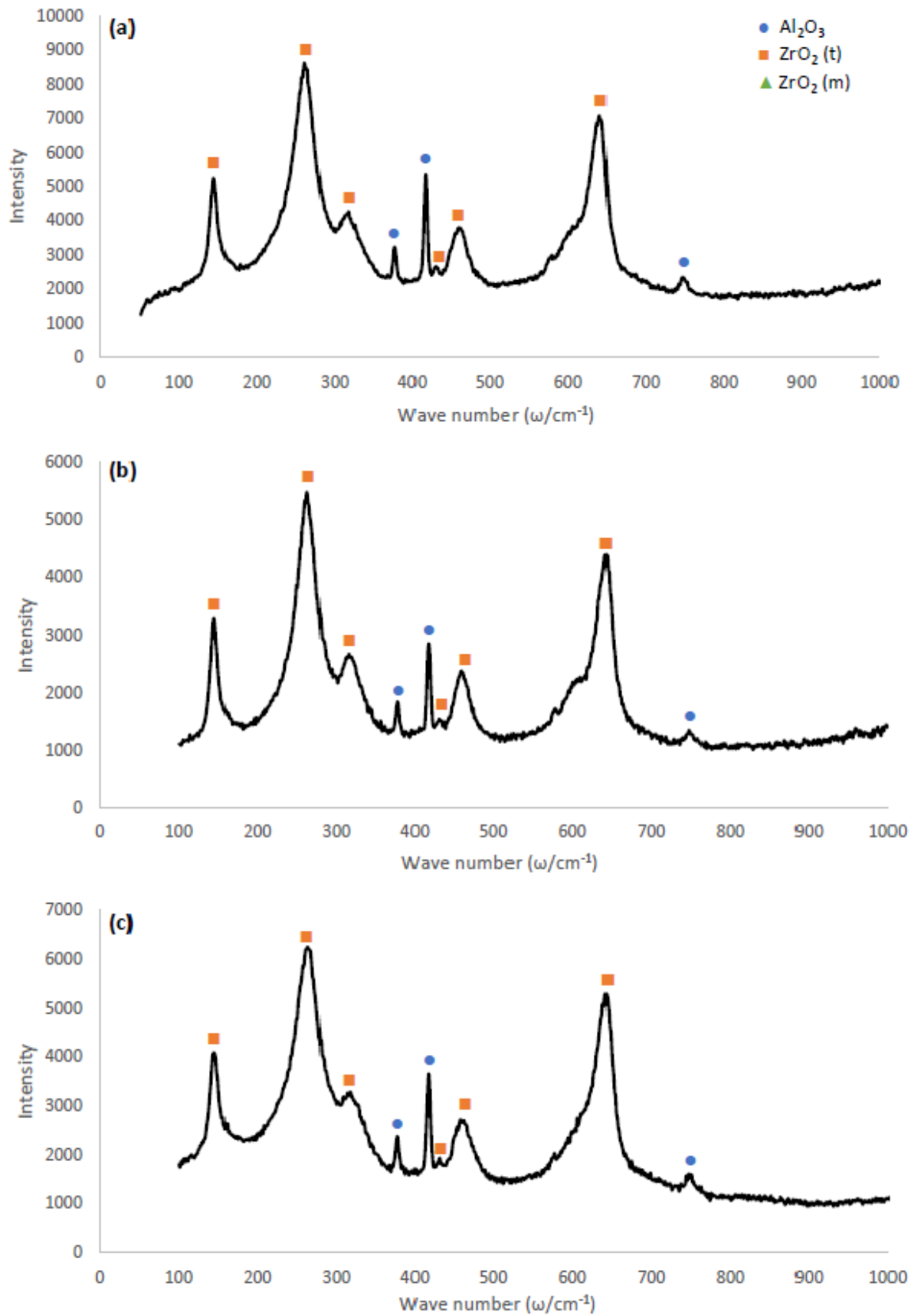


Figure 4.93. Raman spectra of ZTA+0.1 mole.% TiO_2 sample sintered at 1500°C for 5 minutes under the wear condition of 16N-8hr (a), ZTA+0.1 mole.% TiO_2 sample sintered at 1550°C for 5 minutes under the wear condition of 16N-8hr (b), and ZTA+0.5 mole.% TiO_2 sample sintered at 1500°C for 5 minutes under the wear condition of 16N-8hr (c)

4.2.2.4. Worn microstructure characterization

Changes of microstructure in the wear can present valuable information about the mechanism involved in wear and fracture of materials, particularly for composites in which different materials with different wear behavior are involved. Figure 4.94 to Figure 4.120 illustrate the microstructure of wear scar for different wear conditions of each sample. Different magnifications were selected in order to provide reliable and precise demonstration of changes happened in microstructure during wear.

The most common and clear feature found on all of the samples is fractured grains of alumina, represented by red arrows in SEM images, as detected by AFM and LFM images as well. Figure 4.95.d, Figure 4.96.e, Figure 4.99.b,c,d, and e, Figure 4.100.b, c, and d, Figure 4.101.d, e, and f, Figure 4.103.d, Figure 4.105.e, Figure 4.107.c, d, and f, Figure 4.108. e and f, Figure 4.109.d, e, and f, Figure 4.110.d, Figure 4.111.d, e, and f, Figure 4.114.e and f, Figure 4.117.e and f, Figure 4.119.d, and Figure 4.120.e illustrate that fractured alumina grains could be detected in majority of obtained microstructure.

In some of the SEM figures such as Figure 4.94.b, e, and f, Figure 4.103.b, c, e, and f, Figure 4.106.b, d, and e, Figure 4.112.a, c, d, and e, Figure 4.115.d and f, Figure 4.116.c and e, and Figure 4.118.c, e, and f, fine grooves could be observed in microstructure. In addition, grain pull-out was detectable in some figures like Figure 4.94.c and d, Figure 4.96.b, c, and e, Figure 4.98.e, Figure 4.100.e and f, Figure 4.101.c, Figure 4.108.f, Figure 4.115.c and e, Figure 4.118.c and e, and Figure 4.119.d, e and f, which in some of the figures such as Figure 4.101.b and d, Figure 4.102.c and f, and Figure 4.110.c, e and f, the area of grain pull-out seems to be larger than one grains and is considered that clusters of neighboring grains have been removed from the surface.

An interesting feature which could be identified in Figure 4.95.e and f, Figure 4.104.e and f, and Figure 4.116.e was the wear debris trapped in the pores resulted from grain removal. The size of these wear debris as could be estimated from the figures is in nanometer range and the BSE images show that they could be made of both alumina and/or zirconia fractured and smashed particles.

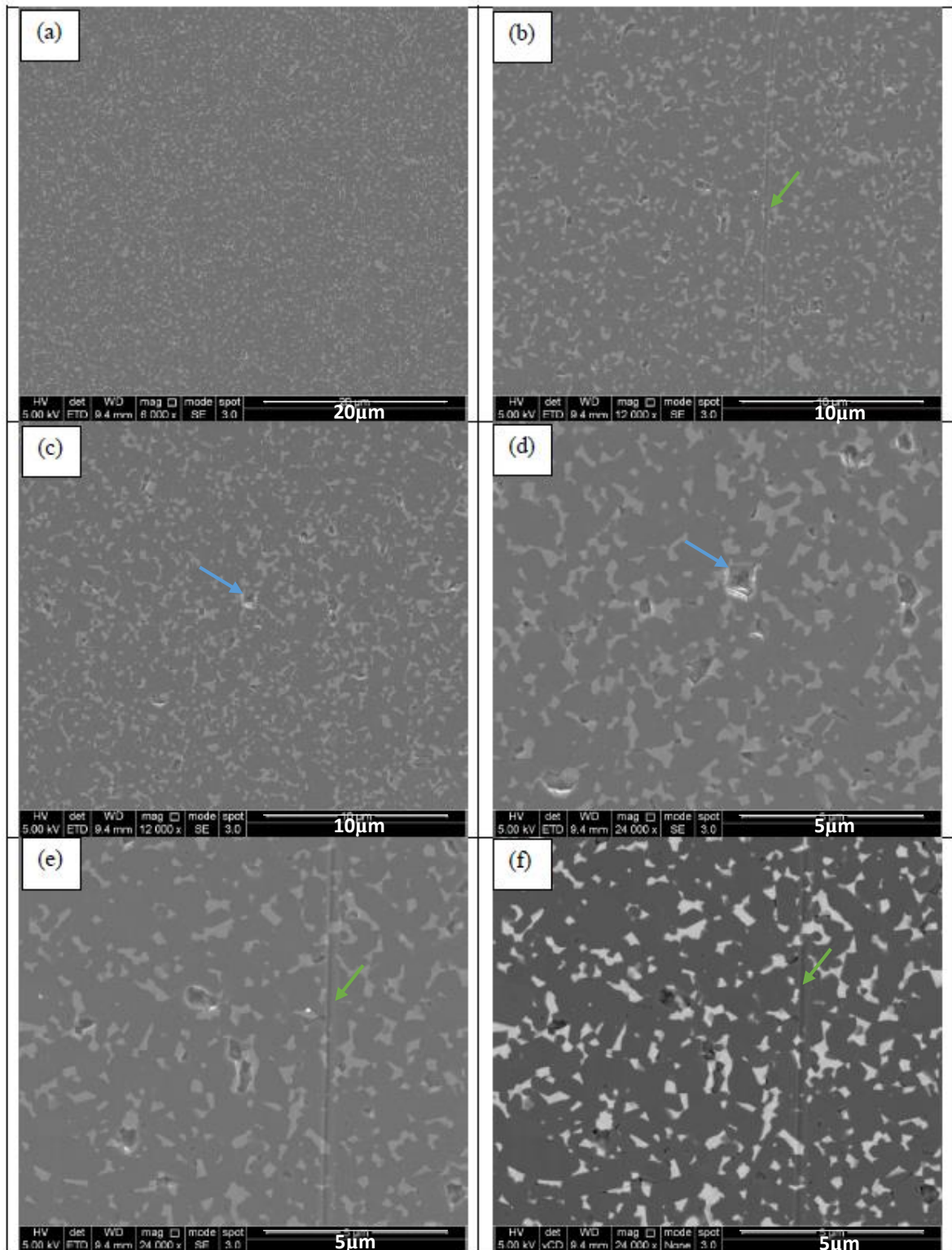


Figure 4.94. Secondary electron and backscattered electrons (f) SEM images of wear scars for ZTA sample sintered at 1450°C for 7 minutes under the wear condition of 4N-24hr, representing grain pull-out with blue arrows, and grooves with green arrows

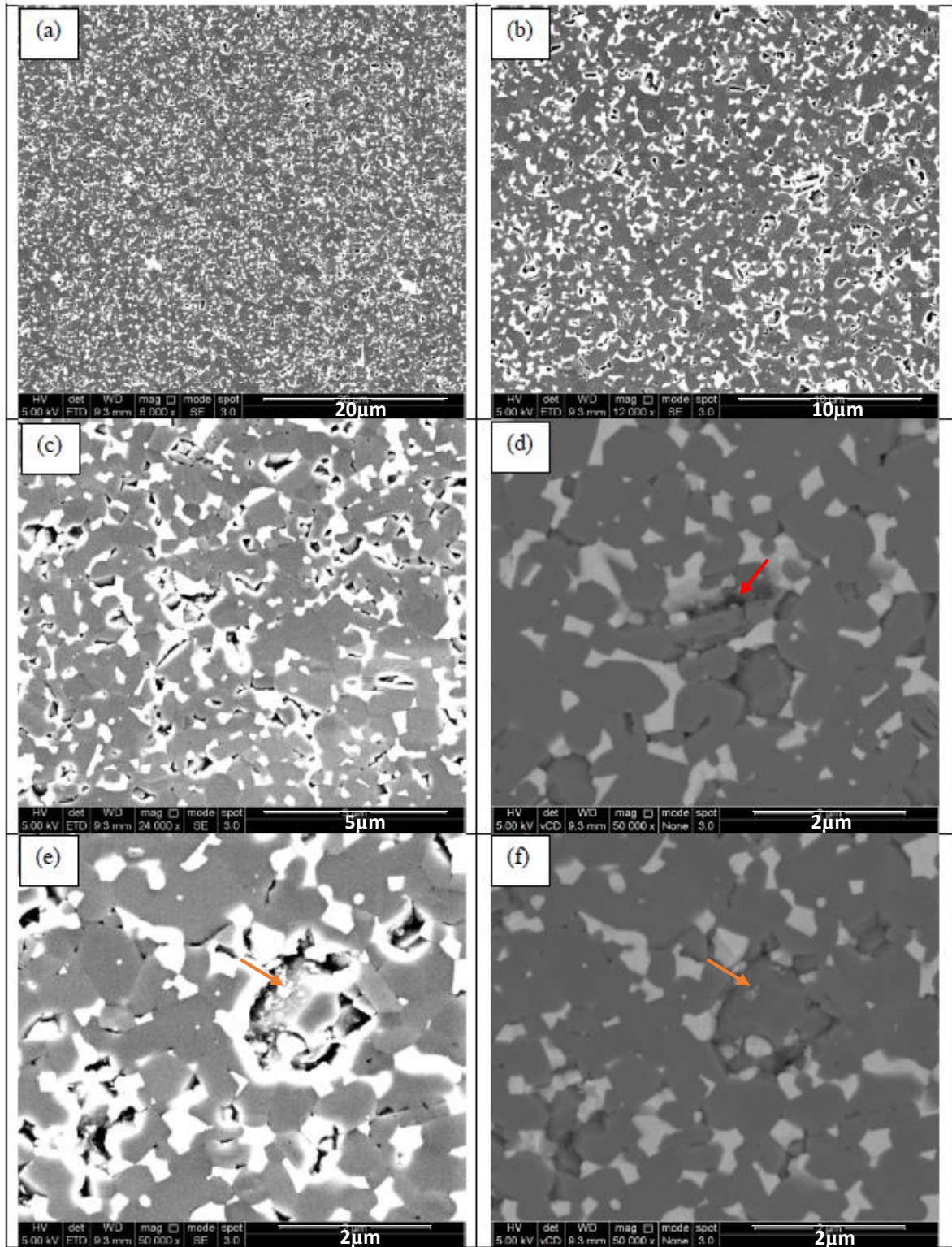


Figure 4.95. Secondary electron and backscattered electrons (d, f) SEM images of wear scars for ZTA sample sintered at 1450°C for 7 minutes under the wear condition of 8N-24hr, representing transgranular fractured alumina grains with red arrows, and wear debris with orange arrows

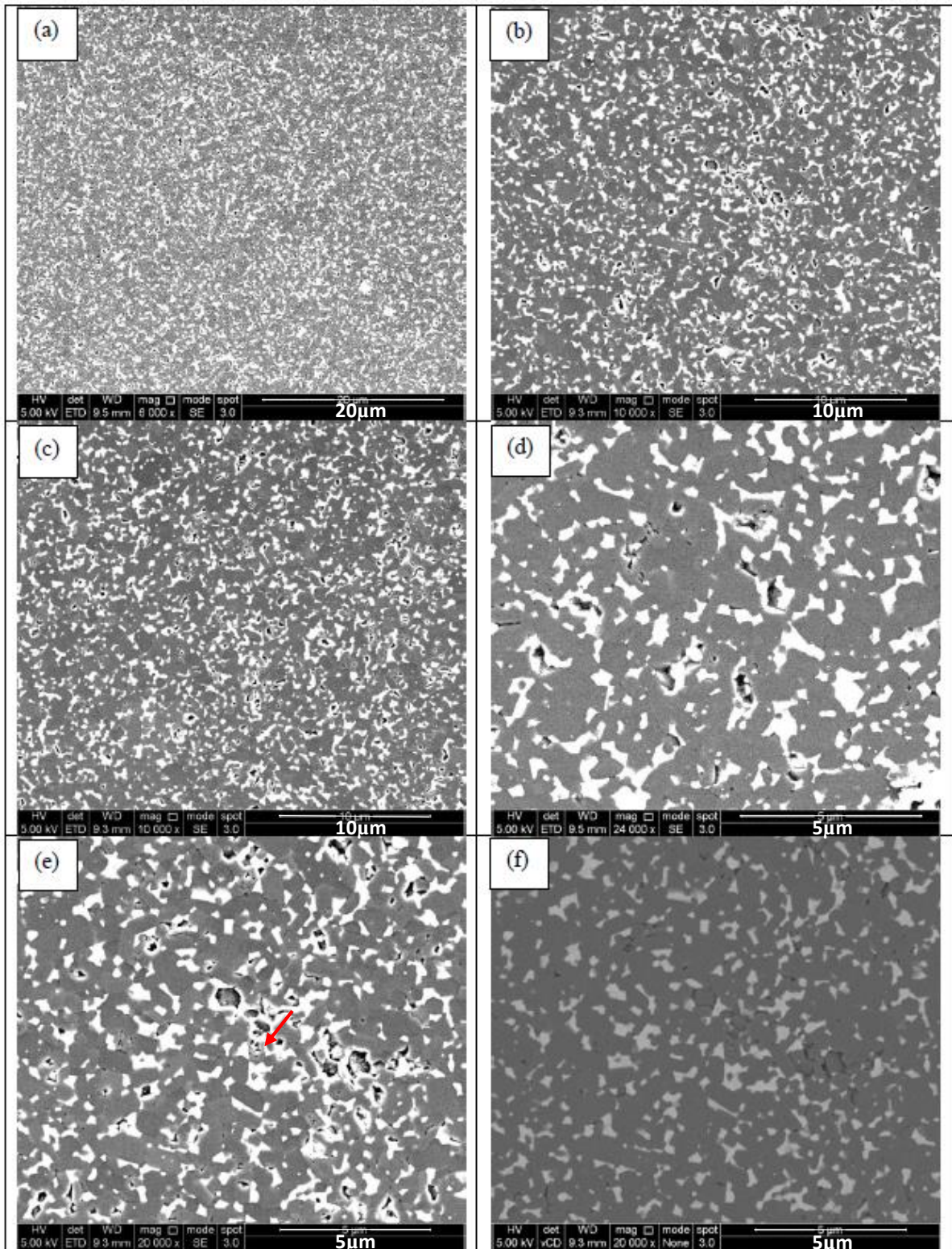


Figure 4.96. Secondary electron and backscattered electrons (f) SEM images of wear scars for ZTA sample sintered at 1450°C for 7 minutes under the wear condition of 16N-8hr, representing transgranular fractured alumina grains with red arrow

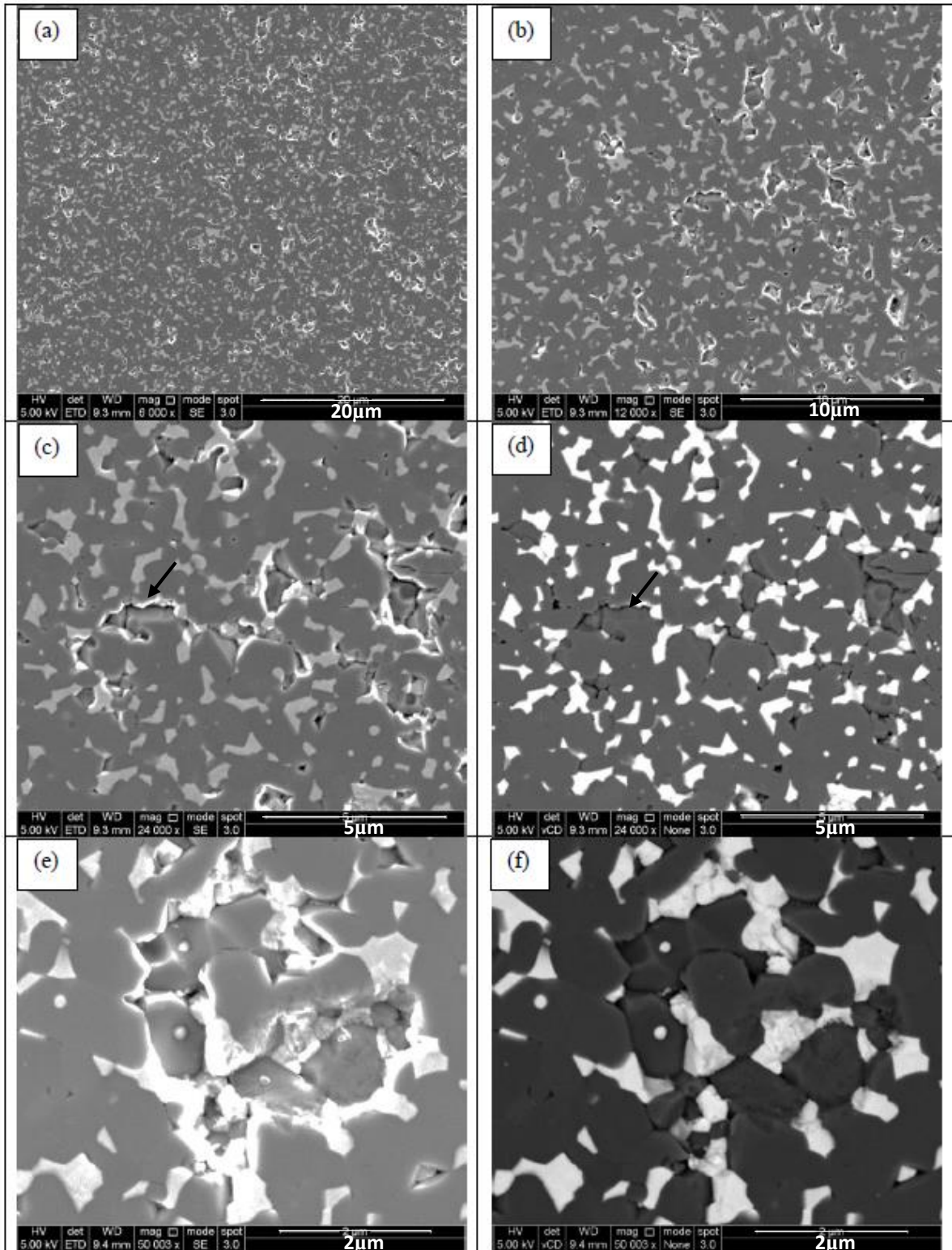


Figure 4.97. Secondary electron and backscattered electrons (d, f) SEM images of wear scars for ZTA sample sintered at 1500°C for 7 minutes under the wear condition of 4N-24hr, representing intergranular fracture with black arrows

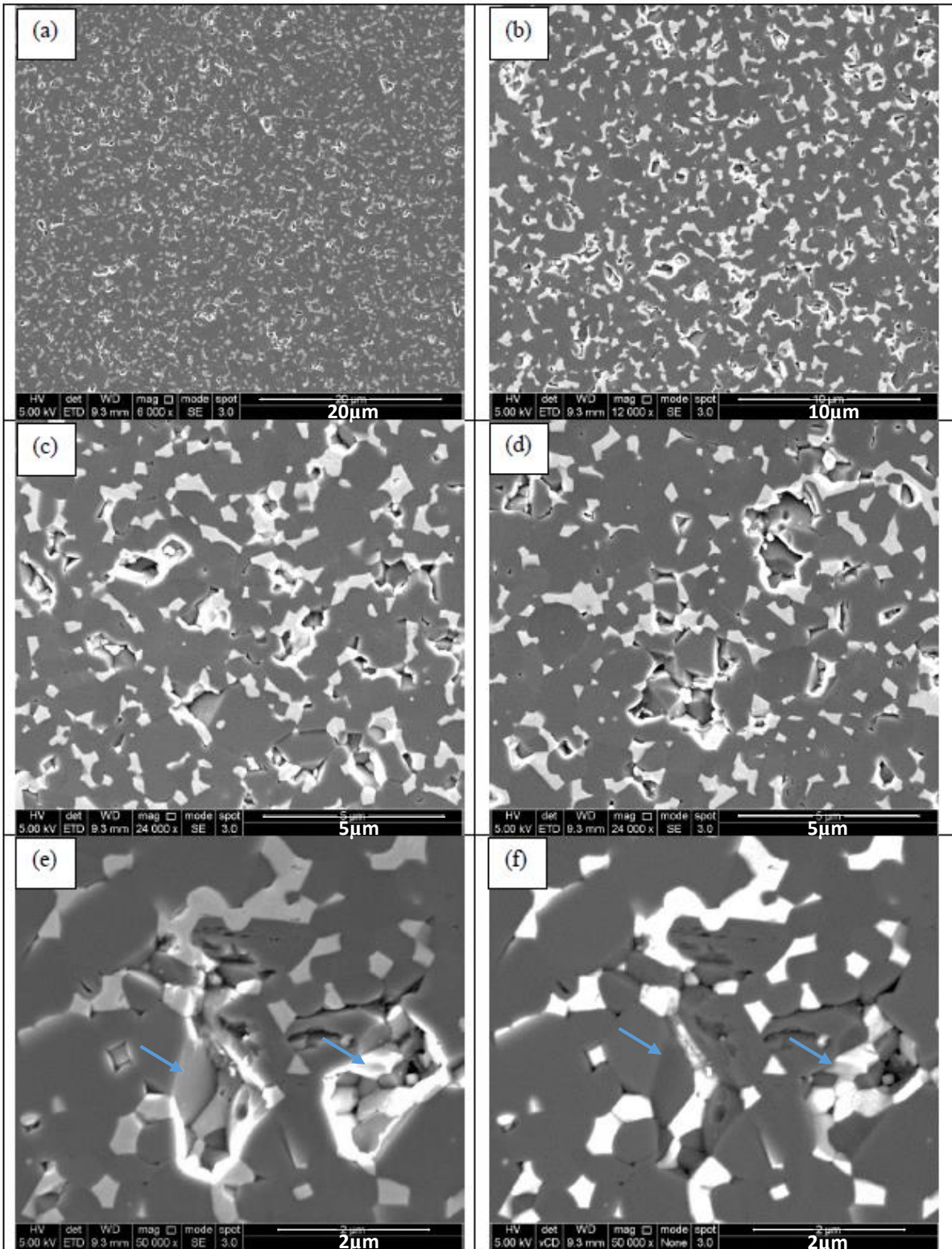


Figure 4.98. Secondary electron and backscattered electrons (f) SEM images of wear scars for ZTA sample sintered at 1500°C for 7 minutes under the wear condition of 8N-24hr, representing grain pull-out with blue arrows

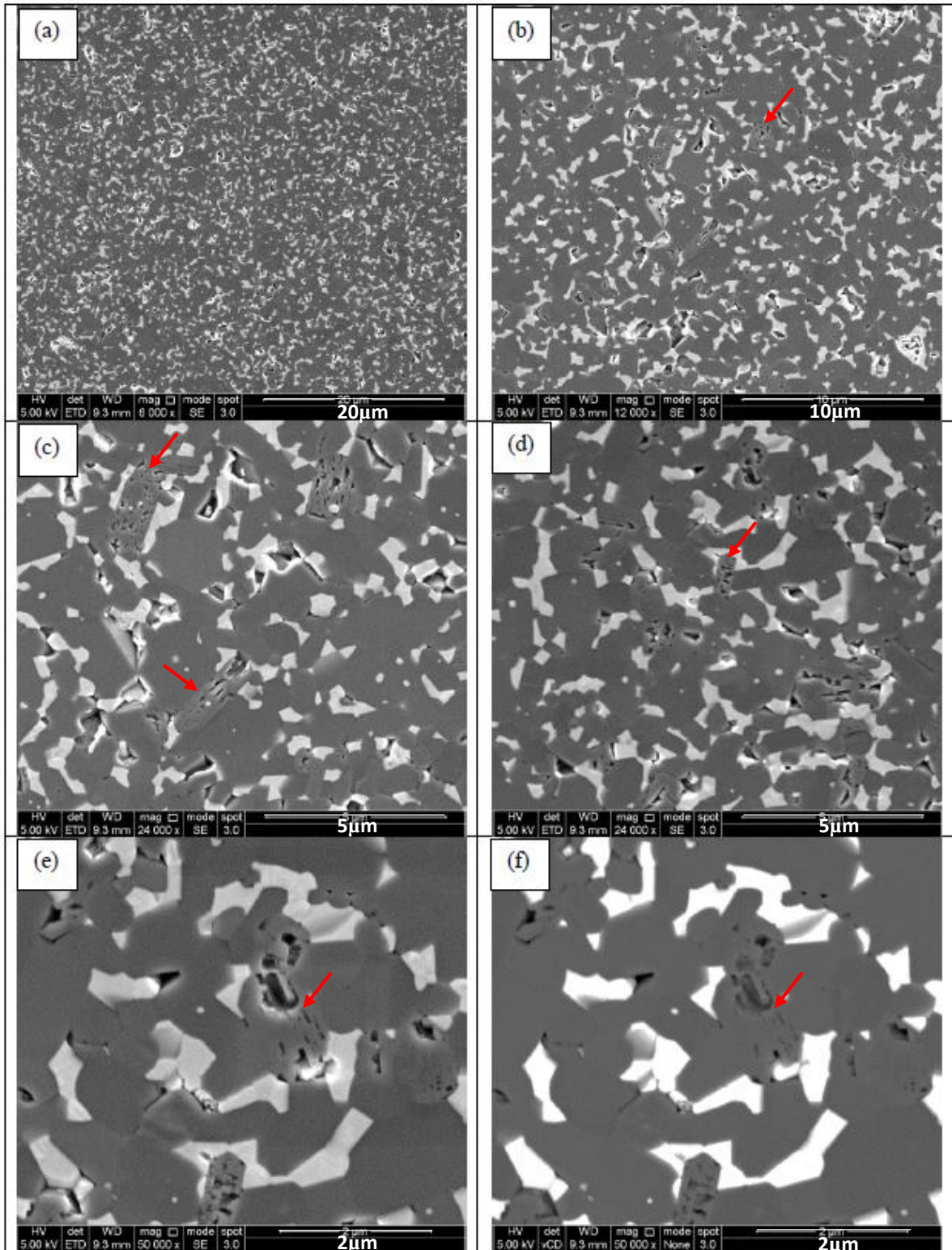


Figure 4.99. Secondary electron and backscattered electrons (f) SEM images of wear scars for ZTA sample sintered at 1500°C for 7 minutes under the wear condition of 16N-8hr, representing transgranular fractured alumina grains with red arrows

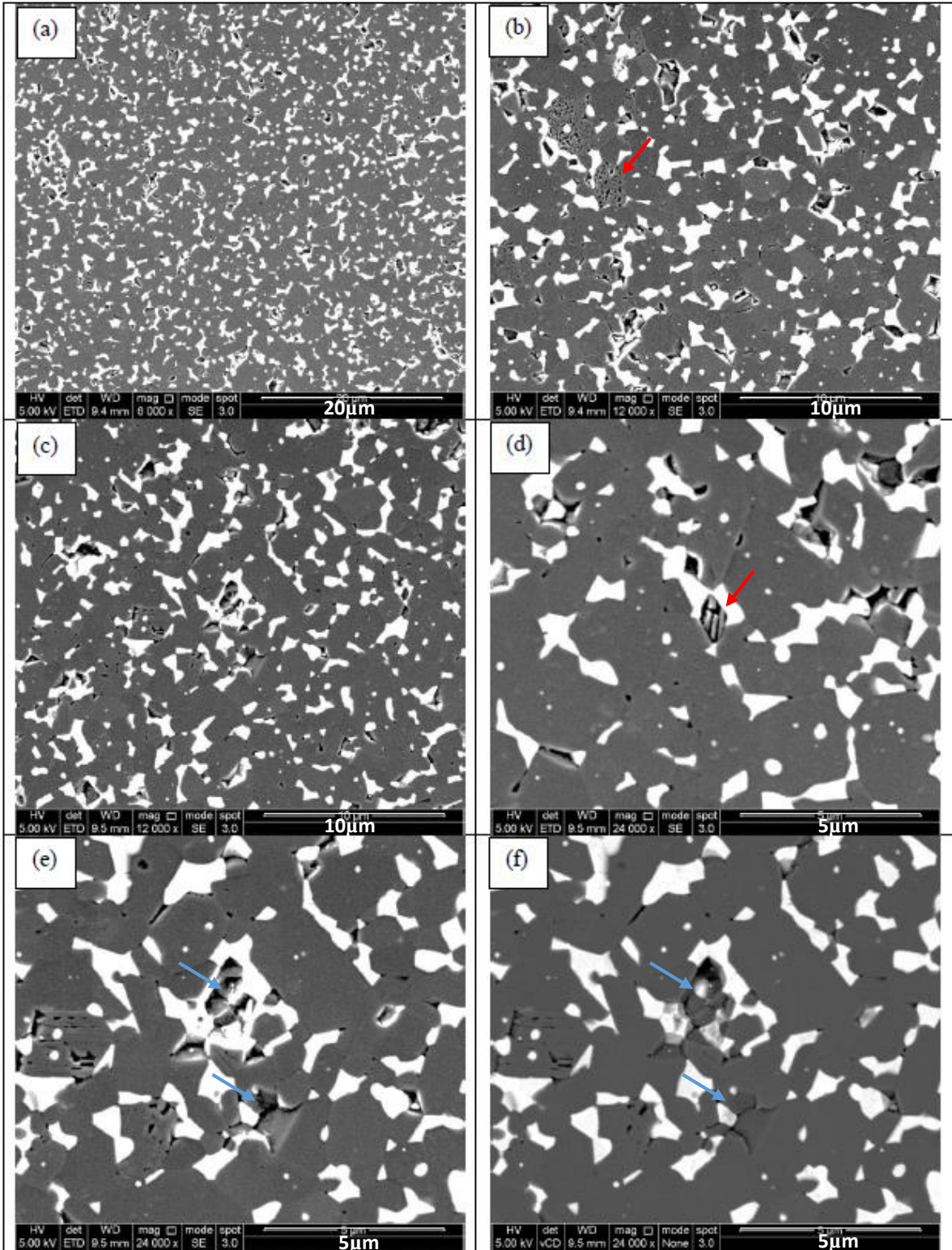


Figure 4.100. Secondary electron and backscattered electrons (f) SEM images of wear scars for ZTA sample sintered at 1550°C for 7 minutes under the wear condition of 4N-24hr, representing transgranular fractured alumina grains with red arrows, and grain pull-out with blue arrows

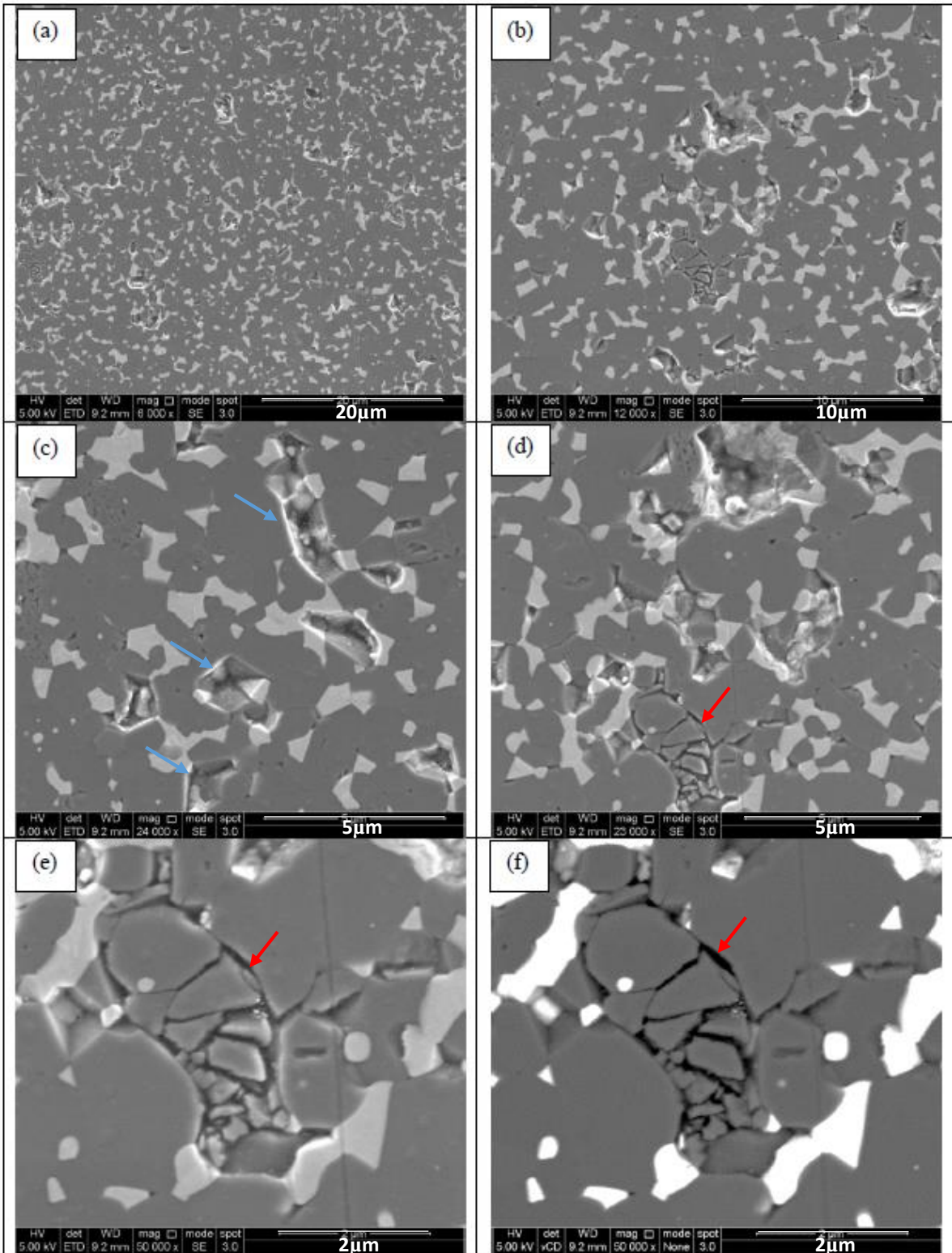


Figure 4.101. Secondary electron and backscattered electrons (f) SEM images of wear scars for ZTA sample sintered at 1550°C for 7 minutes under the wear condition of 8N-24hr, representing transgranular fractured alumina grains with red arrows, and grain pull-out with blue arrows

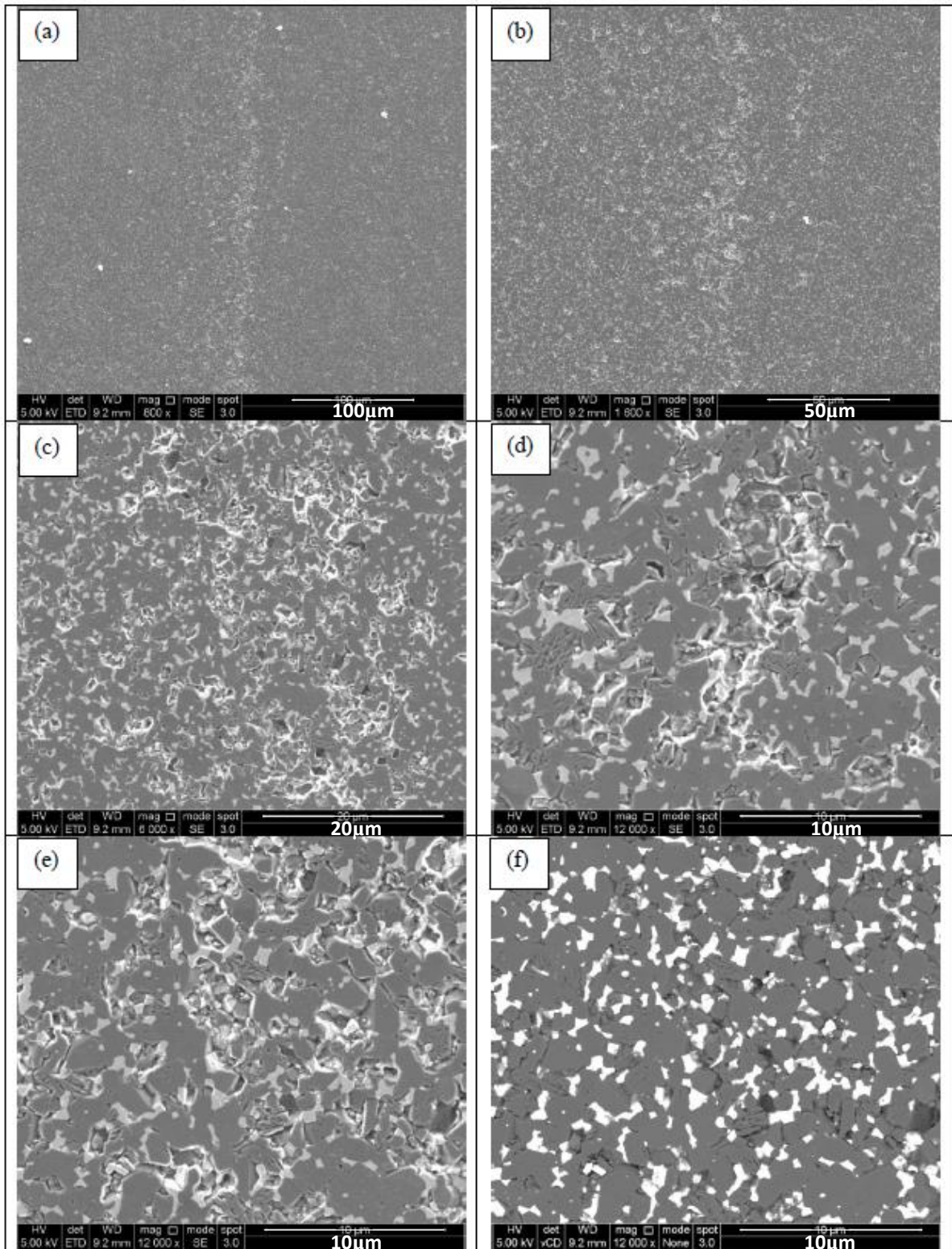


Figure 4.102. Secondary electron and backscattered electrons (f) SEM images of wear scars for ZTA sample sintered at 1550°C for 7 minutes under the wear condition of 16N-8hr

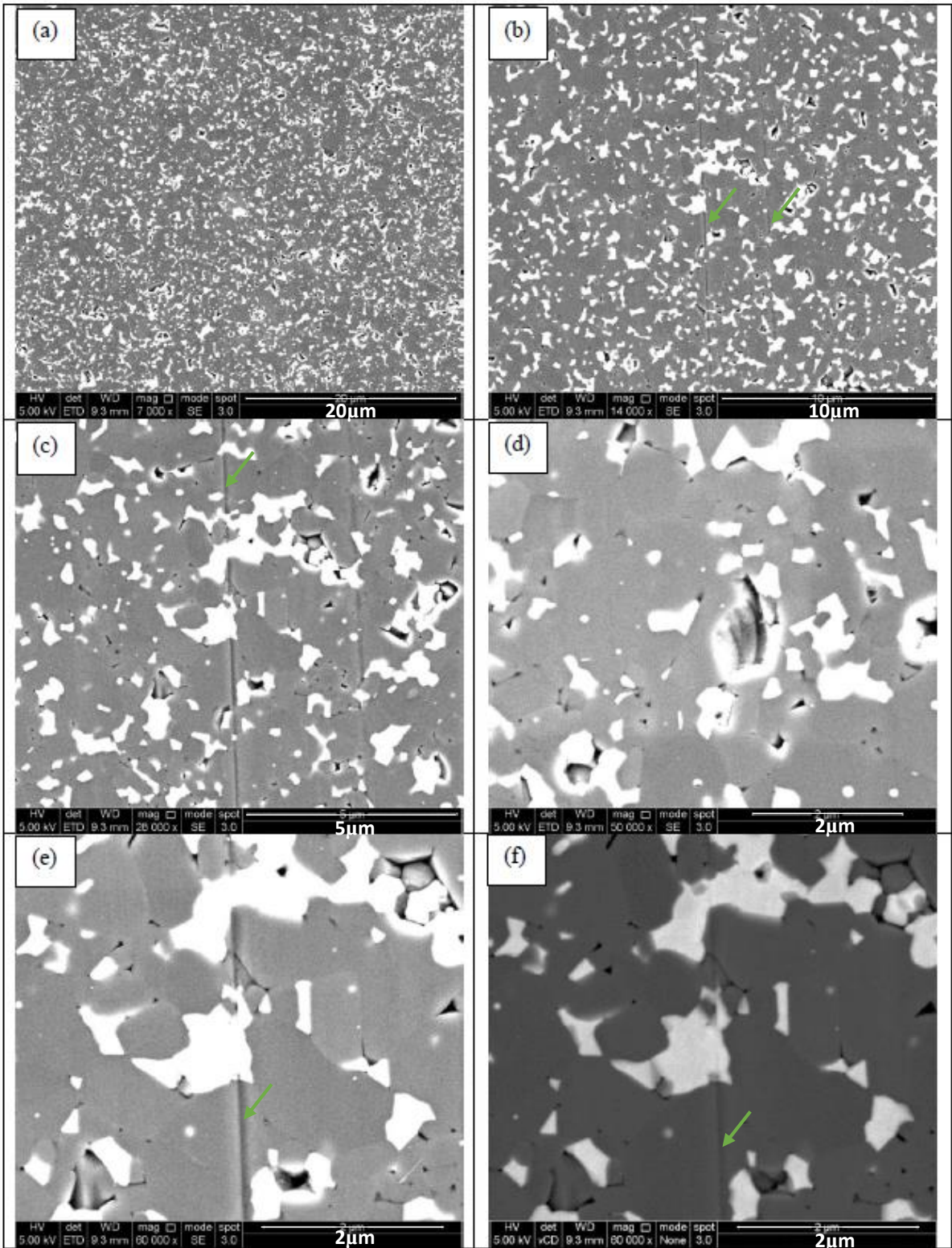


Figure 4.103. Secondary electron and backscattered electrons (f) SEM images of wear scars for ZTA+0.1 mole.% TiO₂ sample sintered at 1450°C for 5 minutes under the wear condition of 4N-24hr, representing grooves with green arrows

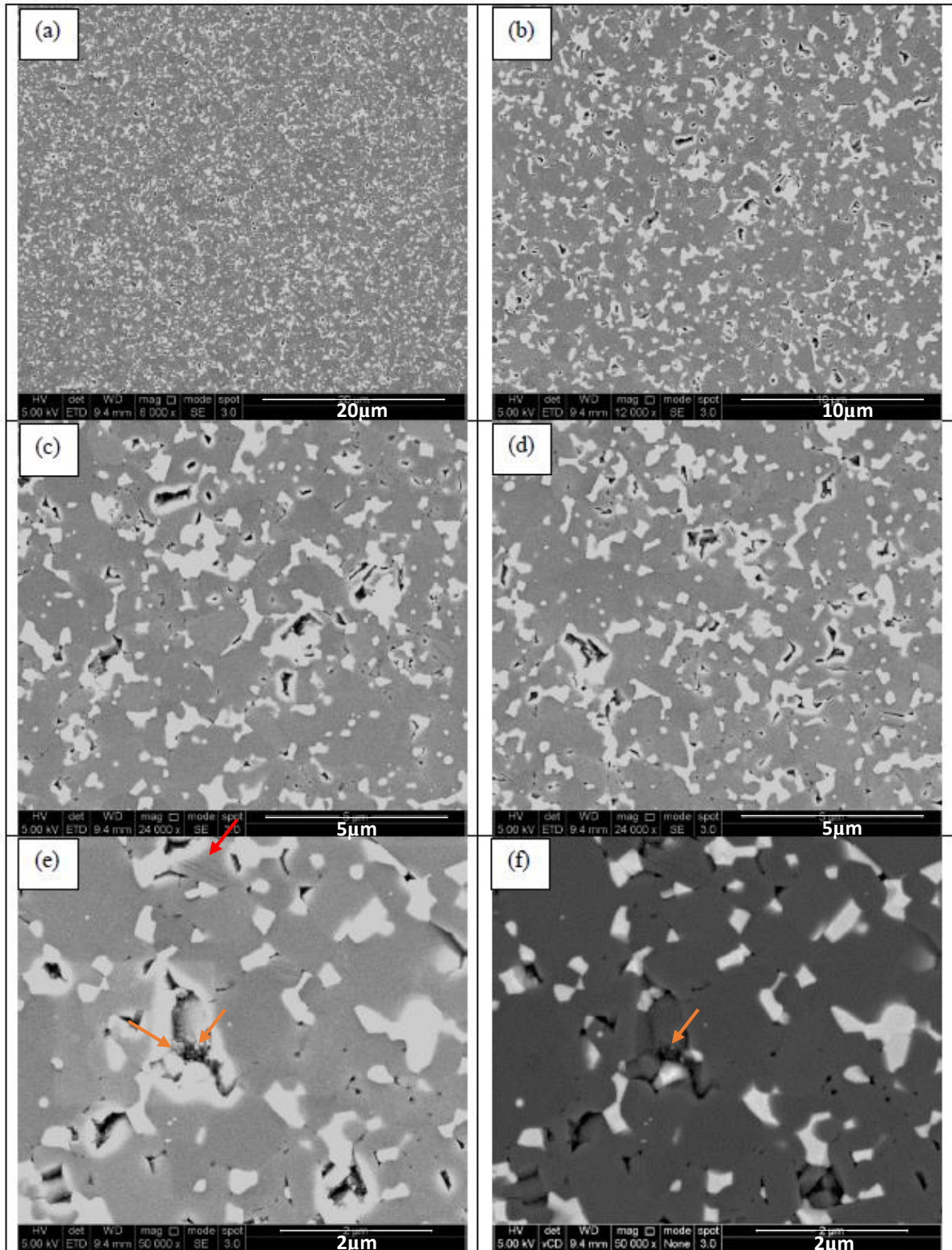


Figure 4.104. Secondary electron and backscattered electrons (f) SEM images of wear scars for ZTA+0.1 mole.% TiO₂ sample sintered at 1450°C for 5 minutes under the wear condition of 8N-24hr, representing transgranular fractured alumina grains with red arrows, and wear debris with orange arrows

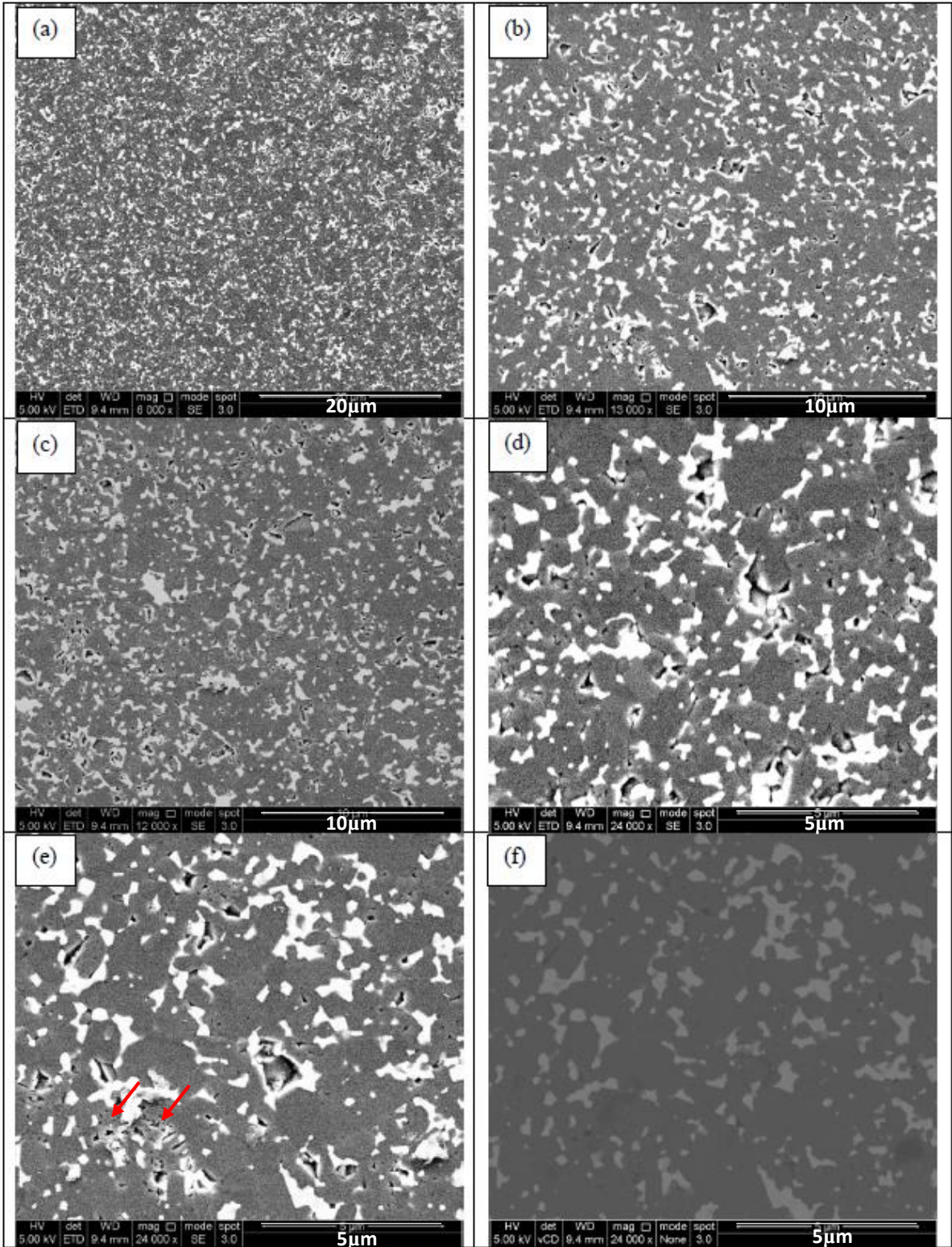


Figure 4.105. Secondary electron and backscattered electrons (f) SEM images of wear scars for ZTA+0.1 mole.% TiO₂ sample sintered at 1450°C for 5 minutes under the wear condition of 16N-8hr, representing transgranular fractured alumina grains with red arrows

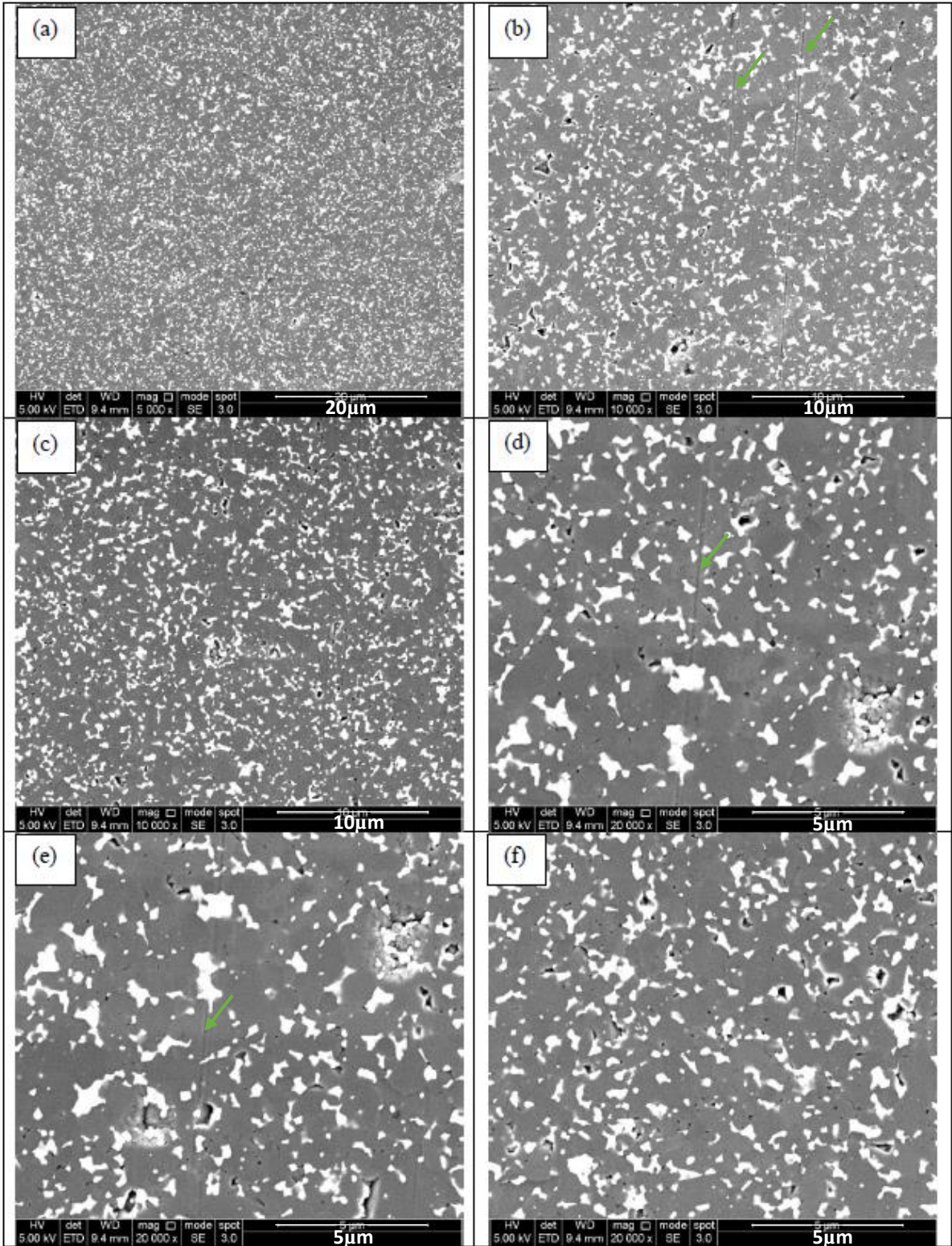


Figure 4.106. Secondary electron SEM images of wear scars for ZTA+0.1 mole.% TiO₂ sample sintered at 1500°C for 5 minutes under the wear condition of 4N-24hr, representing grooves with green arrows

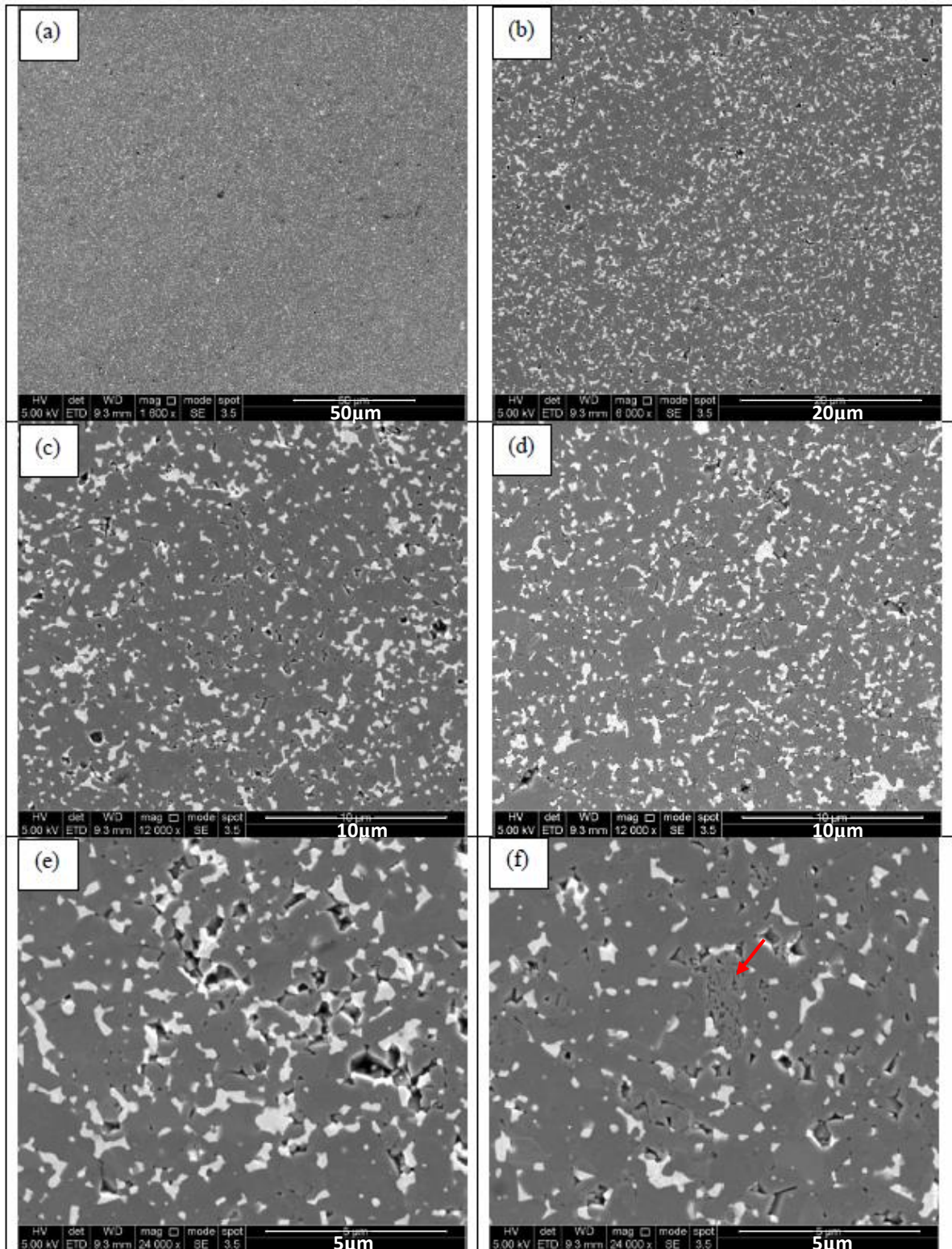


Figure 4.107. Secondary electron SEM images of wear scars for ZTA+0.1 mole.% TiO₂ sample sintered at 1500°C for 5 minutes under the wear condition of 8N-24hr, representing transgranular fractured alumina grains with red arrow

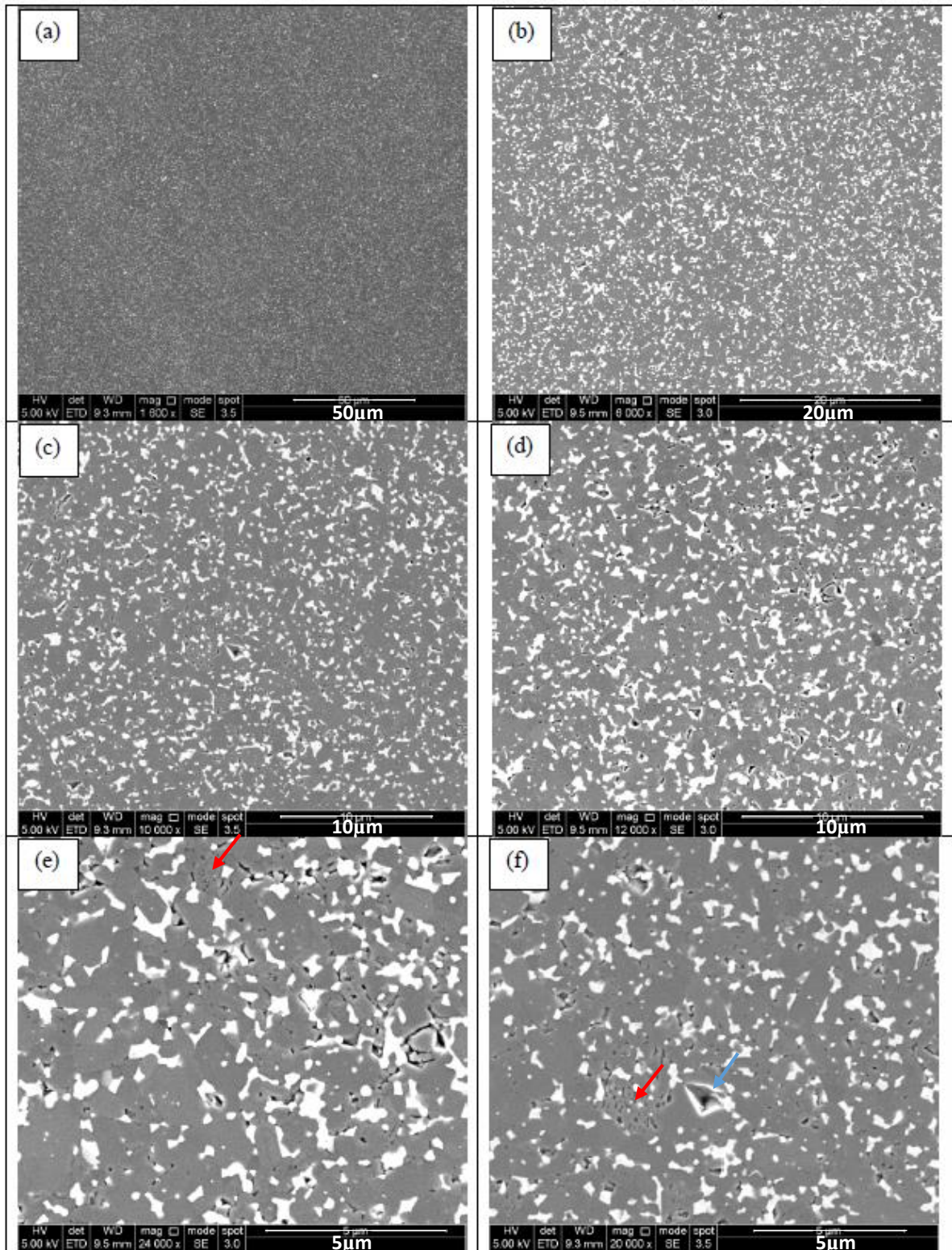


Figure 4.108. Secondary electron SEM images of wear scars for ZTA+0.1 mole.% TiO₂ sample sintered at 1500°C for 5 minutes under the wear condition of 16N-8hr, representing transgranular fractured alumina grains with red arrows, and grain pull-out with blue arrows

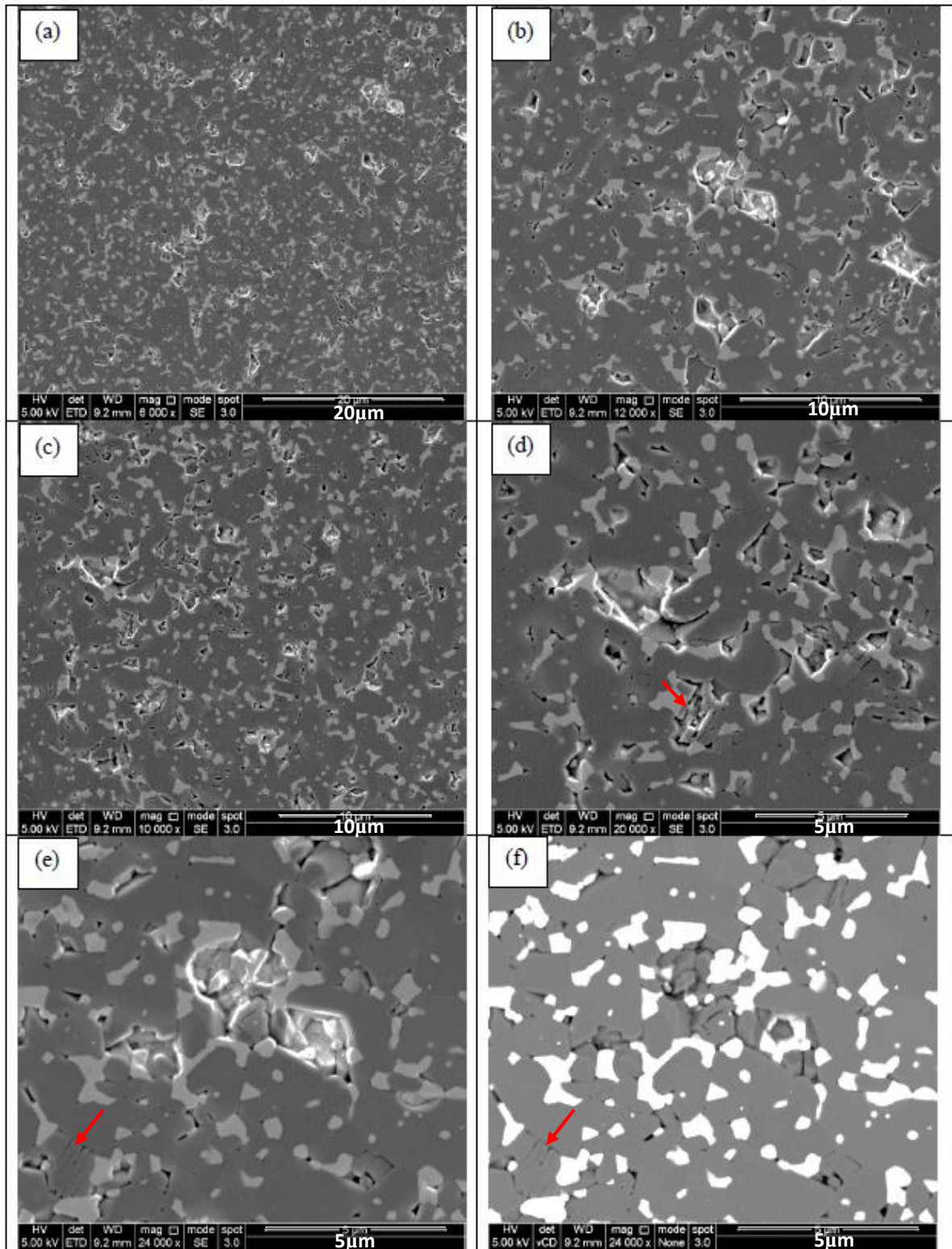


Figure 4.109. Secondary electron and backscattered electrons (f) SEM images of wear scars for ZTA+0.1 mole.% TiO₂ sample sintered at 1550°C for 5 minutes under the wear condition of 4N-24hr, representing transgranular fractured alumina grains with red arrows

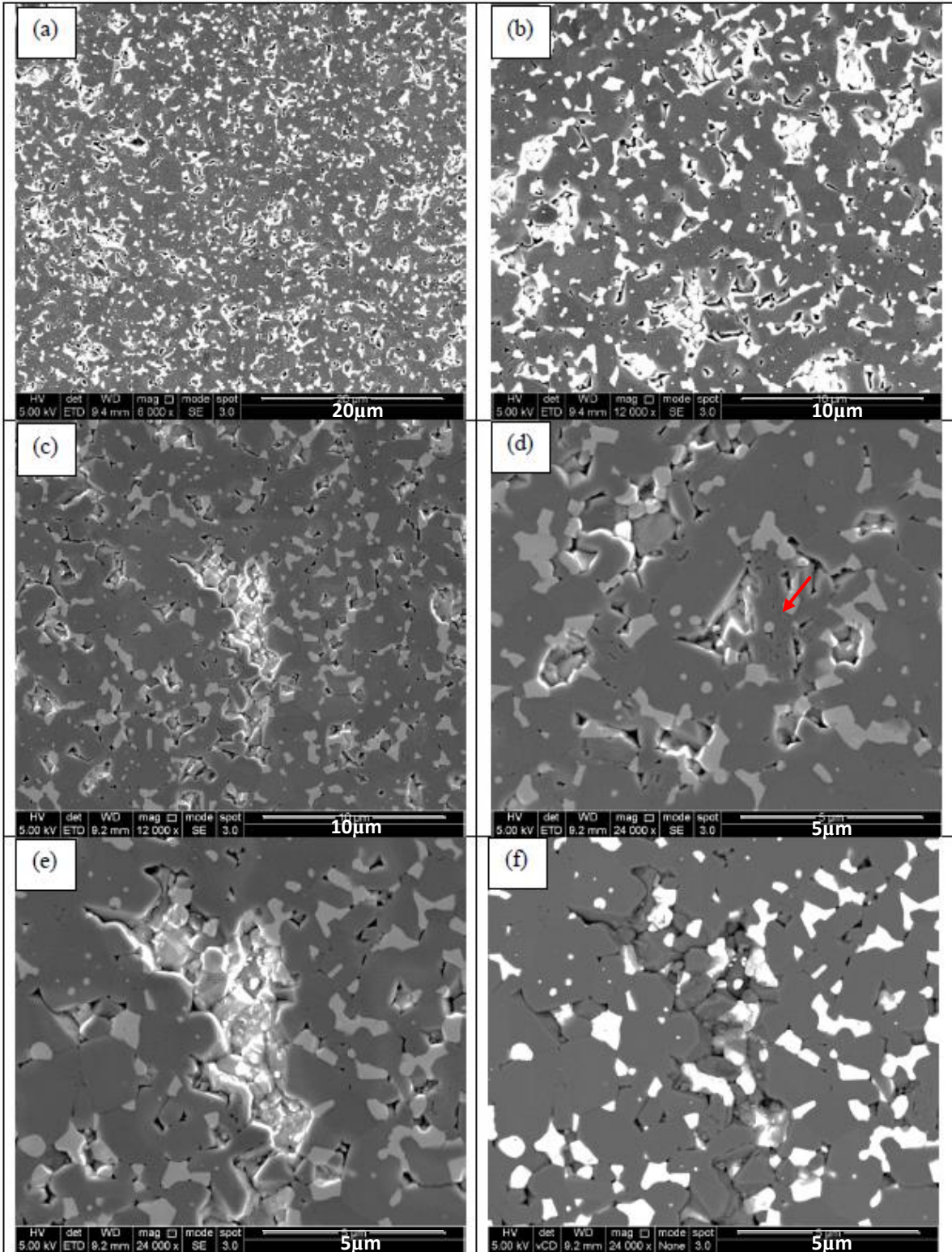


Figure 4.110. Secondary electron and backscattered electrons (f) SEM images of wear scars for ZTA+0.1 mole.% TiO₂ sample sintered at 1550°C for 5 minutes under the wear condition of 8N-24hr, representing transgranular fractured alumina grains with red arrow

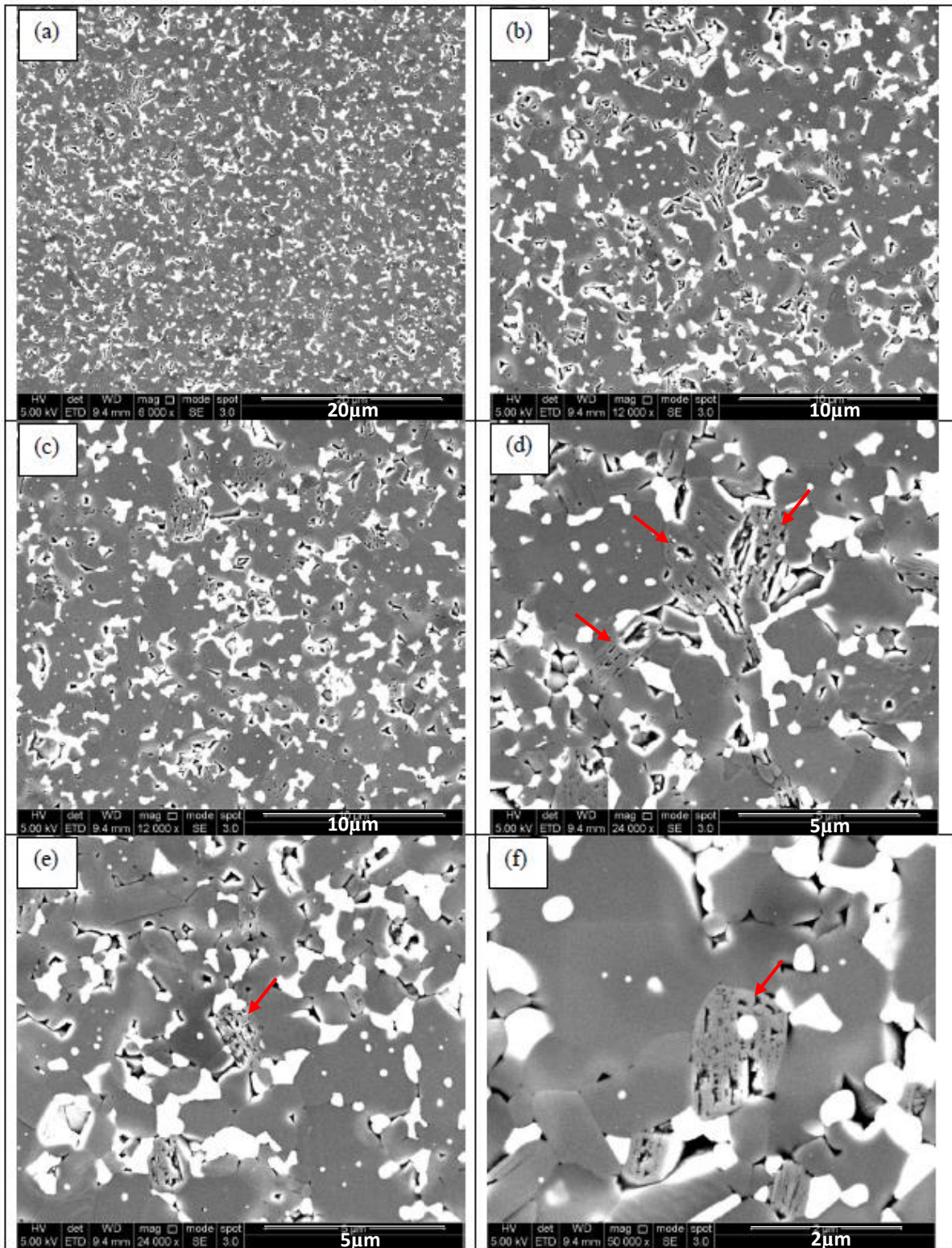


Figure 4.111. Secondary electron SEM images of wear scars for ZTA+0.1 mole.% TiO₂ sample sintered at 1550°C for 5 minutes under the wear condition of 16N-8hr, representing transgranular fractured alumina grains with red arrows

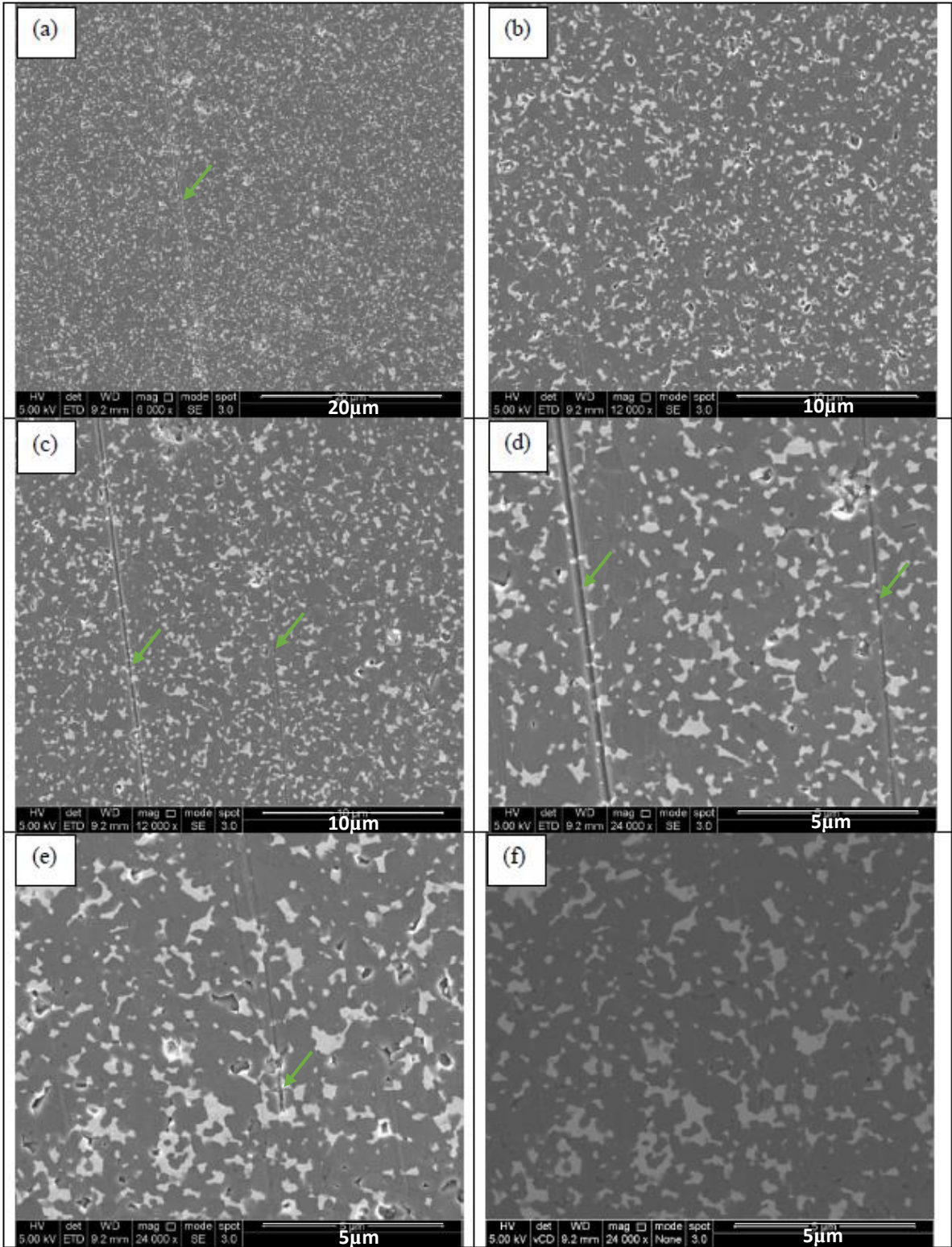


Figure 4.112. Secondary electron and backscattered electrons (f) SEM images of wear scars for ZTA+0.5 mole.% TiO₂ sample sintered at 1400°C for 5 minutes under the wear condition of 4N-24hr, representing grooves with green arrows

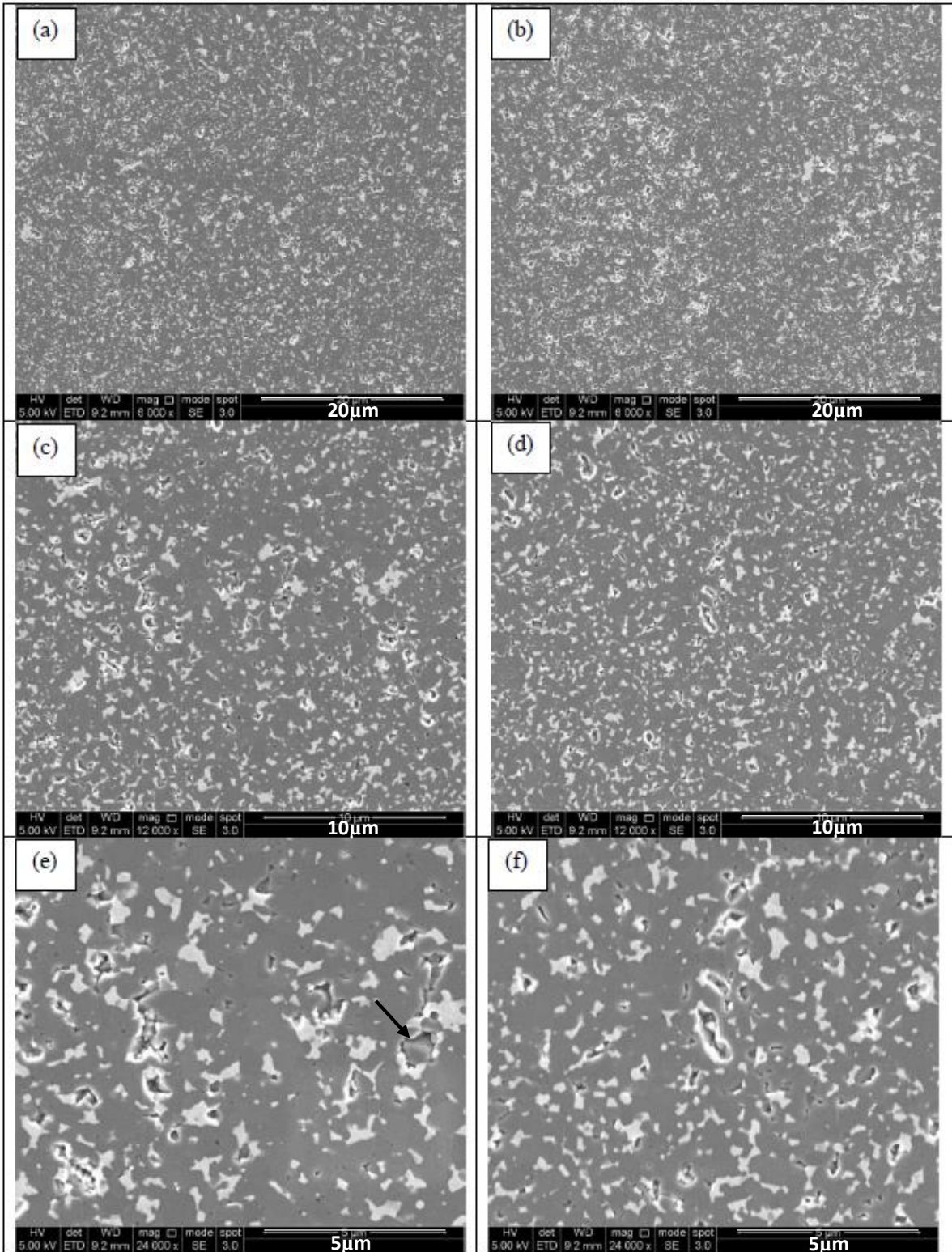


Figure 4.113. Secondary electron SEM images of wear scars for ZTA+0.5 mole.% TiO₂ sample sintered at 1400°C for 5 minutes under the wear condition of 8N-24hr, representing intergranular fracture with black arrow

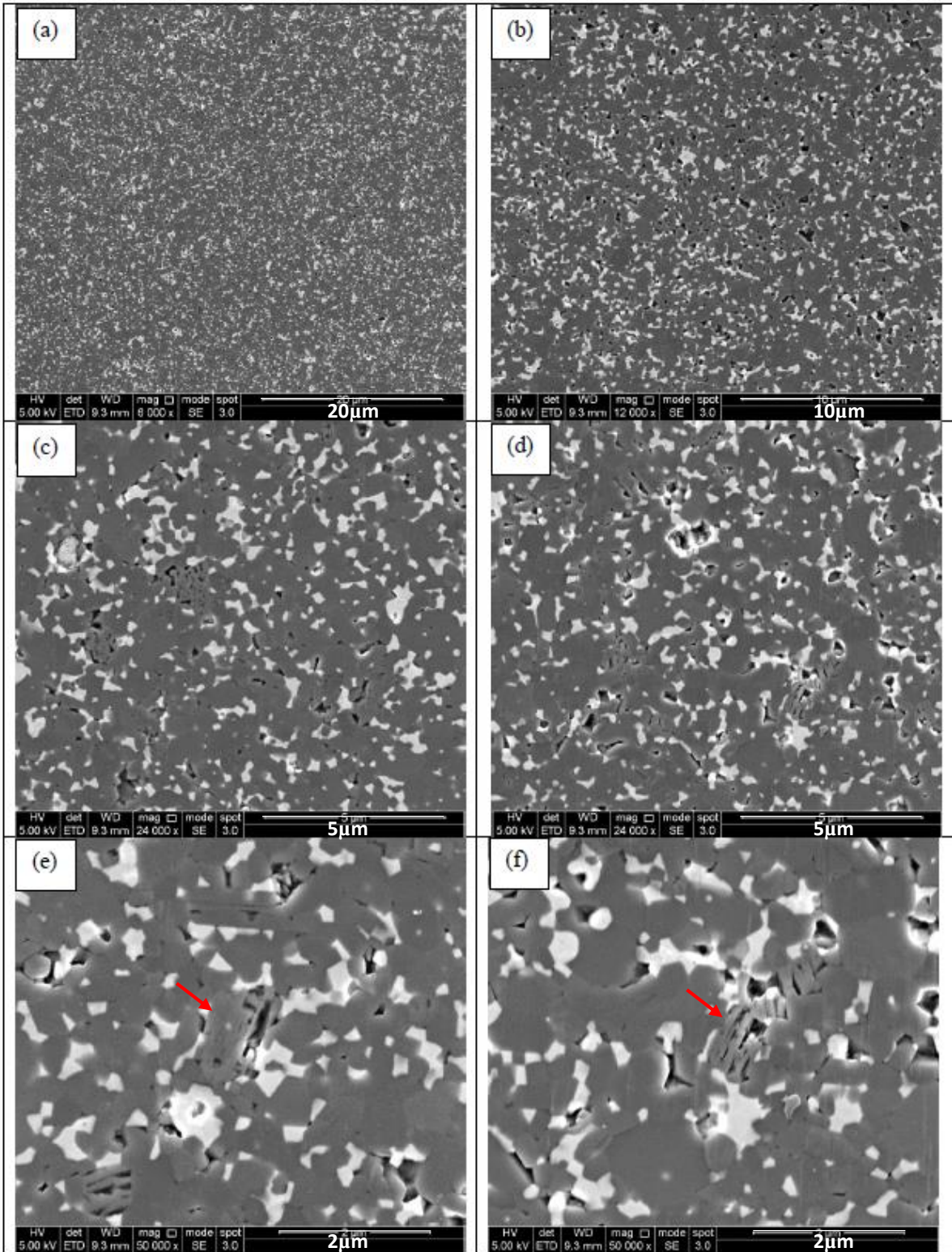


Figure 4.114. Secondary electron SEM images of wear scars for ZTA+0.5 mole.% TiO₂ sample sintered at 1400°C for 5 minutes under the wear condition of 16N-8hr, representing transgranular fractured alumina grains with red arrows

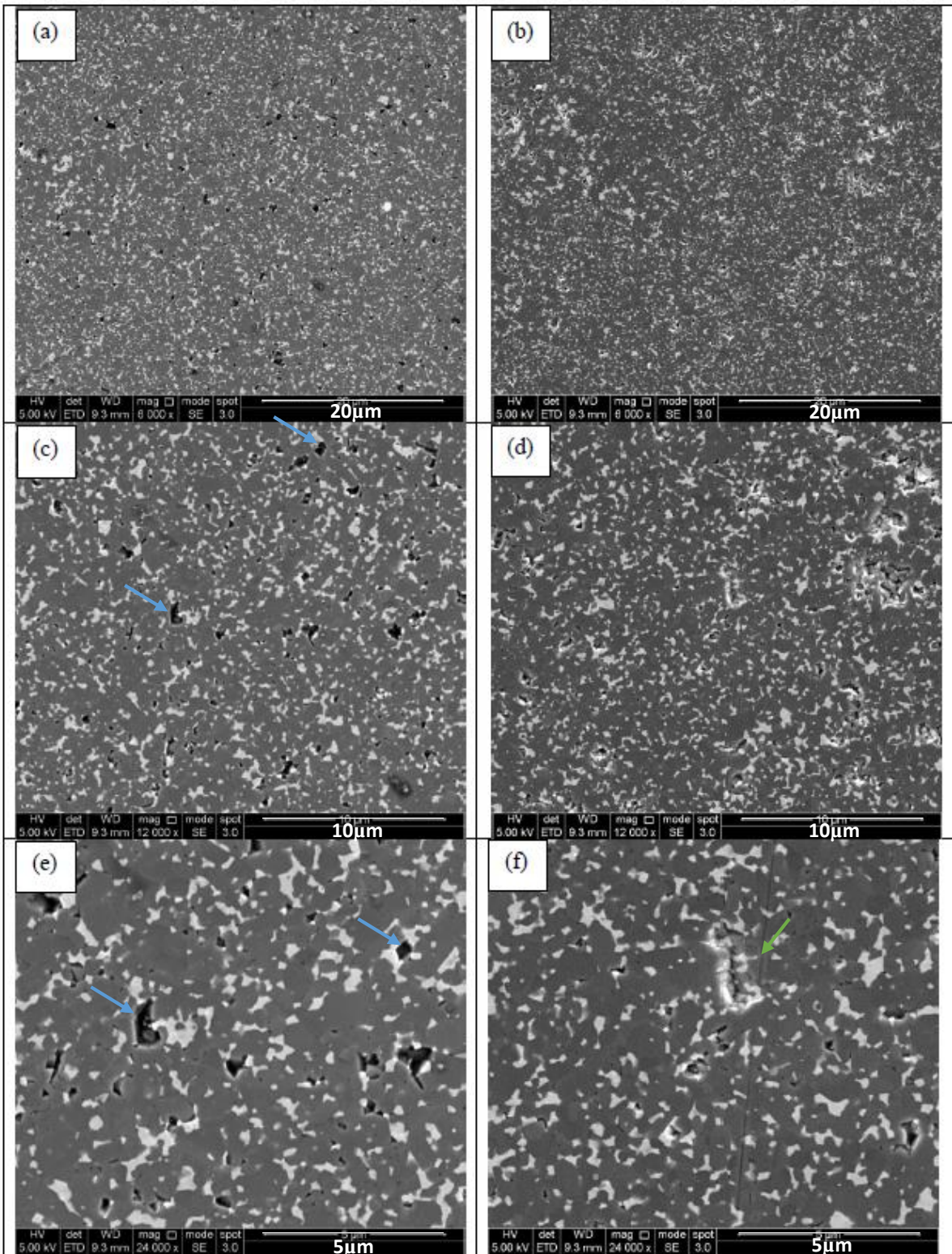


Figure 4.115. Secondary electron SEM images of wear scars for ZTA+0.5 mole.% TiO₂ sample sintered at 1450°C for 5 minutes under the wear condition of 4N-24hr, representing grain pull-out with blue arrows, and grooves with green arrows

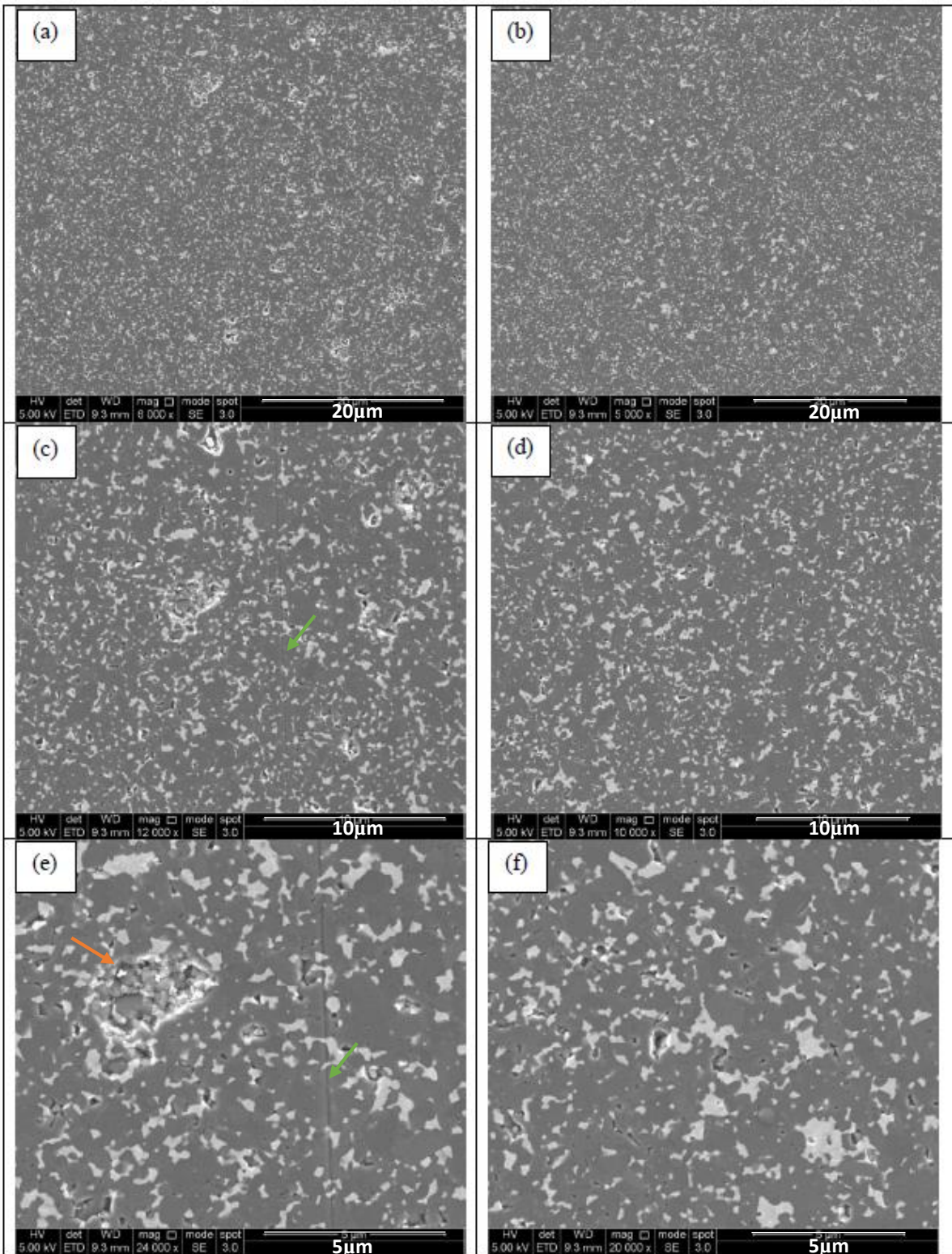


Figure 4.116. Secondary electron SEM images of wear scars for ZTA+0.5 mole.% TiO₂ sample sintered at 1450°C for 5 minutes under the wear condition of 8N-24hr, representing wear debris with orange arrow, and grooves with green arrows

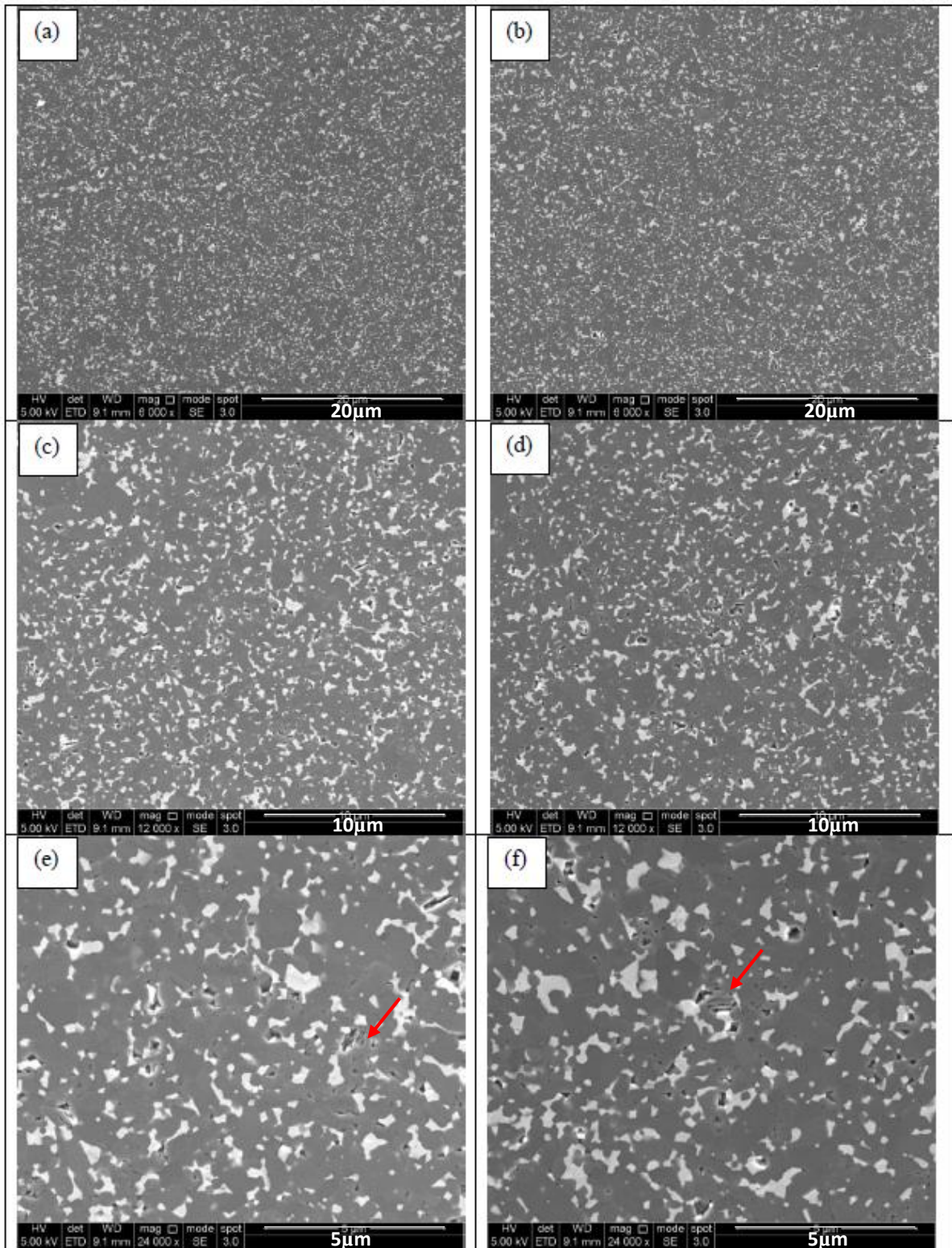


Figure 4.117. Secondary electron SEM images of wear scars for ZTA+0.5 mole.% TiO₂ sample sintered at 1450°C for 5 minutes under the wear condition of 16N-8hr, representing transgranular fractured alumina grains with red arrows

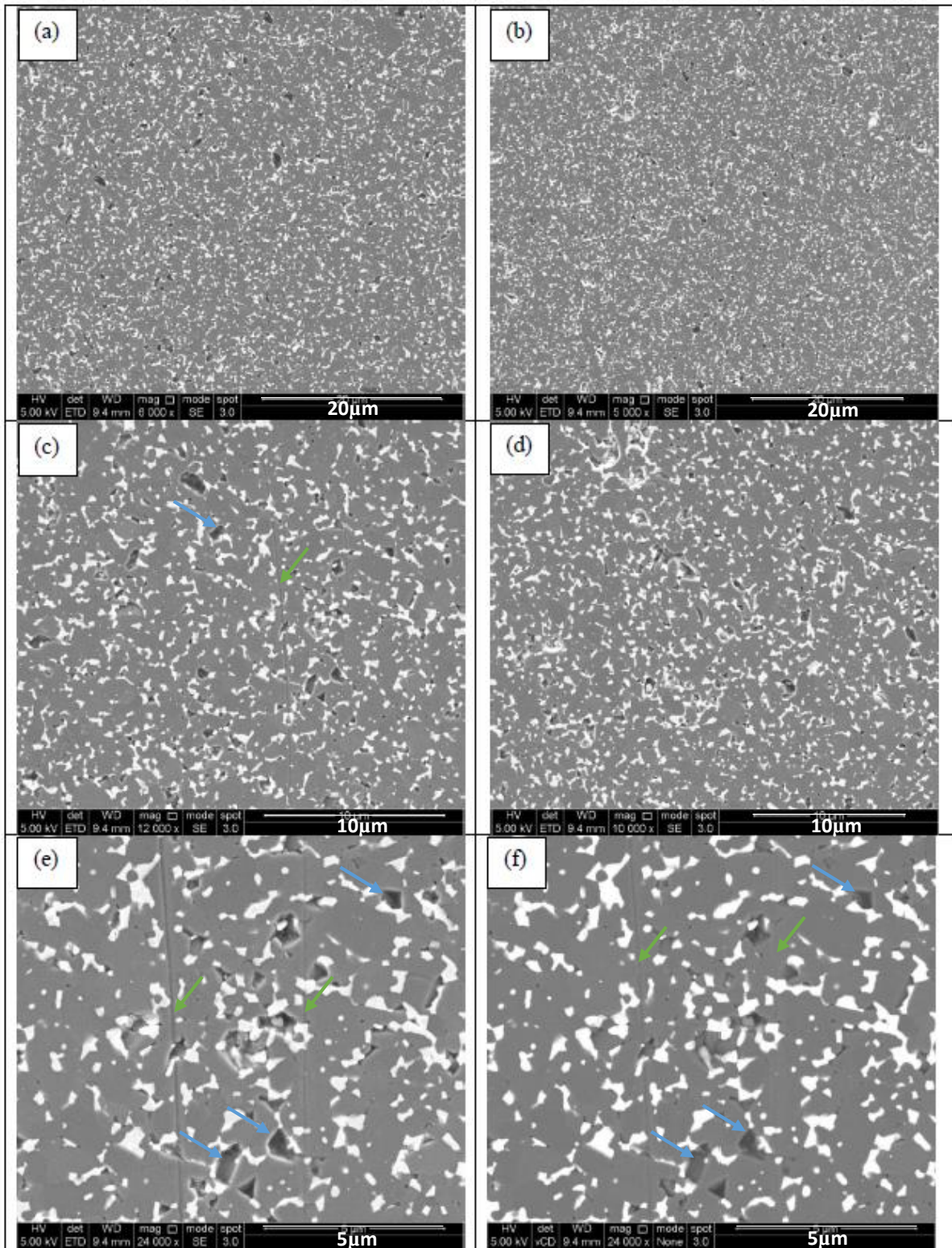


Figure 4.118. Secondary electron and backscattered electrons (f) SEM images of wear scars for ZTA+0.5 mole.% TiO₂ sample sintered at 1500°C for 5 minutes under the wear condition of 4N-24hr, representing grain pull-out with blue arrows, and grooves with green arrows

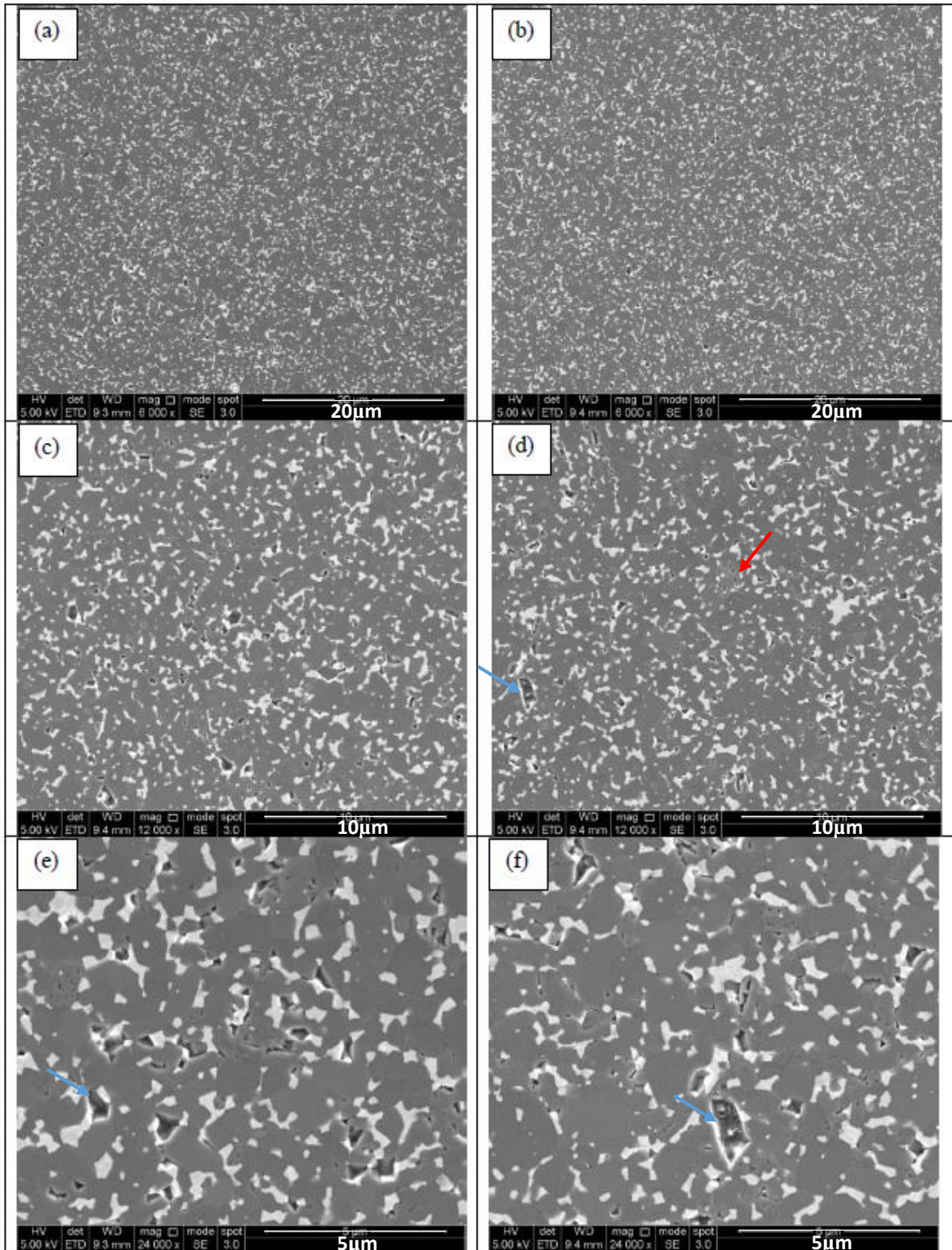


Figure 4.119. Secondary electron SEM images of wear scars for ZTA+0.5 mole.% TiO₂ sample sintered at 1500°C for 5 minutes under the wear condition of 8N-24hr, representing transgranular fractured alumina grains with red arrows, and grain pull-out with blue arrows

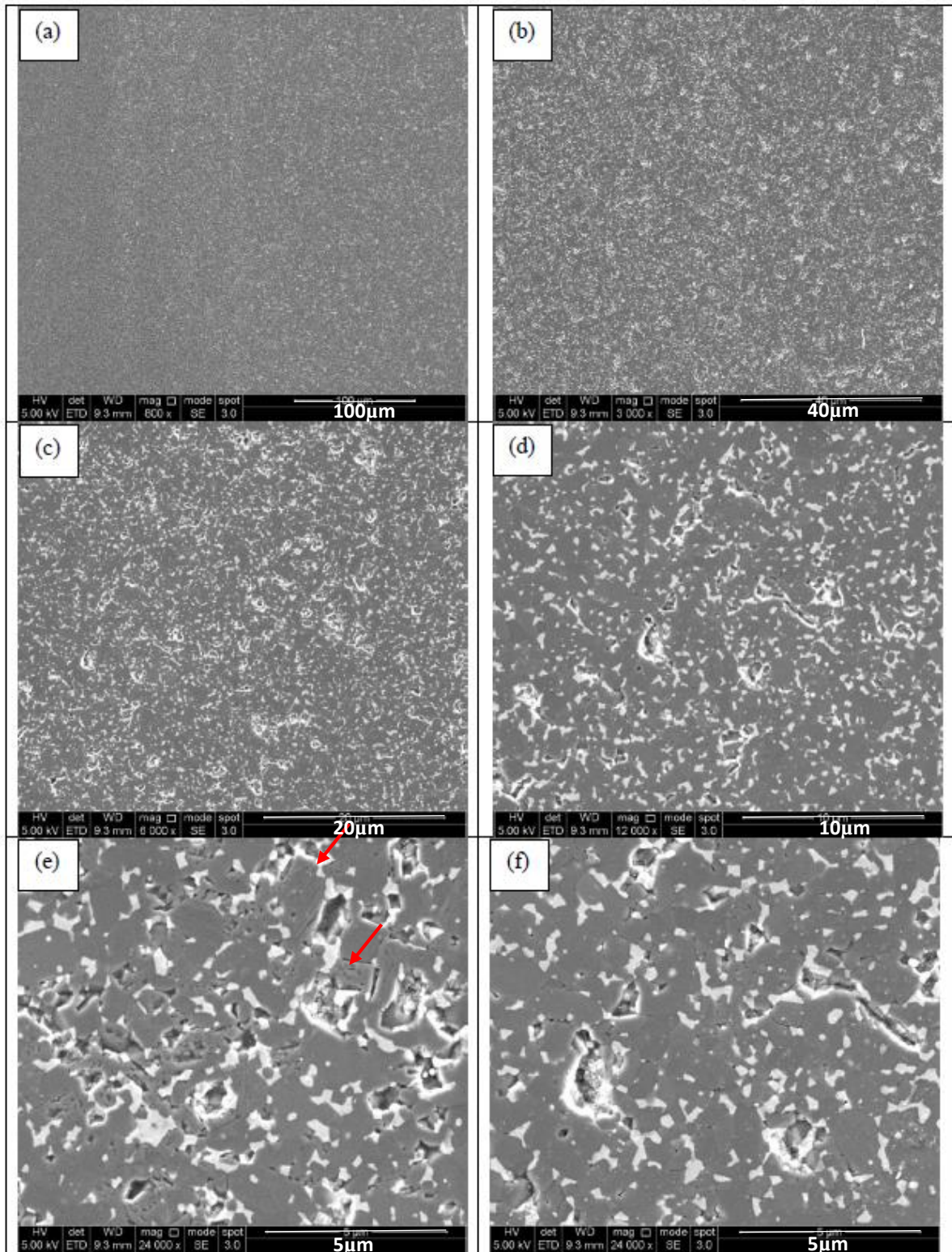


Figure 4.120. Secondary electron SEM images of wear scars for ZTA+0.5 mole.% TiO₂ sample sintered at 1500°C for 5 minutes under the wear condition of 16N-8hr, representing transgranular fractured alumina grains with red arrows

5. DISCUSSION

5.1. Sample Characterization

5.1.1. Relative density

Relative density is defined as “the ratio of the bulk density to the theoretical density often quoted as percentage theoretical density” where the theoretical density of a polycrystalline ceramic is calculated based on zero porosity (Lee & Rainforth, 1994). In processing the ceramics, it is highly preferable to achieve the full density or at least very close to full density of the material. Spark plasma sintering, which was used in this work, is one of the new processes proposed enabling ceramics and composites to be compacted rapidly to full density at low temperatures with short holding time (Garay, 2010; Zhan, et al., 2002; Shen, et al., 2002).

It is stated in Chapter 2, densification is based on mass transport and atomic diffusion in the solid state, which is driven by the kinetic energy of the atoms at higher temperature (Richerson, 2006). However, in SPS sintering, there are three other factors contributing to the rapid densification process: the application of a mechanical pressure, the use of rapid heating rates, and the use of pulsed direct current as explained before (Shen, et al., 2002). This leads to achieving higher relative density in comparison with pressureless techniques.

In this study, all the samples were reasonably dense having relative density more than 97.5% of the theoretical density, like that reported by Shen et al. (2002), Lee and Rainforth (1994), Borrell et al. (2013), Ormanci et al. (2014), and Borrell et al. (2014). This implies that in addition to mechanical pressure, the electric field and its effect on surface phenomena by modifying the grain boundary energy and interface kinetics is beneficial even in poorly conducting materials such as ZTA, as shown by Ghosh et al. (2009), Borrell et al. (2014), and Shen et al. (2002). This can be explained by the reported effect of electrical fields on cleaning the surfaces from absorbed species, activating the particle surfaces, improving surface reactivity, and finally enhancing the grain-boundary diffusion (Shen, et al., 2002; Borrell, et al., 2014; Ghosh, et al., 2009).

Similarly, improving the relative density at higher temperature (as shown in Figure 4.1) could be the result of two effects of densification in the SPS process, first through increasing the kinetics of the sintering process, second through increasing the electric discharge as a result of intensifying the applied pulses used for heating the samples. It should be noted that as the samples prepared were small in size, no tangible effects of the dwell time on the relative density were seen.

Comparing Figure 4.1.a to both Figure 4.1.b and Figure 4.1.c demonstrates that adding TiO₂ in small amounts of 0.1 and 0.5 mole.% to the composite improved sinterability and densification of the samples. It is clear in these figures that the relative density of the samples were all more than 99.92% of the theoretical density for samples containing TiO₂; while they were only more than 98.26% of the theoretical density for ZTA samples. The beneficial contribution of TiO₂ to compactness of alumina and zirconia ceramics and lowering sintering temperature was reported by Wahsh, et al. (2013), Wang et al (2008), Manshor, et al. (2015), Affatato et al. (2001), Ormanci, et al. (2014), Pandolfelli et al. (1991), Horn and Messing (1995), Kim et al. (2000), Hwang and Chang (1996), Osendi and Moya (1988), Wang et al. (2009), Yang et al. (2009), Borrell et al. (2013), and Pandolfelli et al. (1991).

The main reason for improved density in alumina composites has been attributed to effect of titania on increasing Al³⁺ vacancy concentration to maintain the charge neutrality, which results in an increase in intergranular diffusion and grain boundary mobility (Kim, et al., 2000; Hwang & Chang, 1996; Lartigue-Korinek, et al., 2006). It should be noted that results by researchers have confirmed that this vacancy concentration is dependent to the titanium content as they are generated by Ti⁴⁺ substituting for Al³⁺ as discussed before (Kim, et al., 2000; Hwang & Chang, 1996; Lartigue-Korinek, et al., 2006; Wang & Huang, 2008). The presence of liquid phase in the case of co-doping TiO₂ and SiO₂, as proposed by some researchers, could be another reason for the enhancing effect on densification by adding titania (Kim, et al., 2000), although in the current work the SiO₂ level seemed to be too low to consider this effect. The other theory, which might explain the improved density of the samples with increasing TiO₂, is based on anisotropic surface energies. This led to different morphologies of internal pores for titania doped alumina compared with undoped ones, which results in forming a stacking of elongated elementary bricks and removing intra-colony porosity leading to the faceted fully dense grains, shown in Fig. 2.11 (Lartigue-Korinek, et al., 2006).

The same results of enhanced sinterability by small additions of titania has been reported for zirconia ceramics and attributed to its effect on generating defects caused by increasing temperature or reducing conditions which promotes diffusion, and/or chemical changes in the bound nearest neighbors, which affect the diffusion rate, particularly of oxygen ions (Pandolfelli, et al., 1991; Horn & Messing, 1995; Kim, et al., 2000).

When the matrix of composite is made of both alumina and zirconia, based on the argument proposed by Hwang and Chang (1996), TiO_2 firstly goes into solution in zirconia grains rather than the alumina. In this case, $(\text{Zr,Ti})\text{O}_2$ might be reduced to $(\text{Zr,Ti})\text{O}_{2-x}$ in reducing atmosphere which generates the lattice defects and increases the diffusion and density (Hwang & Chang, 1996). Therefore, by increasing the TiO_2 content in the composite, more Ti ions will diffuse out of $(\text{Zr,Ti})\text{O}_{2-x}$ to the alumina and the more Ti^{4+} will be generated, which will improve the sintering of the composite (Hwang & Chang, 1996).

Figure 4.1.b and Figure 4.1.c illustrates that even a small addition of TiO_2 could improve sinterability and densification of the ZTA composites, which is consistent with Winkler et al. (1966) that even very small TiO_2 addition, around 0.1 to 0.2 mole% to Al_2O_3 will alter the effective diffusion constant by a factor of more than 100. The sintering additives and their effect on SPS sintering can also be explained through their contribution to increasing electrical conductivity, or additional electric fields as discussed above (Borrell, et al., 2013).

In samples containing 0.1 mole.% and 0.5 mole.% TiO_2 , the density peaked at 1500°C and then decreased at 1550°C . The same trend was reported by Yang et al. (2009) at 1550°C and Pandolfelli et al. (1990) at $1500\text{-}1600^\circ\text{C}$. They attributed the density reduction to grain growth, presence of liquid phase, or formation of new phases such as monoclinic zirconia, ZrTiO_4 or Al_2TiO_5 , and microcracking.

As discussed before, TiO_2 is dissolvable in both alumina and zirconia grains; therefore, the formation of both new phase of Al_2TiO_5 or ZrTiO_4 is possible according to section 2.3 of the literature review chapter. The sintering temperature for all samples in this work were above the eutectoid temperature of Al_2TiO_5 formation (1280°C) (Borrell, et al., 2013); however, according to researchers, the completion of Al_2TiO_5 formation is highly dependent on the sintering temperature and applied pressure as well as grain size (Duan, et al., 2004; Yang, et al., 2009; Borrell, et al., 2013; Winkler, et al., 1966; McKee & Aleshin, 1963; Bagley, et al.,

1970; Smothers & Reynolds, 1954; Cahoon & Christensen, 1956). It was also reported by Hwang and Chang (1996) that Al_2TiO_5 phase was only found in the specimen with 7.5 mole% TiO_2 in ZTA composites. On the other hand, formation of ZrTiO_4 has been reported by researchers at high amount of titania (higher than 15 mole.%) for temperatures above 980°C (Brown & Duwez, 1954; Pandolfelli, et al., 1991; Bannister & Barnes, 1986; Miao, et al., 2004).

Looking at XRD patterns of samples containing a larger amount of titania (Figure 4.3 and Figure 4.4) reveals that ZrTiO_4 and monoclinic tetragonal phase were formed and its formation got completed with elevating sintering temperature. Thus, one of the main possibilities for deterioration of density at 1550°C in samples with 0.1 and 0.5 mole.% could be formation of this phase or monoclinic zirconia because of higher kinetics of diffusion in SPS technique (Borrell, et al., 2013; Yang, et al., 2009), which resulted in forming macrocracks as reported by Yang et al. (2009), although it could not be detected by XRD because of its low content.

It is clear in Figure 4.1 that the beneficial effect of titania addition was only limited to small amount of it, and at higher content of 2 and 5 mole.% the relative density decreased to less than 98.5% for all sintering temperatures and times. The same trend has been reported by other researchers though their titania limit content had different values (Wang & Huang, 2008; Wahsh, et al., 2013; Manshor, et al., 2015). For instance, Wahsh et al. (2013) showed that the relative density was improved up to 5 wt.% of titania, and after that up to 25 wt.%, it remained constant. Wang and Huang (2008) reported that the decreased density beyond the composite solubility limit of 0.35 mole.% while Manshor et al. (2015) found the maximum density to be with the addition of 3 wt.% TiO_2 , which would start decreasing from the addition of 5 wt.% TiO_2 .

XRD patterns (Figure 4.3 and Figure 4.4) and SEM images (Figure 4.11 to Figure 4.17) confirm coarsening and formation of ZrTiO_4 in the samples containing 2 and 5 mole.% TiO_2 . Coarsening with its effect on suppressing densification due to its dominant grain growth mechanism resulted from its high surface diffusion coefficient could be detrimental for compactness, as illustrated in Figure 2.17 and described in chapter 2.3.1.2. Coarser microstructures would lead to forming microcracks due to higher thermal mismatch stresses and consequently has an adverse effect on the density (Horn & Messing, 1995; Kim, et al., 2000). The same argument could be explained for presence of new phases such as ZrTiO_4 and

its pinning effect for diffusion, lower density and higher thermal mismatch causing high pores and macrocracks due to shrinkage (Manshor, et al., 2015; López-López, et al., 2012; Wahsh, et al., 2013; Wang & Huang, 2008; Horn & Messing, 1995; Kim, et al., 2000). Presence of pores and macrocracks could be detected in SEM images of Figure 4.11 to Figure 4.14 by comparing different images of (d) and (e) with (a), (b), and (c) of each figure.

5.1.2. Phase analysis

XRD patterns of ZTA samples in this study demonstrated characteristic peaks of alumina and tetragonal zirconia and its representative spectrum is given in Figure 4.2.a. No traces of monoclinic phase could be found in these samples showing that using SPS techniques could inhibit transformation of tetragonal to monoclinic phase during cooling. Adding titania in small amounts of 0.1 and 0.5 mole.% resulted to the same XRD pattern as for the ZTA.

The results reported by Ormanci et al. (2014), Wang and Huang (2008), Schaedler, et al. (2008), Hwang and Chang (1996), Nawa et al. (1998) have revealed that at small additions of titania to ZTA ceramics, Ti^{4+} ions first diffuse into ZrO_2 phase to form $t-(Zr,Ti)O_2$ solid solution. Preferred dissolution of titania in zirconia rather than in alumina was related to its higher solubility limit in zirconia and easier accommodation of Ti^{4+} ions in zirconia crystals due to their isovalent cations and larger ionic radius in comparison with Al^{3+} ions (Schaedler, et al., 2008; George, et al., 2012; Nawa, et al., 1998; Nawa, et al., 1998). However, Figures 4.2.b and 4.2.c did not show measurable changes in XRD patterns with Figure 4.2.a, and it could not be concluded from these figures if Ti ions dissolved in the zirconia crystals and formed solid solution. However, tetragonal phase stability could be confirmed from Figure 4.2, which might be related to improved tetragonal phase stability due to lowering the transformation temperature and making a large area of tetragonal zirconia solid solution as illustrated in Figure 2.14 and Figure 2.15 (Schaedler, et al., 2008; Nawa, et al., 1998; Hwang & Chang, 1996; Brown & Duwez, 1954; Pandolfelli, et al., 1991; Noguchi & Mizuno, 1968; Chevalier & Gremillard, 2009).

XRD patterns of 2 and 5 mole.% titania (Figure 4.3 and Figure 4.4) shows new peaks characteristic of $ZrTiO_4$, which has the orthorhombic structure with space group of $\alpha-PbO_2$

and low melting point ($\sim 1840^\circ\text{C}$) (López-López, et al., 2012; George, et al., 2012; Cui & Shao, 2015; Schaedler, et al., 2008; Ormanci, et al., 2014). According to researchers, zirconia and titania could form mixed oxides of different types, but ZrTiO_4 is the only stoichiometric compound which is found under atmosphere pressure (Kim, et al., 2000; George, et al., 2012; Schaedler, et al., 2008). Formation of ZrTiO_4 at higher amount of titania addition, due to entering a high amount of Ti ions in zirconia lattice and their precipitation as ZrTiO_4 , was reported by Wahsh et al. (2013) for the titania amount of higher than 5 wt.%, by López-López et al. (2010) for 39.42 wt.%, by Ormanci et al. (2014) for 5 vol.%, by Wang and Huang (2008) for 2.0 and 4.0 wt.%, by Brown and Duwez (1954) for 15 to 45 mol.%, by Pandolfelli and Rodrigues (1991) in 17.9 and 21.5 mol.%, by Bannister and Barnes (1986) in 20.2, 22.5, and 29.6 mol.%, and by Miao et al. (2004) in 20 and 40 mol.% TiO_2 . The results of this study in finding the traces of ZrTiO_4 peaks in low titania addition, 2 and 5 mole.%, is more close to the results reported by Wahsh et al. (2013), Ormanci et al. (2014), and Wang and Huang (2008).

In addition to ZrTiO_4 characteristics peaks, monoclinic zirconia peaks could also be detected in samples containing 5 mole.% at all sintering temperature (Figure 4.4) and 2 mole.% at 1500°C and 1550°C temperatures (Figure 4.3.c and d). Although Ormanci et al. (2014) did not find any monoclinic zirconia in a Al_2O_3 -YSZ- TiO_2 system sintered by SPS technique and only confirmed formation of ZrTiO_4 and tetragonal zirconia solid solution, other researchers showed the presence of residual monoclinic zirconia associated with formation of ZrTiO_4 . They argued that TiO_2 solubility in tetragonal zirconia was more than that of monoclinic phase and resulted in formation of ZrTiO_4 plus monoclinic solid solution with lower titania content at eutectoid decomposition temperature due to diffusion of Ti ions in short distances (Borrell, et al., 2014; Brown & Duwez, 1954; Pandolfelli, et al., 1991; Bannister & Barnes, 1986; Noguchi & Mizuno, 1968; Pandolfelli, et al., 1990). This argue could be employed for this research in which appearance of ZrTiO_4 peaks are relatively in the same order of detection of monoclinic zirconia peaks.

It should be noted that no traces of aluminum titanate peaks were identified in this research, which might be due to low titania content. The existence of Al_2TiO_5 phase was reported by Hwang and Chang (1996) for the specimen with 7.5 mol.% TiO_2 (Figure 2.22), and by Wahsh et al. (2013) for titania content more than 10 wt.%. These amounts are considered to be higher than the solubility limit of zirconia and regarding amount of solubility limit at different temperature and varied phase diagrams reported by researchers, which was discussed in details

in section 2.3.1.2. However, in a study done by Manshor et al. (2015), no $ZrTiO_4$ phase was reported by addition of titania to ZTA, and except for alumina and tetragonal zirconia peaks, the only peaks which started to appear in XRD patterns after 5 wt.% of titania were Al_2TiO_5 peaks, which is in contrary with the results of this research. Similarly, Wang and Huang (2008) detected both $ZrTiO_4$ and Al_2TiO_5 in ZTA samples with 2 and 4 wt.% TiO_2 sintered at $1450^\circ C$, which was close to the titania amount and sintering temperatures of this study while the results were different.

5.1.3. Microstructure characterization

The microstructures of ZTA with different titania amounts are shown in Figure 4.11 to Figure 4.14, which are clearly characterized by the presence of two specific and recognizable phases, which, as stated in Chapter 2, do not react with each other to form a solid solution (Thompson & Rawlings, 1990).

As discussed before, one of the main concerns about using ZTA in artificial joints is hydrothermal degradation of zirconia, which leads to deterioration of the mechanical properties and wear resistance of the composite. Aging of zirconia is highly sensitive to the presence of aggregates since if one of the zirconia grains transforms to the monoclinic phase, the neighboring zirconia grains inside aggregates will then transform by nucleation-growth mechanism and the whole aggregate would be transformed (Nogiwa-Valdez, et al., 2014; Nogiwa-Valdez, et al., 2013). This might even happen at the temperatures below the transformation temperature and percolation threshold of zirconia content, and cause extensive microcracking during cooling, and allow water to penetrate inside the component due to interconnected network of cracks (Gutknecht, 2007).

Comparing microstructures for different TiO_2 content shown in Figure 4.11 to Figure 4.14 demonstrates more agglomeration of zirconia particles and less homogeneous microstructure by increasing amount of titania to 2 and 5 mole.%, especially at lower sintering temperature. The same inhomogeneity in size and morphology of ZTA microstructure by adding titania was reported by Manshor et al. (2015). The cause of this inhomogeneous microstructure with increase in titania content could be related to the mixing step of processing. In this research,

the first batch of zirconia was prepared by attrition milling in methanol, which gave poor distribution and relatively high agglomeration of zirconia and alumina particles in the composites. Then, the electrostatic dispersion technique proposed by Gutknecht et al. (2007), Wang and Stevens (1989), and De Aza et al. (2002) for ZTA composites was adopted. The principle of this technique is based on using the electrostatic repulsive forces proceeding from a charged electric particles formed in the acidic atmosphere. To estimate the electrostatic effect, the electrokinetic or zeta potential measurement is used which is responsible for the repulsive forces between the particles and controls the suspension stability, in which high zeta potentials and low viscosity indicate that suspensions are very well dispersed (Gutknecht, 2007; Chera, et al., 2007). Based on the findings of Gutknecht et al. (2007) and Wang and Stevens (1989), the acidic pH (~4-5) with its highest zeta potentials and lowest viscosity for both alumina and zirconia powders was adopted for this study.

The microstructure figures show that although this method resulted in favourable uniformity and homogeneity for ZTA samples and for samples containing less titania amount ((a), (b) and (c) of Figure 4.11 to Figure 4.14), it would not be appropriate for higher addition of titania. This could be related to the changes of zeta potential and corresponding viscosity due to presence of Ti ions, which is out of scope of this research.

Grain growth was found in this work by increasing the sintering temperature and time for all samples (Figure 4.5 to Figure 4.9). This is the result of temperature activating process of atomic diffusion and grain boundary movement caused by reducing the grain boundary area and lowering the energy of system to a more stable state (Lee & Rainforth, 1994; Richerson, 2006). The ultimate rate controlling process for grain coarsening in ZTA samples is attributed to the rate at which an individual ZrO_2 particle could migrate, which is dependent on the interfacial zirconia-alumina diffusion kinetics, and is increased with increasing sintering temperature and time (Wang, 1989). The comparison of alumina and zirconia grain sizes for all samples (Figure 4.5 to Figure 4.9) reveals that the rate of grain coarsening for alumina was more than for zirconia grains. This can be related to the greater volume fraction of alumina phase and shorter effective diffusion path length of alumina atoms in comparison with the zirconia.

It should be noted that although the discharge process in SPS is more effective in the first stage of sintering, the grain-boundary diffusion and grain-boundary migration processes have been found to be enhanced in the presence of the electric field (Shen, et al., 2002). This indicates

why the grain growth is fast in the SPS process above a certain critical temperature in comparison with the conventional pressureless sintering (Shen, et al., 2002).

Figure 4.10 shows that the average grain sizes for both alumina and zirconia were increased by increasing the amount of TiO_2 . The same increasing trend in grain sizes of both Al_2O_3 and ZrO_2 by raising TiO_2 content was reported by Hwang and Chang (1996), Wang and Huang (2008), Ormanci et al. (2014), Yang et al. (2009), and Borrell et al. (2013), though Manshor et al. (2015) reported reduction of grain sizes by increasing of titania addition from 3 wt.% to 5 wt.%.

The same argument discussed in section 5.1 for improved density of ZTA composites by adding small amount of TiO_2 would be applicable here. As stated before, adding titania could beneficially affect the grain growth by increasing the intergranular diffusion and grain boundary mobility through increasing amount of defects (Kim, et al., 2000; Hwang & Chang, 1996; Lartigue-Korinek, et al., 2006; Miao, et al., 2004), or by forming a liquid phase at the grain boundaries facilitating the diffusion rate (Kim, et al., 2000), or by removing intra-colony porosity and forming a stacking of larger elongated grains (Lartigue-Korinek, et al., 2006).

The SEM images for samples with small amount of titania ((b) and (c) in Figure 4.11 to Figure 4.14) show that the addition of TiO_2 changed the shape of grains and grain boundaries. On the thermally etched surface, the grains were more faceted after adding TiO_2 , while in ZTA samples the microstructure was more flat and leveled. This phenomenon is a result of differences in surface energies, in which surface diffusion occurs with atoms migrating from higher energy region to lower energy region causing formation of grain boundary morphology and growth steps, ultimately leading to curved grain boundaries to minimize interfacial energy (Yin, et al., 2009; Chinn, 2002; Geels, 2006). Therefore, TiO_2 probably changed the surface and kinetic energy for atom diffusion causing formation of etching grooves, which is detectable in the SEM images of samples containing titania (e.g. Figures 4.13.c and 4.14.e). The development of the grain boundary grooves is dependent on the equilibrium conditions for the interfacial tensions between the solid phases, which are in contact with the surrounding atmosphere (Kebbede, et al., 1997).

Another feature which is more detectable for samples containing 2 and 5 mole.% TiO_2 ((c) and (d) in Figure 4.11 to Figure 4.17) is increased porosity, mainly on grain boundaries and triple points. One possibility for the porosity is the presence of liquid phase during sintering process.

The presence of liquid phase in alumina composites containing titania was reported by Kebede et al. (1997), Horn and Messing (1995), Kim et al. (2000), Kwon et al. (2002), and was attributed to lower ternary eutectic temperature or accumulation of impurities at the boundaries which became liquid after heat treatment (Kwon, et al., 2002; McKee & Aleshin, 1963). In zirconia composites, Pandolfelli et al. (1990) reported the presence of glassy phase at triple points which was increased by increasing sintering temperature, and was collected on the surface as a result of capillary forces. Another possibility is the formation of a new phase associated with volume changes and induced cracks and microcracks. The formation of a new phase in samples containing 2 and 5 mole.% titania was confirmed by XRD results discussed above, which was $ZrTiO_4$. Backscattered electron images of their microstructure shows that in addition to the alumina (dark contrast) and zirconia grains (light contrast), a number of grains with a mid grey contrast could be detected in ZTA+2 mole.% and ZTA+5 mole.% TiO_2 , shown in Figure 4.15 and Figure 4.16. It also can be seen from these figures that at lower temperature, e.g. 1400°C, the new phase is difficult to detect while in higher sintering temperature, e.g. 1550°C, it is easily visible.

BSE images of samples containing 5 mole.% titania (Figure 4.16) shows the stages at different sintering temperature, which can be assumed as the completion stages of $ZrTiO_4$ formation. $ZrTiO_4$ formation started within zirconia grains (Figure 4.16.c and d, and Figure 4.17) and at high temperature of 1550°C, it was completed to form a grain due to high diffusion kinetics at this temperature (Figure 4.16.d). This kind of $ZrTiO_4$ formation can be related to the higher concentration of Ti ions at the centre of $(Zr,Ti)O_2$ grains, as reported by Hwang and Chang (1996), which decreases to the grain boundaries, as illustrated in Figure 2.23 and 2.24. Thus, it seems that when the amount of Ti ions exceeds their solubility limit in zirconia, formation of $ZrTiO_4$ phase begins. On the other hand, solubility of Ti ions is less in monoclinic phase than in tetragonal phase, and since diffusion of Ti^{4+} ions from the matrix to the $ZrTiO_4$ occurs over a short distance, it would be monoclinic phase which is surrounded $ZrTiO_4$ grains. This is completely in agreement with the XRD results of this study and very similar to the results reported by Pandolfelli et al. (1990) in zirconia-titania-ceria system. Interestingly, Pandolfelli et al. (1990) claimed that when this formation is not complete, $ZrTiO_4$ regions are formed within the grains, which could be detected in this work in high magnification BSE image demonstrated in Figure 4.17.

It has been discussed in Chapter 2 that one of the main advantages caused by adding TiO_2 to alumina is producing the anisotropic grains, which are embedded in an equi-axed matrix. However, the microstructures studied in this work did not exhibit any particular anisotropic alumina grains or in-situ fibres. This might be attributed to dissolution of Ti ions mostly in zirconia, and formation of zirconium titanate phase, which reduce the effect of titania on alumina grains. It is notable that elongated grains in microstructure for alumina-zirconia composites have not been reported by most of researchers working on the addition of titania to this composites such as Nawa et al. (1998), Hwang and Chang (1996), Osendi and Moya (1988), and could only be restricted to alumina ceramics. Similarly, no traces of aluminum titanate or Al_2TiO_5 was found on the microstructure images, which is in contrast with the results reported by Manshor et al. (2015) about presence of elongated Al_2TiO_5 grains for more than 3 wt.% addition of titania to ZTA ceramics.

5.1.4. Hardness and toughness characterization

It is clear that mechanical properties of the ZTA composites are strongly related to size, size distribution and location of zirconia particles as well as stabilization of tetragonal zirconia (Hwang & Chang, 1996; Osendi & Moya, 1988), and as titania affects all of these microstructural features it is expected to impact these properties to significant extent.

Figure 4.18 to Figure 4.21 and Table 4.7 to Table 4.11 show the effect of sintering temperature and time on hardness and toughness of the samples. For ZTA samples, hardness values were between 16.3 ± 0.3 GPa for 1550°C and 10 minutes, and 18.1 ± 0.9 GPa for 1450°C and 3 minutes sintering conditions. Figure 4.18 shows that although the values were very close, the trend seems to be lower hardness for higher temperatures and dwell time. This can be related to microstructure coarsening and its effect on formation of microcracks at grain boundaries during cooling. It should also be noted that low sintering temperature will give greater porosity and decreased density, as discussed before, which is expected to decrease the hardness. These two factors, working in opposite ways, result in increases or decreases in hardness by increasing temperature and dwell time.

Hardness values of samples containing 0.1 mole.% titania were very close and in a range of 17.2 ± 0.8 to 18.0 ± 0.6 GPa, which is higher than the values of ZTA samples and in a good agreement with high relative density of these composites (Figure 4.1). This confirms the beneficial effect of small additions of titania on improving density and subsequently improving hardness of ZTA samples, which has been reported by other researchers (Beaule, et al., 2006; Antonio, et al., 2002; Benzaid, et al., 2008; Nawa, et al., 1998; Hwang & Chang, 1996; Yang, et al., 2009; Wang & Huang, 2008; Manshor, et al., 2015; Wahsh, et al., 2013; Borrell, et al., 2014). In addition to the effect of titania on densification of ZTA ceramics, improved hardness have resulted from increasing the cohesion between grains of alumina, titania and zirconia, as well as purifying and strengthening the phase interfaces and/or the grain boundaries as shown by Yang et al. (2009). In agreement with these results, slight hardening was reported by Nawa et al. (1998) for titania addition up to 0.5 mol.% (Figure 2.31.b), attributed to higher amount of transgranular nanodispersion (Beaule, et al., 2006; Nawa, et al., 1998).

Figure 4.20 shows that the hardness curve moved slightly downward comparing to Figure 4.18 and Figure 4.19, showing the slight decrease of hardness with addition of more titania content to ZTA composites. In these samples containing 0.5 mole.% TiO_2 , by neglecting the value of 14.8 ± 2.1 GPa with its high standard deviation, the hardness values were in the range of 16.4 ± 0.2 GPa for 1550°C and 5 minutes to 17.7 ± 0.5 GPa for 1400°C and 7 minutes. Since the relative density of samples containing 0.5 mole.% titania were found to be in the same range of samples with 0.1 mole.%, and are more than 99% (Figure 4.1), the slight decrease of hardness values can be attributed to their coarser microstructure, as shown in Figure 4.7 and Figure 4.11 to Figure 4.14.

The same range of hardness values for samples containing 2 mole.% titania was obtained for sintering for 5 minutes, from 16.4 ± 1.7 GPa to 17.9 ± 1.2 GPa, Figure 4.21 and Table 4.10. However, for the samples with higher amount of titania, 5 mole.%, Vickers hardness was reduced significantly and was in the range of 14.3 ± 0.7 GPa to 15.8 ± 0.9 GPa, as shown in Figure 4.21 and Table 4.11. As discussed before, XRD and SEM results of samples containing 2 and 5 mole.% TiO_2 confirmed formation and evolution of a new phase, found to be ZrTiO_4 , which could be cause of the reduction in Vickers hardness for these samples. ZrTiO_4 has lower elastic modulus and hardness in comparison with zirconia (Miao, et al., 2004; Wang & Huang, 2008; Ormanci, et al., 2014; Borrell, et al., 2014; Osendi & Moya, 1988). Evolution of forming ZrTiO_4 along with the effect of coarsening with its associated microcracks (Yang, et al., 2009)

could be the causes for lower hardness values at higher temperatures, as can be seen in Figure 4.21, particularly for 2 mole.% titania addition.

These results are in a good agreement with the results by Ormanci et al. (2014) who reported the reduction of hardness from 20.7 GPa to 16.9 GPa with the addition of 5 wt.% titania to ZTA samples of 10 vol.% YSZ. They attributed the decreased hardness to the formation of $ZrTiO_4$ phase with its hardness value of 8 GPa. Correspondingly, Wang and Huang (2008) found the same hardness for ZTA and ZTA samples containing 0.5 wt%, similar to the results of this study for ZTA and ZTA+0.5 mole.% TiO_2 , while when the titania content in their work was 2 and 4 wt.%, a gradual decrease of hardness resulted from the presence of $ZrTiO_4$ and/or Al_2TiO_5 . Similarly, Manshor et al. (2015) results presented the maximum hardness with the addition of 3 wt.% TiO_2 , which was decreased by higher addition of titania due to formation of secondary elongated phase of Al_2TiO_5 .

The effect of additives and sintering conditions on toughness of composites is very complicated due to different, and sometimes contradictory mechanisms, as discussed before. These various mechanisms work in different ways to increase or decrease the toughness based on the intrinsic characteristics, volume fraction, shape, and dispersion of the second phase as well as the microstructure of the ceramic composite. In nanoscale composites, it would even get more complex since the materials show different properties when they are in nanometer sizes.

The fracture toughness values for ZTA samples were very similar and in a range of 4.9 ± 0.2 $MPa \cdot m^{1/2}$ and 5.8 ± 0.2 $MPa \cdot m^{1/2}$, as shown in Figure 4.18 and Table 4.7, which was higher than the fracture toughness of monolithic alumina (~ 4 $MPa \cdot m^{1/2}$). These values for samples containing 0.1 and 0.5 mole.% titania were slightly higher with the range of 5.4 ± 0.2 $MPa \cdot m^{1/2}$ to 6.2 ± 0.5 $MPa \cdot m^{1/2}$, and of 5.1 ± 0.2 $MPa \cdot m^{1/2}$ to 5.9 ± 0.1 $MPa \cdot m^{1/2}$ respectively.

Considering toughening mechanisms discussed in section 2.1.1.3, four main mechanisms can be involved in ZTA composites including stress-induced transformation toughening, crack deflection, microcracking, and compressive surface stresses.

The effect of higher sintering temperature and dwell time to toughness could be due to coarsening and its associated effects on toughening mechanisms. When zirconia grain size passes the critical size for t-to-m transformation, i.e. around $0.4 \mu m$ as reported by Trune

(2008), the toughness can be increased by increasing the contribution of stress-induced transformation mechanism to the total toughness of the material. For alumina grains, there is a disagreement among researchers about the toughening mechanism and their changes with microstructure (Kuntz, et al., 2004; Casellas, et al., 2003; Evans, 1990; Guazzato, et al., 2004; Rice, 1996; Mussler, et al., 1982). Despite the fact that crack deflection toughening mechanism is greater in coarse microstructures and improve toughness of the composite through deflecting the path of propagating crack (Thompson & Rawlings, 1990), the microcracking mechanism seems to contribute to toughening in the opposite way. As discussed before, microcracks are generally induced by the combined action of thermal residual stress and applied stress field at the crack tips, particularly in multiphase material with different thermal expansion coefficients between the phases. The presence of these microcracks deflects or branches out the main crack as well as dissipating the fracture energy and shielding stress at the crack tip, which increases the toughness (Lee & Rainforth, 1994; Kuntz, et al., 2004). As these microcracks are typically generated at grain boundaries (Kuntz, et al., 2004), their lower length and higher dispersion in finer microstructures would results in the higher fracture toughness.

In ZTA samples, the combination of these two possible opposing toughening mechanisms might be the cause of absence of an appreciable change in toughness as a function of grain size (Figure 4.18.b). It should be noted that the grain size of zirconia in ZTA samples did not exceed 350 nm even at higher temperature and time in this study (Figure 4.5.a); thus, the transformation toughening mechanism does not seem to play an important role in the samples without TiO₂, as was discussed by Kuntz et al. (2004) showing serious doubts about feasibility of transformation toughening mechanism in nanoceramic composites.

In samples containing 0.1 and 0.5 mole.% titania, toughness values were slightly increased, especially in 0.1 wt.% TiO₂ (Figure 4.19.b), in which all obtained values for fracture toughness were more than 5.4 MPa.m^{1/2}. It also can be seen from Figure 4.18, Figure 4.19, and Figure 4.20 that although the curve is relatively flat for ZTA samples, there is a trend of increasing toughness with increasing temperature for samples containing TiO₂. The increase in toughness values for samples containing 2 mole.% was more visible, reaching 5.9±0.3 MPa.m^{1/2} to 7.8±0.8 MPa.m^{1/2}. Improved toughness by titania additions is in agreement with results has been reported by several researchers (Lee, et al., 2003; Nawa, et al., 1998; Horn & Messing, 1995; Nawa, et al., 1998; Osendi & Moya, 1988; Hwang & Chang, 1996; Wang & Huang, 2008; Yang, et al., 2009; Manshor, et al., 2015; Ormanci, et al., 2014). For instance, Wang and

Huang (2008) found that the low toughness of $4.4 \text{ MPa}\cdot\text{m}^{1/2}$ for ZTA without additives could be improved to $5.2 \text{ MPa}\cdot\text{m}^{1/2}$ (corresponding to 18%) after only 0.5 wt.% TiO_2 addition, and Manshor et al. (Manshor, et al., 2015) reported increasing the fracture toughness from $5.93 \text{ MPa}\cdot\text{m}^{1/2}$ (0 wt.% TiO_2) to $6.56 \text{ MPa}\cdot\text{m}^{1/2}$ (3.0 wt.% TiO_2) in ZTA composites.

The improvement of toughness for samples containing small amounts of titania could be related to the effect of titania on microstructure and tetragonal retention of zirconia. By adding TiO_2 to the composite, the tetragonal to monoclinic transformation temperature becomes lower making a large range of composition having the tetragonal zirconia, as demonstrated by Figure 2.14 and 2.15 (Brown & Duwez, 1954; Hwang & Chang, 1996; Pandolfelli, et al., 1991). Thus, the transformation toughening mechanism that seems to be negligible in case of ZTA composite, might be more significant for samples containing titania as a result of greater transformability of tetragonal zirconia (Ormanci, et al., 2014). This effect can explain the relatively higher toughness for samples with TiO_2 , which is raised by increasing sintering temperature and coarsening of zirconia grain sizes, as can be seen in rising curves of Figure 4.19.b and Figure 4.20.b. However, some researchers such as Nawa et al. (1998), Osendi and Moya (1988), and Pandolfelli et al. (1990) cast doubt on the beneficial effect of tetragonal stabilization on toughness and argued that small amount of titania (less than 1 mole.% as reported by Nawa et al (1998)) would degrade toughness due to high stabilization of tetragonal phase and its resistance to stress induced transformation.

In addition, the addition of titania can affect crack deflection and alteration of crack path, especially when the fracture mode is predominantly intergranular. Different researchers have pointed out the beneficial effect of titania on increased toughness due to crack deflection mechanism in alumina and zirconia composites (Lee, et al., 2003; Nawa, et al., 1998; Horn & Messing, 1995; Nawa, et al., 1998; Osendi & Moya, 1988; Hwang & Chang, 1996; Wang & Huang, 2008; Manshor, et al., 2015). Moreover, it was suggested by Chevalier and Gremillard (2009) that in micro-nano-composites, as in this study, presence of large residual compressive stresses around the zirconia nanoparticles (up to 150MPa compressive stress in the alumina grains with only 1.7 vol.% zirconia transgranular particles) plays an important role. Residual stresses are highly dependent to the volume fraction, the size and the location of the zirconia particles, for example the zirconia particles at grain boundaries would not give rise to the residual stresses (Chevalier & Gremillard, 2009). This effect was also considered by Hwang and Chang (1996) as the main role of titania effect on toughening of ZTA composites in

absence of transformation toughening. It is notable that by using SPS technique, as was used in this work, higher stresses might concentrate at grain boundaries, which limit extensive crack growth and would result in higher toughness (Borrell, et al., 2014).

Despite the increased values of toughness for ZTA samples by titania added up to 2 mole.%, further addition seems to be associated with lowering the toughness as can be seen in Figure 4.21.b. The range of toughness for ZTA+5 mole.% TiO₂ composite was from 5.4±0.3 MPa.m^{1/2} to 6.8±0.7 MPa.m^{1/2}, which was relatively higher than those for ZTA, ZTA+0.1mole.% and ZTA+0.5 mole.% TiO₂, but less than toughness values of ZTA+2 mole.% TiO₂. This is in contrast with Hwang and Chang's (Hwang & Chang, 1996) study, which showed that ZTA samples with 5.5 mol.% titania had higher strength and toughness in comparison with samples having 1.5, 2.5, as well as 7.5 mol.% TiO₂ (Figure 2.30). Similarly, Ormanci et al. (2014) found that samples containing 5 wt.% titania had higher fracture toughness in comparison with samples with 3 wt.%.

The main difference of samples containing 5 mole.% (and relatively 2 mole.%) with other samples in this study was the formation and evolution of new phase of ZrTiO₄. As reported by Miao et al. (2004), and Osendi and Mayo (1988) and illustrated in Figure 2.21.b, formation of ZrTiO₄ with its poorer mechanical properties in comparison to Y-TZP can degrade toughness of zirconia composites. Thermal expansion anisotropy, which is a characteristics of ZrTiO₄ crystals, could develop extensive microcracking after cooling process (López-López, et al., 2012; Borrell, et al., 2014; López-López, et al., 2015). Evolution of ZrTiO₄ formation associated with its induced microcracks, along with its coarser microstructure and associated higher microcracking (Osendi & Moya, 1988) can be the causes for descending graph of toughness by increasing temperature for samples containing 2 and 5 mole.% TiO₂ (Figure 4.21.b).

Figure 4.22 and Figure 4.23 show the hardness and toughness values for different amount of titania addition. The opposite effect of the amount of titania on hardness and toughness values is clearly demonstrated in these two figures. Specifically, in Figure 4.23 with more obtained data, it is noticeable that the titania addition improved toughness significantly although it affects hardness adversely. The maximum and minimum hardness measured for the whole range of samples was for ZTA sintered at 1450°C for 3 minutes (18.1±0.9 GPa) and ZTA+0.5 mole.% TiO₂ sintered at 1400°C for 5 minutes (14.8±2.1 GPa) respectively. The maximum and minimum toughness found for all samples was recorded for ZTA+2 mole.% TiO₂ sintered at

1450°C for 5 minutes ($7.8 \pm 0.8 \text{ MPa}\cdot\text{m}^{1/2}$) and ZTA sintered at 1450°C for 7 minutes ($4.9 \pm 0.2 \text{ MPa}\cdot\text{m}^{1/2}$).

As discussed above, improvement and degradation of toughness can be related to different involved toughening mechanisms; thus, studying the crack path after indentation can provide more clear evidences for understanding the dominant mechanism. In Figure 4.24 the crack propagated in ZTA shows relatively linear path, mostly intergranular, as well as some crack bridging, which were due to fine microstructure of the samples. In some of the indentations, two cracks were developed near the indent (Figure 4.24.d). Relatively similar crack propagation could be detected for sample containing 0.1 mole.% titania as can be seen in Figure 4.25. Figure 4.26 show a linear crack path in low magnification for 0.5 mole.% titania addition sample, while it shows more deflection in high magnifications and a few transgranular fracture which were mainly due to its coarser microstructure.

In Figure 4.27 and Figure 4.28 it is clear that crack propagation was highly deviated from its original path and the cracks propagates over a more tortuous path due to the coarser microstructure. This suggests that the higher toughness values obtained for 2 and 5 mole.% titania could be related to their dominant crack deflection mechanism, which consume higher energies to propagate. On the other hand, despite the crack path seems mostly intergranular in Figure 4.27, some transgranular crack propagation, especially in larger grains, was visible in Figure 4.28, which along with the macrocracks detectable in the neighboring area around the crack could be the reasons for lower toughness values of 5 mole.% titania samples in comparison to samples containing 2 mole.%.

Crack propagation mechanisms similar to those found in this work have been reported by other researchers (Wang & Huang, 2008; Manshor, et al., 2015; Borrell, et al., 2014). For instance, Wang and Huang (2008) showed linear crack and tortuous path for ZTA samples with and without titania addition, and concluded that since toughness increased proportionally to the grain size the dominant toughening mechanism should be attributed to the crack deflection effect. They also attributed intergranular pattern for fracture of these composites to the weaker grain boundary bonding effect after titania addition.

5.2. Wear characterization

5.2.1. Friction

Friction of two contacting materials, as stated before, is a very complicated physical phenomenon which includes elastic and plastic deformation between two surfaces, microfracture, interaction of wear debris and particles, chemical reactions, excitation of electrons and phonons, and adhesion of two contacting surfaces (Popov, 2010). The coefficient of friction (COF), which is a dimensionless value, is widely used to explain the ratio of friction force and normal force between two contacting objects (Budinski, 2014). The values listed in Table 4.12 and shown in Figure 4.31 indicates that the COF in this work were in the range 0.001-0.032, which are slightly lower than the values reported for ceramic-on-ceramic bearings in artificial hip joints as reported by Jin et al. (2006) and shown in Table 2.2. These values were very close to COF range under 0.5, 1, 2 and 4N load and similar lubricant reported by Ma (2010) to be around 0.002–0.015 for ZTA composites and by Shirkhan (2014) to be around 0.002-0.041 for zirconia ceramics. The values reported by other researchers for alumina and zirconia ceramics were in a wide range of 0.007 ± 0.003 by Saikko (1993), 0.05-0.08 by Scholes, et al. (2000), and 0.06 by Scholes and Unworth (2000) for bovine lubricated surfaces; 0.07-0.2 by He et al. (1993), 0.12-0.16 by Wang et al. (1995), and 0.0019-0.73 by Lee et al. (1993) for purified paraffin oil lubricated conditions; 0.0019-0.83 by Lee et al. (1993), 0.15 by Barceinas-Sánchez and Rainforth (1998), 0.52-0.61 by He et al. (1997), 0.13 by Rainforth (1996), and 0.3 by Kato (1990) in water lubricated systems; 0.12-0.44 by Rainforth (1996), 0.45-0.55 by Kerkwijk et al. (1999), 0.45-0.8 by Kerkwijk et al. (1999), 0.68-0.76 by He et al. (1997), 0.06-0.26 by Esposito et al.(1998), 0.47-0.85 by Kerkwijk et al. (2004), 0.41-1.15 by Zum Gahr et al. (1993), 0.35-0.7 by Dey and Biswas (2009), 0.2-0.6 by Wang and Hsu (1996). 0.4 by Rainforth and Stevens (1993), 0.5-0.98 by Kato (1990), and 0.5-0.70 by Lee et al. (1993) for unlubricated surfaces.

Variations of COF in different samples and under varied wear condition, as can be seen in Figure 4.31, is difficult to explain due to complicated factors affecting friction, most of them related to the running system conditions. Particularly, when the values are very low like the results of this work, the small changes in friction appear large on this scale. However, the trend of COF variations, Figure 4.31, demonstrates relatively higher COF in samples containing titania in comparison with the ZTA samples. As stated in Chapter 2, metal oxide additions such

as CuO and MgO, ZnO, B₂O₃, and MnO₂ and also SiC can affect friction in alumina and zirconia ceramics due to modification of microstructure, formation of self-lubricated surfaces, and formation of tribofilms or compacted layer of wear debris (Rainforth, et al., 2002; Rainforth, 2004; Kerkwijk, et al., 2004; Rainforth & Stevens, 1993).

In this study, the effect of titania addition in COF can be related to protein precipitation on the surface which could make a solid-like tribofilm and its presence on the worn surfaces can be confirmed from AFM images (Figure 4.52) and Raman studies (Figure 4.89 and 4.90). In fact, as stated by Ma and Rainforth (2012), Brown and Clarke (2006), Lu and McKellop (1997), Lu et al. (1999), Shirkhan (2014), the protein of bovine serum could be absorbed by the ceramic surfaces and play solid-like film role, which strongly affect the friction. The protein absorption process is a complex process and highly dependent to many factors such as pH, temperature, concentrations of ions and molecules on the surface, the degree of hydrophilicity of the surface, the electrostatic interactions of the protein molecules with each other and with the surface, and the structural stability of the protein molecules, and etc. (Kurrat, et al., 1997; Amadeu do Serro, et al., 1999). Fukuzaki et al. (1996) examined protein absorption on surfaces of different ceramic oxides in various conditions and concluded that electrostatic nature of metal oxides' surfaces, particularly the surface charge density, can extremely affect absorbed amount of protein. Thus, it can be argued that Ti ions might change the surface charge density resulted in higher protein absorption and higher viscosity of solid-like tribofilm led to higher COF values. This is in agreement with the experimental observation of this research in which cleaning the wear scar surface and removing the tribofilm for the samples containing titania were more challenging than cleaning ZTA samples. Although increased COF found in this research was in contrast with the results reported by Key and Biwas (2009) and Morillo et al. (2009) who observed lower friction in case of titania addition, it can confirm relationship of higher COF to protein absorption since none of the mentioned studies were conducted in bovine lubricated system. It should be noted that adsorption of protein on the surface of alumina and zirconia ceramics was observed by Ma (2010) and Shirkhan (2014), although Ma (2010) reported its thickness to be around 20 nm for ZTA ceramics, the tribofilm thickness found in this study was around 100 nm (Figure 4.52).

5.2.2. Wear rate

There was a wide range in the specific wear rate in this study of $2.47\text{E-}09$ to $3.7\text{E-}07$ mm^3/Nm , Table 4.13, which are in the range of specific wear rate reported by Jin et al. (2006) for ceramic-ceramic bearings of hip joint replacements as shown in Table 2.2, and very close to the wear rate of natural synovial joints which is around $\text{E-}09$ mm^3/Nm , as suggested by Dowson (2000). In similar studies investigated on alumina, zirconia and ZTA by Rana (2013), Shirkhan (2014), and Ma (Ma, 2010), the wear rates were calculated at 0.5, 1, 2 and 4 N load in bovine lubricated system. Thus, the results of this study only could be compared with their reported values at 4 N load. These values were $1\text{E-}06$ mm^3/Nm for alumina by Rana (2013), $8\text{E-}08$ mm^3/Nm for zirconia by Shirkhan (2014), and $1.33\text{E-}08$ mm^3/Nm for ZTA by Ma (2010). Similarly, Wang et al. (1995) reported the minimum wear rate in order of $\text{E-}06$ mm^3/Nm for alumina and $\text{E-}07$ mm^3/Nm for alumina with 15 vol.% zirconia in paraffin oil lubricated system. Other values reported by researchers were $\text{E-}07$ mm^3/Nm by Huang et al. (2008) for alumina, $8.9\text{E-}04$ mm^3/Nm for zirconia and $3\text{E-}08$ mm^3/Nm for ZTA in water lubrication by Rainforth (1996), $1.8\text{E-}04$ mm^3/Nm for unlubricated zirconia by Rainforth and Stevens (1998), $4\text{E-}07$ to $8\text{E-}06$ mm^3/Nm for unlubricated alumina and $3\text{E-}04$ to $7\text{E-}04$ mm^3/Nm for unlubricated zirconia by Kato (1990), $\text{E-}02$ to $\text{E-}07$ mm^3/Nm for zirconia in paraffin oil lubricated conditions by Lee et al. (1993), $0.36\text{E-}07$ to $1.04\text{E-}07$ mm^3/Nm for alumina and zirconia composites in water lubrication and $0.1\text{E-}06$ to $78.8\text{E-}06$ mm^3/Nm in dry condition by He et al. (1997), $1.28\text{E-}06$ to $3.40\text{E-}06$ mm^3/Nm for ZTA composites in dry sliding by He et al. (1997), $0.5\text{E-}06$ to $1\text{E-}04$ mm^3/Nm for unlubricated ZTA with different zirconia amount by Esposito et al. (1998), $7.75\text{E-}02$ to $1.37\text{E-}04$ mm^3/Nm for unlubricated ZTA with different zirconia amount by Cherif et al. (1996), $9.2\text{E-}05$ mm^3/Nm for ZTA composite with $\text{TiO}_2\text{-MnO}_2$ in dry condition by Dey and Biswas (2009), and $\text{E-}07$ to $\text{E-}05$ mm^3/Nm for alumina with different amount of zirconia in dry condition by Bartolome et al. (2006).

The wear rates in this study for 4N were mostly in a range of $\text{E-}09$ order, and were much lower than the ones described above. This can be due to the finer microstructure of samples in this work due to using SPS processing technique, and the effect of titania addition and less zirconia content used in this study. The effect of zirconia content on lower wear rate of this research is consistent with finding of He et al. (1993), who showed that the lowest wear rate was found for 15 vol.% ZrO_2 addition (Figure 2.47), which is the amount used in this work while Ma (2010)'s samples were BioloX® delta with 17 vol.% zirconia.

As can be seen in Figures 4.32 to Figure 4.34, higher normal loads caused higher specific wear rate, which is expected due to creating higher shear stress and number of asperities under contact pressure (Fischer, et al., 2000; Rana, 2013). This is in agreement with Fischer et al. (2000) for alumina ceramics and illustrated in Figure 2.41 in which at low loads (less than 19.6N), the wear volume was proportional to load and were raised with the third root of sliding distance. Similarly, Lee et al. (1993) reported the same dependence of wear rate to normal load and sliding velocity (Figure 2.44) for zirconia ceramics, although the severe wear due to induced thermal shock brittle fracture reported by them at high velocity did not occur in this study even though the sliding velocity was higher than used by Lee et al. (1993). This can be related to low content of zirconia in ZTA samples and also bovine lubricated system applied in this work which reduced both frictional heat and contact stresses. This reduction in wear is believed to be due to tribofilm formation which retarded beginning of wear transition as illustrated on shaded region on Figure 2.44.

The other trend which could be realized in Figure 4.32 to Figure 4.34 is that in all series of samples, coarser microstructures exhibited higher wear rates, particularly the highest wear rate were found for ZTA-1550°C-7min, ZTA+0.1mole.%TiO₂-1550°C-5min, and ZTA+0.5mole.%TiO₂-1500°C-5min with the relatively same grain sizes of around 250 nm and 400 nm for zirconia and alumina respectively. This is in agreement with what has been reported by several researchers, namely that fine-grained alumina ceramics show higher wear resistance (Wang, et al., 1995; Zum Gahr, et al., 1993; He, et al., 1993; Krell, 1996; Senda, et al., 1995). This is due to higher anisotropic thermal expansion and elastic properties of neighbouring grains in coarse structures, which results in higher local residual stresses during cooling, and leads to grain boundary failure and intergranular microfracture during the wear tests (Zum Gahr, et al., 1993). These results were also in accordance with Hall-Petch-type relationship between grain size and critical damage stress explained in section 2.4.5.1 as proposed by Wang et al. (1995), He et al. (1993), Kerwijk et al. (1999), and Bartolome et al. (2006). In contrary, the results of this work were in contrast with findings of He et al. (1997) who found that wear rate of coarse-grained ZTA was lower than that of fine-grained ZTA. They attributed this effect to compressive stresses at the surface caused by zirconia transformation and its volume expansion. However, in this study zirconia transformation seems only to happen in the ZTA samples at higher loads as illustrated in Figure 4.92. Thus, the lower wear rates of ZTA samples sintered at 1500°C and 1550°C under 8N and 16 N load in comparison with matching series containing 0.1 mole.% titania could be justified on the basis of this argument. Consequently,

this lower wear rate could be attributed to volume expansion and compressive stresses caused by zirconia transformation, which can improve wear resistance as explained by several researchers (He, et al., 1997; He, et al., 1993; Wang, et al., 1993; Kerkwijk, et al., 1999; He, et al., 1997; Wang, et al., 1993; Dogan & Hawk, 1997).

Moreover, comparing Figure 4.32 and 4.33 to Figure 4.34 demonstrate that samples containing 0.5 mole.% titania showed tangibly higher wear resistance, particularly for coarser microstructures and high loads. The specific wear rate of ZTA+0.5mole.%TiO₂ sample sintered at 1500 °C for 5 minutes (1.16E-07 mm³/Nm) was one third (3.7E-07 mm³/Nm) and one fourth (4.66E-07 mm³/Nm) of ZTA and ZTA+0.1 mole.%TiO₂ with similar grain size and microstructure. In lubricated systems, wear rate is more controlled by tribochemical mechanisms and is mainly dependent on chemical dissolution of the surface and the properties of the adherent film, such as its hardness and inherent friction coefficient and its growth or detachment on the surface, which indicate if it can affect wear properties in a favourable or adverse manner (Rainforth, 1996; Rainforth, 2004). As discussed in the section 5.2.1, protein absorption and presence of tribolayer on the worn surfaces could be confirmed in this study from AFM images (Figure 4.52) and Raman studies (Figure 4.89 and 4.90), which seems to increase COF, as explained. However, it seems to contribute positively in lowering wear rate in samples containing titania, mostly on samples with higher titania amount (0.5 mole%). This is in agreement with what reported by Key and Biwas (2009) and Morillo et al. (2009) who showed beneficial effect of formed tribofilm resulted from titania addition in improving wear resistance of ZTA composites in lubricated systems.

In addition, wear process in lubricated conditions is highly controlled by tribochemical mechanisms in low loads, while in high loads, the effect of involved mechanical mechanisms is prominent. In this case, 16 N can be regarded as a relatively high load and wear rate could be affected by mechanical mechanisms more than 8N and 4N. It was explained in section 5.1.4 that based on the hardness and toughness findings of this research, titania addition could improve hardness and toughness to some extent due to contributed mechanisms discussed. Hardness and toughness values for the samples used for wear studies were almost the same with the hardness value to be around 17 GPa and toughness value to be around 5.5 MPa.m^{1/2}, as reported in Table 4.7 to Table 4.9 and illustrated in Figure 4.18 to Figure 4.20. Thus, other factors such as higher density or microstructural effects of titania addition might be involved

in improving the wear resistance of samples containing 0.5 mole.% TiO₂ which would be discussed later.

It should be noted that in all 27 wear tests in this study, wear regime was in the mild region having the specific wear rate less than 10⁻⁶ mm³/Nm, which is the mild wear upper limit as defined by several researchers (Adachi, et al., 1997; Rainforth, 2004; Kato & Adachi, 2002; Hsu & Shen, 2004; Kerkwijk, et al., 2004; He, et al., 1993).

5.2.3. Worn Surface analysis

The surface analysis of wear scars is the main outstanding method for evaluating wear and modelling wear studies; thus, in this study the particular effort was done to analyze the surface comprehensively. As can be seen in 3D VSI images of wear scars (Figure 4.35 to Figure 4.43) and explained in section 4.2.2.2, depth and width of wear scars were in accordance with wear rate, and the worn surfaces were smooth with roughness value less than 50 nm. This is consistent with the results reported by many researchers that in mild wear regime the surface is mainly smooth and contacting surfaces have preferably polished each other (Adachi, et al., 1997; He, et al., 1997; Rainforth, 1996; Wang, et al., 1995; He, et al., 1993; Dogan & Hawk, 1997; Kerkwijk, et al., 1999; Bartolome, et al., 2006). However, some fine scale features such as pitting, grain pull-out, and fine grooves could be seen on the surfaces as illustrated in AFM and SEM results of this work.

Grain pull-out is one of the dominant wear mechanisms occurs due to intergranular fracture in both mild and severe regime in ZTA ceramics as has been reported by many researchers (Dey & Biswas, 2009; Kerkwijk, et al., 1999; He, et al., 1997; Rainforth, 2004; Rainforth, et al., 2012; Birkby, et al., 1989; He, et al., 1997; Wang, et al., 1995; He, et al., 1993; Rana, 2013). This could be detected on almost all of the high magnification 3D VSI images as well as AFM and LFM images of this research, which was very similar to what illustrated by Ma and Rainforth (2012) in Figure 2.53 and 2.54. The size of single removed grains as stated in section 4.2.2.2 were in range of 100-250 nm which could be considered as detached zirconia grains due to their size, as suggested by Ma and Rainforth (2010; 2012) and Shirkhan (2014).

Removing zirconia grains could be related to thermal expansion mismatch coefficient for

alumina and zirconia (Thompson & Rawlings, 1990), which left alumina grains in tension and zirconia grain in compression and cause internal stresses which could weaken grain boundaries and trigger easier delamination and zirconia grain pull-out. In addition, transformation of zirconia from tetragonal to monoclinic and its associated grain volume expansion can lead to transformed grains to stand proud of the surface. This phenomenon accompanied by microcracking resulted from transformation could be the cause of preferred removal of zirconia grains from the surface, as shown by TEM analysis by several researchers (Kelly & Francis Rose, 2002; Muddle & Hannink, 1986; 2004; Rainforth, et al., 2012; Birkby, et al., 1989; Ma & Rainforth, 2012; Ma, 2010; Shirkhan, 2014). In large pitting areas, like the ones in Figure 4.67.d and Figure 4.76.b, both alumina and zirconia might be lost and the cross section showed different depth size in the pits.

Differential wear between grains is another outstanding feature which can be seen in AFM and LFM images, in which some grains were worn out more than their neighbouring grains. As reported in section 4.2.2.2, some grains were only in height difference around 2 nm with their neighbouring grains while others had higher differences up to 10 nm. Generally, the higher differential wear occurred at lower normal loads, and at high loads such as 16N, the grain height differences were less. However, the fractured alumina grains were found to be present in almost all the wear scars, which stood distinctly higher than neighbouring grains, with the height of 10 to 20 nm. This could be attributed to what is known as grain relief and was reported by Ma (2010), Rainforth et al. (2012), Barceinas-Sánchez and Rainforth (Barceinas-Sánchez & Rainforth, 1998), Shirkhan (2014), and Rana (2013) and is illustrated in Figure 2.42 and Figure 2.46. This finding is in agreement with height difference between the grains reported by Barceinas-Sánchez and Rainforth (1998) in scanning of 30 grains to be 21.2 ± 6.9 nm with the maximum of 33.2 nm. Rainforth et al. (2012) and Barceinas-Sánchez and Rainforth (1998) also found that the density of dislocations is different in adjacent alumina grains and the grains with high dislocation damage stood proud on the worn surfaces. Similarly, grain relief was reported in zirconia ceramics in lubricated condition when frictional heat is removed by conductive counterfaces according to Rainforth (2004) and Shirkhan (2014) (Figure 2.46). It should be noted that in this work, the grains stood proud of the surface contained high density of transgranular cracks. Similarly, these grains were fractured in some cases and some parts of them were removed as could be seen in Figure 4.63.b with transgranular pitting of 37 nm depth.

Different mechanisms have been suggested to explain grain relief process, like different elastic deflection of grains in an asperity contact, different worn mechanisms (e.g. microfracture and plastic flow) due to different crystal orientations, and different tribochemical wear rates (Barceinas-Sánchez & Rainforth, 1998). However, Rainforth et al. (2012), Barceinas-Sánchez and Rainforth (1998) and Ma (2010) attributed grain relief in alumina to tribochemical wear mechanisms in which different rate in formation of amorphous wear debris, which composed of dissolved counterface materials, caused differential wear in alumina and this rate was a function of crystallographic orientation of grains.

As explained in section 5.2.1, formation of a protein layer precipitated from bovine serum on the wear scar surfaces could be confirmed from experimental observations and Raman and AFM results such as Figure 4.52. The presence of soft and thin protein layer on alumina and zirconia ceramics was reported by other researchers like Serro et al. (2006), Martinez et al. (2000), Rana (2013), and Ma (2010) though the film thickness recorded were around 20 nm (Ma & Rainforth, 2010; Ma, 2010) while AFM results of this study measured the layer to be around 100 nm. The presence of this layer can be supposed as the main reason of very low wear rate of these composites and delayed onset of wear transition mechanism as confirmed by Figure 2.40.

LFM images, showing friction force changes at the grain scale, revealed clear cracks and microfracture at grain boundaries especially between grains with differential wear, which could not be detected in AFM images. Unfortunately, distinguishing between alumina and zirconia is not possible in AFM and LFM images; therefore, fractured grain boundaries could not be determined if they were between alumina and/or zirconia grains. Transgranular fractured grains were also more evident in these images and zirconia grains trapped inside of alumina grains were more visible. It should be noted that blurred images were probably due to presence of soft protein layer which had not been removed properly from the surface.

LFM results of this study with their non-uniformity of friction force as a function of grain orientation and highlighted grain boundaries due to different friction force was very similar to that reported by Rana (2013), Ma (2010) and Ma and Rainforth (2012), as shown in Figures 2.51 and 2.54. However, Ma and Rainforth (2012) found that zirconia grains on the surface were transformed from tetragonal to monoclinic phase showing parallel linear features with the twin spacing for monoclinic zirconia, which was confirmed by Chevalier et al. (2007) and TEM

cross-section studies of subsurface layers done by Ma and Rainforth (2010) for 1 N contact load (Figure 2.52). In contrast to their findings, no transformed zirconia grains could be detected in LFM results of this research, which might be due to smaller size of zirconia grains resulted from using SPS processing technique, and their higher resistance to transformation as discussed before. In addition, transgranular fractured alumina grains found in this study were not detected in Ma (2010) and Rana (2013) study as they reported no damage in alumina grains, which should be related to lower load ranges they used or the changes of wear mechanism resulted from finer microstructure.

5.2.4. Worn phase analysis

As explained before, the presence of protein precipitation and formation of tribolayer during wear could be confirmed from SEM and optical image illustrated in Figures 4.89 and 4.90. Raman spectra of precipitated spot confirmed that these spots had both spectra of bovine serum and ZTA ceramics. Formation of such layer were reported by Ma and Rainforth (2012), Brown and Clarke (Brown & Clarke, 2006), Lu and McKellop (1997), Lu et al. (1999), Scholes et al. (2000), Heuberger et al. (Heuberger, et al., 2005), and Shirkhan (2014) though similar evidence of SEM and optical images, while no Raman spectra for such layer was found in their works.

In addition, worn surfaces were studied carefully and very few traces of monoclinic zirconia phase were found (Figure 4.92), and these were only in ZTA samples under high loads, while no transformed grains were detected even for this surfaces in LFM study, probably due to small area of analysis. Rare transformation of zirconia grains in ZTA composites was in contrast with findings of several researchers who reported zirconia grains on surface regions were dominantly transformed to monoclinic zirconia (He, et al., 1997; He, et al., 1993; Wang, et al., 1993; Kerkwijk, et al., 1999; He, et al., 1997; Krell & Blank, 1988; Ma & Rainforth, 2012; Shirkhan, 2014). This could be attributed to finer microstructure used in this work and tribochemical environment, which diminished both high temperature and contact stress on asperities. In addition, as explained earlier, microcracking resulted from tetragonal to monoclinic transformation could enhance transformed grains to be pulled out, which might then be removed from the surface by lubricants.

Careful Raman investigation on samples containing titania revealed that no monoclinic zirconia grains were found on the worn surfaces, as can be seen in some representative spectra illustrated in Figure 4.93. This could be attributed to the tetragonal stability effect of titania on zirconia through lowering the tetragonal to monoclinic transformation temperature and making a large area for having the tetragonal zirconia, as explained before and is depicted in Figure 2.51. It also should be noted that more precise statement about presence or absence of transformed zirconia could only be observed after TEM examination due to the small content and the possibility that the Raman signal came from both the substrate and the surface layers.

5.2.5. Worn microstructure characterisation

As stated before, wear in ceramics is considered as a result of fracture process of ceramics due to their intrinsic brittleness, in which with increasing the contact stresses and exceeding a very low critical value, fracture happens (Fischer, et al., 2000; Miyoshi, 1988). Thus, fractured grain boundaries and pitting are the most common features in ceramics, which can even be seen at very low loads and lubricated condition, as is illustrated in Figure 4.94 to Figure 4.120 of this study. According to Ma and Rainforth (2012), in bovine lubricated system for ZTA, the surface were rougher with higher pitting and more expanded grain pull-out areas than the one in water lubricated system although its wear rate and friction was very low. This was attributed to protein adsorption behaviour of alumina and zirconia grains and the damage accumulation such as dislocation activity, which was reported by Ma and Rainforth (2012) to be higher in bovine serum lubricated environment.

SEM images of this research exhibited smooth worn surface with few and isolated intergranular microcracks and pitting with the size around a single grain for 4N load tests and finer microstructures (Figure 4.94 to Figure 4.120), which are considered as characteristic features for mild wear regime (He, et al., 1997; Rainforth, 1996; Wang, et al., 1995; He, et al., 1993; Rainforth, et al., 2012; Dogan & Hawk, 1997; Kerkwijk, et al., 1999; Bartolome, et al., 2006; Fischer, et al., 2000; Lee, et al., 1993). This kind of microstructure is similar to that reported by Ma and Rainforth (2012) under normal load of 2N while they reported features of severe wear under 4N normal load (Figure 2.53.a). The difference could be related to finer microstructures of this work and the effect of titania on zirconia stability as discussed before.

Other visible features such as very small mechanically-formed debris (one-tenth or less than grain size), microscale abrasion, and differential wear between grains could be found in the images which are considered as other characteristics of mild wear regime by researchers, as shown in Figure 2.37 (Rainforth, 2004; Kato & Adachi, 2002).

Large pitted areas and connected intergranular microfracture is visible in SEM images having coarse microstructure and were tested under higher loads of 8N and 16N. These large pits were mainly filled with agglomerated wear debris such as Figure 4.95, which is comparable with what reported by Ma and Rainforth (2012) and Rana (2013) for testing under 4N (Figure 2.53.b). This kind of microstructure was close to what reported by Rana (2013), Ma (2010), and Zeng (2008) in a region called 'wear transition zone', which is supposed to occur in intermediate time after the initial mild wear regime and the before onset of severe stripe wear. Thus, 4N load claimed by Ma (2010) as the critical contact load for starting transition of ZTA was not approved by this study and depending on microstructure and Ti content, higher load such as 8 N and 16 N could be regarded as the critical load.

In the case of ZTA samples with coarse microstructure worn under 16N (Figure 4.102) large craters of removed grains due to mechanical cracking of grains could be seen. This figure shows that this kind of worn microstructure is only in middle of wear track due to highest contact stress at these areas, and two other sides have the characteristics of transition or mild regime as discussed before. Thus, it could be deduced that in other wear scars as well as at sides of this wear scar, the observed wear regime was in the start of the transition zone, while it could be considered as mid-transition regime in the middle. Consequently, it can be concluded that smaller grain sizes and lower loads could improve wear resistance and retard wear transition of ZTA composites as reported by several researchers (Rainforth, et al., 2012; Barceinas-Sánchez & Rainforth, 1998; Rainforth, 2004).

Another important feature which could be seen on SEM images, particularly in the large pitting areas are wear debris as clearly illustrated in high magnification pictures like Figures 4.95.e, 4.104.e, and 4.120.f. In this case, wear debris observed could be generated from zirconia grains pulling out from the surface or detached transgranular part of alumina grains, as was reported by Rana (2013), Shirkhan (2014), and Ma (2010). BSE images of Figures 4.95.d and 4.104.f demonstrates that wear debris consisted of both alumina and zirconia which is in agreement with results of Rana (2013), Ma (2010), Shirkhan (2014), and Krell and Plank (1988), and as stated by Rainforth et al. (2012) wear debris were chemical mixture of all component in the

tribosystem. They also found that in alumina femoral heads, wear debris had long axis parallel to the trace of the basal planes and had a size equal to the spacing size between the cracks, and concluded that they were formed as a consequence of transgranular fracture.

According to Fischer et al. (2000) and Wang and Hsu (1996), wear debris could be squeezed and removed from the surface by continuing the wear or they can remain and play as a third body generating grooves and affecting the contact stresses and wear rate as observed in this study. They also can crush to finer debris at high stresses as could be seen in few nanometre scale size as illustrated in Figures 4.95.e, 4.104.e, 4.120.f, similar to 50-200 nm size reported by Rana (2013), Ma (2010), Shirkhan (2014) *in vitro* and Hatton et al. (2000) *in vivo*. In lubricated system such as this work, they could attach to each other and form agglomerated wear particles, or trap in surface voids or be removed from the surface. They also could be embedded in the tribofilm and form an amorphous layer with fine nanocrystals, as reported by Ma (2010), Shirkhan (2014) and can be seen in Figure 2.45.

Another feature could be detected on SEM images, particularly in samples worn under 4 and 8 N normal loads, was the presence of abrasive grooves elongated in the sliding direction, which is another characteristic of a mild wear mechanism (He, et al., 1997; Rainforth, 1996; Wang, et al., 1995; He, et al., 1993; Rainforth, et al., 2012; Dogan & Hawk, 1997; Kerkwijk, et al., 1999; Bartolome, et al., 2006). Abrasive grooves in alumina and zirconia ceramics were reported by Rana (2013) in wear scars of 0.5, 1, 2 and 4N for alumina, and Shirkhan (2014) for zirconia ceramics though grooves in this study were fewer, deeper and longer. However, Ma (2010) reported surface with fine abrasive grooves only for 1N normal load in water lubricated system (Figure 2.50.a), and found that no grooves were present for ZTA under 4N normal load in water and under 2 and 4 N load in bovine lubricated system, which is in contrast with finding of this research.

As explained before, grooves initiate from the grains standing proud of the surface as a direct result of differential wear (Figure 2.42) (Rainforth, et al., 2012; Barceinas-Sánchez & Rainforth, 1998; Rana, 2013; Ma, 2010); thus, absence of grooves for samples worn under 16N could be related to the smaller height difference between neighbouring grains. As the grooves in this work were deep and long, finding the origin of them was difficult. However, it could be detected in one case that the groove was initiated from a transgranular fractured alumina grain and caused by the micro fractured 3rd body liberated from the grain (Figure 4.112.e). This is similar to observation by Rana (2013) that deep grooves passing through pits of transgranular

fracture in wear scars. Moreover, it can be seen from SEM images (e.g. Figure 4.106.d) which was confirmed by AFM cross section images (Figures 4.70.c and 4.69.a) that the abrasive grooves depth was varying in adjacent grains and it changed at grain boundaries; for instance, the depth difference up to 20 nm were measured in AFM images. This is consistent with what reported by Rainforth et al. (Rainforth, et al., 2012), Barceinas-sanchez and Rainforth (1998), Rana (2013), Ma (2010), and Steijn (1961) that width, depth and orientation of these abrasive grooves were mostly dependent on crystallographic orientation of the grains. It should be noted that surface damage would be continued by wide-ranging microcracking and dislocation flow at the base of grooves promoting more origination of abrasives, as explained in section 2.4.3.

As discussed before, alumina has higher hardness and Young's modulus, lower fracture toughness and bending strength, lower coefficient of linear thermal expansion and higher thermal conductivity in comparison with zirconia. On the other hand, zirconia with its lower hardness and lower thermal conductivity (around one third than that of alumina), which increases the flash temperature and thermal stresses at the contacting areas, would cause higher wear rate in compare with alumina (Figure 2.38) (He, et al., 1997; Trabelsi, et al., 1989; Dey & Biswas, 2009; Krell & Blank, 1988; Kerkwijk, et al., 1999; Zum Gahr, et al., 1993). Therefore, it is expected that zirconia grains contain more damage and wear at a higher rate than alumina, while the SEM images of this study demonstrated the opposite result and zirconia grains were relatively undamaged even when the grooves were passing them (Figure 4.103).

The same results were reported by Zum Gahr et al. (1993) for ZTA in reciprocating wear conditions, in which zirconia grains showed greater wear resistance than alumina grains. They attributed less wear resistance of alumina grains to their intercrystalline microfracture resulted from their low fracture toughness. This can confirm what was argued by several researchers (Fischer, et al., 1989; He, et al., 1997; Wang, et al., 1993) that in spite of the common dependence of wear resistance to hardness in other materials, for ceramics fracture toughness would be a more reliable factor to predict wear behaviour. However, these findings were in contrast with those reported by Ma (2010) who used relatively similar wear conditions to those used in this research, as she found that alumina grains were not damaged and zirconia grains contained microcracks and twin due to monoclinic transformation (Figure 2.51 and 2.54). The contrasting results might be due to finer microstructure and less zirconia grain sizes of this study, which along with titania addition could inhibit zirconia transformation and improve wear resistance of the composite. Consequently, it could be concluded that transformation of

tetragonal to monoclinic would deteriorate wear properties of ZTA composites, and could be improved by reducing grain sizes.

In contrast to zirconia grains, alumina grains with transgranular microfracture were detected in almost all of the microstructures of this study. Precise observation of fractured grains in SEM and AFM/LFM images revealed that increased load led to more fractured grains as expected, since intercrystalline microfracture is affected by the local stress during wear. As AFM results indicated, these grains were standing proud of the surface and therefore were under raised contact stresses due to lower real contact area. This could promote crack nucleation at these grains, which propagated easily as a result of low fracture toughness of alumina. These cracks could also cause detachment of a wear particle operating as the third body and make abrasive grooves on the surface as explained before.

Formation of transgranular cracks and intercrystalline microfracture for alumina grains were observed by some researchers (Zum Gahr, et al., 1993; Rainforth, et al., 2012; Barceinas-Sánchez & Rainforth, 1998; Wang, et al., 1995) although it was not observed in similar wear conditions for ZTA and alumina ceramics in the study done by Ma (2010) and Rana (2013) respectively. This can again be related to finer microstructure used in this research, which caused lower residual stresses due to smaller grain sizes, and resulted in shifting from intergranular to transgranular fracture. It should be noted that detailed stress analysis is required to explain the interaction of contact stresses, residual stresses and transformation stresses and preferred transgranular fracture in the microstructure, which was out of the scope of this research.

SEM images of alumina grains also demonstrate that most of fractured grains exhibited a distinct fracture direction as is clear in Figures 4.72.c and 4.85.c. This is consistent with what was reported by Rainforth et al. (2012) and Barceinas-Sánchez and Rainforth (1998) that the transgranular fracture of alumina strongly crystallographic. Similarly, Rainforth et al. (2012) argued that transgranular cracks in alumina grains mainly propagated along the basal planes, i.e. basal cleavage. The SEM images could also be interpreted as twinning. It is probable that twinning first occurred in the (0001) direction, which then developed as cracks resulting in transgranular fracture.

Despite the relatively similar microstructural map of worn surfaces for ZTA and ZTA+0.1 mole.%TiO₂, comparing them with SEM images of samples containing 0.5 mole.% titania

shows that these composites exhibited less damages in both intergranular and transgranular cracking. Less craters of removed grains and fewer transgranular fractured grains were detected in this composites, which were more tangible in coarser microstructures and higher loads, as could be confirmed by the wear rate results. This can be due to titania addition effect on toughness and strength of the composite by pore reduction and composite densification, and on increasing transgranular nano dispersions due to its ability to increase grain growth (Figure 2.30.b), or the stabilization effect of tetragonal zirconia, as discussed before. It also might enhance grain boundaries strength and changes residual stress states as argued by Fischer et al. (2000) and Rainforth (2004) that enhancing the strength of grain boundaries through the appropriate additives can affect the wear transition regime and change the mechanism involved in it. All of these effects would alter the stress distribution involved in wear mechanisms and could result in delayed wear transition and improved wear behaviour. This is consistent with that reported by Lee et al. (2003) that wear rate of alumina was reduced greatly by increasing the amount of TiO₂ up to 10 mol.% in the nanocomposite (Figure 2.8), which was attributed to its microstructure and mechanical properties such as fine grains and boundary chemistry. Similar improvement in wear behaviour of alumina and zirconia ceramics with metal oxide additions were reported by Kerkwijk et al. (2004) and Rainforth et al. (2002) for CuO, Rainforth and Stevens (1993) for MgO, Shirkhan (2014) for La₂O₃, and Rainforth (2004) in SiC-Al₂O₃ nanocomposites.

According to five stage grading scale of wear progression by Shishido et al. (2006) explained in section 2.4.2.2, wear of all samples under 4N normal load could be classified as grade III type wear, which is in contrast with what reported by Ma (2010) and Rana (2013) that ZTA and alumina ceramics presented wear type of Grade IV under 4N load. For 8 N and 16 N loads, samples without and with 0.1 mole.% titania showed wear type in category of grade IV, while in samples containing 0.5 mole.% titania, wear type could still be categorized in grade III except for sample sintered at 1500°C under 16N which was more similar to Grade IV.

In general, wear mechanisms of studied samples at low loads and fine microstructures were found to be polishing, differential wear, grain pull-out, 3rd body abrasion and grooves, while large microcracking and craters resulting from fractured grains were found to be dominant wear mechanisms in high loads and coarser microstructures. This is consistent with wear mechanisms reported by several researchers for alumina and zirconia ceramics (He, et al., 1997; Rainforth, 1996; Wang, et al., 1995; Rainforth, et al., 2012; Dogan & Hawk, 1997;

Kerkwijk, et al., 1999; Bartolome, et al., 2006; Rana, 2013; Shirkhan, 2014; Ma, 2010). It should be noted that no evidence of severe wear features as characterized by He et al. (1993), Wang et al (1995), and He et al. (1997) could be seen on wear scars of this study, even at high loads and coarse microstructures, which is in accordance with the wear rate values of the study.

6. CONCLUSION

By studying a large numbers of samples and experiments in this work, it was found that reducing the microstructural scale using SPS technique gave a significant improvement in mechanical and wear properties of ZTA composites compared to materials processed in the conventional manner. Moreover, titania addition was found to be beneficially effective in improving mechanical and tribological characteristics of ZTA composites and could help retard the wear and hydrothermal degradation when used in hip joint replacements. These two main achievements are considered as the significant outcomes of this study.

6.1. Sample Characterization

- All the samples in this study were reasonably dense having relative density more than 97.5% of the theoretical density due to using SPS technique through the application of a mechanical pressure, the use of rapid heating rates, and the use of pulsed direct current, which helped to achieve higher relative density in comparison with pressureless techniques. Even in a poorly conducting materials such as ZTA, the presence of electric field was beneficial in enhancing density.
- Higher sintering temperature resulted in improved density of the samples due to increased kinetics of the sintering process and heightened electric discharge as a result of intensified pulses applied for heating the samples. No tangible effects of the dwell time on the relative density were.
- Adding TiO₂ in small amounts of 0.1 and 0.5 mole.% to the composite improved sinterability and densification of the samples from 98.26% of the theoretical density for ZTA samples to 99.92% for samples containing TiO₂. This might be due to dissolution of Ti ions in alumina and zirconia lattice and reducing conditions, which generated lattice effects and vacancies to maintain the charge neutrality. These defects increased intergranular diffusion and grain boundary mobility and resulted in higher density of the composites. Other contributing factors on improved density might be due to

anisotropic surface energies caused by titania addition, which lead to the formation of a stacking of elongated elementary bricks and removal of intra-colony porosity leading to the faceted fully dense grains.

- At higher titania content of 2 and 5 mole.%, the relative density decreased to less than 98.5% in all sintering temperature and time. This was attributed to coarsening and formation of new phase of $ZrTiO_4$ as confirmed by XRD and SEM results. Coarser microstructures lead to the formation of microcracks due to higher thermal mismatch stresses and consequently had adverse effect on the density. The presence of a new phase such as $ZrTiO_4$ led to higher porosity presumably through reduced diffusion rates and higher thermal mismatch stresses which led to macrocracks. The same factors could be the causes for the decreased density at high temperature of 1550°C for samples containing 0.1 mole.% and 0.5 mole.% TiO_2 .
- XRD patterns of ZTA samples in this study showed characteristic peaks of alumina and tetragonal zirconia without any traces of monoclinic phase indicating that using SPS inhibited transformation of tetragonal to monoclinic phase during cooling. Adding titania in small amounts of 0.1 and 0.5 mole.% resulted in the same XRD pattern as ZTA.
- XRD patterns of 2 and 5 mole.% titania showed the characteristic of $ZrTiO_4$ peaks for all the samples and monoclinic zirconia peaks in samples containing 5 mole.% titania in all sintering temperatures, and samples with 2 mole.% titania at 1500°C and 1550°C sintering temperatures. The presence of residual monoclinic zirconia associated with formation of $ZrTiO_4$ was attributed to higher solubility of TiO_2 in tetragonal zirconia than in monoclinic zirconia and diffusion of Ti ions in short distances to form zirconium titanate phase. No traces of aluminium titanate peaks were identified in this research, which might be due to low titania content.
- The microstructures of ZTA with different titania amount showed two specific and recognizable phases of alumina and zirconia. Increasing amount of titania addition to 2 and 5 mole.% resulted in more agglomeration of zirconia particles and less homogeneous microstructure, especially at lower sintering temperature. This might be

due to changes of zeta potential and corresponding viscosity due to presence of Ti ions in mixing step of processing.

- Grain growth was observed by increased sintering temperature and dwell time for all samples due to temperature activating process of atomic diffusion and grain boundary movement caused by reducing the grain boundary area and lowering the energy of system to a more stable state. The rate of grain coarsening for alumina was more than zirconia grains as a result of its higher volume fraction and shorter effective diffusion path for alumina ions in comparison with the zirconia ones. In addition, the average grain sizes for both alumina and zirconia were increased by increasing amount of TiO₂ content, which might be due to increased intergranular diffusion and grain boundary mobility through increasing amount of defects, or removed intra-colony porosity.
- The SEM images for samples with titania addition showed that TiO₂ changed the shape of grains and grain boundaries. In these composites, grains were more faceted with formed etching grooves within alumina grains by adding TiO₂, while in ZTA samples the microstructure the grain boundaries were more linear probably due to effect of TiO₂ on the surface and kinetic energy for diffusion. Another microscopic feature in samples containing 2 and 5 mole.% TiO₂ was increased porosity, mainly on grain boundaries and triple points, probably due to presence of liquid phase during sintering, or the formation of ZrTiO₄ associated with volume changes and induced cracks and microcracks.
- Formation of a new phase of ZrTiO₄ in samples containing 2 and 5 mole.% titania was also confirmed by BSE images through observing a new phase with grey contrast which started to form within zirconia grains, and since diffusion of Ti⁴⁺ ions from the matrix to the ZrTiO₄ occurred over a short distance, it was probably monoclinic phase surrounded ZrTiO₄ grains, as confirmed by XRD analysis. ZrTiO₄ regions formed within the grains were also detected in high magnification BSE images, which was attributed to incomplete formation of ZrTiO₄.
- The microstructures studied in this work did not exhibit any particular anisotropic alumina grains or in-situ fibres in SEM images probably due to dissolution of Ti ions

mostly in zirconia, and formation of zirconium titanate phase, which reduced the effect of titania on alumina grains.

- For ZTA samples, hardness values were in a range of 16.3 ± 0.3 to 18.0 ± 0.9 GPa with relatively lower hardness for higher temperatures and dwell time probably due to microstructure coarsening and its associated microcracks. Hardness values of samples containing 0.1 mole.% titania were very close and in a range of 17.2 ± 0.8 to 18.0 ± 0.6 GPa, which were higher than the values of ZTA samples and in a good agreement with high relative density of these composites. This might be as a result of the beneficial effect of small additions of titania on improving density and subsequently improving hardness of ZTA samples, or of raising the cohesion between grains of alumina, titania and zirconia, and purifying and strengthening the phase interfaces and grain boundaries. The larger amount of transgranular nanodispersed zirconia grains resulted from greater grain growth could be another cause of improved hardness. In the samples containing 0.5 mole.% TiO_2 , by neglecting the value of 14.8 ± 2.1 GPa with its high standard deviation, the hardness values lay in the range of 16.4 ± 0.2 to 17.7 ± 0.5 GPa. The same range of hardness values for samples containing 2 mole.% titania was obtained varying from 16.4 ± 1.7 to 17.9 ± 1.2 GPa. The slight decrease of hardness values for these samples compared to samples containing 0.1 mole.% titania might be due to their coarser microstructure. Vickers hardness for the samples containing 5 mole.% titania was reduced significantly and lay in the range of 14.3 ± 0.7 to 15.8 ± 0.9 GPa probably due to formation of ZrTiO_4 with its lower elastic modulus and hardness in comparison with zirconia as well as the presence of microcracks associated with the formation of zirconium titanate.
- The fracture toughness values for ZTA samples were very similar and in a range of 4.9 ± 0.2 to 5.8 ± 0.2 $\text{MPa}\cdot\text{m}^{1/2}$, which was higher than the fracture toughness of monolithic alumina (~ 4 $\text{MPa}\cdot\text{m}^{1/2}$). These values for samples containing 0.1 and 0.5 mole.% titania were slightly higher with the range of 5.4 ± 0.2 to 6.2 ± 0.5 $\text{MPa}\cdot\text{m}^{1/2}$, and of 5.1 ± 0.2 to 5.8 ± 0.12 $\text{MPa}\cdot\text{m}^{1/2}$ respectively. The increased toughness for samples containing 2 mole.% was more visible by reaching to the range of 5.9 ± 0.3 to 7.8 ± 0.8 $\text{MPa}\cdot\text{m}^{1/2}$. The range of toughness for ZTA+5 mole.% TiO_2 composite was from 5.4 ± 0.3 to 6.8 ± 0.7 $\text{MPa}\cdot\text{m}^{1/2}$, which was relatively higher than those for ZTA,

ZTA+0.1mole.% and ZTA+0.5 mole.% TiO_2 , but less than toughness values of ZTA+2 mole.% TiO_2 . The improved toughness by titania addition might be due to its effect on microstructure through crack deflection and alteration of crack path, especially when the fracture mode was predominantly intergranular. It might also be as a result of titania effect on tetragonal retention of zirconia and transformation toughening mechanism involved in it, or through residual stress mechanism due to presence of large residual compressive stresses around the zirconia nanoparticles in the current micro-nano-composite. Formation of ZrTiO_4 with its poorer mechanical properties in comparison to Y-TZP and microcracking associated with its characteristic thermal expansion anisotropy found to be the main cause of toughness degradation for samples containing 2 and 5 mole.% titania sintered at high temperatures.

- SEM images of the crack path showed that the cracks propagated in ZTA and ZTA+0.1 mole.% TiO_2 in the relatively linear paths, mostly intergranular, and some crack bridging was observed probably due to fine microstructure of the samples. In samples containing 0.5 mole.% titania, some small deflection and a few transgranular fracture were detected in high magnifications images which were mainly due to its coarser microstructure. In samples with 2 and 5 mole.% titania addition, crack propagation was highly deviated from its original path and the cracks propagates over a more tortuous path due to the coarser microstructure, which resulted in higher toughness values obtained for these composites regarding to their dominant crack deflection mechanism. In addition, intergranular pattern for fracture of these composites might be due to their weaker grain boundary bonding effect after titania addition.

6.2. Wear characterization

- The coefficient of friction values (COF) in this work were in 0.001-0.032 range with the trend of higher COF in samples containing titania in comparison with ZTA samples. The effect of titania addition in COF might be due to protein precipitation on the surface which made a solid-like tribofilm and its presence on the worn surfaces was confirmed from AFM images and Raman studies and experimental observation of difficult cleaning of the surface in samples containing titania.
- The specific wear rate in this study was lied in a wide range of 2.47E-09 to 3.7E-07 mm³/Nm, which in details was in the range of 2.47E-09 to 7.46E-08 mm³/Nm under 4N load, 1.57E-08 to 6.37E-08 mm³/Nm under 8N load, and 4.59E-08 to 4.66E-07 mm³/Nm under 16N load. The wear rates all decreased in the mild region with the specific wear rate less than 10⁻⁶ mm³/Nm. Higher normal loads caused higher specific wear rate as a result of creating higher shear stress and number of asperities under contact pressure. In addition, coarser microstructures exhibited higher wear rates due to higher anisotropic thermal expansion and elastic properties of neighbouring grains in coarse structures resulted in higher local residual stresses and grain boundary failure and intergranular microfracture during the wear. Samples containing 0.5 mole.% titania showed tangibly higher wear resistance, particularly for coarser microstructures and high loads probably due to beneficial effect of the tribofilm which resulted from titania addition in improving wear resistance of ZTA composites in lubricated systems. Some factors such as higher density or microstructural effects of titania addition might also be involved in improving the wear resistance of samples containing 0.5 mole.% TiO₂ particularly at high load of 16N.
- The surface analysis of wear scars showed smooth surface with roughness value less than 50 nm suggesting that the contacting surfaces preferably polished each other. The depth and width of wear scars were in accordance with loads and obtained wear rate. Some fine scale features such as pitting, grain pull-out, and fine grooves were observed on the surfaces. Grain pull-out was detected on almost all of the high magnification 3D VSI images as well as AFM, LFM, and SEM images with the size range of 100-250 nm which probably were detached zirconia grains due to their size. Removing zirconia

grains could be due to thermal expansion mismatch coefficient for alumina and zirconia or microcracking resulted from tetragonal to monoclinic transformation.

- Differential wear between grains was another outstanding feature seen in AFM and LFM images, in which some grains were worn out more than their neighbouring grains. The difference in height between some grains was as small as 2 nm with their neighbouring grains while others had higher differences up to 10 nm. The higher differential wear occurred in lower normal loads, and at high loads such as 16N, the grain height differences were less. The fractured alumina grains were found to be present in almost all the wear scars, which stood distinctly higher than neighbouring grains, with the height of 10 to 20 nm, known as grain relief. These grains contained high density of transgranular cracks, and some were fractured transgranular and lost some parts of grains. This might be due to tribochemical wear mechanisms in which different rate in formation of amorphous wear debris caused differential wear in alumina and this rate was a function of crystallographic orientation of grains.
- Presence of a tribolayer was confirmed in this study through AFM, SEM and Raman studies, which was found to have a thickness of around 100 nm measured by AFM studies. The presence of this layer was believed to be the main reason of very low wear rate of these composites and delayed onset of wear transition mechanism.
- No transformed zirconia grains were detected in LFM results of this research, which might be due to smaller size of zirconia grains resulted from using SPS processing technique, and their higher resistance to transformation as discussed before. However, very few traces of monoclinic zirconia phase were found by Raman study which were only in ZTA samples under high loads, while no transformed grains were detected even by Raman study in samples containing titania, probably due to tetragonal stability effect of titania on zirconia.
- Microstructural studies of the worn surfaces exhibited smooth worn surface with few and isolated intergranular microcracks and pitting with the size around a single grain for 4N load tests and finer microstructures, considered as characteristic features for mild wear regime. Large pitting areas and connected intergranular microfracture was

detected in SEM images of samples with coarse microstructure tested under higher loads of 8N and 16N. These large pits were mainly filled with agglomerated wear debris which had the size of one-tenth or less than a grain size and consisted of both alumina and zirconia. This kind of microstructure was called ‘wear transition zone’ supposed to occur in intermediate time after the initial mild wear regime and the before onset of severe stripe wear. Thus, depending on microstructure and Ti content, high load such as 8N and 16N was regarded as the critical load for starting transition of ZTA composites.

- In the case of ZTA samples sintered at 1550C for 7 minutes and worn under 16N, large craters of removed grains due to mechanical cracking of grains were seen in the middle of the wear track due to the highest contact stress at these areas, and two other sides have the characteristics of transition or mild regime. Thus, it was deduced that in other wear scars as well as at sides of this wear scar, the wear regime was at the start of the transition zone, while it was in mid-transition regime in the middle.
- Despite the relatively similar microstructural map of worn surfaces for ZTA and ZTA+0.1 mole.% TiO₂, SEM images of samples containing 0.5 mole.% titania showed less craters of removed grains and fewer transgranular fractured grains. This effect was more tangible in coarser microstructures and higher loads, as was confirmed by the wear rate results. This was probably due to the effect of the titania addition on toughness and strength of the composite by pore reduction and composite densification, or its effect on increasing transgranular nano dispersions, or on tetragonal zirconia retention, or on enhancement of grain boundaries strength.
- SEM images revealed that increased load had spread more fractured alumina grains since intercrystalline microfracture was mainly affected by mechanical aspect of wear. They also showed that most of fractured grains exhibited a fracture direction in which transgranular cracks mainly propagated along the basal planes as seen by other researchers. On the other hand, zirconia grains were found relatively undamaged even when the grooves were passing them, probably due to their higher fracture toughness in comparison to alumina and their less grain size, which along with titania addition, inhibited their transformation.

- Abrasive grooves elongated in the sliding direction were detected on SEM images, particularly in samples worn under 4N and 8N normal loads, which was another characteristic of a mild wear mechanism. It was detected in one case that the groove was initiated from a transgranular fractured alumina grain and caused by the micro fractured 3rd body liberated from the grain. The abrasive grooves depth varied in the adjacent grains, due to their dependent on crystallographic orientation of the grains, and changed at grain boundaries; for instance, the depth difference up to 20 nm were measured by AFM studies. The absence of grooves for samples worn under 16N was related to their less height difference between neighbouring grains.
- According to five stage grading scale of wear progression by Shishido et al. (2006), wear of all samples under 4N normal load was classified as grade III type wear. For 8N and 16N loads, samples without titania and with 0.1 mole.% titania showed wear type in category of grade IV, while in samples containing 0.5 mole.% titania, wear type was still in grade III except for sample sintered at 1500°C under 16N which was more similar to Grade IV. No evidence of severe wear was found on wear scars of this study, even at high loads and coarse microstructures, which was in accordance with the wear rate values of the study.

7. FUTURE WORK

Titania addition in small amounts was found to improve mechanical properties of ZTA composites. Further investigation including TEM studies is suggested to find out the exact role of its addition on grain boundaries composition and its effect on retention of tetragonal zirconia.

In order to study the effect of improved toughness by titania addition on the wear behaviour of ZTA ceramics, further research with larger amounts of titania is suggested. Similarly, further reciprocating wear tests under different conditions of load and time and various lubricants such as water is suggested to figure out a more complete wear map.

The tribolayer formed on the worn surfaces was highly dependent to protein precipitation. Further XPS studies is suggested to discover the surface protein adsorption behaviour and how it could be affected by dopant additions such as titania.

Due to the high effect of viscosity of lubricants on wear behaviour, doing the reciprocating test in a more controllable environment such as controlled temperature, speed and shear rate is recommended.

Further investigation on the surface and sublayers need to be carried out by FIB and TEM studies to determine the accurate effect of titania addition on microstructure such as crystallographic dislocations, grain boundaries microcracks, and zirconia transformation.

Further detailed stress analysis is required to explain the interaction of contact stresses, residual stresses and transformation stresses and preferred transgranular fracture in the microstructure.

There are limited findings on the performance of ZTA composites with titania additions. There is a need to investigate to carry out the *in vivo* examinations on these composites and compare them with the results of other dopants additions.

8. REFERENCES

- Adachi, K. & Kato, K., 2000. Formation of smooth wear surfaces on alumina ceramics by embedding and tribo-sintering of fine wear particles. *Wear*, Volume 245, p. 84–91.
- Adachi, K., Kato, K. & Chen, N., 1997. Wear map of ceramics. *Wear*, Volume 203-204, pp. 291-301.
- Affatato, S., Goldoni, M., Testoni, M. & Toni, A., 2001. Mixed oxides prosthetic ceramic ball heads. Part 3: effect of the ZrO₂ fraction on the wear of ceramic on ceramic hip joint prostheses. A long-term in vitro wear study. *Biomaterials*, Volume 22, pp. 717-723.
- Ajayi, O. O. & Ludema, K. C., 1990. Mechanism of transfer film formation during repeat pass sliding of ceramic materials. *Wear*, Volume 140, pp. 191-206.
- Antonio, J. D., Capello, W., Manley, M. & Bierbaum, B., 2002. New Experience With Alumina-on-Alumina Ceramic Bearings for Total Hip Arthroplasty. *The Journal of Arthroplasty*, Volume 17, pp. 390-397.
- Bagley, R. D., Cutler, I. B. & Johnson, D. L., 1970. Effect of TiO₂ on initial sintering of Al₂O₃. *Journal of The American Ceramic Society*, 53(3), pp. 136-141.
- Bannister, M. J. & Barnes, J. M., 1986. Solubility of TiO₂ in ZrO₂. *Journal of The American Ceramic Society*, 69(11), pp. C269-C271.
- Ban, S., Sato, H., Suehira, Y., Nakanishi, H. & Nawa, M., 2008. Biaxial Flexure Strength and Low Temperature Degradation of Ce-TZP/Al₂O₃ Nanocomposite and Y-TZP as Dental Restoratives. *Journal of Biomedical Materials Research*, Volume Part B, pp. 492-498.
- Barceinas-Sánchez, J. D. O. & Rainforth, W. M., 1998. On the role of plastic deformation during the mild wear of alumina. *Acta Materialia*, 46(18), pp. 6475-6483.
- Bar, S., 2004. Crystalline rare earth-doped-sesquioxide PLD-films on [alpha]-alumina. *Cuvillier Verlag*, Volume [online access: 25 July 2013], p. p.12.
- Bartolome, J. F., Pecharroman, C., Moya, J. S., Martin, A., Pastor, J. Y. & Llorca, J., 2006. Percolative mechanism of sliding wear in alumina/zirconia composites. *Journal of the European Ceramic Society*, Volume 26, p. 2619–2625.
- Beaule, P. E., Dorey, F. J., Hoke, R., LeDuff, M. & Amstutz, H. C., 2006. The Value of Patient Activity Level in the Outcome of Total Hip Arthroplasty. *The Journal of Arthroplasty*, 21(4), pp. 547-552.
- Benzaid, R., Chevalier, J., Saa[^]daoui, M., Fantozzi, G., Nawa, M., Diaz, L. A., & Torrecillas, R., 2008. Fracture toughness, strength and slow crack growth in a ceria stabilized zirconia–alumina nanocomposite for medical applications. *Biomaterials*, Volume 29, p. 3636–3641.
- Berger, M. & Sayir, A., 2008. Directional solidification of Al₂O₃–Al₂TiO₅ system. *Journal of the European Ceramic Society*, Volume 28, p. 2411–2419.
- Bierbaum, B. E., Nairus, J., Kuesis, D., Morrison, J. C., & Ward, D., 2002. Ceramic-on-Ceramic bearings in total hip arthroplasty. *Clinical Orthopaedics And Related Research*, Volume 405, p. 158–163.

- Birkby, I., Harrison, P. & Stevens, R., 1989. The effect of surface transformation on behaviour of zirconia TZP ceramics. *Journal of the European Ceramic Society*, Volume 5, pp. 37-45.
- Blau, P. J., 1993. Friction microprobe investigation of particle layer effects on sliding friction. *Wear*, Volume 162-164, pp. 102-109.
- Blunn, G., 2013. Bearing surfaces. *Orthopaedics And Trauma*, 27(2), pp. 85-92.
- Borrell, A., Dolores Salvador, M., Rocha, V. G., Fernández, A., Molina, T. & Moreno, R., 2013. Enhanced properties of alumina–aluminium titanate composites obtained by spark plasma reaction-sintering of slip cast green bodies. *Composites: Part B*, Volume 47, pp. 255-259.
- Borrell, A., Salvador, M. D., Rocha, V. G., Fernández, A., Gómez, A., López-López, E. & Moreno, R., 2014. ZrTiO₄ materials obtained by spark plasma reaction-sintering. *Composites: Part B*, Volume 56, pp. 330-335.
- Brown, F. H. & Duwez, P., 1954. The zirconia-titania system. *Journal of The American Ceramic Society*, 37(3), pp. 129-132.
- Brown, S. S. & Clarke, I. C., 2006. A review of lubrication conditions for wear simulation in artificial hip replacements. *Tribology Transactions*, Volume 49, pp. 72-78.
- Buckley, D. H. & Miyoshi, K., 1984. Friction and wear of ceramics. *Wear*, Volume 100, pp. 333-353.
- Budinski, K. G., 2014. *Friction. wear, and erosion atlas*. New York: Taylor & Francis Group.
- Burwell, J. T., 1957/58. Survey of Possible Wear Mechanisms. *Wear*, Volume 1, pp. 119-141.
- Cahn, R., 2001. The coming of materials science. In: *Pergamon Materials Series*. Oxford: Elsevier Science, p. 377.
- Cahoon, H. P. & Christensen, C. J., 1956. Sintering and grain growth of alpha-alumina. *Journal of The American Ceramic Society*, 39(10), pp. 337-344.
- Capello, W. N., D'Antonio, J., Feinberg, J. R., Manley, M. T. & Naughton, M., 2008. Ceramic-on-Ceramic total hip arthroplasty: Update. *The Journal of Arthroplasty*, Volume 23, pp. 39-43.
- Casellas, D., Nagl, M. M., Llanes, L. & Anglada, M., 2003. Fracture toughness of alumina and ZTA ceramics: microstructural coarsening effects. *Journal of Materials Processing Technology*, pp. 143-144, 148-152.
- Ceramtec Website, [access date: 26 July 2013]. Increased fracture strength and excellent wear properties BIOLOX®delta. [online] available: <http://www.ceramtec.com/ceramic-materials/biolox/delta/>.
- Chera, L., Palcevskis, E., Berzins, M., Lipe, A. & Jansone, I., 2007. Dispersion of Nanosized Ceramic Powders in Aqueous Suspensions. *Journal of Physics: Conference Series*, Volume 93, pp. 1-6.
- Cherif, K., Gueroult, B. & Rigaud, M., 1996. Wear behaviour of alumina toughened zirconia materials. *Wear*, Volume 199, pp. 113-121.
- Chevalier, J., 2006. What future for zirconia as a biomaterial?. *Biomaterials*, Volume 27, pp. 535-543.
- Chevalier, J. & Gremillard, L., 2009. Ceramics for medical applications: A picture for the next 20 years. *Journal of the European Ceramic Society*, Volume 29, p. 1245–1255.

- Chevalier, J. & Gremillard, L., 2009. The tetragonal-monoclinic transformation in zirconia: lessons learned and future trends. *Journal of the American Ceramic Society*, 92(9), pp. 1901-1920.
- Chevalier, J., Gremillard, L. & Deville, S., 2007. Low-temperature degradation of zirconia and implications for biomedical implants. *Annual Review of Materials Research*, Volume 37, pp. 1-32.
- Chinn, R. E., 2002. Etching. In: *Ceramography: preparation and analysis of ceramic microstructure*. Ohio: ASM International, pp. 45-53.
- Christel, P., Meunier, A., Dorlot, J. M., Crolet, J. M., Witvoet, J., Sedel, L. & Boutin, P., 1988. Biomechanical compatibility and design of ceramic implants for orthopaedic surgery. *Annals of the New York Academy of Sciences*.
- Cui, W. F. & Shao, C. J., 2015. The improved corrosion resistance and anti-wear performance of Zr-xTi alloys by thermal oxidation treatment. *Surface & Coatings Technology*, Volume 283, pp. 101-107.
- De Azaa, A. H., Chevalier, J., Fantozzi, G., Schehl, M. & Torrecillas, R., 2002. Crack growth resistance of alumina, zirconia and zirconia toughened alumina ceramics for joint prostheses. *Biomaterials*, Volume 23, p. 937-945.
- Denape, J. & Lamon, J., 1990. Sliding friction of ceramics: mechanical action of the wear debris. *Journal of Materials Science*, Volume 25, pp. 3592-3604.
- Devillea, S., Chevalier, J., Fantozzi, G., Bartolome, J. F., Requena, J., Moya, J. S., Torrecillas, R. & Díaz, L. A., 2003. Low-temperature ageing of zirconia-toughened alumina ceramics and its implication in biomedical implants. *Journal of the European Ceramic Society*, Volume 23, p. 2975-2982.
- Dey, A. K. & Biswas, K., 2009. Dry sliding wear of zirconia-toughened alumina with different metal oxide additives. *Ceramics International*, Volume 35, pp. 997-1002.
- Dogan, C. P. & Hawk, J., 1997. Role of zirconia toughening in the abrasive wear of intermetallic and ceramic composites. *Wear*, Volume 212, pp. 110-118.
- Dowson, D., 2001. New joints for the Millennium: wear control in total replacement hip joints. *Proceedings of the Institution of Mechanical Engineers, Part H: Journal of Engineering in Medicine*, 215(4), pp. 335-358.
- Dowson, D., Hardaker, C., Flett, M. & Isaac, G. H., 2004. A hip joint simulator study of the performance of Metal-On-Metal joints: Part I: The role of materials. *The Journal of Arthroplasty*, Volume 19, pp. 118-123.
- Duan, R., Zhan, G., Kuntz, J. D., Kear, B. H. & Mukherjee, A. K., 2004. Processing and microstructure of high-pressure consolidated ceramic nanocomposites. *Scripta Materialia*, Volume 51, p. 1135-1139.
- Erickson, L., Blomberg, A., Hogmark, S. & Bratthall, J., 1993. Tribological characterization of alumina and silicon carbide under lubricated sliding. *Tribology International*, 26(2), pp. 83-92.
- Erkalfa, H., Misirli, Z. & Baykara, T., 1998. The effect of TiO₂ and MnO₂ on densification and microstructural development of alumina. *Ceramics Internationals*, Volume 24, pp. 81-90.
- Esposito, L., Moreno, R., Sanchez Herenciab, A. J. & Tucci, A., 1998. Sliding Wear Response of an Alumina-zirconia system. *Journal of the European Ceramic Society*, Volume 18, pp. 15-22.

- Evans, A. G., 1990. Perspective on the development of high-toughness ceramics. *Journal of American Ceramic Society*, Volume 73, pp. 187-205.
- Evans, A. G. & Fu, Y., 1984. Fracture in Ceramics Materials. In: New Jersey: Noyes, p. p.650.
- Fartash, B., Liao, H., Li, J., Fouda, N. & Hermansson, L., 1995. Long-term evaluation of titania-based ceramics long-term evaluation of titania-based ceramics. *Journal of Materials Science: Materials in Medicine*, 6(8), pp. 451-454.
- FDA, 2001. FDA announces recall of hip implants: device recalled due to high fracture. [online], p. Available: <http://www.fda.gov/ICECI/EnforcementActions/EnforcementStory/EnforcementStoryArchive/ucm106947.htm#orth> [online access: 25 July 2013]..
- Fischer, T., Anderson, M. P. & Jahanmir, S., 1989. Influence of fracture toughness on the wear resistance of yttria-doped zirconium oxide. *Journal of American Society*, Volume 72, pp. 252-257.
- Fischer, T. E., Anderson, M. P., Jahanmir, S. & Salher, R., 1988. Friction, and wear of tough and brittle zirconia in nitrogen, air, water, hexadecane, and hexadecane containing stearic acid. *Wear*, Volume 124, pp. 133-148.
- Fischer, T. E. & Tomizawa, H., 1985. Interaction of tribochemistry and microfracture in the friction and wear of silicon nitride. *Wear*, Volume 105, pp. 29-45.
- Fischer, T. E., Zhu, Z., Kim, H. & Shin, D. S., 2000. Genesis and role of wear debris in sliding wear of ceramics. *Wear*, Volume 245, pp. 53-60.
- Garay, J. E., 2010. Current-activated, pressure-assisted densification of materials. *Annual review of Materials Research*, Volume 40, pp. 445-468.
- Garvie, R. C., Hannink, R. H. & Pascoe, R. T., 1975. Ceramic steel?. *Nature*, 258(5537), pp. 703-704.
- Gates, R. S., Hsu, M. & Klaus, E. E., 1989. Tribochemical mechanism of alumina with water. *Tribology Transactions*, 32(3), pp. 357-363.
- Geels, K., 2006. *Metallographics and materialographic specimen preparation, light microscopy, image analysis, and hardness testing*. s.l.:ASTM international.
- Gee, M. G. & Butterfield, D., 1993. The combined effect of speed and humidity on the wear and friction of silicon nitride. *Wear*, Volume 162-164, pp. 234-245.
- George, A., Solomon, S., Thomas, J. K. & John, A., 2012. Characterizations and electrical properties of ZrTiO₄ ceramic. *Materials Research Bulletin*, Volume 47, pp. 3141-3147.
- Ghosh, S., Chokshi, A. H., Lee, P. & Raj, R., 2009. A Huge Effect of Weak dc Electrical Fields on Grain Growth in Zirconia. *Journal of American Ceramic Society*, 92(8), pp. 1856-1859.
- Guazzato, M., Albakry, M., Ringer, S. P. & Swain, M. V., 2004. Strength, fracture toughness and microstructure of a selection of all-ceramic materials. Part II. Zirconia-based dental ceramics. *Dental Materials*, Volume 20, pp. 449-456.
- Gutknecht, D., 2007. Key Role of Processing to Avoid Low Temperature Ageing in Alumina Zirconia Composites for Orthopaedic Application. *Journal of the European Ceramic Society*, Volume 27, p. 1547–1552..

- Hamadouche, M., Boutin, P., Daussange, J., Bolander, M. E. & Sedel, L., 2002. Alumina-on-Alumina Total Hip Arthroplasty: A Minimum 18.5-year Follow-up Study. *The Journal Of Bone And Joint Surgery*, 84A(1), pp. 69-77.
- Hannink, R. H., Kelly, P. M. & Muddle, B. C., 2000. Transformation toughening in zirconia-containing ceramics. *Journal of American Ceramic Society*, Volume 83, pp. 461-487.
- Hatton, A., Nevelos, J. E., Nevelos, A. A., Banks, R. E., Fisher, J. & Ingham, E., 2000. Alumina-alumina artificial hip joints. Part I: a histological analysis and characterisation of wear debris by laser capture microdissection of tissues retrieved at revision. *Biomaterials*, 23(16), pp. 3429-3440.
- He, C., Wang, Y. S., Wallace, J. & Hsu, S. M., 1993. Effect of microstructure on the wear transition of zirconia toughened alumina. *Wear*, Volume 162-164, pp. 314-321.
- He, Y. J., Winnubst, A. J. A., Burggraaf, A. J., Venveij, H., van der Varst, P. G. T. & de With, G., 1997. Sliding wear of ZrO₂-Al₂O₃ composite ceramics. *Journal of the European Ceramic Society*, 17(11), pp. 1371-1380.
- He, Y. J., Winnubst, A. J. A., Schipper, D. J., Burggraaf, A. J. & Verweij, H., 1997. Effects of a second phase on the tribological properties of Al₂O₃ and ZrO₂ ceramics. *Wear*, Volume 210, pp. 178-187.
- Horn, D. S. & Messing, G. L., 1995. Anisotropic grain growth in TiO₂-doped alumina. *Materials Science and Engineering A*, Volume 195, pp. 169-178.
- Hsu, S. M. & Shen, M., 2004. Wear prediction of ceramics. *Wear*, Volume 256, p. 867-878.
- Huang, C. W., Weng, M. T. & Wei, W. C. J., 2008. Contact wear of low-zirconia toughened alumina (ZTA) produced by a colloidal process. *Journal of Ceramic Processing Research*, 9(3), pp. 221-223.
- Hughes, A. E., St John, H., Kountouros, P. & Schubert, H., 1995. Moisture sensitive degradation in TiO₂-Y₂O₃-ZrO₂. *Journal of the European Ceramic Society*, Volume 15, pp. 1125-1134.
- Hutchings, I. M., 1992. *Tribology: friction and wear of engineering materials*. London: Edward Arnold.
- Hwang, C. & Chang, Y., 1996. Effects of TiO₂ on the microstructure and mechanical properties of Al₂O₃yZrO₂ composites. *Journal of Materials Research*, 11(6), pp. 1545-1551.
- Jin, Z. M., Stone, M., Ingham, E. & Fisher, J., 2006. Biotribology. *Current Orthopaedics*, Volume 20, pp. 32-40.
- Kato, K., 1990. Tribology of ceramics. *Wear*, Volume 136, pp. 117-133.
- Kato, K. & Adachi, K., 2002. Wear of advanced ceramics. *Wear*, Volume 253, p. 1097-1104.
- Kebbede, A., Messing, G. L. & Carim, A. H., 1997. Grain boundaries in titania-doped α -alumina with anisotropic microstructure. *Journal of American Ceramic Society*, 80(11), pp. 2814-2820.
- Kelly, P. M. & Francis Rose, L. R., 2002. The martensitic transformation in ceramics - its role in transformation toughening. *Progress in Materials Science*, Volume 47, pp. 463-557.
- Kerkwijk, B., Garcia, M., van Zyl, W. E., Winnubst, L., Mulder, E. J., Schipper, D. J. & Verweij, H., 2004. Friction behaviour of solid oxide lubricants as second phase in α -Al₂O₃ and stabilised ZrO₂ composites. *Wear*, Volume 256, p. 182-189.

- Kerkwijk, B., Winnubst, L., Mulder, E. J. & Verweij, H., 1999. Processing of homogeneous zirconia-toughened alumina ceramics with high dry-sliding wear resistance. *Journal of American Ceramic Society*, 82(8), p. 2087–2093.
- Kern, F., 2012. Structure-property relations in alumina-zirconia nanocomposites reinforced with in situ formed Ceriumhexaaluminate precipitates. *Scripta Materialia*, Volume 67, pp. 1007-1010.
- Kerwijk, B., Winnubst, A. J. A., Verweij, H., Mulder, E. J., Metselaar, H. S. C. & Schipper, D. J., 1999. Tribological properties of nanoscale alumina–zirconia composites. *Wear*, Volume 225-229, p. 1293–1302.
- Kim, T., Oh, J., Park, B. & Hong, K. S., 2000. Correlation between strain and dielectric properties in ZrTiO₄ thin films. *Applied Physics Letters*, 76(21), p. 3043.
- Kim, Y., Hong, S. & Kim, D., 2000. Anisotropic abnormal grain growth in TiO₂/SiO₂-doped alumina. *Journal of The American Ceramic Society*, 83(11), p. 2809–2812.
- Komvopoulos, K. & Li, H., 1992. The effect of tribofilm formation and humidity on the friction and wear properties of ceramic materials. *Journal of Tribology*, Volume 114, pp. 131-140.
- Krell, A., 1996. Improved hardness and hierarchic influences on wear in submicron sintered alumina. *Materials Science and Engineering*, Volume A209, pp. 156-163.
- Krell, A. & Blank, P., 1988. On abrasive wear of zircon-toughened aluminas. *Wear*, Volume 124, pp. 327-330.
- Kroger, F. A., 1984. Defect models for sintering and densification of Al₂O₃ : Ti and Al₂O₃ : Zr. *Journal of the American Ceramic Society*, 67(6), pp. 390-392.
- Kuntz, J. D., Zhan, G. & Mukherjee, A. K., 2004. Nanocrystalline-Matrix Ceramic Composites for Improved Fracture Toughness. *MRS Bulletin*, Volume January, pp. 22-27.
- Kwon, O., Hong, S., Lee, J., Chung, U., Kim, D. & Hwang, N., 2002. Microstructural evolution during sintering of TiO₂/SiO₂-doped alumina: mechanism of anisotropic abnormal grain growth. *Acta Materialia*, Volume 50, p. 4865–4872.
- Lartigue-Korinek, S., Legros, C., Carry, C. & Herbst, F., 2006. Titanium effect on phase transformation and sintering behavior of transition alumina. *Journal of the European Ceramic Society*, Volume 26, pp. 2219-2230.
- Lee, S. W., Hsu, S. M. & Shen, M. C., 1993. Ceramic Wear Maps: Zirconia. *Journal of American Ceramic Society*, 76(8), pp. 1937-1947.
- Lee, S. W., Morillo, C., Lira-Olivares, J., Kim, S. H., Sekino, T., Niihara, K. & Hockey, B. J., 2003. Tribological and microstructural analysis of Al₂O₃/TiO₂ tribological and microstructural analysis of Al₂O₃/TiO₂. *Wear*, Volume 25, pp. 1040-1044.
- Lee, W. E. & Rainforth, W. M., 1994. *Ceramic microstructures : property control by processing*. London: Chapman & Hall.
- Lin, V. J. C. & Koenig, J. L., 1976. Raman studies of bovine serum albumin. *Biopolymers*, Volume 15, pp. 203-218.
- Li, P., de Groot, K. & Kokubo, T., 1996. Bioactive Ca₁₀(PO₄)₆(OH)₂-TiO₂ composite coating prepared by sol-gel process. *Journal of sol-gel science and technology*, 7(1-2), pp. 27-34.

- Lizaur-Utrilla, A., Sanz-Reig, J. & Trigueros-Rentero, M., 2012. Greater Satisfaction in Older Patients With a Mobile-Bearing Compared With Fixed-Bearing Total Knee Arthroplasty. *The Journal of Arthroplasty*, 27(2), pp. 207-212.
- López-López, E., Baudín, C., Moreno, R., Santacruz, I., Leon-Reina, L. & Aranda, M. A. G., 2012. Structural characterization of bulk ZrTiO₄ and its potential for thermal shock applications. *Journal of the European Ceramic Society*, Volume 32, pp. 299-306.
- López-López, E., Moreno, R. & Baudín, C., 2015. Fracture strength and fracture toughness of zirconium titanate–zirconia bulk composite materials. *Journal of the European Ceramic Society*, Volume 35, pp. 277-283.
- López-López, E., Sanjuán, M. L., Moreno, R. & Baudín, C., 2010. Phase evolution in reaction sintered zirconium titanate based materials. *Journal of the European Ceramic Society*, Volume 30, pp. 981-991.
- Ludema, K. C., 1996. *Friction, Wear, Lubrication: A Textbook in Tribology*. Boca Raton: CRC Press.
- Lu, Z. & McKellop, H., 1997. Frictional heating of bearing materials tested in a hip joint wear simulator. *Proceedings of the Institution of Mechanical Engineers*, 211(H), pp. 101-108.
- Lu, Z., McKellop, H., Liao, P. & Benya, P., 1999. Potential thermal artifacts in hip joint wear simulators. *Journal of Biomedical Materials Research Part A*, 48(4), pp. 458-464.
- Maccauro, G., Iommetti, P. R., Raffaelli, L. & Manicone, P. F., 2011. Alumina and zirconia ceramic for orthopaedic and dental devices. In: *Biomaterials Applications for Nanomedicine*. Shanghai: InTech, pp. 299-309.
- Ma, L., 2010. *Wear Behaviour of Biolox® delta ceramic Composite for Joint Replacements*. PhD Thesis. Sheffield: The University of Sheffield.
- Ma, L. & Rainforth, W. M., 2010. A study of Biolox delta subject to water lubricated reciprocating wear. *Tribology International*, Volume 43, pp. 1872-1881.
- Ma, L. & Rainforth, W. M., 2012. The effect of lubrication on the friction and wear of Biolox delta. *Acta Biomaterialia*, 8(6), pp. 2348-2359.
- Manshor, H., Aris, S. M., Azhar, A. Z. A., Abdullah, E. C. & Ahmad, Z. A., 2015. Effects of TiO₂ addition on the phase, mechanical properties, and microstructure of zirconia-toughened alumina ceramic composite. *Ceramics International*, Volume 41, pp. 3961-3967.
- McKee, W. D. & Aleshin, E., 1963. Aluminum oxide-titanium oxide solid solution. *Journal of The American Ceramic Society*, 46(1), pp. 54-58.
- Miao, X., Sun, D., Hoo, P. W., Liu, J., Hu, Y. & Chen, Y., 2004. Effect of titania addition on yttria-stabilised tetragonal zirconia ceramics sintered at high temperatures. *Ceramics International*, Volume 30, p. 1041–1047.
- Miyoshi, K., 1988. Adhesion, friction, and micromechanical properties of ceramics. *Surface and Coatings Technology*, Volume 36, pp. 487-501.
- Morillo, C., Sawae, Y. & Murakami, T., 2009. Influence of different counterfaces on tribological behaviours of Al₂O₃ nanocomposites for joint prostheses. *Tribology Online*, 4(5), pp. 127-130.

- Muddle, B. C. & Hannink, R. H. J., 1986. Crystallography of the tetragonal to monoclinic transformation in MgO-Partially-Stabilized Zirconia. *Journal of American Ceramic Society*, 69(7), pp. 547-555.
- Murphy, S., Ecker, T., Tannast, M., Bierbaum, B., Garino, J., Howe, J., Hume, E., Jones, R., Keggi, K., Kress, K., Phillips, D. & Zann, R., 2006. Experience in the United States with Alumina Ceramic–Ceramic Total Hip Arthroplasty. *Seminars in Arthroplasty*, Volume 17, pp. 120-124.
- Mussler, B., Swain, M. V. & Claussen, N., 1982. Dependence of fracture toughness of alumina on grain size and test technique. *Journal of the American Ceramic Society*, Volume 65, pp. 566-572.
- Nawa, M., Bamba, N., Sekino, T. & Niihara, K., 1998. The effect of TiO₂ addition on strengthening and toughening in intragranular type of 12Ce-TZP/Al₂O₃ nanocomposites. *Journal of the European Ceramic Society*, Volume 18, pp. 209-219.
- Nawa, M., Nakamoto, S., Sekino, T. & Niihara, K., 1998. Tough and Strong Ce-TZP/Alumina nanocomposites doped with titania. *Ceramics International*, Volume 24, pp. 497-506.
- Nevelos, J. E., Ingham, E., Doyle, C., Nevelos, A. B. & Fisher, J., 2001. Wear of hiped and non-hiped alumina-alumina hip joints under standard and severe simulator testing conditions. *Biomaterials*, Volume 22, pp. 2191-2197.
- Nogiwa-Valdez, A. A., Rainforth, W. M. & Stewart, T. D., 2014. Wear and degradation on retrieved zirconia femoral heads. *Journal of Mechanical Behaviour of Biomedical Materials*, Volume 31, pp. 145-151.
- Nogiwa-Valdez, A. A., Rainforth, W. M., Zeng, P. & Ross, I. M., 2013. Deceleration of hydrothermal degradation of 3Y-TZP by alumina and lanthana co-doping. *Acta Biomaterialia*, 9(4), pp. 6226-6235.
- Noguchi, T. & Mizuno, M., 1968. Phase Changes in the ZrO₂-TiO₂ System. *Bulletin of The Chemical Society of Japan*, Volume 41, pp. 2895-2899.
- Ohama, Y. & Gemert, D. V., 2011. *Application of Titanium Dioxide Photocatalysis to Construction Materials*. s.l.:Springer.
- Ormanci, O., Akin, I., Sahin, F., Yucel, O., Simon, V., Cavalu, S. & Goller, G., 2014. Spark plasma sintered Al₂O₃-YSZ-TiO₂ composites: Processing, characterization and in vivo evaluation. *Materials Science and Engineering C*, Volume 40, pp. 16-23.
- Ortega-Saenz, J., Kalbarczyk, M., Michalczewski, R., Piekoszewski, W., Szczerek, M., 2008. Comparison of wear processes of biomaterials used in hip joint implants. *Scientific Problems of Machines Operation and Maintenance*, 4(156), pp. 15-25.
- Osendi, M. I. & Moya, S., 1988. Role of titania on the sintering, microstructure and fracture toughness of Al₂O₃/ZrO₂ composites. *Journal of Materials Science Letters*, Volume 7, pp. 15-18.
- Pandolfelli, V. C., Rainforth, W. M. & Stevens, R., 1990. Sintering and microstructural studies in the system ZrO₂.TiO₂.CeO₂. *Journal of Materials Science*, Volume 25, pp. 2233-2244.
- Pandolfelli, V. C., Rodrigues, J. A. & Stevens, R., 1991. Effects of TiO₂ addition on the sintering of ZrO₂.TiO₂ compositions and on the retention of the tetragonal phase of zirconia at room temperature. *Journal of Materials Science*, 26(19), pp. 5327-5334.

- Park, D., Danyluck, S. & McNellan, M., 1990. Friction and wear measurements of Si₃N₄ at elevated temperatures in air, Ar, and humid environments. In: *Proceedings of the Symposium on Corrosion and Corrosive Degradation of Ceramics*. Westerville: American Ceramic Society, pp. 159-180.
- Ponton, C. B. & Rawlings, R. D., 1989. Vickers Indentation Fracture Toughness Test Part1: Review of Literature and Formulation of Standardized Indentation Toughness Equations. *Materials Science and Technology*, Volume 5, pp. 865-872.
- Popov, V. L., 2010. *Contact mechanics and friction*. Berlin: Heidelberg.
- Pramanik, S., Agarwal, A. K. & Rai, K. N., 2005. Chronology of Total Hip Joint Replacement and Materials Development. *Trends Biomater. Artif. Organs*, Volume 19, pp. 15-26.
- Rahaman, M. N., Yao, A., Sonny Bal, B., Garino, J. P. & Ries, M. D., 2007. Ceramics for Prosthetic Hip and Knee Joint Replacement. *Journal of the American Ceramic Society*, 90(7), pp. 1965-1988.
- Rainforth, W. M., 1996. The Sliding Wear of Ceramics. *Ceramics International*, Volume 22, pp. 365-372.
- Rainforth, W. M., 2000. Microstructural evolution at the worn surface: a comparison of metals and ceramics. *Wear*, Volume 245, pp. 162-177.
- Rainforth, W. M., 2004. The wear behaviour of oxide ceramics-A Review. *Journal of Materials Science*, Volume 39, p. 6705 – 6721.
- Rainforth, W. M., Leonard, A. J., Perrin, C., Bedolla-Jacuinde, A., Wang, Y., Jones, H. & Luo, Q., 2002. High resolution observations of friction-induced oxide and its interaction with the worn surface. *Tribology International*, Volume 35, pp. 731-748.
- Rainforth, W. M. & Stevens, R., 1993. A transmission electron microscopy study of wear of magnesia partially stabilised zirconia. *Wear*, Volume 162-164, pp. 322-331.
- Rainforth, W. M. & Stevens, R., 1998. Transmission electron microscopy of worn zirconia surfaces. *Journal of Materials Research*, 13(2), pp. 396-405.
- Rainforth, W. M., Zeng, P., Ma, L., Nogiwa Valdez, A. & Stewart, T., 2012. Dynamic surface microstructural changes during tribological contact that determine the wear behaviour of hip prostheses: metals and ceramics. *Faraday Discuss*, Volume 156, pp. 41-57.
- Rana, A., 2013. *Wear resistant alumina for artificial hip replacements*. Sheffield: The University of Sheffield.
- Reis, D. & Levin, D., n.d. Hip with arthritis [online]. Available: <http://www.hipsurgery.co.il/english/introduction.htm> [access: 25 July 2013].
- Rice, R. W., 1996. Grain size and porosity dependence of ceramic fracture energy and toughness at 22°C. *Journal of Materials Science*, Volume 3, pp. 1969-1983.
- Richerson, D. W., 2006. *Modern ceramic engineering : properties, processing, and use in design*. Boca Raton: CRC.
- Rigney, D. A., 1988. Sliding wear of metals. *Annual Review of Materials Research*, Volume 18, p. 141–163.

- Rigney, D. A. & Hammerberg, J. E., 1998. Unlubricated sliding behavior of metals. *MRS Bulletin*, 23(6), pp. 32-36.
- Roy, S. K. & Coble, R. L., 1968. Solubilities of magnesia, titania, and magnesium titanate in aluminum oxide. *Journal of The American Ceramic Society*, 51(1), pp. 1-6.
- Saikko, V., 1993. Wear and friction properties of prosthetic joint materials evaluated on a reciprocating pin-on-flat apparatus. *Wear*, Volume 166, pp. 169-178.
- Schaedler, T. A., Fabrichnaya, O. & Levi, C. G., 2008. Phase equilibria in the TiO₂-YO_{1.5}-ZrO₂ system. *Journal of the European Ceramic Society*, Volume 28, p. 2509-2520.
- Scholes, S. C., Unsworth, A., Hall, R. & Scott, R., 2000. The effects of material combination and lubricant on the friction of total hip prostheses. *Wear*, 241(2), pp. 209-213.
- Scholes, S. c. & Unworth, A., 2000. Comparison of friction and lubrication of different hip prostheses. *Proceedings of the Institution of Mechanical Engineers*, Volume 214, pp. 49-56.
- Senda, T., Drennan, J. & McPherson, R., 1995. Sliding wear of oxide ceramics at elevated temperatures. *Journal of American Ceramic Society*, 78(11), pp. 3018-3024.
- Shen, Z., Johnsson, M., Zhao, Z. & Nygren, M., 2002. Spark plasma sintering of alumina. *Journal of American Ceramic Society*, 85(8), pp. 1921-1927.
- Shim, I. & Lee, C., 2002. Synthesis and characterization of Al₂O₃/ZrO₂, Al₂O₃/TiO₂ and Al₂O₃/ZrO₂/TiO₂ ceramic composite particles prepared by ultrasonic spray pyrolysis. *Bulletin of Korean Chemical Society*, 23(8), pp. 1127-1134.
- Shirkhan, L., 2014. *The Role of Hydrothermal Degradation in the Wear Behaviour of Zirconia*. PhD Thesis. Sheffield: The University of Sheffield.
- Shishido, T., Yamamoto, K., Tanaka, S., Masaoka, T., Clarke, I. C. & Williams, P., 2006. A Study for a Retrieved Implant of Ceramic-on-Ceramic Total Hip Arthroplasty. *The Journal of Arthroplasty*, 21(2), pp. 294-298.
- Siopack, J. & Jergesen, H. E., 1995. Total Hip Arthroplasty. *Western Journal of Medicine*, Volume 162, pp. 243-249.
- Smirnov, A., Bartolomé, J.F., Moya, J.S., Kernb, F. & Gadow, R., 2011. Dry reciprocating sliding wear behaviour of alumina-silicon carbide nanocomposite fabricated by ceramic injection molding. *Journal of European Ceramic Society*, Volume 31, pp. 469-474.
- Smothers, W. J. & Reynolds, H. J., 1954. Sintering and grain growth of alumina. *Journal of The American Ceramic Society*, 37(12), pp. 588-595.
- Stachowiak, G. W. & Stachowiak, G. B., 1993. Environmental effects on wear and friction of toughened zirconia ceramics. *Wear*, Volume 160, pp. 153-162.
- Steijn, R., 1961. On the wear of sapphire. *Journal of Applied Physics*, 32(10), p. 1951-1958.
- Takano, T., Tasaka, A. & Yoshinari, M., 2012. Fatigue strength of Ce-TZP/Al₂O₃ nanocomposite with different surfaces. *Journal of Dental Research*, Volume 9, pp. 800-804.

- Tanaka, K., Tamura, J., Kawanabe, K., Nawa, M., Oka, M., Uchida, M., Kokubo, T. & Nakamura, T., 2002. Ce-TZP/Al₂O₃ Nanocomposite as a Bearing Material in Total Joint Replacement. *Journal of Biomedical Materials Research*, Volume 63, p. 262–270.
- Thompson, I. & Rawlings, R., 1990. Mechanical behavior of zirconia and zirconia-toughened alumina in a simulated body environment. *Biomaterials*, Volume 11, pp. 505-508.
- Tipper, J. L., Ingham, E., Jin, Z. M. & Fisher, J., 2005. The science of Metal-On-Metal articulation. *Current Orthopaedics*, Volume 19, p. 280–287.
- Trabelsi, R., Treheux, D., Orange, G., Fantozzi, G., Homerin, P. & Thevenot, F., 1989. Relationship between mechanical properties and wear resistance of alumina-zirconia ceramic composites. *Tribology Transaction*, 32(1), pp. 77-84.
- Trunec, M., 2008. Effect of grain size on mechanical properties of 3Y-TZP ceramics. *Ceramics – Silikáty*, Volume 52, pp. 165-171.
- Wahsh, M. M. S., Khattab, R. M. & Zawrah, M. F., 2013. Sintering and technological properties of alumina/zirconia/nano-TiO₂ ceramic composites. *Materials Research Bulletin*, Volume 48, pp. 1411-1414.
- Wang, C. & Huang, C., 2008. Effect of TiO addition on the sintering behavior, hardness and fracture toughness of an ultrafine alumina. *Materials Science and Engineering: A*, 492(1-2), pp. 306-310.
- Wang, D., Li, J. & Mao, Z., 1993. Study of abrasive wear resistance of transformation toughened ceramics. *Wear*, Volume 165, pp. 159-167.
- Wang, J. & Steven, R., 1987. *Proceeding of the British Ceramic Society (Vol.39)*. Stoke-on-Trent: British Ceramic Society.
- Wang, J. & Stevens, R., 1989. Review: Zirconia-toughened alumina (ZTA) ceramics. *Journal of Materials Science*, Volume 24, pp. 3421-3440.
- Wang, Y., He, C., Hockey, B. J., Lacey, P. I. & Hsu, S. M., 1995. Wear transitions in monolithic alumina and zirconia-alumina composites. *Wear*, Volume 181-183, pp. 156-164.
- Wang, Y. & Hsu, S., 1996. Wear and wear transition mechanisms of ceramics. *Wear*, Volume 195, pp. 112-122.
- Wang, Y., Yang, Y., Zhao, Y., Tian, W., Bian, H. & He, J., 2009. Sliding wear behaviors of in situ alumina/aluminum titanate ceramic composites. *Wear*, Volume 266, p. 1051–1057.
- Williams, J. A., 1994. *Engineering Tribology*. Oxford: Oxford University Press.
- Winkler, E. R., Sarver, J. F. & Cutler, I. B., 1966. Solid solution of titanium dioxide in aluminum oxide. *Journal of The American Ceramic Society*, 49(12), pp. 634-637.
- Yang, Y., Wang, Y., Tian, W., Wang, Z., Zhao, Y., Wang, L. & Bian, H., 2009. Reinforcing and toughening alumina/titania ceramic composites with nano-dopants from nanostructured composite powders. *Materials Science and Engineering A*, Volume 508, p. 161–166.
- Yang, Y., Wang, Y., Tian, W., Zhao, Y., He, J., Bian, H. & Wang, Z., 2009. In situ alumina/aluminum titanate bulk ceramic composites prepared by SPS from different structured composite powders. *Journal of Alloys and Compounds*, Volume 481, p. 858–862.

Yang, Y., Wang, Y., Wang, Z., Liu, G. & Tian, W., 2008. Preparation and sintering behaviour of nanostructured alumina/titania composite powders modified with nano-dopants. *Materials Science and Engineering A*, Volume 490, p. 457–464.

Yin, Q., Zhu, B. & Zeng, H., 2009. *Microstructure, property and processing of functional Ceramics*. s.l.:Springer.

Yust, C. Y. & Allard, L. F., 1989. Microanalytical characterization of wear damage in an alumina–silicon carbide whisker composites. In: *Ceramic Materials and Components for Engines*. Westerville: American Ceramic Society, p. 1212–1224.

Zanoria, E. & Danyluk, S., 1993. Ball-on-flat reciprocating sliding wear of single-crystal, semiconductor silicon at room temperature. *Wear*, Volume 162-164, pp. 332-338.

Zhan, G., Kuntz, J., Wan, J., Garay, J. & Mukherjee, A. K., 2002. Alumina-Based Nanocomposites Consolidated by Spark Plasma Sintering. *Scripta Materialia*, Volume 47, p. 737–741.

Zhu, W., Sugano, N. & Pezzotti, G., 2013. Nondestructive inspection of phase transformation in zirconia-containing hip joints by confocal Raman spectroscopy. *Journal of Biomedical Optics*, 18(12).

Zum Gahr, K. H., Bundschuh, W. & Zimmerlin, B., 1993. Effect of grain size on friction and sliding wear of oxide ceramics. *Wear*, Volume 162-164, pp. 269-279.

Zutshi, A., Haber, R. A., Niesz, D. E., Adams, J. W., Wachtman, J. B., Ferber, M. K. & Hsu, S. M., 1994. Processing, microstructure, and wear behavior of silicon nitride hot-pressed with alumina and yttria. *Journal of American Ceramic Society*, 77(4), p. 883–890.